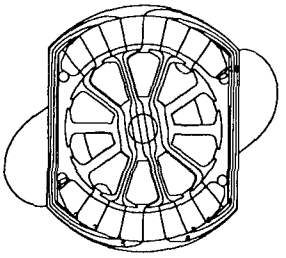

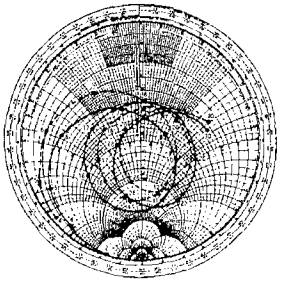

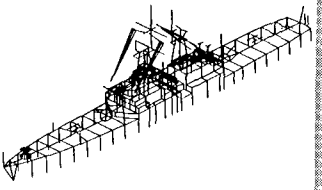

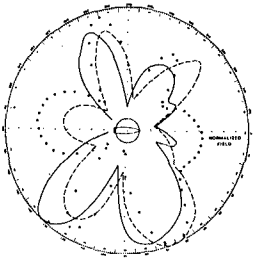

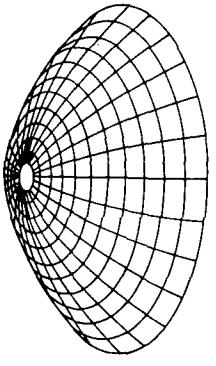

14th Annual Review of Progress in

APPLIED COMPUTATIONAL ELECTROMAGNETICS

at the

Naval Postgraduate School

Monterey, CA

March 16-20, 1998

CONFERENCE PROCEEDINGS

DISTRIBUTION STATEMENT A
Approved for public release;
Distribution Unlimited

DISTRIBUTION STATEMENT A
Approved for public release;
Distribution unlimited

CONFERENCE PROCEEDINGS

VOLUME I

14th Annual Review of Progress in APPLIED COMPUTATIONAL ELECTROMAGNETICS

at the

Naval Postgraduate School

Monterey, CA

March 16-20, 1998

TECHNICAL PROGRAM CHAIRMAN

Jianming Jin

Sponsored by

The Applied Computational Electromagnetics Society

Naval Postgraduate School, University of Illinois at Urbana-Champaign,

Brigham Young University, University of Kentucky, University of Nevada

THE NAVAL POSTGRADUATE SCHOOL

19980709 161

DTIC QUALITY INSPECTED 1

Contents

Table of Contents i

1999 Call for Papers xiii

1998 Symposium Program Committee xv

Technical Program Chairman's Statement xvi

ACES President's Statement xvii

ACES 98 Short Courses xviii

Agenda xix

VOLUME I

SESSION 1: CEM ANALYSIS AND APPLICATION WITHIN AN ENGINEERING ENVIRONMENT
Chairs: Kenneth R. Siarkiewicz and Donald R. Pflug

"Frameworks - Future Paradigm for CEM Analysis"
K.R. Siarkiewicz 2

"REF CEM Data Dictionary"
T. Wharton and J. Evans 9

"Air Force Research and Engineering Framework Control Panel"
D.M. Hallatt and J.A. Evans 15

"Continued Application of the Research and Engineering Framework (REF) at Raytheon"
J. Labelle, B. Hantman, H. Wright, Y. Chang, and R. Abrams 20

"The Innovative Research Testbed: A PC-Based High Performance Computing and Web-Based Collaboratory for Computational Electromagnetics"
D.M. Leskiw, G. Ingersoll, T. Vidoni, and R. Redmond 28

"Illustrating the Application of Expert Systems to Computational Electromagnetics Modeling and Simulation"
A.L.S. Drozd, T.W. Blocher, C.E. Carroll, Jr. and J.M. Allen 36

" Some Present and Future Aspects of the Quality of Solution in Computational Electromagnetics"
D.R. Pflug 42

"On the Use of Computational Electromagnetics in the Radar Cross Section Measurement Calibration Process"
K.C. Hill and W.D. Wood, Jr. 50

"Radar Calibration at Low Frequencies Using a Triangular Trihedral Corner Reflector"
C.Y. Shen 57

SESSION 2: FINITE-DIFFERENCE TIME-DOMAIN APPLICATIONS
Chairs: John Beggs and Melinda Piket-May

"Time Domain Analysis of Small Multi-Sector Monopole Yagi-Uda Array Antenna Mounted on a Finite Ground Plane Using FDTD Method"
T. Maruyama, K. Uehara, T. Hori and K. Kagoshima 66

"Antenna Performance Calculation in Lossy Media with FDTD Method"
M. Cai and N. Ljepojevic 73

"Far-Zone Transformation in FDTD for VHF-band SAR-image Simulations"
T. Martin and L. Ulander 79

"FDTD Simulations Used to Correct for Ground Effects in Aircraft Testing"
G. Eriksson and U. Thibblin 87

"Validation of FDTD-Computed Handset Patterns by Measurement"
C.W. Trueman, S.J. Kubina, J.E. Roy, W.R. Lauber and M. Vall-llossera 93

"FDTD Analysis of Flip Chip Interconnects"
A.Z. Elsherbeni, V. Rodriguez-Pereyra and C.E. Smith 99

"FDTD Analysis of the Celestron-8 Telescope"
R.R. DeLyser 105

"Modifying a Graphically-Based FDTD Simulation for Parallel Processing"
G. Haussmann, M. Piket-May and K. Thomas 113

"A Time Domain Method for High Frequency Problems Exploiting the Whitney Complex", A. Arkko, T. Tarhasaari and L. Kettunen 121

"Treatment of Boundaries in Multiresolution Based FDTD Multigrid"
K. Goverdhanam, E. Tentzeris and L.P.B. Katehi 127

SESSION 3: APPLICATION OF ANALYTIC AND COMPUTATIONAL METHODS TO THE MODELING OF ELECTROMAGNETIC MATERIALS"
Chairs: Rudy Diaz and David H.Y. Yang

"Computing Dispersion Relations and Radiation Spectra in Photonic Band Gap Materials by Plane Wave Expansion Method"
T. Suzuki and P.K.L. Yu 136

"Waveguides in Photonic Band Gap Materials"
M.M. Sigalas, R. Biswas, K.M. Ho, C.M. Soukoulis and D.D. Crouch 144

"Is There a Relationship Between a Random and an Ordered Composite Mixture?"
- STUDENT PAPER CONTEST -
W.M. Merrill, S.A. Kyriazidou and N.G. Alexopoulos 151

"An Analytic Framework for the Modeling of Effective Media"
R.E. Diaz 159

SESSION 3: APPLICATION OF ANALYTIC AND COMPUTATIONAL METHODS TO THE MODELING (cont)

"Finite Grain Boundary Effects for Magnetic Materials: Tunneling and Intergrain Gaps"
G.G. Bush 167

"Numerical Computation of the Complex Dielectric Permittivity: FFT-Based Hilbert Transform Approximation of the Kramers-Kronig Relations".
- STUDENT PAPER CONTEST - , F. Castro and B. Nabet 173

"Rayleigh Analysis of Novel Dense Medium Exhibiting Narrow-Band Transparency Window", S.A. Kryiazidou, R.E. Diaz and N.G. Alexopoulos 179

SESSION 4: INTERACTIVE POSTER SESSION

"Finite Difference Formulation - Expanding the Capabilities"
K. Davey 188

"Time and Frequency Domain Numerical Modeling of Outbound and Standing Power From Perpendicularly Oriented, Electrically Small TM Dipoles"
G. Liu, C.A. Grimes K.G. Ong, D.M. Grimes 194

"Efficient Analysis of Large Two-dimensional Arbitrarily Shaped Finite Gratings for Quantum Well Infrared Photodetectors"
V. Jandhyala, D. Sengupta, B. Shanker, E. Michielssen, M. Feng, G. Stillman 204

"Forward and Backward Propagation Algorithms Applied to the Electromagnetic Scattering by an Inpenetrable Obstacle: A Progress Report"
G.F. Crosta 210

"Analysis of Broad Wall Slots Excited by Tuning Screws"
T. Azar and R. Coren 216

"Closed-Form Expression of the Arc-Length of the Toroidal/Helical Equilibrium Orbit"
R.A. Speciale 224

"Asymptotic Techniques in Naval Ship Design"
R. Routier and R. Burkholder 243

"A BCG-FFT Solution of Scattering and Radiation by Large Finite Arrays of Microstrip Antennas", C-Fu Wang, F. Ling and J-M. Jin 250

"Analytic Solution for Low-Frequency Electric Induction in an Equatorially Stratified Sphere", T.W. Dawson 258

"Parallelizing Computational Electromagnetics Code Using the Parallel Virtual Machine: Examples"
E. Skochinski and S. Rengarajan 264

"SAF Analysis Codes for Predicting the Electromagnetic Effectiveness of Antenna Enclosed in Composite Structures"
B.J. Cown, J.P. Estrada and R. Routier 270

SESSION 4: INTERACTIVE POSTER SESSION (continued)

"Some Concentrated Solutions of Helmholtz Equation with Nonlocal Nonlinearity"
Y.N. Cherkashin and V.A. Eremenko 278

"Hysteresis and Eddy Currents in Ferromagnetic Media"
J. Fuzi and A. Ivanyi 283

"Electrical Circuit Analysis Considering Hysteresis in Coil Cores"
J. Fuzi 291

"A Paradigm for Proving the Convexity Properties of Slowness Curves"
A.R. Baghai-Wadji (8 pages) 297

"On the Strict-Convexity of the Slowness Surfaces for the Fastest Bulk-Acoustic-Waves in Piezoelectric and Piezoelectromagnetic Media"
A.R. Baghai-Wadji 305

"Solving EMC Problems Using the FDTD Method"
F. Gisin and Z. Pantic-Tanner 313

SESSION 5: TLM MODELING AND APPLICATIONS
Chairs: Wolfgang J.R. Hoefer and Peter Russer

"A Hybrid Time Domain TLM-Integral Equation Method for Solution of Radiation Problems", L. Pierantoni, S. Lindenmeier and P. Russer 320

"Comparison of Symmetric Condensed TLM, Yee FDTD and Integer Lattice Gas Automata Solutions for a Problem Containing a Sharp Metallic Edge"
N. Simons, R. Siushansian, J. LoVetri, G. Bridges and M. Cuhaci 326

"Some Observations on Stubs, Boundaries and Parity Effects in TLM Models"
D. De Cogan and C. Kun 331

"Modelling of Dispersive Media in TLM Using the Propagator Approach"
J. Rebel and P. Russer 336

"A Hybrid Time Domain TLM-Integral Equation Method for Solution of Radiation Problems", L. Pierantoni, S. Lindenmeier and P. Russer 320

"Comparison of Symmetric Condensed TLM, Yee FDTD and Integer Lattice Gas Automata Solutions for a Problem Containing a Sharp Metallic Edge"
N. Simons, R. Siushansian, J. LoVetri, G. Bridges and M. Cuhaci 326

"Some Observations on Stubs, Boundaries and Parity Effects in TLM Models"
D. De Cogan and C. Kun 331

"Modelling of Dispersive Media in TLM Using the Propagator Approach"
J. Rebel and P. Russer 336

"Characterization of Quasiplanar Structures Using the TLM Method"
O. Pertz, U. Muller and A. Beyer 344

SESSION 5: TLM MODELING AND APPLICATIONS (continued)

"Generation of Lumped Element Equivalent Circuits from Time-Domain Scattering Signals", T. Mangold and P. Russer 351

"TLM Analysis of an Optical Sensor"
R.R. DeLyser 359

"TLM Modeling and TDR Validation of Soil Moisture Probe for Environmental Sensing"
G. Tardioli, M. Righi, L. Cascio, W.J.R. Hoefer and R. McFarlane 367

"TLM Analysis of the Celestron-8 Telescope"
R.R. DeLyser 374

"Near-to Far Field Transformation Via Parabolic Equation" - STUDENT PAPER CONTEST -
A.N. Kurokhtin, Y.V. Kopylov, A.V. Popov and A.V. Vinogradov 381

SESSION 6: FREQUENCY-DOMAIN FAST ALGORITHMS
Chairs: Jiming Song and Weng Cho CHew

"Recent Advances in the Numerical Solution of Integral Equations Applied to EM Scattering from Terrain"
P. Cullen and C. Brennan 390

"Solution of Combined-Field Integral Equation Using Multi-Level Fast Multipole Algorithm for Scattering by Homogeneous Bodies"
X.Q. Sheng, J.M. Jin, J.M. Song, W.C. Chew and C.C. Lu 397

"Comparisons of FMM and AIM Compression Schemes in Finite Elements - Boundary Integral Implementations for Antenna Modeling"
K. Sertel, D.S. Filipovic, S. Bindiganavale and J.L. Volakis 405

"High-Order Nystrom Discretization for Faster, More Accurate Scattering Calculations"
L.S. Canino, J.J. Ottusch, M.A. Stalzer, J.L. Visher and S.M. Wandzura 413

"Large Scale Computing with the Fast Illinois Solver Code - Requirements Scaling Properties", J. Song and W.C. Chew 420

"A Fast Technique for Determining Electromagnetic and Acoustic Wave Behavior in Inhomogeneous Media"
M.A. Jensen 428

"Rapid Analysis of Perfectly Conducting and Penetrable Quasi-Planar Structures with the Steepest Descent Fast Multipole Method"
V. Jandhyala, E. Michielssen, B. Shanker and W.C. Chew 434

"Iterative Solution Strategies in Adaptive Integral Method (AIM)"
E. Bleszynski, M. Bleszynski and T. Jaroszewicz 441

"A Fast Moment Method Matrix Solver"
F.X. Canning and K. Rogovin 449

"Vector Parabolic Equation Technique for the RCS Calculations"
A.A. Zaporozhets and M.F. Levy 455

SESSION 7: ELECTROMAGNETICS IN BIOLOGICAL AND MEDICAL APPLICATIONS
Chairs: Cynthia Furse and Maria A. Stuchly

"EM Interaction Evaluation of Handset Antennas and Human Head: A Hybrid Technique", K.W. Kim and Y. Rahmat-Samii 462

"Comparison of RGFM and FDTD for Electromagnetic-Tissue Interaction Problems" M.A. Jensen 470

"Isolated vs. *in situ* Human Heart Dosimetry under Low Frequency Magnetic Exposure" T.W. Dawson, K. Caputa and M.A. Stuchly 476

"Faster than Fourier - Ultra Efficient Time-to-Frequency Domain Conversions for FDTD Applied to Bioelectromagnetic Dosimetry", C.M. Furse 482

"Modelling of Antennas in Close Proximity to Biological Tissues Using the TLM Method" J. Paul, C. Christopoulos and D.W.P. Thomas 490

SESSION 8: ADVANCES IN PERFECTLY MATCHED LAYERS (PML)
Chairs: Weng Cho Chew and Qing Huo Liu

"Conformal Perfectly Matched Layers" F.L. Teixeira and W.C. Chew 500

"Stability Analysis of Cartesian, Cylindrical and Spherical Perfectly Matched Layers" F.L. Teixeira and W.C. Chew 507

"A Unified Approach to PML Absorbing Media" D.H. Werner and R. Mittra 515

"Comparison of the Performance of the PML and the Liao Absorbing Boundary Formulation", M. Vall-llossera and C.W. Trueman 523

"A Uniaxial PML Implementation for a Fourth Order Dispersion-Optimized FDTD Scheme", G. Haussmann and M. Piket-May 531

SESSION 9: VISUALIZATION IN CEM
Chairs: Janice Karty and Stanley J. Kubina

"Plate Scattering Visualization: Images, Near Fields, Currents, and Far Field Patterns" J. Shaeffer and K. Hom 538

"Visualization Aids for Effective Aircraft Antenna Simulations" S.J. Kubina, C.W. Trueman, Q. Luu and D. Gaudine 546

"Visualization of Radiation from a Spiral Antenna Using EM-ANIMATE" R.A. Pearlman, M.R. Axe, J.M. Bomholdt and J.M. Roedder 554

"Evolution of an Antenna Training Aid Using Electromagnetic Visualisation" A. Nott and D. Singh 560

"The NEC-BSC Workbench: A Companion Graphical Interface Tool" G.F. Paynter and R.J. Marhefka 568

SESSION 9: VISUALIZATION IN CEM (continued)

" A New Tool to Assist Use of Legacy Programs"
B. Joseph, A. Paboojian, S. Woolf and E. Cohen 576

"Visual EMag: A 2-D Electromagnetic Simulator for Undergraduates"
D. Garner, J. Lebaric and D. Voltmer 581

"Exploring Electromagnetic Physics Using Thin-Wire Time-Domain (TWTD) Modeling"
E.K. Miller 583

AUTHOR INDEX 589

SESSION 10: ABC'S FOR CEM: THEORETICAL AND IMPLEMENTATION
Chairs: Peter G. Petropoulos and Omar M. Ramahi

"The Concurrent Complementary Operators Method for FDTD Mesh Truncation"
O.M. Ramahi 592

"Accurate Boundary Treatments for Maxwell's Equations and their Computational Complexity", T. Hagstrom, B.K. Alpert, L.F. Greengard and S.I. Hariharan 600

"Perfectly Matched Layer Methods in Spherical Coordinates"
B. Yang and D. Gottlieb 607

"The Unsplit PML for Maxwell's Equations in Cylindrical and Spherical Coordinates"
P.G. Petropoulos 615

"A Comparison of the Grote-Keller and Unsplit PML Absorbing Boundary Conditions for Maxwell's Equations in Spherical Coordinates"
N.V. Kantartzis, P.G. Petropoulos and T.D. Tsiboukis 623

"A Systematic Study of Three PML Absorbing Boundary Conditions Through a Unified Formulation in Cylindrical Coordinates"
J-Q. He and Q-H. Liu 631

"Preconditioned Generalized Minimal Residual (GMRES) Solver for Domains Truncated by Perfectly Matched Layer (PML) Absorbers"
Y.Y. Botros and J.L. Volakis 639

"PML Implementation for the Battle-Lemarie Multiresolution Time-Domain Schemes"
E. Tentzeris, R. Robertson and L.P.B. Katehi 647

"A PML-FDTD Algorithm for General Dispersive Media"
G-X. Fan and Q.H. Liu 655

SESSION 11: CEM AND PARAMETER EXTRACTION FOR PACKAGING ANALYSIS
Chairs: Emilie van Deventer and Jose E. Schutt-Aine

"A New Generalized De-embedding Method for Numerical Electromagnetic Analysis"
Y.O. Shlepnev 664

"A Circuit Extraction Approach in PCB Power-Bus Analysis"
H. Shi and J.L. Drewniak 672

"Modeling of Conductor and Dielectric Losses in Packages"
J. Poltz 680

"Extraction of Effective Capacitance and Inductance of a Power Distribution Structure from Numerical Field Data"
A. Byers, B. Boots, M. Piket-May and R. Gravrok 687

"Extraction of Equivalent Circuit Parameters of Interconnections Using FDTD and PML"
F. Liu and J.E. Schutt-Aine 695

SESSION 12: REDUCED-ORDER MODELING IN ELECTROMAGNETICS
Chairs: Andreas C. Cangellaris and R.F. Remis

"The Use of a Correspondence Principle in Reduced-order Modeling of Electromagnetic Wavefields"
R.F. Remis and P.M. van den Berg 704

"The Spectral Lanczos Decomposition Method for Efficient Time-Domain and Frequency-Domain Finite-Element Solution of Maxwell's Equations"
M. Zunoubi, J-M. Jin, K. Donepudi and W.C. Chew 712

"Passivity of Discrete Electromagnetic Systems"
A.C. Cangellaris and L. Zhao 721

"Rational Krylov Reduced Order Modeling of Multiscreen Frequency Selective Surfaces" - STUDENT PAPER CONTEST -
D.S. Weile, E. Michielssen and K. Gallivan 732

SESSION 13: FINITE ELEMENT METHOD
Chairs: John R. Brauer and Jin-fa Lee

"Comparing High Order Vector Basis Functions"
J.S. Savage 742

"Mesh Refinement for Hybrid FEM in the Analysis of Printed Antennas and Arrays"
J. Gong, D. Bernstein and S. Wedge 750

"A Novel, Efficient Algorithm for Scattering from a Complex BOR Using Vector FEM and PML" - STUDENT PAPER CONTEST - A.D. Greenwood and J-M. Jin 756

"Homogenized Finite Element Model of a Beam Waveguide Resonator Antenna with Over One Hundred Coupling Holes"
J.R. Brauer 763

"A Surface Admittance Formulation for the Transient Modeling of Skin Effect and Eddy Current Problems"
K.N. Wassef and A.F. Peterson 771

SESSION 13: FINITE ELEMENT METHOD (continued)

"Verification of Eddy Current Analysis of Engineering Oriented Loss Model (Problem 21)"
N. Takahashi, K. Fujiwara, K. Sugiyama and J. Takehara 779

"Jacobi-Davidson Algorithm for Modeling Open Domain Lossy Cavities"
C. Liu and J-F. Lee 787

"Analysis of Electromagnetic Penetration Through Apertures of Shielded Enclosure Using Finite Element Method",
B-W. Kim, Y-C. Chung and T-W. Kang 795

"hp-Adaptive Edge Finite Elements for Maxwell's Equations"
L. Demkowicz, L. Vardapetyan and W. Rachowicz 799

SESSION 14: RECENT ADVANCES IN TIME-DOMAIN TECHNIQUES
Chairs: Douglas C. Blake and Douglas J. Riley

"An Analysis of Programming Models for Time-Domain CEM Codes on RISC-Based Computers" D.C. Blake and J.S. Shang 808

"The *VOLMAX* Transient Electromagnetic Modeling System, Including Sub-Cell Slots and Wires on Random Non-Orthogonal Cells"
D.J. Riley and C.D. Turner 816

"Using the Finite Integration Time Domain Technique at Low Frequencies"
R. Ehmann and T. Weiland 825

"Modelling Dispersive Media Using the Finite Integration Technique"
S. Gutschling, H. Kruger and T. Weiland 832

"Transient Analysis of Thin Wire Antennas Mounted on Three-Dimensional Perfectly Conducting Bodies"
K. Aygun, A.A. Ergin, B. Shanker, S.E. Fisher and E. Michielssen 838

"A PSTD Algorithm in Cylindrical Coordinates"
Q.H. Liu and J.Q. He 845

"On the PSTD Method for Large-Scale Problems", Q.H. Liu 852

"Pseudospectral Time-Domain Modeling of Diffractive Optical Elements"
J.S. Hesthaven, P.G. Dinesen and J.P. Lynov 858

"Transient Analysis of Acoustic Scattering Using Marching-on-in Time With Plane Wave Time Domain Algorithm"
A.A. Ergin, B. Shanker, K. Aygun and E. Michielssen 866

"A Plane Wave Time Domain Algorithm for the Fast Analysis of Transient Electromagnetic Scattering Phenomena"
B. Shanker, A.A. Ergin, K. Aygun and E. Michielssen 873

SESSION 15: EMI/EMC
Chairs: Todd Hubing and Bruce R. Archambeault

"EMC Modeling of Shielded Enclosures with Apertures and Attached Wires in a Real-World Environment"
B.R. Archambeault, K. Chamberlin and O. Ramahi 880

"Proposed Standard EMI Modeling Problems for Evaluating Tools which Predict Shielding Effectiveness of Metal Enclosures"
B.R. Archambeault 888

"A Study in the Proper Design of Grounding for SMPS Converters and the Role of CEM"
R. Perez 895

"Expert System Algorithms for EMC Analysis"
T. Hubing, N. Kashyap, J. Drewniak, T. Van Doren and R. DuBroff 905

"The Electromagnetic Compatibility Characteristics of Buildings in Mobile Radio Waves Propagation Channel"
Y. Miyazaki and P. Selormey 911

SESSION 16: HYBRID TECHNIQUES
Chairs: Ulrich Jakobus and William D. Wood, Jr.

"Extension of the MoM/PO Hybrid Technique to Homogeneous Dielectric Bodies"
U. Jakobus 920

"EMAPS: A 3D Hybrid FEM/MoM Code"
Y. Ji and T.H. Hubing 928

"Iterative Coupling of MoM and MMP for the Analysis of Metallic Structures Radiating in the Presence of Dielectric Bodies"
H-O. Ruoss, U. Jakobus and F.M. Landstorfer 936

"A Hybrid Algorithm for Frequency Selective Surface Analysis"
M.J. Walker 944

"Generalized Networks for Waveguide Step Discontinuities"
M. Mongiardo, P. Russer, M. Dionigi and L.B. Felsen 957

SESSION 17: SIGNAL PROCESSING TECHNIQUES IN CEM
Chairs: Douglas H. Werner and Ping L. Werner

"Using Windowed, Adaptive Sampling to Minimize the Number of Field Values Needed to Estimate Radiation and Scattering Patterns"
E.K. Miller 958

"Spectral Domain Interpolation of Antenna Radiation Patterns Using Model-Based Parameter Estimation and Genetic Algorithms"
R.J. Allard, D.H. Werner, J.S. Zmyslo and P.L Werner 964

"An Accurate Algorithm for Nonuniform Fast Fourier Transforms (NUFFT) and Its Applications", Q.H. Liu and N. Nguyen 972

SESSION 17: SIGNAL PROCESSING TECHNIQUES IN CEM (continued)

"A Subspace Approach to Fast Moment Method Scattering Predictions Over Limited Sectors", J. Stach 979

"Application of Biorthogonal B-Spline-Wavelets to Telegrapher's Equations" M. Aidam and P. Russer 983

"NEC Acceleration by the Wavelet Matrix Transform" Y.H. Lee and Y. Lu 991

"Adaptive Segmentation Algorithms for Optimal NEC Modelling of Wire-Grid Structures", Y.H. Lee and Y. Lu 999

SESSION 18: HF-UHF PRACTICAL ANTENNA TOPICS
Chairs: W. Perry Wheless, Jr., and Nathan Cohen

"Comparison of Shipboard HF Transmit Fan Characteristics NEC versus Scale-Model Measurements", K. Lysiak and P. Dombowsky 1006

"NEC Model Results for Shipboard Shielded Crossed Loop Antennas with Scale-Model Range Data", K. Lysiak 1012

"A Near-Earth and Buried HF Antenna Computer Modeling Program" W.P. Wheless, Jr., and L.T. Wurtz 1019

"Empirical and Numerical Treatment of Electromagnetic Pulse Induced Currents" M.J. Packer 1028

"Advantages of an Alternate Viewpoint When Designing HF Verticals for 80 and 160 m", R. Severns 1036

"Tower Equivalent Radius", W.F. Cummins 1043

"Simple CP Fractal Loop Array with A Parasitic", N. Cohen 1047

"NEC4 Analysis of a Fractalized Monofilar Helix in an Axial Mode" N. Cohen 1051

"Design of Low Sidelobe Antennas", R.W. Hecht 1058

"EMP Simulations of Near Field Enhancement of Wire Antenna" M. El Hachemi, C. Tosser-Roussey and A. Tosser-Roosey 1066

SESSION 19: OPTIMIZATION TECHNIQUES FOR ELECTROMAGNETICS
Chairs: Eric Michielssen and Randy L. Haupt

"Genetic Algorithm Design of the Conical Interdigitated Log-Periodic Antenna"
P.D. Mannikko, P.J. O'Brien and K.W. Ommodt 1074

"A Comparison of Simple and Complex Genetic Algorithms in Wire Antenna Design"
B.S. Sandlin and A.J. Terzuoli 1080

"Array Failure Correction with a Genetic Algorithm"
B. Beng, K. Yeo and Y. Lu 1087

"Backscattering Synthesis from Tapered Resistive Grids", R.L. Haupt 1095

"Obtaining Linear and Circular Apertures with Smooth Amplitude Distribution and High Efficiency", J.A. Rodriguez and F. Ares 1100

SESSION 20: INTEGRAL EQUATION METHODS AND ERROR CONTROL
Chairs: Goran Eriksson and C.Y. Shen

"Force Calculations and Error Estimates with Boundary Element Methods"
K. Davey and D. Zheng 1106

"Use of Residual Error Bounds to Obtain Stable Numerical Solutions of a Fredholm Integral Equation of the First Kind"
T. Schwengler and E.F. Kuester 1112

"Eigenvalue Studies of Matrices Resulting from EFIE Simulations for Planar Structures"
J.M. Dunn and H. MacMillan 1120

"Iterative Solution of Dense Linear Systems in Electromagnetic Scattering Calculations", J. Rahola 1126

"EMCP2 A Parallel Boundary Element Software Package Using a Novel Parameterisation Technique" G. Eriksson and U. Thibblin 1134

AUTHOR INDEX 1141

THE APPLIED COMPUTATIONAL ELECTROMAGNETIC SOCIETY

CALL FOR PAPERS

The 15th Annual Review of Progress

in Applied Computational Electromagnetics

March 15-19, 1999

Naval Postgraduate School, Monterey, California

"Share Your Knowledge and Expertise with Your Colleagues"

The Annual ACES Symposium is an ideal opportunity to participate in a large gathering of EM analysis enthusiasts. The purpose of the Symposium is to bring analysts together to share information and experience about the practical application of EM analysis using computational methods. The symposium offerings include technical presentations, demonstrations, vendor booths and short courses. All aspects of electromagnetic computational analysis are represented. Contact for details.

Technical Program Chairman
Randy Haupt
EE Dept., 260
University of Nevada
Reno, NV 89557-0153
Phone: (702)-784-6927
Fax: (702)-784-6627
Email:haupt@ee.unr.edu

Symposium Administrator
Richard W. Adler
ECE Dept/Code EC/AB
Naval Postgraduate School
833 Dyer Road, Room 437
Monterey, CA 93943-5121
Phone: (408) 646-1111
Fax: (408) 649-0300
Email:rwa@ibm.net

Symposium Co-Chairman
Indira Chatterjee
EE Dept., 260
University of Nevada
Reno, NV 89557-0153
Phone: (702)-784-1346
Fax: (702)-784-6627
Email:indira@ee.unr.edu

Symposium Co-Chairman
James Hensen
EE Dept., 260
University of Nevada
Reno, NV 89557-0153
Phone: (702)-784-6929
Fax: (702)-784-6627
Email:jmb@proton.ee.unr.edu

The ACES Symposium is a highly influential outlet for promoting awareness of recent technical contributions to the advancement of computational electromagnetics. Attendance and professional program paper participation from non-ACES members and from outside North America are encouraged and welcome.

Early Registration Fees; (approximate*)	**ACES MEMBERS**	**$255**
	NON-MEMBER	**$295**
	STUDENT/RETIRED/UMEMPLOYED	**$115 (no proceedings)**
	STUDENT/RETIRED/UNEMPLOYED	**$150 (includes proceedings)**

*The exact fee will be announced later. Each conference registration is entitled to publish two papers in the proceedings free of charge. Excess pages over a paper limit of 8 will be charged $15/page.

1999 ACES Symposium
Sponsored by: ACES, NPS, U of NV, BYU, U of Illinois at Urbana-Champaign, U. of Kentucky
in cooperation with: The IEEE Antennas and Propagation Society, the IEEE Electromagnetic Compatibility Society and USNC/URSI

Visit ACES on line at: www.emclab.umr.edu/aces

THE APPLIED COMPUTATIONAL ELECTROMAGNETIC SOCIETY

CALL FOR PAPERS

The 15th Annual Review of Progress in Applied Computational Electromagnetics

Papers may address general issues in applied computational electromagnetics, or may focus on specific applications, techniques, codes, or computational issues of potential interest to the Applied Computational Electromagnetics Society membership. Area and topics include:

- Code validation
- Code performance analysis
- Computational studies of basic physics
- Examples of practical code application
- New codes, algorithms, code enhancements, and code fixes
- Computer Hardware Issues
- Partial list of applications:

antennas	wave propagation
radar imaging	radar cross section
shielding	bioelectromagnetics
EMP, EMI/EMC	visualization
dielectric & magnetic materials	inverse scattering
microwave components	MIMIC technology
fiberoptics	remote sensing & geophysics
communications systems	propagation through plasmas
eddy currents	non-destructive evaluation

- Partial list of techniques:

frequency-domain & time-domain techniques	
integral equation & differential equation techniques	
finite difference & finite element analysis	
diffraction theories	physical optics
modal expansions	perturbation methods
hybrid methods	moment methods

+ + + NEW + + + INSTRUCTIONS FOR AUTHORS AND TIMETABLE + + + NEW + + +

November 20, 1998: Submission deadline. Submit four copies of a full-length, camera-ready paper to the Technical Program Chairman. Please supply the following data for the corresponding author: name, address, email address, FAX, and phone numbers. See below for instructions for the format of paper.

December 21, 1998: Authors notified of acceptance.

PAPER FORMATTING REQUIREMENTS

The recommended paper length is 6 pages, with 8 pages as a maximum, including figures. The paper should be camera-ready (good resolution, clearly readable when reduced to the final print of 6 x 9 inch paper). The paper should be printed on 8-1/2 x 11 inch papers with 13/16 side margins, 1-1/16 inch top margin, and 1 inch on the bottom. On the first page, place title 1-1/2 inches from top with author and affiliation beneath the title. Single spaced type using 10 or 12 point front size, entire text should be justified (flush left and flush right). No typed page numbers, but number your pages lightly in pencil on the back of each page.

SHORT COURSES

Short courses will be offered in conjunction with the Symposium covering numerical techniques, computational methods, surveys of EM analysis and code usage instruction. It is anticipated that short courses will be conducted principally on Monday March 15 and Friday March 19. Fees for **Half-day course** will be: $90 per person if booked before 1 March 99; $100, if booked from 1 March to 15 March 99; and $110 if booked at Conference time. **Full-day Courses** will be: $140 if booked before 1 March 1999; $150 if booked from 1 March to 15 March; $160 if booked at Conference time. **Short Course Attendance is not covered by the Symposium Registration Fee!**

EXHIBITS

Vendor booths and demonstrations will feature commercial products, computer hardware and software demonstrations, and small company capabilities.

1998 Symposium Program Committee

for the

14th Annual Review of Progress in

APPLIED COMPUTATIONAL ELECTROMAGNETICS

at the
Naval Postgraduate School
Monterey, CA

Technical Program Chairman:
Jiaming Jin
ECE Department
Univ. of Illinois
1406 West Green Street
Urbana, IL 61801-2991
Phone: 217 333-3801
FAX: 217 333-5962
Email:j-jin1@uiuc.edu

Co-Chair:
Michael A. Jensen
ECE Department, 459 CB
Brigham Young University
Provo, UT 84602
Phone:801 378-5736
Fax: 801 378-6586
Email:jensen@ee.byu.edu

Co-Chair:
Randy L. Haupt
EE Department, 260
Univ. of Nevada
Reno, NV 89557-0153
Phone: 702-784-6927
Fax: 702-784-6627
Email: haupt@ee.unr.edu

Symposium Administrator
Richard W. Adler
ECE Department, Code EC/AB
Naval Postgraduate School
833 Dyer Road, Room 437
Monterey, CA 93943-5121
Phone: 408-646-1111
FAX: 408-649-0300
Email:rwa@ibm.net

Short Course Chairman:
Michael A. Jensen
ECE Department, 459 CB
Brigham Young University
Provo, UT 84602
Phone: 801-378-5736
Fax: 801-378-6586
Email: jensen@ee.byu.edu

Vendor Chairman:
Keith W. Whites
Department of EE
University of Kentucky
453 Anderson Hall
Lexington, KY 40506-0046
Phone: 606-257-1768
Fax: 606-257-3092
Email: whites@engr.uky.edu

Conference Secretary:
Mrs. Pat Adler
Email: pba@ibm.net

Advisory Committee:
Richard W. Adler, Naval Postgraduate School
Duncan C. Baker, University of Pretoria
Robert Bevensee, Consultant
John Brauer, Ansoft Corp.
Andreas Cangellaris, University of Illinois
Pat Foster, Microwave & Antenna Systems
Todd Hubing, University of Missouri-Rolla
Adalbert Konrad, University of Toronto
Ray Perez, Jet Propulsion Lab.
Harold Sabbagh, Sabbagh Assoc. Inc.
Norio Takahashi, Okayama University
W. Perry Wheless, Jr., University of Alabama

PREFACE

On behalf of the ACES Technical Program Committee, I welcome you to "The 14th Annual Review of Progress in Applied Computational Electromagnetics." The Symposium spans the five day period from Monday, March 16 through Friday, March 20, 1998, and takes place at the Naval Postgraduate School (NPS) in Monterey, California. The Symposium is sponsored by the Applied Computational Electromagnetics Society, NPS, and the University of Illinois at Urbana-Champaign.

Monday, March 16 and Friday, March 20 are devoted to short courses. A total of eight short courses will be offered. Technical sessions will take place Tuesday, March 17 through Thursday, March 19, with an Interactive Poster Session and Vendor Exhibits scheduled for Tuesday afternoon. This year's Symposium features a total of 20 technical sessions. For the second time, the Symposium will hold a Student Paper Contest.

The organization of the Symposium would not have been possible without the cooperation of my Symposium Co-Chairmen, Professor Michael Jensen, who organized short courses and Professor Randy Haupt, who reviewed papers. I would also like to thank Professor Keith Whites, our capable Vendor-Chair, for organizing vendor exhibits. My appreciation also goes to Professor Richard Adler for providing access to the NPS facilities and his unending dedication to the annual ACES conferences, to Dr. Bob Bevensee, the ACES Conference Committee Chairman, for his support, and to Professor Eric Michielssen for his suggestions. Pat Adler, Shirley Dipert, and Linda Vogel assisted in the compilation of the author database and the printing of the proceedings. Finally, I would like to thank the session organizers for putting together some excellent sessions.

Enjoy the 14th Annual Review and your stay in Monterey.

Jianming Jin
Technical Program Chair
1998 ACES Conference

ACES PRESIDENT'S STATEMENT

Welcome to the Fourteenth Annual Review of Progress in Applied Computational Electromagnetics. I don't know what El Nino has planned for outdoors, but the weather inside should be nice. Jianming Jin, Michael Jensen, Randy Haupt, Keith Whites, and Dick Adler, have developed an outstanding agenda. The range of session topics continues to increase, which speaks well for the applicability of Computational Electromagnetics to science and engineering.

Since this is my last conference as ACES President, and because I will be absent from the Conference this year, I will give thanks in this note to those people who deserve it. In particular, I want to thank Dick and Pat Adler for their continued hard work on our behalf. Pat has put together an outstanding team of workers, whom you will see when you register, of if you have any questions about the conference, or if you simply want to drop in and say "hi" to. My thanks go, also, to those faithful members of the Board of Directors, who labor on your behalf throughout the year to ensure that our Society, and this Conference, are of the highest professional caliber. If you run into any of these folks, give them a pat on the back; they deserve it. I congratulate all of the winners of this year's awards; it has been my pleasure in the past to shake your hands directly. This year I will do it remotely, but the sincerity is still there.

Finally, my thanks go to each of you who is in attendance, especially those who are presenting papers. You have made the Annual Review one of the outstanding professional-technical conferences in Computational Electromagnetics.

Best wishes,

Harold A. Sabbagh, President
Sabbagh Associates, Inc.
4635 Morningside Drive
Bloomington, IN 47408
(812)339-8273
(812)339-8292 FAX
email: has@sabbagh.com

ACES 1998 SHORT COURSES

MONDAY 16 MARCH FULL-DAY COURSES

0830 - 1630 "Recent Advances in Fast Algorithms for Computational Electromagnetics", Weng Cho Chew, Jiming Song, Eric Michielssen, and Jianming Jin, Center for Computational Electromagnetics, University of Illinois at Urbana-Champaign.

0830 - 1630 "An Introduction to the Fast-MoM in Computational Electromagnetics", Ali R. Baghai-Wadji, Department of Applied Electronics, Vienna University of Technology, Vienna, Austria.

0830 - 1630 "Finite Elements for Electromagnetics", John R. Brauer, Ansoft Corporation, Milwaukee, WI.

MONDAY 16 MARCH HALF-DAY COURSES

0830 - 1200 "A Survey and Comparison of Computational Electromagnetics Options", Edmund K. Miller, Santa Fe, NM.

1300 - 1630 "Using Model-Based Parameter Estimation to Increase the Efficiency and Effectiveness of Computational Electromagnetics", Edmund K. Miller, Santa Fe, NM.

FRIDAY 20 MARCH FULL-DAY SHORT COURSES

0830 - 1630 "Practical Genetic Algorithms," Randy L. Haupt, University of Nevada, Reno, Reno, NV.

0830 - 1630. "Application of the Finite-Difference Time-Domain Method to Simulation of Electromagnetic Coupling to the Human Body," Cynthia Furse, Utah State University, Logan, UT

0830 - 1630 "Using Mathematical Software (MATHCAD and MATLAB) for Computational Electromagnetics," Jovan Lebaric, Naval Postgraduate School, Monterey, CA

FINAL AGENDA

The Fourteenth Annual Review of Progress in Applied Computational Electromagnetics

NAVAL POSTGRADUATE SCHOOL
16-20 MARCH 1998

Jianming Jin, Technical Program Chairman

Michael A. Jensen, Conference Co-Chair & Short Course Chairman

Randy L. Haupt, Conference Co-Chair

Keith Whites, Vendor Chairman

Richard W. Adler, Conference Facilitator

MONDAY MORNING 16 MARCH 1998

0730 - 0820	**SHORT COURSE REGISTRATION**		**Glasgow 103**
0830 - 1630	"Recent Advances in Fast Algorithms for Computational Electromagnetics", Weng Cho Chew, Jiming Song, Eric Michielssen, and Jianming Jin, Center for Computational Electromagnetics, University of Illinois at Urbana-Champaign.		**Full-day course**
0830 - 1630	"An Introduction to the Fast-MoM in Computational Electromagnetics", Ali R. Baghai-Wadji, Department of Applied Electronics, Vienna University of Technology, Vienna, Austria.		**Full-day course.**
0830 - 1630	"Finite Elements for Electromagnetics", John R. Brauer, Ansoft Corporation, Milwaukee, WI.		**Full-day course**
0830 - 1200	"A Survey and Comparison of Computational Electromagnetics Options", Edmund K. Miller, Santa Fe, NM.		**Half-day course**
1300 - 1630	"Using Model-Based Parameter Estimation to Increase the Efficiency and Effectiveness of Computational Electromagnetics", Edmund K. Miller, Santa Fe, NM.		**Half-day course**
0900 - 1800	**CONFERENCE REGISTRATION**		**Glasgow 103**
1200	**BOD MEETING/LUNCHEON**		**Terrace Room, Herrmann Hall**
1630 - 1830	**BOD CONTINUATION MEETING**		**Glasgow 114**

TUESDAY MORNING 17 MARCH 1998

0715 - 0750	**CONTINENTAL BREAKFAST**		**Glasgow Courtyard**
0745 - 0800	**ACES BUSINESS MEETING**	President Hal Sabbagh	**Glasgow 102**
0800-1810	**WELCOME**	Jianming Jin	**Glasgow 102**

SESSION 1: **CEM ANALYSIS AND APPLICATION WITHIN AN ENGINEERING ENVIRONMENT** **(Parallel with Sessions 2 & 3)**
Chair: Kenneth R. Siarkiewicz (Organizer), Co-Chair: Donald R. Pflug (Co-Organizer)

0820	Frameworks--Future Paradigm for CEM Analysis	K.R. Siarkiewicz
0840	REF CEM Data Dictionary	T. Wharton & J.A. Evans
0900	Air Force Research & Engineering Framework Control Panel	D.M. Hallatt & J. A. Evans
0920	Continued Application of the Research and Engineering Framework (REF) at Raytheon	J. LaBelle, B. Hantman H. Wright, Y. Chang, R. Abrams
0940	The Innovative Research Testbed: A PC-Based High Performance Computing and Web-Based Collaboratory for Computational Electromagnetics	D.M. Leskiw, G. Ingersoll T. Vidoni & R. Redmond
1000	**BREAK**	

TUESDAY MORNING 17 MARCH 1998

SESSION 1: CEM ANALYSIS AND APPLICATION WITHIN AN ENGINEERING ENVIRONMENT (cont)

1020	Illustrating the Application of Expert Systems to Computational Electromagnetics Modeling and Simulation	A.L.S. Drozd, T.W. Blocher C.E. Carroll, Jr., & J.M. Allen
1040	Some Present and Future Aspects of the Quality of Solution in Computational Electromagnetics	D.R. Pflug
1100	On the Use of Computational Electromagnetics in the Radar Cross Section Measurement Calibration Process	K.C. Hill & W.D. Wood, Jr.
1120	Radar Calibration at Low Frequencies Using a Triangular Trihedral Corner Reflector	C.Y. Shen
1200	**LUNCH**	

SESSION 2: FINITE-DIFFERENCE TIME-DOMAIN APPLICATIONS (Parallel with Sessions 1 & 3)
Chair: John Beggs (Organizer), Co-Chair: Melinda Piket-May

0820	Time Domain Analysis of Small Multi-Sector Monopole Yagi-Uda Array Antenna Mounted on a Finite Ground Plane Using FDTD Method	T. Maruyama, K. Uehara, T. Hori, K.. Kagoshima
0840	Antenna Performance Calculation in Lossy Media with FDTD Method	M. Cal & N. Ljepojevic
0900	Far-Zone Transformation in FDTD for VHF-band SAR-image Simulations	T. Martin & L. Ulander
0920	FDTD Simulations Used to Correct for Ground Effects in Aircraft Testing	G. Eriksson & U. Thibblin
0940	Validation of FDTD-Computed Handset Patterns by Measurement	C.W. Trueman, S.J. Kubina, J.E. Roy, W.R. Lauber, M. Vall-llossera
1000	**BREAK**	
1020	FDTD Analysis of Flip Chip Interconnects	A Z. Elsherbeni, V. Rodriguez-Pereyra, C.E. Smith
1040	FDTD Analysis of the Celestron-8 Telescope	R.R. DeLyser
1100	Modifying a Graphically-Based FDTD Simulation for Parallel Processing	G. Haussmann, M. Piket-May K. Thomas
1120	A Time Domain Method for High Frequency Problems Exploiting the Whitney Complex	A. Arkko, T. Tarhasaari L. Kettunen
1140	Treatment of Boundaries in Multiresolution Based FDTD Multigrid	K. Goverdhanam, E. Tentzeris L.P.B. Katehi
1200	**LUNCH**	

SESSION 3: APPLICATION OF ANALYTIC AND COMPUTATIONAL METHODS TO THE MODELING OF ELECTROMAGNETIC MATERIALS (Parallel with Sessions 1 & 2)
Chair: Rudy Diaz (Organizer), Co-Chair: David H. Y. Yang

0820	Computing Dispersion Relations and Radiation Spectra in Photonic Band Gap Materials by Plane Wave Expansion Method	T. Suzuki & P.K. L. Yu
0840	Waveguides in Photonic Band Gap Materials	M.M. Sigalas, R. Biswas K.M. Ho, C.M. Soukoulis D.D. Crouch
0900	Is There a Relationship Between a Random and an Ordered Composite Mixture? **- STUDENT PAPER CONTEST -**	W.M. Merrill, S.A. Kyriazidou N.G. Alexopoulos
0920	An Analytic Framework for the Modeling of Effective Media	R E. Diaz
0940	Finite Grain Boundary Effects for Magnetic Materials: Tunneling and Intergrain Gaps	G.G. Bush
1000	**BREAK**	

TUESDAY MORNING 17 MARCH 1998

SESSION 3: APPLICATION OF ANALYTIC AND COMPUTATIONAL METHODS TO THE MODELING OF ELECTROMAGNETIC MATERIALS (cont)

1020	Numerical Computation of the Complex Dielectric Permittivity: FFT-Based Hilbert Transform Approximation of the Kramers-Kronig Relations - **STUDENT PAPER CONTEST -**	F. Castro & B. Nabet
1040	Rayleigh Analysis of Novel Dense Medium Exhibiting Narrow-Band Transparency Window	S.A. Kryiazidou, R.E. Diaz N.G. Alexopoulos
1200	**LUNCH**	

TUESDAY AFTERNOON 17 MARCH 1998

INTERACTIVE POSTER SESSION 1300 - 1530	**Ballroom, Herrmann Hall**
VENDOR EXHIBITS 1300 - 1900	**Ballroom, Herrmann Hall**
WINE AND CHEESE BUFFET 1500 - 1700	**Ballroom, Herrmann Hall**

SESSION 4: INTERACTIVE POSTER SESSION **Ballroom, Herrmann Hall**

Finite Difference Formulation - Expanding the Capabilities	K. Davey
Time and Frequency Domain Numerical Modeling of Outbound and Standing Power from Perpendicularly Oriented, Electrically Small TM Dipoles	G. Liu, C.A. Grimes K.G. Ong
Efficient Analysis of Large Two-dimensional Arbitrarily Shaped Finite Gratings for Quantum Well Infrared Photo-detectors	V. Jandhyala, D. Sengupta B. Shanker, E. Michielssen M. Feng, & G. Stillman
Forward and Backward Propagation Algorithms Applied to the Electromagnetic Scattering by an Impenetrable Obstacle: A Progress Report	G.F. Crosta
Analysis of Broad Wall Slots Excited by Tuning Screws	T. Azar & R.Coren
Closed-Form Expression of the Arc-Length of the Toroidal/Helical Equilibrium Orbit	R.A. Speciale
Asymptotic Techiques in Naval Ship Design	R. Routier & R. Burkholder
A BCG-FFT Solution of Scattering and Radiation by Large Finite Arrays of Microstrip Antennas	C-Fu Wang, F. Ling, J-M Jin
Analytic Solution for Low-Frequency Electric Induction in an Equatorially Stratified Sphere	T.W. Dawson
Parallelizing Computational Electromagnetics Code Using the Parallel Virtual Machine: Examples	E. Skochinski & S. Regarajan
SAF Analysis Codes for Predicting the Electromagnetic Effectiveness of Antennas Enclosed in Composite Structures	B.J. Cown, J.P. Estrada R. Routier
Some Concentrated Solutions on Hemholtz Equation with Nonlocal Nonlinearity	Y.N. Cherkashin V.A. Eremenko
Hysteresis and Eddy Currents in Ferromagnetic Media	J. Fuzi & A. Ivanyi
Electrical Circuit Analysis Considering Hysteresis in Coil Cores	J. Fuzi
A Paradigm for Proving the Convexity Properties of Slowness Curves	A.R. Baghai-Wadji
On the Strict-Convexity of the Slowness Surfaces for the Fastest Bulk-Acoustic-Waves in Piezoelectric and Piezoelectromagnetic Media	A.R. Baghai-Wadji
Solving EMC Problems Using the FDTD Method	F. Gisin & Z. Pantic-Tanner

TUESDAY EVENING 17 MARCH 1998 **BOD DINNER**

WEDNESDAY MORNING 18 MARCH 1998

0730 - 0800	**CONTINENTAL BREAKFAST**	**Glasgow Courtyard**
SESSION 5:	**TLM MODELING AND APPLICATIONS (Parallel with Sessions 6, 7 & 8))** Chair: Wolfgang Hoefer (Organizer), Co-Chair: Peter Russer	
0820	A Hybrid Time Domain TLM-Integral Equation Method for Solution of Radiation Problems	L. Pierantoni, S. Lindenmeier P. Russer
0840	Comparison of Symmetric Condense TLM, Yee FDTD and Integer Lattice Gas Automata Solutions for a Problem Containing a Sharp Metallic Edge	N. Simons, R. Siushansian J. LoVetri, G. Bridges M. Cuhaci
0900	Some Observations on Stubs, Boundaries and Parity Effects in TLM Models	D. de Cogan & C. Kun
0920	Modelling of Dispersive Media in TLM Using the Propagator Approach	J. Rebel & P. Russer
0940	Characterization of Quasiplanar Structures Using the TLM Method	O. Pertz, U. Muller & A. Beyer
1000	**BREAK**	
1020	Generation of Lumped Element Equivalent Circuits from Time-Domain Scattering Signals	T. Mangold & P. Russer
1040	TLM Analysis of an Optical Sensor	R.R. DeLyser
1100	TLM Modeling and TDR Validation of Soil Moisture Probe for Environmental Sensing	G. Tardioli, M. Righi, L. Cascio W.J.R. Hoefer, & R. McFarlane
1120	TLM Analysis of the Celestron-8 Telescope	R.R. DeLyser
1140	Near to Far Field Transformation via Parabolic Equation - **STUDENT PAPER CONTEST**	A.N. Kurokhtin, Y.V. Kopylov, A.V. Popov, & A.V. Vinogradov
1200	**LUNCH**	
SESSION 6:	**FREQUENCY-DOMAIN FAST ALGORITHMS (Parallel with Sessions 5, 7 & 8)** Chair: Jiming Song (Organizer), Co-Chair: Weng Cho Chew (Co-Organizer)	
0820	Recent Advances in the Numerical Solution of Integral Equations Applied to EM Scattering from Terrain	P. Cullen & C. Brennan
0840	Solution of Combined-Field Integral Equation Using Multi-Level Fast Multipole Algorithm for Scattering by Homogeneous Bodies	X.Q. Sheng, J.M. Jin, J.M. Song W.C. Chew, & C.C. Lu
0900	Comparisons of FMM and AIM Compression Schemes in Finite Element - Boundary Integral Implementations for Antenna Modeling	K. Sertel, D.S. Filipovic S. Bindiganavale, & J.L. Volakis
0920	High-Order Nystrom Discretization for Faster, More Accurate Scattering Calculations	L.S. Canino, J.J. Ottusch M.A. Stalzer, J.L. Visher S.M. Wandzura
0940	Large Scale Computing with the Fast Illinois Solver Code --Requirements Scaling Properties	J. Song & W.C. Chew
1000	**BREAK**	
1020	A Fast Technique for Determining Electromagnetic and Acoustic Wave Behavior in Inhomogeneous Media	M.A. Jensen
1040	Rapid Analysis of Perfectly Conducting and Penetrable Quasi-Planar Structures with the Steepest Descent Fast Multipole Method	V. Jandhyala, E. Michielssen B. Shanker, & W.C. Chew
1100	Iterative Solution Strategies in Adaptive Integral Method (AIM)	E. Bleszynski, M. Bleszynski T. Jaroszewicz
1120	A Fast Moment Method Matrix Solver	F.X. Canning & K. Rogovin
1140	Vector Parabolic Equation Technique for the RCS Calculations	A.A. Zaporozhets & M. F. Levy
1200	**LUNCH**	

WEDNESDAY MORNING 18 MARCH 1998

SESSION 7: ELECTROMAGNETICS IN BIOLOGICAL AND MEDICAL APPLICATIONS (Parallel with Sessions 5, 6 & 8)
Chair: Cynthia Furse (Organizer), Co-Chair: Maria A. Stuchly

0820	EM Interaction Evaluation of Handset Antennas and Human Head: A Hybrid Technique	K.W. Kim & Y. Rahmat-Samii
0840	Comparison of RGFM and FDTD for Electromagnetic-Tissue Interaction Problems	M.A. Jensen
0900	Isolated vs. *in situ* Human Heart Dosimetry under Low Frequency Magnetic Exposure	T.W. Dawson, K. Caputa M.A. Stuchly
0920	Faster Than Fourier -- Ultra-Efficient Time-to-Frequency Domain Conversions for FDTD Applied to Bioelectromagnetic Dosimetry	C.M. Furse
0940	Modelling of Antennas in Close Proximity to Biological Tissues Using the TLM Method	J. Paul, C. Christopoulos D.W.P. Thomas
1000	**BREAK**	

SESSION 8: ADVANCES IN PERFECTLY MATCHED LAYERS (PML) (Parallel with Sessions 5, 6, & 7)
Chair: Weng Cho Chew, Co-Chair: Qing Huo Liu

1020	Conformal Perfectly Matched Layer	F.L. Teixeira & W.C. Chew
1040	Stability Analysis of Cartesian, Cylindrical and Spherical Perfectly Matched Layers	F.L. Teixeira & W.C. Chew
1100	A Unified Approach to PML Absorbing Media	D.H. Werner & R. Mittra
1120	Comparison of the Performance of the PML and the Liao Absorbing Boundary Formulation	M. Vall-llossera, C.W. Trueman
1140	A Uniaxial PML Implementation for a Fourth Order Dispersion-Optimized FDTD Scheme	G. Haussmann & M. Piket-May
1200	**LUNCH**	

WEDNESDAY AFTERNOON 18 MARCH 1998

SESSION 9: VISUALIZATION IN CEM (Parallel with Sessions 10, 11 & 12))
Chair: Janice Karty (Organizer), Co-Chair: Stanley J. Kubina

1320	Plate Scattering Visualization: Images, Near Fields, Currents, and Far Field Patterns	J. Shaeffer & K. Hom
1340	Visualization Aids for Effective Aircraft Antenna Simulations	S.J. Kubina, C.W. Trueman Q. Luu, D. Gaudine
1400	Visualization of Radiation from a Spiral Antenna Using EM-ANIMATE	R.A. Pearlman, M.R. Axe J.M. Bomholdt, & J.M. Roedder
1420	Evolution of an Antenna Training Aid Using Electromagnetic Visualisation	A. Nott & D. Singh
1440	The NEC-BSC Workbench: A Companion Graphical Interface Tool	G.F. Paynter and R.J. Marhefka
1500	**BREAK**	
1520	A New Tool to Assist Use of Legacy Programs	B. Joseph, A. Paboojian, S. Woolf, E. Cohen
1540	Visual EMag: A 2-D Electromagnetic Simulator for Undergraduates	D. Garner, J. Lebaric D. Voltmer
1600	Exploring Electromagnetic Physics Using Thin-Wire Time-Domain (TWTD) Modeling	E. K. Miller

SESSION 10: ABCS FOR CEM: THEORETICAL AND IMPLEMENTATION (Parallel with Sessions 9, 11 & 12)
Chair: Peter G. Petropoulos (Organizer), Co-Chair: Omar M. Ramahi

1320	The Concurrent Complementary Operators Method for FDTD Mesh Truncation	O.M. Ramahi
1340	Accurate Boundary Treatments for Maxwell's Equations and Their Computational Complexity	T. Hagstrom, B.K. Alpert L.F. Greengard, S.I. Hariharan
1400	Perfectly Matched Layer Methods in Spherical Coordinates	B. Yang & D. Gottlieb

WEDNESDAY AFTERNOON 18 MARCH 1998

SESSION 10: ABCS FOR CEM: THEORETICAL AND IMPLEMENTATION (cont)

1420	The PML for Maxwell's Equations in Cylindrical and Spherical Coordinates	P.G. Petropoulos
1440	A Comparison of the Grote-Keller and Unsplit PML Absorbing Boundary Conditions for Maxwell's Equations in Spherical Coordinates	N.V. Kantartzis, P.G. Petropoulos, T.D. Tsiboukis
1500	**BREAK**	
1520	A Systematic Study of Three PML Absorbing Bo undary Conditions Through a Unified Formulation in Cylindrical Coordinates	J.-Q. He & Q.-H. Liu
1540	Preconditioned Generalized Minimal Residual (GMRES) Solver for Domains Truncated by Perfectly Matched Layer (PML) Absorbers	Y.Y. Botros & J.L. Volakis
1600	PML Implementation for the Battle-Lemarie Multiresolution Time-Domain Schemes	E. Tentzeris, R. Robertson L.P.B. Katehi
1620	A PML-FDTD Algorithm for General Dispersive Media	G-X Fan & Q.H. Liu

SESSION 11: CEM AND PARAMETER EXTRACTION FOR PACKAGING ANALYSIS (Parallel with Sessions 9, 10 & 12)
Chair: Emilie van Deventer (Organizer), Co-Chair: Jose E. Schutt-Aine

1320	A New Generalized De-embedding Method for Numerical Electromagnetic Analysis	Y.O. Shlepnev
1340	A Circuit Extraction Approach in PCB Power-Bus Analysis	H. Shi & J.L. Drewniak
1400	Modeling of Conductor and Dielectric Losses in Packages	J. Poltz
1420	Extraction of Effective Capacitance and Inductance of a Power Distribution Structure from Numerical Field Data	A. Byers, B. Boots M. Piket-May, & R. Gravrok
1440	Extraction of Equivalent Circuit Parameters of Interconnections Using FDTD and PML	F. Liu & J.E. Schutt-Aine
1500	**BREAK**	

SESSION 12: REDUCED-ORDER MODELING IN ELECTROMAGNETICS (Parallel with Sessions 9, 10 & 11)
Chair: Andreas C. Cangellaris, Co-Chair: R.F. Remis

1520	The Use of a Correspondence Principle in Reduced-Order Modeling of Electromagnetic Wave Fields	R.F. Remis P.M. van den Berg
1540	The Spectral Lanczos Decomposition Method for Efficient Time-Domain and Frequency-Domain Finite-Element Solution of Maxwell's Equations	M. Zunoubi, J-M. Jin K. Donepudi, & W.C. Chew
1600	Passivity of Discrete Electromagnetic Systems	M. Zunoubi, J.-M. Jin A.C. Cangellaris & L. Zhao
1620	Rational Krylov Reduced Order Modeling of Multiscreen Frequency Selective Surfaces - **- STUDENT PAPER CONTEST -**	D.S. Welle, E. Michielssen K. Gallivan

WEDNESDAY EVENING 18 MARCH 1998

1830	**NO HOST BAR**	**Terrace Room, Herrmann Hall**
1930	**AWARDS BANQUET**	**La Novia Room, Herrmann Hall**

THURSDAY MORNING 19 MARCH 1998

0730 - 0800	**CONTINENTAL BREAKFAST**	**Glasgow Courtyard**
SESSION 13:	**FINITE ELEMENT METHOD (Parallel with Sessions 14, 15 & 16)** Chair: John R. Brauer, Co-Chair: Jin-Fa Lee	
0820	Comparing High Order Vector Basis Functions	J.S. Savage
0840	Mesh Refinement for Hybrid FEM in the Analysis of Printed Antennas and Arrays	J. Gong, D. Bernstein S. Wedge
0900	A Novel, Efficient Algorithm for Scattering from a Complex BOR Using Vector FEM and PML -- **STUDENT PAPER CONTEST--**	A.D. Greenwood & J-M. Jin
0920	Homogenized Finite Element Model of a Beam Waveguide Resonator Antenna with Over One Hundred Coupling Holes	J.R. Brauer
0940	A Surface Admittance Formulation for the Transient Modeling of Skin Effect and Eddy Current Problems - **STUDENT PAPER CONTEST** -	K.N. Wassef & A.F. Peterson
1000	**BREAK**	
1020	Verification of Eddy Current Analysis of Engineering Oriented Loss Model (Problem 21) Sugiyama	N. Takahashi, K. Fujiwara, K. J. Takehara
1040	Jacobi-Davidson Algorithm for Modeling Open Domain Lossy Cavities	C. Liu & J-F Lee
1100	Analysis of Electromagnetic Penetration Through Apertures of Shielded Enclosure Using Finite Element Method	B-W. Kim, .-C. Chung T-W. Kang
1120	hp-Adaptive Edge Finite Elements for Maxwell's Equations	L. Demkowicz, L. Vardapetyan W. Rachowicz
1200	**LUNCH**	
SESSION 14:	**RECENT ADVANCES IN TIME-DOMAIN TECHNIQUES (Parallel with Sessions 13, 15 & 16)** Chair: Douglas C. Blake, Co-Chair: Douglas J. Riley	
0820	An Analysis of Programming Models for Time-Domain CEM Codes on RISC-Based Computers	D.C. Blake & J.S. Shang
0840	The VOLMAX Transient Electromagnetic Modeling System, Including Sub-Cell Slots and Wires on Random Non-Orthogonal Cells	D.J. Riley & C.D. Turner
0900	Using the Finite Integration Time Domain Technique at Low Frequencies	R. Ehmann & T. Weiland
0920	Modelling Dispersive Media Using the Finite Integration Technique	S. Gutschling, H. Kruger, T. Weiland
0940	Transient Analysis of Thin Wire Antennas Mounted on Three-Dimensional Perfectly Conducting Bodies	K. Aygun, A.A. Ergin, B. Shanker S.E. Fisher E. Michielssen
1000	**BREAK**	
1020	A PSTD Algorithm in Cylindrical Coordinates	Q.H. Liu & J. Q. He
1040	On the PSTD Method for Large-Scale Problems	Q.H. Liu
1100	Pseudospectral Time-Domain Modeling of Diffractive Optical Elements	J.S. Hesthaven, P.G. Dinesen J.P. Lynov
1120	Transient Analysis of Acoustic Scattering Using Marching-on-in-Time with Plane Wave Time Domain Algorithm	A.A Ergin, B. Shanker K. Aygun, & E. Michielssen
1140	A Two Level Plane Wave Time Domain Algorithm for Fast Analysis of Transient Electromagnetic Scattering	B. Shanker, A.A. Ergin K. Ayugun, & E. Michielssen
1200	**LUNCH**	

THURSDAY MORNING 19 MARCH 1998

SESSION 15: **EMI/EMC (Parallel with Sessions 13,14 & 16)**
Chair: Todd Hubing (Organizer), Co-Chair: Bruce Archambeault

0820	EMC Modeling of Shielded Enclosures with Apertures and Attached Wires in a Real-World Environment	B. Archambeault, K. Chamberlin O. Ramahi
0840	Proposed Standard EMI Modeling Problems for Evaluating Tools which Predict Shielding Effectiveness of Metal Enclosures	B. Archambeault & O. Ramahi
0900	A Study In the Proper Design of Grounding for SMPS Converters and the Role of CEM	R. Perez
0920	Expert System Algorithms for EMC Analysis	T. Hubing, N. Kashyap J. Drewniak, T. Van Doren R. DuBroff
0940	The Electromagnetic Comatibility Characteristics of Buildings In Mobile Radio Waves Propagation Channel	Y. Miyazaki & P. Selormey
1000	**BREAK**	

SESSION 16: **HYBRID TECHNIQUES (Parallel with Sessions 13, 14 & 15)**
Chair: Ulrich Jakobus, Co-Chair: William D. Wood, Jr.

1020	Extension of the MoM/PO Hybrid Technique to Homogeneous Dielectric Bodies	U. Jakobus
1040	EMAP5: A 3D Hybrid FEM/MoM Code	Y. Ji & T. Hubing
1100	Iterative Coupling of MoM and MMP for the Analysis of Metallic Structures Radiating in the Presence of Dielectric Bodies	H-O. Ruoss, U. Jakobus F.M. Landstorfer
1120	A Hybrid Algorithm for Frequency Selective Surface Analysis	M.J. Walker
1140	Generalized Networks for Waveguide Step Discontinuities	M. Mongiardo, P. Russer M. Dionigi & L.B. Felsen
1200	**LUNCH**	

THURSDAY AFTERNOON 19 MARCH 1998

SESSION 17: **SIGNAL PROCESSING TECHNIQUES IN CEM (Parallel with Sessions 18, 19 & 20)**
Chair: Douglas H. Werner (Organizer), Co-Chair: Ping L. Werner (Co-Organizer)

1320	Using Windowed, Adaptive Sampling to Minimize the Number of Field Values Needed to Estimate Radiation and Scattering Patterns	E.K. Miller
1340	Spectral Domain Interpolation of Antenna Radiation Patterns Using Model-Based Parameter Estimation and Genetic Algorithms	R.J. Allard, D.H. Werner J.S. Zmyslo, & P.L. Werner
1400	An Accurate Algorithm for Nonuniform Fast Fourier Transforms (NUFFT) and Its Applications	Q.H. Liu & N. Nguyen
1420	A Subspace Approach to Fast Moment Method Scattering Predictions over Limited Sectors	J. Stach
1440	Application of Biorthogonal B-Spline-Wavelets to Telegrapher's Equations	M. Aidam & P. Russer
1500	**BREAK**	
1520	NEC Acceleration by the Wavelet Matrix Transform	Y.H. Lee & Y. Lu
1540	Adaptive Segmentation Algorithms for Optimal NEC Modelling of Wire-Grid Structures	Y.H. Lee & Y. Lu

SESSION 18: **HF-UHF PRACTICAL ANTENNA TOPICS (Parallel with Sessions 17, 19 & 20)**
Chair: W. Perry Wheless, Jr. (Organizer), Co-Chair: Nathan Cohen

1320	Comparison of Shipboard HF Transmit Fan Characteristics: NEC versus Scale-Model Measurements	K. Lysiak & P. Dombowsky
1340	NEC Model Results for Shipboard Shielded Crossed Loop Antennas with Scale-Model Range Data	K. Lysiak

THURSDAY AFTERNOON 19 MARCH 1998

SESSION 18: HF-UHF PRACTICAL ANTENNA TOPICS (cont)

1400	A Near-Earth and Buried HF Antenna Computer Modeling Program	W.P Wheless, Jr. & L.T. Wurtz
1420	Empirical and Numerical Treatment of Electromagnetic Pulse Induced Currents	M.J. Packer
1440	Advantages of an Alternate Viewpoint when Designing HF Verticals for 80 and 160 m	R. Severns
1500	**BREAK**	
1520	Tower Equivalent Radius	W.F. Cummins
1540	Simple CP Fractal Loop Array with Parasitic	N. Cohen
1600	NEC4 Analysis of a Fractalized Monofilar Helix in an Axial Mode	N. Cohen
1620	Design of Low Sidelobe Antennas	R.W. Hecht
1640	EMP Simulation of Near Field Enhancement of Wire Antenna	M. El Hachemi, C. Tosser-Roussey A. Tosser-Roosey

SESSION 19: OPTIMIZATION TECHNIQUES FOR ELECTROMAGNETICS (Parallel with Sessions 17, 18 & 20)
Chair: Eric Michielssen (Organizer), Co-Chair: Randy L. Haupt (Co-Organizer)

1320	Genetic Algorithm Design of the Conical Interdigitated Log-Periodic Antenna	P.D. Mannikko, P.J. O'Brien K.W. Ommodt
1340	A Comparison of Simple and Complex Genetic Algorithms in Wire Antenna Design	B.S. Sandlin & A.J. Terzuoli
1400	Array Failure Correction with a Genetic Algorithm	B. Beng, K. Yeo & Y. Lu
1420	Backscattering Synthesis From Tapered Resistive Grids	R.L. Haupt
1440	Obtaining Linear and Circular Apertures with Smooth Amplitude Distributions and High Efficiency	J.A. Rodriguez & F. Ares
1500	**BREAK**	

SESSION 20: INTEGRAL EQUATION METHODS AND ERROR CONTROL (Parallel with Sessions 17, 18, & 19)
Chair: Goran Eriksson, Co-Chair: C. Y. Shen

1520	Force Calculations and Error Estimates with Boundary Element Methods	K. Davey & D. Zheng
1540	Use of Residual Error Bounds to Obtain Stable Numerical Solutions of a Fredholm Integral Equation of the First Kind	T. Schwengler & E.F. Kuester
1600	Eigenvalue Studies of Matrices Resulting from EFIE Simulations for Planar Structures	J.M. Dunn & H. MacMillan
1620	Iterative Solution of Dense Linear Systems in Electromagnetic Scattering Calculations	J. Rahola
1640	EMCP2 A Parallel Boundary Element Software Package Using a Novel Parameterisation Technique	G. Eriksson & U. Thibblin

FRIDAY 20 MARCH 1998 FULL-DAY SHORT COURSES

0830 - 1630 "Practical Genetic Algorithms," Randy L. Haupt, University of Nevada, Reno, Reno, NV. **Full - day course**

0830 - 1630. "Application of the Finite-Difference Time-Domain Method to Simulation of Electromagnetic Coupling to the Human Body," Cynthia Furse, Utah State University, Logan, UT. **Full - day course**

0830 - 1630 "Using Mathematical Software (MATHCAD and MATLAB) for Computational Electromagnetics," Jovan Lebaric, Naval Postgraduate School, Monterey, CA. **Full day - course**

SESSION 1:

CEM ANALYSIS AND APPLICATION WITHIN AN ENGINEERING ENVIRONMENT

Chair:K.R. Siarkiewicz and D.R. Pflug

Frameworks—Future Paradigm for CEM Analysis

Kenneth R. Siarkiewicz
Air Force Research Laboratory/IFSB
525 Brooks Road
Rome New York 13441-4505
kens@rl.af.mil

The AF, DoD in general, and the civilian sector, are placing increasing emphasis on the use of modeling and simulation (M&S) in the design, acquisition, and performance evaluation of their various products. Product can be defined as a device, a board, a module, a subsystem (e.g., communications), or a system (e.g., F16). The concept of a product model includes not only the physical characteristics of the product, but also the processes associated with its manufacture and operation. For completeness there must also be included the environment in which it will operate and a consideration of its interaction with and relationship to other products.

Because of this increased emphasis the topics of M&S frameworks and product databases are seeing greater emphasis. A framework can be thought of as an environment in which a particular simulation is executed in concert with a number of other simulations. The framework establishes a set of specifications for the execution of the simulation, specifications for input/output data management, and a run-time infrastructure to coordinate and facilitate the execution of the individual simulations and management of the data.

A common example of a framework is the operating system of a personal computer. Microsoft, for example, has the Windows operating system. It has defined a set of rules for application programs, such as word processors and games. As long as these applications meet the specifications, the user can easily install and successfully execute the applications. The operating system, or framework, works invisibly behind the scenes to allow a particular application to run while others are also executing. The activities are coordinated. Data are managed, and the user concentrates on his or her work.

In addition, Microsoft and other companies have developed and marketed utilities to facilitate program development to meet the specifications, such as GUI builders and Wizards which generate the user interface for execution or assist the user in performing various tasks within the application.

In the same way the DoD and the Services are developing M&S frameworks to accomplish a broad variety of collaborated simulations. DARPA is in the final year of a five-year effort to develop a Simulation Based Design (SBD) environment. Its objective is to develop and demonstrate the concept of Virtual Prototyping in order to exploit the cost and time saving benefits of simulation technology in the design of complex mechanical systems An overview can be found at http://www.arpa.mil/asto/SBD/sbd.html.

The Defense Modeling and Simulation Office (DMSO) is developing a High-Level Architecture (HLA) scheme to establish a common technical framework to facilitate the interoperability of all types of models and simulations among themselves and with C4I systems, as well as to facilitate the reuse of M&S components. The overall DMSO program encompasses M&S specifications, object model definitions, and a run-time infrastructure (RTI) to coordinate the execution of the multiple simulations. Further details can be found on the Web at http://hla.dmso.mil/.

On a somewhat smaller scale, but tying into HLA and product/process models, AFRL at Rome has been developing a framework called the Integrated Computational Environment (ICE) [1-3]. As pointed out in these papers, the models and codes of the CEM community must be designed or retrofitted to work in such an environment in order to make the wealth of highly accurate and sophisticated data available to the higher-level and more-encompassing simulations.

In some cases this has been accomplished on a local scale. Companies are in the process of tying CEM model development to company-based drawing packages in order to start from the current structural and mechanical design of a product. There may also be an interface to other analysis packages, such as thermal and aerodynamic. However, the link to the broader DoD community or civilian sector is lacking. The interface among the members of a team of contractors working on the design and development of a product is difficult and prone to error or misunderstanding.

INTEGRATED COMPUTATIONAL ENVIRONMENT

For all the CEM community the ICE is meant to be a generic framework to link model development to drawing packages, and the CEM analysis domain to the analyses codes of other engineering disciplines [1]. It is also a framework to interface a number of different CEM formulations which may be required to completely characterize the product. The CEM data model [4] is a key element for model development and data re-use, and it serves as a link across formulations and different implementations of the same formulation (e.g. NEC-MOM and GEMACS-MOM).

Many elements are currently coming together within ICE to bring CEM into the realm of concurrent engineering. Figure 1 shows the time-line development of ICE.

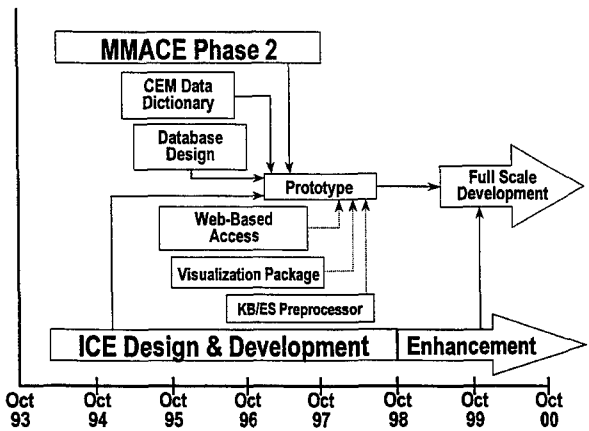

Figure 1. ICE Development Timeline

The Microwave and Millimeter-Wave Advanced Computational Environment (MMACE) is a Naval Research Laboratory (NRL) funded program under the Vacuum Electronics Initiative. Its objective is to develop a design and analysis environment for small project teams working on the design, development and manufacturing of high-power microwave tubes. Version 3 of the MMACE suite of tools consisting of a framework and a number of design tools and utilities has been distributed and is being used by the industry.

The framework provides many of the capabilities now in place in ICE, including an extremely flexible Control Panel, Application Programmer Interfaces (API) for database, distributed processing, geometry and meshing interfaces. Code and file wrapping tools are included to interface user codes with the framework and data between the codes and the product database. Support software for data model development and read/write access is included. The system contains a suite of data visualization, meshing, and framework administration utilities. The MMACE framework has been described previously [5]. It runs on Sun and HP workstations. It is designed to allow the user to interface local design and analysis tools, drawing packages, meshers, and database managers.

AFRL at Rome has funded the modification and the port of the MMACE framework to a Windows 95/NT environment. The user is able to describe the design process locally and spawn jobs remotely on high performance computers to execute the analysis. Output data is returned for post-processing and display. Input and output data storage can be accomplished locally and for transferred to a remotely located product database.

Figure 2 shows the ICE Control Panel. It is readily seen that the "look and feel" are exactly those of most Windows applications. Pull-down and tear-off menus contain and perform functions identical to many common office-oriented applications. Icons are provided with descriptions in the status bar as an alternative means to execute common functions.

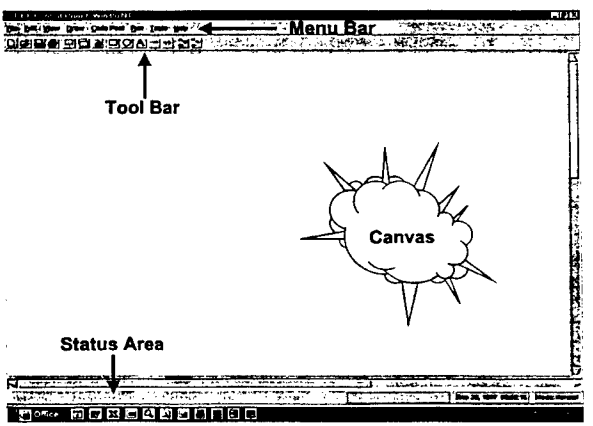

Figure 2. ICE Control Panel

The code pool menu provides access to the various engineering tools that the user has interfaced with the Control Panel. Clicking on a tool name places its icon on the Canvas Area. Double-clicking the icon brings up its properties box (see Figure 3), which shows the location of the executable and the identification of its input and output data files. Several of these analysis codes can be strung together to form an automated or turn-key design process. An example of such a process is shown in Figure 4.

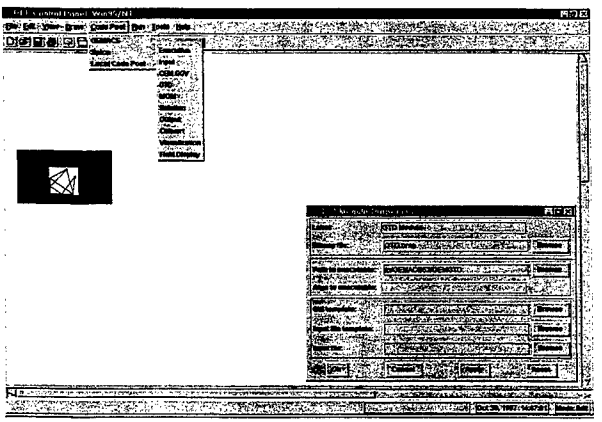

Figure 3. Code Pool Menu and Properties Box

ICE relies on the already developed CEM data dictionary [4]. This dictionary provides access to and re-use of CEM data stored in the product database and shared among many different CEM formulations and code implementations of the same formulation. An example is shown in Figure 4.

Figure 4 also shows that the CEM analysis tools can be interfaced with others to iteratively determine the effects of such phenomena as structural warping (e.g. for conformal antennas) and thermal expansion (e.g., patch antenna heating). Thus a structure can be defined with an embedded patch array, excited, and analyzed for antenna performance in the presence of the structure. Terminal currents cause heating which slightly deform the patch. High altitude flight can cause thermal contraction. Thermal analysis can be used to determine the resulting shapes which can then be re-meshed for further CEM analysis. The loop can be repeated a user-specified number of times. In this way high performance antennas can be analyzed with greater resolution of peak and null depths and widths and higher degrees of accuracy. This is critical for the more demanding air and spacecraft applications.

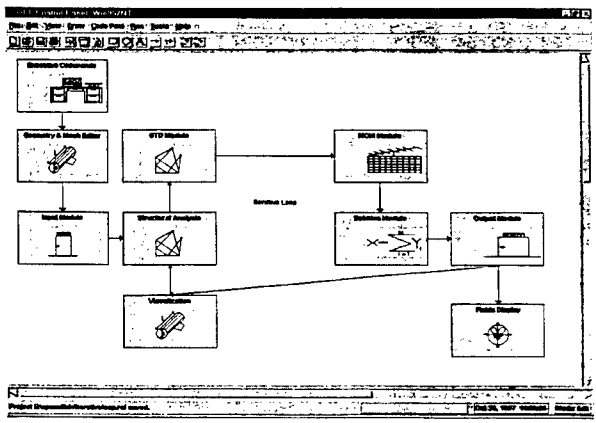

Figure 4. Sample Design Process

Other developments are in progress which will enhance the use of the ICE. A web-based access is now available [6]. At the present time the GEMACS can be accessed on a parallel processor through the World-Wide Web. Batch jobs can be submitted via the Control Panel. A library of output data can be developed and accessed via a browser which can visually present a sample of the data and comments regarding the data. Reduced maintenance and computer transportability result from this scheme. The visual nature of the database access assures that only pertinent data are downloaded, thereby saving analyst time and connection charges.

A generic and powerful visualization package is under development [7]. It features a series of input data screens for several codes for a number of engineering disciplines. This reduces the chance for data input error and allows data input to be performed by less-experienced engineers. Output data is easily formatted and presented in a variety of ways to aid in making decisions.

Finally, on knowledge-based expert system is being designed and built to aid in the process of CEM model development 8. It is planned to extend the system to other engineering disciplines. The result will be a single, unified, consistent "look-and-feel" tool which will be used to develop efficient and internally consistent numerical computation models for use in the iterative loop shown in Figure 4.

Two other major Air Force programs will make the use of this framework and its data more viable and effective. The Collaborative Engineering Environment (CEE) [9] will be used to link the various members of the product development team. This HLA-compliant network will allow for data transfer, e-mail, and virtual meetings among engineers located across the country. This will tie the ICE to a model data repository, thereby ensuring its accessibility, longevity, and self-consistency.

The technology resulting from Air Force research and development efforts in model abstraction [10] will process low-level phenomenological data and develop derived, traceable models for use in mission planning and theater-level system performance studies. The result will be more accurate and reliable battle plan analyses made by senior staff and strategists without sacrificing simulation execution times.

Figure 5 schematically depicts the process of these last two efforts.

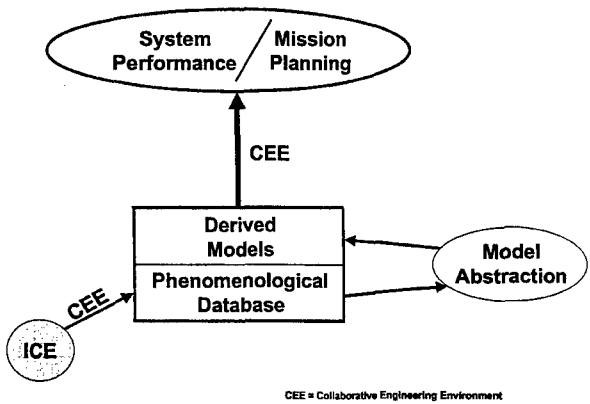

Figure 5. ICE Data Re-Used in High-Level Simulations

SUMMARY

Economics and time schedules preclude the traditional method of build-and-try. Design for both the military and civilian sectors must be accomplished and thoroughly evaluated before any parts are made or structures modified. In both sectors it is also a matter of product quality (ability to meet performance requirements), safety (flight and consumer), and manufacturability (technology availability and cost). A concurrent engineering framework in which the various engineering disciplines can work in concert is a viable and cost-effective alternative which is becoming the design process of choice.

REFERENCES

1. Capraro, Gerard and K. Siarkiewicz, "Computational Electromagnetics' Future Database Architecture," *13th Annual Review of Progress in Applied Computational Electromagnetics Conference Proceedings*, March 1997, pages 1126-1132.
2. Siarkiewicz, Kenneth, "Further Considerations Regarding the Electromagnetic Modeling and Simulation Environment for Systems (EMSES)," *10th Annual Review of Progress in Applied Computational Electromagnetics Conference Proceedings*, March 1994, pages 86-93.
3. Siarkiewicz, Kenneth, et. al., "Computational Electromagnetics Using the Research & Engineering Framework As a Backbone," *Applied Computational Electromagnetics Society Newsletter*, Volume 10, Number 3, November 1995.
4. Evans, Jeffrey, "Research & Engineering Framework (REF) Data Dictionary Specification for Computational Electromagnetics," *12th Annual Review of Progress in Applied Computational Electromagnetics Conference Proceedings*, March 1996, pages 340-346.
5. Hantman, Barry, et. al., "Research and Engineering Framework (REF) for Computational Electromagnetics." *11th Annual Review of Progress in Applied Computational Electromagnetics Conference Proceedings*, March 1995, pages 118-125.
6. Leskiw, Donald, et. al., "Web-Based High Performance Computational Electromagnetics Servers." *13th Annual Review of Progress in Applied Computational Electromagnetics Conference Proceedings*, March 1997, pages 1141-1148.
7. Joseph, Bob, et. al., "Graphical User Interface for Computational Electromagnetics Software." *13th Annual Review of Progress in Applied Computational Electromagnetics Conference Proceedings*, March 1997, pages 1149-1154.
8. Drozd, Andrew, et. al., "An Expert System Tool to Aid CEM Model Generation." *13th Annual Review of Progress in Applied Computational Electromagnetics Conference Proceedings*, March 1997, pages 1133-1140.
9. McQuay, William, *Modeling and Simulation for Collaborative Technology Development in the Air Force Research Laboratory*. Draft document dated May 1997.
10. Frantz, Frederick, *A Taxonomy of Model Abstraction Techniques*. To be found at URL http://www.rl.af.mil/Lab/IR/IR1/ModSim/ModAb/ModAb.html.

REF CEM Data Dictionary

Mr. Thomas Wharton, Mr. Jeffrey Evans
Decision-Science Applications, Inc.
1300 Floyd Ave., Bldg B
Rome, NY 13440
twharton@dsany.com, jevans@dsany.com

Background

The goal of the CEM Data Dictionary effort is to provide the Research and Engineering Framework (REF) [1] with the means to store, retrieve, and manipulate CEM data. This goal is accomplished through the development of a CEM database and a set of tools that are used to access it. This database is part of an increasing subset of databases that provide the REF with discipline specific information. The resulting database from this effort will be incorporated into an administrative database managed by the REF (see figure 1).

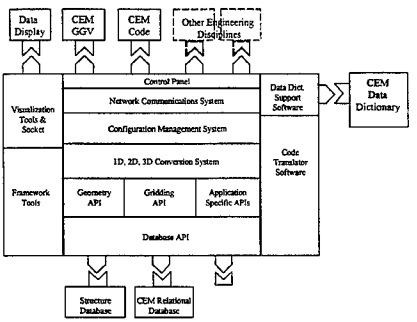

Figure 1. REF Architecture

This paper discusses the three phases of database design used to generate the current CEM database as well as the tools that provide the linkage between the database and the REF. Also addressed is the underlying concern of the generality of the resultant database and the ability to reproduce the CEM data from the database information in a form that deviates marginally from the original.

Conceptual Database Design

Two questions had to be answered from the onset of this effort. The first question is, "What should the resulting database provide to the user?" The second related question is, "What kind of information should the database contain?" The second question is easier to answer. Clearly a CEM database must include geometry elements, materials properties, excitation and observables information, however, this information must be rendered as a cohesive unit in order to provide something meaningful to the user.

This cohesive unit is called the CEM model, which is an aggregate structure composed of executive commands and geometry sets. Figure 2 displays the entity-relationship (ER)

This work was sponsored by Rome Laboratory under BAA 96-02, Contract No. F30602-97-C-0047

diagram. The CEM model is depicted as the primary entity under which other entities, and their attributes and relationships, are specified. This figure also indicates the first level of generalization made, which is that all CEM tools (such as GEMACS, NEC MoM, CARLOS3D, etc.) utilize execution commands and geometry data commands.

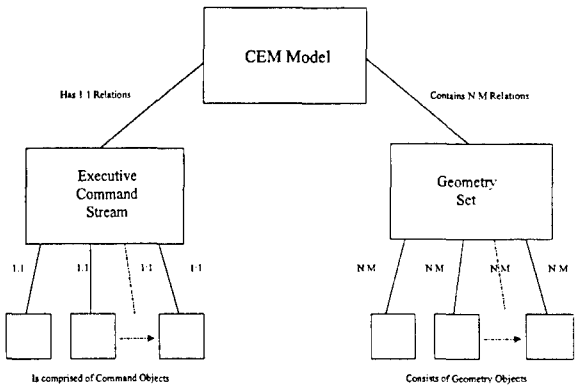

Figure 2 CEM Entity Relationship Diagram

Logical Database Design

From the ER diagram, the CEM data dictionary (DD) can be derived. A data dictionary is a catalog that thoroughly details all the entities, their attributes, and relationships [6]. The current CEM DD has evolved from its original conception and user documentation will detail all the changes.

The changes instituted reflect the desire to generalize the database such that information from a wide variety of CEM tools can be accommodated. An example of a DD generalization is the Surface Object that a CEM tool might use as a patch, plate, or facet. Each of these geometry elements share a certain level of commonality. The Surface Object reduces redundancy by combining those objects into a common divisor. The result may appear less intuitive, but contains all the information necessary to recreate the actual object it represents. This allows existing CEM codes to readily use the DD generic templates, while making it possible for future codes to expand on them.

Certain caveats were applied at this stage as they became apparent:

1. A CEM model must have one command stream.
2. A command stream can belong to one, and only one, CEM model.
3. A CEM model must have at least one region (an element within a geometry set).
4. A region must belong to at least one CEM model.
5. A command stream is composed of one or more commands.
6. A command belongs to one, and only one, command stream.
7. A region must be made up of at least one geometry component.
8. A geometry component must belong to only one region.

From this list of business rules, it is clear that the command stream is tightly bound to the CEM model entity, whereas the region (or geometry set) is loosely coupled. This allows regions to be reused in other models without reiterating the data. Executive commands are bound to the command stream, hence the model, indicating that a CEM model is defined largely by the commands that are invoked on the geometry. From the users stand point, geometry has many applications, but executive commands relate to only one geometry set.

Physical Database Design

The CEM database was implemented using Microsoft Access. The physical schema, shown in figure 3 as an Access relational view, was derived from the DD. The current schema underwent several transformations as the CEM project evolved. The primary table, tblobjMaster, serves to store the CEM model and is the entry point into the database.

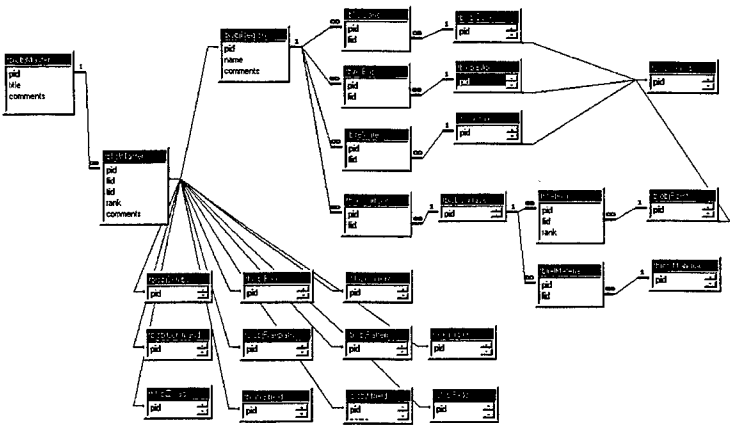

Figure 3 CEM Relations Figure (MS Access)

Originally, a relational table was created between tblobjMaster and every other table that represented an executive command. This was to allow many-to-many relationships and support referential integrity. However, when it became apparent that data entered into the database might have a specific ordering, this schema proved to be too tedious to maintain. (When recalling data from the database you would not want to reference a field source before it was defined.)

To ameliorate this problem a single relational table, called tblrelMaster, was created to link tblobjMaster to each other table. tblrelMaster contains a primary key made up of three fields. The first field stores the primary key of the CEM model, linking in tblobjMaster. The second field stores the primary key from another table that the third field of tblrelMaster defines. Though perhaps not as elegant as the original, this allows the fourth field of tblrelMaster, called rank, to be used to reconstruct the CEM information in the order it was entered.

To insure the generic nature of the database, certain tables had to be constructed and the domain types of other tables required modification. For example:

1. tblobjCommand was created to catch those commands that are not represented by other tables in the database. It is composed of a primary key and a text field which would hold the unknown commands' text.

2. tblobjSymbol was created specifically for GEMACS since it uses variables and expressions in its input data files. As a result, the domain types of all executive commands were converted from their previous types to text type (as appropriate) to accommodate the fact that GEMACS (and perhaps some other CEM tools) might use variables in their command stream.

Accessing the Database

The CEM database is accessed through the REF by three tools that provide the means to take application specific CEM data, convert it into a data dictionary compliant format (DDCF), and either insert it into or extract it from the database. Figure 4 depicts this process as it begins from and returns to the REF.

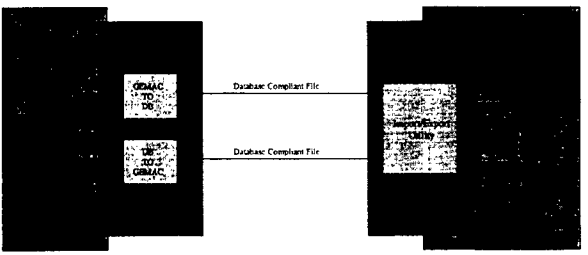

Figure 4 Data Flow between REF and CEM Database

Current CEM tools have their own syntax for executive and geometry commands through which analyses are accomplished. Though future tools can use the CEM data dictionary to support direct connectivity to the database, current tools require an intermediary to transform their specific syntax into a DDCF. Two methods of producing the DDCF were considered:

1. Wrappering – a method whereby the CEM tool is enveloped in another code which directs and/or processes input and output to the CEM tool. This method requires a great deal of developmental overhead in order to produce one wrapper specific to one CEM tool. Changes made to the CEM tool could easily translate to many manhours spent modifying the wrapper (even to simply maintain functionality).

2. Translating – a method whereby an application would be developed that is independent of the CEM tool and simply converts the tools input data files into a DDCF. The CEM tool is free to evolve without seriously jeopardizing the utility of the translator.

This latter method was adopted, and a pair of translators were developed for the GEMACS tool. Available to the REF through its control panel, one translator (GEMTODB) converts a GEMACS input data file into DDCF. This file can then, through the REF, be inserted and subsequently extracted from the database. The second translator (DBTOGEM) can then be called to reproduce the original input data file in functionally the same form as the original.

Both applications were written in C++ and are designed to serve as templates to produce additional translators for other CEM tools.

Aside from the translators, another tool was required to access the database. A Visual Basic application (DBTRANS) allows the REF to insert into and extract data from the CEM database. Input data files, converted to DDCF by a translator, can be placed within the database by invoking DBTRANS from the REF control panel.

When inserting data, DBTRANS prompts the user for a file name. Through the use of insertion queries, it places the data from the specified file into the table structure of the database and creates the necessary links between tables (from the CEM model, to the geometry, to the executive commands.) After successful insertion, a dialog box prompts the user that the operation is complete.

Figure 5 shows the display, as it appears in the REF, which is used to extract a CEM model from the database. When extracting data, DBTRANS prompts the user to click on the title of the CEM model desired. Once the model is selected, the user is prompted to enter a file name under which the data will be saved. Data is then gathered by selection queries which trace through the relationships of the model. The resulting information is then saved to the specified file. Upon successful extraction, a dialog box prompts the user that the operation is complete.

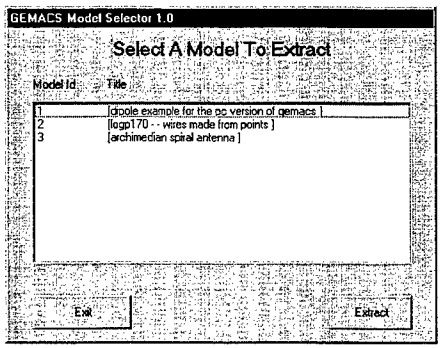

Figure 5 CEM Database Model Extraction

Specific consideration was given to ensure that not only the ordering of the commands is preserved (through tblrelMaster), but also the ordering of components within the commands (i.e., a plate is composed of a series of ordered points so that an outward normal can be produced). This application also removes redundant information (i.e., points which are common to multiple plates are referenced by those plates as opposed to creating duplicate points for each plate).

Future Plans

Future effort will go towards refining the CEM data dictionary and developing tools in the CEM database that will make administration of CEM models plausible. Facilities will be made available to edit and query data from within the database, as well as provide reports on the information therein. Finally, the CEM database may also be used as a template for the creation of other discipline specific databases.

References

[1] Date, C. J., "An Introduction to Database Systems Volume 1, Fourth Edition", Addison-Wesley Publishing Company, Reading MA, 1986.

[2] E.L. Coffey, D.L. Kadlec, General Electromagnetic Model for the Analysis of Complex Systems (GEMACS), Version 5.0, Advanced Electromagnetics, RADC-TR-90-360, Volumes I, II and III, Dec 1990.

[3] E.L. Coffey, D.L. Kadlec, GEMACS Source Book, Advanced Electromagnetics, RADC-TR-87-102, February 1988.

[4] Evans, J. A., "REF Data Dictionary Specification for Computational Electromagnetics", Applied Computational Electromagnetics Society 11th Annual Review of Progress in applied Electromagnetics, p126, March 1996.

[5] Evans, J. A., "REF Data Dictionary Specification for Computational Electromagnetics", Applied Computational Electromagnetics Society 11th Annual Review of Progress in applied Electromagnetics, p126, March 1995.

[6] Evans, J. A., "REF Data Dictionary Specification for Computational Electromagnetics", RL-TR-96-263 Final Technical Report, April 1997.

[7] Hantman Barry, Research & Engineering Framework (REF): MMACE Summary Document, Draft B, March 1996.

[8] Marhefka, R. J., Burnside, W. D., "Numerical Electromagnetic Code (NEC) - Basic Scattering Code (Version 2)," Part I: User's Manual, Technical Report 712242-14, The Ohio State University ElectroScience Laboratory, Columbus; prepared under Contract N00123-79-C-1469 for Naval Regional Contracting Office, December 1982.

Air Force Research & Engineering Framework Control Panel

David M. Hallatt and Jeffrey A. Evans
Decision-Science Applications, Inc.
1300 Floyd Ave.
Rome, NY 13440
dhallatt@dsany.com, jevans@dsany.com

The Research & Engineering Framework (REF) Control Panel is a Graphical User Interface designed to provide a common integrated environment which allows the user to have a standardized method for accessing and analyzing data. The REF Control Panel, originally written in Python for the UNIX operating system, has been ported to a Windows 95/NT based platform and modified to have the look and feel of a standard Windows program.

The REF Control Panel provides the user with a canvas area to build projects. The projects are created using customizable icons that provide access to any application on the host computer. These icons, once created, can then be saved to a local code pool to be used multiple times. When the user has added and positioned the icons on the Control Panel's canvas they can then be connected, thus allowing control over the flow of execution of the icons. Once all desired connections are made the project can be stored to disk for repeated use.

The REF Control Panel also provides standard icons that can be edited for use in projects, eliminating the need to search for the program path and icon bitmap. Standard Windows accessories, such as the calculator, and text editor, have been added to the code pool to aid in the creation of a project. A new version of the scriptwriter has been added that utilizes the advantages of the Windows environment.

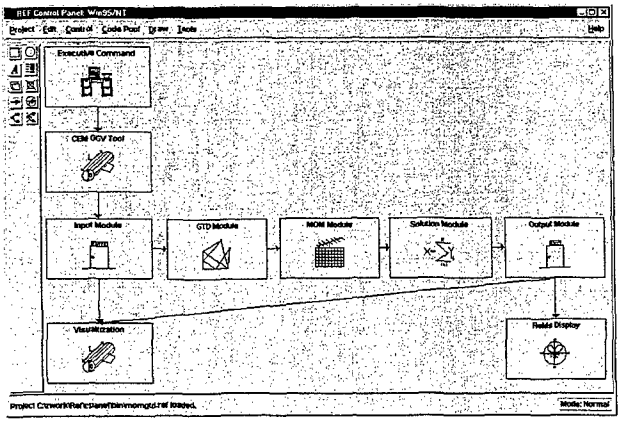

Figure 1. MMACE Control Panel

This work was sponsored by Rome Laboratory under BAA 96-02, Contract No. F30602-97-C-0047

Figure 1 shows the Control Panel as it was created for the MMACE. The functionality of the control panel was satisfactory and therefore the core portion of the Control Panel was retained. The goal for the Air Force Research & Engineering Framework (AFREF) Control Panel was to have it operate on a Windows 95/NT based platform. The REF CEM Database was being developed using the Microsoft Access relational database management system on Windows 95 and could be directly used in the a Control Panel resident on the Windows Platform. The conversion of the existing MMACE Control Panel, written in Python on a UNIX platform, was accomplished with little difficulty due to the fact that version of the Python interpreter had been created for the Windows platform. The major changes were to swap "\" for "/" within the source code to account for the difference in disk drive path name separators.

Once the move to the Windows platform was complete, the next step was to have the Control Panel conform more to the standard look and feel of a native Windows application. The necessary changes were made and the resulting control panel was the REF Control Panel, as seen in Figure 2.

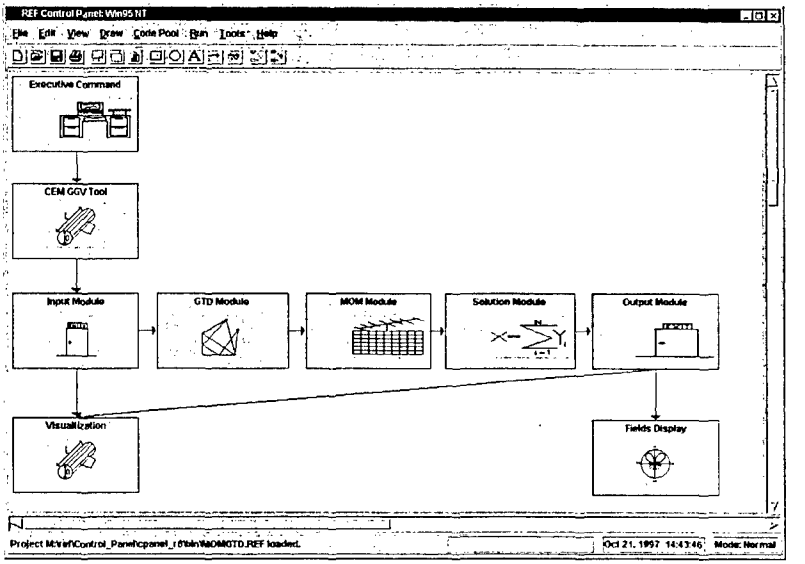

Figure 2. REF Control Panel

The modifications to the REF Control Panel can be divided into four major component areas, the menubar, the toolbar, the canvas and the statusbar. The major visual differences can be seen in Figure 2. The menubar's options have all been packed to the left and the toolbar has been moved to just below the menubar, thus giving the REF Control Panel more of a Windows look. The other changes are not as immediately visible but provide the program with the standard feel of a windows program. These changes are described in more detail in the following sections.

Menubar

Changes were made to the menubar in order to provide more familiar Windows menu options, such as File instead of Project and Run instead of Control. Also, other menu options were added. The View menu option allows the user to change the look of the Control Panel. Other Code Pool options and Tools were added to enhance the overall functionality of the Control Panel.

These menus follow standard Windows logic. For example, when a menu option does not apply, such as deleting an icon when there are no icons selected, the appropriate menu options are grayed out and cannot be selected. Figure 3 shows the complete layout of the menu structure. Indented items indicate submenus below the main menu item.

File	Edit	View	Draw	Code Pool	Run	Tools	Help
New	Copy	Tool Bar	Rectangle	GEMACS	Start	Scripts	Control Panel
Open	Delete	Script Area	Circle	Executive	Stop	Converter	Code Pool
Save	Properties	Status Bar	Label	Input	Reset	GEMACS to DB	GEMACS
Save As		Drag Update	Connect	CEM GGV		DB to GEMACS	Spice
Revert			Disconnect	GTD		Spice to DB	About REF
Print				MOM		Calculator	
Exit				Solution		Matlab	
				Output		Explorer	
				Convert		Notepad	
				Visualization		Nutmeg	
				Field Display		Database	
				Spice		TechPlot	
				Spice			
				Convert			
				Local Code Pool			
				Add			
				Show			

Figure 3. Menu Structure

Toolbar

The REF Control Panel's toolbar was updated to follow the more familiar Windows format. The toolbar was moved to the top of the window just under the menubar, and x-bitmaps were replaced with color Windows bitmaps on the toolbars buttons, as can be seen in Figure 4. Also, the familiar Windows toolbar buttons were added, such as New, Open, Save and Print.

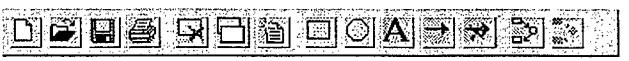

Figure 4. Toolbar

Canvas

The canvas area of the REF Control Panel is where the work is done. Each icon placed on the canvas is a process to be completed. The icons can be connected so that as one icon finishes its process

the next icon begins its processing, thus providing a graphical layout that allows for the control of the work flow. The layout of some icons and their connections can be seen in Figure 2.

Each icon has a property page associated with it. This page allows for the customization of the icon. Figure 5 is an example of a property page filled out to execute a GEMACS MOM Module. The browse buttons to the right of each text entry field were added to allow the use of standard file open dialog boxes to find the desired files and applications. This keeps the user from having to remember what can be long path names for these items and is thus an easier implementation. The first section on the property page allows for the customization of the look of the icon. The second section identifies what action the icon is to perform. The last section is used for the wrappering capability of the original REF control panel.

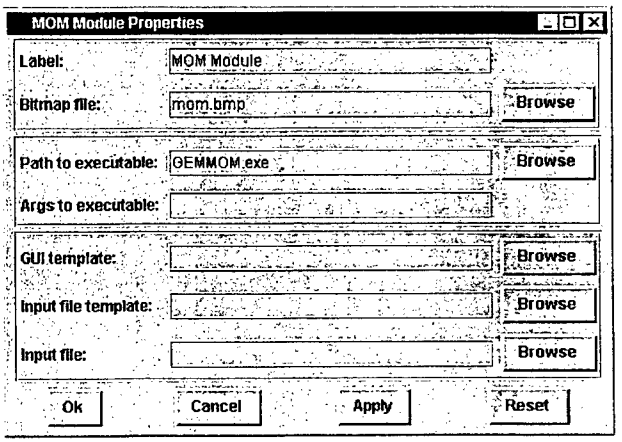

Figure 5. Icon Property Page

Some other changes made to the REF Control Panel's canvas area are shortcuts. By clicking on the canvas area with the right mouse button a user will be presented with a popup menu providing the options that are applicable at that time. Also, an icon can be double-clicked to bring up its property page. Scrollbars were also added to the canvas area to accommodate larger projects.

In the original control panel an option would be selected first and then the object to which the option was to be performed. This is backward to the way a Windows program usually works, so this was changed to allow an object (icon or label) to be selected and then the applicable option to perform is selected. If an option does not apply to the selected object, that option is grayed out and cannot be selected.

Statusbar

The REF Control Panel's statusbar provides general information about the program. As can be seen in Figure 6, from left to right the current process is displayed, the help box provides information regarding the toolbar buttons, the date and time are displayed, and the current operating mode of the Control Panel is displayed.

Figure 6. Statusbar

Future Considerations

The future outlook for the REF Control Panel would be to migrate it to a native Windows programming language. Some languages to consider would be Visual Basic, Visual C++ or Java. Currently Visual C++ would be the preferred language because of its power and widespread use. Java would also be a good choice because of its cross-platform and Internet capabilities, but the programming language is still in its infancy.

References

[1] Evans, J. A., "REF Data Dictionary Specification for Computational Electromagnetics", Applied Computational Electromagnetics Society 11th Annual Review of Progress in applied Electromagnetics, p. 126, March 1996.

[2] Evans, J. A., "REF Data Dictionary Specification for Computational Electromagnetics", Applied Computational Electromagnetics Society 11th Annual Review of Progress in applied Electromagnetics, p. 126, March 1995.

[3] Evans, J. A., "REF Data Dictionary Specification for Computational Electromagnetics", RL-TR-96-263 Final Technical Report, April 1997.

[4] Hantman Barry, Research & Engineering Framework (REF): MMACE Summary Document, Draft B, March 1996.

CONTINUED APPLICATION OF THE RESEARCH AND ENGINEERING FRAMEWORK (REF) AT RAYTHEON*

J. LaBelle[§], B. Hantman[§], H. Wright[§], Y. Chang[†], R. Abrams[‡]

Correspondence to:
Barry Hantman
Raytheon Company, Mailstop T3MR8
Tewksbury, MA 01876
Phone: (508) 858-5778
FAX: (508) 858-5976
Email: hantman@caesun.msd.ray.com

ABSTRACT

Scientific and engineering research and design codes are typically FORTRAN-based, having vastly different data structures and I/O, and unique and inconsistent user interfaces resulting in long learning curves and difficulties in usage. This is true of the codes implementing the various computational electromagnetics (CEM) and thermomechanics (TM) formulations. Manual manipulation of data from code to code is required to ensure validity of the input. Coupled with the difficulty of graphically viewing the geometry and translating it to an analysis model, the result is numerous opportunities for the introduction of human errors into the design process. This situation also adversely affects the cost (human and software/hardware) of maintaining and extending design capabilities as the theoretical foundation and design needs advance. The Research and Engineering Framework (REF) provides a coherent, integrated design environment which is the first step toward addressing the above problems. Although the REF was initially developed to address the problems of the US power tube industry, the underlying framework is open; it can accommodate a broad range of scientific and engineering disciplines, including antenna design.

During the past year, Raytheon continued development of an integrated antenna design system based on the REF. While the framework had been used elsewhere for power tube design, this was the first usage in the antenna community. Two additional design codes were integrated into the antenna design system. The system is based in part on a data dictionary developed by DSA (under contract from the Air Force Rome Laboratory). Based on the success of the application of the REF to antenna design, Raytheon proceeded to apply the REF to electro-optic design. A number of enhancements were developed to support the use of the REF in a distributed environment because of the number of electro-optic design tools are utilized on the PC platform.

Earlier papers presented at ACES and IEE CEM conferences[1-7] and an article in the ACES Newsletter[8] provided an overview of how the REF could be applied to computational electromagnetics. This paper expands on that concept to provide the results of the continued application of the REF to antenna design and electro-optic design at Raytheon Company.

* Work supported by the Naval Research Laboratory, Contract #N00014-94-C-2064, Raytheon's RESCAD IR&D Initiative and technical support from Mr. Kenneth Siarkiewicz, Rome Laboratory.
§ Permanent Address: Raytheon Co., 50 Apple Hill Dr. T3MR8, Tewksbury, MA 01876
† Permanent Address: Raytheon Co., 528 Boston Post Rd., Sudbury, MA 01776
‡ Permanent Address: Naval Research Lab., Code 6840, Washington, DC 20375-5347

BACKGROUND

The Research and Engineering Framework (REF) was developed as part of the DoD MMACE Program. The MMACE program has been underway for over five years and has just completed its second phase. The first phase, which began in 1992, was an investigation phase. Four teams were put in place to study the problems of the Microwave Power Tube industry and develop roadmaps for the implementation of a framework to address those problems. The teams found an existing design environment that: was based largely on in-house developed software; was largely unsupported by commercial vendors; did not take advantage of the latest advances in CAD, visualization, database technology, and networking; was addressing technically difficult problems; contained a collection of tools that were not well integrated with each other; and was crucial to projects deemed important to the US government. While these items were true of the power tube industry, the same can be said of many specialized scientific disciplines including antenna design and electro-optic design.

In 1994, the Air Force Rome Laboratory expressed interest in extending MMACE to accommodate the requirements of the antenna design community. The idea was to use the REF as the basis for an antenna design environment into which the various antenna codes can be inserted as shown in the following diagram.

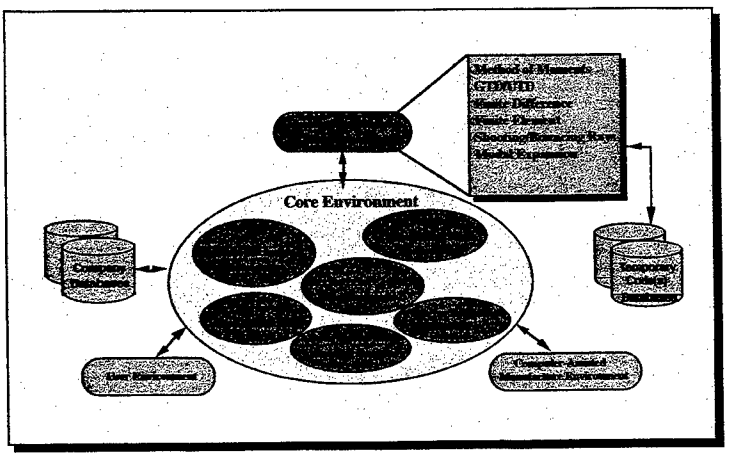

Source: EMCC Conference, 1995, K. Siarkiewicz, Rome Laboratory

While Rome Laboratory may at some point integrate many of the Air Force codes into the REF, they would not be integrating the specific, proprietary codes used within Raytheon. Therefore, Raytheon funded this activity themselves. A proof-of-principle was developed in 1996 and a full implementation is now underway.

REF ANTENNA ENVIRONMENT

During the past year Raytheon continued the integration of their antenna design tools into the REF environment. So far, four code have been integrated including the Shapebeam and Anabeam codes developed in-house and the Periodic Moment Method (PMM) code and Basic Scattering Code (BSC) developed at by Ohio State University. Utilizing some of the control panel enhancements developed at Raytheon, the antenna design process was improved as shown in the figure. Shapebeam is a recursive code, utilizing its output as the input for subsequent executions of the synthesis. The original intent was that the designer would iterate an arbitrary number of times reviewing the output of each run. After deciding which run met the desired performance criteria, the Shapebeam code would then need to run the necessary number of times to preserve the desired results. Now with the control panel enhancements, the user can use the **IF** conditional to examine the results of each iteration and exit the looping function when the desired performance criteria is met.

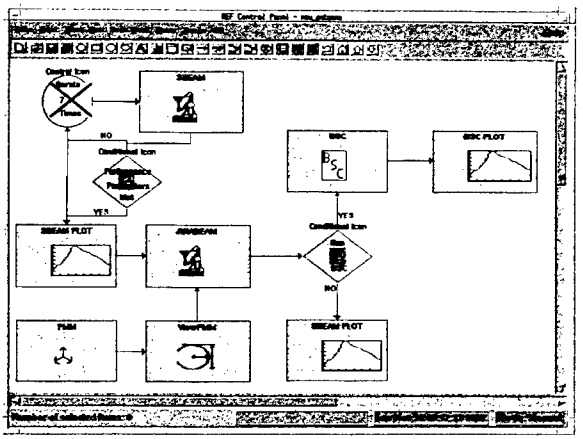

AutoCAD was included in the process to visualize the geometry of the PMM code relevant to creation of dipole and slot arrays. The dipole or slot array description is used to generate an

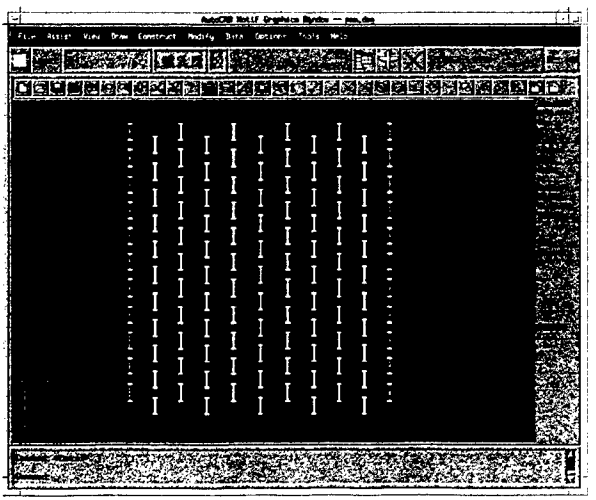

autolisp script which when loaded into AutoCAD generates the display shown right. A method for automating the process to generate the necessary photoplots from AutoCAD was developed eliminating the need for a man-in-the-loop.

Both the PMM and BSC are command driven codes which proved a challenge to wrapper. Although the wrapper software lacked the necessary capabilities to simplify the integration of these codes, they provided enough flexibility to allow us to accomplish the wrappering without having to modify the codes. We have successfully provided a GUI front end to the command language for these codes automatically generating the execution scripts for running the codes. Relevant database information used by the various commands is automatically extracted from the database by the wrappering software allowing these codes to share data. At right is pictured the initial GUI for the BSC which specifies the number of commands and individual command codes. The subsequent GUI which is automatically generated based on the choices made in the initial GUI, allows the user to edit the specific commands for the desired execution.

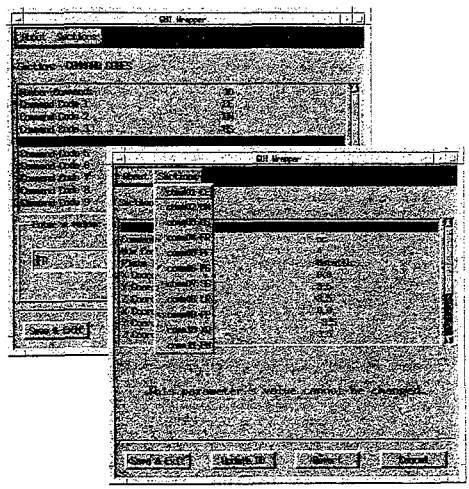

As design and analysis codes were integrated into the environment the data dictionary support software was utilized to modify the on-line data dictionary. The antenna data dictionary was developed using the data dictionary developed by DSA under contract to Rome Laboratory, as a foundation. A new version of the Data Dictionary Support Software using exclusively Python scripts makes modifying the on-line data dictionary much simpler. Now whenever a table is displayed, the field name is a link to the form for modifying the associated record. Another enhancement included in the Data Dictionary Support Software simplifies keyword searching by allowing users to search only selected sections of the data dictionary instead of searching the entire data dictionary.

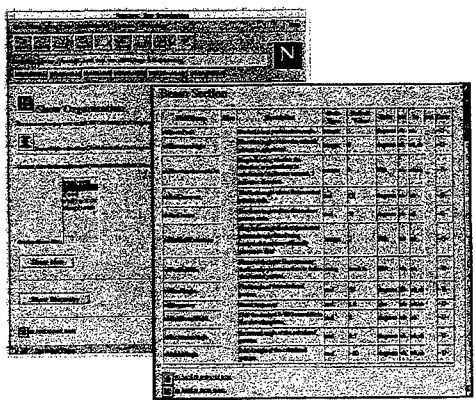

To complete the integration of the BSC we created the ability to translate the output of the BSC to NetCDF, the recommended file format for using FERRET to visualize the results of the analysis performed by the code. Now all visualization requirements are satisfied by tools included in the framework. at right are examples of the types of plots generated by the Basic Scattering Code. The plot on the right is a far zone pattern of an electric dipole located above a square plate. The plot on the left is of a slot antenna mounted in the center of a square ground plane.

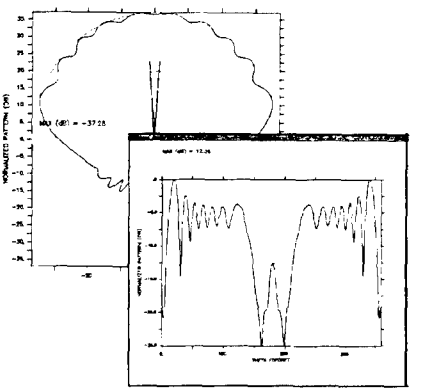

REF ELECTRO-OPTIC ENVIRONMENT

Based on the successful application of the REF to Raytheon's antenna design environment, Raytheon funded additional application of the REF for electro-optic design. Initial discussions with electro-optic designers indicated additional diversity and uniqueness in tools and methods from both antenna and power tube design. It became clear that successful application of the REF would require support of a distributed environment. The principal platform of choice by Raytheon's Electro-optics Lab is the PC. Many of the design and analysis tools utilized are PC based tools including MS Office. Preliminary models for the various components of the optics in seeker design are actually captured using Microsoft Excel.

We began investigating enabling technology in the areas of distributed computing. Since the REF was developed using Python/TK, which is available for UNIX, Windows 95/NT, and even Macintosh, we began experimenting with porting the REF control panel to the Windows environment. Before getting too involved in the port we discovered that Rome Laboratory contracted DSA to port the control panel to the PC and Windows. Rome Labs was gracious enough to share their results with Raytheon and hence expedited the Windows version of the control panel at Raytheon.

Before deciding on the initial approach to utilizing the REF in a distributed environment, we researched the world wide web for topics related to distributed computing. We discovered that a Python plugin for Netscape had been developed. If it worked, we could actually make the REF control panel web based, running within a Netscape window and simplify the launching of PC based tools from the control panel. It turned out that the Python plugin didn't work, wasn't fully tested by the developer and there wasn't enough interest in the plugin to continue to support it. Since we didn't have the knowledge to try and fix the plugin, it was shelved and another approach was investigated.

Included in the Python distribution are interface modules to TCP/IP, HTTP, CGI, and a Python server. Our WWW research even turned up a testbed for development of a Internet browser totally written in Python called GRAIL. Some examples included running Python applets within GRAIL. Python provides enough

functionality to utilize a server running on a workstation for data management and access via the Common Gateway Interface (CGI) to workstation applications while running the REF control panel on a PC. The approach requires that an X emulator, such as Hummingbird's Exceed, must be running in the background to display workstation applications locally. Since Python is a platform independent language and supports server access, we avoided having to port the entire REF to the PC. Tools available only on a UNIX workstation will continue to be run on the workstation and PC tools will continue to run locally on the PC. To support this approach it was necessary to develop the ability to both download and upload data to the server on the workstation.

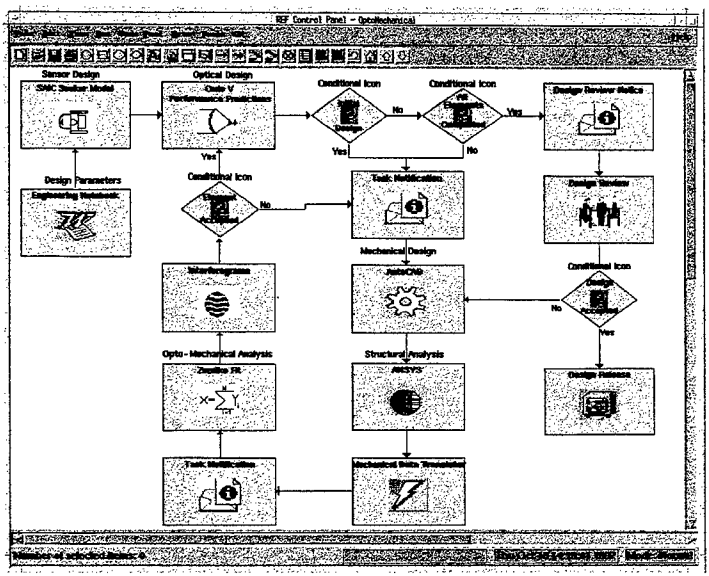

As for code integration, since the wrapper software only runs on UNIX platforms, we needed to ensure that PC tools could actually be wrappered and share data. Using an X emulator on the PC with the ability to download and upload data via an HTTP server, we can actually run the wrapper software on the UNIX workstation, download the automatically generated input file for the PC tool, launch and run the PC tool, and then upload output data from the PC tool back to the server. This approach to a distributed environment proved to be a viable solution and has been implemented to support the opto-mechanical design process shown in the figure above. In this process, the seeker model, AutoCAD, ANSYS, and the translator are UNIX based applications. The rest of the tools are PC based. In the case of CodeV and the Zernike Fit tools the wrapper software runs on the workstation, downloading the required input files to make them available for the application running on the PC. The goal is to develop similar project flows for other aspects of a seeker design such as gimble, servo, detector, and electronics design.

The opto-mechanical design flow pictured here is performed by two different labs. The Electro-Optics Lab designs the optics while the detailed mechanical design and various stress analysis is done in the Mechanical Engineering Lab. The concept behind this flow is that the REF control panel is used in both labs. When the design flow reaches a point where the design needs to be transitioned from one lab to the other, email is used to notify the other laboratory that the design is ready for them to continue with the next step in the flow. Because the design data is managed on the server side of the distributed architecture, each laboratory working on the design has transparent access to the data required for their task.

The particular program for which the application of REF to electro-optic design required the control panel to support additional controls over the design and data flow for a project. Based on these new requirements a number of enhancements have been developed.

- The connection lines indicating project and data flow have been constrained to orthogonal lines to improve the observability of the flow. Additional enhancements are being done to allow more specific definition and editing of connection lines to eliminate ambiguity in the project flow.
- A true/false branching capability has been added for additional flow control based on the evaluation of python IF statements looking at the state of database variables.
- A Pause/Continue capability has been added to allow users to pause in the middle of an executing project to perform other functions, such as CM of the design database.
- The ability to select and manipulate multiple canvas objects was added to simplify creating/editing of project flows.
- Text annotation of the canvas has been improved to allow text to be selected, edited, copied, and deleted. Previously text annotation could only be added and moved around on the canvas.
- Added the ability to undo the last canvas modification.
- Developed the ability to create, traverse, and run a project hierarchy (sub-projects).

These enhancements provide a lot more flexibility in development of not just a project flow for a particular design discipline, but allows the REF control panel to be used as a more general workflow management system.

Besides the enhancements developed by Raytheon to support the desired REF architecture and workflow control, a number of new features were incorporated by DSA as part of porting the control panel to the Windows NT environment. A majority of these features make the control panel window consistent with the appearance and behavior of most Windows applications. Included with the latest version of the Python distribution is a new imaging library and TK widget library that allows the same appearance and behavior to be incorporated in UNIX versions of the REF control Panel.

LONG TERM GOALS

The long term goals for the REF is to completely port the entire toolbox to the PC. Steps have been taken to ensure portability of various pieces of the REF such as the GUI wrapper. The GUI wrapper software included in version 3.0 of the REF was developed using X/MOTIF. To make it portable, Raytheon has converted it to Python/TK. The Data Dictionary Support Software was developed using UNIX scripting languages, Cshell and AWK along with C functions. The Data Dictionary Support Software has been re-written using Python scripts.

Raytheon will continue to research web enabling technologies in an attempt to make the REF web based. We will attempt to complete the Python plugin for Netscape and if successful, develop a distributed architecture based on running the REF control panel within Netscape or any other comparable Internet browser. The proposed architecture is intended only for an Intranet and therefore has no security requirements.

SUMMARY

Raytheon has embraced the REF for development of integrated design environments for those unique design disciplines where custom design and analysis tools are developed in house, and there is no commercial vendor to provide these tools. Raytheon has begun developing integrated design environments for antenna and electro-optic design. The scope of the design process in both arenas will be expanded over the next years to accommodate the entire design process. A third potential application for the REF at Raytheon is acoustic design.

REFERENCES

1. Siarkiewicz, K. "The Electromagnetic Modeling and Simulation Environment for Systems (EMSES)." *9th Annual Review of Progress in Applied Computational Electromagnetics Conference Proceedings*, March 1993, pages 114-121.
2. Siarkiewicz, K. "Further Considerations Regarding the Electromagnetic Modeling and Simulation Environment for Systems (EMSES)." *10th Annual Review of Progress in Applied Computational Electromagnetics Conference Proceedings*, Volume II, March 1994, pages 86-93.
3. Hantman, B et. al. "Research and Engineering Framework (REF) for Computational Electromagnetics." *11th Annual Review of Progress in Applied Computational Electromagnetics Conference Proceedings*, Volume I, March 1995, pages 118-125.
4. Woo, L. W. et. al. "Standardized Grid Generation for the Research and Engineering Framework." *11th Annual Review of Progress in Applied Computational Electromagnetics Conference Proceedings*, Volume I, March 1995, pages 135-142.
5. Woo, L. W. et. al. "Continuing Development of the Research and Engineering Framework (REF) for Computational Electromagnetics." *Proceedings of the IEE 3rd International Conference on Computation in Electromagnetics*, April 1996, pages 96-101.
6. Hantman, B. et. al. "Overview of the Research and Engineering Framework (REF) for Computational Electromagnetics." *12th Annual Review of Progress in Applied Computational Electromagnetics Conference Proceedings*.
7. LaBelle, J. et. al. "Application of the Research and Engineering Framework (REF) for Antenna Design at Raytheon" *13th Annual Review of Progress in Applied Computational Electromagnetics Conference Proceedings*.
8. Siarkiewicz, K. et. al. "Computational Electromagnetics Using the Research & Engineering Framework as a Backbone." *Applied Computational Electromagnetics Society Newsletter, Volume 10, Number 3*, November 1995.

The Innovative Research Testbed: A PC-Based High Performance Computing and Web-Based Collaboratory for Computational Electromagnetics†

Donald M. Leskiw, Grant Ingersoll, Thomas Vidoni, and Reneè Redmond

The Ultra Corporation, P.O. Box 50, University Station,
1004 E. Adams St. Syracuse, NY 13210
www.ultracorp.com

I. Abstract

An approach to building high performance collaboratories (collaboration+laboratory) using PCs and the Internet is presented. A PC hosts a Web server for a non-trivial computational electromagnetics system to enable world-wide Simulation-on-Demand. Several other PCs are interconnected via fast-Ethernet and the message passing interface runtime system. A client/server architecture implementation allows users to configure input files and simulations using the Web-browser at their location. The remote server launches the high performance simulation on the network of PCs. We use a new parallel version of the Air Force computational electromagnetics code GEMACS for the demonstration of this PC-based high performance computing and Internet collaboratory.

II. Introduction

The need for high performance computing for solving complex simulations is a well established fact. High Performance Computing (HPC) has made inroads into such diverse areas as: Grand Challenge problems, computational chemistry and computational electromagnetics[1]. In the electromagnetics area, high performance is driven by both the military's and the private sector's requirements to calculate more accurate internal and external electromagnetic fields for more analysis cases, but in less time[2]. The General Electromagnetic Model for the Analysis of Complex Systems (GEMACS) is a tool designed by the Air Force Rome Laboratory to solve large scale antenna radiation problems[3]. GEMACS solves radiation and scattering problems by examining the exterior and interior of a structure as a complete solution, using both low and high frequency techniques. A new parallel version of GEMACS uses high performance computing.[4] It is currently being run on the Rome Laboratory Paragon to support government analyses of antenna siting issues for the DARPA Airborne Communication Node, an excursion to the Global Hawk program. However, despite the gains made by applying parallel processing techniques to computational simulations in general, and electromagnetics in particular, there remains one large, prohibitive factor for most users who wish to run such simulations: accessibility to high performance computing platforms.

In addition to the requirement to parallelize large problems for high performance, the need also exists to support the distribution of the work among user input-output client interfaces and (parallel) simulation servers. This is especially true for systems of simulations that support multi-disciplinary analysis and integrated product engineering. A specimen application requiring this class of simulation support is the development of an aerospace system. Here, several specialized simulations may address disparate engineering domains: thermal, structure, electromagnetic, aerodynamic, etc. The data and knowledge

† The research reported here was funded in part by the Ballistic Missile Defense Organization under Army Space and Strategic Defense Command contract DASG60-92-C-0155 and by the Air Force under Rome Laboratory contract F30602-95-C-0221. We also wish to acknowledge the research of the Northeast Parallel Architectures Center and the Parallel Compiler Runtime Consortium, both directed by Geoffrey Fox of Syracuse Univeristy, with whom we are collaborating. The views expressed herein are those of the authors and not necessarily those of the Department of Defense or its agencies.

bases for each code are usually where the expert users are located. Integrated product engineering requires those experts to collaborate.

In 1989 the term "collaboratory" was coined by William Wulf as a combination of the words collaborate and laboratory, and defined as *"a center without walls, in which the nation's researchers can perform their research without regard to physical location– interacting with colleagues, accessing instrumentation, sharing data and computational resources, and accessing information in digital libraries."* [5] Two related studies, chaired by Wulf, focused on detailing the concept and setting up collaboratory testbeds, at a cost of several hundred millions of dollars.[6, 7]. Their examples for collaboration domains included scientific databases, remote instrumentation, collaboration technology, and data fusion. During that period, The Ultra Corporation, under contract to the Army, began a project for the Strategic Defense Initiative Organization (now Ballistic Missile Defense Organization) to investigate whether a low-cost alternative was possible by simply using the Internet and PCs.[8] Now, recent developments (indeed revolution) in Internet technologies make this the implementation method of choice for building collaboratories. The Web provides the architecture standards for software and hardware interoperability. The world-wide software development base for Internet tools, i.e., browsers, visualization languages, videoconferencing, ensures that the best systems will emerge from Internet-based developers as these have the widest user base possible.[9] Some even claim that Java will replace Fortran as the language of choice for scientific and engineering simulations.[10]

In this paper we provide a practical demonstration of how to build a PC-based collaboratory testbed. This system, the Innovative Research Testbed (IRT), provides world-wide accessibility to high-performance parallel computing (built entirely of PCs). Figure 1 below illustrates the basic concept and system functions. As a specimen test-article, we host the new parallel version of the Air Force computational electromagnetics code GEMACS. Web browsers provide the user access and the means to input data and view results. An on-line data archiving system allows the results of many runs to be visually browsed and retrieved for comparison. Videoconferencing, voice-phone, white-board, and the other basic Internet technologies (email, FTP, etc.) support collaboration among participants. The IRT architecture enables high performance phenomenological models to be integrated into remote simulations such as real-time, high-fidelity battle management/command, control, and communications simulations and models, or commercial tools for interactive, integrated product design and engineering.[11]

III. The Innovative Researcher Testbed

We have developed object-oriented reusable software building blocks for constructing low-cost distributed collaboratories using PC's and the Internet. This is continually being pushed by advances in PC-based multimedia technology, the emerging availability of wide area high-speed data networks, and of course, the World Wide Web. The basic functions required by a collaboratory are shown in figure 1 below. We focus here on the IRT functions of DigitalLibraries-on-Demand and Simulation-on-Demand. We have addressed the function Instrumentation-on-Demand within another context using special purpose neural computing hardware at the NASA Jet Propulsion Laboratory for remote data fusion and image processing collaboration. Also, we have developed our own videoconferencing and Internet-phone software for PCs, the function VideoConferencing-on-Demand. These collaboration tools are widely available and do not need to be discussed here.

The Simulation-on-Demand capability provides world-wide availability of supercomputing via the Internet. We use the client/server model for the simulation architecture with a classical, but highly interactive "input-process-output" sequence to divide the processing between distributed users and computational servers: scripts (JavaScript and Visual Basic) written into standard Web-browser pages provide forms for data entry and Java aplets allow information to be displayed on the user's client PC. The Web-server employs Common Gateway Interface (CGI) scripts written in Perl to parse user input submitted through forms to build an input file, which is then submitted to the PC-based parallel processor at Ultra through a scripting system. Upon completion (the user is notified via email for non-real time cases), another script is run to display the results using Web-browser forms, aplets, and VRML on the user's client PC.

We discuss first the PC-based supercomputer, then the use of Web-browsers for sophisticated user interfaces, and finally the Web-based database management for simulation archives

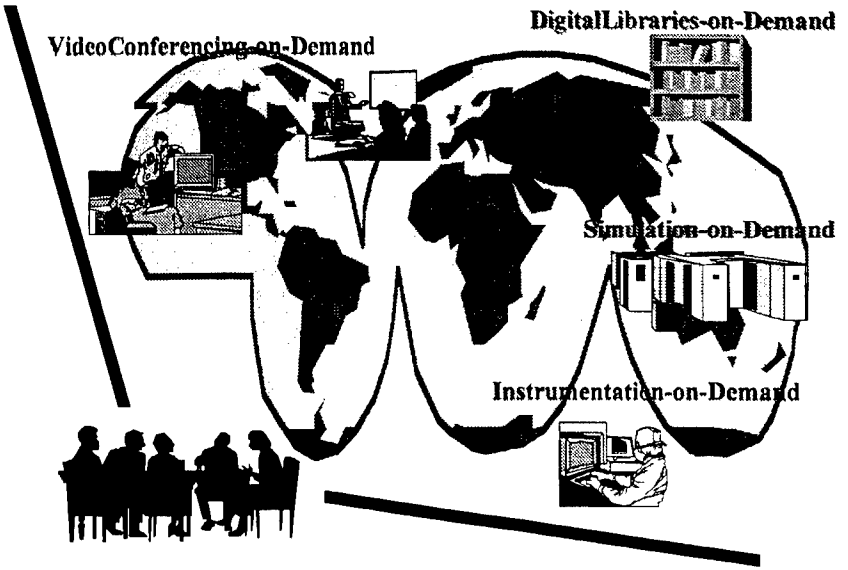

Figure 1 Innovative Research Testbed's Collaboratory Functions

A. PC-Based Supercomputing

The potential of PC's for scientific and engineering parallel computing was introduced over a decade ago by Geoffrey Fox at the California Institute of Technology.[12] Since then, tremendous advances in microprocessor performance and networking technology in the past decade have dramatically changed the perspective of supercomputing. Today's PC not only delivers higher performance than a supercomputer did twenty years ago, but also a well configured PC cluster can even deliver comparable performance against today's supercomputers (not to mention performance/cost ratio benefits). This is best exemplified by Beowulf.[13] The original Beowulf as conceived by Thomas Sterling combined sixteen PCs using Ethernet to provide a one GOPS peak performance, half a Gbyte of disk storage, and up to eight times the disk I/O bandwidth of conventional workstations to a single user. More recently, at Supercomputing96, 1.17 Gflops was demonstrated on a system costing $50,000 for a cosmological N-body simulation — high performance and very high performance/cost ratio on real applications! That system was composed of sixteen single-processor 200 MHz Pentium Pros.[14]

As a test-article for our testbed, we use GEMACS, an evolving computer simulation system developed by the Air Force that provides sophisticated phenomenological simulation of electromagnetic fields associated with radiating or scattering systems.[15] GEMACS is an electromagnetics code capable of analyzing any phase of system engineering: design, development, production, or maintenance. The

latest version makes significant leaps beyond previous upgrades by taking advantage of high performance computing. Figure 2 provides results from running GEMACS to simulate a non-trivial aircraft electromagnetic compatibility problem. The results are compared with those obtained from running the same problem on the Rome Laboratory Paragon. The code in each case was identical and used the Message Passing Interface (MPI) standard as interface to the respective parallel machines.[16]

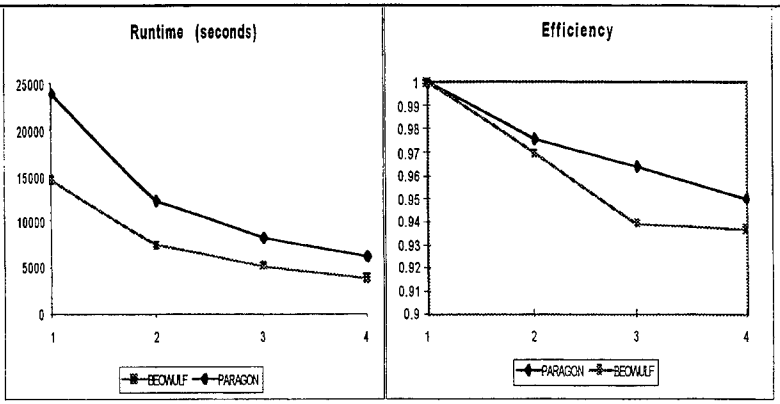

Figure 2 Comparison Between Ultra 4-PC Beowulf and Air Force Paragon

The left side of figure 2 shows how the runtime decreases as the number of processors is increased. We see that the processors of our Beowulf (which happened to be AMD5X86-based) are faster than those of the Paragon and our runtime decreases as we add more computer nodes. For an ideal parallel application, we would like the time for an N -node run to take $1/N$ the time of a serial, without parallelization run, i.e., on 1-node. In real-world the time on N nodes may be expressed as

$$T_N = \frac{T_1}{\varepsilon N}, \quad (0 < \varepsilon \leq 1$$

where ε is defined as the efficiency of the parallel implementation. The ideal is to have $\varepsilon = 1$. Inefficiency (i.e., $\varepsilon < 1$), however, can be caused by several factors: some of the code remains as a serial program (Amdahl's Law), communication among parallel processors (not present in the original serial code), etc. Typically, an $\varepsilon > .8$ is considered very satisfactory. In the right side of figure 2 we compare the efficiency between the PC-based system (Beowulf) and the Paragon, where we have computed efficiency using

$$\varepsilon = \frac{T_1}{NT_N}.$$

B. The IRT Client/Server User Interfaces

Current developments in the client/server design are focusing on creating intuitive, easy-to-use user interfaces by employing Web-technologies. With new Web-technologies emerging almost daily from various vendors, a GUI can be developed to run as plug-ins for Netscape and Microsoft's Internet Explorer browsers that takes advantage of C++ and it's large collection of libraries. Of course, aplets written in Java are expected to have the advantage of security compliance, although this is presently

debatable. Presently, Java does not have the properties required to offer a full-featured integrated interface, but this is expected to change in the near future as more libraries are developed and related security issues are solved.

Figure 3 presents the top-down structure of the client/server user interface.

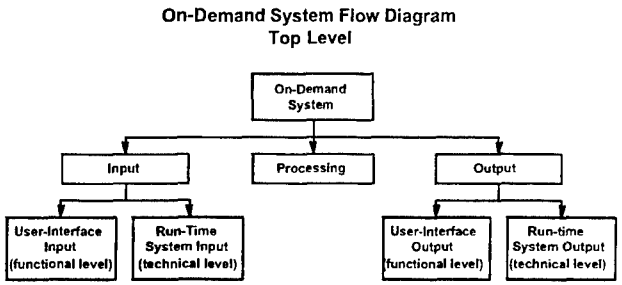

Figure 3 Top-Down View of Test-Article User Interfaces

Figure 4 below provides further detail of the input functions of figure 3.

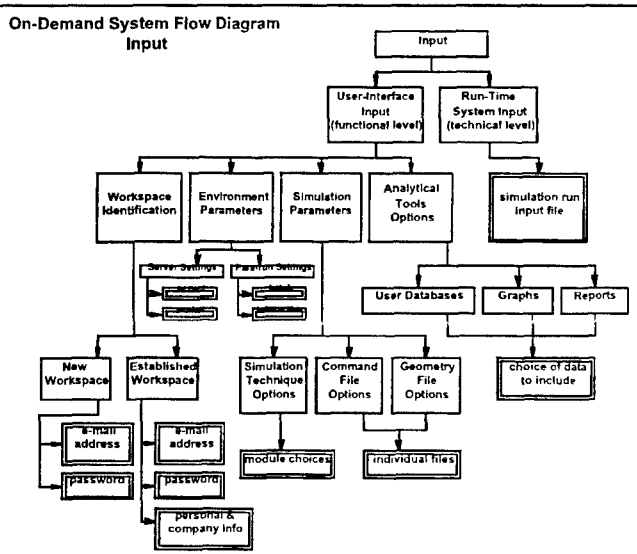

Figure 4 Input Module Structure

The user proceeds through identification and authentication security checkpoints. Once admitted into a workspace, the user may proceed directly to the analysis section, or make a new run. If the latter, then the user selects which computational resources of the collaboratory to use, i.e., Paragon, Beowulf, and how many nodes. Next, simulation input paramenters are specified. A level is provided to permit an expert user to interact with the details, while a less-senior analyst or technician can be restricted to making only parametric adjustments. This allows the expert to set up detailed simulation templates for a set of runs and then have an analyst make the variations and excursions. The input module parses the user's responses and interprets them for the (typically non-user friendly) simulation code. This is also an illustration of a simulation wrapper whereby user interfaces may be rapidly prototyped and customized by the user, who does not need to know the details of configuring any highly technical input file and scripts for running the code.

Figure 5 provides examples of the user identification and simulation input Web-pages. Also, a view of an actual detailed input file is given, whereby the expert user can make changes and redefine the template.

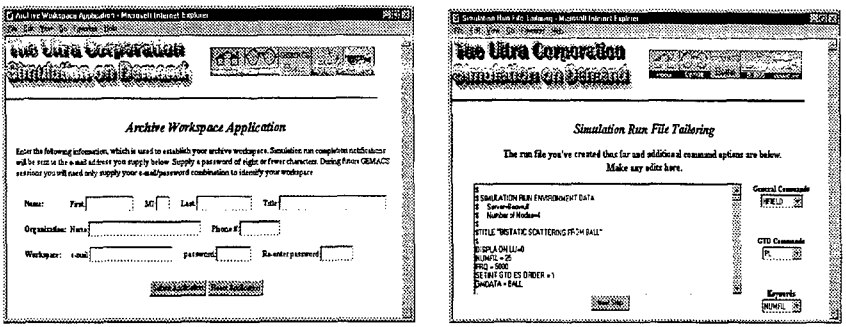

Figure 5 Examples of System Input Web-Pages

After completing the input phase, the system creates appropriate files for the simulation and produces the scripts which specify the execution environment, runtime libraries, and locations to place the results. After a simulation run (which can take hours on a parallel processor in contrast to days using a serial version), the user is automatically sent email and the serial numbers for accessing the results. The user may then re-enter the workspace and examine the new results and make comparisons with previous runs. Data can be displayed in text, graphical, or 3-D volumetric forms. As with the input side, an expert user can interact with the output at a detailed level, select variables and parameters to be extracted from the databases, and set up templates for graphs, reports, or slides.

C. *Examples of Analysis and Database Web-Pages*

Figure 7 provides examples of Web-pages for the output side of figure 3. The user can select an archive (or databases) of simulation runs to work with. Each run belonging to a selected database is listed in a visual (text plus graphics) format. The user may select any to work further with. A set of plots may be generated using the templates or a custom format. Viewers are also available should the user want a 3-D view and rotation of the view-point. Quick-look reports are then readily generated (documents, tables, or viewgraphs). A free set of viewers, in this case Microsoft Office (Word, Excel, PowerPoint, and Access), can be downloaded to format the data and create quick-look analysis reports and presentation slides.

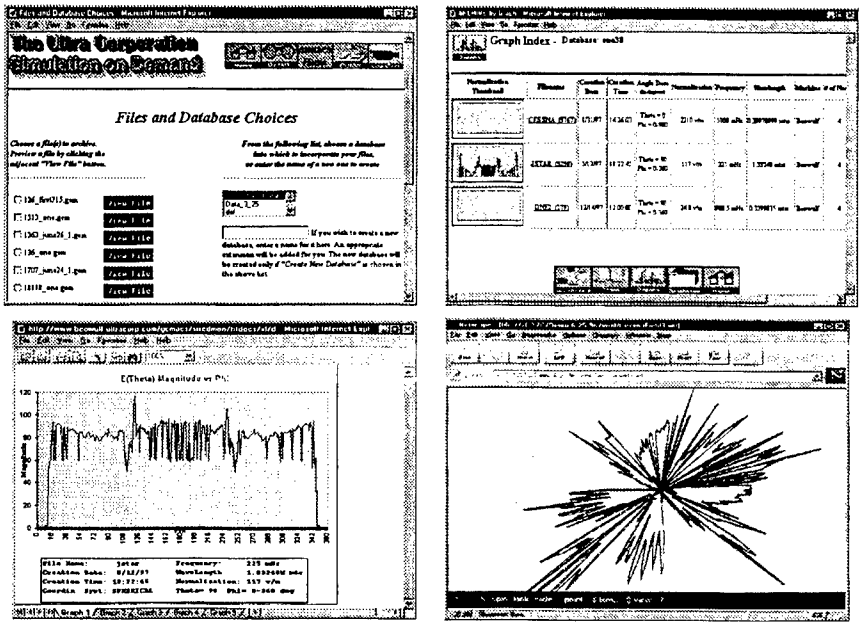

Figure 7 Examples of System Output Web-Pages

IV. Next Steps

The system we have presented will be generalized to support distributed and parallel simulation of multiple heterogeneous systems. The user interfaces are written such that codes, rather than humans can interact with a given program. The use of Internet technologies provides us with standards that greatly simplify the challenge of making such programs interoperable with each other. A key feature of the IRT collaboratory is the use of PC-based parallel processing to provide the high performance computing capability. When we bring together multiple codes, a common runtime system for high performance computing will be needed. This must provide runtime functions of array distribution and mapping that are compatible for the languages of the individual codes (Fortran, C/C++, Java, and Ada). We expect the area of Internet security to continue to evolve and eventually provide us with certified policies and procedures.

The exclusive use of PCs for this demonstration proves that desk-top supercomputing and Web-based Simulation-on-Demand works. We will continue to adopt new developments in the PC-technology base. This will lead to the use of distributed-shared memory clusters of PCs. Such systems, which we call Advanced-Beowulf, are expected to provide a rich and affordable computational resource for interoperable virtual environments, phenomenological models, and system simulations. A basic Advanced-Beowulf consisting of four nodes, each having four processors (a total of sixteen) and a quarter gigabyte of on-board RAM (a total of one gigabyte), plus a terabyte of secondary storage

distributed among the four mother boards (i.e., parallel I/O), can be easily built. Moreover, future developments in wrapper technology promises to require less specific knowledge of the actual working of the test-article, as is now the case with GEMACS. Implementations of wizards, or small helper applications, will step the user through the process of creating, submitting and analyzing simulations. Thus, the learning curve required to operate a Simulation-On-Demand site will be lowered and the site will be more accessible to a larger number of users. In the GEMACS case, analysis tools for in-depth analysis of electromagnetic fields make the user more productive. The Innovative Research Testbed framework will continue to evolve and expand to meet Collaboratory demands of the future. Additionally, with efforts to increase the speed of computers and the networks they communicate with, PC-based Web-enabled collaboratories will become a valuable, integrated, fully interactive tool embedded into many powerful applications.

---

[1] D. Loshin, High Performance Computing Demystified, Academic Press, 1994

[2] D. Leskiw, The Ultra Corporation, "High Performance Computing for C3I Computational Electromagnetics Applications", Air Force Rome Laboratory Technical Report RL-TR-94-181, October 1994

[3] RADC-TR-90-360, "General Electromagnetic Model for the Analysis of Complex Systems (GEMACS) — Version 5," RL/ERPT, Griffiss AFB.

[4] D. M. Leskiw, T. Vidoni, G. Ingersoll, R. Redmond, "Parallelization of GEMACS", The Ultra Corporation Internal Technical Report Under U.S. Air Force Rome Laboratory Contract F30602-95-C-0221.

[5] W. Wulf, "The Collaboratory Opportunity", Science, Vol 261, 13 August 1993.

[6] J. Lederberg and K Uncapher, "Towards a National Collaboratory", Report of an Invitational Workshop at the Rockefeller University, March 13-15, 1989.

[7] National Collaboratories, Applying Information Technology for Scientific Research, National Research Council, National Academy Press, Washington, DC 1993.

[8] D. Leskiw and G. Ingersoll, "The Innovative Research Testbed", The Ultra Corporation Internal Technical Report Under U.S. Army Space and Strategic Defense Command Contract DASG60-92-C-0155.

[9] G. Fox, W. Furmanski, K. Hawick, D. Leskiw, The Ultra Corporation, "Exploration of the InfoMall Concept "Building the Electronic InfoMall", ", Air Force Rome Laboratory Technical Report RL-TR-95-156, August 1995.

[10] G. Fox, "Special Issue: Jave for Computational Science and Engineering/Simulation and Modeling", Concurrency Practice and Experience, Vol. 9, No. 6, June 1997.

[11] Lettes, T., "Flexible Computer Integrated Manufacturing and the Ability to Compete in Global Markets," Office of the Assistant Secretary for Technology Policy, DoC, December 1991.

[12] Angus, I., Fox, G., Kim, J., Walker, D., Solving Problems on Concurrent Processors Volume II: Software for Concurrent Processors, Englewood Cliffs, Prentice Hall, 1990

[13] T. Sterling, D. Becker, D. Savarese, et al. "BEOWULF: A Parallel Workstation for Scientific Computation," Proceedings of the International Conference on Parallel Processing, 1995

[14] Cohen, Jarrett, "Beowulf Workstations Exceed Sustained GigaFLOPS," NASA, Ames Research Center HPCC Program Office, Nov. 15, 1996

[15] K. R. Siarkiewicz, "GEMACS — An Executive Summary," Proceedings of the 1985 International Symposium on Electromagnetic Compatibility, Wakefield, MA, August 1985, pp. 75-81.

[16] W. Gropp, E. Lusk, and A. Skjellum, Using MPI: Portable Parallel Programming with the Message-Passing Interface, The MIT Press, 1995.

ILLUSTRATING THE APPLICATION OF EXPERT SYSTEMS TO COMPUTATIONAL ELECTROMAGNETICS MODELING AND SIMULATION

Andrew L.S. Drozd*
Timothy W. Blocher†
Clifford E. Carroll, Jr.*
James M. Allen*

1.0 INTRODUCTION

This paper presents another in a series of topics on the application of knowledge-based techniques to CEM computer modeling and simulation. The strength of the knowledge-based approach is described for a simple canonical problem and a subset of relevant modeling concerns to illustrate the basic concept. The approach can readily be extended to more complex geometries and modeling scenarios. The modeling examples and concerns are discussed in the context of applying a smart pre-processor for government, university, and industry CEM codes called the Intelligent Computational Electromagnetics Expert System (ICEMES).[1-7] The ongoing research and development work is funded under Contract F30602-96-C-0163 for the US Air Force Research Laboratory's Information (IF) Directorate at Rome.

2.0 BACKGROUND

The reader may recall from previous literature on this subject that the pursuit of knowledge-based, expert system techniques is for the purpose of instituting an "intelligent agent" in the CEM computer modeling and simulation task. Such techniques are meant to better automate the modeling process and enhance the analyst's efficiency in generating validated CEM models in accordance with appropriate electromagnetic physics formalisms and within the constraints of selected codes. ICEMES is being developed for this very purpose.

The CEM formalisms supported by ICEMES include MoM, GTD/UTD, SBR/PO/PTD, and hybrid MoM/GTD. The CEM codes of interest here are current versions of GEMACS, NEC-MOM, NEC-BSC, Carlos-3D, Apatch, and Xpatch. ICEMES will validate existing input models for these CEM codes and formalisms. It will also accept a limited set of computer-aided design (CAD) data to automatically produce CEM structure models for these same codes and formalisms. Selected CAD file types and data formats include facet, DXF, and subsets of the Initial Graphical Exchange Specification (IGES) superset list of entities. Additionally, ICEMES provides a shapes pallet from which canonical objects can be "dragged and dropped" on a workspace to synthesize a complex system model.

Whereas past treatments of this subject have focused on the general knowledge-based approach, concept design, system framework and software-related issues this paper illustrates how the concept and approach are applied. Specifically, this paper will help answer an often asked question posed by many in the CEM community; that is, *"How are expert system rules actually applied to assure a valid CEM structure model?"* We will address this by way of a simple illustration from which the reader can grasp the concept and gain insight into some of the subtle modeling issues that ICEMES is designed to handle. The cases described below will also help the reader develop an appreciation for extending the technique to a variety of real-world, complex system modeling scenarios. The mechanics of translating user inputs and other external data which drive the process, as well as the methods employed to generate corresponding CEM models for selected codes will not be addressed in this paper. These aspects will be the subject of a future paper.

In this paper we will briefly discuss a few modeling and validation issues particularly as they relate to: geometry object connectivity and alignment; surface attachment; surface planarity (flatness or curvature); the orientation of surface normals with respect to electromagnetic sources; frequency-dependent object-element transformations and resizing; and the impacts on model reasoning processes caused by selecting regions, and specifying observables and field points. We will also discuss the effect of introducing certain modeling violations which are intended to evoke a predictable cause-effect response from the expert system's inferencing engine (i.e., the knowledge/rule base). Such violations, if not corrected in the final model, can result in CEM model instabilities, problematic singularities, and invalid solutions.

*ANDRO Consulting Services, P.O. Box 543, Rome, NY 13442-0543, andro1@aol.com, ccarrollJ@aol.com, jma@borg.com
†US Air Force Research Laboratory/IFSB, 525 Brooks Road, Rome, NY 13441-4505, blochert@rl.af.mil

Each cause-effect relationship or *if-then-else* action is defined by a rule set that applies to one or more of the CEM formalisms, software codes, and modeling methodologies. The methodologies are drawn from CEM experts who are theorists, experienced analysts, code developers, and proficient code users.

3.0 MODEL VALIDATION EXAMPLES

Figure 1 illustrates a simplified, canonical model for the purposes of this discussion. The model consists of two basic objects: a thin wire radiator perpendicularly attached to a flat plate. This could represent, for example, a radiating monopole or whip antenna effectively mounted atop a vehicle roof, hut, or an aircraft wing which acts as a ground reference. In CEM parlance, this represents a hybrid model comprised of MoM and GTD objects. Interest here may be in analyzing antenna performance and/or predicting the field pattern of the antenna over a finite ground plane.

The physical dimensions of the objects and the manner in which voltage feeds are applied are not critical to the discussion. Hence, we will approach the application of model validation rules and reasoning methodologies qualitatively rather than quantitatively. The illustrations given below assume that a predefined CEM model (consistent in whole or in part, for example, with GEMACS, NEC-BCS, NEC-MOM, and Carlos 3D) has been imported and is being validated by the ICEMES Pre-processor.

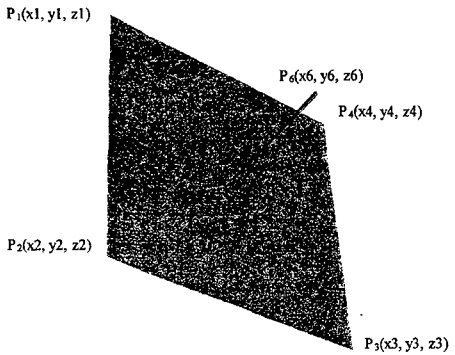

Figure 1. Canonical Example of an MoM Radiator Over a Conductive GTD Plate

3.1 Geometry Object Connectivity and Surface Attachment

One of the initial validations that the expert system engine performs is to check for intra-object as well as inter-object connectivity. This means that the system first looks for missing or incomplete physical parameters (scaled to frequency, of course) that define the geometry including voids, disconnected regions, and so on for each main object. For example, the thin-wire antenna is checked to determine if its end points including any intermediate wire segments are connected to each other in a contiguous manner.

Checks are then performed to verify antenna-to-plate attachment and surface planarity of the plate object. The surface planarity check is accomplished using the generalized equation for a plane. This equation assumes that the plate can be "discretized" and equivalently defined by a series of contiguous triangular finite elements or patches. As such, the equation for a plane is expressed as:

$$a(x-x_0) + b(y-y_0) + c(z-z_0) = 0$$

where

$$a = y_1z_2 - z_1y_2$$
$$b = -(x_1z_2 - z_1x_2)$$
$$c = x_1y_2 - y_1x_2.$$

The coefficients a, b, and c are computed by the cross product of two vectors connecting three points in the triangular finite element. The number of planes is tracked by assigning a "plane parameter" to each finite element. ICEMES verifies whether each element has assigned to it some initial value (x_0, y_0, z_0). The first element considered acts as a "basis" in determining plate planarity where all other elements are considered in a recursive manner.

One of the approaches used to verify wire-to-plate connectivity is based on an equation for a generalized curved surface. For the sake of brevity, the mathematical equations and approach are not presented here. For example, a useful method is to employ the equations for attachment to cylindrical surfaces. The equations reduce to the case of a flat plate after modifying assumptions are applied with regard to the off-axis angle, θ, and assuming very large cylinder radii. Other equations and simplifying techniques can be used to determine attachment and "welding" criteria for the wire and plate.

In the event that the antenna object's base coordinates are not within some acceptable tolerance value with respect to the plate surface to assure attachment or if it is not at a valid attachment point on the surface, the expert system will issue a warning and a recommended action of the following form to the user:

Antenna is not connected to the plate surface at a valid attachment point or is offset from the surface!

Do you want ICEMES to reposition/translate the antenna base element and all connecting segments to the plate surface using distance-minimization criteria?

3.2 Geometry Object Alignment

The next validity test involves the detection of misaligned objects. Such objects may be all or partially misaligned due to differences in the (x, y, z) coordinates at the interfaces between two or more separate objects or for individual elements of a single object. For example, in the case of Figure 1 a misalignment effectively occurs if the wire object is inadvertently defined to lie partially or completely in the plane of the plate. The misalignment also leads to the extreme case of a shallow wire angle with respect to the plate surface. In this case, the following message is issued:

Wire subsections lie completely or partially in the plane of the plate resulting in the potential for shallow angles ($\leq 20°$) with respect to the surface!

Do you want ICEMES to raise the wire segment(s) within the range of $20°$ to $90°$ relative to the base attachment point?

Shallow angles are an important consideration in view of possible model transformation and resizing (see Subsection 3.4 below) where, for example, the solid plate surface may be redefined as an equivalent wire mesh depending upon frequency and accuracy constraints.

Another practical example of misalignment can be observed for 3D object attachments where, for example, a cone frustum is not properly attached to a cylinder object, or when multiple frustum sections are improperly connected when forming a single, contiguous object.

3.3 Surface Normals With Respect to EM Sources

For the most part, surface normals for CEM objects (e.g., GTD plates) should be defined to point in the direction of incident or applied sources. The situation is complicated when multiple objects and sources are present in the problem. In the case of our plate-wire problem, if the user has defined the order of (x, y, z) plate vertices such that the right-hand rule defines a normal opposite to the location, direction, or orientation of the wire then the following warning and corrective action are issued:

Plate corners are currently ordered in a manner that produces a normal which is opposite in direction from the source(s) in the problem!

Do you wish ICEMES to reorder the points to assure a normal in the direction of the source(s)?

3.4 CEM Model Transformations and Element Resizing

The user will have the ability to specify frequency information (start, stop, Δf) and certain accuracy constraints to the expert system for any given problem. In Figure 1, we started out by assuming a hybrid MoM/GTD model. Let us now assume that the frequency and accuracy constraints are redefined such that the model transforms completely into a wire meshed surface where subsection element lengths are typically in the range 0.1λ-0.25λ, and where λ is the wavelength of interest. The new model may be a result of lowering frequency and requesting increased modeling accuracy or by increasing frequency and imposing high-accuracy constraints. The expert system computes the corresponding mesh elements which are used to define the surface. For any other frequency and/or accuracy limit adjustments, the expert system rules will redetermine the appropriate mesh densities and wire subsection dimensions. The following message would then be issued:

Wire subsections are valid at x MHz and adhere to proper length-to-radius ratios, and minimization of nearest neighbor segments that differ by a factor of ≥2x in length.

3.5 Geometry Region Selection, Observables, and Field Point Specifications

The impacts of collectively selecting geometry regions, specifying observables (surface currents or current densities, magnetic fields, electric fields), and considering the relative proximities of electromagnetic sources in the problem places a tremendous burden on the inferencing engine and its decision making ability. These aspects are currently being researched and implemented in a piecewise manner. A smart 3D graphical editor is being implemented to provide an interactive display environment to aid in the decision-making process. This environment will allow the user to select/highlight all or part of the geometry using a "lasso" function. Selecting only a portion of the total geometry will result in either one of two events or both: (1) only that portion of the geometry will be "extracted" and considered in the CEM model generation process and/or (2) the selected region will be modeled accurately within some nλ volume or boundary limit whereas the remainder of the model will be approximated or perhaps completely neglected in the final generated model. Event 2 will depend on frequency, accuracy, and other specified problem constraints. Other constraints that influence how the final CEM structure model will be defined, partitioned, or modified include the type(s) of observable(s) desired and the location of electromagnetic sources relative to the geometry and field point(s) of interest.

Generally, the result will be a complete, valid CEM structure model which is accurately defined over the selected region of interest (e.g., using a series of contiguous, discrete patches or a wire-gridded surface), and less accurately defined beyond the nλ boundary limit dictated by the extent of the selected region or by wavelength, whichever criterion is the more accurate. The effects of region selection, and the general influence of observables and sources on the generated model are illustrated in Figure 2. The method of successfully accomplishing this is dependent upon the following: the manner in which selected objects (subregions) are grouped or tagged; determining the 2D to 3D transfer function or extent to which the 2D lasso area relates to a 3D volume; and assuring valid boundary conditions at the interface between the higher- and lower-fidelity regions of a model.

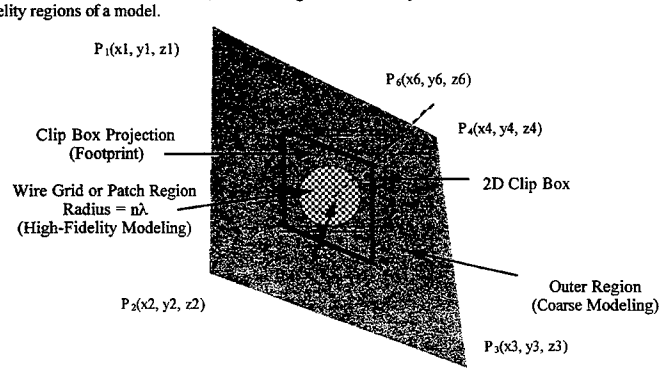

Figure 2. Illustrating the Influence of Region Selection

3.6 Other Hybrid Modeling Violations

We are also concerned with avoiding the attachment of wire segments at or near a GTD plate edge (see Figure 1). The general rule is to avoid attachment points that are $\leq \lambda/4$ from any plate edge. When this condition exists, a warning and corrective action of the following type are issued to the operator:

> **Base of wire segment(s) is attached at a point that is $\leq 0.25\lambda$ from plate edge x!**
>
> **Do you wish ICEMES to relocate the wire segment(s) using distance-minimization criteria?**

4.0 DEVELOPING THE ANALYSIS DEFINITION (COMMANDS AND GEOMETRY)

ICEMES is being designed with a capability to aid in the development of the analysis definition. This involves the generation of appropriate structure models and executive commands for the corresponding CEM tool(s). The analyst specifies the general output that he/she desires and ICEMES asks pertinent questions to provide the appropriate commands and geometry models as output. Using an interactive dialogue approach to communicate with the expert system, the operator can perform the following: (a) import a CAD (IGES, DXF, or facet) model; (b) define the top-level analyses parameters (frequency, source definitions, observables and solution controls); (c) translate one CEM tool command set into another CEM tool command set; and (d) modify a CEM command set for a different user-defined scenario. These aspects are illustrated in Figure 3.

It is important to note that importing CAD or existing CEM models results in a "mapping" of the corresponding model data into an object-oriented metafile environment which is effectively mirrored into a generic KB object network resident within the inference engine. CEM and executive control parameters input by the user are associated with the geometrical description establishing a synergy between the command and model development tasks. This approach allows for the generation of structure models and executive commands for the CEM code(s) of interest in a single session. The translation of one CEM tool command set to another is accomplished by exploiting the metafile environment and the generic KB object definitions, rather than directly performing file translations (e.g., GEMACS to NEC-BSC input formats, and so on). The rules operate upon the generic KB objects to produce the desired modeling results. This methodology results in a complete and robust pre-processor.

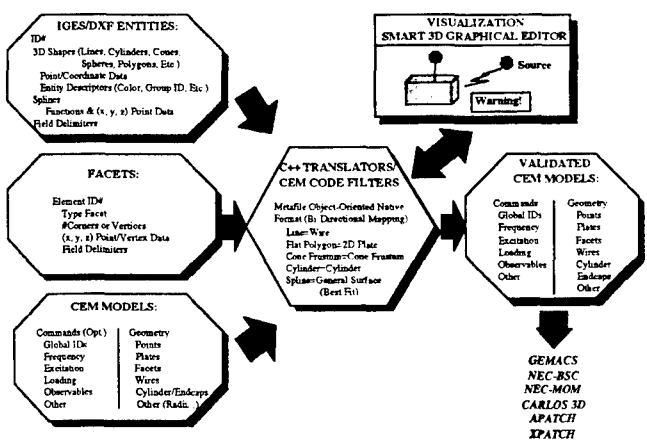

Figure 3. ICEMES Analysis Definition and Data Flow

5.0 SUMMARY AND FUTURE DIRECTIONS

A knowledge-based, expert system approach to CEM computer modeling and simulation is discussed in this paper. The concept and approach are based on the ICEMES capability which is in the process of development and demonstration. This paper represents another in a series of technology updates on the development and application of the ICEMES knowledge-based capability.

ICEMES assists the CEM analyst in efficiently generating CEM structure models based on a number of widely-used physics formalisms, proven numerical techniques, and validated software codes. The CEM structure models are generated in accordance with the modeling guidelines and input data requirements for selected CEM codes. The ICEMES model validation and correction measures ultimately act upon generic CEM objects resident in the knowledge base. Any size adjustments, position changes, connectivity modifications, etc. are applied directly to the generic CEM model components. Once the geometry model complies with the set of applicable CEM rules, it passes through a "filter" for the application code selected. The filter converts generic knowledge-based parameters into a specific format required by the CEM code(s).

A number of typical examples illustrating the application of expert system rules to the CEM modeling and validation task is presented above. These examples are only a small subset of what is achievable using ICEMES. The various rules, checks and balances applied to these examples and cases represent a fraction of the total knowledge base and decision-making capability resident in ICEMES.

REFERENCES

[1] A. Drozd, T. Blocher, et. al., "The Intelligent Computational Electromagnetics Expert System (ICEMES)", Conference Proceedings of the 12th Annual Review of Progress in Applied Computational Electromagnetics at the Naval Postgraduate School, Monterey, CA, 18-22 March 1996, pp. 1158-1165.

[2] A. Drozd, T. Blocher, et. al., "The Intelligent Computational Electromagnetics Expert System (ICEMES)", Applied Computational Electromagnetics Society Newsletter, Vol. 11, No. 2, ISSN 1056-9170, July 1996, pp. 28-40.

[3] A. Drozd, T. Blocher, et. al., "The Intelligent Computational Electromagnetics Expert System (ICEMES)", Newsletter Technical Features Article for the Applied Computational Electromagnetics Society, Vol. 11, No. 2, ISSN 1056-9170, July 1996, pp. 28-40.

[4] A. Drozd, T. Blocher, et. al., "Expert Systems for Computational Electromagnetics", Conference Proceedings of the Society for Computer Simulation (SCS) Summer Computer Simulation Conference, Portland, OR, 21-25 July 1996.

[5] A. Drozd, T. Blocher, et. al., "An Expert System Tool to Aid CEM Model Generation", Conference Proceedings on the 13th Annual Review of Progress in Applied Computational Electromagnetics, Monterey, CA, 17-21 March 1997, pp. 1133-1140.

[6] A. Drozd, T. Blocher, et. al., "An Expert System Tool to Aid CEM Model Generation", Newsletter Technical Features Article for the Applied Computational Electromagnetics Society, Vol. 12, No. 2, ISSN 1056-9170, July 1997, pp. 17-23.

[7] A. Drozd, T. Blocher, et. al., "Technology Update: ICEMES, A Tool for Generating Complex CEM Models Using an Expert System Approach", Conference Proceedings of the Society for Computer Simulation (SCS) Summer Computer Simulation Conference, Arlington, VA, 13-17 July 1997, pp. 395-400.

ACKNOWLEDGMENTS

The authors wish to acknowledge the continuing support and contributions made on behalf of the ICEMES development program by Kenneth R. Siarkiewicz of the US Air Force Research Laboratory/IFSB, Dr. Edgar L. Coffey III of Advanced Electromagnetics, Dr. Ronald J. Marhefka of The Ohio State University, Jeffrey A. Evans of Decision-Science Applications, Inc., James B. McCreary of Innovation Strategy Group, Inc.

Some Present and Future Aspects of the Quality of Solution in Computational Electromagnetics

Donald R. Pflug
Air Force Research Laboratory
Rome Research Site
525 Brooks Road
Rome, NY 13441-4505

INTRODUCTION

Practitioners and researchers in Computational Electromagnetics (CEM) have made enormous strides over the last thirty years in their ability to analyze a wide variety of complex electromagnetic phenomena. Before this time rigorous solutions to electromagnetic problems usually were limited to those having a canonical geometry in which the vector Helmholtz equation was separable. Approximate solutions also existed for electrically large problems by using the classical methods of geometric and/or physical optics together with the Geometrical Theory of Diffraction (GTD) as developed by Keller [1]. The application of modern numerical methods to solve Maxwell's equations for more general CEM problems began in earnest with the development of the Method of Moments (MoM) by Harrington [2] for integral equations, the Finite Difference Time Domain (FDTD) method by Yee [3] and Taflove [4] for differential equations, and the Uniform Theory of Diffraction by Kouyoumjian and Pathak [5] for high frequency solutions. These techniques were developed from the mid 1960s to the mid 1970s and have been applied to a wide variety of general CEM problems up to the present day. MoM proved to be very versatile for radiation and scattering but was limited to problems whose characteristic sizes were, at most, on the order of a wavelength. FDTD methods proved excellent for similarly sized interior problems, especially those containing complex materials, but encountered accuracy limitations due to numerical dispersion, stair step effects at curvilinear boundaries and insufficiently accurate absorbing boundary conditions (ABCs) for exterior problems. UTD provided solutions of good accuracy to a variety of electrically large problems involving metal structures but it proved difficult to extend the theory rigorously to nonmetallic structures. Finally, a major constraint on all numerical methods until recently were the limitations on the computer hardware.

The advent of fast workstations, massively parallel computers, CAD programs, advanced visualization tools, and major advances in CEM solution algorithms have greatly changed this picture. Computer speed and memory have made possible the solution of very large problems in reasonable times. A very complex general geometry can be represented very accurately in a standard (e.g., IGES) geometry file. Sophisticated graphics hardware and software make the presentation of computed results clear and informative. Iterative methods and fast solvers, such as the Fast Multipole Method (FMM) [6] and the Adaptive Integral Method (AIM) [7], have expanded the applicability of MoM integral equation formulations to electrically sizable problems. Similar advances have taken place in FDTD due to development of the very accurate Perfectly Matched Layer (PML) absorbing boundary condition by Berenger [8]. More recently the finite element method (FEM) has been developed in

both the frequency and time domains and applied to very general radiation and scattering problems. Finally, the hybridization of different CEM frequency domain techniques coupled with massive computer power have brought CEM into the realm of "real world" problems. Two examples of such problems are calculation from first principles of the radar cross section (RCS) for a complete fighter aircraft at ever higher frequencies and the performance of antennas mounted on complex platforms.

While CEM technology has continued to advance into more and more areas of electromagnetics, the methods of determining the quality of the CEM solution and the validity of the CEM software have remained essentially unchanged over the past thirty years. In this paper, CEM solution quality and code validation now and in the future will be reviewed and discussed from several points of view. Emphasis will be placed on CEM codes that analyze the electromagnetic performance of large complex platforms such as aircraft. Both hardware and software validation benchmark problems are discussed and the quality of the CEM solution is given in terms of software error analysis and control as well as algorithms for the extrapolation/interpolation of computed CEM data. This discussion is not meant to be complete but to indicate how CEM code solution quality is determined today and a few promising approaches for improving the solution quality in the future.

CEM CODE VALIDATION:

The most common, and best, way to validate a CEM code is to compare the computed results of a carefully defined test problem with the measured results of the same problem. This test problem is represented in the real world by a material test body upon which specific measurements are to be performed in a carefully controlled environment to generate the measured data. Ideally a measurement error budget is constructed by careful calibration of the test body and measurement environment and an estimate of the measurement accuracy is determined. Measurements are expensive and time consuming but they touch the real world without which computer modeling and simulation is lost.

The test problem is represented within the CEM code by a digital data set. This data set is made up of two major subsets, geometry data and electromagnetic data, each representing a separate CEM model. In most modern CEM codes geometry data is generated externally by a CAD program and is usually passed to the CEM code using a standard file format (e.g. IGES). The CEM electromagnetic data is generated internally using a limited set of externally specified parameters (e.g. frequency, material constitutive parameters) required for specific material and electromagnetic source models within the code. CEM solution algorithms then operate on this data in a carefully within the CEM code to produce the computed results. As is evident the simulation procedure is analogous to the measurement procedure. Currently, however, only limited effort goes into estimating simulation accuracy. This is due primarily to the fact that simulation accuracy is a complex combination of the accuracies of the geometry, CEM algorithms (including their specific implementation in a given code) and their numerical procedures, and computer roundoff error. The usual approach is to compare measurements and calculations without error bars on either data set.

Over the years a number of test bodies have been recognized as being particularly valuable as CEM validation benchmarks. For RCS calculations the sphere is perhaps the best known since it is the one 3D test body whose RCS can be calculated exactly using the well known Mie series.

More general benchmark problems, however, have been developed recently. Perhaps the most well known problem set is the one sponsored by the Electromagnetic Code Consortium (EMCC) that has become recognized in the CEM community as benchmarks for RCS calculation. One such set of problems consist of various flat plate configurations, two of which are shown below in Figures 1a and 1b.

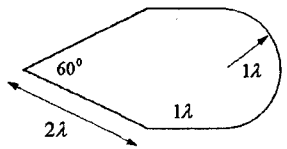

Figure 1a. Wedge-Plate-Cylinder

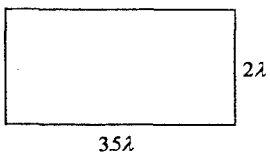

Figure 1b. Plate (Business Card)

These benchmarks are designed to be used with first principles CEM techniques such as MoM , FEM or FDTD. These problems are characterized by an electrically thin plate structure possessing edges, corners and tips which stress CEM code modeling capabilities. A detailed description of these plate target benchmarks along with a selection of measured and calculated data is published elsewhere [9].

A second set of EMCC benchmarks consists of several bodies of revolution (ogive, double ogive, cone-sphere and cone-sphere with gap) [10], a more general 3D target (NASA almond) [10] and an aircraft model, the VFY 218. Depending on the frequency, these targets can be used to benchmark a variety of CEM codes and techniques. Three of these targets, the NASA almond, double ogive and cone-sphere with groove are shown in Figure 2 while the VFY 218 is illustrated in Figure 3. As with the plate benchmarks these targets contain regions that stress CEM code modeling and solution capability. These 3D targets show increasing levels of structural sophistication starting from the body of revolution structures having an axis of symmetry to the full 3D almond to the VFY 218 which represents a highly complex and general airframe.

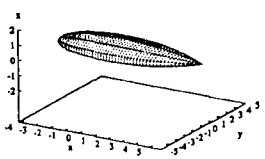
Figure 2a. NASA Almond

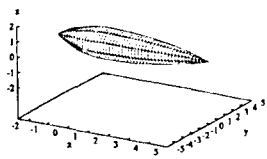
Figure 2b. Double Ojive

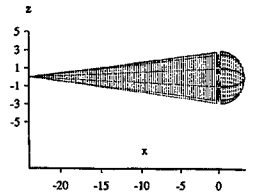

Figure 2c. Cone-Sphere with Groove

Figure 3. VFY 218

Besides RCS, the performance of antennas mounted on platforms such as aircraft or other vehicles represents another major CEM "real world" problem . In contrast to RCS, antenna/platform integration has major commercial applications which suggests the need for validation procedures that are practical in the commercial as well as in the DoD world. Antennas represent relatively strong EM sources close to many parts of the platform giving rise to significant surface wave and near field phenomena on the platform.

Antenna performance validation typically has been restricted either to the antenna in the absence of a platform or in the presence of a simple platform such as a highly conducting planar or curved surface. Since modern antennas usually reside on a complex structure, the "realistic" problem is to include the antenna and platform as one system. Platform effects can significantly degrade the antenna radiation pattern. In addition other antenna characteristics, such as efficiency, input impedance or array scan impedance, are sensitive functions of the nature of the platform.. In particular it can be difficult to determine those parts of the platform whose influence significantly degrades the antenna performance.

A test article for validating antenna/platform CEM codes was constructed recently at the Rome Research Site of the Air Force Research Laboratory (AFRL) to help answer this question. The test article, called the Transformable Scale Aircraft-Like Model (TSAM) [11], is an approximately 1/20 scale model of a wide bodied aircraft with a simplified canonical geometry on which six monopole antennas have been mounted, three on top of the fuselage and three on the bottom. The use of a simplified geometry allows geometry modeling accuracy to be high with insignificant modeling error. Simulation error then is due primarily to algorithm errors within the code which is the major focus of CEM code validation. A set of principal plane radiation patterns have been measured and have been used to validate the Rome Laboratory GEMACS code. A unique feature of TSAM is that all its components can be removed so that the electromagnetic scattering from each TSAM component on the TSAM antenna radiation patterns can be determined easily. These data serve not only to validate CEM codes but also as a troubleshooting guide in determining problem areas in the software. A view of TSAM assembled and disassembled into its component parts is shown in Figure 4 and typical platform effects on a monopole mounted on TSAM are illustrated in Figure 5.

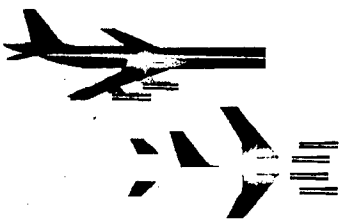

Figure 4 The TSAM Test Article [11]

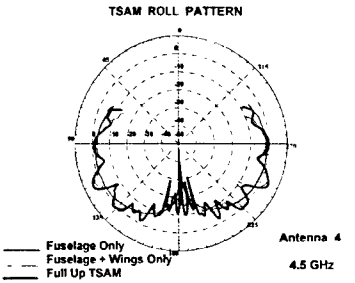

Figure 5. TSAM Antenna Platform Effects

Another antenna/platform test article being constructed at Wright Patterson AFB is a 1/3 scale model of a C29 aircraft [12]. This platform was originally designed for RCS measurements but is being modified to include both a monopole antenna and an array. Antenna pattern measurements currently are underway which will provide additional data showing various platform effects on antenna patterns.

In addition to measurements on hardware test bodies, CEM software validation can be done using computed results from other CEM codes on selected problems. One such collection of CEM validation problems has been compiled by ACES into a canonical problem set that was published in 1990 [13]. This would work best if the computed results of the various canonical problems were done using CEM codes of known accuracy which is usually not the case. Still, these problem sets are valuable in helping to check CEM code quality for problems in which benchmark measured data are not available.

CEM QUALITY OF SOLUTION:- NOW AND IN THE FUTURE

The most accepted procedure for validating CEM codes and judging the quality of CEM solutions is comparing the calculations to the results of well designed and carefully conducted experiments. The absence of error bars, or at least error estimates, for most published measured data makes the CEM code validation process ambiguous. Certainly rough estimates of measurement accuracy based on experience often are available for many kinds of electromagnetic measurements. However what is needed for benchmark measurements is a quantitative error estimate (and an error budget) of the observable being measured on a specific test body at a particular measurement facility with specific calibrated equipment at a specific time. If the computed results fall within the error bars of the measurements, the code is validated to within the accuracy of these measurements.

Unfortunately most comparisons of benchmark measurements to calculations usually show areas of reasonable agreement and areas of disagreement. If the measurement accuracy is not known, then it is usually impossible to determine the cause of the disagreement. If the measurement accuracy

is known then it is usually difficult to determine the source of the disagreement within the CEM code. Modern CEM codes are complex in the extreme and their accuracy is a function of geometry modeling error, electromagnetic modeling error, algorithm error and computer machine accuracy. Even worse, these errors are not independent of each other and the dependencies usually are not known. A start has been made, however, to include error estimates in CEM codes. These estimates typically are associated with the CEM solver algorithms and involve quantities such as condition number and residual error. Basic research to determine error estimates for differential and integral equations of electromagnetics is being pursued actively. A recent example for integral equations is found in [14]. While such research is essential it must be extended to include error estimates on the electromagnetic observables of interest in terms of quantities that are under the control of the CEM analyst (e.g. grid density, number of terms in a sum, quadrature points). In addition error estimates must be developed for CEM hybrid code algorithms. Such algorithms are combinations of different CEM techniques and are much more difficult to analyze but they represent currently the only practical way to analyze "real world" problems using CEM.

In addition to the accuracy of a given CEM solution over a domain of parameter values, another aspect of the quality of solution in CEM is the development of "smart" extrapolation/interpolation procedures to extend the range and domain of a given CEM solution while preserving solution accuracy. Two techniques developed recently are Model Based Parameter Estimation (MBPE) and Asymptotic Waveform Evaluation (AWE). Recent development of MBPE can be found in [15, 16, 17].and AWE in [18, 19]. Both methods replace the exact electromagnetic model with a reduced order model. For example, in the frequency domain the algorithm for a scattered field or an antenna impedance can be viewed as a transfer function which varies with frequency. A suitable reduced order model for the transfer function is a ratio of polynomials whose coefficients are determined from the CEM computed data. This approach allows the CEM analyst to avoid having to do calculations over a dense set of points. Instead, accurate calculations for an electromagnetic observable are done for a smaller set of points and the results at other neighboring points are estimated. Important questions remain concerning how far the computed data can be extrapolated and how accurately the data can be interpolated.

The CEM codes of the future will be used in support of virtual prototyping and acquisition of future commercial and military systems and high level modeling of C4I assets. In virtual prototyping and acquisition, electromagnetic analysis tools will be used together with the tools of other engineering disciplines (e.g. structural, thermal, fluid mechanics) in an integrated computational environment to develop a set of manufacturing specifications for a given system that is consistent with user requirements and acquisition issues such as affordability, manufacturability and reliability. The best example to date is the development of the Boeing 777 done largely by computer analysis and simulation. To work in this design arena most effectively the CEM codes of the future requires careful validation and rigorous accuracy estimation.

A further use of the CEM codes of the future is in providing support for the modeling and simulation of C4I systems. A number of different modeling and simulation levels are required for C4I simulation and are best illustrated by the pyramid structure shown in Figure 6. At the base of the pyramid are the engineering physics simulations, including CEM, which are essential to determine the

detailed virtual performance of an electronic system. These simulations are the most accurate but do not run in real time. Toward the top of the pyramid are the various command and control simulations which are essential for evaluating how a given electromagnetic system performs in a C4I environment. These simulations are less accurate but run in near real time.

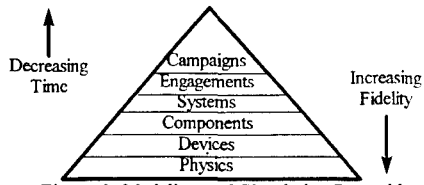

Figure 6. Modeling and Simulation Pyramid

At a given level, a set of system models are required that can be derived from the models and data at the level below it by a process called model abstraction. Such a process systematically reduces the model complexity of lower levels to a model appropriate for the modeling and simulation tools at higher levels. CEM codes, along with other engineering physics disciplines, will provide the bedrock of accurate information to be passed up to the higher level simulation tools to give accuracy and to the results. Essential to this process is the existence of validated CEM tools of known accuracy and wide applicability to be used in the acquisition and testing of DoD and commercial systems of the future.

REFERENCES:

1. J. P. Keller, "Geometrical Theory of Diffraction", *J. Opt. Soc. Amer.*, vol. 52, p. 116, Feb. 1962.
2. R. F. Harrington, "Matrix Methods for Field Problems", *Proc. IEEE*, vol. 55, p. 136, Feb. 1967.
3. K. S. Yee, "Numerical Solution of Initial Boundary Value Problems Involving Maxwell's Equations in Isotropic Media", *IEEE Trans. Antennas & Propagat.*, vol. 14, p. 302, 1966.
4. A. Taflove, *Computational Electromagnetics: The Finite-Difference Time Domain Method*, Artech House, Norwood MA, 1995.
5. R. G. Kouyoumjian and P. H. Pathak, "A Uniform Theory of Diffraction for an Edge in a Perfectly Conducting Surface", *Proc. IEEE*, vol.62, p.1448, Nov. 1974.
6. R. Coifman, V. Rokhlin and S. Wandzura, "The Fast Multipole Method: A Pedestrian Prescription, *IEEE Antennas & Propagation Society Magazine*, vol. 35, no. 3, p.7, June 1993.
7. E. Bleszynski, M. Bleszynski and T. Jaroszewicz, "AIM: Adaptive Integral Method for Solving Large-Scale Electromagnetic Scattering and Radiation Problems", *Radio Science*, vol. 31, no. 5 p.1225, Sep-Oct 1996.
8. J. P. Berenger, "A Perfectly Matched Layer for the Absorption of Electromagnetic Waves", *J. Computational Physics*, vol. 114, p.185, 1994.
9. A. C. Woo, H. T. Wang, M. J. Schuh and M. L. Sanders, "Benchmark Plate Radar Targets for the Validation of Computational Electromagnetics Programs", *IEEE Antennas and Propagation Magazine*, vol. 34, no. 6, p. 52, December 1992.

10. A. C. Woo, H. T. Wang, M. J. Schuh and M. L. Sanders, "Benchmark Radar Targets for the Validation of Computational Electromagnetics Programs", *IEEE Antennas and Propagation Magazine*, vol. 35, no. 1, p. 84, February 1993.
11. D. R. Pflug, "A Novel Test Article for Computational Electromagnetics (CEM) Code Testing and Validation: The Transformable Scale Aircraft-Like Model (TSAM), *IEEE Antennas and Propagation Magazine*, vol. 39, no. 3, p. 92, June 1997.
12 Dr. Kueichien Hill, Wright Laboratory (WL/XPN), private communication.
13. The ACES Collection of Canonical Problems (Set 1), Harold A. Sabbagh, Ed., Applied Computational Electromagnetics Society (ACES), Spring 1990.
14. G. C. Hsiao and R.E Kleinman, "Mathematical Foundations for Error Estimation in Numerical Solutions of Integral Equations in Electromagnetics", *IEEE Trans. Antennas Propagat.*, vol.45, no. 3, p.316, March 1997.
15 E. K. Miller, "Model-Based Parameter Estimation in Electromagnetics:I—Background and Theoretical Development", *Applied Computational Electromagnetics Society Newsletter*, vol. 10, no. 3, November 1995.
16 E. K. Miller, "Model-Based Parameter Estimation in Electromagnetics:II—Applications to EM Observables", *Applied Computational Electromagnetics Society Newsletter*, vol. 11, no. 1, November 1995.
17. R. S. Adve, T. K. Sarkar, S. M. Rao, E. K. Miller and D. R. Pflug, "Application of the Cauchy Method for Extrapolating/interpolating Narrowband System Responses", *IEEE Trans. Microwave Theory Tech.*, Vol 45, no. 5, p.837, May 1997.
18. A. C. Cangellaris and L. Zhao, "Reduced Order Modeling of Electromagnetic Systems with Pade via Lanczos Approximations", *Proceedings of the Thirteenth Annual Review of Progress in Applied Computational Electromagnetics*, ACES, vol. II, p. 148, March 1997.
19. J. Volakis, private communication.

On the Use of Computational Electromagnetics in the Radar Cross Section Measurement Calibration Process

Kueichien C. Hill and William D. Wood, Jr.
Air Force Research Laboratory
2591 K Street, Building 254
Wright-Patterson AFB OH 45433-7602

Abstract

This paper describes how recent advances in computational electromagnetics can be used by the radar cross section (RCS) measurement community to design improved calibration targets. We present numerical examples for three calibration targets: a right circular cylinder, a modified bicone, and a dihedral. Several different computational electromagnetics codes are used for each target, and the accuracy of each is assessed.

1 Introduction

RCS measurement ranges are complex systems used to measure the radar cross section of arbitrary targets. Recent advances in instrumentation radar technology have greatly improved the accuracy of measured RCS data, as well as the speed with which it is acquired. New sophisticated software tools transform broadband and/or wide-angle RCS data into various types of images, useful for analyzing target scattering characteristics.

One aspect of the RCS measurement process which has received relatively little attention is the calibration process. Calibration is accomplished by measuring the electric field scattered by the target under test, and then repeating the measurement using a calibration target. The calibration measurement is then correlated with the known RCS of the calibration at the frequency, polarization, and aspect angle of interest. Traditionally, a conducting sphere is the target which has been used almost exclusively for calibration, primarily because it is one of the few objects whose theoretical RCS can be computed exactly. Conversely, other targets have not been used for calibration purposes because of the lack of high-quality theoretical scattering data. The emergence of powerful new computational electromagnetics tools can remove this barrier.

In Section 2, we briefly discuss the conducting sphere as an RCS calibration target, focusing on its advantages and disadvantages. In Section 3, we discuss the use of the right circular cylinder as a calibration target, while in Sections 4 and 5 we address the bicone and dihedral, respectively.

2 Conducting Sphere

Conducting spheres are by far the most widely used RCS calibration target. This popularity is based on several factors. First, conducting spheres are relatively easy to fabricate. Second, the RCS of a conducting sphere is independent of azimuth and elevation angle. Third, and most important, the theoretical RCS of a perfectly conducting sphere is readily given by the classical Mie series [2].

Conducting spheres have several serious disadvantages. First, conducting spheres scatter strongly in all directions, providing secondary illumination of target support hardware and corrupting the calibration.

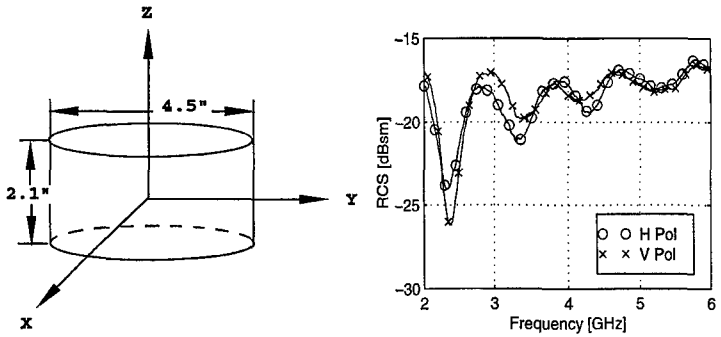

(a) Geometry of the "squat" cylinder. The cylinder is 4.5 inches in diameter and 2.1 inches in height.

(b) Measured RCS as a function of frequency.

Figure 1: Measured monostatic RCS of a right circular cylinder as a function of frequency. The elevation angle is 0°; that is, the cylinder is edge-on to the incident field.

Second, the RCS of a conducting sphere is very sensitive to fabrication defects. For instance, a conducting "sphere" with radius a and 1.5% eccentricity corrupts an RCS measurement by as much as 0.5 dB at wavelengths below $0.25a$ [3]. Third, spheres are not compatible with modern rotator-pylon supports.

3 Right Circular Cylinder

Right circular cylinders are currently being used as the primary calibration target at the Air Force Research Laboratory's Advanced Compact Range at Wright-Patterson AFB, OH. These so-called "squat" cylinders, shown in Figure 1(a), look like metallic hockey pucks and are oriented edge-on to the illuminating radar. Their advantages include 1) ease of fabrication with extremely tight physical tolerances, 2) reduced secondary illumination of target support hardware, 3) compatibility with rotator-pylon supports, and 4) azimuthal invariance. Their disadvantages are primarily limited to 1) RCS sensitivity to elevation angle, and 2) lack of exact theoretical RCS.

The first disadvantage can often be mitigated in practice by elevation alignment, although this can often not be done at large outdoor RCS measurement ranges due to ground bounce effects. The second can be overcome by the application of computational electromagnetics. Figure 1(b) shows the measured RCS of the "squat" cylinder as a function of frequency. Figures 2(a) and 2(b) show the difference between the calculated and measured RCS of the 450 "squat" cylinder as a function of frequency. Data from two body of revolution (BOR) moment method codes, a general-purpose moment method code incorporating "fast" solution techniques, and a physical optics code are shown. As can be plainly seen, the agreement with measured data for the three moment-method techniques is excellent. As might be expected, the agreement for the physical optics result is less impressive, especially at the lower frequencies.

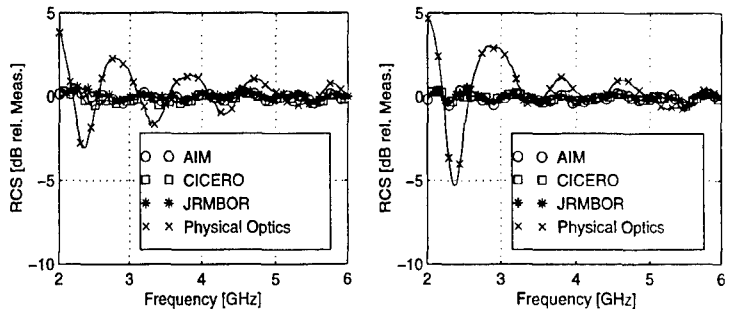

(a) Difference between calculated and measured RCS – HH Polarization

(b) Difference between calculated and measured RCS – VV Polarization

Figure 2: Calculated RCS data versus frequency for the "squat" cylinder. Calculated data is provided by AIM [1] (a "fast" general-purpose moment-method code), CICERO [4] and JRMBOR [5] (two body of revolution moment method codes), and XPATCH [7] (a shooting-and-bouncing ray/physical theory of diffraction code) with no edge diffractions included. Results are plotted as RCS relative to measurements.

4 Bicone

The "squat" cylinder provides superior calibration performance over the conducting sphere. However, it possesses one serious shortcoming – its RCS is relatively sensitive to elevation angle, especially at higher frequencies. The bicone, shown in Figure 3(a), is designed to give better elevation performance than the "squat" cylinder while maintaining the cylinder's advantages over the sphere. The bicone can be thought of as a body of revolution analogue of a dihedral; the geometrical optics scattering mechanism is a double bounce reflection from the top and bottom sections of the bicone rather than the single bounce reflection from the side of the "squat" cylinder. Figure 3(b) shows the measured RCS of the bicone as a function of frequency.

Calculated RCS data for the bicone was generated using a "fast" general-purpose moment method code, FISC [6], and a body of revolution moment method code, CICERO [4]. The difference between the calculated and measured RCS is shown in Figures 4(a) and 4(b). It is clear that both codes agree very well with each other and with measurements.

Figure 5 shows the calculated RCS of the bicone and "squat" cylinder as a function of elevation angle. The calculations are scaled in frequency so that the two objects are approximately the same number of wavelengths in height. The results clearly show that the bicone is less sensitive to variations in elevation than the "squat" cylinder.

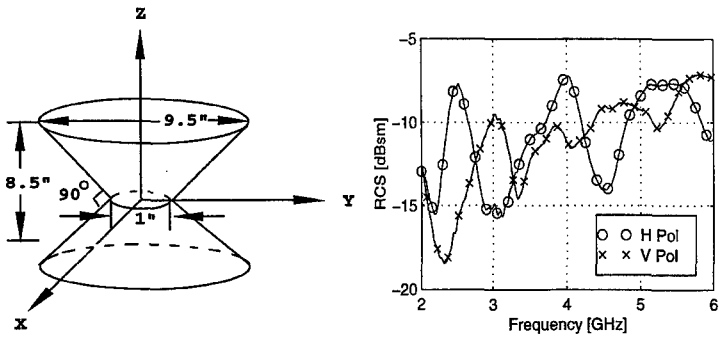

(a) Geometry of the bicone. The bicone is 9.5 inches in diameter, 8.5 inches in height, and the waist is 1.0 inches in diameter.

(b) Measured RCS as a function of frequency.

Figure 3: Measured monostatic RCS of the bicone as a function of frequency. The elevation angle is 0°; that is, the bicone is edge-on to the incident field.

5 Dihedral

Dihedrals are used as calibration targets mainly to calibrate the radar cross-pol responses. Shown in Figure 6(a) is the dihedral used in this study. Figure 6(b) shows comparison between the measured and predicted radar cross sections for the VV and HH polarizations with the incident field illuminating from the positive X direction. The predicted data were obtained using the AIM code [1]. The HH curves compare very well with less than one dB error; while the VV curves compare well from 4 to 6 GHz but have a substantial discrepancy from 2 to 4 GHz. The discrepancies are due to the interactions between the vertical edges of the dihedral and the rotator mount. This target/rotator interaction is stronger for V-pol than for H-pol and is more significant at lower frequencies. The calibration measurement data shown in Figures 7(a) and 7(b) were taken with the dihedral rotating 360 degrees around the x-axis. The dihedral has one plane of symmetry. Thus, the VV and HH responses have a 180-degree periodicity and the VH and HV responses have a 90-degree periodicity. The VV and HH responses should be the same except for a 90-degree phase shift. The VH and HV responses are identical. Only two data points, the VV and HH backscattering responses along the x-axis (Azimuth angle equal to zero), are calculated. These VV and HH responses are then projected to the properly transformed coordinate system to generate the 360-degree pattern cut shown in Figure 7. The asymmetry of the measured data is due to the indentations in one of the vertical edges of the dihedral. The discrepancies at the peaks are due to the target/rotator interactions.

6 Summary

We have discussed the RCS calibration process from the viewpoint of designing RCS calibration targets to enhance the accuracy of RCS measurements. We have shown that the state-of-the-art in computational electromagnetics is sufficient to accurately predict the RCS of candidate calibration targets. We have pre-

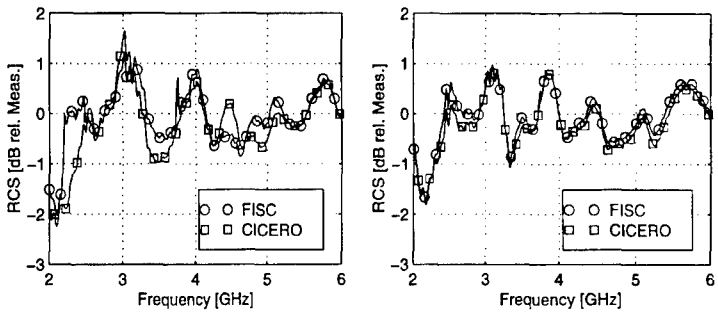

(a) Difference between calculated and measured RCS – HH Polarization

(b) Difference between calculated and measured RCS – VV Polarization

Figure 4: Calculated RCS data versus frequency for the bicone, provided by FISC [6], a "fast" general-purpose moment-method code, and CICERO [4], a body-of-revolution moment-method code. Results are plotted as RCS relative to measurements.

sented results for the "squat" cylinder, bicone, and dihedral calibration targets, as well as calculated data from two different "fast" moment-method codes, two different body of revolution moment-method codes, and a physical theory of diffraction code. Excellent agreement with measurements was observed for the moment-method codes.

7 Acknowledgments

The authors gratefully acknowledge the valuable assistance provided by the following persons: Dr. Marek Bleszynski, Mr. Alan Buterbaugh, Mr. Richard Porter, Dr. Brian Kent, and Mr. Ed LeBaron. The authors are further indebted to the High Performance Computing (HPC) Major Shared Resource Center (MSRC) at Wright-Patterson AFB OH for providing some of the computational resources used in this study.

References

[1] Bleszynski, E. and Bleszynski, M., *Development and Implementation of Computational Electromagnetic Techniques on Massively Parallel Computing Architectures*, DRAFT Final Technical Report, Boeing North American Aviation Division, Seal Beach CA, June 1997.

[2] Hulst, H.C. van de, "Light Scattering by Small Particles," Wiley, New York, 1957.

[3] Kent, B.M., Chizever, H.M., and Soerens, R.J., "On Reducing Primary Calibration Errors in Radar Cross Section Measurements," *Proc. AMTA*, Seattle WA, 1996.

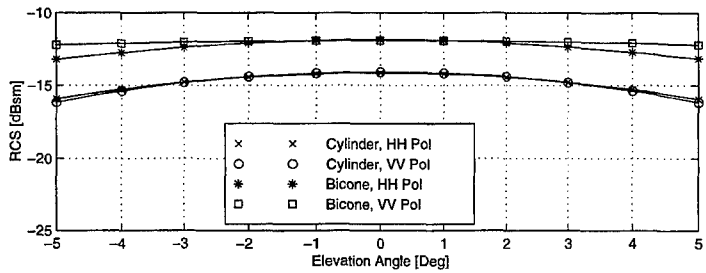

Figure 5: Calculated RCS versus elevation angle for the "squat" cylinder and bicone calibration bodies. The calculations are provided by FISC [6], and are scaled in frequency so that each body is approximately two wavelengths in height.

[4] Putnam, J.M., and Medgyeshi-Mitschang, L.N., *Combined Field Integral Equation Formulation for Axially Inhomogeneous Bodies of Revolution (Combined Field Formulation of CICERO)*, Report MD-CQA003, McDonnell Douglas Research Laboratory, St Louis MO, Dec 1987.

[5] Rogers, J., *JRMBOR: Computation of Scattering from a General Body of Revolution, Vol. 1: Formulation and MoM Algorithm, Vol. 2: Test Cases, Vol. 3: Code Listing*, Technical Report JR-2, Atlantic Aerospace Corporation, Greenbelt MD, 1989.

[6] Song, J. *et al*, *User's Manual for FISC: Fast Illinois Solver Code, Version 1.0*, DEMACO, Inc., Champaign IL, 1997.

[7] *XPATCH 2.4 User's Manual*, DEMACO, Inc., Champaign IL, 1997.

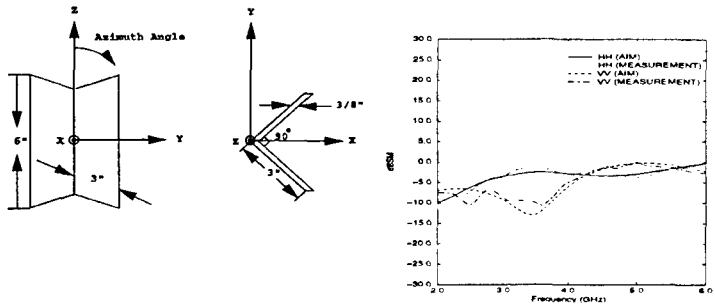

(a) Geometry of the dihedral. Each plate of the dihedral is 6 inches high, 3 inches wide, and 0.375 inches thick.

(b) Measured and calculated monostatic RCS of the dihedral as a function of frequency.

Figure 6: Monostatic RCS of the dihedral as a function of frequency. The elevation angle is 0°; that is, the incident wave is parallel to the front edges of the dihedral. Calculated values are provided by AIM [1], a general-purpose moment-method code employing a "fast" solution technique.

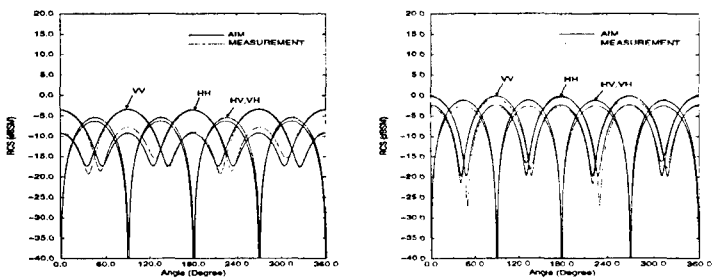

(a) Monostatic RCS as a function of rotation angle; frequency = 3 GHz.

(b) Monostatic RCS as a function of rotation angle; frequency = 6 GHz.

Figure 7: Measured and calculated RCS of the dihedral as a function of rotation angle about the x-axis. Calculated values provided by AIM [1]. Peaks of the cross-pol and co-pol RCS are within 5 dB of each other.

Radar Calibration at Low Frequencies Using a Triangular Trihedral Corner Reflector

C. Y. Shen
XonTech, Inc
6151 West Century Blvd. Suite 600
Los Angeles, CA 90045

In recent years, instrumentation radars have been widely used to make radar reflectivity measurements or images. The usefulness of the data collected by an instrumentation radar depends on the ability to accurately calibrate such a system (see [1]). For most calibration schemes, measurements of a reference target are often used, and the true radar cross section (RCS) and the polarization characteristics of such a target must be known.

Simple geometrical objects, such as spheres, plates, or dihedral reflectors, are often used as the reference target. An important reason for choosing these objects as reference targets is that simple formulas are available for calculating their RCS in the high frequency region. However, these formulas are known to become inaccurate in the resonant or low–frequency region, and a different means must be found to obtain the RCS of such targets.

Computational methods are natural candidates to be used to obtain the RCS of reference targets. In particular, the integral equation technique has proven to be very successful in calculating the RCS of different scatterers over a wide frequency range. However, the integral equation technique places a heavy demand on the computer resources and requires a careful numerical treatment of the singular nature of the kernel of the integral equation. For a certain class of problems such as plates or corner reflectors, these difficulties can be circumvented by exploiting the particular mathematical structure associated with these problems.

Among some of the commonly used reference targets, the triangular–shaped trihedral corner reflector possesses many desirable qualities:

1) It offers a large return with relation to its size, and this large return is sustained over a broad range of aspect angles.

2) The polarization of the reflected wave is known to be the same as that of the incident wave.

3) From the computational standpoint, a triangular trihedral corner reflector can be treated basically as three mutually interacting triangular plates.

The first property mentioned above provides a greater tolerance to the calibration target orientation. The last observation can be used in designing an efficient numerical technique to solve the electric field integral equation (EFIE) associated with a triangular trihedral corner reflector.

Results and Discussion

A modular electromagnetic computation algorithm (MECA) is used to compute the RCS of a triangular–shaped trihedral corner reflector of dimension 2.4384 meters (see Fig. 1). The most important feature of this algorithm lies in the decomposition of the dihedral corner reflector into three triangular plates S_j, j = 1, 2, and 3, and will be briefly described below.

Suppose the surface current over S_j is denoted by $\underline{J}_j$. Then the scattered field at an arbitrary spatial point $\underline{x}$ due to the current $\underline{J}_j$ can be symbolically written as

$$\underline{E}^S(\underline{x}) = L\,(\underline{J}_j)\,(\underline{x})\,,$$

where L is a linear differential integral operator (see [2, eq. 1]). The tangential component of $\underline{E}^S$ to S_i is given by

$$\underline{n}_i \times \underline{E}^S = \underline{n}_i \times L(\underline{J}_j) = L_{ij}(\underline{J}_j)\,,$$

where $\underline{n}_i$ is the unit normal vector to S_i. From the enforcement of the usual boundary condition, the following EFIE can be obtained:

$$\begin{pmatrix} L_{11} & L_{21} & L_{31} \\ L_{12} & L_{22} & L_{32} \\ L_{13} & L_{23} & L_{33} \end{pmatrix} \begin{pmatrix} \underline{J}_1 \\ \underline{J}_2 \\ \underline{J}_3 \end{pmatrix} = \begin{pmatrix} \underline{E}_1^{(i)} \\ \underline{E}_2^{(i)} \\ \underline{E}_3^{(i)} \end{pmatrix}$$

In the above equation, $\underline{E}_j^{(i)}$, j = 1, 2, and 3, denotes the tangential component of the incident field over S_j. The above system of integral equations is in a format which can be solved in an efficient manner on a parallel supercomputer.

Various tests have been conducted to validate the numerical technique and the resulting computer code. An easy test is to blank out one of the three sides and to reduce the target to a dihedral corner reflector. Results on dihedral corner reflectors have been obtained earlier by the author [2] and can be used for comparison. Also, for the present situation, the computed results should be the same regardless of which side is blanked out. This symmetry property would indicate that the mutual interaction terms were correctly modeled numerically. The code has produced extremely good accuracy in this regard.

As another test, an H–pol sweep ($\theta = 54.74^\circ$, $-180^\circ \leq \varphi \leq 180^\circ$) was made of a rectangular dihedral corner reflector at 300 MHz. The dimension of the dihedral reflector is 5.6088 wavelengths for all sides. A resolution of approximately 10 divisions per wavelength was used in this calculation, and a logarithmic RMS error of –1.6 was achieved. This result is presented in Fig. 2 , and it agrees well with the values given by the high frequency formula.

A third test was made to test the convergence of the numerical method. The RCS of a triangular dihedral reflector vs. the error is shown in Fig. 3. The incident angles are $\varphi = 45^\circ$ and $\theta = 54.74^\circ$, and the dimension of the corner reflector is 2.4384 meter for each of its three vertical sides.

Next, the numerical technique MECA is used to compute the RCS of a triangular dihedral corner reflector of the dimension as shown in Fig. 1. RCS over a frequency sweep from 100 MHz to 300 MHz was calculated at a look angle where the propagation vector coincided with the unit normal vector $\underline{n}$ of the open triangular face (see Fig. 1). A resolution of 15 divisions per meter and an error criterion of –1.8 were used in this calculation.

For the purpose of comparison, the RCS was also calculated by using the high frequency formula

$$\sigma = \frac{4\pi a^4}{3\lambda^2}.$$

The MECA–computed RCS and that obtained by the high frequency approximation are both shown in Fig. 4. Note that the RCS fluctuates around the curve given by the high frequency formula and that a deep null is present around 150 MHz. This result shows clearly that the high frequency approximation is not valid in the resonat region. Fig. 4 should be used for any calibration references.

References

1. N. C. Currie, Radar Reflectivity Measurement: Techniques and Application. Artech House, 1989.

2. C. Y. Shen, Application of the Discrete Fourier Transform Method to Nonorthogonal Dihedral Reflectors, IEEE Trans. Antennas Propagat., vol. 38, No. 12, pp. 1913–1919, December 1990.

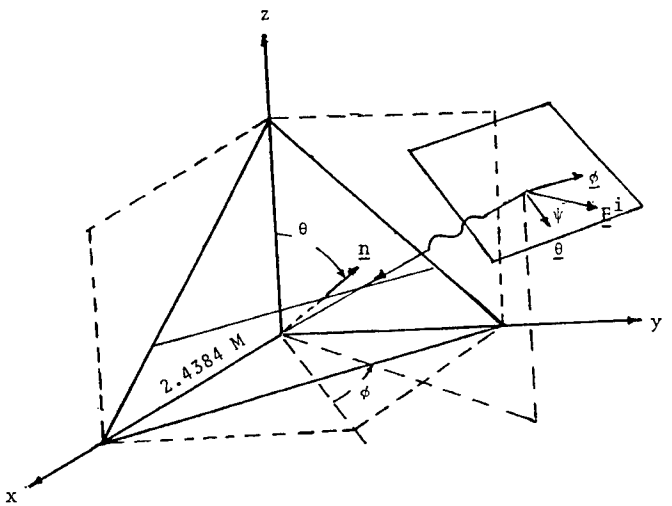

Fig. 1 The geometry of a trihedral reflector

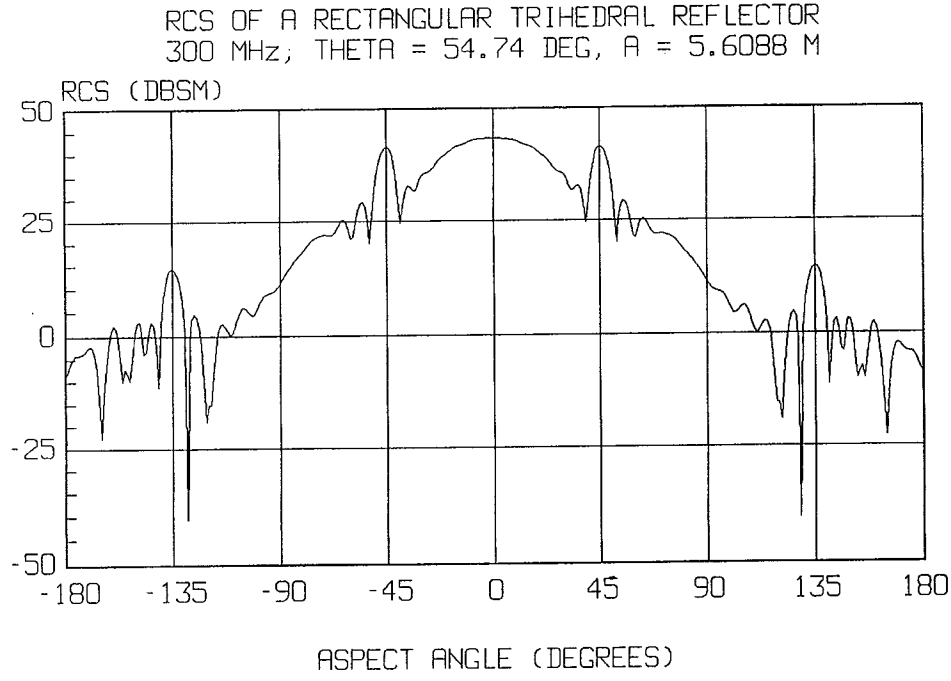

Fig. 2 The H–pol sweep of a rectangular trihedral reflector

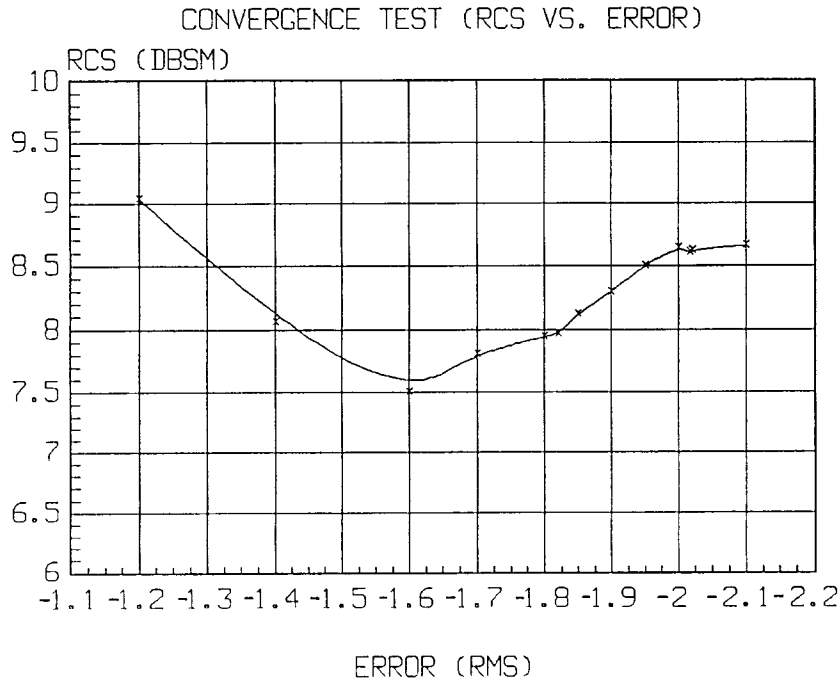

Fig. 3 RCS vs. error for a triangular trihedral reflector

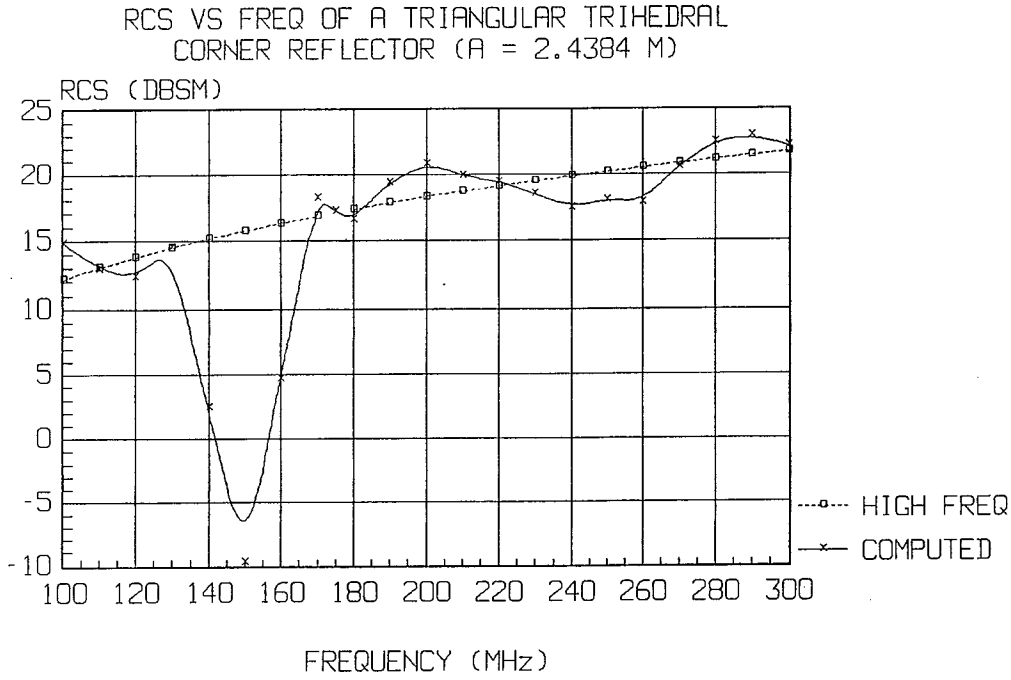

Fig. 4 Frequency sweep for a triangular trihedral reflector

SESSION 2:

FINITE-DIFFERENCE TIME-DOMAIN APPLICATIONS

Chair:J. Beggs and M. Piket-May

Time Domain Analysis of Small Multi-Sector Monopole Yagi-Uda Array Antenna Mounted on a Finite Ground Plane Using FDTD Method

T. Maruyama, K. Uehara, T. Hori and K. Kagoshima

NTT Wireless Systems Laboratories, JAPAN

Summary:

This paper shows a time domain analysis, using the FDTD method, of the Multi-Sector Monopole Yagi-Uda Array Antenna (MS-MPYA) mounted on a finite ground plane. The MS-MPYA has an interesting feature. That is, we can sharpen the beams using the adjacent array effect if we set metallic fins between the arrays so as to hide the excitors. Without the fins, undesired radiation causes beam division. To examine this mechanism, this paper provides FDTD results for three types of Multi Sector Monopole Yagi-Uda Antenna: without adjacent arrays, with adjacent arrays but without fines, and with arrays and fins. Experimental and MOM results confirm the accuracy of the FDTD model. The transient solution tells us that without the fins, the beams propagate in three directions. Adding the fins, however, delays the onset of reradiation from the adjacent arrays as well as reducing the level of reradiation which suppresses beam division.

1. Introduction:

The Multi Sector Monopole Yagi-Uda Antenna can achieve the low profile multi-sector antennas[1] ,[2] that are needed for realizing high speed indoor wireless LANs. The monopole Yagi-Uda antenna is a surface wave antenna and offers a lower profile than is possible with corner reflectors. MS-MPYA is one third the height of an ordinary three dimensional corner reflector antenna. The multi-sector configuration sharpens the beam width, so we can get same level of directivity but with a shorter array than the One-Array model. The MS-MPYA sets metallic fins between the arrays to suppress undesired radiation from adjacent arrays. The fin length is optimum when it just hides the excitors; lengths longer than this reduce the level of directivity. A previous study[3] reported these interesting characteristics as determined from Near field calculations based on MOM[7]; mutual interaction, isolation, and poynting vectors were considered. This paper, uses time domain analysis to examine MS-MPYA characteristics. Three kind of models are examined: without adjacent arrays, with adjacent arrays but without fines, and with arrays and fins.

Kashiwa et al. [5] provided the time domain analysis of a two element Yagi-Uda Antenna. Reference [5] compares the instantaneous distributions of electric field intensity for two cases: the parasitic elements work as the director and the parasitic elements work as the reflector. However, no one has considered in detail the case of a multi sector Yagi-Uda antenna that consists of many elements, a finite ground plane, and a reflector. This paper considers, for the first time, the existence of reradiation from the adjacent arrays in determining the final main beam pattern.

At first, we compare the results of FDTD analysis, MOM analysis, and experiments, and show that they match very well which confirms the accuracy of the calculation models. Next, we show the radiation patterns of the three models. Proof is given that the model with fins and adjacent arrays achieves the sharpest beam width and highest level of directivity. Next, we show the Poynting powers transient solution of these three models. Finally our conclusions are given.

2.Antenna configuration and analysis models:

The MS-MPYA's antenna configuration is shown in Figure 1. This antenna consists of twelve monopole Yagi-Uda array antennas, a cylindrical reflector, circular ground plane, and metallic fins. Beam tilt is realized by the finite ground plane effect. One design goal is half power beam width of 30 degrees in horizontal plane. The antenna structural parameters are shown in Table1. These values are almost the same as those in reference [1]; the design conditions are shown in Table 2. The FDTD analysis model is shown in Fig.2 and calculating conditions are shown in Table 3.

As the total size of the MS-MPYA is almost ten wavelengths, we reduce the analysis model to three arrays. The three array model reproduces the adjacent array effect and is adopted in MOM calculations[1]. For MS-MPYA's main array, the adjacent array effect is dominant. The results of the model analysis well match those of an actual 12 sector array [1].

We use Cartesian coordinates for FDTD analysis model

shown in Fig.2. We paint white for perfect conductor shown in Fig.2. Fins and circular reflector are 1mm thick to match the experimental antenna and the MOM analysis model for MS-MPYA[1]. As to the ground plane, its thickness doesn't have a significant effect so we set it to 0. We assume that the thickness of each element is virtually zero compared to the wavelength. Therefore, the z-direction electric field of each element is set to 0. Please note that the elements in Figure 2 are drawn proportionally larger than their real size for better understanding. Generally speaking, the difference in the height of the Yagi-Uda antenna's elements is almost 1/200 wavelengths. If we define the unit cell length to be 1/200 wavelengths, the memory required and calculation time would be excessive. To simplify FDTD calculations, we use the cell dimensions shown in table3. For FDTD calculations the MS-MPYA is fed at #1 element of the center array with a Gaussian pulse voltage.

Table1 Antenna structure parameter

Simbol		*name*
λ		*:wavelength*
f	*19.5GHz*	*: frequency*
n	*:12*	*: number of sector*
r	*:4.9 λ*	*: ground plane radius*
s	*:1.0 λ*	*: center space radius*
hr	*:0.39 λ*	*: reflector height*
lr	*:0.52 λ*	*: fin length*
d0	*:0.39 λ*	*: space between reflector and element #1*
dp	*:0.31 λ*	*: pitch between elements*
#1		*: excitor*
#2		*: director*
..#k		
k	*9*	*: array number*
hi		*: height of elements*
h1	*0.209 [λ]*	*:3.3 [mm]*
h2..h4	*0.193 [λ]*	*:2.97[mm]*
h5..h9	*0.171 [λ]*	*:2.64 [mm]*

Table 2 Design condition

HPBW in H-plane	30°
Tilt Angle in V-plane	$15^\circ \leqq \alpha \leqq 20^\circ$
Front to Back ratio	≧ 20dB
Directivity	≧ 15dBi
Isolation	≧ 30dB

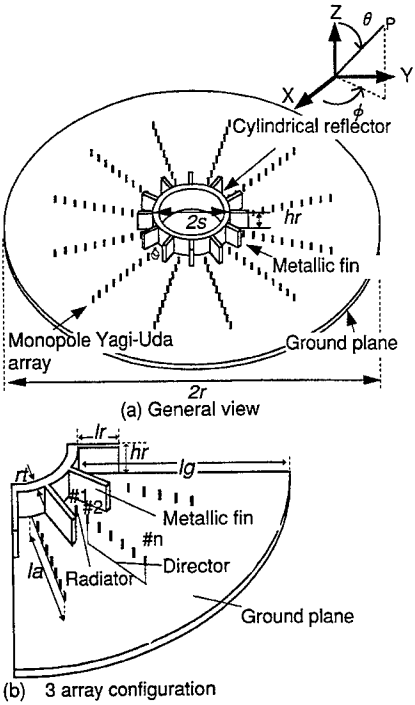

Figure1 show MS-MPYA antenna structure.

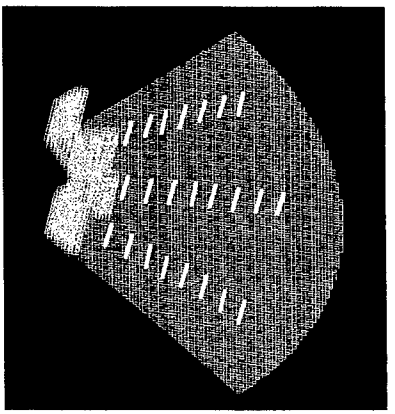

Figure2 Analysis model

Table 3 The calculation condition

Coordinate	Cartesian
number of cell	157×213×209
Cell dimensions	△x=0.66mm,△y=0.66mm, △z=0.33mm
ABS	Second Order Mur Absorbing boundaries
time step	2000

3 Calculation result

3.1 Basic characteristic of MS-MPYA

Figure3 compares FDTD analysis, MOM [1], and experimental results on the radiation pattern in the horizontal plane for the MPYA with fin and with adjacent arrays (same as in Figure 2). MOM results follow those in reference[1]. Figure 3 shows that the FDTD analysis results well match the others in terms of main lobe and back lobe. Only side lobe direction shows a slight difference; this is because MOM calculations considered element radius but FDTD did not. Another reason is because element height in the FDTD analysis model was somewhat coarser than in the MOM model. Reflection Power vs. Frequency is shown in Figure 4. At the desired frequency; 19.5GHz, the Reflection Power was almost 15dB. Figures 3 and 4 confirm that the FDTD model of MS-MPYA is accurate.

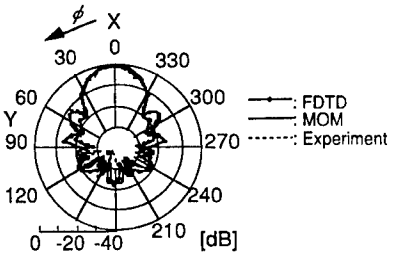

Fig.3 Comparing result of two kind of numerical calculation result; using FDTD and MOM, and Experimental Result method of MS-MPYA about Horizontal plane radiation pattern. This antenna structure is with fin and setting adjacent arrays model.

Next, to examine the adjacent array effect, the radiation pattern in horizontal plane of the three models were determined and plotted in Figure 5. We can see that the adjacent arrays sharpens the beam width if the metallic fins are present. The largest beam width is seen without the fins. This is same phenomenon with shown in reference [1],[3] that calculated by MOM

The radiation patterns in the horizontal plane of these three models at three frequencies are shown in Figure 6. Comparing Fig.6 (b) to Fig.6 (c) shows us that adding side arrays sharpens the main beam. Comparing Fig.6 (a) to Fig.6 (b) shows that the fins suppress undesired side lobes. These phenomena match the MOM results of our previous studies [1], [2], [3].

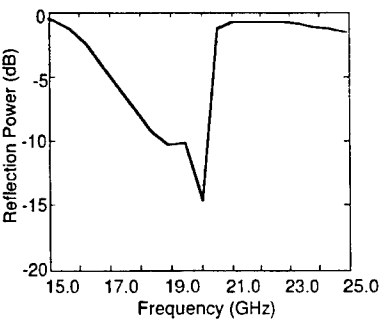

Fig.4 FDTD Calculation Result Reflection Power vs Frequency

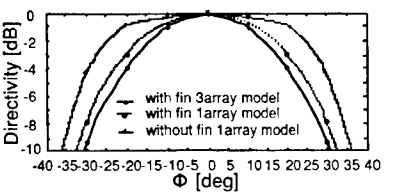

Fig.5 Radiation pattern in Horizontal plane

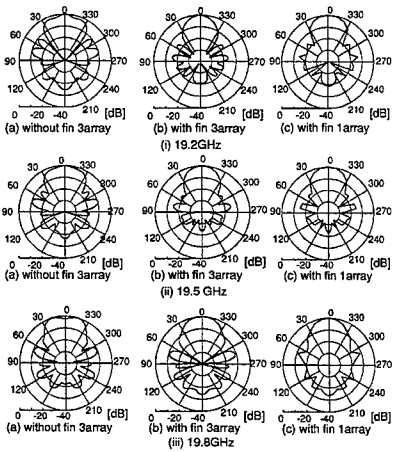

Fig.6 Radiation pattern in Horizontal Plane of three array model.

3.2. Transient solution

To understand how the metallic fins and adjacent arrays influence antenna performance, Fig 8. shows the transient solution of the three models. The Poynting powers are those on the X-Y plane placed 1.32mm above the ground plane. The analysis space and coordinates are shown in Fig.7. Transient solutions at five times (286.9ps, 477.6ps, 954.2ps, 1431ps, and1812 ps) are shown in Fig.8 to Fig.12, respectively. The 3 array model without fins exhibits reradiation from adjacent arrays at 286.9ps while the other two models shown no such effect even up to 477.6ps. At 954.2ps, the response of the 3 array model with fins differs from that of the 1 array model with fins. From this time, we find that the 3 array model with fins exhibits some slight reradiation from adjacent arrays. These results indicate that the fins delay the onset of reradiation from adjacent arrays. An examination of the field strength indicates that the fins also weaken the side lobe levels.

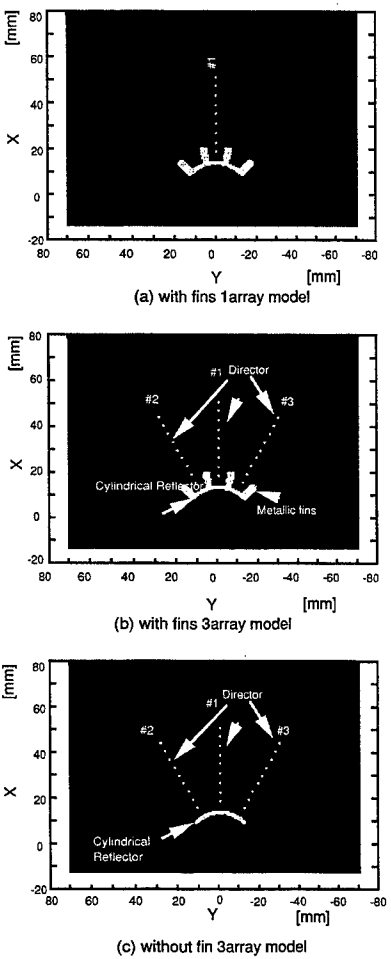

Fig.7 Antenna Configuration and Coordinate in X-Y plane that is made at 1.32mm above of ground plane ■: Analytic space

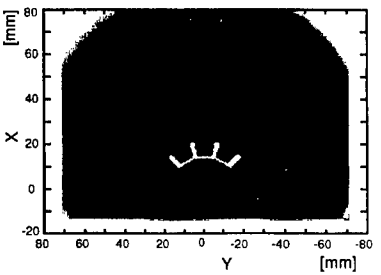

(a) with fins 1array model

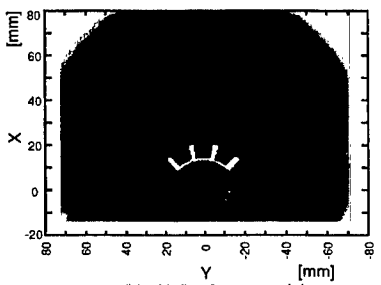

(b) with fins 3array model

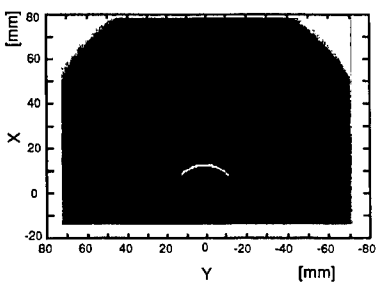

(c) without fin 3array model

Fig. 8 Instaneous distributions of poynting power of t=286.9ps

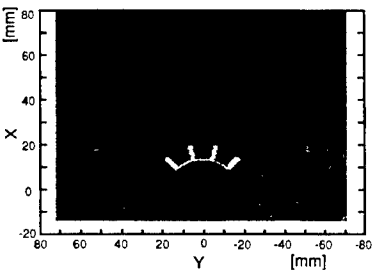

(a) with fins 1array model

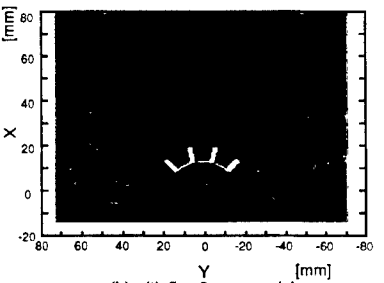

(b) with fins 3array model

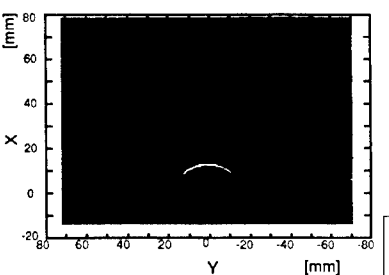

(c) without fin 3array model

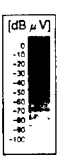

Fig. 9 Instaneous distributions of poynting powe of t=477.6ps

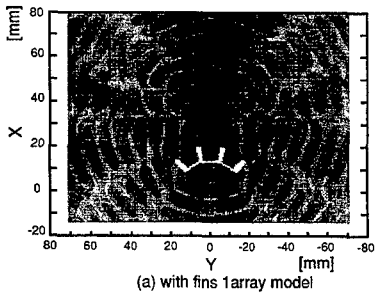

(a) with fins 1array model

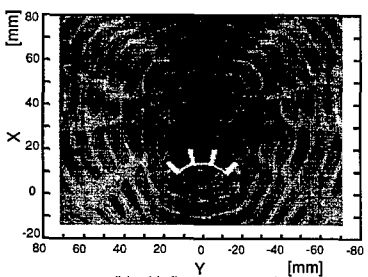

(b) with fins 3array model

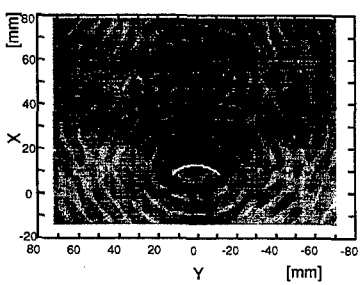

(c) without fin 3array model

Fig. 10 Instaneous distributions of poynting power of t=954.2ps

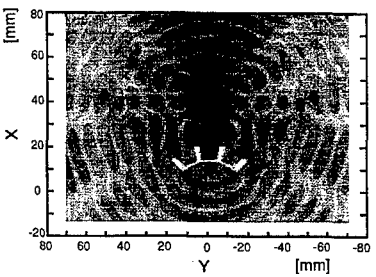

(a) with fins 1array model

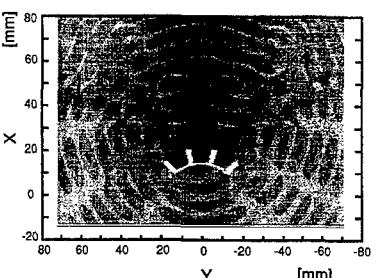

(b) with fins 3array model

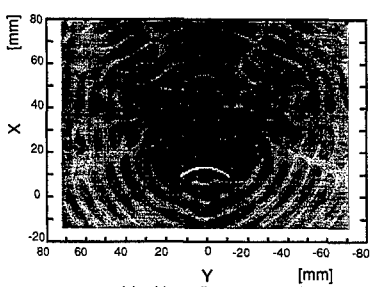

(c) without fin 3array model

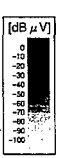

Fig. 11 Instaneous distributions of poynting power of t=1431ps

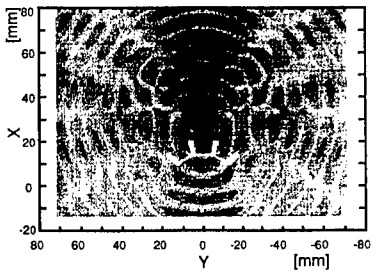

(a) with fins 1array model

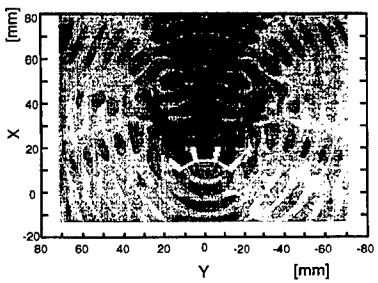

(b) with fins 3array model

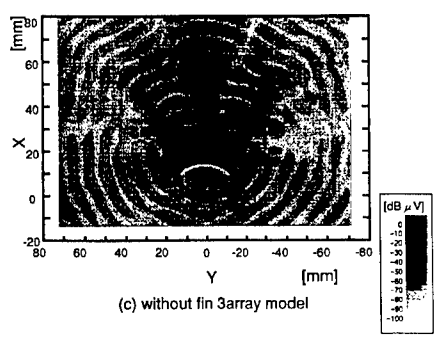

(c) without fin 3array model

Fig. 12 Instaneous distributions of poynting power of t=1431ps

5 Conclusion

This paper showed the results of a temporal analysis of the Multi-Sector Monopole Yagi-Uda antenna by the FDTD method. The analysis results well match with the corresponding experimental and numerical results. The transient response shows the different responses of three models: 3 array model without fins, 3 array model with fins, 1 array model with fins. Setting metallic fins between the arrays, appears to interfere with the establishment of reradiation from the adjacent arrays.

Acknowledgments

The authors would like to acknowledge Dr. Shuichi Samejima and Dr. Takehiro Murase for their continuous encouragement.

References

[1]T.maruyama, K.Uehara, K.Kagishima: "Design and Analysis of Small Multi-Sector Antenna for Wireless LANs Made by Monopole Yagi-Uda Array Antenna", IEICE. Trans., vol. J80 B-II, No. 5, pp.424-433, MAY. 1997 (in Japanese).

[2]T.maruyama, K.Uehara, K.Kagishima: "Analysis and Design of Multi-Sector Monopole Yagi-Uda Array Mounted on a Ground Plane Using Moment Method" IEE, Conf. Publication, 420, 3rd computation in electromagnetics, pp.289-294, April, 1996.

[3]T.maruyama, K.Uehara, K.Kagishima: "Rigorous Analysis of A Multi-Sector Monopole Yagi-Uda Antenna with metallic Fins" Proc. 1996 Int'l Symp. Antennas and Propagation, ISAP'96, Japan, pp.1017-1020, Sept. 1996.

[4]K. Kunz, R. J. Luebbers:" The Finite Difference Time Domain Method for Electromagnetics", CRC Press. 1993.

[5]T. Kashiwa, S. Tanaka, I. Hukai:"Time Domain Analysis of Yagi-Uda Antennas Using the FD-TD Method", IEICE. Trans., vol. J76-B-II, No. 11, pp.872-879, Nov. 1993 (in Japanese).

[6]P. P. Viezbike, "Yagi Antenna Design," NBS Tech. Note, 688, Dec. 1976.

[7]G. J. Burke, and A. J. Poggio, "Numerical Electromagnetics Code (NEC) - Method of Moments, Part I-III," Lawrence Livermore National Laboratory, 1981.

Antenna Performance Calculation in Lossy Media with FDTD Method

M. Cai N. Ljepojevic

Centre for Computer and Mathmatical Modelling, School of EEIE
South Bank University, London
103 Borough Road, London, SE1 OAA, UK

December 1, 1997

Abstract

The antenna input admittance in lossy media is computed by FDTD method. The Ideal Absorption Condition, an extension of Perfectly Matched Layers (PMLs), is used to confine the lossy media with the same advantages of PMLs. The calculated results are compared with existing experimental results. A good agreement is found. Results for a mobile antenna are also given.

Summary

Antenna performance in lossy media is of interest, because antennae are used in many lossy media, for example, undersea and underground etc. Various methods have been developed for theoretical analysis of the antenna performance in lossy media. However the analytical solution is rather complicated even just for the dipole antennas [5]. In this paper, we use FDTD method to solve the problem. In order to confine the computation lossy area, we use a new absorbing boundary, an extension of the Perfectly Matched Layers (PMLs) [1], the Ideal Absorption Condition (IAC) [2] [3] which is based on the equivalent constitutive parameters. If (E_c, H_c) represent the fields in the original lossy media and (E_s, H_s) represent the fields in the equivalent media, the relationship between (E_s, H_s) and (E_c, H_c) is given by:

$$E_s = \sqrt{A}E_c, \quad H_s = \sqrt{A^m}H_c \tag{1}$$

where $A = 1 - jp_e$, $A^m = 1 - jp_m$, $p_e = \frac{\sigma}{\omega\epsilon}$ is the electrical loss tangent and $p_m = \frac{\sigma^m}{\omega\mu}$ is the magnetic loss tangent. The formula (1) can be written in the following form:

$$E_s = (C_R^e + jC_I^e)E_c, \quad H_s = (C_R^m + jC_I^m)H_c \tag{2}$$

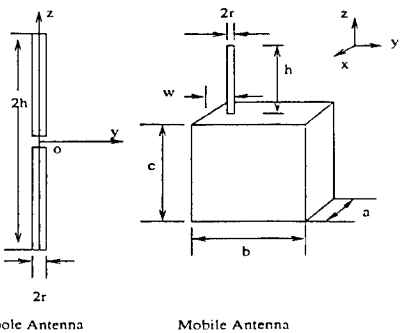

Figure 1: Geometry of Dipole and Mobile Antennae.

Table 1: The parameters of dipole antenna

Frequency = 1.5 GHz	h = 50 (mm)	r = 0.266 (mm)
cell sizes = 2.5 (mm)	total cell number = 60x60x80	time steps = 800

where

$$C_R^e = \sqrt{\frac{\sqrt{1+p_e^2}+1}{2(1+p_e^2)}}, \quad C_I^e = \sqrt{\frac{\sqrt{1+p_e^2}-1}{2(1+p_e^2)}} \tag{3}$$

$$C_R^m = \sqrt{\frac{\sqrt{1+p_m^2}+1}{2(1+p_m^2)}}, \quad C_I^m = \sqrt{\frac{\sqrt{1+p_m^2}-1}{2(1+p_m^2)}} \tag{4}$$

We use the above formulae to obtain the fields in the original media from those in the equivalent media.

The modelling results are given in the following.

Input admittance of dipole: The dipole antenna is shown in Fig.1. In order to include the effects of the relatively small radius of wire antennas, the magnetic fields surrounding the electric field components along the wire were treated by the method explained in the reference [4]. The parameters of the dipole are given in Table.1. The source is the Gaussian pulse source voltage $V(t)$ as shown in Fig.2, which is represented by E component with one cell length along the wire axis at the middle of dipole antenna. The voltage source is used throughout in the numerical impedance calculations. When compared with the experimental results [5], we see the

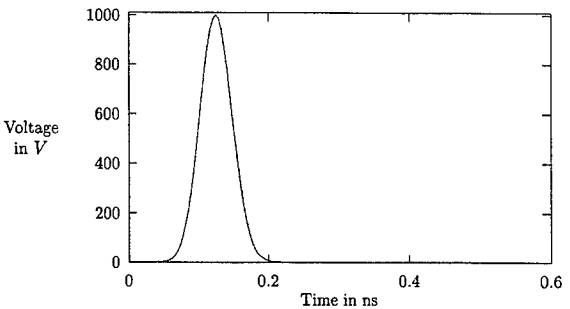

Figure 2: The Gaussian voltage used in FDTD method for mobile antenna

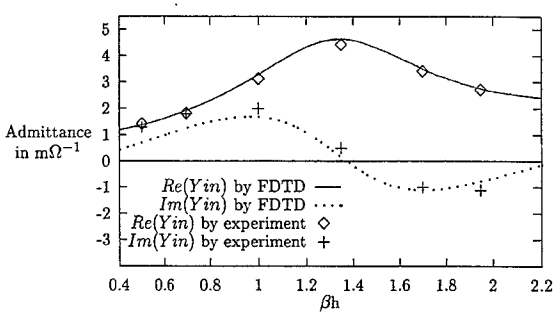

Figure 3: The input impedance of dipole antenna in lossy media

Table 2: The equivalent constitutive parameters for dipole

σ (S/m)	σ_g (S/m)	σ_g^m (Ω/m)	ε_g (F/m)	μ_g (H/m)
0.0	0.0	0.0	$8.85e^{-12}$	$1.256e^{-6}$
0.0552	0.0328	3735.435	$9.28e^{-12}$	$1.32e^{-6}$

Table 3: The parameters of mobile antenna

Frequency = 1.5 GHz		
a = 60 (mm)	b = 10 (mm)	c = 50 (mm)
w = 30 (mm)	h = 50 (mm)	r = 0.5 (mm)
cell sizes = 2.5 (mm)	total cell number = 60x60x60	total time step = 2400

Table 4: The equivalent constitutive parameters for mobile antenna

σ (S/m)	σ_g (S/m)	σ_g^m (Ω/m)	ε_g (F/m)	μ_g (H/m)
$1.0e^{-10}$	$5.0e^{-11}$	$7.1e^{-6}$	$8.85e^{-12}$	$1.256e^{-6}$
$5.0e^{-2}$	$2.402e^{-2}$	$3.409e^{3}$	$9.21e^{-12}$	$1.307e^{-6}$

FDTD modelling results agree very well, as shown in Fig.3 where

$$\beta = \frac{2\pi}{\lambda}\sqrt{\frac{1+\sqrt{1+p_e^2}}{2}}$$

and λ is the wavelength and p_e is the electrical loss tangent. Table.2 gives the equivalent constitutive parameters related to different conductivities σ in lossy media.

Mobile antenna: The geometry of mobile antenna is shown in Fig.1. A monopole antenna is connected to a conducting box and fed at the junction between the monopole and the box. The parameters for FDTD calculation are given in Table.3. We are not aware of any experimental data for the mobile antenna in lossy media. However, in the lossless media, the agreement between the FDTD calculations and experiment results obtained from [6] is quite good. The equivalent constitutive parameters for $\sigma = 1.0^{-10}(S/m)$ media are similar to the constitutive parameters in lossless media. Table.4 gives the equivalent constitutive parameters related to different conductivities σ in lossy media. Fig.4 shows the transient currents calculated by FDTD method with IAC. Although the variation of currents with time in different lossy media is similar, the amplitude of current in $\sigma = 5.0^{-2}(S/m)$ medium is much less than that in $\sigma = 1.0^{-10}(S/m)$ medium. The same phenomena are observed in the impedence calculation results shown in Fig.5. The absolute values of $Re(Z_{in})$ and $Im(Z_{in})$ in $\sigma = 5.0^{-2}(S/m)$ medium is much less than that in $\sigma = 1.0^{-10}(S/m)$ medium.

Conclusion: The FDTD method with IAC has been used in the lossy media to analyze the antenna performance. A good agreement is obtained with the available experimental data. Results for a mobile antenna are also given.

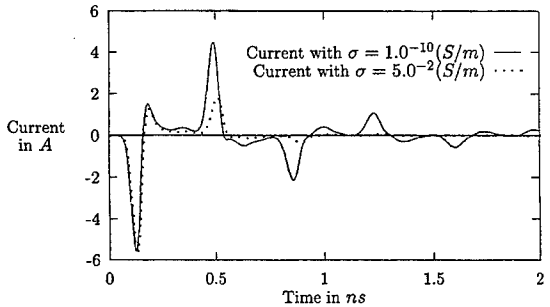

Figure 4: The transient current on mobile antenna excited by Gaussian voltage in lossy media

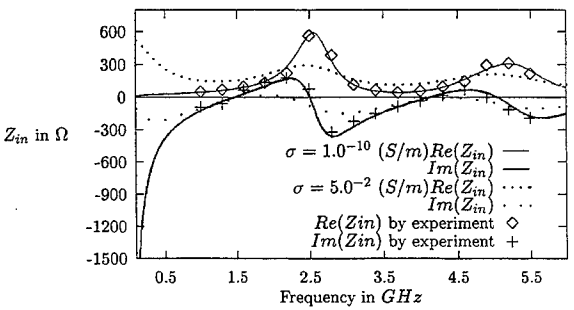

Figure 5: The input impedance of mobile antenna in lossy media

References

[1] J.-P. Berenger, *"A Perfectly Matched Layer for the Absorption of Electromagnetics Waves"*. *J. Comput. Phys.*, Vol. 114, No. 1, pp. 185-200, 1994.

[2] M. Cai, H. Zhou and N. N. Ljepojevic, *"Ideal Absorption Condition for the FDTD Method in Isotropic Lossy Dispersive Media"*, *2nd High Frequency Postgraduate Student Colloquium, UMIST, Manchester, U.K.*, Sept., 1996.

[3] M. Cai and H. Zhou, *"Constitutive Equivalent Principle and an Ideal Absorption Condition for the FDTD Method in Isotropic Lossy Dispersive Media"*, *Microwave Opt. Technol. Lett.*, Vol. 13, No. 4, pp. 190-193, 1996.

[4] K. R. Umashankar and A. Taflove and B. Beker, *"Calculation and experimental validation of induced currents on coupled wire in an arbitrary shaped cavity"*, *IEEE trans. Antenna Propagat.*, Vol. AP-35, pp. 1248-1257, Nov., 1987.

[5] S. R. Mishra, *"Three-Term Exponential Product Solution for the Current on Dipole Antenna in homogeneous Isotropic Media"*, *Division of Engineering and Applied Physics, Harvard Univ. Technical Report No. 636*, 1972.

[6] R. Luebbers and L. Chen and T. Uno and S. Adachi, *"FDTD Calculation of Radiation Patterns, Impedance, and Gain for a Monopole Antenna on a Conducting Box"*, *IEEE Trans. Antennas Propagat.*, Vol. 40,No. 12, pp. 1577-1583, 1992.

Far-zone transformation in FDTD for VHF-band SAR-image simulations

Torleif Martin, Lars Ulander
Defence Research Establishment (FOA)
P.O. Box 1165, S-581 11 Linköping, Sweden
email: tormar@lin.foa.se

1. INTRODUCTION

The CARABAS-II radar system is an airborne synthetic-aperture radar (SAR) which operates in the lower VHF band (20-90 MHz) using horizontal polarization on both transmit and reception. It has mainly been designed for foliage penetration and detection of concealed man-made objects [1]. The choice of frequency and polarization is dictated by the fact that a typical tree is vertically-oriented and has a trunk diameter of a few decimetres, whereas the size of a typical man-made object is a few meters or more. Hence, by choosing a wavelength matched to the object size and horizontal polarization ensures both low attenuation and backscattering by foliage and large scattering cross-section from man-made objects. In addition, the incidence angle is chosen to be small or intermediate ($< 60°$) to avoid reflection-interference from the ground which otherwise tends to cancel the returned signal from low objects. Due to the relatively long wavelengths (3-15 m), it is clear that the spatial resolution needs to approach the fundamental wavelength limit in order to resolve man-made objects from foliage and other background objects. These requirements together lead to the design of an ultra-wideband SAR system operating in the lower part of the VHF band.

It is important to theoretically study the radar cross section (RCS) of different types of targets in order to understand system performance. In particular, trihedral retroreflectors are used for system calibration. For this purpose an FDTD-code has been developed for simulation of far field scattering of objects above a dielectric ground. The advantage of using FDTD is the capability of obtaining results in a broad frequency band, which reduces computational efforts. Also useful is the capability to model complex objects with dielectric properties. By using far-zone transformation in FDTD the scattered field at large distances can be found either in the time domain or in the frequency domain [2]. When the scattering object is placed on an infinite dielectric ground plane the transformation procedure becomes more complicated. We solve this problem by using the reciprocity theorem as described in [3]. In addition to the far-zone transformation, the incident field must be created either by using the scattered field formulation or the total field formulation [2]. The total field formulation was chosen since it only requires source terms at a Huygen's surface [4] surrounding the object, while the scattering field formulation requires source terms at every field component where material exist [2]. The latter can be time consuming if large dielectric objects are studied.

Traditionally, far-zone transformation is performed by integrations of the equivalent currents on a single surface where either the magnetic or the electric fields are spatially averaged, due to the spatial

shift between the E- and H-fields in FDTD. We use a different approach where the equivalent currents for the far-zone transformation are the same as those derived for the Huygen's sources in [4], whereby no averaging is necessary. It will be shown that this method is also more accurate than the averaging method, especially if the wavenumber is compensated due to numerical dispersion. The accuracy of the transformation routine is demonstrated for some simple objects and an example of image formation using the CARABAS-II system is presented.

2. NEAR- TO FAR-ZONE TRANSFORM

A description of the free-space version of the near- to far-zone transform used in this study has been reported elsewhere [5]. The derivation below is slightly different from [5], in that it is not restricted to the free-space situation. The far-zone transformation can be derived in various ways. Below we will derive it from the reciprocity theorem, utilizing the source currents derived in [4]. Within a volume V, assume that the sources $\boldsymbol{J}_i$ and $\boldsymbol{M}_i$ give the fields $\boldsymbol{E}_i$ and $\boldsymbol{H}_i$ and that the sources $\boldsymbol{J}_s$ and $\boldsymbol{M}_s$ give $\boldsymbol{E}_s$ and $\boldsymbol{H}_s$. Then according to the reciprocity theorem [6]

$$\iiint_V (\boldsymbol{E}_s \cdot \boldsymbol{J}_i - \boldsymbol{H}_s \cdot \boldsymbol{M}_i) dV = \iiint_V (\boldsymbol{E}_i \cdot \boldsymbol{J}_s - \boldsymbol{H}_i \cdot \boldsymbol{M}_s) dV \tag{1}$$

where the currents $\boldsymbol{J}_i$ and $\boldsymbol{M}_i$ may be equivalent sources on a surface S that reproduces fields $\boldsymbol{E}_i$ and $\boldsymbol{H}_i$ inside this surface. It is also assumed that the sources creating $\boldsymbol{E}_s$ and $\boldsymbol{H}_s$ are inside S. Before converting this into the equivalent numerical equations for FDTD, it is useful to recapitulate the derivation of the equivalent source currents derived for the Huygen's sources in FDTD. In [4] this is done by defining two closed surfaces in the FDTD-lattice, one outer surface spanned by tangential H-fields and one inner surface spanned by tangential E-fields. In a rectangular FDTD-lattice these two artificial surfaces form two cubes, separated by a half cell-size. In [4] it is shown that the equivalent source currents that reproduces the fields inside the surface S, and zero field outside S, can be written as

$$\boldsymbol{J}_i^{S_e} = \frac{\hat{\boldsymbol{n}} \times \boldsymbol{H}_i^{S_h}}{\Delta s}, \quad \boldsymbol{M}_i^{S_h} = \frac{-\hat{\boldsymbol{n}} \times \boldsymbol{E}_i^{S_e}}{\Delta s} \tag{2}$$

where $\hat{\boldsymbol{n}}$ is the surface normal pointing *into* the volume, i.e. into the region where the fields are non-zero, and Δs is the cell size in the $\hat{\boldsymbol{n}}$-direction. It is important to note that the electric source currents appears on the surface of tangential E-fields (denoted S_e) since they are sources for the electric fields, but they are computed on the surface of tangential H-fields (denoted S_h), at the H-fields' time step. Vice versa holds for the magnetic source currents. Converting the left side of equation 1 into its numerical equivalent and using equation 2, the following equation can be derived:

$$\sum_S [\boldsymbol{E}_s^{S_e} \cdot (\hat{\boldsymbol{n}} \times \boldsymbol{H}_i^{S_h}) + \boldsymbol{H}_s^{S_h} \cdot (\hat{\boldsymbol{n}} \times \boldsymbol{E}_i^{S_e})] \Delta S = \tag{3}$$
$$-\sum_S [\boldsymbol{E}_i^{S_e} \cdot (\hat{\boldsymbol{n}} \times \boldsymbol{H}_s^{S_h}) + \boldsymbol{H}_i^{S_h} \cdot (\hat{\boldsymbol{n}} \times \boldsymbol{E}_s^{S_e})] \Delta S$$

where the summation over S denotes the summation over all indices of tangential electric and magnetic fields on the two surfaces S_e and S_h in the FDTD-lattice. By inspection it can be seen that the RHS of eq. 3 corresponds to the RHS of eq. 1, if the currents $\boldsymbol{J}_s$ and $\boldsymbol{M}_s$ are defined analogous to eq. 2, but with $\hat{\boldsymbol{n}}$ pointing out of the volume. In this case $\boldsymbol{J}_s$ and $\boldsymbol{M}_s$ are the equivalent source currents that reproduces the fields $\boldsymbol{E}_s$ and $\boldsymbol{H}_s$ outside S and zero fields outside S. Thus, eq. 3 can be regarded as the FDTD-version of the reciprocity theorem. If $\boldsymbol{J}_s$ and $\boldsymbol{M}_s$ are calculated using averaged H-fields (or E-fields) the FDTD reciprocity theorem will not hold. To simplify the derivation below it is assumed that the scattered fields on the surfaces have been transformed into the frequency domain by an FFT or DFT. The derivation is similar to the one described in [3]. By keeping the RHS of eq. 3, replacing the LHS with the original volume integral in eq. 1 and letting the original current source $\boldsymbol{J}_t$ be a test current consisting of an electric dipole on a position far away outside S, it can be shown that

$$E_s^{fz}(r) = i\frac{\eta k}{4\pi r}\sum_S [\boldsymbol{E}_t^{S_e} \cdot (\hat{\boldsymbol{n}} \times \boldsymbol{H}_s^{S_h}) + \boldsymbol{H}_t^{S_h} \cdot (\hat{\boldsymbol{n}} \times \boldsymbol{E}_s^{S_e})]\Delta S \tag{4}$$

where $E_s^{fz}(r)$ is the electric field parallel to the dipole in the far-zone, at distance r from the scattering object, η is the free-space wave impedance and k is the wavenumber. $\boldsymbol{J}_t$ is normalised to give an incident field of 1 V/m at the scattering object. The fields $\boldsymbol{E}_t^{Se}$ and $\boldsymbol{H}_t^{Sh}$ in eq. 4, created by $\boldsymbol{J}_t$, can either be the sum of the incident and reflected fields above a dielectric ground or the refracted fields below the ground. If no ground is present $\boldsymbol{E}_t^{Se}$ and $\boldsymbol{H}_t^{Sh}$ at the surfaces S_e and S_h are simply

$$\boldsymbol{E}_t^{S_e} = \hat{\boldsymbol{E}} e^{-ikr + ik(\hat{\boldsymbol{r}} \cdot \boldsymbol{r}_e')}, \boldsymbol{H}_t^{S_h} = (\hat{\boldsymbol{k}} \times \hat{\boldsymbol{E}})\frac{1}{\eta} e^{-ikr + ik(\hat{\boldsymbol{r}} \cdot \boldsymbol{r}_h')} \tag{5}$$

where $\boldsymbol{r}_e'$ and $\boldsymbol{r}_h'$ are the position vectors to the S_e and S_h surfaces respectively. By choosing the dipole to be parallel to either of the unit vectors $\hat{\theta}$ or $\hat{\varphi}$. eq. 4 can then be rewritten to

$$\begin{aligned} E_\theta^{fz} &= -i\frac{ke^{-ikr}}{4\pi r}\sum_S \left[\hat{\theta} \cdot (\hat{\boldsymbol{n}} \times \boldsymbol{H}_s^{S_h})\eta e^{ik(\hat{\boldsymbol{r}} \cdot \boldsymbol{r}_e')} - \hat{\varphi} \cdot (\hat{\boldsymbol{n}} \times \boldsymbol{E}_s^{S_e}) e^{ik\hat{\boldsymbol{r}} \cdot \boldsymbol{r}_h'}\right]\Delta S \\ E_\varphi^{fz} &= -i\frac{ke^{-ikr}}{4\pi r}\sum_S \left[\hat{\varphi} \cdot (\hat{\boldsymbol{n}} \times \boldsymbol{H}_s^{S_h})\eta e^{ik(\hat{\boldsymbol{r}} \cdot \boldsymbol{r}_e')} + \hat{\theta} \cdot (\hat{\boldsymbol{n}} \times \boldsymbol{E}_s^{S_e}) e^{ik(\hat{\boldsymbol{r}} \cdot \boldsymbol{r}_h')}\right]\Delta S \end{aligned} \tag{6}$$

The important difference between eq. 6 and the traditional FDTD far-zone transformation is that the summation of the fields in eq. 6 is done over two surfaces where the phase factor multiplied with the H-field is evaluated at the position of the E-field a half cell size away, and vice versa for the E-field. Since the summation is done over two surfaces with the position vectors $\boldsymbol{r}'$ switched, the transformation procedure is called a "mixed" surface transform. In [5] it is shown that this transformation gives more accurate result than the traditional transform using averaged fields, and that it can be even further improved if the wavenumber k occurring in eq. 6 is compensated due to numerical dispersion.

3. VALIDATION

In order to verify the improvement of the far-zone transform it was applied on a plane wave propagating through the computational volume with no scattering object present. Since the scattered field is zero this far-zone transformation must result in a zero field in all directions, but since FDTD is suffering from numerical dispersion the result will not be exactly zero. In Fig. 1a the scattering cross section of an empty 30x30x30 cells volume is shown both for the mixed surface transform and for the single (averaged) surface transform. If the transformation is made in the frequency domain it is also possible to compensate for numerical dispersion [5], which is done for the mixed surface transform. As seen from the result the mixed surface transform yields much lower RCS than the single surface transform. Figure 1b shows the result of the bistatic RCS of a circular disk at 2 GHz (15 cells/wavelength). The disk with a radius of 20 cells (dx=1cm) was illuminated with normal incidence from θ=180°. These results are compared with the exact solution (series solution).

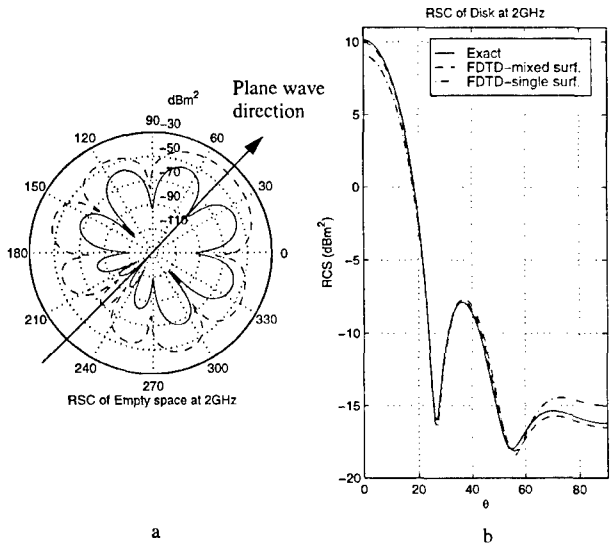

Figure. 1. FDTD-RCS calculations of a) Empty space. The arrow shows the direction of the incident plane wave (θ=45°,ϕ=0°). The bistatic RCS is shown in the X-Z plane. b) Circular disk. plane wave incidence from θ=180°. The cell size was 1cm in both cases.

In order to validate the FDTD-code for scattering of objects above a dielectric lossy groundplane, comparison with NEC-3 was done. One of the calibration objects, a 5 m triangular trihedral was modelled using FDTD and NEC-3, the latter with the Sommerfeld solution. The results can be seen in Figure 2. As seen from the figure the NEC-3 Sommerfeld solution and the FDTD-solution agrees well.

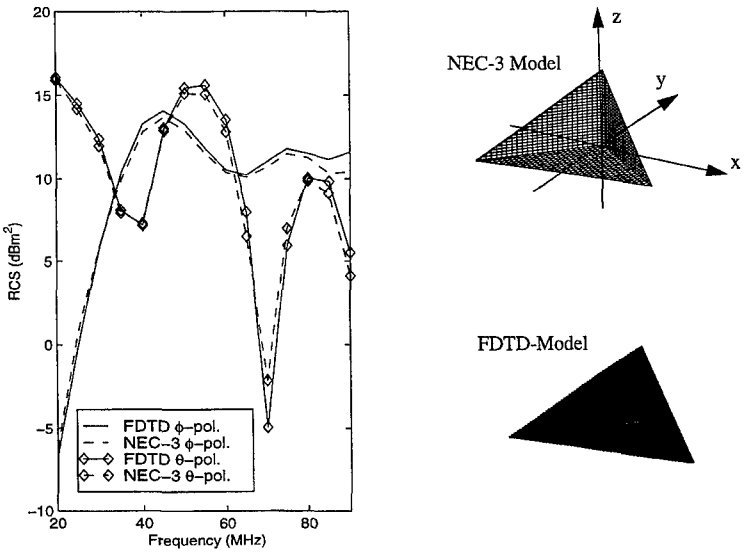

Figure. 2. Comparison between NEC-3 and FDTD. The incident angles are θ=55.9°, ϕ=202.3° and the polarization angle is 31.1°. For NEC, the segment length was 20cm and the wire radius 1cm. The FDTD cell size was 10cm. The trihedral was placed 10cm above the ground (ε_r=10, σ=0.01 S/m).

4. IMAGING PRINCIPLES OF CARABAS-II SAR

The basic imaging geometry is shown in Fig.3 with the antenna and airborne platform moving along a nominally straight flight track. The antenna is designed to illuminate a half-plane to either the right- or left-hand side of the flight track. A number of coded pulses are transmitted at each indicated position and the returned signals as a function of delay time are recorded and stored. After decoding of the pulse returns, the returned signal equivalent to a transmitted short pulse is obtained. A particular target will thus appear at a given delay time corresponding to the slant range (distance) between the antenna phase centre and the target. As the platform moves, the slant range variation is hyperbolic. Each target on the ground surface has a unique hyperbola which is used to "focus" the target at the vertex during image formation. In practise, the returned signals are only acquired out to a maximum slant range and along a finite flight track ("synthetic array") which define the minimum and maximum Doppler cone angles as illustrated in Fig. 3.

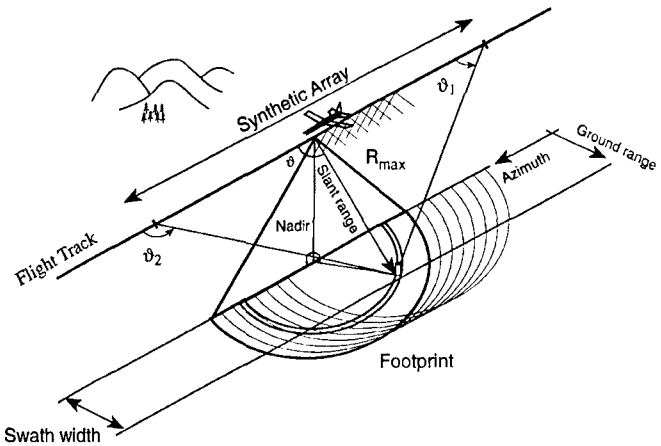

Figure. 3. Illustration of the SAR imaging geometry.

5. IMAGE FORMATION

SAR image formation is accomplished by processing the acquired radar data using time- or frequency-domain signal processing algorithms. The particular choice of algorithm is dependent on a number of trade-offs related to system, processor and required image quality parameters. Common to all algorithms, however, is that the support of the resulting SAR image spectrum is confined to an annular segment as illustrated in Fig. 4. Each point in the spectrum is uniquely defined by its polar coordinate $(2K,\vartheta)$, i.e. directly related to the transmitted frequency $f = cK/2\pi$ and the Doppler cone angle ϑ [7]. The image spectrum for a particular target can thus be determined from knowledge of the scattering amplitude over the relevant frequency band and Doppler cones angles.

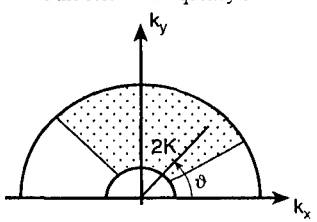

Figure. 4. SAR transfer function after image formation. The frequency domain support is confined to an annular segment defined by the min. and max. transmitted frequency and Doppler cone angle.

6. SAR IMAGE RESPONSE OF CALIBRATION TARGETS

A major problem when attempting to calibrate an ultra-wideband and widebeam SAR system such as CARABAS-II is to find suitable calibration targets. In an earlier study near-resonant horizontal dipoles at a variable height above ground where used for this purpose [8]. This configuration was quite useful for calibrating sub-band images but the large variability of the radar-cross section with frequency inhibited full-bandwidth calibration. Another candidate target for calibration purposes is the triangular trihedral. The FDTD algorithm has been used to compute the scattering matrix for a 5-m trihedral placed on ground ($\varepsilon_r = 10, \sigma = 0.01$S/m). The scattering amplitude as a function of frequency and Doppler cone angle is computed assuming that the antenna is a wideband dipole and the zero-Doppler frequency incidence angle is 60°. The result after interpolation to the image spectral coordinates (k_x, k_y) is shown in Fig. 5. We assume that the processing uses Doppler cone angles in the range 45°-135°, i.e. an aperture angle of 90°, and frequencies in the band 20-90 MHz. A compensation for the range-spreading loss in the radar equation is also included. In this case, the radar-cross section increases with frequency, reaches a maximum of 28 dBm^2 at 90 MHz and $\vartheta = 90°$, and has a dynamic range of about 20 dB. The reduction for lower frequencies and non-zero Doppler frequencies is mainly caused by cancellation due to ground reflection interaction. The SAR image is obtained by inverse Fourier transformation of the image spectrum which is shown in Fig. 4. Measurements of the spatial resolution between half-power points gives 2.6 x 1.4 = 3.5 m^2, and the peak sidelobe ratio is -12 dB. These values can be compared with an ideal point target, i.e. with no amplitude or phase distortion, which give a spatial resolution of 3.1 m^2 and a peak sidelobe ratio of -16 dB. The broadening of the resolution is mainly caused by the amplitude distortion, whereas the increase in sidelobe ratio is mainly due to the phase distortion.

7. CONCLUSIONS

The FDTD near- to far-zone transformation in free space or above a dielectric lossy ground has been improved. The FDTD-method has been used to assess calibration targets for the CARABAS-II system, where in particular scattering from large trihedrals has been studied. In conclusion, the 5-m triangular trihedral is found useful for system calibration across the full bandwidth and beamwidth of CARABAS-II. Only at the low frequency end (< 30 MHz) does the radar cross section fall considerably due to ground interaction and will limit the calibration accuracy.

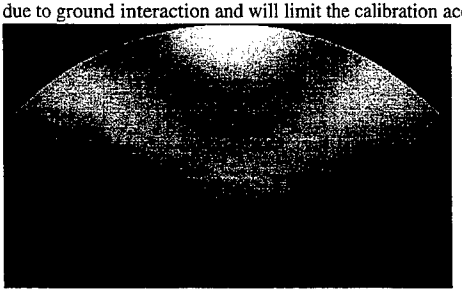

Figure. 5. Simulation of the image spectrum of a 5-m triangular trihedral on a dielectric ground surface. Transmitted frequency band is 20-90 MHz and Doppler cone angles cover the range 45°-135°.

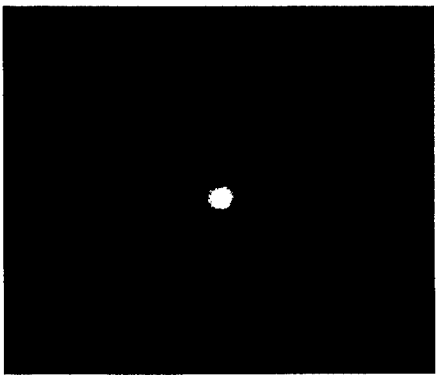

Figure. 6. Image amplitude response corresponding to the spectrum in Fig. 5. Rectangular 3 dB resolution is $3.5m^2$ and peak side lobe ratio is -12dB.

8. REFERENCES

[1] Hellsten, H., Ulander, L.M.H., Gustavsson, A., and B. Larsson, 1996, "Development of VHF CARABAS II SAR", *Proceedings SPIE Conference on Radar Sensor Technology*, Orlando, Fl., 8-9 April 1996, SPIE, 2747, 48-60.

[2] A. Taflove, *Computational Electrodynamics*. London: Artech House, 1995.

[3] K. Demarest, Z. Huang, and R. Plumb, "An FDTD near- to far-zone transformation for scatterers buried in stratified grounds," *IEEE Trans. Antennas Propagat.*, vol. 44, pp. 1150 - 1157, Aug. 1996

[4] D. E. Merewether, R. Fischer, F. W. Smith, " On implementing a numeric Huygen's source scheme in a finite difference program to illuminate scattering bodies," *IEEE Trans. Nucl. Science.*, vol. NS-27, pp. 1829- 1833, Dec. 1980.

[5] T. Martin, "An improved near to far zone transformation for the Finite-Diference Time-Domain method," Submitted to the *IEEE Trans. Antennas Propagation*.

[6] C. A. Balanis, *Advanced Engineering Electromagnetics*, New York: Wiley, 1989.

[7] Ulander, L.M.H., and H. Hellsten, 1996, "A New Formula for SAR Spatial Resolution", AEÜ, 50, 117-121

[8] Ulander, L.M.H., and Z. Sipus, 1996, "RCS of Dipoles used for SAR Calibration", Proc. EUSAR held in Königswinter, 1996.

FDTD SIMULATIONS USED TO CORRECT FOR GROUND EFFECTS IN AIRCRAFT TESTING

Göran Eriksson and Ulf Thibblin
Ericsson Saab Avionics AB, Electromagnetic Technology Division,
S-581 88 Linköping, Sweden

ABSTRACT

During so-called LLSC (Low Level Swept Coupling) tests, induced currents on cables inside the aicraft are measured while it is illuminated from the outside by electromagnetic radiation. To correct for the fact that LLSC tests are performed with the aircraft on ground, while the quantities of interest are the induced cable currents under free-flight conditions, the so-called compensation (K) factor method has been developed at Saab AB and Ericsson Saab Avionics AB. By comparing measured surface current densities during the ground testing and numerically computed surface currents in free-flight, a frequency-dependent compensation factor $K(f)$ can be determined. The measured currents on internal cables are then multiplied by this factor, yielding the currents which would be expected during free-flight illumination. The computations of the surface current distributions are performed using the classical FDTD method. It is demonstrated that, compared to the method of applying a constant safety margin for all frequencies, the method may provide considerable savings.

1. INTRODUCTION

Since modern aircraft, both civil and military, depend heavily on safety critical electronic systems for stearing, engine control, navigation, communication, etc., the issue of protection against interfering electromagnetic radiation is of highest priority. Apart from natural sources of electromagnetic energy, such as lightning discharges, the steadily growing number of different kinds of radar and radio transmitters has in this respect become a considerable problem. This has resulted in requirements that aircraft have to be certified for incident electrical field strengths of several hundreds of volts per meter. During so-called LLSC (Low Level Swept Coupling) tests the aircraft is illuminated from the outside by electromagnetic radiation while at the same time the induced currents on internal cables are measured. These currents are then compared with those current levels which are defined as the highest acceptable with respect to their interference with connected electronic devices. For practical reasons, during the test the illuminating electromagnetic field strength is an order of magnitude lower than the threat level and hence the measured currents are scaled linearly to correspond to the real threat. The frequency range covered by the LLSC tests is 10 kHz - 400 MHz (for even higher frequencies only local illumination of possible penetration apertures is required). Finally, it is important to have in mind that the many resonances caused by the internal and external structure generate a highly complex response, implying a need for very good frequency resolution.

The actual threat situation is defined as an aircraft in free-flight illuminated by an approximately plane electromagnetic wave. The LLSC test, however, is performed with the aircraft on ground and the elec-

tromagnetic radiation generated by an antenna in its vicinity, see Fig. 1.

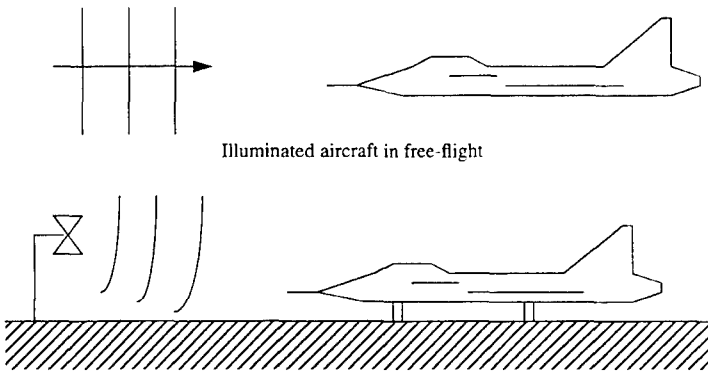

Illuminated aircraft in free-flight

LLSC test

Figure 1. The threat situation and the test setup.

Obviously, the test and free-flight situations are not identical. For instance, induced ("mirror") currents in the ground and other conducting objects in the vicinity distort the field pattern and, in particular for lower frequencies, the field may deviate from that of a plane wave. Moreover, illumination from below and above is not possible, unless the aircraft is lifted and tilted. A simple way of taking these effects into account is to multiply all measured cable currents with a constant factor. However, since the test setup effects are strongly frequency-dependent, this may lead to a situation where the aircraft becomes over-protected within some frequency intervals. In order to optimize the protection measures, the compensation (K) factor method [1,2] has been developed by Saab AB and Ericsson Saab Avionics AB. Here, the measured cable currents are multiplied by a frequency-dependent function $K(f)$, which is determined from a comparison of the exterior surface current densities induced during free-flight illumination and the LLSC test. The method relies on the assumption that the electromagnetic field penetrating into the interior of the aircraft through small apertures, seams, etc. is approximatively proportional to the induced surface current density (without the apertures present). This assumption is supported by theory as well as by experimental results [3]. Consequently, the compensation factor $K(f)$ is defined as the ratio between the surface currents in free-flight and in the test setup (at the same incident field strength). Since the free-flight currents cannot be measured, they are calculated numerically. This is done via FDTD simulations [4,5], where the mesh describing the aircraft is automatically generated from a CAD model. As is shown below, a detailed analysis of the method provides support for the use of a single function $K(f)$, at least for the test setup used today.

2. THE NUMERICAL SIMULATION TECHNIQUE

Starting from a CAD model of the two-seated Saab JAS 39B Gripen fighter aircraft, the commercial software FAM was used to generate a Cartesian FDTD mesh with 9 cm unit cell size, see Fig. 2.

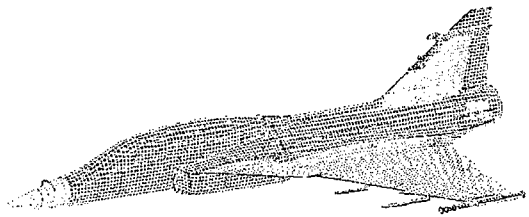

Figure 2. The mesh of the Gripen aircraft.

For these simulations a computational box consisting of $177 \times 107 \times 54$ unit cells was used. Furthermore, the incident plane wave was generated on a Huygen's surface [4] and the outgoing radiation was taken care of by an eight-layer perfectly matched layer (PML) absorbing boundary condition [4]. A time step $\Delta t = 1.70 \times 10^{-10}$ s was chosen to satisfy the CFL criterion for numerical stability. Finally, with the spatial resolution used here, waves with frequencies $f < 300$ MHz are expected to be well described. Using the FDTD algorithm, where the time evolution of the electromagnetic field is followed, the aircraft is illuminated from different angles by a plane wave having a Gaussian puls shape which contains all the frequencies of interest. After making a Fourier transform, the frequency domain response is obtained.

3. THE K-FACTOR METHOD

As mentioned above, what is needed in order to transform the induced cable currents during testing to those expected during free flight is thus the ratio between the surface current densities (for the same incident field strength) in the two cases [1,2]. However, the exact definition of the single function $K(f)$ is not self-evident, since the angle of incidence and the polarization of the plane wave can vary. Also, the surface current density varies along the surface of the aircraft.

So, in order to find a suitable definition of $K(f)$, a limited number (5) of representative points on the aircraft surface are chosen. At these positions the surface current density J_{LLSC} is measured during the LLSC test and, in parallel, the corresponding surface current densities J_{ff} are calculated numerically for the free flight situation. With E_{LLSC} and E_{ff} being the corresponding electric field strengths (without the aircraft present), a compensation factor $K_{mji}(f)$ is defined as a function of frequency f for each point of measuring ($m = 1, ...,5$), surface current component ($j = 1,2$), and incident wave ($i = 1, ..., 6$):

$$K_{mji}(f) = \frac{J_{ff}/E_{ff}}{J_{LLSC}/E_{LLSC}} \tag{1}$$

A single, global compensation factor $K(f)$ is then formed, a procedure that will be discussed below. Assuming that the penetrating field, and consequently the induced cable currents, is proportional to the

surface currents, the free-flight cable current I_{ff} is consequently found from

$$I_{ff} = \alpha K(f) I_{LLSC}, \tag{2}$$

where I_{LLSC} is the measured LLSC cable current and α is the scaling factor up to the threat level. It is, at this point, not obvious that a single function $K(f)$ can be defined, such that it with an acceptable degree of accuracy can be used to represent the situation at all points on the aircraft surface and for all possible incident waves. If such a function cannot be defined, the situation will become very complicated. In order to study the statistical properties of the 60 individual K-factors defined in (1), let us plot the maximum, average, and minimum values as functions of frequency. This is shown in Fig. 2.

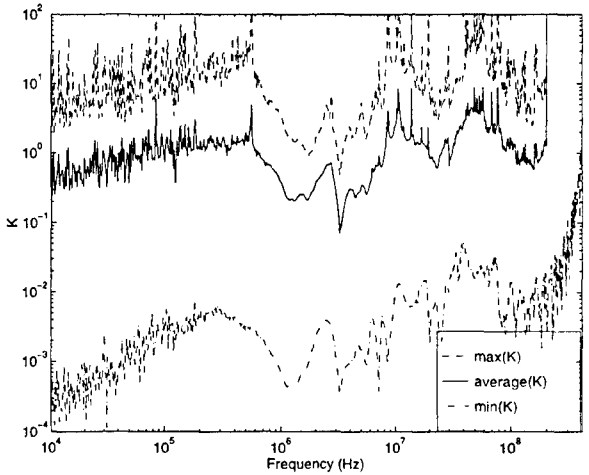

Figure 2. Maximum, average, and minimum values of the 60 K-factors defined in Eq. (1).

From this figure a number of observations can be made. We see that the maximum envelope K_{max} is roughly a factor 10 larger than the average <K>. Having in mind that the relative standard deviation is 2-3, typically, this means that choosing $K(f) = K_{max}$ would result in compensation factors too large to be of practical use. This is also true taking into account the fact that some of the rapid and strong oscillations seen in Fig. 2 do not necessarily represent the effects of the test setup; instead they may originate from the different resolutions and accuracies of the measured and computed surface currents. Clearly, some, but not all, of these unwanted oscillations disapear during the averaging process. Also, since all the three curves in Fig. 2 have the same slow frequency dependence, it seems likely that it indeed represents the effects of ground testing.

We have seen that the relative standard deviation taking all the 60 K-factors into account is typically 2-3. A question of particular interest is whether the K-factors differ between the different probe positions or not. If they do, a single function $K(f)$ cannot be used for the whole aircraft. In order to investigate this, let us plot the separate K-factors for the five probe positions. This is done in Fig. 3, where each curve is calculated as the average over the two orthogonal current directions and the six incident waves.

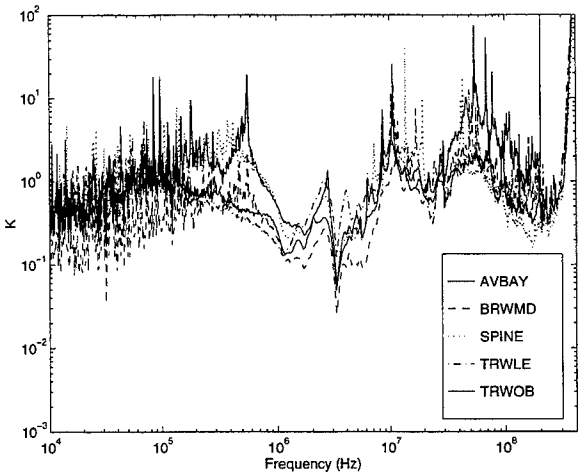

Figure 3. Local compensation factors for the five different probe positions.

Also here the relative variation is seen to be of the order of 3, i.e. 10 dB. Having in mind that the total error introduced in the measurement and computational processes is roughly of the same size, we can draw the conclusion that a single K-factor, preferably defined as the average (1), can be used to represent the whole aircraft and every possible illumination within reasonable accuracy.

4. FURTHER IMPROVEMENTS

In order to avoid the unwanted rapid oscillations due to the resolution differences between the measurements and the simulations, the next step is to develop a fully numerical model of the test situation as well. The K-factors could then be determined by simulations alone, thus making it possible to further reduce the (expensive) time needed for the test. With a detailed model of the test setup it would also be possible to study the importance of the electromagnetic properties of the ground and the deviations from an exact plane wave illumination. Moreover, the K-factors could be calculated for any angle of incidence, including those corresponding to illumination from above and below.

5. SUMMARY

Using measured and computed data for the Saab JAS 39B Gripen aircraft as an example, we have demonstrated that the expected induced cable currents during illumination in free-flight can be found from those measured in the LLSC test setup by multiplying the latter with a frequency-dependent compensation factor $K(f)$. This function is preferably defined as the average of all the individual K-factors given by Eq. (1), with the average taken over all probe positions, surface current directions, and incident waves. It is shown that the error introduced by using a single K-factor is of the same order of magnitude as those introduced by other sources. Clearly, the consequent use of K-factors gives a more detailed description of the unwanted effects from the test setup and may therefore be exploited in the optimization of the protection against electromagnetic threats. In particular, it may be used to reduce the requirements within certain frequency intervals.

6. REFERENCES

[1] Bäckström, M., "Analyser för 39-3 prov", TUST-39-89.14.

[2] Palmqvist, J., "JAS39. ELMILJÖ. Utvärdering av metodiken för uppskalning av uppmätta kabelströmmar vid LLSC-mätning. Slutrapport.", TUST-39-91.85.

[3] Palmqvist, J., "Relevanta parametrar vid bestämning av strukturdämpningen däplanvågsbelysning simuleras med närfältsbelysning.", TUST-TS-90.115.

[4] Taflove, A., *Computational Electrodynamics: The Finite-Difference Time-Domain Method*. Norwood, MA, Artech House, 1995.

[5] Yee, K.S., "Numerical Solution of Initial Boundary Value Problems Involving Maxwell's Equations in Isotropic Media", *IEEE Trans. Antennas and Propagation*, **AP-14**, pp. 302-307, 1966.

Validation of FDTD-Computed Handset Patterns by Measurement

C. W. Trueman
S.J. Kubina
Electromagnetic Compatibility Laboratory, Concordia University, Montreal

J.E. Roy
W.R. Lauber
Communications Research Centre, Ottawa

M. Vall-llossera
Department of Signal Theory and Communications, Universitat Politècnica de Catalunya (UPC), Barcelona

Abstract-This paper compares the radiation patterns of a portable radio handset at 850 MHz in free space with those of the radio operating near box and sphere models of the head. The patterns are computed with the finite-difference time-domain method, using measured parameters for the liquid representing the brain. The head is found to introduce considerable changes to the radiation patterns, especially for directions where the head lies between the handset and the receiver. The computed radiation patterns are validated in this paper against measured patterns. Excellent agreement is found for the handset alone. The agreement is good for the handset and head models, with some differences in the minima of the radiation patterns, particularly for the sphere head. These may be due to the styrofoam-and-fiberglass-bolts mounting jigs, not included in the FDTD models, or to the cubical cell approximation of the shape of the heads.

Introduction

The finite-difference time-domain method has been used extensively to evaluate the radiation patterns and near fields of a portable radio handset operating near a representation of a human head, for example in Refs. [1] to [4]. The head is a complex three-dimensional structure made up of high-permittivity, lossy dielectric materials and as such is a challenging computational problem. A realistic head phantom is difficult to construct physically and complex to represent in terms of FDTD cells. This paper deals with simplified heads that are easy to build and straightforward to model with FDTD, as a preliminary step to studying a full head phantom. The "box head" is a thin-walled plexiglas box filled with liquid with the electrical parameters of the brain[5]. A simple box has surfaces parallel to planes of FDTD cells and so can be modelled with good accuracy. The "sphere head" is a thin plexiglas spherical shell filled with brain liquid. The sphere head introduces staircasing error into the FDTD model and so we might expect the accuracy of the computations to be poorer. This paper compares the radiation patterns of a handset operating near the box head and near the sphere head with measurements, as a validation of the FDTD computations.

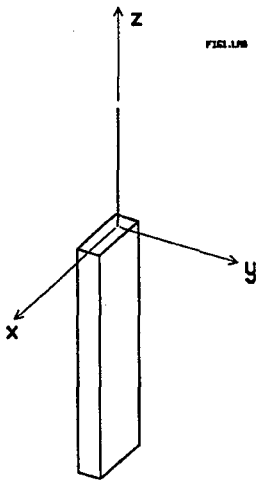

Fig. 1 The portable radio handset in the *xyz* coordinate system.

Measurement of the Radiation Patterns

The radiation patterns were measured by mounting the handset and head in a jig atop a styrofoam rotator column in a 6x6x6 meter anechoic chamber[6]. The handset contains a battery-operated oscillator at 850 MHz. An open-ended waveguide was mounted on the rotating table near the base of the rotator column to sample the field to provide a reference signal to phase-lock a network analyzer. The horizontal and vertical components of the field were measured by a dual-polarized ridged waveguide horn mounted about 330 cm from the handset. The mounting jig shown in Fig. 2, consisting of styrofoam blocks and fiberglass nuts and bolts, holds the handset in a well-known, reproducible position relative to the head. Fig. 2 shows the jig positioned for rotation in the *yz* plane in Fig. 1, for measurement of the $\phi = 90$ degree elevation. The elastic bands attached to the nuts in Fig. 2 were removed for the measurement. The patterns were measured in one degree increments.

Considerable care was taken to optimize the quality of the measured data. Unwanted reflections in the anechoic chamber were identified and reduced with absorber. The position of the handset was aligned as accurately as possible using a laser beam as a reference, to reduce alignment error as much as possible. However, the absorber in the chamber is designed for best performance above 1.5 GHz. The relatively short range from the handset to the horns may not be adequate for a true "far field" measurement. These problems will primarily affect the measured patterns in the minima.

Patterns of the Handset

Fig. 1 shows the handset oriented with the broad face of the case parallel to the *xz* plane, the antenna parallel to the *z*-axis and adjacent to the $-x$ side of the case. The handset is an aluminum box 5.35 by 1.74 by 16.77 cm, with an antenna 8.82 cm in length. These dimensions were chosen so that, using a cell size of 0.441 cm, the handset case is very close to 12 by 4 by 38 cells with a 20 cell antenna. The antenna is positioned 0.87 cm from three edges of the case. The FDTD code uses the perfectly-matched layer[7](PML) absorbing boundary condition. The PML was set to 6 cells in thickness with a surface reflection coefficient of 0.001 and parabolic evolution of the conductivity. The surfaces of the handset and the tip of the antenna were separated from the first layer of the PML by 4 cells of free space or "whitespace". The integration surface for the near-to-far zone transformation was centered within the whitespace. The FDTD computation was run for 2048 time steps with a sinusoidal generator at 850

Fig. 2 The handset and box head mounted in the styrofoam jig, positioned on top of the rotator in the anechoic chamber.

MHz at the base of the monopole. The computed radiation patterns are true "far field" and do not account for the 330 cm range to the measurement horns. The computed patterns were scaled to have an "isotropic level" field strength[4] of 0 dB.

The radiated power in the measurement is not known, hence the measured patterns need to be scaled for comparison with the computations. The RMS field strength found from the computed principal plane patterns for $\phi = 0$, $\phi = 90$, and $\theta = 90$ was used as a reference level. Then the corresponding RMS field strength was found from the measured principal plane patterns, and the measured patterns were scaled to have the same RMS field strength as the computation.

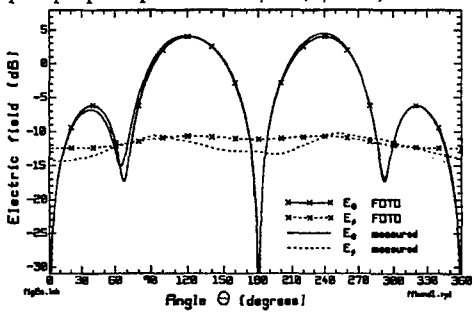

(a) Elevation pattern for $\phi = 90$ degrees.

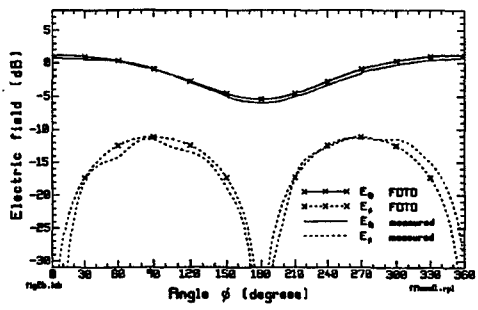

(b) Azimuth pattern.

Fig. 3 The radiation patterns of the handset.

Fig. 3 compares the measured and computed radiation patterns for the handset in free space, in decibels above the isotropic level field strength. In the measurement the handset was held in a simpler styrofoam jig than that in Fig. 2, having no fiberglass nuts and bolts. The computed $\phi = 90$ pattern in Fig. 3(a) is symmetric about the xz plane. It has the main lobe of field strength 4.0 dB directed at θ =121, that is downward, and a minor lobe of field strength –6.2 dB directed upward at $\theta = 39$ degrees. The measured E_θ polarization agrees very well with the computation, with a difference in the minor lobe near 40 degrees of 0.6 dB and in the major lobe near 240 degrees of 0.4 dB. The differences in the minima are larger. The computed minimum at 68 degrees has level –17.3 dB, whereas the measurement has a minimum at 65 degrees of –15.1 dB. The cross-polarized or E_ϕ field is roughly circular in shape and at a level of about –10.8 dB in the computation. The measured E_ϕ component has maxima at about the same level as the computed field, but has minima about 1.8 to 2.2 dB below the computed field.

Fig. 3(b) compares the measured and computed azimuth patterns. The principal polarization is very roughly circular, with quite good agreement between the computation and the measurement, with a difference of about 0.5 dB in the minimum. The cross-polarization is a figure-eight pattern and agrees quite well between the measurement and the computation.

Some differences between the measurement and the computation in Fig. 3 can be attributed to the styrofoam mount for the handset, which was not included in the computation. The agreement in Fig. 3 is about the best that we have been able to achieve between computations and measurements.

The Handset and the Box Head

Fig. 2 shows the handset and the box head, mounted in the support jig. The box head has outside dimensions 17.07 by 13.89 by 21.06 cm and wall thickness 0.5 cm. It is filled with a mixture of de-ionized water, sugar and salt having the electrical parameters of the brain[5] at 850 MHz. The relative permittivity and conductivity were measured to be 40.42 and 1.064 S/m, respectively[8]. The box head is positioned in the coordinates of Fig. 1 on the $+y$ side of the handset, such that if the operator faces in the $+x$ direction, the handset is held in the right hand with the antenna towards the back. The handset is spaced from the box by 0.96 cm. The box is positioned such that if the antenna is on the z-axis, then the back surface of the box is at x=-5.95 cm. The bottom of the box aligns with the bottom of the handset. The box is modelled with FDTD cells of size 0.441 cm. This puts the handset case in the FDTD model two cells or 0.882 cm from the box head, and approximates the box dimensions as 17.12 by 14.11 by 21.12 cm. The FDTD code uses the average permittivity and conductivity to update field components that lie in planes that are interfaces between two dielectric materials. The styrofoam blocks and fiberglass nuts and bolts of the positioning jig were not included in the FDTD model.

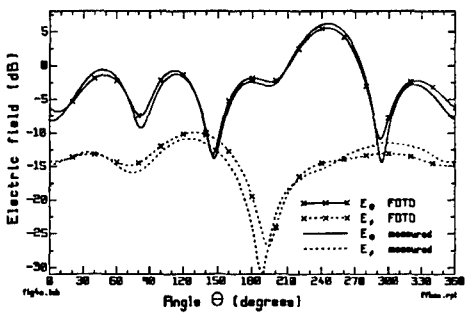

(a) Elevation pattern for $\phi = 90$ degrees.

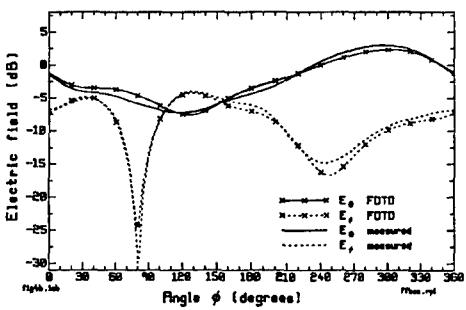

(b) Azimuth pattern.

Fig. 4 The radiation patterns of the handset and box head.

Fig. 4 shows two principal plane patterns of the handset and box head. The $\phi = 90$ pattern from $\theta = 0$ to 180 degrees has the head between the handset and the observer, and comparing Fig. 3(a) and Fig. 4(a), the head changes the pattern considerably. From $\theta = 180$ degrees to 360 degrees (this corresponds to $\phi = 270$ degrees, $180 < \theta < 0$) the pattern of the handset and box head resembles the pattern of the handset alone. The large lobe near 245 degrees is seen in both patterns as is the smaller lobe near 325 degrees. The cross-polarized field is about –11 dB for the handset alone, and about –15 dB for the handset and box head.

The agreement between the computation and the measurement in Fig. 4(a) is quite good. The lobe in E_θ in the computation at 50 degrees of –1.4 dB is seen in the measurement at 48 degrees and –0.6 dB. The lobe at 114 degrees and –1.2 dB is reproduced in the measurement at 112 degrees, -0.74 dB. The minimum at 82 degrees of –9.2 dB falls at 81 degrees and –7.5 dB in the measurement. These features are in the part of the pattern where the head is between the handset and the observer. The largest difference in E_θ is at the minimum at 294 degrees and –14.5 dB in the computation, which is seen at 293 degrees, -10.9 dB in the measurement. The cross-polarized field agrees well in shape and level. Again the largest difference is in the minimum at 188 degrees of –30.8 dB in the computation, and and 194 degrees and –26.9 dB in the measurement.

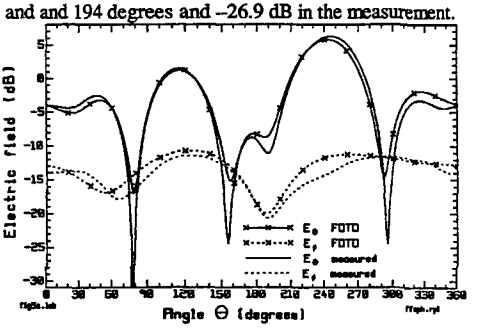

(a) Elevation pattern for $\phi = 90$ degrees.

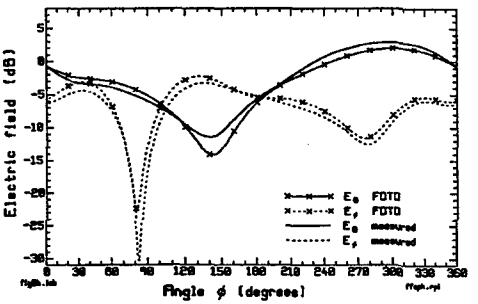

(b) Azimuth pattern.

Fig. 5 The radiation patterns of the handset and sphere head.

The azimuth pattern is shown in Fig. 4(b). The head causes the azimuth pattern to be less circular and raises the level of the cross-polarized field. The measured and computed patterns again agree quite well, with the largest differences in the minima of the patterns.

The Handset and the Sphere Head

The sphere head is a plexiglas sphere of outside diameter 20.68 cm and wall thickness 0.365 cm. The sphere is filled with the same "brain liquid" mixture used for the box head. The sphere was positioned such that if the base of the antenna is at the origin, the centre of the sphere is at $(x = +1.81, y = 12.14, z = 6.42)$ cm. The curved surface of the sphere is approximated with a staircase of FDTD cells of size 0.441 cm. The model was constructed such that over the whole surface of the sphere the edge of a cell filled with brain liquid never touches the edge of a free-space cell; that is, there is always a plexiglas cell separating the outside from the inside.

Fig. 5(a) shows the elevation pattern for ϕ=90 degrees. The pattern is not greatly different from that of the handset and box head. The sphere head changes the pattern from θ=0 to 180 degrees where the sphere lies between the handset and the observer. The sphere introduces deep minima in E_θ near 78 and 155 degrees. The measured and computed fields agree quite well except in the minima. The large lobe at 242 degrees and 5.8 dB in the computed field is seen at 246 degrees and

6.2 dB in the measurement. The cross-polarized field is at about the same level for the handset and sphere as it was for the handset and box. The computed and measured patterns agree quite well in both shape and level.

Fig. 5(b) shows the azimuth pattern, which is very similar to that for the box head in Fig. 4(b). The minimum at 143 degrees is deeper for the sphere than for the box. The cross-polarized fields are remarkably similar. The agreement between the computation and the measurement is somewhat better for the box than it is for the sphere. This may be attributable to the staircased approximation of the sphere's curved surface.

Conclusion

This paper has compared measured and computed radiation patterns for a portable radio handset and two simple representations of the head. One objective was to validate the FDTD method for solving lossy, high-permittivity materials such as human tissue. A second objective was to discover the changes in the radiation patterns of a handset when a head is introduced very close to the handset surfaces.

The radiation patterns for the handset alone, Fig. 3, establish the best agreement that we have been able to achieve between the measurement and the computation. The box head is well represented with cubical FDTD cells, with some error in the overall size and relative position of the box to the handset. Fig. 4 for the handset and box head shows agreement that is somewhat poorer than in Fig. 3, but still very good. The sphere's shape is represented approximately by a staircase in the FDTD model. Still, the agreement between the measured and computed data in Fig. 5 is good, with differences in the depth of the minima being the major problem. By including the styrofoam mounting jig with its fiberglass nuts and bolts in the FDTD cell model, somewhat improved agreement may be possible. The limitations of the absorber in the anechoic chamber and the short range from the handset to the measurement horn may account for some of the differences between the measured data and the computation.

References

1. M.A. Jensen, Y. Rahmat-Samii, "E.M. Interaction of Handset Antennas and a Human in Personal Communication", *Proc. IEEE*, Vol. 83, No. 1, pp. 7-17, January, 1995.
2. Q. Balzano, O. Garay and T.J. Manning, "Electromagnetic Energy Exposure of Simulated Users of Portable Cellular Telephones", *IEEE Trans. On Vehicular Technology*, Vol. 44, No. 3, pp. 390-403, August, 1995.
3. J. Toftgard, S.N. Hornsleth, and J. Bach Andersen, "Effects on Portable Antennas of the Presence of a Person", *IEEE Trans. on Antennas and Propagation*, Vol. 41, No. 6, pp. 739-746, June, 1991.
4. C.W. Trueman, S.J. Kubina, D. Gaudine and B. Lorkovic, "A Research Study on Electromagnetic Fields Produced by Portable Transceivers", Technical Note TN-EMC-97-01, ECE Dept., Concordia University, March 31, 1997.
5. G. Hartsgrove, A. Kraszewski and A. Surowiec, "Simulated Biological Materials for Electromagnetic Radiation Absorption Studies", *Bioelectromagnetics*, Vol. 8, pp. 29-36, 1987.
6. J.E. Roy, W. Lauber, and J. Bertrand, "Measurements of the Electromagnetic Far Field Produced by a Portable Transmitter", Communications Research Centre, Ottawa, September 24, 1997.
7. J. P. Bérenger, "Perfectly Matched Layer for the FDTD Solution of Wave-Structure Interaction Problems", *IEEE Trans. Antennas and Propagation*, Vol. 4, No. 1, pp. 110-117, January 1996.
8. J. Seregelyi, private communication, September 24, 1997.

FDTD ANALYSIS OF FLIP CHIP INTERCONNECTS

Atef Z. Elsherbeni, Vicente Rodriguez-Pereyra, and Charles E. Smith
Department of Electrical Engineering, The University of Mississippi
University, MS 38677
atef@sphinx.ee.olemiss.edu

Abstract- Multichip and flip chip technology has become increasingly popular in the past years. It employs a series of chips flipped and connected through metallic bumps [1]. A study for improving the performance of flip chip interconnects was recently presented by Ghouz and El-Sharawy [2,3] for frequencies up to 50 GHz. They introduced the idea of staggering the signal line interconnect with respect to the ground plane bumps to reduce reflection and insertion loss. In this paper we concentrate on re-shaping the discontinuity region in order to provide a better impedance match between the CPW-motherboard and the CPW-chip, and thus reducing reflection. The use of bumps of different thickness located at different positions, and the use of tilted bumps or "ramps" indicate that the performance of these flip chips can be greatly enhanced and extended to frequencies beyond 100 GHz.

I. INTRODUCTION

Coplanar Waveguides (CPW's) represent an important transmission line technology at RF, microwave, and millimeter-wave frequencies. Among the advantages of these lines are the ease of parallel and series connection of both active and passive components. The increase in popularity of this type of transmission line has brought increased interest in flip chip technology. The flip chip structure consists of a CPW chip flipped over and mounted onto a CPW mother board, as shown in Fig. 1. Several chips may be mounted on to a mother board, thus increasing the density of the circuit. To connect from the mother board to the chip, metallic bumps are usually used. The effect of these interconnects on the performance of a high frequency circuit is important since the discontinuity on the transmission line creates undesirable reflections [4,5]. These bumps should be designed such that the induced reflections are minimum. Published analyses of these flip chip structures are related to the determination of the proper positioning of the bumps. As an example, the staggering of the signal bump was studied in [2], showing improvements for the return loss. In our study, we extend the analysis in [2] by allowing the connecting bumps to vary in shape. The main objective of these approaches is to match the impedance of the

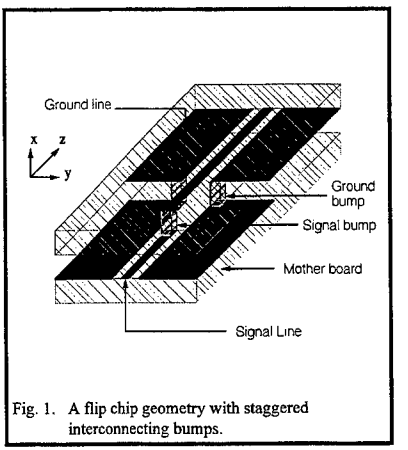

Fig. 1. A flip chip geometry with staggered interconnecting bumps.

interconnection to the impedance of the CPW.

II. ANALYSIS METHOD

The Finite Difference Time Domain (FDTD) technique is used here to analyze a flip chip structure as shown in Fig. 1. The frequency spectrum of the voltage and current at points on the CPW close to the interconnecting bumps are obtained using Discrete Fourier Transform (DFT). By choosing the sampling points close to the discontinuity of the interconnecting bumps the effects of these bumps are isolated from the rest of the structure [6]. Our sampling points are located 0.6mm away from the ground bumps. These sampling points were left fixed for all cases studied in this paper. To obtain the S parameters the incident signal must be isolated from the reflected signal. The method used here consists of the simulation of a long feed line with the same dimensions as the input line of the structure considered for this study. Using the same FDTD code and the same excitation waveform as the one used in the analysis of the flip chip structure, a set of reference current and voltages are obtained. The backward traveling wave is then computed by subtracting the incident or reference voltage or current from the total voltage or current computed at the sampling point in the flip chip structure. To compute the S parameters, the following equations were used:

$$S_{11} = 20\,Log_{10}\left(\sqrt{\frac{V_1^- I_1^-}{V_1^+ I_1^+}}\right), \qquad (1)$$

$$S_{21} = 20\,Log_{10}\left(\sqrt{\frac{V_2 I_2}{V_1^+ I_1^+}}\right)$$

where V_1^+, I_1^+ are the incident voltage and current at the input port; which are the responses for the reference long line. The reflected voltage and current V_1^-, I_1^- at the input port and the total voltage and current V_2, I_2 at the output port are computed with the actual flip chip geometry.

III. NUMERICAL RESULTS

Numerical results were obtained for the geometry shown in Fig. 1. This geometry has the same dimensions as that shown in [2]. The width of the center conductor is 0.12mm, the gap between the conductor and the coplanar ground plane is 0.12mm, the thickness of the substrate of both the chip and the mother board is 0.36mm and the height of the bumps is 0.12mm. The substrate is made of gallium arsenide (*GaAs*, ϵ_r=12.9). The geometry is discretized using Yee cubical cells with the following dimensions; $\Delta x=\Delta y=\Delta z$=0.04mm. The structure was excited by a pair of resistive voltage sources having a magnitude of 10 Volts and opposite polarities and internal resistance of 74Ω and located between the signal line and the side ground planes. The excitation waveform was a Gaussian pulse. The Gaussian pulse is defined for a stationary source by

$$g(t) = e^{-\frac{(t-t_0)^2}{T^2}} \tag{2}$$

where the period of the pulse (T) is defined by [7],

$$T = \frac{m\Delta s}{2\sqrt{3}v} \tag{3}$$

where Δs is the largest edge of the cell, m is an integer number, and v is the velocity of propagation of the pulse. The maximum usable frequency is determined based on the value of T. For our simulations, m was set to 30.

To verify our computations, a case reported in [3] was analyzed. The geometry consists of cubical in-line bumps. Figure 2 shows our results, which are in good agreement with the results reported in [3]. The results for this geometry along with the cases where the signal bump is staggered, where the staggered distance (S) is 0.32mm, and thin in-line bumps case are shown in Fig.3. The thin in-line bumps are bumps with zero thickness along the z

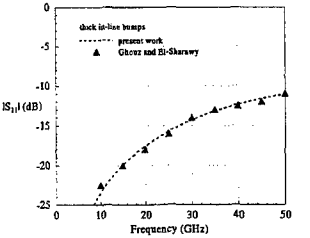

Fig. 2. Comparison of this work results with previously presented results.

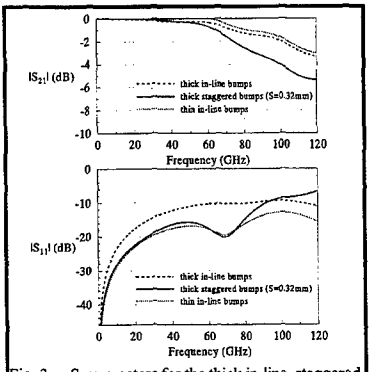

Fig. 3. S parameters for the thick in-line, staggered, and thin in-line bumps.

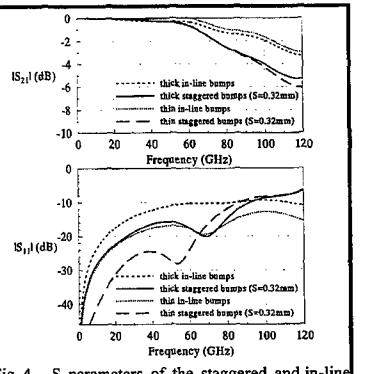

Fig. 4. S parameters of the staggered and in-line bumps for both thick and thin bumps.

direction. It is obvious that the use of thin in-line bumps appears to give better results, specially at high frequencies where staggering the bumps fails to improve the performance.

Figure 4 shows how the use of thin bumps gives a better performance than thick bumps, for both in-line and staggered cases (S=0.32mm). Figure 5 shows the combination of both ides of staggering and thin bumps, for different staggering distances. It appears that staggering works better at frequencies below 60GHz for this geometry while the thin in-line bumps continue to yield good performance at much higher frequencies. Reducing the thickness

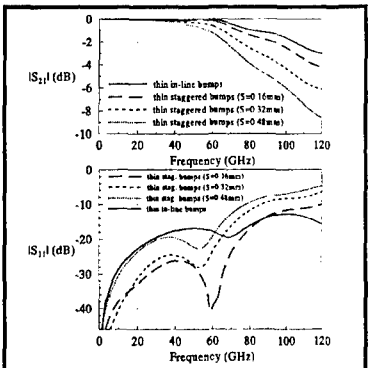

Fig. 5. S parameters for different staggering distances using thin bumps.

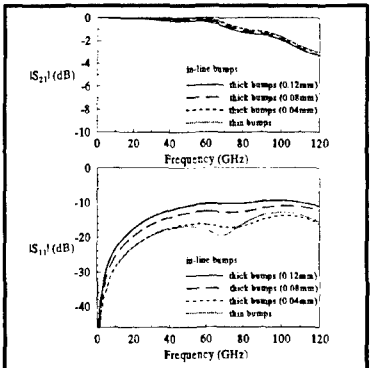

Fig. 6. S parameters for in-line bumps of different thickness.

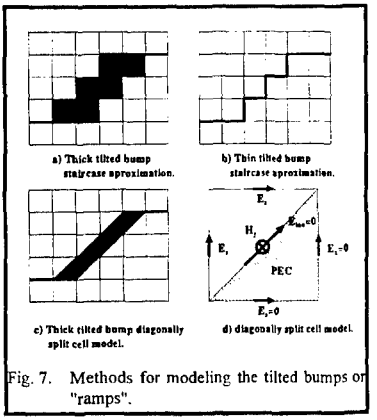

Fig. 7. Methods for modeling the tilted bumps or "ramps".

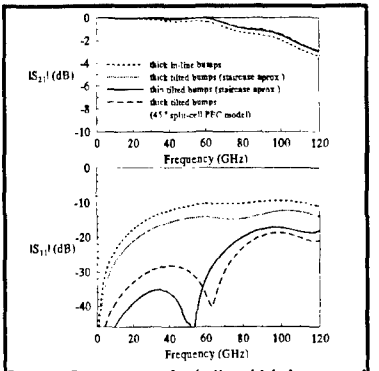

Fig. 8. S parameters for in-line thick bumps and tilted bumps.

of the bumps to thin sheets has proven to give better performance than thick bumps. Figure 6 shows the S parameters for bumps with different thickness. It proves that thinner bumps reduce the reflection.

The concept of tilted bumps (or ramps) is introduced and investigated in this paper. Figure 7 shows how these "ramps" were modeled in the FDTD technique. Figure 7a and 7b show the thick and thin staircase tilted bump, respectively. Figure 7c shows the "ramp" modeled using the diagonally split cell technique. Figure 7d shows the H_y of a single cell and the surrounding electric field components. The H_y within the cell is computed using the integral form of Faraday's law. The contour is given by the sides of the cell that are not defined as PEC, and the diagonal. The electric field on this diagonal is zero, since it is tangential to a PEC boundary. The surface surrounded by this contour is half the area of the original cell [8]. This procedure leads to a simple modification to the regular update equation of the H_y field component as previously reported in [9]. Figure 8 shows that these "ramps" give a much better performance. Again the thinner the bump or "ramp" the lower the reflection coefficient. The split cell model provides good results for high frequencies. The results obtained in Fig. 8 using this technique also show a great improvement when compared with the vertical bumps.

IV. CONCLUSION

Reducing the return loss due to connections within multichip structures is important in order to allow for the fabrication of microwave and millimeter wave integrated circuits that were not possible because of large internal reflection problems. Our investigation indicate that thin bumps give better performance than the original flip chip design with thick in-line or staggered thick bumps. The staggering of bumps is useful in reducing the return loss for frequencies up to 60 GHz. With tilted bumps or "ramps", the return loss is greatly reduced for a very wide range of frequencies.

V. ACKNOWLEDGEMENT

This research was supported by the Army Research Office under grant No. DAAH04-94-G-0355.

VI. REFERENCES

[1] K. Heinen, W. Schroen, D. Edwards, A. Wilson, R. Stierman, and M. Lamson, " Multichip Assembly with Flipped Integrated Circuits," *IEEE Trans. On Components, Hybrids and Manufacturing Technology,* Vol. 12, No. 4, pp.650-657, Dec. 1989.

[2] H. Ghouz and E. El-Sharawy, "Finite-Difference Time-Domain Analysis of Flip-Chip Interconnects with Staggered Bumps," *IEEE Trans. On Microwave Theory and Tech.*, Vol. 44, No. 6, pp. 960-963, June 1996.

[3] H. Ghouz and E. El-Sharawy, "An Accurate Equivalent Circuit Model of Flip Chip and Via Interconnects," *IEEE Trans. On Microwave Theory and Tech.*, Vol. 44, No. 12, pp. 2543-2554, Dec 1996.

[4] W. D. Becker and R. Mittra, "FDTD Modeling of Noise in Computer Packages," *IEEE Trans. On Components, Packaging and Manufacturing Technology,* Part B, Vol. 17, No. 3, pp. 240-247, Aug 1994.

[5] J-G Yook, N. Dib, and L. P B. Katehi, "Characterization of High Frequency Interconnects Using Finite Difference Time Domain and Finite Element Methods," *IEEE Trans. On Microwave Theory and Tech.*, Vol. 42, No. 9, pp. 1727-1736, Sep. 1994.

[6] E. El-Sharawy, private communications.

[7] X. Zhang and K. Mei, " Time-Domain Finite-Difference Approach to the Calculation of Frequency-Dependent Characteristics of Microstrip Discontinuities," *IEEE Trans. On Microwave Theory and Tech.*, Vol. 36, No. 12, pp. 1775-1787, Dec. 1988.

[8] A. Taflove, *Computational Electrodynamics: The Finite-Difference Time-Domain Method,* Boston, Massachusetts: Artech House, Inc., 1995.

[9] O. M. Ramahi, A. Z. Elsherbeni, and C. E. Smith, "Dynamic Analysis of V Transmission Lines," *The 12th Annual Review of Progress in Applied Computational Electromagnetics,* ACES'96, Monterey, CA, pp 1260-1266, March 1996.

FDTD Analysis of the Celestron-8 Telescope

Ronald R. DeLyser, University of Denver, Denver, CO

1 Introduction

Numerical analysis of optical sensors at microwave frequencies is essential in order to compliment measurements and to determine vulnerability of internal components. TEMAC3D [1] is a Finite Difference Time Domain code developed by John H. Beggs of Mississippi State University for use in modeling high power microwave antennas, ultra-wideband antennas and for electromagnetic coupling calculations. It is a FORTRAN code which is based on the three dimensional implementation of the FDTD method [2] which was used for the analysis of a Celestron-8 telescope and a satellite optical sensor. In the past, the Finite Element Method [3] was used to analyze the Celestron-8, and the FDTD Method [4] was used to analyze the satellite optical sensor. This paper addresses the FDTD analysis of the Celestron-8 telescope.

Supplementing TEMAC3D, is a suite of peripheral software which is needed to generate solid models, generate the Finite Difference (FD) mesh, view the mesh for consistency, generate the problem namelist and header files, and view the results of the analysis. The solid model geometry file is generated by BRL-CAD which is available from Ballistics Research Laboratory, Aberdeen Proving Ground, MD. The geometry file is then used as input to ANASTASIA, a component of TSAR (Temporal Scattering And Response) from Lawrence Livermore National Laboratory, CA. ANASTASIA generates a mesh given the number of "pad" cells[1] and the size of the cell. IMAGE (another component of TSAR) is used to view the mesh to be sure that the FD mesh is really the desired mesh. This mesh file is then an input for XTEAR (X-window Temporal Electromagnetic Analysis and Response) [1] which is a graphical user interface designed for input of all relevant parameters for the FDTD simulations using TEMAC3D. Since XTEAR was written using the scripting language, TCL/TK, these software packages (version 7.3 of TCL and version 3.6 of TK) have to be installed on the same computer that runs XTEAR. Finally, software is needed to view output fields as a function of time, frequency and/or position (Axum 5.0 is used here), to generate far-field scattering and/or radiation plots (these programs were provided by John Beggs), and to do Fast Fourier Transforms (FFTs) (Mathcad was used) in order to determine the frequency response.

2 The Model

A drawing and a cross-section of the simulation model of the Celestron-8 are shown in Figures 1 and 2. The scattering problem was done with an x-polarized, Gaussian pulse wave incident on the aperture. The locations (in mm) of the field point sensors are relative to a lower corner of the computational space assuming the aperture of the telescope is at a plane which is five pad cells below the most positive z value and the extension for the eye-piece has its lowest point in the plane which is five pad cells above the lowest z value. The computational space is 252 mm x 252 mm x 400 mm. The locations of the sensors are: (1) 126, 126, 30; (2) 126, 126, 235; (3) 70, 126, 235; (5) 35, 126, 235; (6) 15, 126, 235.

[1]Pad cells occupy the space between the outermost cells of the modeled object and the outermost cells of the problem space which implement the absorbing boundary conditions.

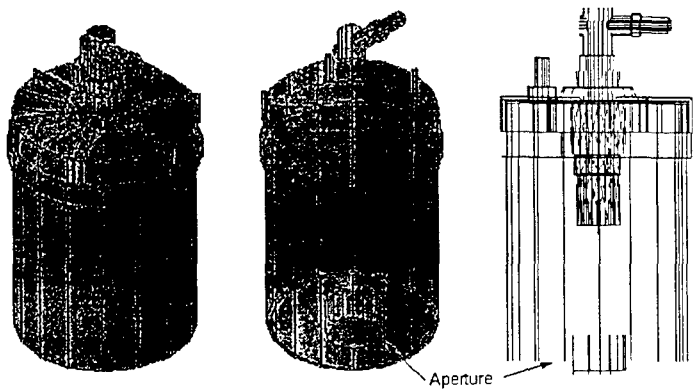

Figure 1: The Celestron-8 telescope.

Location 1 is at the eyepiece and location 5 is at the probe that was installed for testing at Phillips Lab, Kirtland AFB, NM. The model used 320 MBytes of RAM and 345 MBytes of paging space. The number of time steps taken was 32,768 at a cpu time of 29.25 seconds per time step. Since the glass region (shown in gray in Figure 2) is fairly large, that material was used for the calculation of the usable upper frequency which is 11.2 GHz. Since measured data [5] extends to 18 GHz, the numerical results will be compared to the measured results up to that frequency.

3 The Scattering Problem Results

The time domain results are exponentially decaying as expected. However, there is one unusual time domain response - the z component of the electric field at the location of the eye-piece shown in Figure 3. The corresponding frequency domain plot for all of the electric fields at this location are shown in Figure 4. The frequency of oscillation appearing late in time as shown in Figure 3 corresponds to a frequency of 9.33 GHz, clearly seen in Figure 4. If a closed cylinder of the same size as the small cylinder leading to the eye-piece is postulated, the TM_{111} (this is the lowest mode with a z component of the electric field) resonance frequency for this cylinder would be 9.24 GHz.

Figure 5 shows a comparison of the normalized magnitudes of the electric fields at the eye-piece location, the probe location, and the measured data reported in [5]. For those measurements, a sensor was placed in the location of the eye-piece for the telescope and transmission to that sensor from a radiating source was measured. For a radiation measurement, a probe was inserted into the large central cavity region of the telescope and S_{11} data taken. In the low frequency range, the measured data track the probe location data fairly well, even though the measured data is taken at the location of the eye piece. The Phillips lab testers believe that this can be explained by poor isolation between the large cavity region and the location of the test sensor at the eye piece. Note also that the characteristic high pass filter response of the small cylinder leading to the eyepiece is evident in the "Eye piece location"

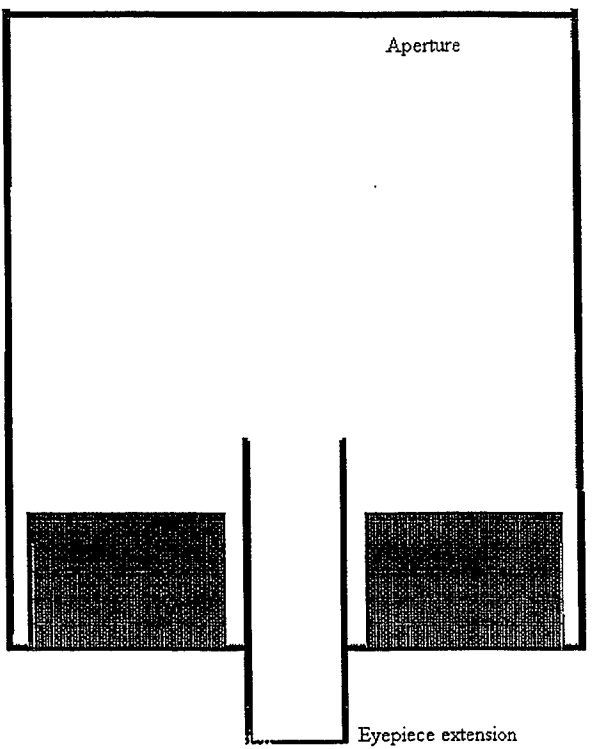

Figure 2: Cross-section of the mesh for the Celestron-8.

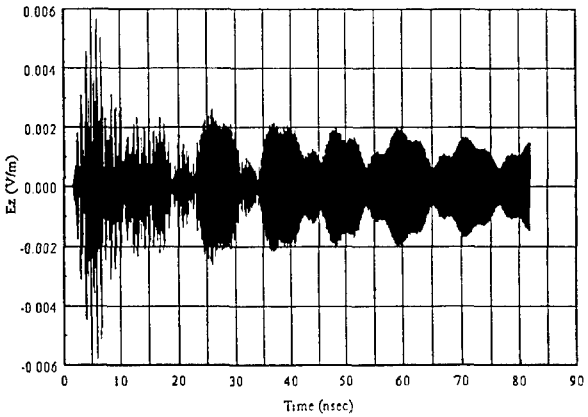

Figure 3: The z component of the electric field at the eye-piece location.

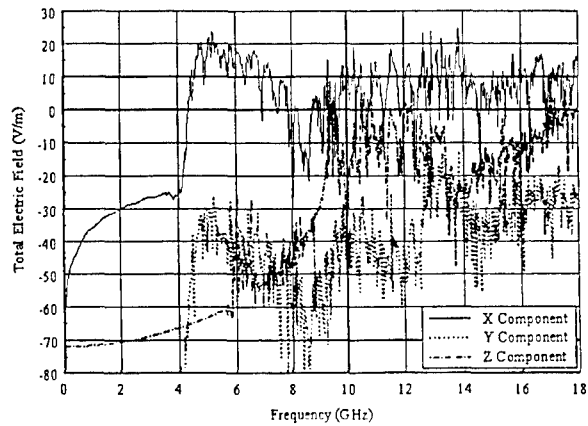

Figure 4: The electric field components at the location of the eye-piece.

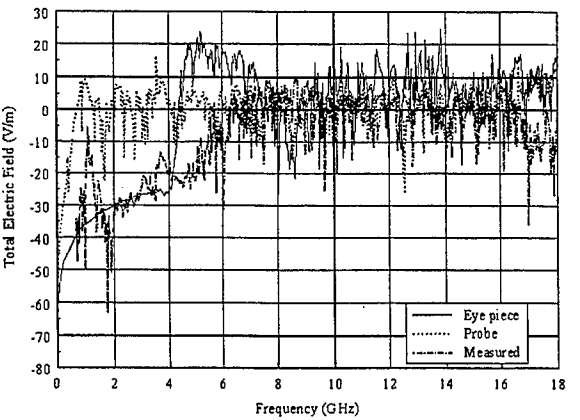

Figure 5: Comparisons of numerical and measured results.

data.

The frequency domain plots for the electric fields at locations 3, 4 and 5 are similar in the low frequency region. Resonances at the higher frequencies are very different for these locations as is expected of a large, multi-moded cavity. This frequency response behavior is seen in a comparison of the normalized magnitudes of the electric fields at locations 2 - 5 shown in Figure 6. Results at the different locations are very similar up to about 3 GHz indicating that only a few modes exist up to that frequency. Above 3 GHz, the responses at the different locations begin to diverge substantially indicating that more and more modes are generated at the higher frequencies.

4 The Radiation Problem Results

The resonances at 1.02 GHz, 1.45 GHz, 1.61 GHz and 1.76 GHz were investigated by doing the radiation problem with an x directed point source at the probe location specified for the measurements reported in [5]. The radiation patterns for 1.61 GHz[2] in the xz ($\phi = 0$) and yz ($\phi = 90$) planes are shown in Figure 7. Notice that the maximum response does not occur on boresight. Other far field plots at other frequencies have maximum responses at other angles including on boresight. This information is important to determine vulnerable angles of incidence.

A slice sensor for the electric fields was placed in the plane of the aperture. A magnetic field slice sensor was defined for the xz plane, the plane containing the probe. Figures 8 and 9 show surface plots corresponding to the magnitudes of the fields for these slice sensors. The vertical scale for Figure 9 has been defined to clearly show the field variations at locations away from the source. Thus, at locations near the source, field magnitudes are clipped.

[2]Details of the entire study are in preparation for publication and can be obtained from the author.

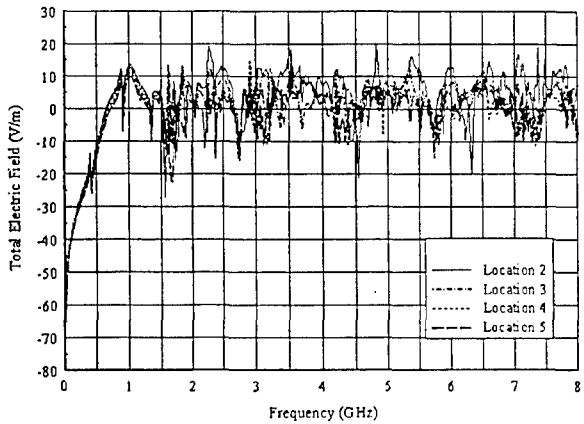

Figure 6: Normalized magnitudes of the electric fields at locations 2 - 5.

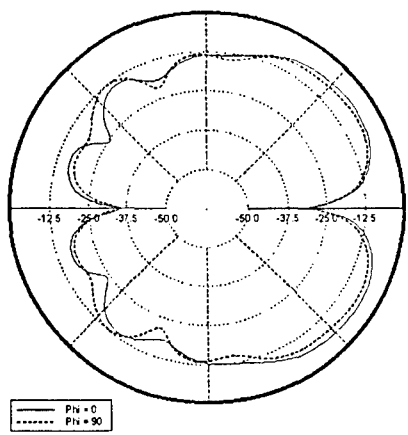

Figure 7: Radiation plot for 1.45 GHz.

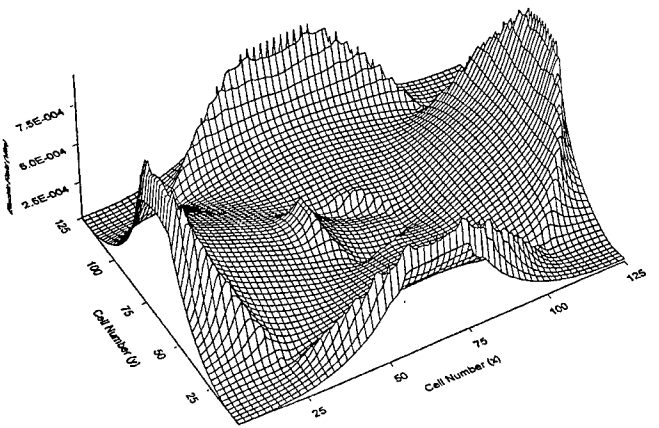

Figure 8: Electric field in the aperture - 1.45 GHz.

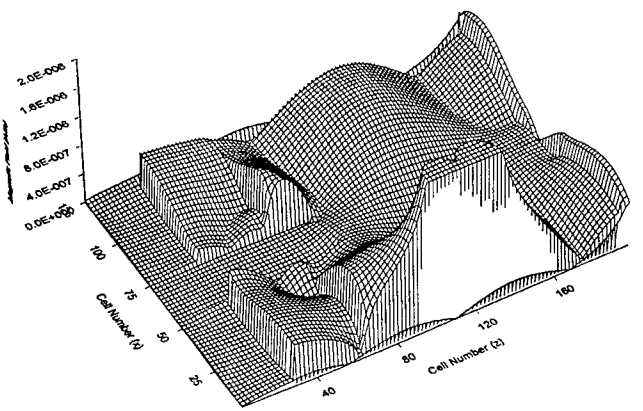

Figure 9: Magnetic field in the plane of the probe - 1.45 GHz.

At this point, it is prudent to refer to a mode chart for circular waveguides in order to identify some of the modes that may be present at these resonant frequencies. One such chart can be found in [6]. This comparison will give the type and first two mode numbers for the transverse resonance modes. Identification of the third mode number which corresponds to resonances for the length of the cavity is not possible because of the open end at the aperture of the cavity. For 1.45 GHz, TM_{21} can be identified as the transverse resonance mode.

5 Conclusions

The results reported here show that TEMAC3D is an effective tool for analysis of complex cavities. It can be used to treat a cavity as a scatterer in order to find frequency response of a particular field location inside the cavity. Once frequencies of interest are identified, TEMAC3D can be used to analyze the cavity as a radiator (antenna with a specified point source internal to the cavity) in order to find angles of incidence that are particularly sensitive. Once these are found, the frequency response can be repeated at these angles. TEMAC3D results for Celestron-8 when compared to testing results are quite good. Where possible, this information should be used to define test parameters for future experiments on the Celestron-8.

References

[1] John H. Beggs, James D. Letterio and Sydney A. Blocher, Jr., *User Manual for XTEAR and TEMAC3D Computational Electromagnetic Time-Domain Codes*, available from Sydney A. Blocher, Jr., Phillips Laboratory/WSM, 3550 Aberdeen Ave. SE, Kirtland AFB, NM 87117.

[2] K. S. Kuntz and R. J. Luebbers, "The Finite Difference Time Domain Method for Electromagnetics," CRC Press, Boca Raton, FL, 1993.

[3] R. R. DeLyser and H. Pohle, "Finite Element Method Analysis of the Celestron-8 Telescope," *The Twelfth Annual Review of Progress in Applied Computational Electromagnetics*, Naval Postgraduate School, Monterey, CA, 18-22 March, 1996.

[4] R. R. DeLyser, "Computational Evaluation of an Optical Sensor using the Finite Difference Time Domain Method," The Thirteenth Annual Review of Progress in Applied Computational Electromagnetics, Naval Postgraduate School, Monterey, CA, 17-21 March, 1997.

[5] R. R. DeLyser and Peyman Ensaf, "Quality Factor Evaluation of Complex Cavities," Final Report, Summer Research Extension Program, Sponsored by Phillips Laboratory, December, 1995.

[6] Constantine A. Balanis, "Advanced Engineering Electromagnetics," John Wiley & Sons, Inc., New York, 1989.

Modifying a Graphically-Based FDTD Simulation for Parallel Processing

Gary Haussmann, Melinda Piket-May
Department of Electrical and Computer Engineering
Campus Box 425, University of Colorado, Boulder,CO 80309
phone 303-492-7891, fax 303-492-5323
mjp@colorado.edu

Kevin Thomas
Cray Research, Inc.
655 Lone Oak Road, Eagan, MN 55121
phone 612-683-3624, fax 612-683-3099
kjt@cray.com

Abstract

This paper discusses the graphical FDTD simulation tool "LC" [3] and the special problems posed when parallelizing such a tool, one designed for rapid graphical editing and analysis instead of direct low-level numerical simulation. In particular, the simulation is represented by numerous data structures specifying material positions and type, excitation types, and data gathering (probe) configurations. Parallelizing the FDTD simulation portion is relatively straightforward, but managing the flexible portion inherent to the functionality of "LC" is not.

I. Introduction

This paper will discuss parallelizing an EM analysis development called "LC". [4] [5] Essentially LC is a Finite-Difference Time-Domain (FDTD) based integrated EM model editor, simulator, and analysis tool. It consists of a GUI interface with the ability to automesh a graphically defined user geometry. A number of different excitations are possible, and the outputs can yield not only field data, but also voltages, currents, impedances, inductances, capacitances and fluxes. Further, both time and frequency-domain data is available on output. It also allows for 2-D visual simulations of the full 3-D problem being simulated during time-stepping. This is very useful in identifying problem areas with a particular design. Another very important and relevant feature of the LC tool is an interface to SPICE [6]which will analyze a circuit based on FD-TD field values linked to SPICE at each time step. The SPICE interface also generates output voltages and/or currents that modify the FD-TD field values which are then used during the next FD-TD time-step. The efficient implementation of LC on scalable parallel computers will allow for the examination of problems that are currently too computationally large or complex, conceivably making inroads into some of the grand challenges facing the electromagnetic engineering community.

II. Parallelizing the FDTD Method

Implementing a parallel version of the FDTD method involves splitting the computation work into pieces for each processor, and then making sure that these processors are properly coordinated with each other, via synchronization and/or message passing. Because the standard FDTD method uses a regular uniform grid, these two tasks are relatively straightforward.

A. Spatial Decomposition

The computations are allocated to multiple processors. The most straightforward method to divide up work is to assign a part of the computational space to each processor (figure 1). Each processor then performs FDTD style updates for only those cells in it's local space, transferring field values as needed to other processors.

A.1 Distributing Work Evenly

In order to achieve good parallel speedup, some sort of load balancing is needed to give each processor the same amount of work; if one processor gets too much computational work to do, the other processors will stall waiting for the overloaded processor to finish. The FDTD method has two characteristics that make the load balancing problem relatively easy:

- The FDTD grid is regular, so that the grid points are evenly spaced over the space being simulated. Therefore, if we cut out specific volume amount of simulation space, that volume always contains the same number of grid points anywhere in the simulation space.
- The FDTD implementation is such that the same computations (update equations) and the same amount of work is done at each grid point.

As a result of these characteristics, any decomposition method that gives each processor an equal volume also gives each processor an equal number of grid points and computational work.

If the grid points were instead distributed in some irregular fashion, or if some grid points required more computation than others, than we need to use some other, more sophisticated method to divide up the work. Some FDTD variants, such as Finite-Volume and Generalized Yee [2, p. 369] will produce an irregular grid, complicating the FDTD parallelization problem. However, the typical FDTD does fit the above mentioned criteria, so a straightforward uniform partitioning does a very good job of distributing the computational load over multiple processors.

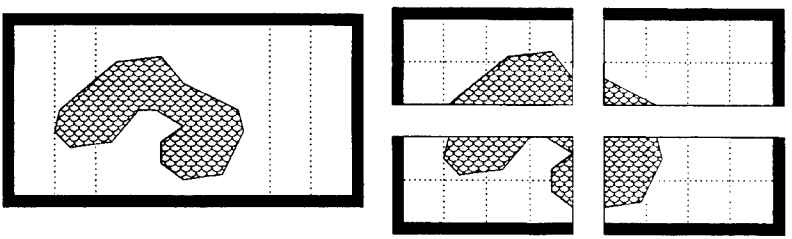

Fig. 1. Spatial partitioning of the problem to four independent processors

B. Data Distribution with MPI

After the array has been partitioned, the simulation begins and field values are updated; on each processor there will be field values that, in order to be properly updated, depend on data values that reside on a different processor (figure 2). The processors must transfer

data to each so that every processor has a copy of the field data needed to update all of the grid points that processor is responsible for.

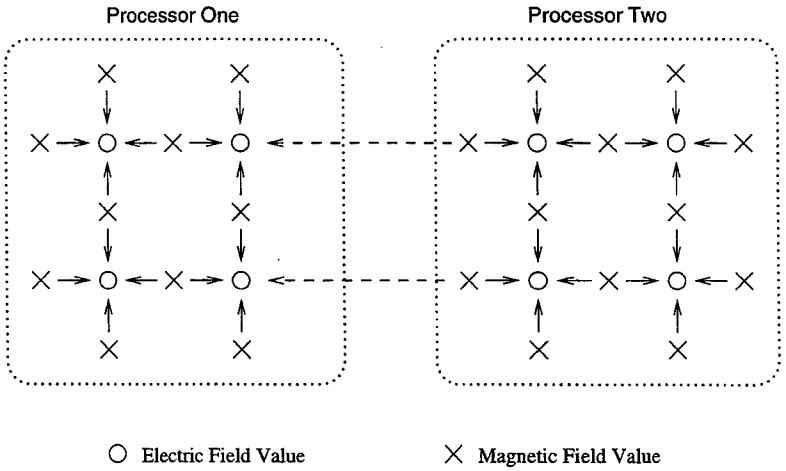

Fig. 2. Data dependency graph for an FDTD grid distributed across two processors. Arrows show that each electric field is dependent on the four surrounding magnetic fields; two electric fields depend on magnetic fields located on the other processor

For FDTD, these transfers occur at every time step, for both types of field values. To update the electric field points, the magnetic field values must be transferred between processor; to update magnetic fields, the electric field values must be transferred. Just as the electric and magnetic field updates themselves are staggered, so too is the transfer of electric and magnetic field values between processors.

The parallel bookkeeping and passing of data between processors is done using the MPI parallel Message Passing Interface [1]. MPI was chosen because it provides good performance combined with portability, allowing the parallel version to run on a wide variety of architectures just as the original program "LC" did. MPI also has built in functionality to configure the parallel machine as a Cartesian array (i.e., as an $N \times M \times P$ array of processors, where N, M, P are user selected), in whatever manner is appropriate for the current hardware. This is achieved using a "virtual Cartesian array", created by the `MPI_CREATE_CART` function.

The MPI interface is capable of transferring simple arrays of data between processors, but can also transfer projections of arrays via strided access. This capability is important because almost all of the data transfer between processors consists of small 2D slices of the 3D simulation grid (figure 3). If MPI only supported transfer of simple 1D arrays, we would have to manually extract the projections into a 1D buffer, transfer that buffer to another processor, and then insert the 1D buffer data into the 3D grid on the new processor. However, after specifying the grid's array structure to MPI with `MPI_CREATE_HVECTOR`, the

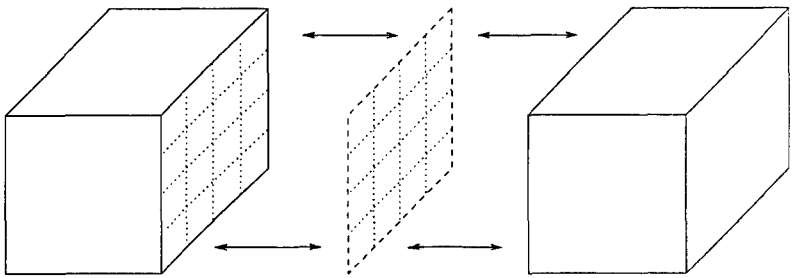

Fig. 3. Processors exchange 2D slices of 3D data

entire 2D projections is transferred to its destination with single MPI function call.

III. Specific Implementation Difficulties

The difficulties particular to paralleling this FDTD implementation stem from the very loose restrictions on the problem space. Because the problem input can be a rather large number of shapes and excitations, input in a more or less arbitrary order and location, the parallel program must do quite a bit of data manipulation. The program could have restricted the user in ways to make implementation of LC easier – requirements such as only allowing one source and probe, or requiring the first block listed to encompass the entire grid – but such restrictions run against the original design goals for LC.

Much of the information about the simulation, such as the grid size and shape, is not known explicitly but deduced at run time. The user can specify the grid size and shape, as well as the structure to analyze at run-time, just as the program is starting execution. If instead the simulation parameters (material values needed, waveform frequency and shape, etc.) were found at compile time and not run time, then every time a parameter changed, the user would need to enter all these parameters, recompile the program, and then run the simulation. By delaying these choices until run time, the user is spared a good deal of time and overhead usually involved in the programming/compiling phase.

However, the same run time properties that make design easy for the user make implementation hard for the programmer. If everything had been specified at compile time, such issues as dividing up the problem amongst multiple processors, and inter-processor communication, would have been examined and solved at compile time. But because the program doesn't have enough information at compile time, it must wait until run time, and as it is running the program must properly redistribute the problem over all of it's processors and set up communication channels to transfer data between processors, and funnel the analysis results into various (one to many) output data files. It is this process of data decomposition and inter-process communication that presents the most implementation problems.

The internal data storage of LC records the structure as a list of "blocks" which can represent a material, data probe, source excitation, or several other objects. The overall structure being studied is manipulated by adding, examining, and destroying these blocks. Just before a simulation is run, the representation is frozen and converted into an FDTD

mesh, along with some extra data representing the sources, probes, and other information not directly stored in the FDTD mesh. This conversion process – the transforming of a block list into an FDTD mesh, called "meshing" in the program – is where most of the actual programming problems arise for the parallel implementation.

A. Variable Spatial Decomposition

The first problem stems from the fact that the grid size and shape is not explicitly defined at compile time, or even at run time. The serial program deduces the grid size by examining all of the LC blocks and finding the size and location of the smallest cube that will completely enclose all the defined blocks. Then all of the grid data is allocated and block locations are mapped from the "real world" coordinates, in meters or mils or perhaps some other unit length, into simulation grid coordinates, so that the blocks may be put into the grid.

The code structure implies that by the time enough information is known about the grid to do a sensible partitioning on parallel processors, the grid itself is in the process of being built. Therefore, the parallel version has to analyze the entire block list before meshing, and form a suitable parallel partition, assigning disjoint spaces to each processor.

B. Variable Block Placement

Once the problem is partitioned onto the parallel processors, meshing can proceed just as it did in the serial version. However, we cannot use the original block list on each processor - if we did, each processor would then be meshing and simulating the entire grid. Therefore, each processor obtains a private copy of the block list, and modifies that copy to contain only relevant blocks (figure 4). Each processor is responsible for computing a certain region of the total grid; any blocks outside that region are discarded, and the remaining blocks are clipped so that they are totally contained in the processor's computational region.

After the block list on each processor has been modified, it is processed normally using the original serial meshing algorithm. Since the block list only specifies blocks within the processor's computational region, the meshing algorithm will only allocate and mesh that region. The process occurs on all the processors in parallel, each transforming the block list into a local grid. Proper manipulation of the block list before this step insures that no two processors try to allocate and simulate the same region, or overlapping regions.

C. Partitioning of Arbitrary Source and Probe Blocks

The process of discarding and clipping blocks in the block list will automatically divide up material blocks correctly, so the overall structure under study will be properly partitioned and meshed on the parallel array of processors. However, non-material elements will not function correctly once they have been split onto multiple processors. The serial code will process a given source or probe block as if it existed only on that processor; if a probe block is split across two processors, for instance, then each processor will collect probe data for its "local" probe. Some mechanism must exist to gather up the data from all the local probes into the larger probes in the original block list. Similarly, the source blocks must be configured to spread their voltage or current energy across multiple processors.

Source blocks are modified to generate a smaller current or voltage, based upon their new size; for instance, if voltage excitation is split exactly in half across two processors, the two new blocks will now generate $\frac{1}{2}$ the original voltage. Voltage excitations split in other

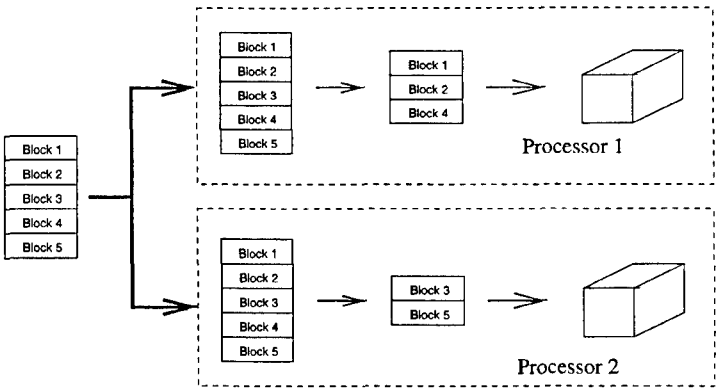

Fig. 4. Each processor obtains and clips its own copy of the block list

ways will generate voltage amplitudes in proportion to their new size. Also, depending on whether the source is a voltage or current source, splitting the block along certain axes does not change the generated value; if a voltage source produced a voltage along the y axis, splitting it down the yz plane, into two voltage sources side by side,

Probe blocks gather their data locally on each processor, and then must somehow combine the data into a final, single, value. The parallel implementation does this by collecting probe information data from every processor. This probe information lists what probes exist on what processors. If a probe is split across multiple processors, then one of those processors is selected to manage the overall data for that probe. All other processors containing that probe send their data to the managing processor, which combines the data together and outputs it as the original serial code did.

D. Virtual Boundary Conditions

Except for some block modification and extra probe processing, the code running on each processor is basically unmodified from the serial version. Each processor really thinks that it is running the entire FDTD simulation, and that the modified block list it was given represents the entire simulation domain.

To prevent excessive code modification, this illusion continues with the boundary conditions. Each processor grid is the shape of a cube; the sides and edges of this cube need some sort of boundary conditions, typically an electric wall or absorbing layer. However, there is really no limitation on the boundary condition implementation; we can put whatever boundary conditions we want there. The boundaries that are needed are those that somehow connect all the processors together.

These virtual boundaries look to the simulation to be just a special sort of boundary condition, and in fact are implemented as another entry in the list of boundaries: 1^{st} order Mur, PML, virtual boundaries. These virtual boundaries on a certain processor simply

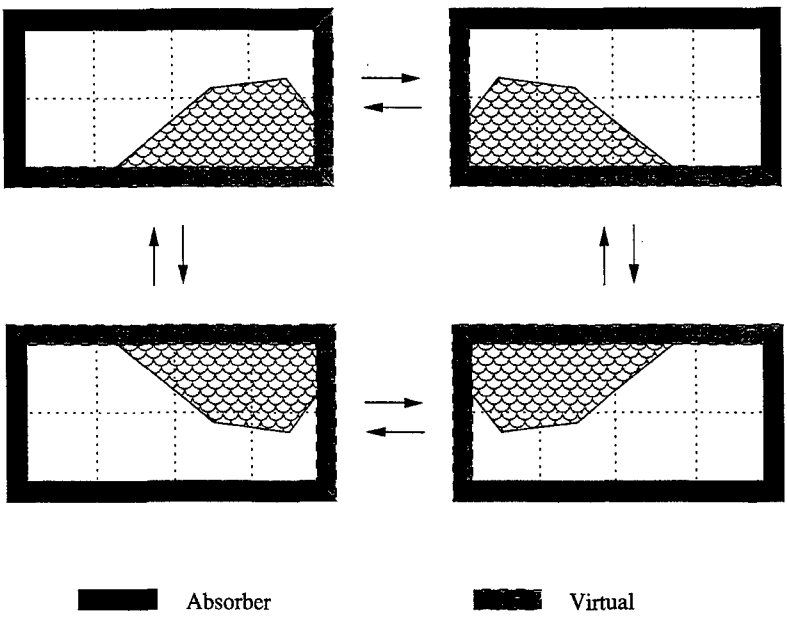

Fig. 5. Parallel configuration with four processors, showing the placement of virtual boundary conditions

transfer the appropriate electric and magnetic fields to and from other processors. These boundaries are only placed on grid sides where communication with other processors is needed (figure 5); other grid sides use an absorbing boundary instead, as they would have if the program was not running in parallel.

IV. Conclusion

This paper reported the special problems posed when parallelizing a graphically based EM simulation tool, one designed for rapid graphical editing and analysis instead of direct low-level numerical simulation. Parallelizing the FDTD simulation portion is relatively straightforward. Spatial decomposition, even work distribution, and distributing data with MPI in relation to the FDTD algorithm were discussed. Managing the flexible portion of LC inherent to its functionality is not straitforward. An explanation of how we used variable spatial decomposition, variable block placement, partitioning of arbitrary source and probe blocks and virtual boundary conditions to parrallelize LC was included. The efficient implementation of LC on scalable parallel computers will allow for the examination of problems that are currently too computationally large or complex, conceivably making inroads into

some of the grand challenges facing the electromagnetic engineering community.

REFERENCES

[1] The message passing interface (MPI) standard 1.2 and 2.0. http://www.mpi-forum org/.

[2] Allen Taflove. *Computational Electrodynamics: The Finite-Difference Time-Domain Method* Artech House, Inc., 685 Canton Street, Norwood, MA 02062 USA, 1995.

[3] Kevin Thomas. LC web home and documentation. http://www.cray.com/lc.

[4] Piket-May Thomas, Haussmann and Gravrok. Packaging and inteconnect design and analysis using fdtd *IEEE EPEP Conference Proceedings*, 1997.

[5] Piket-May Thomas, Haussmann and Gravrok. Implementation and application of a fdtd simulation tool for the analysis of complex 3d structures. *Applied Computational Electromagnetics Society Journal*, submitted 1997.

[6] Piket-May Taflove Thomas, Jones and Harrigan. The use of spice lumped circuits as subgrid models for fdtd analysis. *Microwave and Guided Wave Letters*, 4:141–143, 1994.

A Time Domain Method For High Frequency Problems Exploiting The Whitney Complex

Aimo Arkko, Timo Tarhasaari and Lauri Kettunen
Tampere University of Technology
Laboratory of Electricity and Magnetism
P.O.Box 692
FIN-33101 Tampere, Finland

***Abstract*—In this paper the basic tools needed in generalizing the classical finite difference time domain method for irregular simplicial meshes are introduced. Our main tools are the Whitney complex, primal and dual meshes and a discrete counterpart of the Hodge operator. A simple example demonstrating the main idea is also shown.**

I. Introduction

The finite difference time domain (FDTD) method, first introduced by Yee [1], is widely used for solving high frequency electromagnetic problems. This paper is a step along the way to find a proper extension of Yee's algorithm for any simplicial mesh. Our approach is of more general nature than those of relying on Voronoi duality, such as reference [2]. We do not make any assumptions of perpendicular (dual) edges to (primal) facets and thus any simplicial mesh is acceptable. The aim of this paper is mainly to introduce the basic tools needed in this process. The Whitney complex is our basic tool to represent electromagnetic field quantities in discrete spaces.

II. Whitney Complex

The problem domain is assumed to be tesselated by a finite number of tetrahedra with the usual properties of finite element meshes: two distinct tetrahedra share a facet, an edge, a node or nothing. Whitney forms generate discrete spaces W^0, W^1, W^2 and W^3 associated with nodes, edges, facets and tetrahedra, respectively [3]. Let λ_i be the barycentric function associated with node $n = \{i\}$. The basis functions of W^0, W^1 and W^2 are then given such that for node $n = \{i\}$

$$w_n = \lambda_i, \tag{1}$$

for edge $e = \{i, j\}$

$$w_e = \lambda_i \nabla\lambda_j - \lambda_j \nabla\lambda_i \tag{2}$$

and for facet $f = \{i, j, k\}$

$$w_f = 2(\lambda_i \nabla\lambda_j \times \nabla\lambda_k + \lambda_j \nabla\lambda_k \times \nabla\lambda_i + \lambda_k \nabla\lambda_i \times \nabla\lambda_j). \tag{3}$$

The basis functions of W^3 are not needed here. A field U in space W^p, $p = 0, 1, 2, 3$, is represented as a linear combination of Whitney p-form basis functions. Node elements yield continuous scalar fields, edge elements tangentially and facet elements normally continuous vector fields and volume elements piecewise constant scalar fields. The degrees of freedom (DoF's) are nodal values at nodes, circulations along edges, fluxes across facets or volume integrals over tetrahedra, respectively [3].

The gradient of a node element is a linear combination of edge elements, the curl of an edge element is a linear combination of facet elements and the divergence of a facet element is a linear combination of volume elements. Formally these injective properties of the Whitney complex can be given by [4]

$$\text{grad}\, W^0 \subset W^1,\ \text{curl}\, W^1 \subset W^2,\ \text{div}\, W^2 \subset W^3,$$

or in a form of a diagram such that

$$W^0 \xrightarrow{\text{grad}} W^1 \xrightarrow{\text{curl}} W^2 \xrightarrow{\text{div}} W^3.$$

A same kind of a diagram for spaces $\mathbf{W}^p$, spanned by the vectors of DoF's, can be given such that

$$\mathbf{W}^0 \xrightarrow{\mathbf{G}} \mathbf{W}^1 \xrightarrow{\mathbf{C}} \mathbf{W}^2 \xrightarrow{\mathbf{D}} \mathbf{W}^3,$$

where $\mathbf{G}$, $\mathbf{C}$ and $\mathbf{D}$ denote connectivity matrices, with all entries -1, 0 or 1, representing gradient, curl and divergence operators, respectively [3].

Whitney forms provide us with a tool to represent discrete electromagnetic field quantities in a natural way. Both E- and H-fields are tangentially continuous vector fields, if no surface currents are present, and thus best represented by Whitney 1-forms. DoF's of E and H correspond with EMF's or MMF's along edges, respectively. In the same way, D- and B-fields are normally continuous vector fields, if no surface charges exist, and thus best represented by Whitney 2-forms. DoF's of D and B correspond with electric or magnetic fluxes across facets, respectively [3].

III. Duality

In the high frequency case Faraday's and Ampère's laws need to be solved simultaneously. This can be done by assigning one of the equations on the primal mesh and the other on the dual side. The dual mesh consists of the dual counterparts of each primal simplex e.g. for each primal element, facet, edge and node there exists a dual node, edge, facet and element, respectively. The dual nodes are located at the barycenters (i.e. 'centroids') of primal elements. Each primal facet is pierced by a dual edge and vice versa [5], [6]. In Fig. 1 a dual edge and a dual facet are shown.

The duality involved in Maxwell's equations can be illustrated by 'Maxwell's house' shown in Fig. 2 [5]. Faraday's law is represented on the right side and Ampère's law on the left side of the diagram proposing the decomposition onto primal and dual side. In the discrete case this means that field quantities on one side should be represented in spaces associated with the primal mesh while field quantities on the opposite side should be represented in spaces associated with the dual mesh.

In general, the Whitney elements, associated with the dual of a simplicial (i.e. 'tetrahedral') mesh, are not known. That is why we need to find a way to represent the dual field quantities in

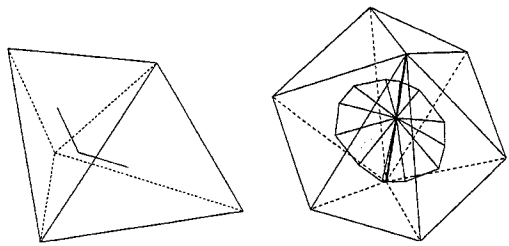

Fig. 1. A dual edge (left) and a dual facet.

term of primal ones. For continuous differential forms the operator that builds up this connection is called the Hodge star operator [7]. For instance, a 1-form U can be transformed into 2-form $^*U$, which is the dual counterpart of U. However, the proper way of doing this in discrete spaces is still an open question.

In electromagnetics, as shown in Fig. 2 the Hodge operator is typically associated with constitutive laws, as represented in the middle of the diagram. In discrete spaces the relation $\tilde{D} = \epsilon\, ^*E$ takes form $\tilde{\mathbf{d}} = \mathbf{E}\mathbf{e}$, where the matrix $\mathbf{E}$ now represents the discrete Hodge operator (quantities on the dual side are equipped with a tilde). According to our current best knowledge, an entry $(\mathbf{E})_{ij}$ in the matrix $\mathbf{E}$ should be given such that

$$(\mathbf{E})_{ij} = \int_{\tilde{e}_i} \epsilon\, ^*w_{e_j}, \tag{4}$$

where $^*w_{e_j}$ corresponds to the normal component of the edge basis function of primal edge j on the oriented dual facet $\tilde{e}_i$. In the same way, the relation $\tilde{H} = \frac{1}{\mu}\, ^*B$ can be written in the discrete case as $\tilde{\mathbf{h}} = \mathbf{M}\mathbf{b}$, where

$$(\mathbf{M})_{ij} = \int_{\tilde{f}_i} \frac{1}{\mu}\, ^*w_{f_j}. \tag{5}$$

$^*w_{f_j}$ now corresponds to the tangential component of the facet basis function of primal facet j on the oriented dual edge $\tilde{f}_i$.

IV. A Time Domain Method

We assign now Faraday's law on the primal and Ampère's law on the dual side (their roles could be interchanged). For simplicity, we assume that charge density $\tilde{\rho}$ and current density $\tilde{J}$ vanish within the domain. Hence Faraday's and Ampère's laws imply $\frac{\partial}{\partial t}\mathrm{div}\tilde{\mathrm{D}}$ and $\frac{\partial}{\partial t}\mathrm{divB}$ to be null. We look for an approximation of E-field in W^1 and B-field in W^2 i.e.

$$E = \sum_e e_e w_e \tag{6}$$

and

$$B = \sum_f b_f w_f. \tag{7}$$

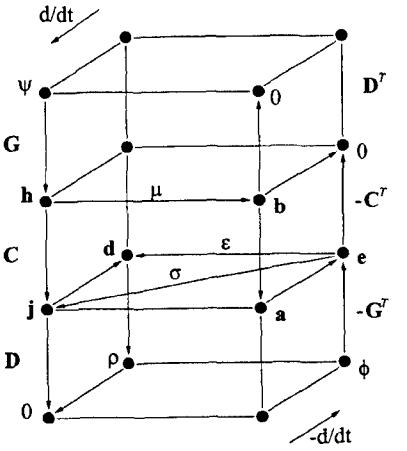

Fig. 2. Maxwell's house.

Starting from Faraday's law we approximate E and the time derivative of B at time step t such that

$$E^t = \frac{E^{t+1} + E^{t-1}}{2} \tag{8}$$

and

$$\frac{\partial}{\partial t} B^t = \frac{B^{t+1} - B^{t-1}}{\Delta t}. \tag{9}$$

Faraday's law can thus be written such that

$$\mathbf{C}\frac{\mathbf{e}^{t+1} + \mathbf{e}^{t-1}}{2} = -\frac{\mathbf{b}^{t+1} - \mathbf{b}^{t-1}}{\Delta t}, \tag{10}$$

where matrix $\mathbf{C}$ is the discrete counterpart of the curl operator. This gives the $\mathbf{b}$-vector at step $t+1$

$$\mathbf{b}^{t+1} = \mathbf{b}^{t-1} - \frac{\Delta t}{2}\mathbf{C}\mathbf{e}^{t+1} - \frac{\Delta t}{2}\mathbf{C}\mathbf{e}^{t-1}. \tag{11}$$

In the same way, $\tilde{H}$ and $\tilde{D}$ on the dual side at time step t can be written as

$$\tilde{H}^t = \frac{\tilde{H}^{t+1} + \tilde{H}^{t-1}}{2} \tag{12}$$

and

$$\frac{\partial}{\partial t} \tilde{D}^t = \frac{\tilde{D}^{t+1} - \tilde{D}^{t-1}}{\Delta t}. \tag{13}$$

Ampère's law is then written such that

$$\mathbf{C}^T\frac{\tilde{\mathbf{h}}^{t+1} + \tilde{\mathbf{h}}^{t-1}}{2} = \frac{\tilde{\mathbf{d}}^{t+1} - \tilde{\mathbf{d}}^{t-1}}{\Delta t}, \tag{14}$$

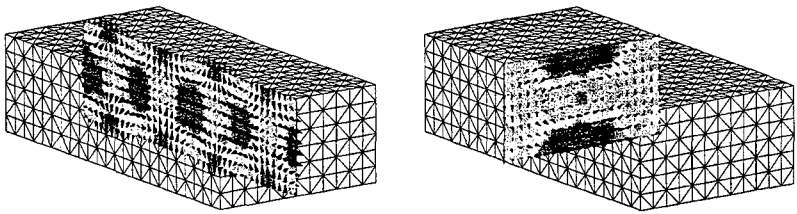

Fig. 3. Electric field strength (left) and magnetic flux density distributions along a rectangular waveguide.

where the adjoint of curl on the dual side is the transpose of the corresponding matrix $\mathbf{C}$ of the primal side [3]. This gives the $\tilde{\mathbf{d}}$-vector at step $t+1$

$$\tilde{\mathbf{d}}^{t+1} = \tilde{\mathbf{d}}^{t-1} + \frac{\Delta t}{2}\mathbf{C}^T\tilde{\mathbf{h}}^{t+1} + \frac{\Delta t}{2}\mathbf{C}^T\tilde{\mathbf{h}}^{t-1}. \tag{15}$$

The discrete Hodge operators are now chosen as given by (4) and (5). Permittivity ϵ and permeability μ are assumed constants within a primal element. Hence

$$\tilde{\mathbf{d}} = \mathbf{E}\mathbf{e} \tag{16}$$

and

$$\tilde{\mathbf{h}} = \mathbf{M}\mathbf{b}. \tag{17}$$

Ampère's law for primal quantities can now be written such that

$$\mathbf{E}\mathbf{e}^{t+1} = \mathbf{E}\mathbf{e}^{t-1} + \frac{\Delta t}{2}\mathbf{C}^T\mathbf{M}\mathbf{b}^{t+1} + \frac{\Delta t}{2}\mathbf{C}^T\mathbf{M}\mathbf{b}^{t-1}. \tag{18}$$

Finally, equations (11) and (18) are combined yielding

$$\begin{bmatrix} \mathbf{I} & \frac{\Delta t}{2}\mathbf{C} \\ -\frac{\Delta t}{2}\mathbf{C}^T\mathbf{M} & \mathbf{E} \end{bmatrix} \begin{bmatrix} \mathbf{b}^{t+1} \\ \mathbf{e}^{t+1} \end{bmatrix} = \begin{bmatrix} \mathbf{I} & -\frac{\Delta t}{2}\mathbf{C} \\ \frac{\Delta t}{2}\mathbf{C}^T\mathbf{M} & \mathbf{E} \end{bmatrix} \begin{bmatrix} \mathbf{b}^{t-1} \\ \mathbf{e}^{t-1} \end{bmatrix}. \tag{19}$$

V. Test Results

A very simple example, the TM_{11} wave in a hollow rectangular waveguide with perfectly conducting walls, is shown to demonstrate the idea. The frequency ($f = 30$ GHz) chosen is above the cutoff frequency. Starting from the analytical solution, a time period of one wavelength is computed. The input mode is defined as boundary conditions on the input and output ports. The left side of Fig. 3 shows the electric field strength over the longitudinal section of the waveguide. The magnetic flux density over the cross section is showed on the right side of Fig. 3. The electric field strength and magnetic flux density at the center of the waveguide are also computed at each time step. A comparison between analytical and computed results is showed in Fig. 4.

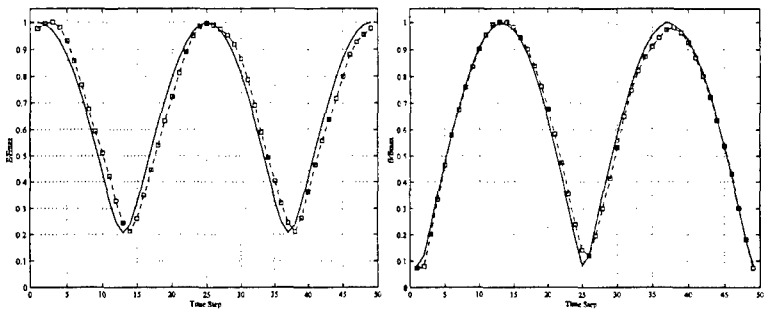

Fig. 4. Electric field strength (left) and magnetic flux density at the center of a rectangular waveguide. Solid line refers to analytical solution and squares represent computed values.

VI. Summary

In this paper we examine the generalization of the classical time domain method for high frequency problems exploiting the Whitney complex. The duality involved in Maxwell's equations is imposed by fulfilling one curl equation on the primal mesh and the other on the dual side. The primal and dual sides are connected with a discrete operator representing (possibly) the Hodge star operator in discrete spaces. An elementary test problem is shown to demonstrate the main ideas.

References

[1] K. S. Yee, "Numerical solution of initial boundary value problems involving maxwell's equations in isotropic media," *IEEE Trans. Antennas Propagat.*, vol. 14, pp. 302–307, May 1966.

[2] T. Weiland, "Time domain electromagnetic field computation with finite difference methods," *Int. J. Num. Modell.*, vol. 9, pp. 295–319, 1996.

[3] A. Bossavit, "Simplicial finite elements for scattering problems in electromagnetism," *Comp. Meth. in Appl. Mech. and Eng.*, vol. 76, pp. 299–316, 1989.

[4] A. Bossavit, "Whitney forms: a class of finite elements for three-dimensional computations in electromagnetism," *IEE Proc.*, vol. 135, Pt. A, no. 8, pp. 493–500, 1988.

[5] A. Bossavit, *Computational Electromagnetism, Variational Formulations, Edge Elements, Complementarity.* Boston: Academic Press, 1997.

[6] D. Adams, "A discrete analogue of a basic formula in hodge-de rham theory," September 1997. Submitted.

[7] H. Flanders, *Differential Forms with Applications to the Physical Sciences.* Dover Publications, 1989.

TREATMENT OF BOUNDARIES IN MULTIRESOLUTION BASED FDTD MULTIGRID

Kavita Goverdhanam, Emmanouil Tentzeris, Linda P.B. Katehi
Radiation Laboratory, EECS Department, University of Michigan,
Ann Arbor, MI 48109-2122, USA

I Introduction

In the last few years, Multiresolution analysis has been successfully applied to finite difference time domain (FDTD) technique in solving a variety of electromagnetic problems [1], [2], [4], [5]. Multiresolution Time Domain (MRTD) approach uses Multiresolution Analysis (MRA) to discretize Maxwell's equations in time domain. The Electric and Magnetic field components are expanded in terms of scaling as well as wavelet bases. The new discretized equations can be derived by applying the Method of Moments in space and time domain. MRTD technique has demonstrated excellent capability in solving Electromagnetics problems [1], [2], [4], [5]. This technique lends itself very naturally to multigrid schemes due to the combined use of scaling and wavelet functions in selective regions of the computational domain.

The advantage of using a combination of wavelets and lower resolution scaling bases instead of higher resolution scaling functions alone is that wavelet coefficients are significant only in the areas of strong field variation and coefficients below a certain threshold level can be dropped without adversely affecting the conditioning of the formulated mathematical problem. This leads to significant economy in memory and computation time while enhancing field resolution in selective regions where both scaling and wavelet coefficients are used.

The use of different basis functions leads to a variety of MRTD schemes, each one carrying the signature of the basis used. Recently, MRTD based on Haar and Battle-Lemarie functions have been successfully applied to microwave propagation and transmission problems [4], [5]. In all these schemes, the method of formulation of the appropriate boundary condition at discontinuities is not very obvious. This paper focuses on the methodology of applying specific boundary conditions at dielectric and metal interfaces. Also, included is a discussion of MRTD as applied at the source region.

II 3-D Haar-MRTD Scheme

For simplicity we begin with of the 3D MRTD scheme with wavelets along the z direction. Consider the following equation obtained from Maxwell's H-curl equation:

$$\epsilon \frac{\partial E_x}{\partial t} = \frac{\partial H_z}{\partial y} - \frac{\partial H_y}{\partial z} \tag{1}$$

This equation is rewritten in a differential operator form as shown below:

$$L_1(f_1(x,y,z,t)) + L_2(f_2(x,y,z,t)) = g \tag{2}$$

where L_1 and L_2 are the operators and f_1(x,y,z,t) and f_2(x,y,z,t) represent the electric/magnetic fields. We now expand the fields using the Haar based MRA with scaling functions ϕ in all three directions

and wavelet functions ψ [3] in the z direction alone. The field expansion can be represented as follows:

$$f(x,y,z,t) = [A][\phi(t)\phi(x)\phi(y)\phi(z)] + [B][\phi(t)\phi(x)\phi(y)\psi(z)] \quad (3)$$

where $[\phi(t)\phi(x)\phi(y)\phi(z)]$ and $[\phi(t)\phi(x)\phi(y)\psi(z)]$ represent matrices whose elements are the corresponding basis functions in the computation domain of interest and, [A] and [B] represent the matrices of the unknown coefficients which give information about the fields and their derivatives.

Application of Galerkin's technique leads to the following schemes:

$$< [\phi\phi\phi], L_1(f_1) + L_2(f_2) > = < [\phi\phi\phi], g >: \phi\phi\phi Scheme$$
$$< [\phi\phi\psi], L_1(f_1) + L_2(f_2) > = < [\phi\phi\psi], g >: \phi\phi\psi Scheme$$

Thus, by sampling Maxwell's differential equations with scaling and wavelet functions, we obtain a set of simultaneous discretized equations. For the first resolution level of Haar wavelets, the above schemes decouple and coupling can be achieved only through the excitation term and boundaries. In the following sections, the conditions to be applied at these locations will be discussed.

For the Haar based MRTD scheme, the parallel plate waveguide shown in Fig. 1 is used to illustrate the treatment of the aforementioned interfaces. The plates are assumed to be infinite in width for simplicity and are separated by a distance of 24mm. A single mode (TEM) operation is chosen throughout this study. For simplicity, the examples in the following sections specifically focus on MRTD scheme with only the first level of wavelet resolution. However, this techniques could easily be extended to a general scheme with multiple levels of wavelets.

In characterizing the circuits below, the Perfectly Matched Layer (PML) is used as an absorber. PML can be applied by assuming that the conductivity is given in terms of scaling and wavelet functions instead of pulse functions with respect to space [6]. The spatial distribution of the conductivity for the absorbing layers is modeled by assuming that the amplitudes of the scaling functions have a parabolic distribution. The MRTD mesh is terminated by a PEC at the end of each PML layer.

III Application of Source term in the Haar-MRTD scheme:

The considered parallel plate waveguide is excited such that it operates in the Dominant TEM mode. A signal with uniform spatial distribution along the waveguide cross section and Gaussian time distribution is chosen as the excitation. The amplitude of the scaling coefficients at the excitation plane is derived by sampling the excitation with pulse (Haar scaling) functions. The total electric field at the interface of the source and its adjacent cell must be continuous. Assuming that the field variation between these two cells is of the first order, it can be proved that the value of the first order wavelet coefficient is half that of the first derivative of the field. Thus, for a specific cell k with scaling and wavelet field amplitudes $E_k^{\phi\phi\phi}$ and $E_k^{\phi\phi\psi}$ respectively, the total field value at the position $(k - 0.5)\Delta z$ equals $E_{tot,k-0.5}^{+} = E_k^{\phi\phi\phi} + 2E_k^{\phi\phi\psi}$ and location $(k + 0.5)\Delta z$ equals $E_{tot,k+0.5}^{-} = E_k^{\phi\phi\phi} - 2E_k^{\phi\phi\psi}$. The amplitude of the wavelet coefficients at the excitation plane can be given by applying the continuity condition at the interface between the source and its adjacent cell: $E_{tot,k+0.5}^{-} = E_{tot,k+0.5}^{+}$. This leads to the following condition on the wavelet coefficients at the source location:

$$E_k^{\phi\phi\psi} = -0.5[E_{k+1}^{\phi\phi\phi} + 2E_{k+1}^{\phi\phi\psi} - E_k^{\phi\phi\phi}] \quad (4)$$

Figs 2. shows the scaling, wavelet and total electric fields, in a parallel plate waveguide which is shorted at one end with a PEC, without the use of the continuity condition, at an arbitrary time step after the incident pulse is reflected. It can be observed from the figure that the total field is not smooth; each cell interface introduces a spurious discontinuity. This implies that the coupled wavelet coefficients are not correct. Fig.3 on the other hand shows the scaling and wavelet coefficients along with the total field for the same geometry after applying the continuity equation (4). The smoothness of the total field here indicates that the wavelet coefficients have the right magnitude and phase when the source condition is applied. Without the continuity condition, the boundary conditions are satisfied only for the average field values (scaling coefficients), whereas, continuity condition ensures that the appropriate boundary conditions are satisfied on the total field which depends on the average field as well as the derivatives of the field (wavelet coefficients).

IV Treatment of PECs in the Haar-MRTD Scheme:

At the interface of a PEC, the total tangential Electric field is equal to 0. Since the location of the origin of the wavelet function coincides with the PEC, the requirement that the scaling functions have a zero value for this specific cell is a sufficient condition for the satisfaction of the boundary condition. Since the wavelet coefficients indicate the local derivatives of the field, they can have a nonzero value and can be calculated by applying continuity condition on the tangential electric field as shown in equation (4) above. For a PEC located at cell k = 0, applying equation (4) and noting that the scaling coefficient $E_0^{\phi\phi\phi}$ is zero at the PEC, we obtain the following equation for the wavelet coefficients.

$$E_0^{\phi\phi\psi} = -0.5[E_1^{\phi\phi\phi} + 2E_1^{\phi\phi\psi}] \tag{5}$$

Fig. 4 shows the reflected scaling, wavelet and total fields at an arbitrary instant of time in the aforementioned shorted parallel plate waveguide, before using equation (5) for the wavelet coefficient at the location of the PEC. Fig. 5 shows the same fields in the case where Equation (5) is used. The smoothness of the total electric field obtained here in contrast to the non-smooth field seen in Fig. 3 validates the necessity of applying the continuity condition at the PEC location.

V Treatment of Dielectric Interfaces in the Haar-MRTD Scheme:

At the interface of two dielectrics, the scaling and wavelet coefficients couple, even for the first order of wavelet resolution. Consider a dielectric interface at location k (assume the dielectric interface to be perpendicular to the direction of propagation) for the parallel plate waveguide considered above. Let the dielectric constant of the material to the left of the interface be ϵ_{r1} and that of the material to the right be ϵ_{r2}. By expanding the electric flux density (D) and electric field (E) in terms of the scaling and wavelet functions and applying the method of moments to the constitutive relationships, it can be shown that for the first resolution level of wavelets at the interface location k, their coefficients are related by the following coupled equations:

$$D_k^{\phi\phi\phi} = 0.5\epsilon_0[(\epsilon_{r1} + \epsilon_{r2})E_k^{\phi\phi\phi} + (\epsilon_{r1} - \epsilon_{r2})E_k^{\phi\phi\psi}] \tag{6}$$

$$D_k^{\phi\phi\psi} = 0.5\epsilon_0[(\epsilon_{r1} + \epsilon_{r2})E_k^{\phi\phi\psi} + (\epsilon_{r1} - \epsilon_{r2})E_k^{\phi\phi\phi}] \tag{7}$$

In addition to the coupled equations above, the continuity of the total tangential electric field at nodes adjacent to the interface needs to be ensured. Following the same procedure that leads to

equation (4), we obtain the following equations one cell to the left and right of the interface k.

$$E^{\phi\phi\psi}_{k-1} = +0.5[E^{\phi\phi\phi}_{k-2} - 2E^{\phi\phi\psi}_{k-2} - E^{\phi\phi\phi}_{k-1}] \quad (8)$$

$$E^{\phi\phi\psi}_{k+1} = -0.5[E^{\phi\phi\phi}_{k+2} + 2E^{\phi\phi\psi}_{k+2} - E^{\phi\phi\phi}_{k+1}] \quad (9)$$

Figs. 6 and 7 show plots of the scaling, wavelet and total flux density with and without the use of the above continuity equations respectively for the waveguide described above whose first half is filled with air and second half with a material of $\epsilon_r = 10$. As mentioned earlier, the plane of discontinuity in this case is perpendicular to the direction of propagation. The smoothness of the total field in Fig. 6 in comparison to its roughness in Fig. 5 validates the continuity conditions in equations 8 and 9.

VI Comparison with MRTD Schemes based on Entire-Domain Basis:

When entire-domain functions are used as scaling and wavelet basis for the development of Multiresolution schemes [2] [5], hard boundaries (e.g.PEC's) and excitation can be modeled in a similar way. E- and H- field components are expanded in terms of scaling and wavelet functions and the discretized equations are derived by using the method of moments. To obtain a desired excitation waveform at a certain position , a finite number of field coefficients surrounding the source point have to be updated. The stencil size varies from 8-12 for phase error less than 1° per wavelength. The desired spatial distribution of the excitation is sampled with scaling and wavelet functions in space-domain to derive the appropriate coefficients for the neighboring points. Usually, the source is applied in the vicinity of one or more metallic planes. Unlike the FDTD where the consistency with the image theory is implicit in the application of the boundary conditions, for MRTD schemes based on entire-domain functions, this theory must be applied explicitly in the locations of Perfect Electric (PEC) or Magnetic Conductors (PMC). The total value of a field component at a specific cell is affected by a finite number of neighboring cells due to the entire-domain nature of the basis functions. Inserting the field expansions, the PEC boundary conditions of zeroing out the tangential-to-PEC E-field and the vertical-to-PEC H-field can be discretized by applying the method of moments. Due to the orthonormal nature of the expansion basis, it can be proved that the contribution of each neighbor at the location of the PEC has to be zero,a condition that can be satisfied with the explicit application of the Image theory. For example, even symmetry is applied for the normal-to-PEC electric field components and odd symmetry for the parallel-to-PEC. The Image Theory can be implemented automatically for an arbitrary number of hard boundaries.

Dielectric discontinuities are modeled by discretizing the constitutive relationships using the scaling and wavelet functions and solving a linear matrix equation [7]. Again, the stencil of the considered neighboring coefficients depends on the desired dispersion characteristics and usually range from 8-14 for dielectrics with ϵ smaller than 20. The conventional PML numerical absorber [8] can be extended assuming a spatial electric and magnetic conductivity distribution in terms of scaling and wavelet functions [6]. Generally, for MRTD Schemes based on entire-domain basis functions, the effect of discontinuities is not numerically localized, but is seen on a number of neighboring coefficients. Nevertheless, the procedure to apply the Boundary Conditions is the same for all MRTD schemes, though the details of implementation may be different.

VII Conclusion

The treatment of excitation condition, PEC boundaries and dielectric interfaces for the Haar as well as Entire Domain based MRTD schemes has been presented. These conditions have been validated by applying them to obtain the fields in a Parallel Plate waveguide. It has been shown that using the appropriate boundary conditions derived here is essential for obtaining smooth reconstructed fields.

VIII Acknowledgments

The authors are greatful to ONR (N00014-95-1-0546) and ARO (DAAH04-95-1-0321) for their support.

References

[1] M .Krumpholz, L. P. B. Katehi, "New Prospects for Time Domain Analysis", IEEE Microwave and Guided Wave Letters, pp. 382-384, November 1995.

[2] M. Krumpholz, L. P. B. Katehi, "MRTD: New Time Domain Schemes Based on Multiresolution Analysis", IEEE Transactions on Microwave Theory and Techniques, pp. 385-391, April 1996.

[3] K. Goverdhanam, E. Tentzeris, M. Krumpholz and L.P.B. Katehi, "An FDTD Multigrid based on Multiresolution Analysis", Proc. AP-S 1996, pp. 352-355.

[4] K. Goverdhanam, A. Cangellaris and L. P. B. Katehi, "Applications of Multiresolution Based FDTD Multigrid", Proc. MTT-S 1997, pp. 333-336.

[5] E.Tentzeris, M.Krumpholz and L.P.B. Katehi, "Application of MRTD to Printed Transmission Lines", Proc. MTT-S 1996, pp. 573-576.

[6] E.Tentzeris, R.Robertson, M.Krumpholz and L.P.B. Katehi, "Application of the PML Absorber to the MRTD Technique", Proc. AP-S 1996, pp. 634-637.

[7] R. Robertson, E. Tentzeris, M. Krumpholz, L.P.B. Katehi, "MRTD Analysis to Dielectric Cavity Structures", Proc. MTT-S 1996, pp. 1861-1864.

[8] J.-P. Berenger, "A Perfectly Matched Layer for the Absorption of Electromagnetic Waves", J. Computational Physics, vol. 114, pp. 185-200, 1994.

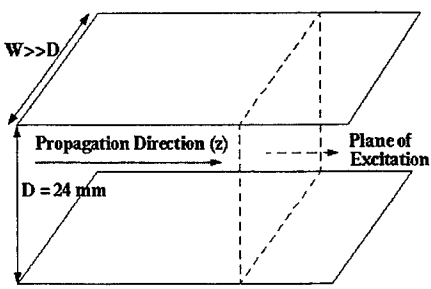

Figure 1: Parallel Plate Waveguide

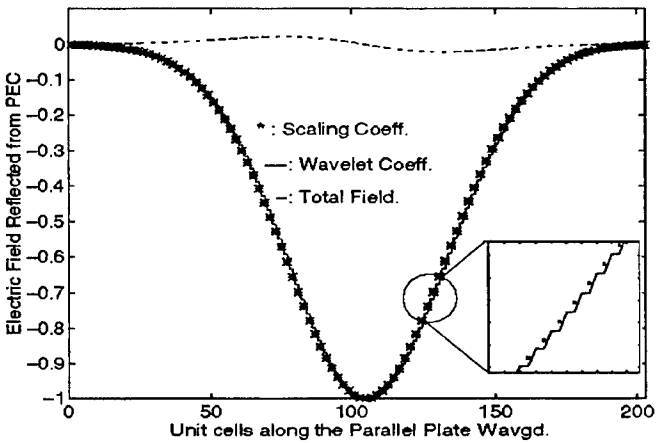

Figure 2: E field WITHOUT wavelet excitation condition in a Plate Waveguide.

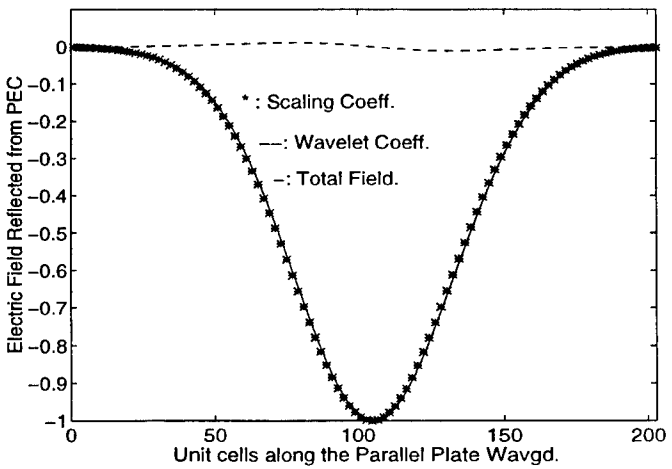

Figure 3: E field WITH wavelet excitation condition in a Plate Waveguide.

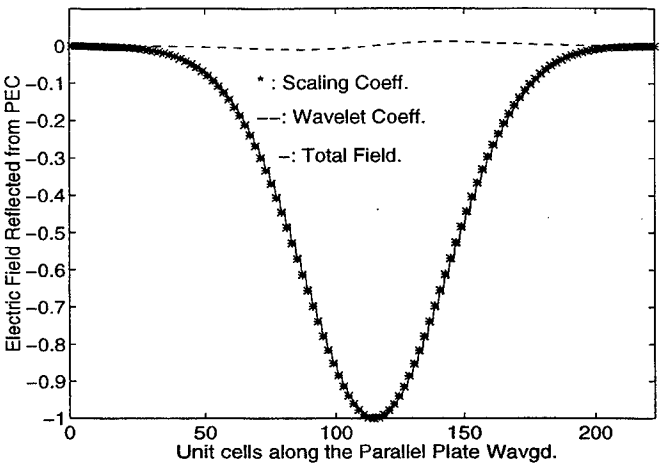

Figure 4: E field WITHOUT continuity condition at PEC in a Parallel Plate Waveguide shorted at one end.

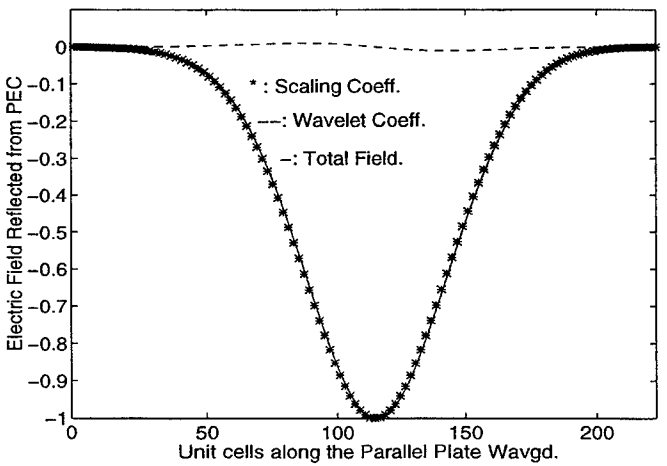

Figure 5: E field WITH continuity condition at PEC in a Parallel Plate Waveguide shorted at one end.

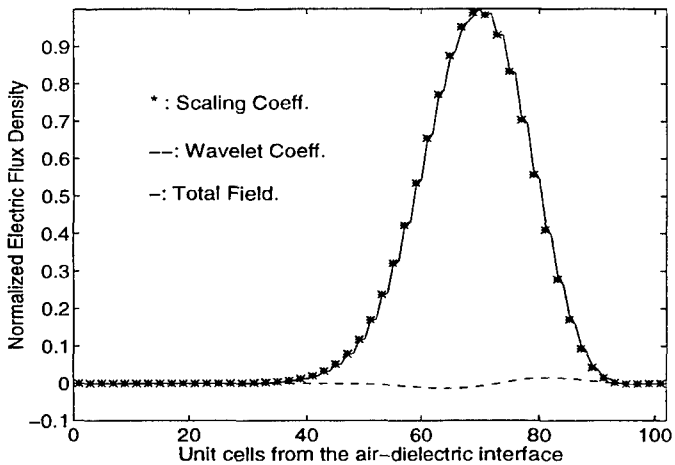

Figure 6: Flux density (D) WITHOUT wavelet continuity conditions in a Parallel Plate Waveguide half filled with dielectric of $\epsilon_r = 10$.

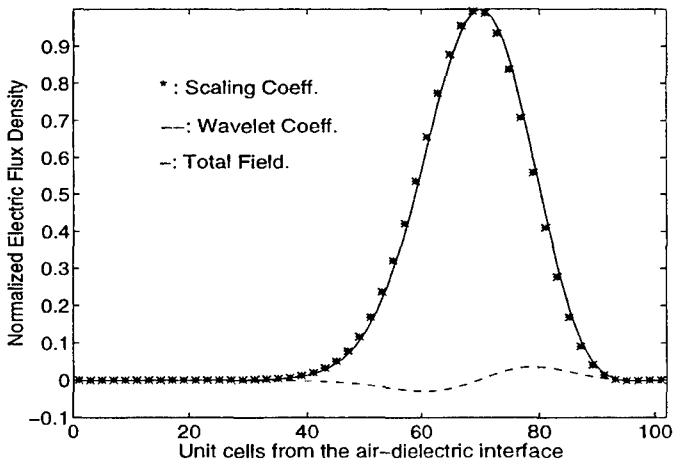

Figure 7: Flux density (D) WITH wavelet continuity conditions in a Parallel Plate Waveguide half filled with dielectric of $\epsilon_r = 10$.

SESSION 3:

APPLICATION OF ANALYTIC AND COMPUTATIONAL METHODS TO THE MODELING OF ELECTROMAGNETIC MATERIALS

Chairs: R. Diaz and D.H.Y. Yang

Computing Dispersion Relations and Radiation Spectra in Photonic Band Gap Materials by Plane Wave Expansion Method

Toshio Suzuki and Paul K. L. Yu
Department of Electrical and Computer Engineering
University of California, San Diego
La Jolla, California 92093-0407

Abstract -We present a theoretical formalism to compute electromagnetic dispersion relations and radiation spectra in periodic structures, incorporating a matrix form of Maxwell's equations based on plane wave expansion, the dyadic Green's function, eigenfunction expansion, Poynting theorem and tetrahedron integration method.

1. Introduction

Wave propagation in periodic structures exhibit numbers of interesting physical phenomena such as radiation alteration. Inside periodic structures, waves unusually interact with radiators in both frequency and spatial domains, and the process is governed by the local behaviors of the electromagnetic modes coupling to the source radiator at the precise radiating frequency in the exact location of the radiator. This type of irregular radiation (compared to the counterparts in free space or uniform media), especially, enhancement and suppression of electromagnetic radiation in artificial periodic structures which come to be called "photonic crystals" or sometimes "photonic band gap materials (PBG) materials", is scientifically quite stimulating, and probably most useful for a large number of diverse engineering purposes.[1~4] It has been suggested[1~4,5,8,12] that electromagnetic radiation can be inhibited completely if radiation frequencies fall inside photonic band gaps, --frequency stop bands generated in three- (or two-) dimensional photonic crystals. In photonic crystals, electromagnetic waves exhibit non-free-space dispersion relations, namely, "photonic band structures", and under special circumstances, photonic band structures exhibit frequency regions (i.e. "photonic band gaps") in which propagating electromagnetic waves are entirely forbidden in every direction.[1~4]

There have been numbers of computational methods proposed in this area. They are generally categorized into two major groups, namely, Fourier type methods (e.g. plane wave expansion methods[1~4,6,7,8~13]) and real space methods (e.g. finite element/difference methods[1~4,14~16]). In general, both methods are applicable to any materials, dimensions, geometry, and crystallographic structures. Compared with real space counterparts, to our knowledge, plane wave expansion methods are known to have following advantages/disadvantages. (Advantage): (1) Easy implementation, (2) Suitable to interpret physical meanings behind the numerical data, (3) Dense information in resulting eigensolutions. (Disadvantage): (1) Slower convergence of eigenvalues[6,7], (2) Dense matrices. The plane wave method initially developed for dielectric photonic crystals[1~4,6,7] has been extended to more general materials such as absorptive or active[10], finitely conducting[10,11] media, and perfectly conducting lattices[13]. The method can also compute tunneling dispersion relations[9], and reflection and transmission coefficients through finite structures by introducing boundary functions to infinite crystals[17]. Localized waves in defect crystals have been extensively investigated with supercell approximation based on plane wave expansion.[1~4,7,18]

2. Theory

Our method for calculating radiation spectra in photonic crystals is divided in three major steps: (1) We numerically solve the matrix representation of Maxwell's equations to obtain eigenfunctions. (2)

The dyadic Green's function is constructed with the computed eigenfunctions. (3) The resulting radiation power which involves a k-space integral is numerically approximated by the tetrahedron integration method.

2.1 Matrix Maxwell's Equations (Source Free)

We expand media's periodicity and electromagnetic fields in the Fourier domain, in sums of plane waves such as Fourier and Bloch-Flouque series respectively, for instance,

$$f(\mathbf{r}) = \sum_{\mathbf{K}} F(\mathbf{K}) \exp[i\,\mathbf{K}\cdot\mathbf{r}]. \tag{1}$$

$$\mathbf{A}(\mathbf{r}) = \sum_{\mathbf{K}} \mathbf{A}(\mathbf{K}) \exp[i\,(-\mathbf{k}+\mathbf{K})\cdot\mathbf{r}], \tag{2}$$

where **K**s are the NP reciprocal lattice vectors of the periodic structures, scalar function $f(\mathbf{r})$ denotes periodic dielectric constant $\varepsilon(\mathbf{r})$, or conductivity $\sigma(\mathbf{r})$ and vector function $\mathbf{A}(\mathbf{r})$ indicates $\mathbf{E}(\mathbf{r})$ or $\mathbf{H}(\mathbf{r})$ for the E-field and H-field respectively. In periodic structures, Maxwell's equations can be easily transformed into a set of simple matrix equations by plane wave expansion. If conductivity of the media $\sigma(\mathbf{r})$ is finite, Maxwell's equations can be expressed as

Maxwell's Equations		Matrix Maxwell's Equations	
$\nabla\times\mathbf{E}(\mathbf{r}) = i\,\omega\mu_0\mathbf{H}(\mathbf{r}),$	(3)	$\mathbf{TE} = -\,\mu_0\omega\mathbf{H},$	(7)
$\nabla\times\mathbf{H}(\mathbf{r}) = -i\,\omega\varepsilon_0\mathbf{E}(\mathbf{r}) + \sigma(\mathbf{r})\mathbf{E}(\mathbf{r}),$	(4)	$\mathbf{TH} = \varepsilon_0\omega\mathbf{U}_\varepsilon\mathbf{E} - i\mathbf{U}_\sigma\mathbf{E},$	(8)
$\nabla\cdot[\varepsilon(\mathbf{r})\mathbf{E}(\mathbf{r})] = \mathbf{0},$	(5)	$\mathbf{KU}_\varepsilon\mathbf{E} = \mathbf{0},$	(9)
$\nabla\cdot\mathbf{H}(\mathbf{r}) = \mathbf{0},$	(6)	$\mathbf{KH} = \mathbf{0},$	(10)

where ε_0 and μ_0 are the permittivity and permeability of vacuum, **E** and **H** are 3NP by 1 vectors including Fourier expansion coefficients of the E-field and H-field respectively, **T** is 3NP by 3NP matrix operator for rotation operator $\nabla\times$, **K** is a NP by 3NP matrix operator for divergence operator $\nabla\cdot$, $\mathbf{U}_\varepsilon$ and $\mathbf{U}_\sigma$ are 3NP by 3NP Fourier expansion matrices for the dielectric and conductivity function respectively (See reference (8)~(13) for more details). If the media contain perfectly conducting elements, conductivity σ in the conductors become infinity. In the limit of $\sigma\to\infty$, equations (4), (5), (8), and (9) can be further transformed by introducing the configuration potential,

$$V(\mathbf{r}) \equiv \begin{cases} 1 & \text{inside periodic conductors} \\ 1 & \text{on the surfaces} \\ 0 & \text{otherwise} \end{cases} \tag{11}$$

For photonic crystals containing perfectly conducting lattices (metal or metallodielectric photonic crystals), Maxwell's equations (4) and (5) and periodic boundary conditions on the surfaces of the perfect conductors can be rewritten as

Maxwell's Equations		Matrix Maxwell's Equations	
$\nabla\times\mathbf{H}(\mathbf{r}) = -i\,\omega\varepsilon_0\varepsilon(\mathbf{r})\mathbf{E}(\mathbf{r}) + \mathbf{J}_s(\mathbf{r}),$	(12)	$\mathbf{TH} = \varepsilon_0\omega\mathbf{U}_\varepsilon\mathbf{E} - i\mathbf{J},$	(14)
$\nabla\cdot[\varepsilon(\mathbf{r})\mathbf{E}(\mathbf{r})] = q_s(\mathbf{r}),$	(13)	$\mathbf{K}\mathbf{U}_\varepsilon\mathbf{E} = \mathbf{Q},$	(15)
Boundary Conditions		**Matrix Boundary Conditions**	
$[\nabla V(\mathbf{r})]\times\mathbf{E}(\mathbf{r}) = \mathbf{0},$	(16)	$[\mathbf{TU} - \mathbf{UT}]\mathbf{E} = \mathbf{0},$	(20)
$[\nabla V(\mathbf{r})]\times\mathbf{H}(\mathbf{r}) = -\mathbf{J}_s(\mathbf{r}),$	(17)	$[\mathbf{TU} - \mathbf{UT}]\mathbf{H} = i\mathbf{J},$	(21)
$[\nabla V(\mathbf{r})]\cdot[\varepsilon(\mathbf{r})\mathbf{E}(\mathbf{r})] = -q_s(\mathbf{r}),$	(18)	$\mathbf{U}'\mathbf{U}_\varepsilon\mathbf{E} = \mathbf{Q},$	(22)
$[\nabla V(\mathbf{r})]\cdot\mathbf{H}(\mathbf{r}) = 0,$	(19)	$\mathbf{U}'\mathbf{H} = \mathbf{0},$	(23)

where $\mathbf{J}$ is a 3NP by 1 vectors including Fourier expansion coefficients of surface current density on the conductors, $\mathbf{Q}$ is a NP by 1 vector containing Fourier coefficients for the surface charge, $\mathbf{U}$ is a Fourier coefficient matrix for configuration potential, and $[\mathbf{TU}-\mathbf{UT}]$ and $\mathbf{U}'$ are 3NP by 3NP and NP by NP commutative matrix relations with respect to differential operators $\nabla\times$ and $\nabla\cdot$ respectively. From equations (7) and (8), we obtain a quadratic and cubic eigensystem as

$$\mathbf{T}^2\mathbf{E} + i\eta\frac{\omega}{c}\mathbf{U}_\sigma\mathbf{E} + \frac{\omega^2}{c^2}\mathbf{U}_\varepsilon\mathbf{E} = \mathbf{0}, \tag{24}$$

$$\mathbf{T}[\mathbf{I} - \frac{i}{\varepsilon_0\omega}\mathbf{U}_\sigma]^{-1}\mathbf{U}_\varepsilon^{-1}\mathbf{TH} + \frac{\omega^2}{c^2}\mathbf{H} = \mathbf{0}, \tag{25}$$

where $\eta = \sqrt{\mu_0/\varepsilon_0}$, quadratic eigensystem (24) and cubic eigensystem (225) can be numerically solved by linearlization scheme[10,11,13]. From (7), (14), (20) and (21), the matrix wave equations can be expressed as

$$\mathbf{T}^2\mathbf{E} + [\mathbf{TU} - \mathbf{UT}]\mathbf{TE} + \frac{\omega^2}{c^2}\mathbf{U}_\varepsilon\mathbf{E} = \mathbf{0}, \tag{26}$$

$$\mathbf{TU}_\varepsilon^{-1}\mathbf{TH} + \mathbf{TU}_\varepsilon^{-1}[\mathbf{TU} - \mathbf{UT}]\mathbf{H} + \frac{\omega^2}{c^2}\mathbf{H} = \mathbf{0}. \tag{27}$$

By applying projection operator $\mathbf{W}_2$ constructed from eigenvectors of matrix $\mathbf{U}$, eigensystem (26) and (27) can be further transformed into real symmetric or Hermitian matrices,

$$\mathbf{W}_2^a\mathbf{T}^2\mathbf{W}_2\mathbf{C}_E + \frac{\omega^2}{c^2}\mathbf{W}_2^a\mathbf{U}_\varepsilon\mathbf{W}_2\mathbf{C}_E = \mathbf{0}, \tag{28}$$

$$\mathbf{T}[\mathbf{W}_2\mathbf{W}_2^a\mathbf{U}_\varepsilon^{-1}]\mathbf{TH} + \frac{\omega^2}{c^2}\mathbf{H} = \mathbf{0}, \tag{29}$$

where $\mathbf{E} = \mathbf{W}_1\mathbf{C}_E$, $\mathbf{W}_1^a$ is the adjoint of projection operator $\mathbf{W}_1$ and $\mathbf{U} = \mathbf{W}_2\mathbf{W}_2^a = \mathbf{I} - \mathbf{W}_1\mathbf{W}_1^a$. Note matrix $[\mathbf{W}_1, \mathbf{W}_2]$ forms a unitary matrix. If the media is not conductive ($\sigma \rightarrow 0$), eigensystem (24) and (25) can be further reduced to well known eigensystems[1~4,6,7],

$$\mathbf{T}^2\mathbf{E} + \frac{\omega^2}{c^2}\mathbf{U}_\varepsilon\mathbf{E} = \mathbf{0}, \tag{30}$$

$$\mathbf{T}\mathbf{U}_\varepsilon^{-1}\mathbf{T}\mathbf{H} + \frac{\omega^2}{c^2}\mathbf{H} = \mathbf{0}. \tag{31}$$

We numerically solve a three-dimensional vector wave equation expressed in a matrix eigensystem by a eigensystem package (e.g. LAPACK)[19], since both dispersion relations and solutions for Maxwell's equations were prerequisites for radiation computations. The formulated matrix equations and eigensystems are structurally simple and symmetric in the Cartesian coordinate system, which is convenient in dealing with the dyadic Green's functions (where dyadics are usually expressed in the Cartesian coordinates).

2.2 Dyadic Green's function

The dyadic Green's function satisfying, for instance,

$$\nabla\times\nabla\times\overline{\mathbf{G}}(\mathbf{r},t;\mathbf{r}',t') + \frac{1}{c^2}\varepsilon(\mathbf{r})\frac{\partial^2}{\partial t^2}\overline{\mathbf{G}}(\mathbf{r},t;\mathbf{r}',t') = \overline{\mathbf{I}}\delta(\mathbf{r}-\mathbf{r}')\delta(t-t'), \tag{32}$$

can be constructed with the eigenfunctions (i.e. eigenvalues and eigenvectors) computed by eigensystem (30) or (31) in **2.1**. The dyadic Green's function is given as

$$\overline{\mathbf{G}}(\mathbf{r},t;\mathbf{r}',t') = \frac{c^2\eta^{-2}}{(2\pi)^3}\frac{1}{(NP)}\sum_{n=1}^{3NP}\int d^3k\,\widehat{\mathbf{E}_0^n}(\mathbf{r},\mathbf{k})\widehat{\mathbf{E}_0^{n*}}(\mathbf{r}',-\mathbf{k})\,\theta(t-t')\,\frac{\sin[\omega_n(t-t')]}{\omega_n}, \tag{33}$$

where the nth eigenfunction $\widehat{\mathbf{E}_0^n}(\mathbf{r},\mathbf{k})$ satisfies homogeneous wave equation,

$$\nabla\times\nabla\times\widehat{\mathbf{E}_0^n}(\mathbf{r},\mathbf{k}) - \frac{\omega_n^2}{c^2}\varepsilon(\mathbf{r})\widehat{\mathbf{E}_0^n}(\mathbf{r},\mathbf{k}) = \mathbf{0}. \tag{34}$$

The inhomogeneous Maxwell's equation with a source term,

$$\nabla\times\nabla\times\mathbf{E}(\mathbf{r},t) + \frac{1}{c^2}\varepsilon(\mathbf{r})\frac{\partial^2}{\partial t^2}\mathbf{E}(\mathbf{r},t) = -\mu_0\frac{\partial}{\partial t}\mathbf{J}(\mathbf{r},t), \tag{35}$$

was then solved by the dyadic Green's function[8,12]. Assuming a Hertzian dipole located in the photonic crystal (as in Fig. 1), namely,

$$\mathbf{J}(\mathbf{r},t) = \mathbf{J}(\mathbf{r})J(t) = I_0\Omega\mathbf{d}\,\delta(\mathbf{r}-\mathbf{r}_0)\,\theta(t)\,e^{-i\Omega t} \tag{36}$$

where $\mathbf{d}$ is the dipole moment and $\theta(t)$ is the unit step function, we obtain the radiated field expressed as

$$\mathbf{E}(\mathbf{r},t) = \frac{-i\mu_0 c^2 \theta(t)}{2(2\pi)^2 \eta^2} \frac{1}{NP} \sum_{n=0}^{3NP} \int dk^3 \, \widehat{\mathbf{E}_0^n}(\mathbf{r}_0,\mathbf{k}) \, \widehat{\mathbf{E}_0^{n*}}(\mathbf{r},-\mathbf{k}) \left[\frac{e^{i\omega_n t} - e^{-i\Omega t}}{(\Omega+\omega_n)} + \frac{e^{-i\omega_n t} - e^{-i\Omega t}}{(\Omega-\omega_n)} \right]. \qquad (37)$$

In the steady state (the limit of $t \to \infty$), radiation power from the dipole is calculated by the Poynting theorem with equation (37),

$$P_{lattice} = \frac{I_0 \Omega \mu_0 c^2 \eta^{-2} \pi}{2(2\pi)^3} \frac{1}{(NP)} \sum_{n=1}^{3NP} \int d^3k \left| \mathbf{d} \cdot \widehat{\mathbf{E}_0^n}(\mathbf{r}_0,\mathbf{k}) \right|^2 [\delta[\Omega+\omega_n(\mathbf{k})]+\delta[\Omega-\omega_n(\mathbf{k})]]. \qquad (38)$$

2.3 K-space integration

Radiation power (38) derived in **2.2** still contains a difficulty -- a k-space integral which cannot be solved in closed form because the dispersion relation and eigenfunctions usually cannot be found analytically but numerically as in **2.1**. However, we can reduce this volume integral down to the surface integral of the well-known Fermi surface integral type which can be approximated numerically by the tetrahedron method.[20] Volume integral (38) can be transformed into the surface integral as,

$$P_{Lattice} = \frac{I_0 \Omega \mu_0 c^2 \eta^{-2} \pi}{2(2\pi)^3} \sum_{n=1}^{2NP} \int_{\substack{\Omega=\omega_n(\mathbf{k}) \\ 1st\ BZ}} \frac{dS}{|\nabla \omega_n(\mathbf{k})|} \left| \mathbf{d} \cdot \widehat{\mathbf{E}_0^n}(\mathbf{r}_0,\mathbf{k}) \right|^2, \qquad (39)$$

In the tetrahedron method, the irreducible Brillouin zones in the k-space are divided into numbers of tetrahedra in which energy surfaces are linearly interpolated. In these tetrahedra, the surface integral is evaluated with the linearly approximated integrand[8,20]. (For two-dimensional cases, triangles can be used instead of tetrahedra.[12])

3. Results and Conclusion

In Fig. 2 (a), we present an example band structure[6] for the FCC lattice structure obtained from eigensystem (31) (NP=125). A photonic band gap appears between the neighborhood of the eighth and ninth mode. See references (1) ~ (4) for various types of photonic band structures. In Fig 2 (b), (c) and (d), the corresponding density of states (DOS), the computed radiation power and normalized radiation power (normalized by free space radiation) are shown respectively. The position of the dipole is (0.25,0.25,0.0) and the direction is (0, 0, 1) as depicted in Fig. 1. The results show that the total inhibition of the emission in the photonic band gap as well strong enhancement near the band edges. The dipole position was also shifted in the (1,1,1), (1,1,0) directions in a unit cell with the dipole moment fixed to the (0,0,1) direction as shown in Fig 3 (a), Fig. 4 (a) respectively .Our computation (plotted in Fig. 3 (b) and 4 (b) for (1,1,1) and (1,1,0) directions respectively) indicates that the strong position dependence of the radiation spectrum on the dipole position in the photonic crystal. In the talk, we will also present results in photonic crystals with perfectly conducting elements computed by method of projection operators.

Acknowledgments

This research is partially supported by National Science Foundation. The authors acknowledge the allocation of CRAY time from San Diego Supercomputer Center.

References

(1). (Edited by) C. M. Bowden, J. P. Dowling, and H. O. Everitt, Development and Applications of Materials Exhibiting Photonic Band gaps, J. Opt. Soc. Am. B **10**, Special Issue (1993).

(2). (Edited by) G. Kurizki, and J. W. Haus, Photonic Band Structures, J. Mod. Optics **41**, Special Issue (1994).

(3). (Edited by) C. M. Soukoulis, *Photonic Band Gaps and Localization* , NATO ASL series, Series B: Physics, Vol. 308 (1993), *Photonic Band Gap Materials*, NATO ASL series, Series E: Applied Science; Vol. 315 (1996).

(4). J. D. Joannopoulos, R. D. Meade, and J. N. Winn, *Photonic Crystals, Molding Flow of the Light* (Princeton University Press, 1995).

(5). E. Yablonovitch, "Inhibited Spontaneous Emission in Solid State Physics and Electronics." Phys. Rev. Lett **58**, 2059 (1987).

(6). H. S. Sozuer, J. W. Haus, and R. Inguva, "Photonic bands: Convergence problems with the plane wave method." Phys. Rev. B **45**, 13962 (1992).

(7). R. D. Meade, A. M. Rappe, K. D. Brommer and J. D. Joannopoulos, "Accurate theoretical analysis of photonic band-gap materials." Phys. Rev. B **48**, 8434 (1992).

(8). T. Suzuki and P. K. L. Yu, "Emission power of an electric dipole in the photonic band structure of the FCC lattice." J. Opt. Soc. Am. B. **12**, 570 (1995).

(9). T. Suzuki and P. K. L. Yu, "Tunneling in photonic band structures." J. Opt. Soc. Am. B. **12**, 804 (1995).

(10). T. Suzuki and P. K. L. Yu, "Dispersion relation at L point in the photonic band structure of the FCC lattice with active or conductive dielectric media." J. Opt. Soc. Am. B. **12**, 583 (1995).

(11). T. Suzuki and P. K. L. Yu, "Complex photonic band structures of a conductive metal lattice by a quadratic eigensystem." Opt. Lett **20**, 2520 (1995).

(12). T. Suzuki and P. K. L. Yu, "Experimental and theoretical study of dipole emission in the two-dimensional photonic band structure of the square lattice with dielectric cylinders." J. Appl. Phy. **79** , 582 (1996).

(13). T. Suzuki and P. K. L. Yu, "Method of Projection Operators for Photonic Band Structures with Perfectly Conducting Elements." To appear in Phys. Rev. B.

(14). J. B. Pendry, "Calculating photonic band structure.", J. Phys. Condens. Matter **8**, 1086 (1996). "Photonic band structures.", J. Mod. Optics **41**, 209 (1994). "A program for calculating photonic band structures and transmission coefficients of complex structures.", Comp. Phys. Comm. **85**, 306 (1995).

(15). S. Fan, P. R. Villeneuve and J. D. Joannopoulos, "Large omindirectional bandgaps in metallodielectric photonic crystals.", Phys. Rev. B **54**, 11245 (1996).

(16). H. Y. D. Yang, "Finite Difference Analysis of 2-D Photonic Crystals.", IEEE Trans. Microwave Theory Tech. **44**, 2688 (1996).

(17). K. Sakoda, "Transmittance and Bragg Reflectivity of Two-Dimensional Photonic Lattices." Phys. Rev. B **52** 8992 (1995). "Optical Transmittance of a Two Dimensional Triangular Photonic Lattices." Phys. Rev. B **51** 4672 (1995).

(18). K. Sakoda and H. Shiroma, "Numerical method for localized defect modes in photonic lattices." Phys. Rev. B **52** 4830 (1997).

(19). E. Anderson, et al., *LAPACK User's Guide, Second Edition.* (SIAM 1995).

(20). Hans. L. Skriver, *The LMTO method* (Springer-Verlag 1984).

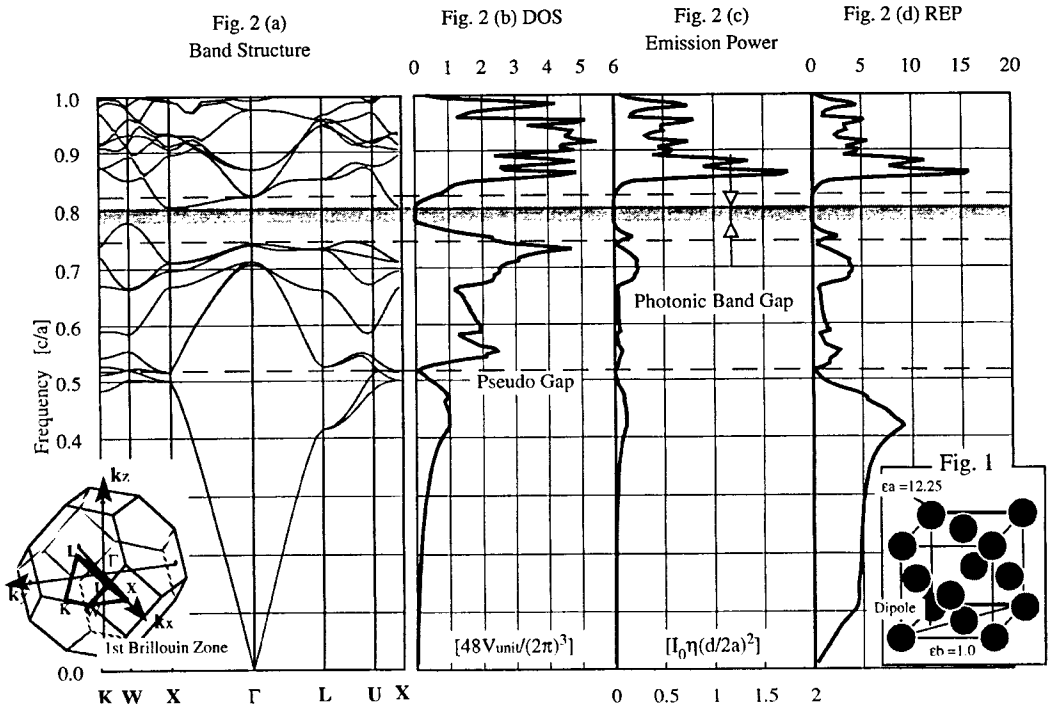
Fig. 2 (a)
Band Structure
Fig. 2 (b) DOS
Fig. 2 (c)
Emission Power
Fig. 2 (d) REP
0 1 2 3 4 5 6
0 5 10 15 20
1.0
0.9
0.8
0.7
0.6
0.5
0.4
0.0
Frequency [c/a]
Photonic Band Gap
Pseudo Gap
kz
ky
kx
Γ
L
U
X
K
W
1st Brillouin Zone
K W X Γ L U X
[48Vunit/(2π)3]
[I0η(d/2a)2]
0 0.5 1 1.5 2
Fig. 1
εa =12.25
Dipole
εb =1.0

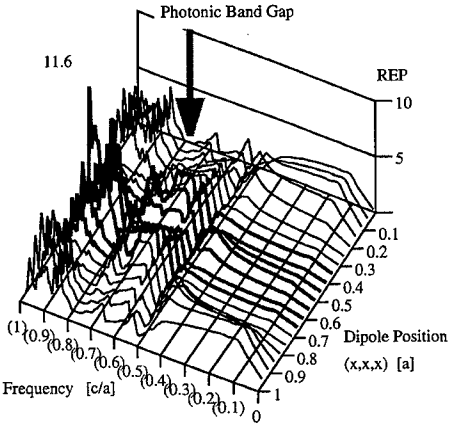

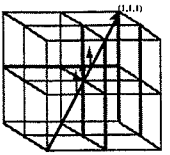

Fig. 3 (a)

Fig. 3 (b) Normalized padiation Power in (1,1,1) direction.

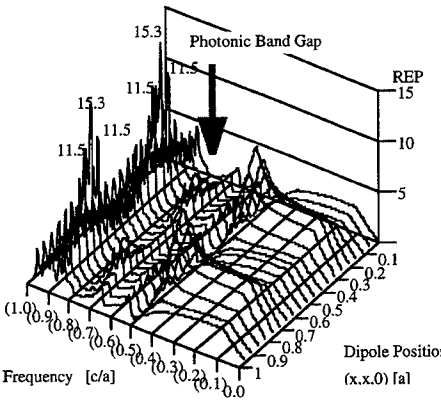

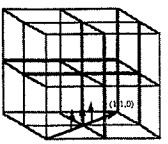

Fig. 4 (a)

Fig. 4 (b) Normalized radiation power in the (1,1,0) direction.

WAVEGUIDES IN PHOTONIC BAND GAP MATERIALS

M. M. Sigalas[1], R. Biswas[1], K. M. Ho[1], C. M. Soukoulis[1], and D. D. Crouch[2]

[1]Ames Laboratory and Department of Physics and Astronomy, Iowa State University, Ames IA 50011

[2]Advanced Electromagnetic Technologies Center, Hughes Electronics Corporation, Rancho Cucamonga, CA 91729

1. INTRODUCTION

Photonic crystals are a novel class of artificially fabricated structures which have the ability to control and manipulate the propagation of electromagnetic waves. Properly designed photonic crystals can prohibit the propagation of light, or allow it only in certain frequency regions, or localize light in specified areas. They can be constructed in one, two, and three dimensions (1D, 2D, and 3D) with either dielectric and/or metallic materials. [1,2] The interest in photonic band gap (PBG) materials arises from their possible applications in several scientific and technical areas such as filters, optical switches, cavities, waveguides, design of more efficient lasers, etc. [1-2]

Recently, Mekis, et. al., showed that highly efficient transmission of light can be achieved around sharp corners in photonic band gap waveguides. [3] They used a 2D photonic crystal consisting of dielectric cylinders. Their numerical calculations revealed complete transmission at certain frequencies, and very high transmission over wide frequency ranges. One limitation of their approach is that it is two dimensional, so, one expects a leakage of the waves even for small components of the k-vectors parallel to the axis of the cylinders and for polarizations with E-fields perpendicular to the axis of the cylinders.

Here, we study waveguides with 3D photonic band gap materials. We are using a photonic crystal which has been suggested and used extensively by our group. This layer by layer structure is shown in Fig. 1. [4] The structure is assembled by stacking layers consisting of parallel rods with a center-to-center separation of a. The rods are rotated by 90° in each successive layer. Starting at any reference layer, the rods of every second neighboring layer are parallel to the reference layer, but shifted by a distance 0.5a perpendicular to the rod axes. This results in a stacking sequence that repeats every four layers. This lattice has face-centered-tetragonal (fct) lattice symmetry with a basis of two rods. This structure has a robust photonic band gap when both the filling ratio and the dielectric contrast meet certain requirements. The photonic band gap is not sensitive to the cross-sectional shape of the rods. Several different structures have been constructed with midgap frequencies at 13 GHz, 100 GHz, and 450 GHz using etching techniques and Al_2O_3 or Si as materials.[5-10] Recently, the same structure has been fabricated with a measured PBG at around 2 THz using laser-induced direct-write deposition from the gas phase. [11]

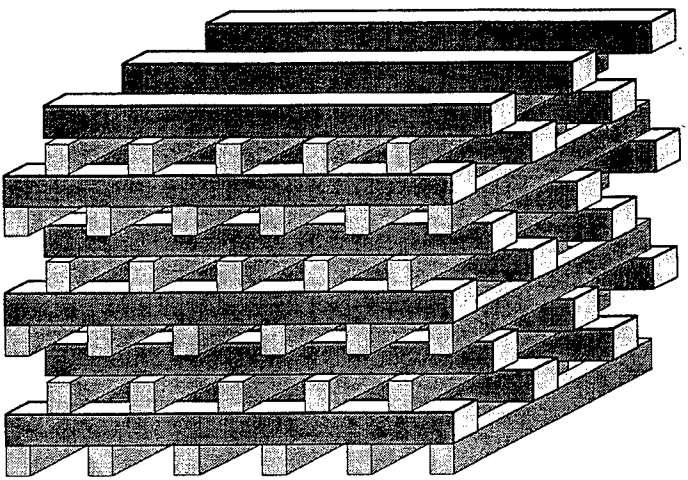

Figure 1: Layer-by-layer structure constructed by orderly stacking of dielectric rods. The periodicity is 4 layers in the stacking direction. Layers in the second neighbor layer are parallel to those in the original layer but are shifted by a/2 in the plane.

2. NUMERICAL METHOD

We are using the finite difference time domain (FDTD) method in order to calculate the propagation of EM waves inside the waveguide. The photonic crystal consists of circular cylinders with 0.32 cm diameter and a center-to-center separation a=1.12 cm. There are 14 rods along the x and y directions and the total thickness of the system along the z direction is 7 unit cells (8.9 cm). The dielectric constant of the cylinders is 9.61 (alumina rods). In order to achieve good accuracy, 8 grid points have been used along the diameter of each cylinder, so, $\Delta x = \Delta y = \Delta z = 0.04cm$. The time step is $\Delta t = 6.6 \times 10^{-13}$ seconds. In order to reduce the memory and time requirements for this calculation, a magnetic wall has been used in the y-z plane at the center of the structure, and an electric wall in the x-z plane at the center of the structure. The excitation is created by a dipole with its axis along the y-direction, a length of 0.6 cm, and located 1.43 cm from the

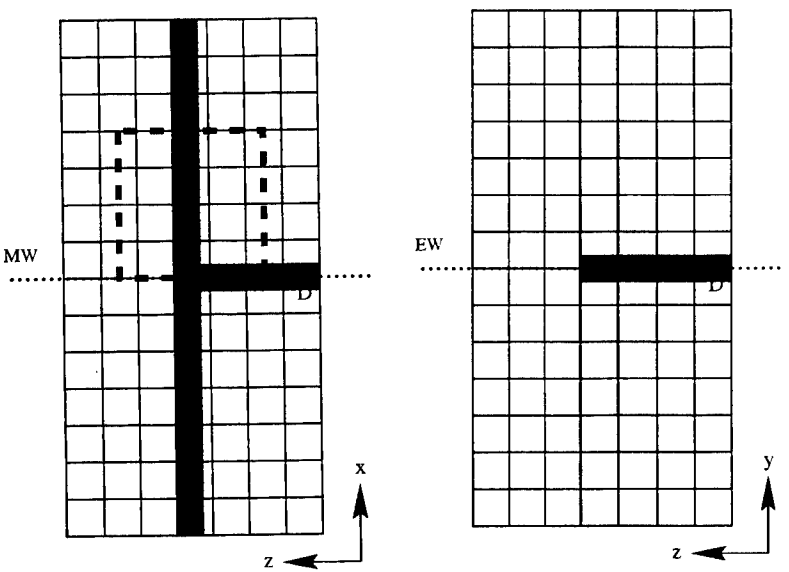

Figure 2: The x-z plane and y-z plane slices of the photonic crystal waveguide structure taken through the middle of the structure. Squares represent the unit cells of the photonic crystal consisting of 4 layers of rods with one rod in each layer. The shaded area shows the section where we put the waveguide. D is the position of the dipole which creates the excitation. The dashed lines indicate the area where the electric fields are plotted. Dotted lines indicate the locations of the magnetic (MW) and electric (EW) walls.

beginning of the waveguide (see Fig. 2).

The waveguide is created by introducing holes in the structure (grey area in Fig. 2) and filling these holes with alumina. It consists of two connected sections. The section which is parallel to the z axis (see Fig. 2) has a square cross section in the x-y plane with width of 0.82 cm. The section which is along the x direction has a width of 0.82 cm and 0.95 cm along the y and z directions, respectively.

The grid points used in our calculation were 240 by 240 by 264 along the x, y, and z directions. The numerical space is terminated with second order Liao boundary conditions. [12] The present method has previously been used to study the problem of dipole antennas placed on top of layer by layer photonic band gaps structures. [13]

3. RESULTS

Figure 3 shows the magnitude of the electric field in a plane parallel to the x-z plane, $3 \times \Delta y$ above the center of the waveguide structure. The slices shown in Fig. 3 are 4 unit cells wide along both x and z axes. The origin of the x axis is the center of the waveguide structure; only one half of the structure is shown since the plane x=0 is a magnetic wall (see Fig. 2). The slices along the z axis start one and a half unit cells from the beginning of the waveguide. Similarly, in Fig. 4, we show the electric field in the same waveguide in the absence of the photonic crystal. Dotted lines in Fig. 2 represents the part of the structure in which the fields in Fig. 3 and 4 are presented.

We can clearly see how the wave is marching along the waveguide by comparing the 3 panels which correspond to three different times. For example, in Fig. 3a, the wave is just past the bend of the waveguide while in Fig. 3c, the wave is more than 3 unit cells past the bend.

There are some important differences between Figs 3 and 4. As we can see in Fig. 4, for the simple waveguide cases, there is a considerable amount of power leaking out of the waveguide. This leakage is greater in the area close to the bend. The leakage is much smaller in the case where the waveguide is enclosed by the photonic crystal.

Comparing the maximum of the fields two unit cells before and after the bend, we find that for the simple waveguide case (Fig. 4c) the maximum of the fields is almost 3 times smaller after the bend relative to the maximum of the field before the bend. In contrast, the maximum of the field is almost the same for the case where the waveguide is covered with the photonic crystal. This is an indication that with the addition of the photonic crystal the wave is more confined inside the waveguide. We are currently working on the calculation of the Poynting vector along the two sections of the waveguide which will tell us how much power is transmitted along the bend of the waveguide.

However, it seems that the wave propagates more slowly when the photonic crystal is added. The field patterns for the simple waveguide case at $T = 2300 \times \Delta t$ and $2900 \times \Delta t$ are very similar indicating that the wave has reached a steady state condition in this particular region. In contrast, when the photonic crystal is added, the field patterns at $T = 2300 \times \Delta t$ and $2900 \times \Delta t$ are different especially for locations more than 3 unit cells after the bend. The slow down of the wave when the photonic crystal is added is related to the confinement of the wave in that case. We expect that when the wave is confined its velocity decreases. Calculations of the phase velocity are in progress and they will clear this point.

4. CONCLUSIONS

We studied photonic crystal waveguides using the finite difference time domain method. We found that by embedding the waveguide in a photonic crystal and operating inside the region of the full band gap, leakage due to the bending of the waveguide can be significantly reduced. However, the wave is slower in the photonic band gap waveguide case. In the future, we will study similar cases where the waveguide is filled with air. We will study also the individual sections of the waveguide using the plane wave expansion method. [1,2] Using that method, one can calculate the dispersion of the waves inside the waveguide. [3]

Acknowledgment - Ames Laboratory is operated by the U.S. Department of Energy by Iowa State University under Contract No. W-7405-Eng-82. We also acknowledge support by the Department of Commerce through the Center of Advanced Technology Development (CATD) at Iowa State University.

REFERENCES

1. See the proceedings of the NATO ASI, *Photonic Band Gap Materials* ed. C. M. Soukoulis, (Plenum, New York, 1996).
2. J. D. Joannopoulos, R. D. Meade, J. N. Minn, "Photonic Crystals," (Princeton University Press, 1995).
3. A. Mekis, J. C. Chen, I. Kurland, S. Fan, P. R. Villeneuve, and J. D. Joannopoulos, *Physical Review Letters,* 77, pp. 3787, 1996.
4. K. M. Ho, C. T. Chan, C. M. Soukoulis, R. Biswas, and M. M. Sigalas, *Solid State Communications,* 89, pp. 413, 1994.
5. E. Ozbay, A. Abeyta, G. Tuttle, M. Tringides, R. Biswas, C.M . Soukoulis, C.T. Chan and K. M. Ho, *Phys. Rev.,* B 50, 1945, 1994.
6. E. Ozbay, G. Tuttle, R. Biswas, M. Sigalas, and K.M. Ho, *Appl. Phys. Lett.,* 64, 2059, 1994.
7. E. Ozbay, E. Michel, G. Tuttle, R. Biswas, K.M. Ho, J. Bostak, and D.M. Bloom, *Optics Letters,* 19, 1155, 1994.
8. E. Ozbay, G. Tuttle, M. Sigalas, R. Biswas, K.M. Ho, J. Bostak, and D.M. Bloom. *Appl. Phys. Lett.,* 65, 1617, 1994.
9. E. Ozbay, G. Tuttle, J. S. McCalmont, M. Sigalas, R. Biswas, and K.M. Ho, *Appl. Phys. Lett.,* 67, 1969, 1995.
10. E. Ozbay, G. Tuttle, M. Sigalas, C. M. Soukoulis, and K.M. Ho, *Phys. Rev.,* B51, pp. 13961, 1995.
11. M. C. Wanke, O. Lehmann, K. Muller, Q. Wen, M. Stuke, *Science,* 275, pp. 1284, 1997.
12. Z. P. Liao, H. L. Wong, B. P. Yang, and Y. F. Yuan, *Sci. Sin.,* A27, pp. 1063, 1984.
13. M. M. Sigalas, R. Biswas, K. M. Ho, W. Leung, G. Tuttle, and D. Crouch, Conference Proceedings of Applied Computational Electromagnetics, 13, pp. 412, 1997; M.M. Sigalas, R. Biswas, Q. Li, D. Crouch, W. Leung, R. Jacobs-Woodbury, B. Lough, S. Nielsen, S. McCalmont, G. Tuttle, K.-M. Ho, Microwave and Optical Technology Letters, 15, pp. 153, 1997.

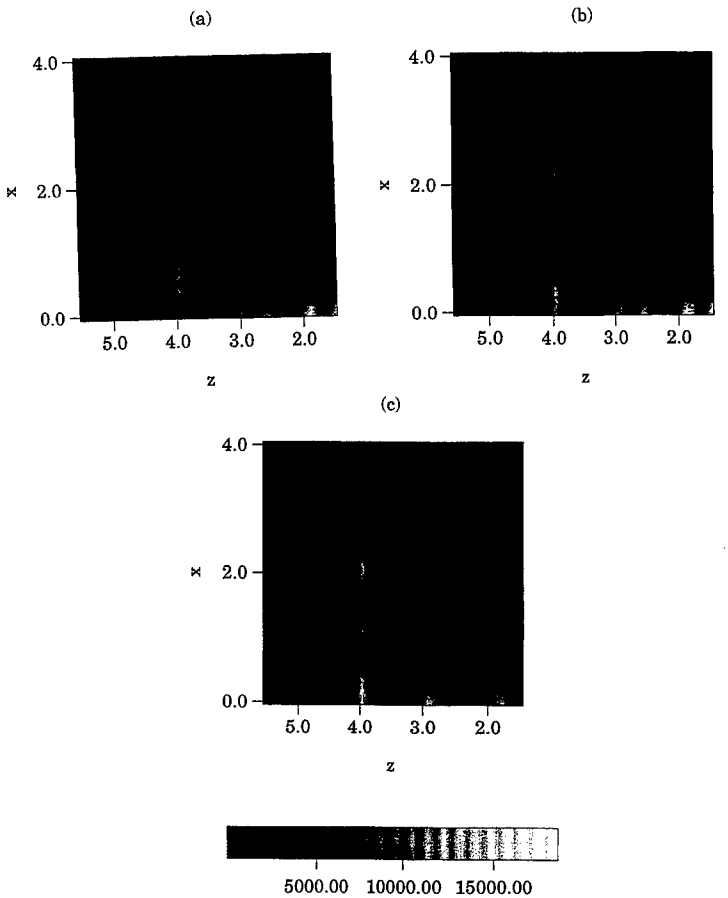

Figure 3: The magnitude of the electric field propagating in a photonic crystal waveguide for T= 1700, 2300, 2900 Δt (a, b, and c panels respectively). The frequency is 12.5 GHz.

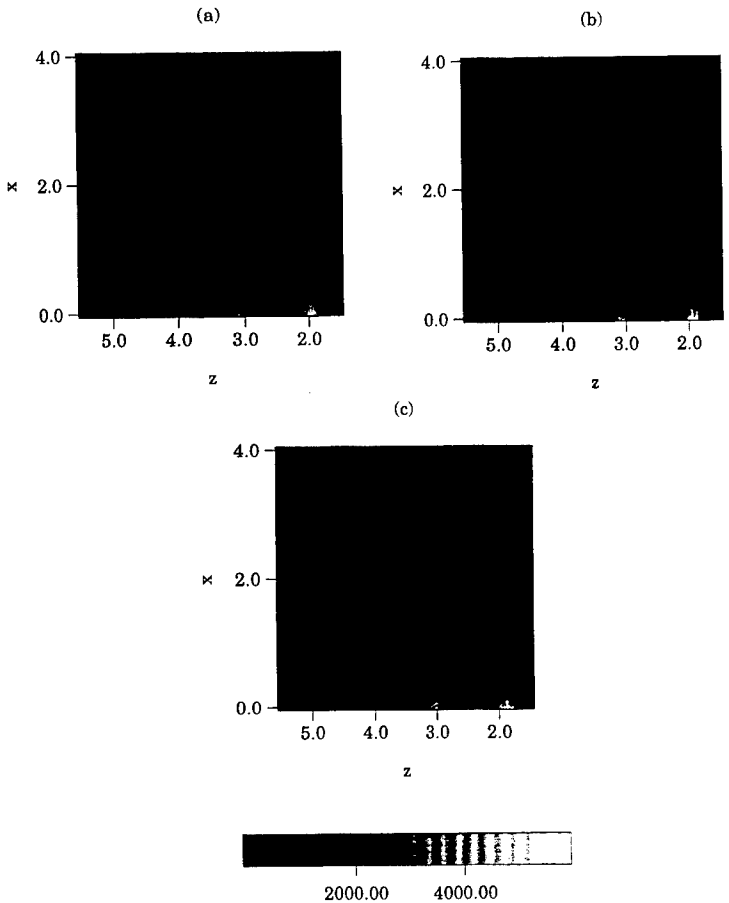

Figure 4: The magnitude of the electric field propagating in single waveguide for T= 1700, 2300, 2900 Δt (a, b, and c panels respectively). The frequency is 12.5 GHz.

Is there a relationship between a random and an ordered composite mixture?

W. M. Merrill*, S. A. Kyriazidou† and N. G. Alexópoulos‡

Abstract

This paper investigates the accuracy of representing a disordered mixture of materials (randomly distributed) with an equivalent homogeneous effective response, or conversely of representing the complex dispersive electromagnetic response of a disordered mixture with an equivalent ordered mixture. First, the accuracy of replacing a disordered mixture using effective parameters representing an equivalent homogeneous material is considered in general, and then specifically for a quasi-static analysis of mixtures of coated spheres. In the quasi-static regime there is also shown to be equivalence between the average field in an amorphous, disordered mixture of coated spheres and the field in an ordered simple cubic lattice arrangement of the same coated spherical inclusions. Next, numerical simulations of the array factors of a randomly filled linear and planar arrays are considered (assuming non-interacting elements) as a conceptual model to study the average and variance of the coherent combinations of the scattered field, and better understand the local and global properties of the disordered mixtures electromagnetic response.

I. Introduction

Engineering applications may require materials with both a specified electromagnetic response at a specific frequency as well as a desired frequency response around that frequency. Disordered mixtures of materials provide one method to design this electromagnetic response, as well as other possible benefits such as lower cost or more attractive mechanical and thermal properties. However, to design these disordered materials the dependence of the material's electromagnetic response must be well characterized in terms of the properties and volume fraction of each component and must result in a reproducible or unique response so that the same type of mixture can be expected to have similar EM properties every time they are manufactured. This paper explores the validity of representing a disordered mixture with its average response.

In this paper the disordered mixtures considered are limited to two-component (binary) mixtures, for which one component can be considered a host material in which the other component is randomly distributed as inclusions. These disordered mixtures will be considered to be specified only by the materials used for inclusion and host, the shape and size of the inclusive particles, and the set volume fraction of inclusions (p) or host ($1-p$). Within this description each disordered mixture will have multiple realizations due to the various possible configurations that represent each possible random distribution. One focus of this paper is to describe how similarly the electromagnetic response of each iteration is (i.e how large the variance is) and whether that response can be well represented with an ordered equivalent effective material. In addition the possibility of representing the disordered mixtures average response in terms of an equivalent ordered mixture is considered. A completely random distribution is assumed in all disordered mixtures considered in this paper. In actual mixtures the inclusions would not be completely randomly distributed, but would be subject to constraints dependent on the mixing process utilized, such as the breaking up of very tenuous clusters if the mixture is mechanically stirred.

II. Equivalent Average Response versus Variance

Generally a disordered mixture is represented with its average response to an electromagnetic field in terms of effective complex parameters $\hat{\epsilon}_{eff}$ and $\hat{\mu}_{eff}$. These effective parameters describe the average electromagnetic response expected of the disordered material and represent a homogeneous material which if it replaced the disordered medium (i.e. of the same size and shape as the total disordered region considered) would create the same average field either scattered from or within the material. This is represented in Figure 1. For this assumption to be true the disordered mixture must be much larger than the inclusion size (a_0) so that the most likely distributions of inclusions can be well represented and so that the scattering from all the inclusions will average out in an ergodic sense. These constraints require either that the wavelength in the effective material be much larger than

*EE Dept. UCLA, Los Angles, CA 90095-1594, williamm@ee.ucla.edu
†EE Dept. UCLA, Los Angles, CA 90095-1594, kyria@ee.ucla.edu
‡ECE Dept. UCI, Irvine, CA 92697-2700 alfios@uci.edu

the inclusion size ($\lambda_{eff} >> a_0$), which is considered in section III. and [1], or that the electromagnetic response, which can be represented with an effective permittivity and permeability or as an array factor A_a (that is the effect of combining coherently into an array factor the scattering off all inclusions, assuming all scattered field to have the same form), has a small variance about its average value when comparing different likely locations of inclusions for a given volume fraction. Consideration of comparison of the Clausius-Mossotti equation to describe the average quasi-static response of disordered mixtures of coated spheres and the Rayleigh formulation which assumes periodic spheres are shown to coincide in section III., for low volume fractions of inclusions. To investigate the average response of disordered mixtures when the local scale of the mixture is on the order of wavelength a simplified model of the disordered mixture is used, with each inclusion representing an element of an array. The array factor of this array is treated in a simplified manner in section IV. by considering all inclusions to be of the same form and to scatter the same incident field so that mutual coupling or multiple scattering between inclusions is neglected, and the incident field on each inclusion is of the same phase and magnitude for each inclusion.

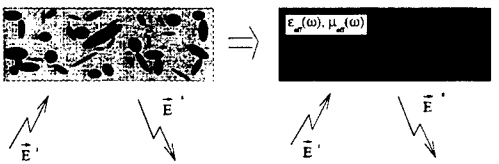

Figure 1: Representing a disordered mixture's average response as an equivalent homogeneous material.

III. Quasi-static mixtures

First we compare quasi-static formulations for an ordered and a random mixture composed of identical, spherical, lossy particles dispersed into a homogeneous nonlossy dielectric. The spherical inclusions are plain or coated with a resonant dielectric layer (Lorentzian medium). We compare the EM response of a random mixture of spheres with that of an ordered arrangement of spheres in a simple cubic lattice by determining the dispersive behavior of the effective (average) permittivity and bulk conductivity of the mixtures. We examine the response of this medium in the quasi-static limit , where the size and spacing of the particles are small with respect to the wavelength.

For low density media , i.e., within range of validity of the effective medium theory (EMT) Clausius Mossotti model, we compare the results between a random and an ordered arrangement of spheres. The results are in excellent agreement indicating that the ordered structure is an excellent representation of the random medium when the quasi-static analysis is applicable.

A. Amorphous Composite

An amorphous composite, with random arrangement of spheres, is analyzed in terms of the Clausius-Mossotti model which considers the dipole approximation of the induced field. The effective permittivity [2] is given in terms of ϵ_1, ϵ_2, ϵ_3, the permittivities of the core , layer and host, respectively, as

$$\epsilon_{eff} = \epsilon_3 \frac{1 + 2f\alpha'}{1 - f\alpha'} \quad . \tag{1}$$

The volume fraction f is given in terms of the number density N of scatterers, and α' is the dimensionless polarizability with

$$f \equiv \frac{4\pi}{3} b^3 N \quad , \alpha' \equiv \frac{\alpha}{b^3} = 1 - \frac{3\left(2 + r + (1-r)\frac{\epsilon_1}{\epsilon_2}\right)}{\left(2 + \frac{\epsilon_1}{\epsilon_2}\right)\left(2 + \frac{\epsilon_2}{\epsilon_3}\right) + 2r\left(1 - \frac{\epsilon_1}{\epsilon_2}\right)\left(1 - \frac{\epsilon_2}{\epsilon_3}\right)}, \tag{2}$$

and $r \equiv (a/b)^3$ is the ratio of the core to the total volume of the coated spheres.

B. Ordered Composite

A mixture of plain or coated spheres occupying the sites of a simple cubic lattice is analyzed in terms of a method devised by Lord Rayleigh [3] and extended more recently for the calculation of the conductivity and magnetic permeability of a lattice of conducting spheres[4, 5, 6]. We apply this method for the case of coated spherical particles [7]. In fact this formulation is a rigorous semi-static solution and takes into account all multipole moments

in the expansion of the induced field which are ignored in the EMT approach. Thus it also extends the analysis to high density media. Following the analysis in [4, 5, 6, 7] a formula for the effective permittivity of coated metallic spheres in a simple cubic lattice configuration is:

$$\epsilon_{eff} = \epsilon_3 \left(1 + \frac{3\,f}{\Lambda(f)}\right) \tag{3}$$

where,

$$\Lambda(f) = -\frac{1}{R_1} - f + 1.3045\,R_3 f^{10/3} + 0.0723\,R_5 f^{14/3} - 0.5289\,R_3^2 f^{17/3} + 0.1526\,R_7 f^6, \tag{4}$$

the volume fraction f is $f = \frac{4\pi b^3}{3c^3}$, b is the radius of the sphere, c is the lattice size,

$$R_l \equiv \frac{1 + \frac{l}{l+1}\,p_l - \frac{\epsilon_2}{\epsilon_3}(1-p_l)}{\frac{l+1}{l} + p_l + \frac{\epsilon_2}{\epsilon_3}(1-p_l)}, \text{ and } p_l = \left(\frac{a}{b}\right)^{2l+1} \frac{1 - \frac{\epsilon_1}{\epsilon_2}}{1 + \frac{l}{l+1}\frac{\epsilon_1}{\epsilon_2}}. \tag{5}$$

C. Comparison of effective permittivities

The dispersive properties over four frequency decades for the plain conducting spheres immersed in a nonlossy dielectric are shown in figure 2. The medium exhibits Debye-type permittivity. We observe a complete agreement

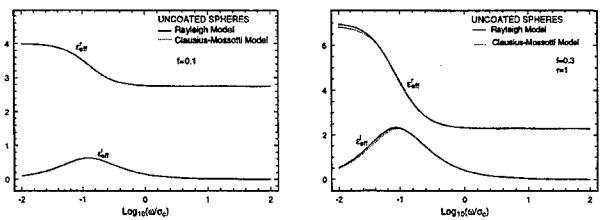

Figure 2: Model comparison for uncoated inclusions (σ_c is sphere bulk conductivity).

between the ordered and disordered models at filling fractions up to $f = 0.1$, which is maintained at higher f with only slight disagreement until $f > 0.3$. The disagreement between these approaches for dense mixtures is attributed to the fact that the Clausius-Mossotti formula accounts for only the dipole moments of inclusions, rather than disagreement between the response of the ordered (Rayleigh) and disordered (Clausius-Mossotti) mixtures since spacing of inclusions are assumed to be much smaller than wavelength in both cases so the field in the disordered mixture should average to the field in the ordered mixture with corresponding volume fraction f.

For a composite with coated spheres the analogy is apparent in figure 3.

IV. The array factor of randomly dispersed non-interacting scatterers

To investigate the variance between disordered mixtures formulated with the same types of inclusions, host material, and volume fractions of each, we use as a simplified model the array factor of a randomly filled array. This array factor assumes that all the inclusions are non-interacting and so does not give a model of the self-similar structure which is built up (and becomes infinite at the percolation threshold) as inclusions are brought in contact to form complex continuous clusters. However, the array model does describe the variation in spacing between inclusions as more inclusions are added and how any constraints placed on that spacing can create fluctuations in the scattered field on average within the disordered structure.

A. Randomly Filled Linear Array

First, a randomly filled linear array is analyzed such as represented in Figure 4. This array represents a one dimensional disordered mixture of inclusions (the inclusion type is general since only the array factor is investigated although each inclusion is considered to scatter the same incident field).

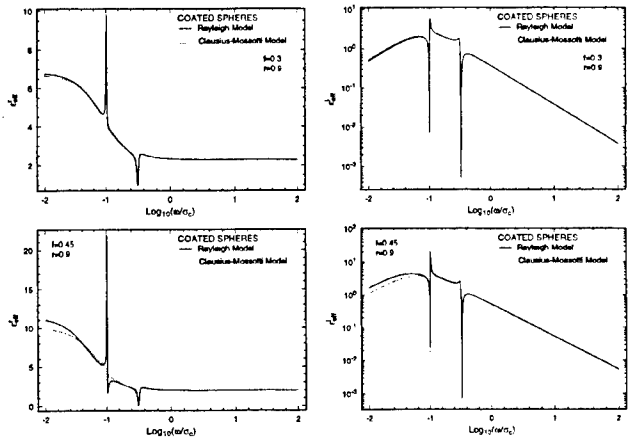

Figure 3: Model comparison for inclusions coated with a highly resonant dielectric (σ_c is sphere core conductivity).

For a one dimensional array along the z-axis the magnitude of the array factor is written for an M site array and spacing d, neglecting multiple scattering following [8] as:

$$|\mathcal{A}_a| = \left| \sum_{m=1}^{M} X_m I_m e^{j\beta dm\cos\theta} \right| = \left| \sum_{m=1}^{M} X_m e^{j\beta dm\cos\theta} \right| \tag{6}$$

where $\{X_n; n = 1, 2, 3, \ldots M\}$ is a Bernoulli random process with $P[X_n = 1] = p$, with expectation $E[X_n] = p$ and variance $Var[X_n] = p - p^2$. The propagation constant in the surrounding media is assumed to be that of free space for the host material $\beta = 2\pi/\lambda_0$, θ is the angle measured off the z axis (the array axis in this case), d is the spacing between sites, I_m represents the amplitude of the incident field at each inclusion which is assumed to be the same and in phase at each inclusion and normalized to one. The expectation of this array factor is:

$$E[|\mathcal{A}_a|] = p \left| \sum_{m=1}^{M} e^{j\beta md\cos\theta} \right| = p\,|\mathcal{A}_a(p=1)| \tag{7}$$

and the variance is:

$$Var[|\mathcal{A}_a|] = \left| \sum_{m=1}^{M} Var[X_m] e^{j\beta md\cos\theta} \right| = (p-p^2) \left| \sum_{m=1}^{M} e^{j\beta dm\cos\theta} \right| = (p-p^2)|\mathcal{A}_a(p=1)| \tag{8}$$

The variance in equation (8) is seen to go to zero only at zero filling, complete filling (when the structure is completely ordered), or at the angles coinciding with nulls for the completely filled array. This variance however, is calculated by considering all possible sites in the array to be filled with an independent filling probability of p rather than what is stated as the constraint for the material that the inclusions had a set volume fraction and so the filling of each site can not be considered completely independently. Thus if the first Mp sites are filled all the remaining sites should be empty (considering each site filled in the array to represent a volume fraction of $1/M$ in the mixture modeled, i.e. to represent one inclusion with a volume fraction $1/M$). As a result the expectation and variance for a disordered mixture which is considered to have a set volume fraction of inclusions (as would be expected for one mixed batch of a disordered mixture) will not be predicted by the above formulas.

Figure 4: Randomly filled linear array, each circle (shown equi-spaced) represents a possible element (inclusion location) with each filled sphere represents a scattering inclusion or occupied location on the array.

However, upon parceling the original batch up, a wider range in filling fractions would result per portion although any potions which contained a wide deviance from the initial mixture ratio would most likely be screened out in the manufacturing process.

In order to investigate the expected value and variance of the magnitude of the array factor of a randomly filled lattice, numerical evaluations of randomly filled linear arrays are investigated in a Monte-Carlo simulation. The number of combinations possible at a given filling probability p increases drastically as M increases (at p=0.5 the number of possible combinations is larger than $2^M/M$) thus rather than sum up all possible combinations and average, random locations in an M sized linear array are filled until a filling fraction of sites of p is achieved, then numerous iterations of this process are used to determine the expectation and variance of the array factor (with the convergence of these values determining when enough simulations had been performed). Plots of the expectation (figure 5) and variance (figure 6) are shown, for a 500 site linear array at various lattice spacing between sites of possible occupation, for a half filled linear array $p = 0.5$ (d/l is the spacing of possible element locations normalized to the wavelength in the surrounding host material, i.e. the spacing between sites). For a 500 site linear array (half filled so 250 scatterers) upon comparing averaging of 4000 iterations and 10000 iterations the difference are within five percent.

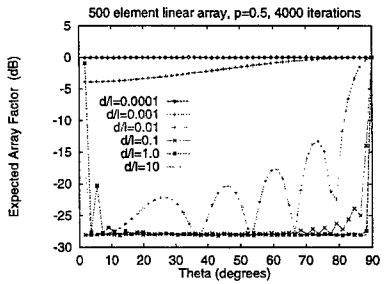

Figure 5: $E[|A_a|]$ computed from Monte-Carlo simulation of linear arrays.

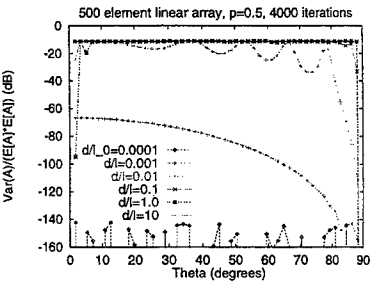

Figure 6: Normalized variance $Var(|A_a|)/(E[|A_a|])^2$ for randomly filled linear arrays.

As expected for spacing between lattice sites (between sites of possible occupation) much smaller than the wavelength the variance predicted goes to zero (as demonstrated in section III.) and for $d/l = 0.0001$ is below the machine error in the calculation thus giving the highly oscillatory behavior of this case in figure 6. The expectation of the normalized array factor decreases from being isotropic in θ to predicting highly directional scattering with an apparently even sidelobe level around $-28dB$ since the array is only one dimensional. Evident in the case that $d/l = 10$ are peaks which result from the constraint that each lattice site is a set distance d apart. These peaks in figure 5 result when all the scatterers act in phase and so $\beta d\, m \cos\theta$ is a multiple of 2π.

Next, the expectation and variance of the array factor at different filling fractions is investigated. The variance is seen to remain constant as the filling fraction is increased contrary to the prediction of equation (8). This is demonstrated in figure 8 which along with figure 7 are plotted for a 500 site array with half-wavelength spacing between sites, for various filling fractions. The variance goes to zero at both endpoints $p = 0$ and $p = 1$ however while it monotonically decreases as p approaches $p = 1$ their is an apparently discontinuous drop at $p = 0$ due to the discrete nature of the array. Once two sites are filled their is large jump in the possible array factors as compared with one site when there are no coherent combinations and thus a variance in the array factor of zero. From figure 7 the expectation is seen to peak at broadside where in the far-field all scattering off each element is in phase and the average scattering off broadside decreases as p increases or as the number of scatterers considered increases. The expectation also does not change linearly with p as predicted by equation (7).

Next, in order to more accurately simulate a completely disordered random mixture, the numerical simulation of the array factor of a randomly filled linear array array is extended to randomly spacing the possible locations of sites. Possible spacing between sites are considered as a continuously distributed random variable in $[0, 2d/l]$ in order to give the same average length as for the equi-spaced randomly filled sites. The expectation and variance for a 500 site half filled linear array are shown in figure 9 and 10. The most noticeable effect of changing the spacing from an ordered structure of sites to random spacing is the smoothing of the expectation and the elimination of

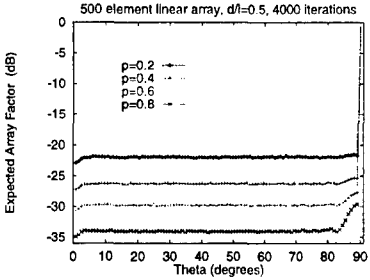

Figure 7: $E[|\mathcal{A}_a|]$ for a randomly filled linear array.

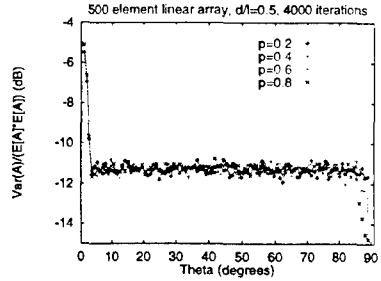

Figure 8: $Var(|\mathcal{A}_a|)/(E[|\mathcal{A}_a|])^2$ from Monte-Carlo simulation of a randomly filled linear array.

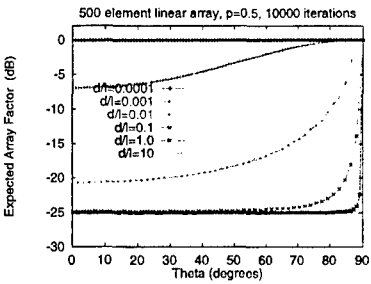

Figure 9: $E[|\mathcal{A}_a|]$ of a randomly filled linear array with site random spacing uniformly distributed from $[0, 2d/\lambda_0]$.

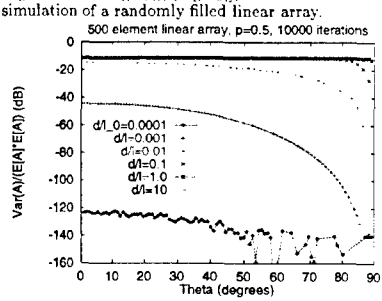

Figure 10: Normalized variance $Var(|\mathcal{A}_a|)/(E[|\mathcal{A}_a|])^2$ for a randomly filled linear array with random site spacing uniformly distributed from $[0, 2d/\lambda_0]$.

the peaks in the expectation for the 10λ spacing.

B. Randomly filled Square Array

As an extension to the treatment of the linear array of non-interacting scatterers a planar array of non-interacting scatterers in the $x-y$ plane is treated in the same manner. For this planar array the array factor can be written as:

$$|\mathcal{A}_{ap}| = \left| \sum_{m=1}^{M} \sum_{n=1}^{N} X_{mn} I_{mn} e^{j\beta \sin\theta (d_x m \cos\phi + d_y n \sin\phi)} \right| = \left| \sum_{m=1}^{M} \sum_{n=1}^{N} X_{mn} e^{j\beta \sin\theta (d_x m \cos\phi + d_y n \sin\phi)} \right| \quad (9)$$

Then following the same procedure as for the linear array the expectation and variance for an array in which each site is independently filled with probability p are: $E[|\mathcal{A}_{ap}|] = p|\mathcal{A}_{ap}(p=1)|$ and $Var[|\mathcal{A}_{ap}|] = (p-p^2)|\mathcal{A}_{ap}(p=1)|$.

Plots of the expectation and variance of the numerically simulated array factor for a constant filling fraction are shown in figures 11 and 12 for randomly filled and randomly spaced sites in a square array (M=N=25). These plots show the array factor versus θ the angle off the normal to the array (the array is in the $x-y$ plane) for a $\phi = \pi/4$ cut (along the array's diagonal). The main difference between the plots of the array factor for the planar array and for the linear array is that the average distance between closest elements decreases so that the average spacings between possible element sites must be larger for comparable isotropic nature and variance as compared to the linear array.

In addition the effect of size of the square array (that is to say the number of elements or scatterers considered) is investigated through computing the expectation and variance of the array factor for various sized square arrays all with $p = 0.5$ filling and $d/l = 0.5$ spacing as shown in figures 13 and 14. The array factor becomes less isotropic as the array becomes larger as expected, the variance however appears to stabilize to around $-10dB$ for most of the angular range, except at broadside where since all elements combine in phase regardless of spacing in the $x-y$ plane the variance goes to zero.

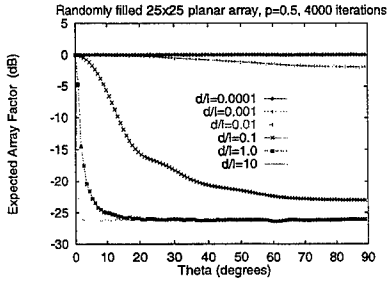

Figure 11: $E[|\mathcal{A}_{ap}|]$ for $\phi = \pi/4$ off the normal to the array, and random spacing uniformly distributed from $[0, 2d/\lambda_0]$.

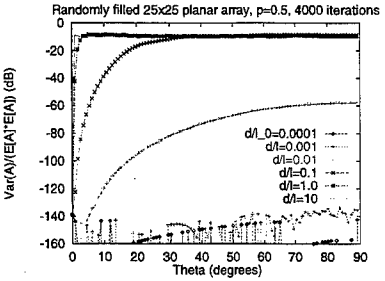

Figure 12: $Var(|\mathcal{A}_{ap}|)/(E[|\mathcal{A}_{ap}|])^2$ for $\phi = \pi/4$ and random spacing uniformly distributed from $[0, 2d/\lambda_0]$.

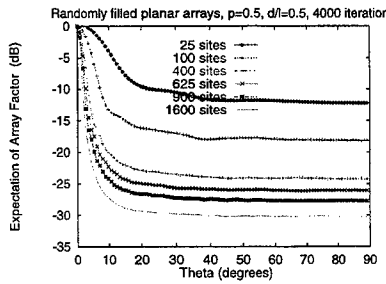

Figure 13: $E[|\mathcal{A}_{ap}|]$ for various sized square arrays, for $\phi = \pi/4$ and site spacing uniformly distributed in the range $[0, 2d/\lambda_0]$.

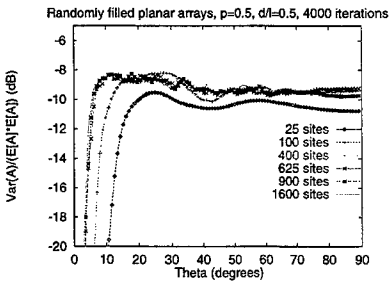

Figure 14: $Var(|\mathcal{A}_{ap}|)/(E[|\mathcal{A}_{ap}|])^2$ for various sized square arrays, for $\phi = \pi/4$ and site spacing uniformly distributed in the range $[0, 2d/\lambda_0]$.

V. Conclusions

To determine when a disordered mixture can be represented accurately with an equivalent ordered structure two regimes are considered. The first regime is when the inclusion size and average spacing between inclusions is small compared to the wavelength in the surrounding material, and the second is when the local spacing or size of inclusions is on the order of or greater than the wavelength so that coherent scattering from inclusions must be considered on a local scale within the disordered mixture to describe the mixture well. In the first regime the local scale of the mixture (local to inclusion size) is small compared to wavelength and thus within one wavelength the spatial variation within the mixture is well represented so that all coherent scattering effects will average out, and only small variation in the electromagnetic response is expected for disordered mixtures fabricated in the same process with the same types of components. This conclusion is supported by a quasi-static analysis of the average effective permittivity of an amorphous mixture of coated spheres and of a corresponding ordered mixture, as well as by the numerical investigation into the array factor of a randomly filled array. This result has been utilized in quasi-static analysis of disordered mixtures to generate effective permittivities or effective permeabilities which present the same EM response as the disordered mixtures modeled [1]-[7], [9]. In the second regime the coherent interactions between the waves scattered off inclusions must be accounted for on a local scale. As demonstrated through the variance of a randomly filled array the average response characterization of a disordered mixture is only likely to be accurate to about a $-10dB$ power level or within about 30% for the array factor. Thus in designing or describing composite mixtures this possible variance between mixtures must be incorporated into the analysis or design. To account for other global properties in the disordered structure (such as the effect of the self-similar structure of clusters which form) possible phase progression and dependence between the scattered

fields at each scatterer must be taken into account in this array model. The same average behavior and variance is expected in multiple scattering of widely spread inclusions as the same distribution of scatterers will scatter each multiple scattered field (assuming the mixture is large enough and the spacing of the scatterers is random enough to average out any additional effects due to phase progression of the scattered field, loss of power due to scattering, and absorption in the material) and so for non-contacting mixtures. or disordered mixtures without a global structure, the average response should characterize the mixture with about the same accuracy However, when self-similar clusters form (such as near the percolation threshold for the inclusions as is considered briefly in [9]) the global structure of these clusters must be accounted for, for example within an equivalent ordered material (either homogeneous effective material or equivalent ordered structure).

Two types of ordered representation are considered in this paper. The first is a representation of the disordered mixture with an effective permittivity or effective permeability representing an equivalent homogeneous material. In this representation all the spatial and frequency dispersion (boundary conditions within the disordered structure) are represented through the functional dependence (value, anisotropy, and time dependence) of the effective permittivity or permeability. The second model considered represents the disordered mixture in terms of an ordered material in which the ordered boundary conditions provide the same electromagnetic interaction as for its disordered equivalent. The Rayleigh and Clausius-Mossotti analysis of mixtures of spherical inclusions demonstrated the equivalence of the effective permittivity description for both an ordered and disordered model when a mixture of coated spheres in a host can be treated quasi-statically. The randomly filled array demonstrated some of the differences in the two structures, such as the averaging out of all nulls and side lobes for the disordered mixture. To create an accurate comparison the ordered equivalent presents a problem in that the periodic nature of the ordered structure must be suppressed, or a deterministic equivalent must be generated without the periodic response. For example in considering the equi-spaced linear array, even with random filling, as the spacing became larger than wavelength the periodicity of the lattice structure imposed a structure on the average array factor not seen in the randomly spaced array counterpart.

VI. Acknowledgements

The authors would like to thank Dr. Rudolfo Diaz for many helpful discussions.

References

[1] A.N. Lagar'kov, A.K. Sarychev, Y.R. Smychkovich, and A.P. Vinogradov, "Effective Medium Theory For Microwave Constant and Magnetic Permeability of Conducting Stick Composites", *J. of Electromagnetic Waves and Applications*, **6**, 1159, (1992).

[2] S.A. Kyriazidou, R.E. Diaz, N.G. Alexópoulos, "Coated Spheres as Constituents of a Novel Artificial Dielectric and as scatterers in a Photonic Band Gap Material", 1997 U.R.S.I. North American Radio Science Meeting. Montreal, Canada, p.747.

[3] Lord Rayleigh, Philos. Mag. **34**, 481 (1892).

[4] R. C. McPhedran, D. R. McKenzie, "The conductivity of lattices of spheres I. The simple cubic lattice", Proc. R. Soc. Lond. A **359**, 45 (1978).

[5] R.C. McPhedran, D. R. McKenzie, G.H. Derrick, "The conductivity of lattices of spheres II. The body centered and face centered cubic lattices", Proc. R. Soc. Lond. A **362**, 211 (1978).

[6] John Lam, "Magnetic permeability of a simple cubic lattice of conducting magnetic spheres", J. Applied Phys **60**, 4230, (December 1986).

[7] S. A. Kyriazidou, R. E. Diaz, and N.G. Alexópoulos, "Rayleigh Analysis of novel dense medium exhibiting narrow-band transparency window", submitted to The 14th Annual Review of Progress in Applied Computational Electromagnetics, Monterey, CA, March 16-20, (1998).

[8] R. S. Elliott, *Antenna Theory and Design*, Prentice Hall, Inc., Englewood Cliffs, New Jersey, 1981. pp. 114-118.

[9] W. M. Merrill, R. E. Diaz, and N. G. Alexópoulos, "A Recasting of the Effective Parameters of Composite Mixtures into the Language of Artificial Dielectrics," *Physica A*, **241**, 334, (June 27, 1997). as part of the proceedings for the ETOPIM4 conference.

An Analytic Framework for the Modeling of Effective Media

R. E. Diaz
Northrop Grumman Corp.
Military Aircraft Systems Division
2500 W. Frye Rd.
Chandler, AZ 85224

Abstract - Synthetic materials in which new electromagnetic properties are obtained from the combination of two or more materials have been of theoretical and practical interest for nearly a century. The ability to explain and predict the properties of these materials has traditionally relied on combining physico-mathematical models of the effective environment seen by the various constituents of the mixture with some assumptions about the way these microscopic properties should translate into macroscopic homogeneous parameters. Thus, even in the simplest case of the binary mixture, with every new set of assumptions, a new effective medium theory (EMT) results, and, with each new theory, stronger claims of correctness and applicability are made. This issue of correctness becomes critical when the properties of one of the constituents is unknown *a priori* and the claim is made that by inverting the fit of experimental results to the EMT model those properties can be ascertained. For this inverse procedure to be possible, the EMT theory should not only be correct, it should be unique in the analytic sense. In this paper, a generalized framework is developed through which the analytic properties of all binary mixture EMTs can be deduced and compared. In the process it is shown that in the complex plane of the variable $u = i/(\varepsilon_{filler}-1)$, it is straight forward to separate the morphology dependent properties of the EMT from its dependence on the susceptibilities of the components. The frequency dependence of the EMT model as a function of arbitrary complex properties of the filler is easily summarized as a compact sum of the poles of a complex function.

I- Introduction

The synthetic composite material is the mainstay of the advanced engineering structures of our century, and its importance continues to grow as we approach the next one. The motivation for initiating this program is the multiplicity of Effective Medium Theories (EMTs) that can be found describing one or more aspects of binary mixtures. Which theories are right, which are wrong, where the assumptions apply and where they break down, whether the empirical data supports them or not, are all questions that the investigator must face in attempting to choose an EMT to model his particular material. If the EMT is to be used for analysis as well as synthesis, specially in the solution of an inverse problem, an unambiguous answer to these questions becomes even more critical. All these concerns can be summarized into one practical question: Does one "best" EMT exist which most accurately models most materials?

Such an EMT would have to account for all the phenomena encountered in binary mixtures. These can be summarized as arising from five major variables involved in the physics of an effective medium: the host permittivity, the filler permittivity, the volume fraction, the frequency, and the total effective morphology of the mixture. The latter is an intricate function of all the parameters affecting the output of the manufacturing process. Therefore, the question that must be addressed by a truly useful EMT is: Can the output of a real manufacturing process yield arbitrary forms of this effective morphology, or is there a set of most probable characteristics common to all mixtures? In other words, just as the properties of an ensemble of Avogadro's number of gas particles can be summarized with a few state variables, is it possible that the average properties of a mixture can be likewise summarized with a few parameters? For the answer to be positive, there must be certain universal properties of mixtures that are independent of the filler and host particulars. In this paper it is established that binary mixtures of dielectrics have certain analytic properties that are indeed universal. It is further shown that these properties are compactly summarized as a sum of poles of a complex function. Such a sum of poles has as its only parameters the strengths of the poles and their positions.

II Derivation of the analytic model

Let us focus our attention on EMTs that yield local, homogeneous, effective permittivity values for the ensemble of particles. It follows that the microscopic granularity of the material occurs on a scale that is small compared to the

wavelength. Therefore the properties of the medium can be derived by considering the quasi-electrostatic limit, and it is in principle derivable from a solution of Laplace's equation over a representative parcel of the medium. Therefore, consider such a parcel of unit volume as suggested in Figure 1, inserted between the plates of an ideal capacitor. The effective relative permittivity of the medium, ε_{eff}, is defined as the ratio of the capacitance of the capacitor when filled with the medium, to the capacitance of the empty capacitor. What are the limiting properties of the effective permittivity?

First, they must depend on the properties of the filler and host. Since free space is always present in filler and host, the quantity of interest is the susceptibility $e_{eff} = \varepsilon_{eff}-1$ and its dependence on $e_{filler} = \varepsilon_{filler}-1$ and the filler's volume fraction, p.

When the properties of host and filler are held fixed, the dependence on the volume fraction has the following trivial limits: At $p = 0$, $e_{eff}+1 = \varepsilon_{host}$, and at $p = 1$, $e_{eff} = e_{filler}$. In addition, it is reasonable to expect for most materials that the following assumption is valid: If the morphology of the filler does not permit 100% filling (as in the case of a monodisperse ensemble of spheres), then for purely real filler and host (with $e_{filler} > e_{host}$), at the maximum volume fraction, $e_{eff}(p = p^{max}) = e_{eff}^{max1}$. Where e_{eff}^{max1} is the maximum value of the effective susceptibility, when the filler properties are held constant. This is the limit of the assumption of process uniformity. Namely, that whatever manufacturing process was used to yield a mixture of volume fraction p, will yield a similar mixture when p is increased to p+dp. This statement is more restrictive than the requirement that the partial derivative of e_{eff} with respect to p be continuous because it also implies that, for the case of purely real filler and host, e_{eff} is a monotonic function of p. Such a requirement is reasonable for most materials because the addition of greater amounts of filler should move the mixture towards a greater resemblance to a pure filler medium. It should be noted that chemical mixtures in which a critical volume fraction of one component can trigger a phase change that dramatically alters the morphology of the mixture do not obey this rule.

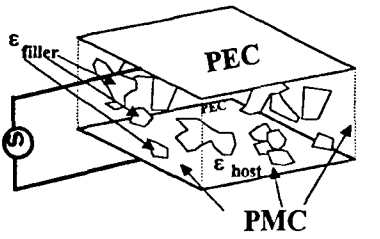

Figure 1. An ideal capacitor filled with a unit volume of the mixture can be used to define the effective permittivity.

Assuming for now that $\varepsilon_{host} = 1$, and that the filler permittivity is purely real and greater than 1, then when the volume fraction is held fixed, the dependence on the filler properties has the following trivial limits: At $e_{filler} = 0$, $e_{eff}=0$. At $e_{filler} = \infty$, $e_{eff} = e_{eff}^{max2}$. Where e_{eff}^{max2} is the maximum value of the effective susceptibility at a given constant volume fraction. Obviously, this maximum is in general less than or equal to the filler's susceptibility. Therefore if we define the new variable,

$$u = \frac{i}{e_{filler}} \tag{1}$$

then $e_{eff}(u)$ has a maximum at $u = i0$, and a minimum of 0 at $u = i\infty$. The function $e_{eff}(u)$ is a monotonically decreasing function of u for all imaginary u.

When e_{filler} is allowed to be complex (that is, when the radiofrequency is non zero), the analytic function properties of u as a function of frequency are also uniquely defined (within a 90 degree rotation): Wherever in the complex frequency plane e_{filler} has zeros, u has poles, and wherever e_{filler} has poles, u has zeros. Wherever e_{filler} is an analytic meromorphic function, u is analytic and meromorphic [1]. Similarly, we expect e_{eff} to be analytic over the same range that e_{filler} is analytic. Knowing this, we can now inquire as to the properties of the function $e_{eff}(u)$ for complex $u = u_r + iu_i$.

First we recall that the permittivity function has a special symmetry in the complex frequency ($\omega = \omega_r + j\omega_i$) plane.

$$\varepsilon(-\omega^*) = \varepsilon^*(\omega) \tag{2}$$

Then, given that the only frequency dependence that can enter a quasistatic EMT comes from the frequency dependence of the filler,

$$e_{eff}(\omega) = f(e_{filler}, morphology, p, \ldots) = g\left(\frac{i}{e_{filler}(\omega)}\right) = g(u) \tag{3}$$

Now let, $\omega \rightarrow -\omega^*$

$$e_{eff}(-\omega^*) = g\left(\frac{i}{e_{filler}(-\omega^*)}\right) \tag{4}$$

Since the filler is a real material, its susceptibility must have the symmetry of equation 2:

$$g\left(\frac{i}{e_{filler}(-\omega^*)}\right) = g\left(\frac{i}{e_{filler}{}^*(\omega)}\right) = g\left(\left[\frac{-i}{e_{filler}(\omega)}\right]^*\right) = g(-u^*) \tag{5}$$

Likewise, since the effective medium is a real material it too must obey the symmetry of equation 2:

$$e_{eff}(-\omega^*) = e_{eff}{}^*(\omega) = g^*(u) \tag{6}$$

And so, equations 3 through 6 imply that:

$$g^*(u) = g(-u^*) \tag{7}$$

So that the causal symmetry of the permittivity as a function of complex frequency implies a causal symmetry of the effective susceptibility as a function of complex filler susceptibility. And since the complex filler susceptibility maps one-to-one to the complex variable u, the effective susceptibility has causal symmetry in the complex u plane. Figure 2 illustrates this similarity between the permittivity function and the effective susceptibility function. The analytic function properties of the permittivity function in the complex frequency plane mirror the analytic function properties of the effective susceptibility function in the complex u plane.

Both functions have a finite real maximum (or at worst a simple pole) at the origin. Both functions tend to a finite limit (=0 for susceptibilities) as ω goes to +infinity or as u goes to +infinity. Both functions have causal symmetry about one axis. In the upper ω half plane the permittivity is known to be devoid of poles or zeros. In the case of the effective susceptibility, since the upper u half plane corresponds to real values of the filler permittivity it can have no poles or zeros either. Therefore the Cauchy Riemann integral can be closed over that half plane and the real and imaginary parts of the functions must form Hilbert Transform pairs. Most importantly, the functions can be continued into their respective lower half planes to obtain their representation in terms of poles. Since this has already be done for the permittivity function [1] we can apply that knowledge to the effective susceptibility.

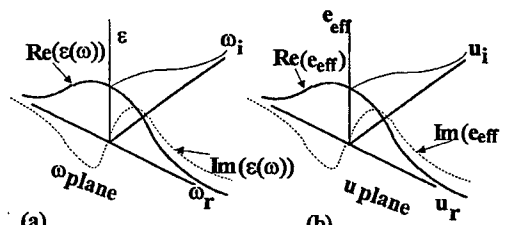

Figure 2. The analytic function properties of the permittivity function in the frequency plane (a) mirror the analytic properties of the susceptibility in the u-plane.

The only difference between the work of [1] and the present application is that the known data for permittivity as a function of frequency is known along the axis where the function has both real and imaginary parts. Whereas here, since we have assumed the filler permittivity to be purely real, u is purely imaginary, and the effective susceptibility has only taken real values. Nevertheless, just as it is easy from the shape of the permittivity curves as a function of frequency to deduce the poles contained in a given set of permittivity data [2], it is easy to deduce from the effective susceptibility as a function of real filler permittivity the poles associated with the given mixture (or EMT). By virtue of the analyticity of the functions involved, once these poles are known, everything about that given mixture (EMT) has been defined, uniquely.

From the results of [1] it follows that all binary mixture EMTs defining an effective susceptibility as a result of adding a dielectric filler to a host must be expressible in the form:

$$e_{eff}(u) = \sum_n \frac{A_n}{(u - \pi_n)(u + \pi_n^*)} \tag{8}$$

where π_n is the nth pole located in the lower half plane. When this pole is on the imaginary axis ($-u_i$) the function of equation 8 has the limiting form of a Debye relaxation function. When the pole is off the imaginary axis, equation 8 yields a Lorentz resonance. Once the poles are found, not only is the function known for all real filler values, it is also

known for all complex values of the filler. This analytic continuation into complex filler values can be performed on numerically computed as well as experimentally measured data.

Note that by the method of derivation, the five major variables that determine the properties of the mixture have been reduced to three: filler permittivity, total effective morphology and volume fraction. The host permittivity has been eliminated by normalization to 1. And the frequency dependence has been included implicitly through the frequency dependence of the filler. It can be shown that accounting for non-unity complex host values is straightforward within this analytic framework, however, because of space limitations, that derivation cannot be included here. Of the three remaining independent variables, the filler permittivity comprises the complex plane in which the effective susceptibility function exists. Therefore it follows that the two other variables must correspond to features in this plane. The total effective morphology is summarized by the sum of poles of equation 8, and the effect of the volume fraction (consistent with the uniformity assumption) is to modify the strength, quantity and position of these poles. Therefore, whenever we cast a given EMT expression in the form of an effective susceptibility as a function of u, we will call that representation the morphology function.

III - Application of the model to the cataloguing of EMTs

It is first convenient to define the limiting forms of EMTs. The minimum effective permittivity for any binary mixture that preserves three dimensional symmetry is the case where all the filler particles are collected into a single cubical region of volume p (side $l = \sqrt[3]{p}$ and cross sectional area $A = l^2$) at the center of the unit volume parcel.
Similarly, the maximum permittivity with three dimensional symmetry would be obtained if the filler particles were combined into a single region which lines the sides of the cubical unit parcel. In this arrangement the maximum amount of uninterrupted Displacement vector can flow from one capacitor plate to the other through the high dielectric filler material. This case is clearly equivalent to collecting all the air in the unit parcel into a cube of volume $(1-p$ centered in the unit parcel. By adding the elementary capacitances in these configurations we conclude that:

$$\varepsilon_{eff}^{\min} = \frac{1-A}{1} + \frac{1}{\frac{l}{\varepsilon A} + \frac{1-l}{A}} \tag{9}$$

Let $t = 1 - \sqrt[3]{1-p}$, then

$$\varepsilon_{eff}^{\max} = \frac{1}{\frac{t}{\varepsilon} + \frac{1}{\frac{(1-t)^2}{1-t} + 2\frac{\varepsilon t(1-t)}{1-t} + \frac{\varepsilon t^2}{1-t}}} \tag{10}$$

These two expressions turn out to be derivable from one of the oldest EMTs, the Clausius-Mosotti expression. For the minimum case of equation 9, the Clausius-Mosotti expression is simply modified by derating the volume fraction term with the ratio of the dipole moment of a dielectric sphere to the dipole moment of a metal sphere of the same dimensions: $(\varepsilon-1)/(\varepsilon+2)$. Thence:

$$\varepsilon_{cm} = \frac{1+2p\frac{\varepsilon-1}{\varepsilon+2}}{1-p\frac{\varepsilon-1}{\varepsilon+2}} \tag{11}$$

This expression is also known as the Maxwell-Garnet formula. The case of the maximum is obtained by exchanging the roles of the filler and the host in the Clausius-Mosotti expression. Therefore, we call this the Reverse-Mosotti expression:

$$\varepsilon_{rm} = \varepsilon\frac{1+2(1-p)\frac{1-\varepsilon}{1+2\varepsilon}}{1-(1-p)\frac{1-\varepsilon}{1+2\varepsilon}} \tag{12}$$

The equivalence of equations 11 and 12 to the sum of capacitance approximations of equations 9 and 10 is easily demonstrated by plotting the effective permittivity as a function of volume fraction, for a filler dielectric constant of 1000. The lower solid line of Figure 3 is the Clausius-Mosotti (CM) expression, the upper solid line of the figure is the Reverse-Mosotti (RM) expression, the dashed lines nearly overlapping them are the capacitance expressions. The reason these expressions are important is that they frame the space in which all EMTs must reside. They represent the two limits of total effective morphology: The first is a filler that never percolates until p=1 (CM), and the second is a filler that percolates immediately, even at p=0 (RM). Note specially that the CM expression converges to Maxwell's expression,

$$\varepsilon_{Maxwell} = 1 + 3p\frac{\varepsilon - 1}{\varepsilon + 2} \tag{13}$$

as p goes to zero, whereas the RM expression does not. Instead, it converges to:

$$\varepsilon_{perc}^{\min} = 1 + \frac{p(\varepsilon - 1)}{3} \tag{14}$$

Clearly, any given arbitrary binary mixture must have a behavior as a function of p that lies in between the two boundaries of Figure 3. How much of the filler percolates and how much remains isolated, as a function of p, will dictate where its curve falls in that space, and what its low p limit is. It is impossible to declare, *a priori*, that all binary mixtures must tend to the Maxwell limit. This is borne out by Doyle and Jacobs [3] who have shown that extreme particle morphologies can have such unexpected effects as percolation at very low volume fractions and the formation of large hollow clusters. Both phenomena violate the Maxwell limit.

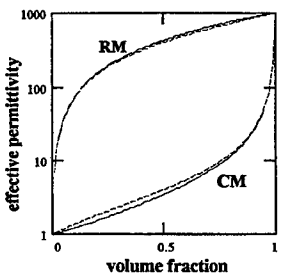

Figure 3. The upper and lower bounds of any EMT are given by the Reverse-Mosotti and Clausius-Mosotti expressions

Let us derive the total morphology function for these two limiting cases. By replacing ε with 1+*i*/*u* in equation 11, and assuming p>0, it is easy to show that, along the upper imaginary *u* axis:

$$e_{eff-cm}(u_i) = \left(\frac{3p}{1-p}\right)\frac{1}{1+\frac{u_i}{1-p}} \tag{15}$$

This is exactly the form a classic Debye relaxation takes on the imaginary frequency axis:

$$\varepsilon_{Debye} - 1 = \varepsilon_1 \frac{1}{1-j\omega\tau} \Rightarrow \varepsilon_1 \frac{1}{1+\omega_i\tau} = \varepsilon_1 \frac{1}{1+\frac{f_i}{f_{relax}}} \tag{16}$$

Thus, the quantity 3p/(1-p) plays the role of the excess permittivity ε_1 , *u* plays the role of the frequency, and 1-p plays the role of the relaxation frequency. For the RM expression it is easier to work with the equation 10. After some algebra it can be reduced to:

$$e_{eff-rm}(u_i) = \frac{1}{u_i}\left[2t(1-t) + t^2\right] + t(1-t)\frac{1}{1+\frac{u_i}{1-t}} \tag{17}$$

So that, in the case of the Reverse-Mosotti equation, the total morphology contains a pole at u_i=0 of strength $2t(1-t)+t^2$ and a Debye pole of strength $t(1-t)$ located at $u_i = -(1-t)$.

Consider now the Asymmetric Bruggeman EMT [4] obtained from solving the equation:

$$\frac{\varepsilon_{filler} - \varepsilon_{eff}}{\varepsilon_{fille} - \varepsilon_{host}} = (1-p)\left(\frac{\varepsilon_{eff}}{\varepsilon_{host}}\right)^{\frac{1}{3}} \tag{18}$$

Although as a function of p, this EMT is significantly different from CM (see Figure 4) , it consists of a distribution of Debye terms with relaxation frequencies so close to each other that it can be represented by a sum of only two terms. (Figure 5). This EMT does not percolate until p=1. On the other hand, the spherical cluster theory of Doyle and Jacobs [3] recast for non metallic inclusions yields a dielectric mixture that percolates at p=0.63 (see Figure 4). Its total morphology contains a pole at u=0 for p=0.63, but essentially only one Debye term below this threshold. In Figure 5, the morphology functions for the EMTs are shown as solid lines. To show how close they are to being single pole Debye curves, two such functions are plotted as dotted curves. The Asymmetric Bruggeman EMT is slightly flatter than a single pole of strength 14.8 at u_i=0.039, while the Cluster theory is nearly identical to a single pole of strength 48.4 at u_i=0.012.

As was done with these two functions, any desired EMT can be plotted as a function of u_i, and its poles numerically extracted by a suitable optimization procedure. Note that the differences between the two theories in the volume fraction plot of Figure 4 do not translate to significant differences in morphology. The lesson to be learned is that the volume fraction dependence curves can be deceiving. They reveal something about the total strength of the poles of the function, but not much more than that. And even this information tends to get lost if the curves are generated using conducting filler.

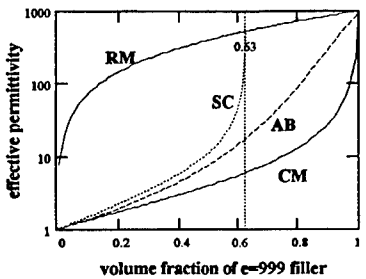

Figure 4. The Asymmetric Bruggeman (AB) EMT (dashed line) and the Spherical cluster (SC) theory of Doyle and Jacobs (dotted line) are similar at low volume fractions, p, but differ at high p.

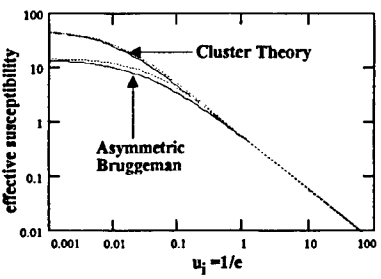

igure 5. Despite the differences in the EMTs of Figure 4 at p=0.6, their morphology functions (solid lines) are very close to single pole Debye expressions (dotted lines).

For reasons that will be explained in section IV, the most realistic EMTs should contain multiple Debye terms in their morphology function. They should also allow for the possibility of early percolation, which implies the existence of poles at u_i=0. And the approach to percolation should be characterized by a rapid increase in the spread of relaxation frequencies of the constituent Debye terms. One EMT exhibiting all these features is based on Percolation Theory [5], regularized to tend to the correct limits as p goes to 0 or 1. Figures 6 and 7 shows the behavior of this function, given by the solution to equation 19, for a percolation threshold p_c of 0.3. Figure 6 shows the function on the volume fraction plane. Figure 7 is a plot of the morphology function as the percolation threshold is approached from above and below.

$$b^2x^3 = (h + a\tau x)^2 \tag{19}$$

where $\varepsilon_{eff} = x\varepsilon_{filler}$, $h = \frac{\varepsilon_{host}}{\varepsilon_{filler}}$, $a = \frac{1-h^{1.5}}{1+\frac{1-p_c}{p_c}\sqrt{h}}$, $b = \frac{1-p_c+hp_c}{p_c+(1-p_c)\sqrt{h}}$, $\tau = \frac{p-p_c}{p_c}$

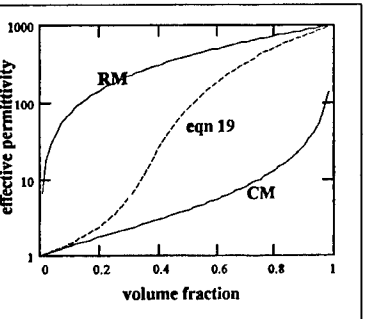

Figure 6. Volume fraction dependence of the realistically percolating EMT of equation 19.

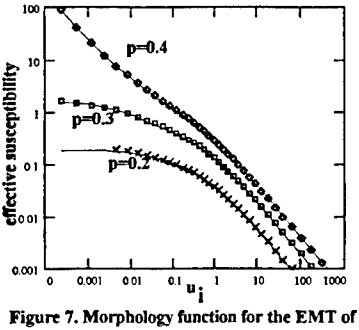

Figure 7. Morphology function for the EMT of equation 19, for pc=0.3, p=0.06, 0.2, 0.4

As done for the other EMTs, the poles of the morphology function for equation 18 can be extracted by a suitable optimization procedure. The solid lines in Figure 7 correspond to the following expressions:

$$\text{for p=0.06, } e_{eff} = \frac{0.092}{1+\frac{u_i}{0.6}} + \frac{0.092}{1+\frac{u_i}{0.038}}, \tag{20}$$

$$\text{for p=0.2, } e_{eff} = \frac{0.28}{1+\frac{u_i}{0.6}} + \frac{0.28}{1+\frac{u_i}{0.05}} + \frac{0.28}{1+\frac{u_i}{0.015}} + \frac{0.75}{1+\frac{u_i}{0.0035}} \tag{21}$$

$$\text{for p=0.4, } e_{eff} = \frac{0.52}{1+\frac{u_i}{0.6}} + \frac{0.52}{1+\frac{u_i}{0.08}} + \frac{0.52}{1+\frac{u_i}{0.02}} + \frac{2.2}{1+\frac{u_i}{0.009}} + \frac{0.021}{u_i} \tag{22}$$

As the percolation threshold is approached from below, the relaxation frequencies of the poles spread apart. One pole travels towards the origin and makes contact at $p = p_c$, and remains there, growing, as more material is added.

IV- The connection between dispersion in the u and ω planes

Consider a binary mixture properly described by an EMT that has been expressed in terms of its total morphology function as a sum of several Debye terms. For arbitrary complex u:

$$e_{eff}(u) = \sum_n \frac{A_n}{1 - i\frac{u}{u_{0n}}} \tag{23}$$

Let the filler's permittivity be $1 + i\frac{\sigma}{\omega\varepsilon_0}$. Then, $u = \frac{\omega\varepsilon_0}{\sigma}$ and therefore 35 is:

$$e_{eff} = \sum_n \frac{A_n}{1 - i\frac{\omega}{\omega_{0n}}}, \tag{24}$$

where

$$\omega_{0n} = \frac{\sigma}{\varepsilon_0} u_{0n} \tag{25}$$

is the Debye relaxation frequency of the nth term. Therefore, to every Debye relaxation in the u plane corresponds a Debye relaxation in the ω plane. This case of the purely conducting filler shows that the morphology function in the u plane can be observed in the ω plane. In particular, any binary mixture which is represented by a morphology function with multiple u-plane Debye relaxations, will also exhibit a highly dispersive, multiple relaxation behavior as a function of frequency. This is precisely the behavior of highly filled synthetic dielectrics. Figure 8 shows a plot of the permittivity of Emerson & Cumings' LS-20 carbon loaded foam material.

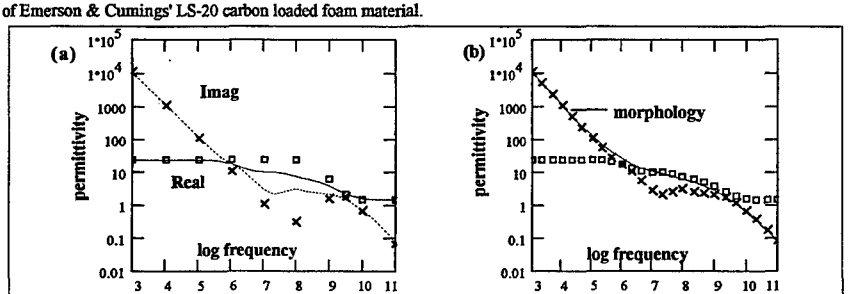

Figure 8. A manufactured carbon loaded foam exhibits a highly dispersive permittivity (a) (data=points, fit=lines). The form of the morphology function can be seen in this plane (b).

In Figure 8a, the published data is shown as points and the lines represent the closest physically realizable analytic fit to that data. Since the morphology function in the u-plane mirrors the value of the susceptibility along the imaginary axis in the ω-plane, it can be evaluated from this data. This is the solid line of Figure 8b, superimposed on the Real and Imaginary parts of the analytic fit of the permittivity (points).

The multiple Debye character of this frequency domain data (6 poles were used) is typical of most filled lossy materials. Therefore, by the connection between dispersion in the frequency domain and dispersion in the u-plane it follows that most effective media must be rich in Debye poles. This is why realistic EMTs must exhibit this behavior.

V- Conclusion

The synthetic dielectric composite is becoming increasingly important as an engineering material. The binary mixture, as its simplest instance, is the prototypical testbed for all theories that attempt to explain and predict its properties. An understanding of its functional behavior and its dependence on frequency, filler properties, host properties and the myriad parameters that result from the manufacturing process can only form a tractable problem if that behavior can be summarized in a few "state" variables. In this paper an analytic framework has been proposed that identifies those variables. The most important of those variables is the total morphology of the mixture, the result of the sum total of all manufacturing steps that yields a unique network of filler particles, clusters and chains inside the host medium. It has been shown that this total morphology, regardless of the manufacturing process, or the filler and host particulars, must take the form of an analytic function in the complex u-plane. This function can be compactly represented as a sum of poles whose locations and trajectories determine the behavior of the mixture.

It was pointed out that not all EMTs converge to the Maxwell limit at low volume fractions. On the volume fraction plane, early dispersing mixtures tend to align with the Clausius-Mosotti expression, while early percolating mixtures tend to align with the Reverse-Mosotti expression. The connection between dispersion in the u-plane and dispersion in the frequency domain led to the observation that realistic morphologies must contain multiple Debye poles. Therefore realistic EMTs are expected to transition from the CM limit to the RM limit as chains and clusters form, and induce percolation. By comparing the morphology of these candidate EMTs with the morphology that can be physically expected from a given manufacturing process, the engineer can select a realistic EMT that best fits that process. Once the EMT is selected, the morphology is fixed and can be used to examine the full range of material values obtainable from the manufacturing process as a function of filler and host properties.

References

[1] R. E. Diaz, and N. G. Alexopoulos, "An analytic continuation method for the analysis and design of dispersive materials", *IEEE Trans. Antennas Propagat.*, vol. 45, pp. 1602-1610, November 1997.

[2] N. G. Alexopoulos and R. E. Diaz, "A procedure for developing compact models of materials for numerical electromagnetics", in *Int. Radio Sci. Union Meet. Abstracts*, Ann Arbor, MI, June 28- July 2, 1993, p.264.

[3] W. T. Doyle and I. S. Jacobs, "The influence of particle shape on dielectric enhancement in metal-insulator composites.", *J. Appl. Phys.* vol. 71 (8), p.3926, 1992

[4] D. S. McLachlan, A. Priou, I.Cheniere, E. Isaac, F. Henry, "Modeling the permittivity of composite materials with a general effective medium equation", *J. Elec. Wav. Appl.*, vol. 6, (9), p.1099, 1992.

[5] Merrill, W. M., *Percolation theory in the design and analysis of artificial dielectrics*, Masters Thesis, UCLA Electrical Engineering, 1996.

Finite Grain Boundary Effects for Magnetic Materials: Tunneling and Intergrain Gaps

Gary G. Bush
Lockheed Martin Missiles and Space Company
1111 Lockheed Martin Way
Sunnyvale, CA 94088-3504

Introduction

Higher magnetic moment materials are required for magnetic storage media and high permeability magnetic materials are needed for VHF to microwave electromagnetic devices and applications. The advent of nanostructured materials holds the promise of providing these properties with very small nano scale grain structure. The ability to control the RF penetration of these nanostructured magnetic materials appears to lay in understanding the conductivity of these materials. The conductivity is proportional to the electron mean free path. This paper will discuss the effects on conductivity of finite grain size and various width gaps or barriers between individual grains. A Monte Carlo model has been devised to calculate the effect of tunneling between grains on the bulk conductivity of the material. The reduction in conductivity for various separations of grain boundaries are presented. The final conclusion is that the effect of tunneling on bulk conductivity for magnetic materials is small if the intergrain separation is more than about 20 angstroms (about 10 atomic diameters).

Conductivity, Grain Size, and Magnetics

The interaction of an electromagnetic field with matter, especially thin films, is a strong function of the conductivity, permeability, and permittivity of the material. The depth of penetration of a field into a surface is often described by the skin depth which is the depth at which the electric field intensity has decreased by 1/e or about 63%. The skin depth can be described by a complex number indicating a phase shift is also involved.

For materials with large grain size, the main effect on skin depth is due to permeability. The grain size can strongly influence the magnetic behavior as shown in Figure 1[1]. In storage applications, the coercivity of a material is quite important. Measurements by Herzer [1] indicate that for 5 common magnetic systems, the coercivity is a function of grain size. Permeability and grain size have been linked as described in Figure 2 [2] for manganese zinc ferrites. This paper will describe the connection between grain size and conductivity.

For a material with a grain size equal to many electron mean free path lengths, the size of the grain has little effect on conductivity. It is when the dimensions of a grain or material, such as a thin film, approach the electron mean free path length that

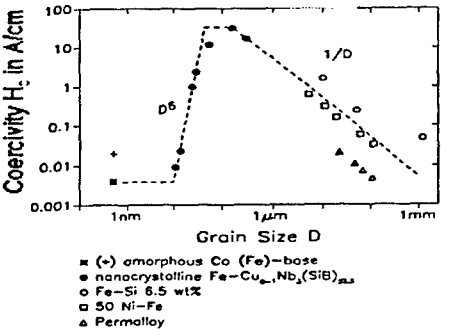

Figure 1. The effect of grain size on five common magnetic materials systems [1].

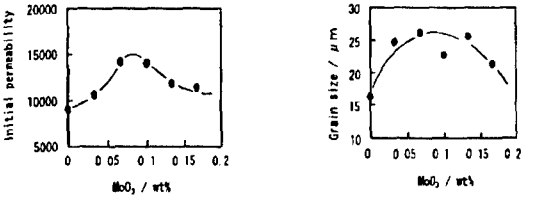

Figure 2. Grain size effects on permeability with wt% as the parameter for Manganese zinc ferrites [2].

the conductivity is affected. The impact on conductivity of having a very thin planar material is displayed in Figure 3 [3]. The normalized conductivity σ/σ_0 is plotted as a function of the thickness, λ, of an thin slab (a slab that is infinite in two dimensions and very thin in the third direction) with thickness normalized to the bulk electron mean free path length. The three solid curves represent various assumptions about the electron scattering at the boundary. P=1 would corresponds to a simple specular reflection (the largest P shown is 15/16) and P=0 then corresponds to a random reflection direction. The dashed curve represents the measured results. As is shown, the conductivity decreases dramatically as the slab becomes thin compared to an

electron mean free path. This research presented in references 1-3 motivated the calculations reported here on grain effects on conductivity.

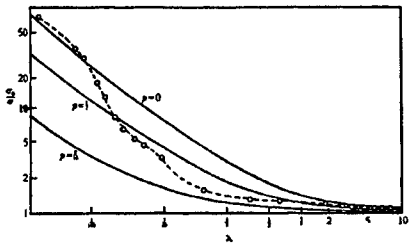

Figure 3. The electron mean free path length as a function of the thickness of an infinite planar slab of conductor [3].

Grain Size, Gaps, and Tunneling

As described earlier, when grain dimensions approach the electron mean free path length, a decrease in conductivity would be expected. A typical path length at room temperature is about 200 angstroms. Thus nanostructured materials are within the range of this phenomena. A very simple calculation was done that assumed the grain shape was square and the grains were regularly spaced on a rectangular lattice. The Monte Carlo calculation presented here was done to find the effect of the grain size on conductivity. With reference to Figure 4, a random number is used to pick an initial location for an electron. A second random number determines the angle, θ, of travel for the electron.

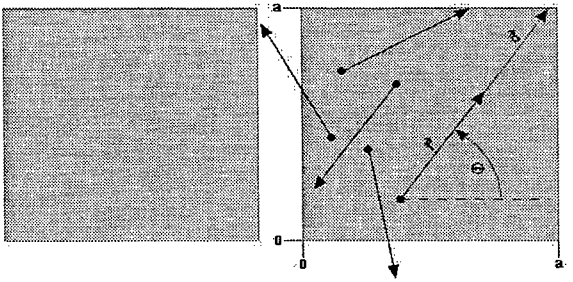

Figure 4. Square grains and electron paths for the Monte Carlo calculation of effective electron mean free path length.

The first case treated was for an insulating grain boundary which did not allow the electron to tunnel to another grain and continue its path. In this first case, if the distance from the starting point to the boundary of the grain is more than a mean free path, the electron path is assigned to be one mean free path length. If the distance is less than one path length, the path length becomes the actual distance between the starting point and the boundary. The path length for many thousands of simulated electrons are then averaged to get the new mean free path length. If the grain shape had been circular, the expected result would be that the new average path length would be half of the grain diameter when the grain diameter was at or less than the mean free path length. For the square grain used here, the result should be a little greater as the electron can travel further when it is going in the direction of one of the four corners. Figure 5 shows the result of this calculation and as expected the new path length is slightly longer than the grain dimension. In Figure 5 the effective mean free path normalized to the bulk mean free path is plotted as a function of the grain size, A, as in Figure 4.

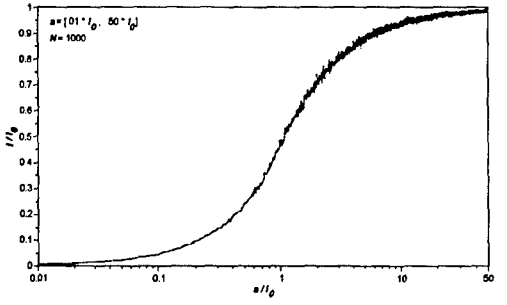

Figure 5. Reduced effective electron mean free path length verses square grain size for infinite intergrain gaps, isolated grains.

The new path length varies smoothly from a very small value for tiny grains to an asymptotic value (the bulk mean free path length) as the grain size becomes large compared to the bulk mean free path. The effect is only strongly evident when the grain size is below 200 angstroms. It is worth noting that there is an effect of a few percent even when grain sizes are several thousand angstroms.

The most efficient way to extend the path from one grain to the next is to assume a resonant coupling between energy levels in atoms on either side of a grain boundary. Under this condition, the electron does not experience an energy loss and thus travels its full mean free path. The probability of this occurring is given by the tunneling probability. The Monte Carlo calculation reported here was done for several gap widths. Figure 6 shows the effect on the effective mean free path due to intergrain

tunneling. The axes are the same as in Figure 5 with the various curves referring to finite gap widths between grains. The effect is only evident when the gap length is less than 20 angstroms. This case is often met in practical materials where grain boundaries are defined by dislocation, inclusion , and voids. The effect is still not a very strong one.

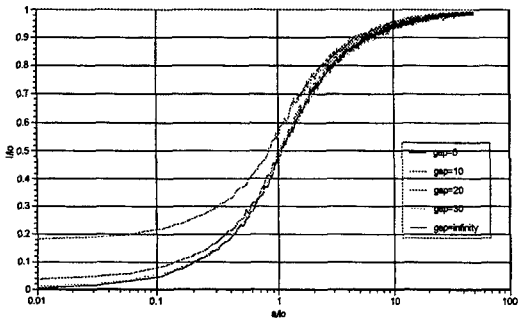

Figure 6. Tunneling effect on the effective mean free path for various intergrain gaps.

If a larger gap is assumed, a potential barrier theory would account for the change in new mean free path and thus conductivity. The wave function of the electron decreases in amplitude exponentially as it traverses the gap. This mechanism would not be as efficient as the resonant tunneling effect. Since the tunneling calculation did not indicate a significant increase in conductivity, it would not be expected that barrier penetration would be a strong contributor to electron path length.

Conclusions

When nonstructural materials have grain sizes below the 200 to 400 angstrom range, the conduction of the material will be effected by the grain size. The skin depth will be greater and thus provide stronger interaction between RF fields and the material. Conductivity effects extending between grains are not likely to prove important if the gap exceeds 30 angstroms regardless of the mechanism. If the grains are touching such that the energy bands of the surface atoms of each grain are overlapping, the conduction will be anisotropic and greatest in along the axis of the joined grains. The question then arises as to whether to consider this case as two or more grains or simply as a larger agglomerated grain with a larger characteristic dimension. The control of the conductivity of a material is key to their application at higher frequencies. A better understanding of grain boundaries and impurities on the boundary will lead to the effective tailoring of the constitutive parameters.

Acknowledgments

The author would like to acknowledge the efforts of Ms. Patricia Maloney, who wrote the software for the Monte Carlo calculations and did the graphics for the plots and this paper.

References

1.) G. Herzer, IEEE Trans. On Magn. Vol. 26, pg. 1397 (1990).

2.) Y. Matsuo, K. Ono, M. Ishikura, I. Sasaki, To be published in IEEE Trans. On Magn., Nov., 1997.

3.) A. H. Wilson, The Theory of Metals, 2nd edition, Cambridge Press, pg. 246, 1958.

Numerical Computation of the Complex Dielectric Permittivity: FFT-Based Hilbert Transform Approximation of the Kramers-Kronig Relations

Francisco Castro and Bahram Nabet
Electrical and Computer Engineering Departmnet
Drexel University

Introduction

The complex nature of some physical parameters is such that their frequency-dependent real and imaginary components cannot be specified independently from each other [1]. This is the case for the complex dielectric permittivity, $\varepsilon(\omega)=\varepsilon'(\omega)+i\varepsilon''(\omega)$, and the complex magnetic susceptability, $\chi(\omega)=\chi'(\omega)-i\chi'(\omega)$, where the coupling between real and imaginary components is provided by the Kramers-Kronig relations, one of the most commonly encountered cases of dispersion relations in physical systems. Since $\varepsilon(\omega)$ provides a parametric relationship for the interaction of solids with electromagnetics fields, then the Kramers-Kronig relations becomes the analogous to a data compression algorithm for this relationship, i.e., only the real or the imaginary component of the complex function is necessary to fully define its operation.

For semiconductor materials $\varepsilon(\omega)$ also becomes a fingerprint tof the physical phenomena acting in the medium; these phenomena include electric field profiles, doping concnetration profiles, temperature variations, etc. It is this underlying information provided by the dielectric permittivity which allows its use as a diagnostic parameter from which to extract, isolate, identify, and fully describe physical effects. Because of these features, information about $\varepsilon(\omega)$ becomes particularly suitable for modeling and analyzing multilayer and non-symmetrical semiconductor structures.

In most experimental procedures the dispersion relation of the real and imaginary components of a complex physical parameter are obtained simultaneously. For the complex dielectric permittivity this is achieved by photoreflectance measurements where both amplitude and phase readings provide a full description of the complex function. However, occasions arise when only one of the components of the complex function can be readily obtained from experimental procedures or theoretical analysis. In these cases the other component must be found through the Kramers-Kronig relations [2,3]. The analytical technique which defines one component in terms of the other i the Hilbert transform since the real and imaginary parts of the complex function are Hilbert transform pairs. To construct this Hilbert transform pair is not an easy task, in most instances we cannot produce an analytic function, i.e., an equation, which fully describes the frequency-dependent readings of the known component in order to obtain its Hilbert transform. Even if we were able to produce such a function, we have no guarantee that the solution is a managable equation which is easily computed by numerical methods. Fanning et. al. have demonstrated an efficient numerical algorithm that constructs the imaginary part of the complex magnetic susceptability from its real part based on the computation of the Hilbert transform with Fast Fourier Transform (FFT) techniques. This approach untilizes the speed and common availability of FFT routines in commercial packages to compute the complex magnetic susceptability without the need to produce analytical solutions.

In this paper we show that the complex dielectric permittivity of semiconductor materials can be numerically computed from its imaginary component following a similar computational algorithm to that used by Fanning et. al. Because of the cyclic nature of the computation, it is possible to make use of

Fourier transform properties to apply currently available Hilbert transform routines in commercial packages directly on experimental readings without need for unit conversions. We then show how this technique works efficiently for semiconductor materials such as GaAs and InAs when the spectral bandwith of the experimental readings is relatively large. We have not included the effects that limited bandwidth or bandpassed spectral readings of $\varepsilon''(\omega)$ have in constructing $\varepsilon'(\omega)$; additional signal processing techniques are required in such cases to construct an accurate respresentation of $\varepsilon'(\omega)$ over the sampled range of $\varepsilon''(\omega)$.

Complex Dielectric Permittivity

The induced electric polarization P in a semiconductor material is due to the causal response of the medium to an electric field E as given by [4]

$$P(t) = \varepsilon_o \int_{-\infty}^{t} \chi(t-\tau) E(\tau)\, d\tau \tag{1}$$

where $\chi(t)$ is the electric susceptability of the medium and ε_0 is the permittivity of free space; the integration over τ is from $-\infty$ to t since the response $P(t)$ results from the excitation field before time t. Since

$$D(t) = \varepsilon_b E(t) + P(t) \tag{2}$$

we find in the frequency domain

$$D(\omega) = \varepsilon(\omega) E(\omega) \tag{3}$$

by taking the Fourier transform of equation (2), where

$$\varepsilon(\omega) = \varepsilon_b + \varepsilon_o \int_0^{\infty} \chi(\tau) e^{i\omega\tau}\, d\tau \tag{4}$$

is the complex dielectric permittivity function and ε_b is the background permittivity of the medium. Since $\chi(t)$ is a real function, from the symmetry properties of the Fourier transforms we see that

$$\varepsilon(\omega) = \varepsilon^*(\omega) \tag{5}$$

If we write $\varepsilon(\omega)$ in terms of its real and imaginary parts,

$$\varepsilon(\omega) = \varepsilon'(\omega) + i\varepsilon''(\omega) \tag{6}$$

we find that

$$\varepsilon'(-\omega) = \varepsilon'(\omega) \tag{7}$$

$$\varepsilon''(-\omega) = -\varepsilon''(\omega) \tag{8}$$

in other words, $\varepsilon'(\omega)$ has even symmetry about the origin, while $\varepsilon''(\omega)$ has odd symmetry about the origin.

In addition to the previous physical description of $\varepsilon(\omega)$, the Kramers-Kronig realtions provide a way to specify $\varepsilon'(\omega)$ and $\varepsilon''(\omega)$ in terms of each other by

$$\varepsilon'(\omega) = \varepsilon_b + \frac{1}{\pi}\int_{-\infty}^{\infty} \frac{\varepsilon''(\omega')}{\omega' - \omega} d\omega' \tag{9}$$

$$\varepsilon''(\omega) = -\frac{1}{\pi}\int_{-\infty}^{\infty} \frac{\varepsilon'(\omega') - \varepsilon_o}{\omega' - \omega} d\omega' \tag{10}$$

Under low electromagnetic field conditions we can assume that the system remains linear and causal so that the relations just desribed hold.

Numerical Computation of the Hilbert Transform

The Hilbert transform of a function x(t) is defined as

$$\hat{x}(t) = \frac{1}{\pi t} * x(t) = \frac{1}{\pi}\int_{-\infty}^{\infty} \frac{x(\lambda)}{t - \lambda} d\lambda \tag{11}$$

where * indicates the convolution operation. The Hilbert transform operation corresponds to phase-shifting all frequency components of x(t) by 90° and it is equivalent to passing the signal x(t) through a linear system with frquency response

$$h(t) = \frac{1}{\pi t} \tag{12}$$

whose Fourier transfer function is given by

$$H(f) = -j\,\mathrm{sgn}(f) \tag{13}$$

Using the convolution theorem, equation (11) can be written in the frequency domain as

$$\hat{X}(f) = H(f)X(f) = -j\,\mathrm{sgn}(f)X(f) \tag{14}$$

where $\hat{X}(f)$ and $X(f)$ are the Fourier transforms of $\hat{x}(t)$ and $x(t)$ respectively. From the previous section we see that equations (9) and (10) are of the same frequency-dependent integral form as equation (11) and can be rewritten as

$$\varepsilon'(\omega) = \varepsilon_b - \frac{1}{\pi}\int_{-\infty}^{\infty} \frac{\varepsilon''(\omega')}{\omega - \omega'} d\omega' = \varepsilon_b - \hat{\varepsilon}''(\omega) \tag{15}$$

$$\varepsilon''(\omega) = \frac{1}{\pi}\int_{-\infty}^{\infty} \frac{\varepsilon'(\omega') - \varepsilon_o}{\omega - \omega'} d\omega' = \hat{\varepsilon}'(\omega) \tag{16}$$

where ε_o in equation (16) dissapears since the Hilbert transform of a constant value is zero. We see clearly in this new representation of equations (9) and (10) that they are indeed Hilbert transforms of each other.

Rather than describe the implementation of the Hilbert transform or "noise-free derivative" in the frequency domain, which happens to be a straightforward and methodic algorithm, it is of far more relevance to prepare the experimental data of $\varepsilon''(\omega)$ to produce $\varepsilon'(\omega)$ in a fast and easy to hanlde manner. While the Hilbert transform is more easily thought of as a phase-shifting procedure once the information is transformed to the frequency domain, we need to consider that the experimental data is already a function of frequency. We overcome this fact by the duality principle of Fourier transforms; thus, the experimental data is more conveniently written as

$$e''(t) = \varepsilon''(-\omega) = \varepsilon''(-f) \tag{17}$$

where the last equality arises from the cyclic nature of the overall computation, i.e., variable scaling into one domain is cancelled when the data is transformed back to the original domain. Because we need both positive and negative values of $e''(t)$, we use the symmetry property outlined in equation (8) and write the data to be Hilbert-transformed in the following format

$$e''(t) = -\varepsilon''(\omega) \tag{18}$$

$$e''(-t) = \varepsilon''(\omega) \tag{19}$$

The frequency-dependent function represented by equations (18) and (19) is first Fourier-transformed with the FFT routines and then Hilbert-transformed by phase-shifting as described in equation (13). Once this operation is performed the inverse-FFT returns the Hilbert-transformed vesion of $e''(t)$. Backtracking our previous steps we see that

$$\hat{e}''(t) = \hat{\varepsilon}''(-\omega) = -\hat{\varepsilon}''(\omega) \tag{20}$$

and therefore

$$\varepsilon'(\omega) = \varepsilon_b - \hat{\varepsilon}''(\omega) = \varepsilon_b + \hat{e}''(t) \tag{21}$$

such that the real part of $\varepsilon(\omega)$ results directly from the computation of equation (21). So far the steps to obtain the complete complex dielectric permittivity has been outlined but a few items remain to be clarified. The experimental data set which has been used to produce $e''(\omega)$ assumes that equally spaced samples in frequency have been taken and that a DC or f=0 value has been included. Large spectral bandwidth is also necessary to guarantee that the integral form of the Hilbert transform, with range of $[-\infty,\infty]$, is approximated as accurately as possible by the numerical computation. Band-limited samples require additional signal processing similar to those used in short-time Fourier transfroms and wavelet transforms [5,6].

Applications to Semiconductor Materials

The need to test this technique on known Hilbert transform pairs is imperative, but must become a simple computational exercise. For this purpose we have found that the complex dielectric permittivity properties of semiconductor materials provide the needed and essential ground for proving the effectiveness of this procedure. Figure 1 and Figure 2 show experimentally obtained complex dielectric permittivity components of InAs and GaAs respectively [7] with the computed real component also shown. It is clear from these figures that the computed real component of $\varepsilon(\omega)$ is to some extent accurate, although slight variations arise in places where the original $\varepsilon''(\omega)$ changes rapidly. This problem is inherent to the frequency domain-based Hilbert transform computation, and is similar in nature to frequency-based derivative operations.

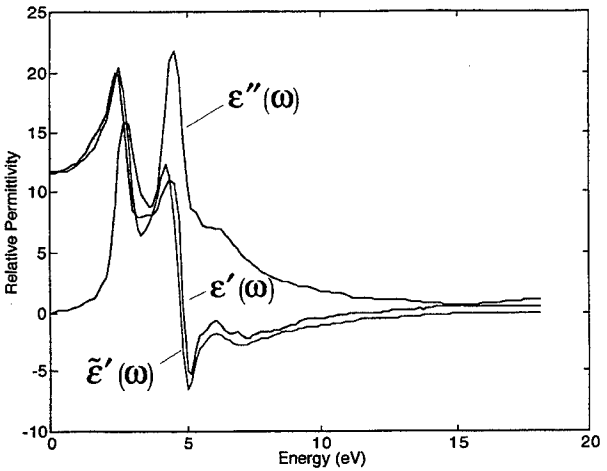

Figure1. Complex dielectric permittivity $\varepsilon(\omega)$ of InAs with reconstructed real part $\tilde{\varepsilon}'(\omega)$.

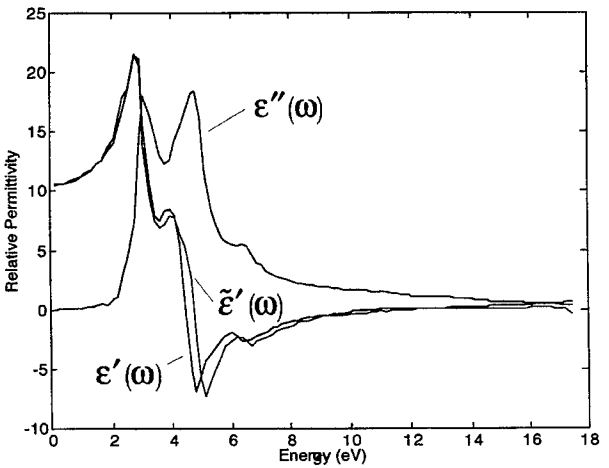

Figure 2. Complex dielectric permittivity $\varepsilon(\omega)$ of GaAs with reconstructed real part $\tilde{\varepsilon}'(\omega)$.

Conclusions

The possibility of providing a full picture of the complex behavior of physical phenomena from either the real or imaginary component becomes a useful tool when limitations arise in the experimental analysis of different materials or when theoretical computations prove to be managable for only one of the components. Furthermore, it can be used to improve and speed up some experimental procedures and modeling processes by reducing the information required in order to completely understand the events at hand. It is for this reason that to numerically compute the complex dielectric permittivity making use of the Hilbert transfrom pair relation between its real and imaginary components becomes immediately applicable to the understanding of semiconductor structures and materials.

The computational outline described in this paper shows encouraging results and proves its usefulness in studying the optical properties of semiconductor materials. A clear advantage arises from the simple data manipulation which allows for available computational algorithms and routines in commercial software applications to be used. One of the original objectives of the analysis was to provide an implementable and practical methodology to study and model physical phenomena in multilayer semiconductor structures. Even with this early success, additional work is required for cases when the available data sample is limited in bandwidth and the ideal limits of the Kramers-Kronig relations become bounded by the finite sample range.

References

[1] G. W. Milton, D. J. Eyre, and J. V. Mantese, "Finite Frequency Range Kramers Kronig Relations: Bounds on Dispersion," *Physical Review Letters*, vol. 79, no. 16, 1997, pp. 3062-3065.

[2] J. Bertie, Shuliang Zhang, "Infrared intensities of liquids. IX. The Kramers-Kronig transform, and its approximation by the finite Hilbert transform via Fast Fourier Transforms," *Canadian Journal of Chemistry*, vol. 70, no. 2, 1992, p. 520-539.

[3] P. C. Fannin, A. Molina, and S. W. Charles, "On the generation of complex susceptability data through the use of the Hilbert transform," *Journal of Physics D: Appied Physics*, vol. 26, 1993, pp. 2006-2009.

[4] Shun Lien Chuang, *Physics Of Optoelectronics Devices*, John Wiley and Sons, New York, 1995, pp. 337-345.

[5] Huang Dishan, "A Wavelet-Based Algorithm for the Hilbert Transform," *Mechanical Systems and Signal Processing*, vol. 10, no. 2, 1996, pp. 125-134.

[6] H. Boche and M. Protzmann, "A New Algorithm for the Reconstruction of Bandlimited Functions and Thier Hilbert Transform," *IEEE Transactions on Instrumentation and Measurements*, vol. 46, no. 2, 1997, pp. 442-444.

[7] H. R. Philipp and H. Ehrenreich, "Optical Properties of Semiconductors," *Physical Review*, vol. 129, no. 4, 1963, pp. 1550-1560.

Rayleigh Analysis of Novel Dense Medium Exhibiting Narrow-Band Transparency Window

Sissy A. Kyriazidou[a], Rodolfo E. Diaz[b], Nicólaos G. Alexópoulos[c],

[a]Department of Electrical Engineering
University of California Los Angeles, Los Angeles, CA 90095
Fax: (310) 206-5306, e-mail: kyria@ee.ucla.edu

[b]Northrop Grumman Corporation
Chandler, AZ 85224

[c]Department of Electrical and Computer Engineering
University of California Irvine, Irvine, CA 92697
Fax: (714) 824-7966, e-mail: alfios@uci.edu

Abstract

The effective permittivity function has been calculated for a dense amorphous mixture consisting of a dielectric host loaded with lossy spheres coated with a highly resonant dielectric layer. The problem is solved exactly by assuming an ordered rather than random arrangement for the inclusions and thus applying the Rayleigh model for the composite medium. This study completes our previous examination of a sparse such material and indicates the existence of two sharp narrow-band transparency windows in an otherwise reflecting spectrum. Unique only to the dense medium is a characteristic region with real permittivity function less than unity, applicable in printed circuit antenna systems.

1 Introduction

Media with frequency selective properties have been traditionally constructed by forming periodic structures of size comparable to the wavelength, for use in radomes, filters, multiband antenna systems or radio frequency absorbers. In reference [1], we presented an alternative approach of creating filtering properties from an amorphous composite structure based on the physical resonant properties of the constituents and the geometry of the inclusions. In this manner, a bulk material rather than a lattice formation is used to manipulate and shape electromagnetic propagation. In particular, we considered an amorphous sparse composite consisting of a dielectric loaded with lossy spheres coated with a highly resonant dielectric layer. The concentric geometry of the inclusions simulated a similar structure which was postulated in order to explain the optical transparency of water according to the Analytic Theory of Dielectrics [2]. Based on the Theory of Effective Media (EMT), our analysis revealed a lossy, reflective medium over its entire spectrum, except of two narrow-band transparency windows with adjustable

depth, shape and positioning controlled by the choice of constituent media and geometry.

In the present work we complete the analysis by extending it to high density media beyond the limits of the EMT, i.e., for filling fraction greater than 0.35, where the size of spherical inclusions increases up to the point where they almost touch. Our motivation is to examine the effects on the window formation and in particular the window shaping capabilities. This extension requires a rigorous semi-static solution, beyond the dipole approximation of EMT, that takes into account all multipole moments in the expansion of the induced field. The analytical study of such structures is possible in terms of a method devised by Lord Rayleigh[3] and extended more recently for the calculation of conductivity and magnetic permeability of lattice of conducting spheres[4, 5, 6]. In the Rayleigh model the composite is represented by a simple cubic lattice of coated spheres imbedded in a dielectric host material. The regular rather than random arrangement of the inclusions is a very good approximation in the case of a random medium that is dense. Moreover, it allows to take into account all multipole interactions analytically in the form of a series expansion in powers of the filling fraction[6].

The design of the dense composite medium complements and completes our previous study[1] of a sparse medium with transparency windows in the bulk, to be applied for fabrication of Thin Absorbing Films. A result that characterizes uniquely the dense composite is the existence of a region of real effective permittivity, ϵ^r_{eff}, less than unity. Such media are shown to be valuable for antenna applications since when used as substrates in multilayered geometries they lead to elimination of surface waves and thus increased antenna efficiency[7].

2 High-density Medium - Rayleigh Formalism

The Rayleigh model is applied to an infinite simple cubic lattice of identical spherical coated particles depicted in figure 1, where,

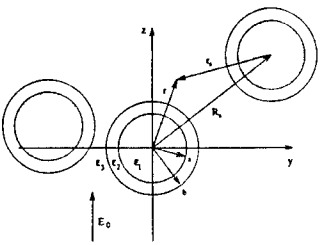

Figure 1: Composite with concentric inclusions.

$$\epsilon_1 = \epsilon_1^r - j\,4\pi\frac{\sigma_c}{\omega}, \quad \epsilon_2 = 1 + \frac{A}{\omega_0^2 - \omega^2 + j\omega\Gamma}, \quad \epsilon_3 = \epsilon_3^r, \tag{1}$$

are the permittivities of the core, layer and host dielectric, respectively. The medium response to an external slowly-varying electromagnetic field is given by the solution of Laplace's equation. The multipole expansions appropriate to the core, shell and exterior of this central sphere are:

$$r < a: \qquad V_1(r,\theta,\phi) = C_0 + \sum_{l=1}^{\infty}\sum_{m=-l}^{l} C_{lm}\left(\frac{r}{b}\right)^l Y_{lm}(\theta,\phi), \tag{2}$$

$$a < r < b: \qquad V_2(r,\theta,\phi) = D_0 + \sum_{l=1}^{\infty}\sum_{m=-l}^{l}\left(D_{lm}\frac{r^l}{b^l} + E_{lm}\frac{b^{l+1}}{r^{l+1}}\right)Y_{lm}(\theta,\phi), \tag{3}$$

$$r > b: \qquad V_3(r,\theta,\phi) = A_0 + \sum_{l=1}^{\infty}\sum_{m=-l}^{l}\left(A_{lm}\frac{r^l}{b^l} + B_{lm}\frac{b^{l+1}}{r^{l+1}}\right)Y_{lm}(\theta,\phi), \tag{4}$$

respectively. The symmetry of the problem requires V to be antisymmetric in θ about $\theta + \pi/2$ and symmetric with ϕ about $\phi = \pi/2$ which yield:

$$l = 1, 3, 5..., \; m = 0, \pm 4, \pm 8... \tag{5}$$

The coefficients A_{lm}, B_{lm}, C_{lm}, D_{lm}, E_{lm} are determined by applying the standard boundary conditions at the interfaces among core, shell and host media

$$B_{lm} = R_l\, A_{lm} \tag{6}$$

where,

$$R_l \equiv \frac{1 + \frac{l}{l+1}\,p_l - \frac{\epsilon_2}{\epsilon_3}(1-p_l)}{\frac{l+1}{l} + p_l + \frac{\epsilon_2}{\epsilon_3}(1-p_l)}, \qquad p_l = \left(\frac{a}{b}\right)^{2l+1}\frac{1 - \frac{\epsilon_1}{\epsilon_2}}{1 + \frac{l}{l+1}\frac{\epsilon_1}{\epsilon_2}}. \tag{7}$$

In the limit $\epsilon_2 \to \epsilon_1$ or $r \equiv \frac{a}{b} \to 1$ we obtain

$$R_l \to \frac{1 - \frac{\epsilon_1}{\epsilon_3}}{\frac{l+1}{l} + \frac{\epsilon_1}{\epsilon_3}} \tag{8}$$

which is precisely the value for uncoated spherical inclusions.

A second relation among A and B is obtained by means of the Rayleigh technique which utilizes the periodicity of the system. The idea is to recognize that in equation (4), terms with negative powers of r are contributions to the potential coming from induced multipole moments on the central sphere, while terms with positive powers of r stem from the multipole moments on all other spheres and the external field:

$$A_0 + \sum_{l=1}^{\infty}\sum_{m=-l}^{l} A_{l,m}\left(\frac{r}{b}\right)^l Y_{l,m}(\theta,\phi) + E_0 r\cos\theta = \sum_{s=1}^{\infty}\sum_{l=1}^{\infty}\sum_{m=-l}^{l} B_{l,m}\left(\frac{b}{r_s}\right)^{l+1} Y_{l,m}(\theta_s,\phi_s). \tag{9}$$

This is an identity with respect to $\mathbf{r}$ valid in the immediate environment of the central sphere. The subscript s enumerates all spheres except the one at the origin and r_s, θ_s, ϕ_s are the coordinates of the observation point $\mathbf{r}$ with respect to the center of the sth sphere. Referring to figure 1, we have:

$$\begin{aligned} \mathbf{r}_s &= \mathbf{r} - \mathbf{R}_s \\ \mathbf{R}_s &= \alpha_s c\hat{\mathbf{x}} + \beta_s c\hat{\mathbf{y}} + \gamma_s c\hat{\mathbf{z}}, \qquad \alpha_s,\ \beta_s,\ \gamma_s = 0, \pm 1, \pm 2, ... \end{aligned} \tag{10}$$

The simultaneous solution of equations (7) and (9) determines the quantity $p = B_{10} b^2$ which is precisely the dipole moment per sphere in the presence of all other spheres, that is, taking into account the multipole moment interactions with the external field as well as the interactions among spheres. Following the iterative solution of ref. [6], the effective permittivity is found

$$\epsilon_{eff} = \epsilon_3 \left(1 + \frac{3f}{\Lambda(f)} \right) \tag{11}$$

where,

$$\begin{aligned} \Lambda(f) \equiv \frac{E_0 b}{B_{10}} &= -\frac{1}{R_1} - f + 1.3045\ R_3 f^{10/3} \\ &+0.0723\ R_5 f^{14/3} - 0.5289\ R_3^2 f^{17/3} + 0.1526\ R_7 f^6 \end{aligned} \tag{12}$$

where, the volume fraction $f = 4\pi b^3/3c^3$, c being the lattice size and R_l, as given in eq. (7), expresses the composition of the spherical inclusions.

3 Transparency Windows

The dispersive properties of the novel composite over four frequency decades are shown in figure 2. For $r \to 1$ the resonant shell disappears and the effective medium exhibits Debye-type permittivity represented in dashed line.

The narrow-band, low-loss transparency windows are driven by the Lorentzian permittivity of the coating. Such dielectric functions are common in spectroscopy and they represent atomic phenomena which may be modeled to a great accuracy by the single or multiple damped oscillator model[8]. The values of the Lorentzian parameters, Γ, ω_0, A, indicated in the figures actually represent quantities scaled with respect to the core conductivity σ_c (with units sec^{-1} in the Gaussian system of units). The values chosen for these parameters reflect known spectroscopic data[9]. In particular, the parameter A, also known as the plasma frequency, $A = \omega_p^2$, when computed from its fundamental definition[8], is estimated to be the same order of magnitude as the resonant frequency ω_0.

Similarly to the results of the Clausius-Mossotti model[1], the window location depends exclusively on the Lorentzian parameters given as

$$\omega_{left} = \omega_0, \qquad \omega_{right} = \omega_0 \left(1 + A/\omega_0^2 \right)^{1/2} . \tag{13}$$

The window formation for a variety of r, f values is depicted in figure 3. In particular, the bandwidth depends mainly on the layer thickness and increases for thicker shell.

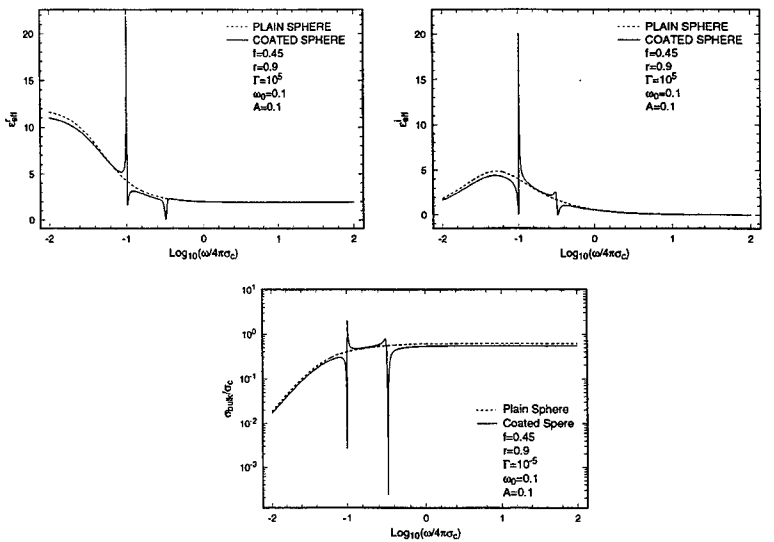

Figure 2: Effective permittivity from Rayleigh formulation of composite. Two narrow-band low-loss transparency windows appear in the bulk conductivity σ_c.

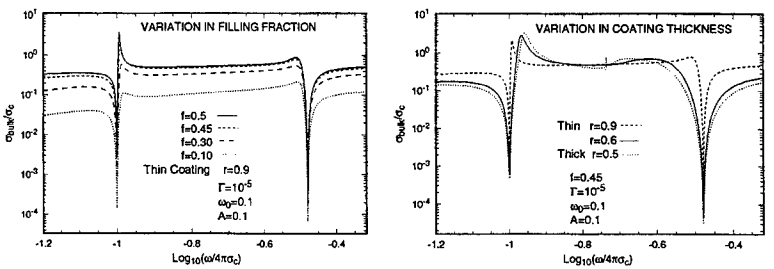

Figure 3: Variation in f (left) and r(right) of window formation from Rayleigh formulation of composite.

4 Real Effective Permittivity Less than Unity

The dispersion of the real effective permittivity, shown in figure 2a, also exhibits interesting characteristics in dense media. In particular, as the filling fraction becomes larger, the right-side disturbance of figure 2a increases in depth and width. The disturbance drops below unity for filling fractions above 0.30 and becomes negative for filling fractions greater than 0.46, as indicated in figure 4a. These results are even more pro-

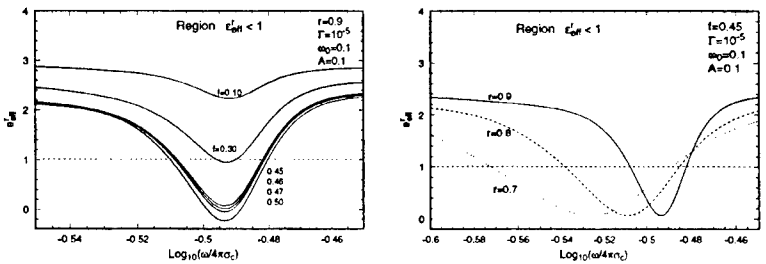

Figure 4: Region $-\infty < \epsilon^r_{eff} < 1$ from Rayleigh formulation of dense composites

nounced as the real part of the permittivity of the core increases. Moreover, according to figure 4b, this region becomes broader with increasing layer thickness.

The values $-\infty < \epsilon^r_{eff} < 1$ characterize a medium with quite unique properties in the sense that the phase and group velocities are greater than the speed of light in vacuum. Nonetheless, Brillouin and Sommerfeld[10, 11] have shown that these are physically realizable media, satisfying the causality requirements and characterized by the non-local nature of the wave propagation. Accordingly, it may be shown that the actual speed of signal propagation within our composite is less than the speed of light in vacuum and the physical picture of the wave propagation does not have the standard features. The wave packets are not formed in some strictly localized region, but rather consist of initial transient waves, the 'Sommerfeld' and 'Brillouin precursors', followed by a steady-state wave propagating in the medium according to the given complex permittivity functions. In particular, during absorption the amplitude is diminished according to the complex nature of the refractive index. The performance of a thin film made out of the novel mixture is described in figure 5.

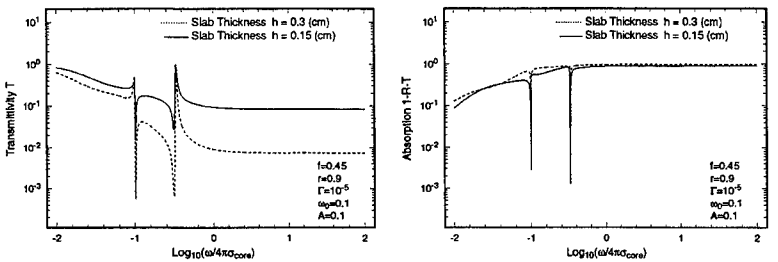

Figure 5: Thin film performance in normal incidence.

5 Conclusion

We have combined two items, namely, the physical sharp resonances of the medium used in the layer, and the particular concentric geometrical design, to create a novel medium with natural frequency selective properties exhibited in the bulk. We have analyzed a dense such medium in terms of the Rayleigh model which gives an exact characterization of the medium response to an external slowly varying electromagnetic field. In comparison to the design of the sparse medium[1] we observe a similar window formation with a small (less than one order of magnitude) increment in the window depth.

The artificial composite is seen to have two interesting engineering applications. First, it constitutes a lossy reflecting medium exhibiting in the bulk two narrow-band, sharp, transparency windows within its entire spectrum. Such a medium may be applied as a Thin Absorbing Film, bypassing the drawbacks of traditional media. Secondly, it possesses a region in the frequency spectrum where the real dielectric function is less than unity. This property is applicable in printed circuit antenna technology since it may result in enhancement of antenna efficiency. This is due to the elimination of surface waves[7] which requires thin substrates, thus leading to a diminished radiative power, unless such small permittivities are used.

References

[1] S.A. Kyriazidou, R.E. Diaz, N.G. Alexópoulos, "Coated Spheres as Constituents of a Novel Artificial Dielectric and as scatterers in a Photonic Band Gap Material", 1997 U.R.S.I. North American Radio Science Meeting, Montreal, Canada, p.747.

[2] N.G. Alexópoulos, R.E. Diaz, "An Analytic Continuation Method for the Analysis and Design of Dispersive Materials,", IEEE Trans. Ant. and Prop., November 1997.

[3] Lord Rayleigh, Philos. Mag. 34, 481 (1892).

[4] R. C. McPhedran, D. R. McKenzie, "The conductivity of lattices of spheres I. The simple cubic lattice", Proc. R. Soc. Lond. A.359, 45 (1978).

[5] R.C. McPhedran, D. R. McKenzie, G.H. Derrick, "The conductivity of lattices of spheres II. The body centred and face centred cubic lattices", Proc. R. Soc. Lond. A.362, 211 (1978).

[6] John Lam, "Magnetic permeability of a simple cubic lattice of conducting magnetic spheres", J. Applied Phys. 60, December 1986.

[7] N. G. Alexópoulos, D.R. Jackson, "Fundamental Superstrate (cover) Effects on Printed Circuit Antennas", IEEE Trans. Ant. and Prop., AP-32. NO. 8, August 1984.

[8] C.F. Bohren, D.R. Huffman. "Absorption and Scattering of Light by Small Particles", John Wiley & Sons, 1983, chapter 9.

[9] A. R. von Hippel, "Dielectrics and Waves", John Wiley & Sons, pp. 166-169.

[10] L. Brillouin, "Wave Propagation and Group velocity", Academic, New York, 1960.

[11] A. Sommerfeld, "Optics", Academic, New York, 1954.

SESSION 4:

INTERACTIVE POSTER SESSION

Finite Difference Formulation - Expanding the Capabilities

by Kent Davey
2275 Turnbull Bay Rd, New Smyrna Beach, FL 32168-5941

Abstract - The finite difference method has an attractive simplicity in handling partial differential equations. In its classical implementation, it lacks flexibility in matching arbitrary boundaries and in grid refinement. This paper explores a method that greatly expands the flexibility of the finite difference approach, even allowing for a random placement of grid points. The partial derivative terms are rapidly computed in terms of the nearest neighbors. The technique is successfully applied to a two dimensional Laplacian problem. The technique has the drawback that the solution is somewhat dependent on the grid. When the points are "too random", the solution accuracy declines.

Introduction

Finite difference techniques and their electrical network models have been useful over the years [1]. It is commonly taught that finite difference methods cannot easily handle irregular boundaries [2]. A generalized finite difference approach fits any geometry and is easily refined to achieve higher accuracy [3]. Grid refinement is achieved by a random increase in grid point density within the portion of a region where the greater accuracy is desired.

Consider a magnetic field problem where the H field is represented as either a total or reduced scalar potential. For the latter, the appropriate defining equation becomes

$$\vec{H}=\vec{T}-\nabla\Phi \tag{1}$$

where T is the magnetic intensity source term and is found in the current carrying region using the Biot-Savart law. The problem reduces to solving Laplace's equation for the unknown □,

$$\nabla\cdot(\mu\nabla\Phi)=\nabla\mu\cdot\nabla\Phi+\mu\nabla^2\Phi=0. \tag{2}$$

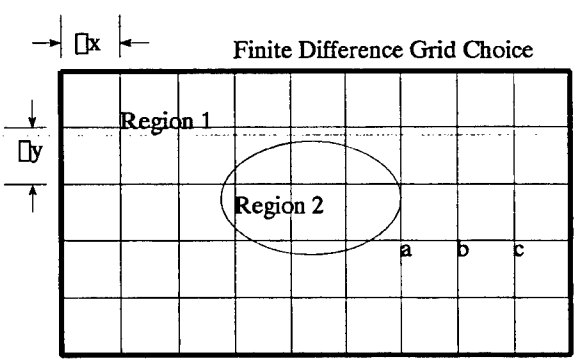

Figure 1. Grid continuation through the boundary of a dissimilar medium.

The simplest discretization for a multi-region problem is to continue a homogeneous grid through the problem space as indicated in Figure 1. The Laplacian operator is easily represented in either 2 or 3 dimensions for such a grid.

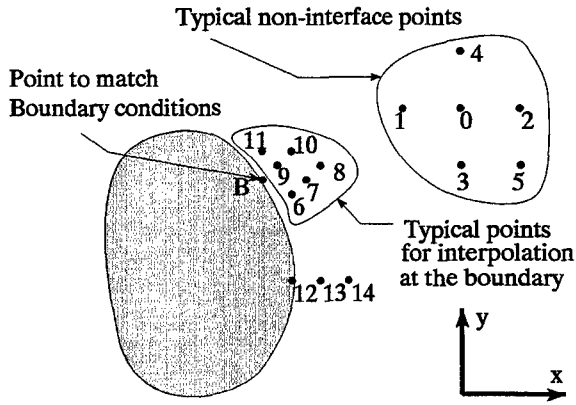

Figure 2. Typical points used for evaluating the Laplacian operator in the bulk and for interpolation near interfaces.

Referring to Figure 2, the 2-D expansion about point 0 is

$$\frac{\Phi_4+\Phi_3-2\Phi_0}{\Delta x^2}+\frac{\Phi_1+\Phi_2-2\Phi_0}{\Delta y^2}=0, \tag{3}$$

where □x, □y refer to the grid distance between points in the x and y directions. The problem setup proceeds by writing the Laplacian operator for □ in all regions. It is assumed the material inhomogeneities are at least piecewise homogeneous, i.e., that the $\nabla\mu$ terms are negligible within any such piecewise homogeneous region. The only precaution to be taken is to use points from a common region when using a finite difference representation of the problem operator such as (3). In close proximity to the boundary interface, the one-sided second-order derivative should be used to represent the Laplacian. The second-order horizontal derivative represented in terms of the potential at adjacent horizontal positions b and c in Figure 1 is

$$\frac{\partial^2\Phi}{\partial x^2}=\frac{\Phi_a-2\Phi_b+\Phi_c}{\Delta x^2}+\mathscr{E}(\Delta x^3) \tag{4}$$

The final term in (4) indicates the error terms are correct to order Δx^3.

The one sided expansion is the same regardless of which side of the boundary the derivative is taken. After writing (2) for all the grid points in the problem, the result is an N by N matrix for N unknowns. Over the bulk region of the problem, the standard finite difference representation of the Laplacian is employed because of its ease of implementation. This is, in fact, the motivation for using the finite difference method as opposed to the finite element method.

The intent of this section is to show that it is possible to set up an evenly spaced finite difference grid irrespective of boundaries, and match boundary conditions after the bulk system equations are modeled. Furthermore, in a standard grid, 4 surrounding points (or 6 in 3D) are used to represent the Laplacian. Here it is shown that using five neighboring points (or 9 points in 3D) provides flexibility in modeling a variety of shapes while preserving the numerical accuracy to order Δ^3 where Δ represents the largest distance to any one of the

neighboring points. Indeed, the technique allows one to place points on the interface randomly. The only penalty is the requirement of solving a 5 by 5 matrix for each interfacial point. The technique is also useful for increasing accuracy where the field has a high gradient, i.e., adding points randomly within a certain region of the problem.

This is made clear by the alternative representation of the second derivatives on x and y at point 0 in Figure 2, obtained by the set of equations

$$\Phi_j=\Phi_0+\frac{\partial\Phi_0}{\partial x}\Delta x_j+\frac{\partial\Phi_0}{\partial y}\Delta y_j+ \frac{1}{2}\frac{\partial^2\Phi_0}{\partial x^2}(\Delta x_j)^2+\frac{1}{2}\frac{\partial^2\Phi_0}{\partial y^2}(\Delta y_j)^2+\frac{1}{2}\frac{\partial^2\Phi_0}{\partial x\partial y}\Delta x_j\Delta y_j+\mathcal{O}(\Delta^3) \tag{5}$$

where the index j refers to one of the nearest neighbors, and Δx_j, Δy_j refer respectively to the x and y differences from the point j to the field point at Φ_0. When (5) is repeated for each of the 5 nearest neighbors, there results a matrix equation for the unknown partial derivatives of Φ at point 0 in terms of the potential values at the nearest neighboring points and the self point Φ_0,

$$\begin{bmatrix} \Delta x_1 & \Delta y_1 & \frac{\Delta x_1^2}{2} & \frac{\Delta y_1^2}{2} & \frac{\Delta x_1\Delta y_1}{2} \\ \Delta x_2 & \Delta y_2 & \frac{\Delta x_2^2}{2} & \frac{\Delta y_2^2}{2} & \frac{\Delta x_2\Delta y_2}{2} \\ \Delta x_3 & \Delta y_3 & \frac{\Delta x_3^2}{2} & \frac{\Delta y_3^2}{2} & \frac{\Delta x_3\Delta y_3}{2} \\ \Delta x_4 & \Delta y_4 & \frac{\Delta x_4^2}{2} & \frac{\Delta y_4^2}{2} & \frac{\Delta x_4\Delta y_4}{2} \\ \Delta x_5 & \Delta y_5 & \frac{\Delta x_5^2}{2} & \frac{\Delta y_5^2}{2} & \frac{\Delta x_5\Delta y_5}{2} \end{bmatrix} \begin{bmatrix} \frac{\partial\Phi_0}{\partial x} \\ \frac{\partial\Phi_0}{\partial y} \\ \frac{\partial^2\Phi_0}{\partial x^2} \\ \frac{\partial^2\Phi_0}{\partial y^2} \\ \frac{\partial^2\Phi_0}{\partial x\partial y} \end{bmatrix} = \begin{bmatrix} \Phi_1-\Phi_0 \\ \Phi_2-\Phi_0 \\ \Phi_3-\Phi_0 \\ \Phi_4-\Phi_0 \\ \Phi_5-\Phi_0 \end{bmatrix}. \tag{6}$$

It is straightforward to invert this 5 by 5 matrix to arrive at the result

$$\begin{bmatrix} \frac{\partial\Phi_0}{\partial x} \\ \frac{\partial\Phi_0}{\partial y} \\ \frac{\partial^2\Phi_0}{\partial x^2} \\ \frac{\partial^2\Phi_0}{\partial y^2} \\ \frac{\partial^2\Phi_0}{\partial x\partial y} \end{bmatrix} = C \begin{bmatrix} \Phi_1-\Phi_0 \\ \Phi_2-\Phi_0 \\ \Phi_3-\Phi_0 \\ \Phi_4-\Phi_0 \\ \Phi_5-\Phi_0 \end{bmatrix}. \tag{7}$$

C is the 5 by 5 inverse of the left hand side of (6). Thus, the Laplacian equation could be written at the point Φ_0 as

$$\sum_{j=1}^{5} C_{3j}\Phi_j+\sum_{j=1}^{5} C_{4j}\Phi_j-\sum_{j=1}^{5}(C_{3j}+C_{4j})\Phi_0=0. \tag{8}$$

The entire matrix is then built up from this principle, implementing (2) for every point in a piecewise homogeneous region. Because the $\nabla\mu$ term of (2) is zero in such regions, the permeability of the material will not appear in any of these equations.

It should be noted that the next higher order of accuracy in two dimensions involves all products of the third order derivatives and thus includes 9 terms. Including all of the fourth order derivatives brings the total number of unknowns to 14. The number added is incremented by one each time, 5-9-15.

The remaining step necessary to properly model the problem is to impose the boundary conditions. Referring back to Figure 2, it is necessary to interpolate [] at the boundary points B in terms of the potential values on one side of the boundary only. As the boundary is approached from a given region, this interpolation must be realized using potentials located in the same region. To evaluate a Neumann condition such as

$$\frac{\partial A_1}{\partial n} = \frac{\partial A_2}{\partial n}, \tag{9}$$

the five nearest neighbors to a point on the boundary in region 1 are first determined. This includes both points on the boundary and those in region 1. Next (6) is inverted to determine $\frac{\partial A_1}{\partial x}$ and $\frac{\partial A_1}{\partial y}$. The process is repeated, but allowing only nearest points in region 2 and the boundary to be included. The boundary condition is realized as

$$\hat{n}\cdot\left(\frac{\partial A_1}{\partial x}\hat{a}_x + \frac{\partial A_1}{\partial y}\hat{a}_y\right) = \hat{n}\cdot\left(\frac{\partial A_2}{\partial x}\hat{a}_x + \frac{\partial A_2}{\partial y}\hat{a}_y\right). \tag{10}$$

An Example Using the Flexible Finite Difference Approach

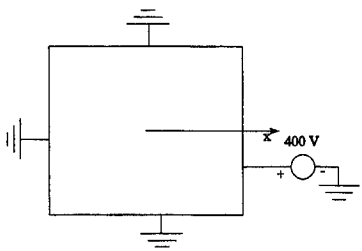

Figure 3 Box with 3 walls grounded, and the right wall held at 400 volts.

By way of testing this concept, the problem in Figure 3 is examined. The right wall is raised to 400 volts with respect to the other 3 grounded walls. The points are filled in somewhat arbitrarily throughout the interior of the box. With 64 points, allowing N=6,10, or 15 showed no noticeable difference of the potential or the E field along the x-axis.A strong field is witnessed along the right wall edge.

The "exact" field was predicted using a boundary element technique with a 60 elements distributed along the perimeter of the box. The comparison of the voltage and the x component of the electric field is witnessed in Figure 4. No difference can be witnessed with 64 points distributed within the box.

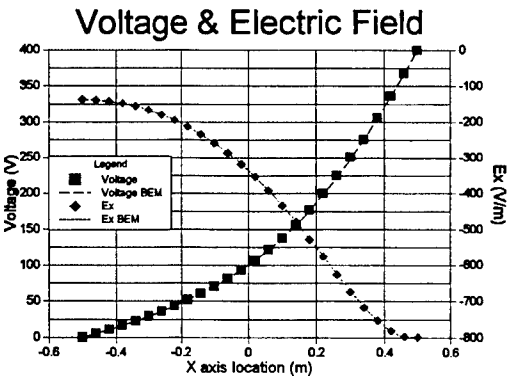

Figure 4 Prediction accuracy for the finite difference approach to predicting the electric field in the box.

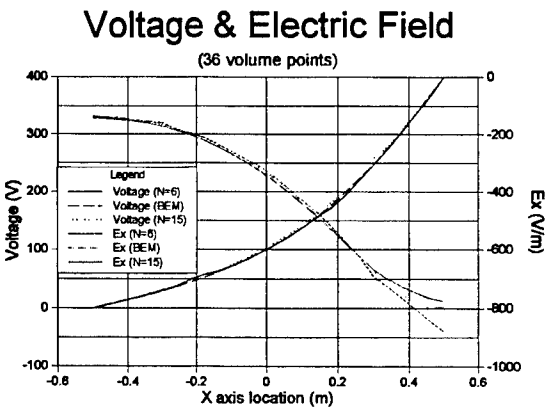

Figure 5 Voltage and Electric field predicted with only 36 internal points.

As the number of points begins to drop, the importance of maintaining a higher order approximation becomes more evident. Shown in Figure 5 is the same comparison for a 36 point analysis. The greater accuracy of the 15 point approximation surfaces.

Getting data out requires one additional variation. Suppose the potential and electric field are desired along a specified line of points. At each desired output point, the 6 nearest neighbors must be determined using a sort algorithm as before. However now the nearest 6 neighbors (Δx^3 accuracy) must be determined to compute the values of the potential and the derivatives. This number is increased to 10 for Δx^4 accuracy and to 15 for Δx^5 accuracy. For Δx^3 accuracy, the defining equation becomes

$$\begin{bmatrix} 1 & \Delta x_1 & \Delta y_1 & \frac{\Delta x_1^2}{2} & \frac{\Delta y_1^2}{2} & \frac{\Delta x_1 \Delta y_1}{2} \\ 1 & \Delta x_2 & \Delta y_2 & \frac{\Delta x_2^2}{2} & \frac{\Delta y_2^2}{2} & \frac{\Delta x_2 \Delta y_2}{2} \\ 1 & \Delta x_3 & \Delta y_3 & \frac{\Delta x_3^2}{2} & \frac{\Delta y_3^2}{2} & \frac{\Delta x_3 \Delta y_3}{2} \\ 1 & \Delta x_4 & \Delta y_4 & \frac{\Delta x_4^2}{2} & \frac{\Delta y_4^2}{2} & \frac{\Delta x_4 \Delta y_4}{2} \\ 1 & \Delta x_5 & \Delta y_5 & \frac{\Delta x_5^2}{2} & \frac{\Delta y_5^2}{2} & \frac{\Delta x_5 \Delta y_5}{2} \end{bmatrix} \begin{bmatrix} \Phi_0 \\ \frac{\partial \Phi_0}{\partial x} \\ \frac{\partial \Phi_0}{\partial y} \\ \frac{\partial^2 \Phi_0}{\partial x^2} \\ \frac{\partial^2 \Phi_0}{\partial y^2} \\ \frac{\partial^2 \Phi_0}{\partial x \partial y} \end{bmatrix} = \begin{bmatrix} \Phi_1 \\ \Phi_2 \\ \Phi_3 \\ \Phi_4 \\ \Phi_5 \\ \Phi_6 \end{bmatrix}. \quad (11)$$

Here Φ_1 through Φ_6 are the six nearest known neighbors to the desired output point Φ_0. After inversion of (11), either the potential itself or the derivatives follow from the first or second and third rows of the inversion matrix respectively.

Although the solutions presented look encouraging, it was found in practice that as the randomness of the grid increases, the accuracy of the solution decreases. In other words, although the technique is sound, the predictive accuracy of the higher order derivatives declines for a random grid even when a higher solution (n=10 or 15) is employed. The better solutions follow from an evenly spaced grid.

Conclusions

A technique is presented and successfully tested which expands the flexibility of the finite difference technique by defining partial derivatives in terms of nearest neighbors. When the nearest neighbor points are randomized, often the partial derivatives are not well defined in terms of the nearest neighbors. This causes reduced accuracy in the field prediction. The dependence of the solution on a somewhat even distribution of field points detracts from the advantages of the increased flexibility.

References

1. G. Liebmann, "Precise Solution of Partial Differential Equations by Resistance Networks", Nature, vol. 164, 1949.

2. S.R.H. Hoole, Computer-Aided Analysis and Design of Electromagnetic Devices, Elsevier, New York, 1989, p. 136.

3. P. Silvester and R. Ferrari, Finite elements for electrical engineers, Cambridge University Press, Cambridge, 1983.

Time and Frequency Domain Numerical Modeling of Outbound And Standing Power From Perpendicularly Oriented, Electrically Small TM Dipoles

Gang Liu, Craig A. Grimes, and Keat Ghee Ong
Department of Electrical Engineering
453 Anderson Hall
The University of Kentucky
Lexington, KY 40506-0046

Dale M. Grimes
Department of Physics and Astronomy
The University of Kentucky
Lexington, KY 40506

Abstract - The outbound and local power emitted from a pair of identical, perpendicularly oriented electrically small TM dipoles are determined using time and frequency domain numerical techniques. Earlier work [1,2] showed that a complete description of power in a radiation field required the use of three numbers, while the frequency domain mathematics inherent in the complex Poynting theorem provided only two; frequency domain mathematics lack phase information that is of significant consequence for certain antenna designs. In this paper we numerically model, using commonly accepted techniques, the simplest antenna design that clearly illustrates the differences in the time and frequency domain representations of power.

INTRODUCTION

In earlier work [1,2] we compared and contrasted analytic power calculations obtained using the time dependent Poynting theorem (TDPT) and the frequency domain complex Poynting theorem (CPT). We concluded that the complex Poynting theorem is an inadequate basis for a full description of power in a radiation field. The difficulty is very simple: The time domain results show it takes three numbers to fully describe power in a radiation field, and the complex theorem supplies only two. How significant this result is depends upon the details of a particular radiation field.

The TDPT and CPT calculate the same far-field power, but are not in agreement for determination of the standing energy and the power that returns to the source twice each field cycle to affect antenna operation. Generally speaking, for electrically small single-terminal pair antennas the differences in the TDPT and CPT local power calculations are small. However, for multi-element antennas driven by a single source, differences between the TDPT and CPT calculations of local power can be quite large. In this work we use widely accepted frequency and time domain numerical techniques, MoM and FDTD respectively, with the corresponding frequency or time domain versions of the Poynting theorem to illustrate the differences in calculated powers. Since, to coin a phrase, the results are a little eye-opening, the 'correctness' of the time domain results are checked in the following manner. We take the discrete Fourier transform of the time domain fields obtained via FDTD (the same time domain fields used with the TDPT to determine time domain power), and combine the complex phasor values of the fields with the CPT to determine frequency domain power: the frequency domain results determined in this fashion are in complete agreement with those obtained via MoM + CPT. In wondering what is right, and what is not, the reader in encouraged to remember that frequency domain mathematics are but a convenient mathematical way of describing physics, they are not inherent in the physics themselves.

The input reactance of an antenna is determined by the standing energy or what we call local bidirectional power- power within a half wavelength that returns to the source twice each field cycle (see [1,2] for a discussion on why this quantity is not what has historically been called reactive power) that an antenna supports. Consequently, for design of efficient, electrically small antennas, determining the local bidirectional power is of vital concern.

Using both numerical methods, we calculate the outbound (unidirectional) and local power (bi-directional) emitted from an antenna that consists of two electrically small, superimposed but spatially orthogonal electric dipoles, as a function of phase difference between the two antennas. The frequency domain results show no affect, in both the unidirectional outbound and bidirectional local power, regardless of the relative phase difference between the two dipoles. In contrast, and in complete agreement with time domain based theory [1,2], the time domain numerical results show that the quantity of local, bidirectional power can be controlled by adjusting the relative phase difference between the drives of the two dipoles.

Consequently, by the CPT the input reactance of the two dipoles is the same as that of a single dipole multiplied by two; power is unaffected by the phase difference between the two antennas. However, the TDPT results show that the input reactance is dependent upon the relative phasing between the two spatially orthogonal electric dipoles. The time domain results show that the reactive portion of the antenna input impedance can be reduced independently of the size to wavelength ratio: This result has profound consequences for the design and fabrication of efficient, electrically small antennas.

ANALYTICAL METHOD

The antenna consists of two electric dipole radiators [3], oriented symmetrically about a common origin, with one dipole oriented along the x axis, and one dipole oriented along the y axis. We use spherical coordinates with θ representing the zenith angle measured from the z axis and ϕ the azimuth angle measured from the x axis. $P_1^1(\cos\theta)$ represent associated Legendre polynomials of order and degree one. F_X represents the field coefficient of the dipole oriented along the x axis, and F_Y the field coefficient of the dipole oriented along the y axis. The radial distance from the origin is denoted by r, the wavevector $k = 2\pi/\lambda$, and $\sigma = kr$. $i = \sqrt{-1}$.

$h_1(\sigma)$ represents spherical Hankel functions of the second kind. It is convenient to define letter functions A_1 and B_1 by the equation

$$h_1(\sigma) = \frac{e^{-i\sigma}}{\sigma}\ (B_1 + iA_1) \tag{1}$$

and C_1 and D_1 by the equations

$$C_1 = \frac{dA_1}{d\sigma} - B_1 \qquad D_1 = A_1 + \frac{dB_1}{d\sigma} \tag{2}$$

Since only order dipole terms, $1 = 1$, are considered in this paper, A_1 is replaced by A, etc.

Frequency Domain Analyses

Letting F_X be the constant field coefficient, the radial component of the field generated by the x axis antenna is [1-4]:

$$\begin{aligned} \sigma E_r &= 2F_X\, h_1(\sigma)\, P_1^1(\cos\theta)\cos\phi\ e^{i\omega t} \\ &= 2F_X\, \frac{B_1 + iA_1}{\sigma}\, P_1^1(\cos\theta)\cos\phi\ e^{i(\omega t - \sigma)} \\ &= 2F_X\, \frac{B_1 + iA_1}{\sigma}\, P_1^1(\cos\theta)\cos\phi\ e^{i\omega t_r} \end{aligned} \tag{3}$$

where t_r represents retarded time:

$$t_r = t - \sigma/\omega \tag{4}$$

Given Eq.(1), the angular fields can be derived and for the x oriented dipole are listed in the left-hand column of Table I.

Table I. Angularly directed field components, frequency domain.

Field Component	*x* dipole	*y* oriented dipole in phase with *x* oriented dipole	*y* oriented dipole 90° out of phase with *x* oriented dipole
σE_θ	$F_x(D_1+iC_1)\frac{\partial P_1^1}{\partial\theta}\cos\phi e^{i\omega t_r}$	$F_y(D_1+iC_1)\frac{\partial P_1^1}{\partial\theta}\sin\phi e^{i\omega t_r}$	$-iF_y(D_1+iC_1)\frac{\partial P_1^1}{\partial\theta}\sin\phi e^{i\omega t_r}$
$\eta\sigma H_\phi$	$-iF_x(B_1+iA_1)\frac{\partial P_1^1}{\partial\theta}\cos\phi e^{i\omega t_r}$	$-iF_y(B_1+iA_1)\frac{\partial P_1^1}{\partial\theta}\sin\phi e^{i\omega t_r}$	$-F_y(B_1+iA_1)\frac{\partial P_1^1}{\partial\theta}\sin\phi e^{i\omega t_r}$
σE_ϕ	$-F_x(D_1+iC_1)\frac{P_1^1}{\sin\theta}\sin\phi e^{i\omega t_r}$	$F_y(D_1+iC_1)\frac{P_1^1}{\sin\theta}\cos\phi e^{i\omega t_r}$	$-iF_y(D_1+iC_1)\frac{P_1^1}{\sin\theta}\cos\phi e^{i\omega t_r}$
$\eta\sigma H_\theta$	$-iF_x(B_1+iA_1)\frac{P_1^1}{\sin\theta}\sin\phi e^{i\omega t_r}$	$iF_y(B_1+iA_1)\frac{P_1^1}{\sin\theta}\cos\phi e^{i\omega t_r}$	$F_y(B_1+iA_1)\frac{P_1^1}{\sin\theta}\cos\phi e^{i\omega t_r}$

If the antennas are driven in phase and if F_y is the constant field coefficient of the *y* axis antenna, the corresponding radial field component is:

$$\sigma E_r = 2F_y h_1(\sigma)P_1^1(\cos\theta)\sin\phi\, e^{i\omega t} \tag{5}$$

for which the angular fields are listed in the middle column of Table I.

If the antennas are driven by voltage sources 90° out of phase, the *y* axis antenna field changes to:

$$\sigma E_r = -i2F_y h_1(\sigma)P_1^1(\cos\theta)\sin\phi\, e^{i\omega t} \tag{6}$$

for which the angular fields listed in the right-hand column of Table I.

Taking the radial component of the complex Poynting vector, by combining the angular fields of the *x* oriented dipole and the fields of either the in or out of phase *y* oriented dipole, and integrating over an enclosing virtual sphere of radius σ gives the complex surface power, $P_c(\sigma)$, with either phase on the *y* oriented antenna:

$$P_c(\sigma) = \frac{4\pi}{3\eta k^2}[(AD-BC) + i(AC+BD)][F_x^2+F_y^2] \tag{7}$$

Equation 7 shows the same reactive power value independently of whether the two antennas radiate in or out of phase. Inserting the values [1,2]:

$$B = -1, \qquad A = D = \frac{1}{\sigma} \qquad C = 1 - \frac{1}{\sigma^2} \tag{8}$$

shows that:

$$P_c(\sigma) = \frac{4\pi}{3\eta k^2}\left[1 - \frac{i}{\sigma^3}\right][F_x^2+F_y^2] \tag{9}$$

Again, the frequency domain mathematics show no significance to a phase difference between the two antennas. The local (reactive) power calculated for the two-antenna ensemble is the same as that of a single dipole multiplied by two.

Time Domain Analyses

The actual portions of the time domain fields follow from the above, and are shown in Table II. If the x and y oriented dipoles are in phase, the time dependent surface power on a virtual, circumscribing sphere is found to be:

$$p(t_r) = \frac{4\pi}{3\eta k^2}[F_x^2+F_y^2][(AD-BC) + (AD+BC)\cos(2\omega t_r) - (AC-BD)\sin(2\omega t_r)] \tag{10}$$

which, after inserting the values of Eq. (8), goes to:

$$p(t_r) = \frac{4\pi}{3\eta k^2}[F_x^2+F_y^2][\{1-\cos(2\omega t_r)\} + \frac{2}{\sigma^2}\cos(2\omega t_r) - (\frac{2}{\sigma} - \frac{1}{\sigma^3})\sin(2\omega t_r)] \tag{11}$$

The term within the { } brackets represents outbound power, the remaining two terms have time average values of zero, and are responsible for the input reactance.

If the voltage source of the y oriented dipole is 90° out of phase with the x oriented dipole the time dependent surface power is:

Table II. Angularly directed fields, time domain.

	x dipole	y oriented dipole in phase with x oriented dipole	y oriented dipole 90° out of phase with x oriented dipole
σE_θ	$F_x(D_1\cos(\omega t_r)-C_1\sin(\omega t_r)) \times \frac{\partial P_1^1}{\partial\theta}\cos\phi$	$F_y(D_1\cos(\omega t_r)-C_1\sin(\omega t_r)) \times \frac{\partial P_1^1}{\partial\theta}\sin\phi$	$F_y(C_1\cos(\omega t_r)+D_1\sin(\omega t_r)) \times \frac{\partial P_1^1}{\partial\theta}\sin\phi$
$\sigma\eta H_\phi$	$F_x(A_1\cos(\omega t_r)+B_1\sin(\omega t_r)) \times \frac{\partial P_1^1}{\partial\theta}\cos\phi$	$F_y(A_1\cos(\omega t_r)+B_1\sin(\omega t_r)) \times \frac{\partial P_1^1}{\partial\theta}\sin\phi$	$-F_y(B_1\cos(\omega t_r)-A_1\sin(\omega t_r)) \times \frac{\partial P_1^1}{\partial\theta}\sin\phi$
σE_ϕ	$-F_x(D_1\cos(\omega t_r)-C_1\sin(\omega t_r)) \times \frac{P_1^1}{\sin\theta}\sin\phi$	$F_y(D_1\cos(\omega t_r)-C_1\sin(\omega t_r)) \times \frac{P_1^1}{\sin\theta}\cos\phi$	$F_y(C_1\cos(\omega t_r)+D_1\sin(\omega t_r)) \times \frac{P_1^1}{\sin\theta}\cos\phi$
$\sigma\eta H_\theta$	$F_x(A_1\cos(\omega t_r)+B_1\sin(\omega t_r)) \times \frac{P_1^1}{\sin\theta}\sin\phi$	$-F_y(A_1\cos(\omega t_r)+B_1\sin(\omega t_r)) \times \frac{P_1^1}{\sin\theta}\cos\phi$	$F_y(B_1\cos(\omega t_r)-A_1\sin(\omega t_r)) \times \frac{P_1^1}{\sin\theta}\cos\phi$

$$p(t_r) = \frac{4\pi}{3\eta k^2}\{F_x^2[\{1-\cos(2\omega t_r)\} + \frac{2}{\sigma^2}\cos(2\omega t_r) - (\frac{2}{\sigma} - \frac{1}{\sigma^3})\sin(2\omega t_r)] + F_y^2[\{1+\cos(2\omega t_r)\}$$
$$- \frac{2}{\sigma^2}\cos(2\omega t_r) + (\frac{2}{\sigma} - \frac{1}{\sigma^3})\sin(2\omega t_r)]\} \qquad (12)$$

In Eq.12, note that the local power terms from the x and y oriented dipoles are of different signs. If $F_x = F_y$ the local power terms cancel.

The frequency domain results, Eq. 9, show that input impedance is unaffected by the phase relationship between the x and y oriented antennas, and therefore from the point of view of the input impedance relative phase differences are unimportant. However Eqs. 11 and 12 show quite a different result: relative phase differences between the two elements affect the amount of local power that returns to the source. For in-phase antennas, Eq. 10 shows the same character as Eq. 9, the source supports local power seen as a reactive input impedance. Eq. 12 shows that when the two antennas support power 180° out of phase the bi-directional, local power of the two antennas cancels. Therefore if the multi-element antenna can be driven from a single transmission line, the input impedance presented to the source would be purely resistive.

NUMERICAL RESULTS

FDTD Power Computations

Using FDTD we have calculated the power passing through an imaginary spherical shell of variable radius (Gaussian sphere), centered at the origin of the two orthogonally oriented dipoles. The two wire dipoles are identical, both center fed, 3 cm in length, 2 mm x 2 mm in cross section, and oriented perpendicular to each other as described above; see Figure 1. The dipole oriented along the x axis is labeled as dipole 1, driven with voltage $V_1(t)$; the dipole oriented along the y axis is labeled dipole 2 with voltage $V_2(t)$.

The FDTD computations were made using a rectangular, three-dimensional computer code based on the Yee [5-7] cell. The problem space was chosen as 140x140x140 cells, with the cell dimensions $\Delta x = \Delta y = \Delta z = 0.5$ cm; second order Mur [8] absorbing boundaries were used. Integration over a spherical boundary was done by interpolation of the fields from the rectangular coordinate points. For the FDTD calculations the dipoles are fed at the center with a modified sinusoidal wave of frequency f [9]. The working frequency is 1.18 GHz, $\lambda = 25$ cm. The time steps were 9.6 ps, the courant stability limit for the cell size chosen.

The electric fields in the gap of dipole 1 and 2 are specified as:

$$E_x(t) = \frac{-V_1(t)}{2\Delta x} \qquad E_y(t) = \frac{-V_2(t)}{2\Delta y} \qquad (13)$$

where $V_1(t)$ and $V_2(t)$ are the voltage source with the modified sinusoidal wave of frequency f in order to cancel spurious fields in time-domain computations [9].

$$\begin{aligned} V_1(t) &= V_0 ft \sin(2\pi ft) && 0 \le t \le T \\ &= V_0 \sin(2\pi ft) && t > T \\ V_2(t) &= V_0 f(t-\tau)\sin[2\pi f(t-\tau)] && 0 \le t-\tau \le T \\ &= V_0 \sin[2\pi f(t-\tau)] && t-\tau > T \end{aligned} \qquad (14)$$

where τ is a time delay, T is the period of sinusoidal wave with frequency f and V_0 is the maximum amplitude of the source voltage. For the work described here, V_0 was set to 1000 V. For orthogonal electric dipoles producing circular polarization τ is 0.25T, which corresponds to a phase delay between voltage sources of 90°.

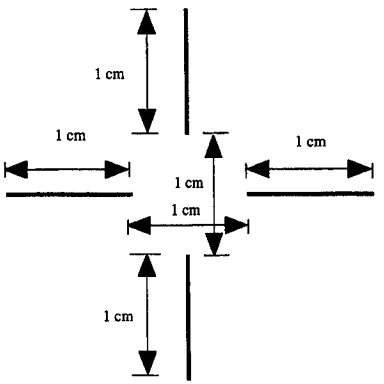

Figure 1. Antenna geometry used for numerical modeling.

Figure 2 is a plot of the instantaneous time varying power, calculated using FDTD, passing through a sphere of radius 0.1, 0.3, and 0.6 wavelengths from the origin when both dipoles are in phase, that is there is no time delay between the drives of the two dipoles. Figure 2 clearly demonstrates outbound real power and time varying local power that oscillates between the field and source. Figure 3 is similar to that of Figure 2, except there is now a time delay between the drives of the two antennas of 0.25T, corresponding to a voltage source phase difference of 90°. The constant valued power output of Figure 3 indicates that the source emits only outbound real power, no bidirectional power is supported, hence no energy returns to the source, hence the input reactance of the source is zero. The relative phasing between the two dipoles plays a crucial role in determining the local power, and hence overall operating characteristics. The power calculations are equal for relative voltage source time delays of 0.25T or 0.75T.

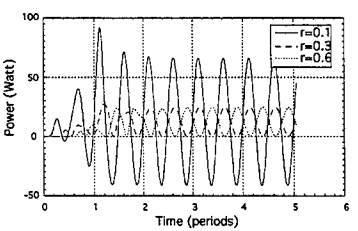

Figure 2. Instantaneous time varying power passing through Gaussian sphere of radius 0.1, 0.3, and 0.6 wavelengths from origin, calculated using FDTD with the TDPT for both antennas when driven in phase. Time average output power is 12.26W.

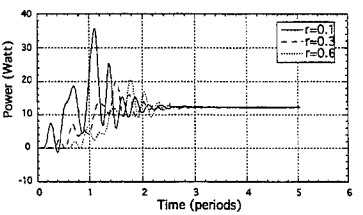

Figure 3. Instantaneous time varying power passing through Gaussian sphere of radius 0.1, 0.3, and 0.6 wavelengths from origin, calculated using FDTD with the TDPT when antennas are driven with a relative voltage source time delay of 0.25 period, corresponding to a relative phase delay of 90°. Time average output power is 12.26 W.

The zero input reactance of Figure 3 is highly dependent upon the phase difference, or time delay, between the dipoles; Figure 4 is the total power calculated for a voltage source time delay of 0.236T, or 85°. Figure 5 is the total instantaneous power calculated for a voltage source time delay between dipoles of 0.125T, or 45°.

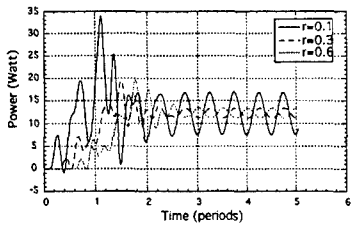

Figure 4. Instantaneous time varying power passing through Gaussian sphere of radius 0.1, 0.3, and 0.6 wavelengths from origin, calculated using FDTD with the TDPT, when antennas are driven with a relative voltage source time delay of 0.236 period, corresponding to a relative phase delay of 85°. Time average output power is 12.26 W.

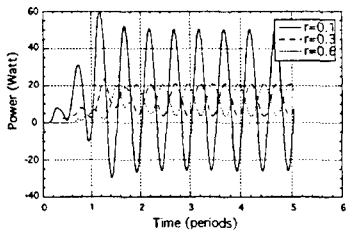

Figure 5. Instantaneous time varying power passing through Gaussian sphere of radius 0.1, 0.3, and 0.6 wavelengths from origin, calculated using FDTD with the TDPT when the antennas are driven with a relative voltage source time delay of 0.125 period, corresponding to a relative phase delay of 45°.

Figure 6 is the power per polarization, at 0.1λ radius, for the case of Figure 2, with the two dipoles in phase. Figure 7 is the power per polarization for the case of Figure 3, with the dipole voltage sources delayed from each other by 0.25T, corresponding to a phase delay of 90°.

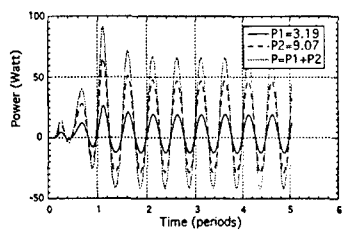

Figure 6. Instantaneous time varying power, per polarization, passing through Gaussian sphere of radius 0.1 wavelengths from origin, calculated using FDTD with the TDPT, when the two antennas are driven in phase. P1 = power in $E_\theta H_\phi$ polarization, P2 = power in $E_\phi H_\theta$ polarization, P = P1 + P2.

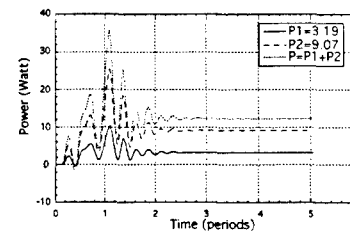

Figure 7. Instantaneous time varying power, per polarization, passing through Gaussian sphere of radius 0.1 wavelengths from origin, calculated using FDTD with TDPT, when the antennas are driven with a relative time delay between voltage sources of 0.25 period, corresponding to a phase delay of 90°. P1 = power in $E_\theta H_\phi$ polarization, P2 = power in $E_\phi H_\theta$ polarization, P = P1 + P2.

Except for Figures 3 and 7 which demonstrate zero input reactance, we are not able to translate the time domain data into the frequency domain, assigning them real and reactive power values since, as was earlier shown [1,2], *it takes three numbers to correctly describe power in a radiation field, not two, and there is no mathematically unique way to transform three numbers into two.*

Frequency Domain Power Computations

One method used to illustrate the differences between the CPT and TDPT descriptions of power in radiation fields was to begin with the time domain electromagnetic fields from the FDTD calculations of the previous section, then obtain the complex phasor values of the field components via a discrete Fourier transform of the time domain fields (FTFDTD). The complex phasor fields were then combined with the CPT, and the real and reactive power passing through the surrounding Gaussian sphere determined.

The other method used for determining the frequency domain power was through the use of the Burke NEC MoM code to obtain the phasor fields surrounding the antenna, which were then combined with the CPT to determine power. The antennas are oriented perpendicular to each other, centered at the origin, each antenna is three centimeters long, driven with 1000 V across infinitesimal gaps. Since the NEC code modeled cylindrical wires and the FDTD code modeled rectangular wires, the diameter of the wire antennas in the MoM description was chosen as 1.4 mm radius; for this diameter the time and frequency domain codes gave the same outbound (real) power values.
We first show comparison between the power calculations obtained using FTFDTD and MoM. Figure 8 shows real and reactive powers as a function of distance, in wavelengths, from the origin, when both dipoles are in phase. Figure 9 shows real and reactive powers when the two dipole voltage sources are phase delayed 90°, supporting circular polarization. Inspection of the two figures shows that: {1} the FTFDTD and MoM results are in agreement, and {2} there is no significance to phase differences between sources. The power calculations are equal to that of a single electric dipole of similar size.

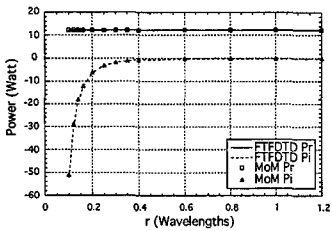

Figure 8. Comparison between FTFDTD and MoM computations of real (Pr) and reactive (Pi) power from two antennas driven in phase, 0° relative phase difference.

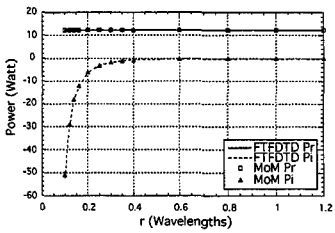

Figure 9. Comparison between FTFDTD and MoM computations of steady state real (Pr) and reactive (Pi) power from two antennas driven with a relative phase difference of 90° between the dipole voltage sources.

Time and Frequency Domain Power Calculations

Figure 10 shows outbound and local power as calculated using FDTD and FTFDTD = MoM numerical techniques when the two antennas support circular polarization, that is with a delay between the dipole voltage sources of 0.25T or 90° (power phase difference of 180°). The outbound, real power values are equal, however the local power calculations are very different, as can be seen in Figure 10 (dashed lines versus filled in triangles). Why the difference? Time domain results [1,2] show that three numbers are required to correctly describe power in a radiation field, yet the frequency domain representation of power provides only two. This missing information is vital for accurate determination of the standing

energy an antenna supports. The standing energy an antenna supports determines the input reactance a source sees in driving an antenna. As illustrated in Figure 10, the consequences of this can be significant for certain antenna structures. The results indicate that it may be possible to build an electrically small antenna structure that does not support large quantities of local power.

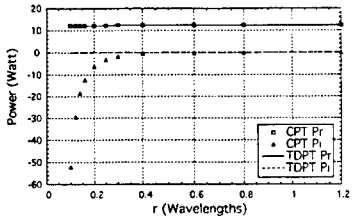

Figure 10. Comparison between steady state powers calculated using time and frequency domain techniques. The time and frequency domain techniques are in agreement for outbound, real power. There is a significant difference between the frequency and time domain computations of local, standing power near the source where the majority of the standing energy is located. The time domain results indicate ways in which the standing energy supported by an electrically small antenna can be reduced independently of the size-to-wavelength ratio.

CONCLUSIONS

Earlier work showed analytically [1,2] that the CPT does not correctly determine the local power in a radiation field that oscillates between the field and source. While the errors are insignificant for electrically small single terminal pair antennas, such as a single electric dipole, they can be large for multi-element antenna designs supporting specific phase relationships. The purpose of this paper is to illustrate these differences using widely accepted numerical computational techniques for the simplest possible case. Since the physics of the world are inherent in the time domain, and the frequency domain but a convenient mathematical technique, the differences illustrated in Figure 10 are of importance to future antenna design. The time domain results illustrated in Figure 10 demonstrate that it is possible to minimize the standing energy, or local power, associated with an antenna through control of the relative phasing between antenna elements.

ACKNOWLEDGMENTS

The authors gratefully acknowledge support of this work by the Air Force Office of Scientific Research under contract F49620-96-1-0353. The authors would also like to thank Professor Stephen D. Gedney of the University of Kentucky for suggesting the FTFDTD calculations.

REFERENCES

[1] D.M. Grimes, C.A. Grimes, Power In Modal Radiation Fields: Limitations of the Complex Poynting Theorem and the Potential for Electrically Small Antennas, Journal of Electromagnetic Waves and Applications, vol. 11, pp. 1721-1747, 1997.

[2] C. A. Grimes, D. M. Grimes, "The Poynting Theorems and the Potential for Electrically Small Antennas," 1997 IEEE Aerospace Conference, Vol. 3, pp. 161-176, 1997.

[3] D.M. Grimes, C.A. Grimes, "Standing energy density, standing energy, and Q of dipole radiation fields," Proceedings, 1998 Aerospace Conference.

[4] W.K.H. Panofsky, M. Phillips, *Classical Electricity and Magnetism*, 2nd.ed., Addison-Wesley, pp.229-233 and pp.255-270, 1962.

[5] K.S.Yee, " Numerical solution of initial boundary value problems involving Maxwell's equations in isotropic media," IEEE Trans. A & P, vol. 14, pp.302-307, 1966.

[6] A. Taflove, Ed., *Finite Difference Time Domain Methods for Electrodynamic Analyses*, NY: Artech House, May 1995.

[7] K.S. Kunz and R.J. Luebbers, The Finite Difference Time Domain Method for Electromagnetics, CRC Press, 1993.

[8] G.Mur, "Absorbing boundary conditions for the finite difference approximation of the time-domain electromagnetic field equations," IEEE Trans. EMC, vol. 23, pp.377-382, 1981.

[9] U.Kangro and R.Nicolaides, "Spurious fields in time-domain computations of scattering problems," IEEE Trans. A & P, vol. 45, pp.228-234, 1997.

Efficient Analysis of Large Two-dimensional Arbitrarily Shaped Finite Gratings for Quantum Well Infrared Photodetectors

Vikram Jandhyala*, Deepak Sengupta**,
Balasubramaniam Shanker*, Eric Michielssen*,
Milton Feng**, and Greg Stillman**
*Center for Computational Electromagnetics
and **Microelectronics Laboratory
Dept. of Electrical and Computer Engineering.
1406 West Green St.
University of Illinois at Urbana-Champaign,
Urbana Il 61801
Email: vikram@decwa.ece.uiuc.edu

Abstract

In this work, a recently developed full-wave electromagnetic analysis technique is applied to the simulation of two-dimensional finite quasi-random and rough surface gratings for quantum well infrared photodetectors. This new steepest descent fast multipole method (SDFMM) is a mathematically rigorous technique that permits the rapid and accurate solution of the electric field integral equation governing scattering from a quasi-planar structure. In the present application, it enables the efficient and accurate simulation of scattering by finite two-dimensional grating structures interfacing with GaAs. Grating absorption is predicted by evaluating the scattered optical electric field component at the device layer along the growth direction. Numerical examples illustrating the functional dependence of the absorption on grating parameters and wavelength are discussed. The simulation approach presented here should prove to be a useful tool for the *a priori* design of novel aperiodic, quasi-random and rough surface two-dimensional gratings for infrared imaging applications.

1 Introduction

Quantum well infrared photodetectors (QWIPs) with AlGaAs/GaAs quantum wells have shown great potential as sensors in large imaging arrays [1, 2]. Owing to quantum mechanical selection rules, most unstrained n-type QWIPs respond only to the longitudinal component of the optical electrical field, i.e. the field along the growth direction. For such devices to sense normally incident radiation, optical grating couplers are necessitated to scatter the optical field in directions favorable to intersubband absorption [3, 4]. While periodic gratings [3, 5] have been extensively studied and modeled using modal expansion methods, aperiodic or quasi-random gratings [6, 4] have not been analyzed in comparable detail. Nonetheless, quasi-random gratings have been experimentally observed to produce better absorption over broad spectral ranges than periodic ones. Unfortunately, the computational burden associated with the solution of a large-scale, three-dimensional, vector electromagnetic problem has restricted the numerical analysis of quasi-random gratings to modal expansions for computationally simpler one-dimensional profiles [4]. In this paper, a recently developed accurate and efficient integral equation based technique is applied to the analysis of finite two-dimensional quasi-random gratings. This technique, termed the steepest descent fast multipole method (SDFMM) [7], is based on an alternate representation of the dyadic Green's function governing free space electromagnetic radiation using a steepest descent integral form and inhomogeneous plane wave expansions. Such an approach permits a fast and memory efficient iterative solution of the integral equation associated with scattering from quasi-planar structures. Furthermore, new rough surface gratings are proposed for QWIP applications. These gratings, that cannot be analyzed by analytical methods or modal expansions, are simulated efficiently using the SDFMM. It is seen that these gratings display remarkable spectral properties and can potentially improve absorption in QWIPs to a substantial degree.

2 Problem Formulation

The back-illuminated QWIP structure to be analyzed is shown in Fig. 1(a). The metallic grating layer S (modeled as a perfect conductor [3, 4]), which interfaces with GaAs, prevents radiation loss and serves as a contact. An

optical wave impinges normally on the grating from the substrate side, and the scattered wave excites the quantum wells owing to its non-zero electric field along the growth direction. The incident field $\mathbf{E}_{inc}(\mathbf{r})$ is assumed to be a tapered Gaussian beam, which suppresses edge scattering effects at the mesa boundary. This assumption is consistent with the observation that a substantial portion of the grating and device near the mesa edge is optically inactive [3]. A surface current $\mathbf{J}(\mathbf{r})$ is generated at the grating due to $\mathbf{E}_{inc}(\mathbf{r})$. The total electric field tangential to S must vanish on S, and hence the following integral equation holds

$$\hat{\mathbf{t}}(\mathbf{r}) \cdot \mathbf{E}_{scat}(\mathbf{r}, \mathbf{J}) = -\hat{\mathbf{t}}(\mathbf{r}) \cdot \mathbf{E}_{inc}(\mathbf{r}) \qquad \mathbf{r}, \mathbf{r}' \in S \,, \tag{1a}$$

with

$$\mathbf{E}_{scat}(\mathbf{r}, \mathbf{J}) = \frac{k_0 \eta_0}{i} \int_S \bar{\mathbf{G}}(\mathbf{r}, \mathbf{r}') \cdot \mathbf{J}(\mathbf{r}') \, dS' \qquad \mathbf{r} \in S \,. \tag{1b}$$

where k_0 and η_0 are the free-space wave number and impedance, $\hat{\mathbf{t}}(\mathbf{r})$ denotes a unit tangent to S at $\mathbf{r}$, and $\bar{\mathbf{G}}(\mathbf{r}, \mathbf{r}')$ is the free-space dyadic Green's function. The solution of Eqn.(1) yields $\mathbf{J}(\mathbf{r})$, and the total longitudinal electric field at the device layer can then obtained via $\bar{\mathbf{G}}(\mathbf{r}, \mathbf{r}')$. A standard approach to solving Eqn.(1) is to use the method of moments (MoM), wherein $\mathbf{J}(\mathbf{r})$ is expressed as a linear combination of basis functions $\mathbf{j}_n(\mathbf{r}), n = 1, ..., N$ as

$$\mathbf{J}(\mathbf{r}) \cong \sum_{n=1}^{N} I_n \, \mathbf{j}_n(\mathbf{r}) \,. \tag{2a}$$

Subsequently testing the resulting equations with a set of functions $\mathbf{f}_m(\mathbf{r}), m = 1, ..., N$ leads to a dense matrix equation of order N of the form

$$\bar{\mathbf{Z}} \cdot \mathbf{I} = \mathbf{V} \,, \tag{2b}$$

with

$$Z_{mn} = \langle \mathbf{f}_m(\mathbf{r}), \mathbf{E}_{scat}(\mathbf{r}, \mathbf{j}_n) \rangle \,, \tag{2c}$$

and

$$V_m = \langle \mathbf{f}_m(\mathbf{r}), \mathbf{E}_{inc}(\mathbf{r}) \rangle \,, \tag{2d}$$

where $\langle , \rangle$ denotes surface integration. A popular choice for the functions $\mathbf{j}_n(\mathbf{r})$ and $\mathbf{f}_m(\mathbf{r})$ is the Rao-Wilton-Glisson (RWG) basis, which will be utilized here. For a grating of size $L \times L$ square wavelengths, N grows approximately as $200L^2$. For the QWIP grating structure under analysis, N can be of the order of 10^4 or 10^5. Hence, direct inversion of $\bar{\mathbf{Z}}$, which entails a computational cost proportional to N^3, is practically impossible. An iterative solution has a cost proportional to N^2 per iteration, which also prohibits the solution of large problems. Moreover, both these approaches require the storage of $\bar{\mathbf{Z}}$, necessitating memory requirements proportional to N^2.

3 The Steepest Descent Fast Multipole Method

The SDFMM, a hybrid between the fast steepest descent path algorithm [8] and the two-dimensional multilevel fast multipole method [9], relies on a hierarchical decomposition of the scatterer into blocks at several levels of coarseness. In the SDFMM, the elements of the MoM matrix $\bar{\mathbf{Z}}$ are formally expressed as

$$\begin{aligned} Z''_{mn} \cong & \sum_{j=1}^{n_{sd}} \sum_{j'=1}^{P} w_j^{sd} w_{j'}^{fmm} \int_S d\mathbf{r} \, \mathbf{f}_m(\mathbf{r}) \, e^{i\mathbf{k}^{(j)} \cdot (\mathbf{r} - \mathbf{r}_t)} \times \\ & \mathcal{T}_{jj'}(\mathbf{r}_t - \mathbf{r}_s) \left(\bar{\mathbf{I}} - \frac{\mathbf{k}^{(j)} \mathbf{k}^{(j)}}{k_0^2} \right) \int_S d\mathbf{r}' \, \mathbf{j}_n(\mathbf{r}') \, e^{i\mathbf{k}^{(j)} \cdot (\mathbf{r}_s - \mathbf{r}')} \,, \end{aligned} \tag{3}$$

where $\mathbf{k}^{(j)}$ are complex wavenumbers, and n_{sd} and w_j^{sd} are the number of points and integration weights associated with integration along the steepest descent path of the Sommerfeld integral representation of the free-space Green's

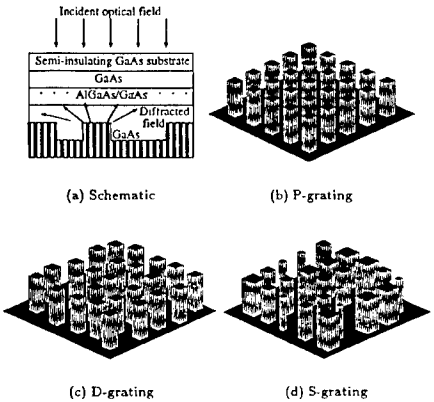

Figure 1: 1(a): Schematic cross section view of grating coupled QWIP device. 1(b): Periodic (P) grating. 1(c): Displaced (D) grating. 1(d): Scaled (S) grating. One corner of each raised portion is fixed, while the other corner is shifted diagonally.

function [7]. Source and testing block centers are denoted by $\mathbf{r}_s$ and $\mathbf{r}_t$, respectively. The translation operator $\mathcal{T}_{jj'}(\mathbf{r}_t - \mathbf{r}_s)$, integration weights w_j^{fmm}, and number of harmonics P are analogous to those defined in well known fast multipole algorithms [10, 11]. The SDFMM enables the aggregation and disaggregation of basis and testing functions through the two far-field integrals appearing in Eqn.(3). This results in a dramatic reduction in the complexity of matrix-vector products involving $\bar{\mathbf{Z}}$ and memory requirements from $O(N^2)$ to $O(N)$.

4 Numerical Results

Three kinds of periodic and quasi-random gratings, shown in Fig. 1, have been studied. The P-grating (Fig. 1(a)) is a doubly *periodic* grating. *Displacing* raised portions of this grating produces a D-grating (Fig. 1(b)), while *scaling* raised portions of a P-grating generates an S-grating (Fig. 1(c)). A single realization of a rough surface grating, which will be discussed later, is depicted in Fig. 1(d). The P-, D-, and S- gratings used here are of dimensions $38 \times 38\mu m$. As a precursor to employing the RWG basis in conjunction with the SDFMM, the grating surfaces are tesselated into planar triangles, with the nodes separated by approximately 0.14λ, where λ is the optical wavelength in the GaAs layer. For infrared radiation with a free-space wavelength of $10\mu m$, $\lambda \cong 3.03\mu m$. Current on each grating is modeled in terms of approximately $N = 30,000$ basis functions. With the SDFMM, such a problem can be solved in 3-7 hours (depending on the number of iterations required) on a single processor R8000 SGI Power Challenge. Detailed memory and cpu time comparisons for the SDFMM, for standard iterative solvers, and for LU decomposition have been carried out earlier for rough surface scattering problems, and are reported in [7].

The periodicity of the P-grating is $4.0\mu m$ along each lateral direction and the raised portions measure $2.0 \times 2.0\mu m^2$. The average shift relative to the period size for the specific D-grating considered is 14 %, and the

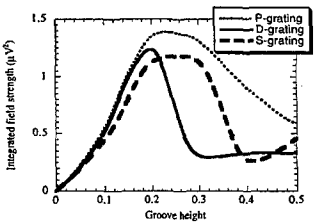

Figure 2: Integrated field strength versus groove height for P- D-, and S- gratings. Groove height is in wavelengths.

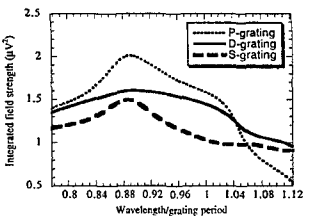

Figure 3: Integrated field strength versus wavelength/period. The ratios of maximum to minimum integrated field strength are 3.83, 1.75, and 1.70 for the P-, D-, and S- gratings respectively.

maximum is 50 %. The average deviation in size (relative compression/ elongation) for the S-grating is 32 % and the maximum deviation is 50 %. Figure 2 shows the integrated field strength as a function of grating height for the three gratings. The integrated field strength is computed by integrating the square of the longitudinal electric field over the cross section of the QWIP at the device layer. Grating absorption is proportional to this measure [4]. As can be seen, the absorption of the P- and S-gratings is maximum when the grating height is approximately 0.25λ, while the D-grating response peaks at a grating height close to 0.2λ. As in the one-dimensional case, the peak absorption due to a P-grating is larger than that due to the quasi-random gratings. The importance and need for quasi-random gratings is evident when one observes the spectral behavior of the absorption due to the gratings, which is depicted in Fig. 3. For the P-grating, the absorption diminishes rapidly at larger wavelengths, due to the evanescent nature of the higher order Floquet modes. If such a grating were designed to operate optimally at the nominal wavelength of $10\mu m$, its performance at the extremal wavelengths ($8\mu m$ and $12\mu m$) would be poor. The D- and S- gratings, on the other hand, do exhibit a much smoother spectral behavior over the range of interest, albeit with a slightly reduced peak absorption. Hence there exists a tradeoff between peak absorption and smooth spectral behavior.

The SDFMM has also been used to analyze rough surface gratings (shown in Fig. 4(a)), which are proposed here as suitable candidates for QWIP applications. These rough surfaces are typically assumed to be correlated Gaussian surfaces [7], and are characterized by two parameters, a correlation length and a mean square height. Prior to the analysis of such surfaces, it was expected that their strongly random nature would result in desirable spectral properties without substantial deterioration in peak absorption. This conjecture has been borne out to be true on the basis of the following simulation results. The relationship between grating absorption and root mean

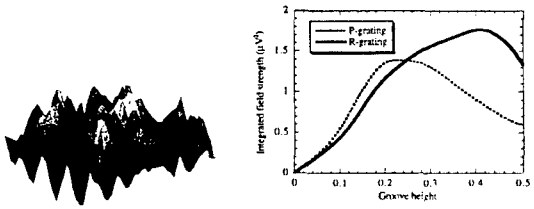

(a) (b)

Figure 4: (a): One realization of a rough surface grating. (b) Integrated field strength versus groove height for periodic and rough surface gratings. The statistical root mean square height is used in lieu of groove height for rough surfaces.

square height of a rough surface grating is presented in Fig. 4(b). The response is seen to peak at around 0.42λ, and is dramatically improved as compared to the peak response of a periodic grating. The correlation length of the grating is 1.0λ. Figure 5 shows the spectral dependence of the grating absorption for three rough surface gratings with different root mean square heights. It can be seen that all three gratings yield a spectral performance that is markedly better than that due to a periodic grating or indeed due to the afore-mentioned quasi-random gratings The grating absorption is remarkably constant over the entire wavelength band of interest. Such behavior as seen in Figs. 4(b) and 5 suggests that rough surface gratings should be particularly suitable for QWIP applications.

5 Conclusions

This work reports on the application of a rigorous full-wave technique to the performance analysis of two-dimensional quasi-random and rough surface gratings for QWIPs. The SDFMM, developed earlier for analyzing arbitrary quasi-planar structures, is well-suited for analyzing scattering from large-scale gratings because its memory requirements and cpu time per matrix-vector product scale as $O(N)$. Using the SDFMM, it has been shown that there is a tradeoff between peak absorption and spectral smoothness. Introducing randomness into a grating leads to a reduced peak absorption but improves spectral properties, which are important when the wavelengths of interest cover a broad band, such as the popular 8μ-12μ range. The results presented here are qualitatively consistent with the findings reported by Xing and Liu in Ref. [4], for one-dimensional gratings. Hence, we confirm these authors' conjecture that the afore-mentioned tradeoff demonstrated for one-dimensional gratings in their work should extend to two-dimensional gratings. Rough surface gratings, analyzed here for the first time in the context of QWIP applications, appear to have great potential because of excellent grating absorption and spectral behavior. It is expected that the techniques suggested in this work will assist in the *a priori* design of novel and efficient QWIP gratings.

References

[1] B. Levine, "Quantum-well infrared photodetectors," *J. Appl. Phys.*, vol. 74, pp. R1–R81, October 1993

[2] C. Bethea, B. Levine, M. Asom, R. Leibenguth, J. Stayt, K. Glogovsky, R. Morgan, J. Blackwell, and W. Parish, "Long wavelength infrared $128\times128 Al_xGa_{1-x}As/GaAs$ quantum well infrared camera and imaging system," *IEEE Trans. Electron Devices*, vol. 40, pp. 1957–1963, November 1993.

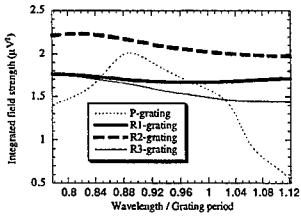

Figure 5: Integrated field strength versus wavelength/period for rough surface gratings and a periodic grating. The three gratings R1, R2, and R3 possess root mean square heights of 0.2λ, 0.4λ, and 0.6λ respectively. For these gratings, their correlation length is varied analogously to the period. The ratio of maximum to minimum integrated field strength is less than 1.2 for all three cases.

[3] J. Andersson and L. Lundquist, "Grating-coupled quantum-well infrared detectors: theory and performance," *J. Appl. Phys.*, vol. 71, pp. 3600–3610, April 1992.

[4] B. Xing and H. Liu, "Simulation of one-dimensional quasi-random gratings for quantum well infrared photodetectors," *J. Appl. Phys.*, vol. 80, pp. 1214–1218, July 1996.

[5] L. Lundqvist, J. Andersson, Z. Paska, J. Borglind, and D. Haga, "Efficiency of grating coupled algaas/gaas quantum well infrared photodetectors," *Appl. Phys. Lett.*, vol. 63, pp. 3361–3363, December 1993.

[6] G. Sarusi, B. Levine, S. Pearton, K. Bandara, R. Leibenguth, and J. Andersson, "Optimization of two dimensional gratings for very long wavelength quantum well infrared photodetectors," *J. Appl. Phys.*, vol. 76, pp. 4989–4994, November 1994.

[7] V. Jandhyala, E. Michielssen, B. Shanker, and W. Chew, "A combined steepest descent –fast multipole algorithm for the fast analysis of three-dimensional scattering by rough surfaces," Tech. Rep. CCEM-3-97, Center for Computational Electromagnetics, University of Illinois, Urbana, March 1997.

[8] E. Michielssen and W. Chew, "Fast steepest descent path algorithm for analyzing scattering from two-dimensional objects," *Radio Science*, vol. 31, pp. 1215–1224, September 1996.

[9] C. C. Lu and W. C. Chew, "A multilevel algorithm for solving a boundary integral equation of wave scattering," *Microwave Opt. Tech. Lett.*, vol. 7, pp. 466–470, July 1994.

[10] R. Coifman, V. Rokhlin, and S. Wandzura, "The fast multipole method for the wave equation: a pedestrian description," *IEEE Antennas Propagat. Mag.*, vol. 35, pp. 7–12, June 1993.

[11] J. M. Song and W. C. Chew, "Multilevel fast-multipole algorithm for solving combined field integral equations of electromagnetic scattering," *Microwave Opt. Tech. Lett.*, vol. 10, pp. 14–19, September 1995.

FORWARD AND BACKWARD PROPAGATION ALGORITHMS APPLIED TO THE ELECTROMAGNETIC SCATTERING BY AN IMPENETRABLE OBSTACLE. A PROGRESS REPORT

GIOVANNI F CROSTA
UNIVERSITÀ DEGLI STUDI DI MILANO
Dipartimento di Scienze dell' Ambiente e del Territorio
via Emanueli, 15 - I 20126 MILANO (IT); e_mail: crosta@imiucca.csi.unimi.it

ABSTRACT

Approximate backpropagation (ABP) methods are used to identify the shape of acoustic and electromagnetic scatterers in the resonance region from full aperture data. Said methods rely on a heuristic relation i.e., ABP, between the expansion coefficients, which represent the scattered wave in the far zone and, respectively, on the obstacle boundary, Γ. The unknown is the shape parameter vector, $\vec{\psi}$, which must be in a suitable admissible set. The objective function to be minimized is the $L^2(\Gamma)$ – norm of the boundary defect. A sample numerical result is given, which comes from the inversion of an IPSWICH data set. In order to justify the well - posedness of ABP some related problems are examined. An error bound is given, which compares the far zone to the least squares boundary coefficients. The approximate forward propagation (AFP) map is defined and its consistency on disks and spheres is stated. Finally, a property of forward propagation in the infinite dimensional case (ℓ_2) is provided.

INTRODUCTION

Let the obstacle, Ω, be a perfectly electrically conducting (PEC) right cylinder lying along the z axis. Let the cross section, D, of Ω be smooth. Denote the boundary of D by Γ. The direct problem consists of determining the scattered wave from knowledge of the (unit amplitude) incident monochromatic plane wave, which may be either vertically or horizontally polarized. A typical inverse problem is the reconstruction of Γ from suitable data and constraints e.g., the incident wave, the (complex) scattering amplitude and a few pieces of prior knowledge about Γ.

SECT. 1 briefly describes a reconstruction method, known as $X_1^{(L)}$ – approximate back propagation ($X_1^{(L)}$ –ABP for short) and its application to the inversion of experimental data, a set of the IPSWICH data [MK1]. The method was developed a few years ago to solve the inverse obstacle problem in acoustics [C1, C2], when the obstacle is axially symmetric and when its diameter is comparable to wavelength. More recently, the method has been extended to scalar and vector electromagnetic cases in 2 spatial dimensions [C3].

SECT. 2 deals with some preliminary results, which aim at proving the well - posedness of $X_1^{(L)}$ –ABP, at least under additional hypotheses on the obstacle and on the incident wave.

1 – SHAPE RECONSTRUCTION FROM EXPERIMENTAL DATA

1.1 – Notation and Basic Properties

Only the vertical polarization case will be described, which is the simplest.
Prior knowledge about the obstacle is summarized by parameterization and constraints. Namely, the class of admissible obstacle contours is described by those functions $r_\Gamma \in \mathcal{C}^2[0, 2\pi]$ of azimuth ϕ, which are linear combinations of the first I trigonometric functions

$$\frac{1}{r_\Gamma^2(\phi)} = \psi_1 + \psi_2 \cos\phi + \psi_3 \sin\phi + \psi_4 \cos 2\phi + \ldots \tag{1.1}$$

Here $\{\psi_1, \psi_2, \ldots, \psi_I\}$ are the shape parameters, which form the entries of the vector $\vec{\psi} \in \mathbb{R}^I$. When smoothness and two sided constraints

$$(0<)\ r_{\min} \le r_\Gamma[\phi] \le r_{\max} \quad \forall \phi \in [0, 2\pi] \tag{1.2}$$

are taken into account, one must select $\vec{\psi} \in \Psi_{ad} \subset \mathbb{R}^I$, where Ψ_{ad} is the bounded set of admissible parameters.

A key role in the approximation of the scattered wave is played by the family of outgoing cylindrical wave functions

$$v_\lambda[\mathbf{x}] = \sqrt{\epsilon_m}\, H_m^{(1)}[k\sigma]\,((1-p)\cos m\,\phi + p \sin m\,\phi)\,, \tag{1.3}$$

where $r := |\mathbf{x}|$, $H_m^{(1)}[.]$ are HANKEL's functions of the 1st kind, ϵ_m is the NEUMANN factor and $\lambda = \{p,m\}$ is the index pair. Indices range in $\Lambda := \{p,m \mid p = 0, 1;\ p \le m\}$. Real waves are defined by $u_\lambda := \mathrm{Re}[v_\lambda]$. If one fixes an approximation order, L, and lets $\lambda \in \Lambda(L) := \{p,m \mid p = 0, 1;\ p \le m \le L\}$, then one can define the following subspace of $L^2(\Gamma)$

$$X_1^{(L)}(\Gamma) := \mathrm{Span}\,\{v_\lambda\,|_\Gamma \mid \lambda \in \Lambda(L)\}, \tag{1.4}$$

which motivates the name of the method, and the two arrays, the matrix $\Re\mathbf{L}^{(L)}$ and the vector $\mathbf{b}^{(L)}$, respectively

$$\Re\mathbf{L}^{(L)} := -\frac{i}{4}\,[\langle u_\lambda\,|_\Gamma\ \partial_N\, v_\mu\,\rangle]\ ,\quad \mathbf{b}^{(L)} := -\frac{i}{4}\,[\langle u_\lambda\,|_\Gamma\ \partial_N\, E_z^{(inc)}\,\rangle];\ \lambda\ ,\mu \in \Lambda(L)\,, \tag{1.5}$$

where $\langle \cdot\,|_\Gamma\,\cdot\,\rangle$ is the inner product in $L^2(\Gamma)$ and ∂_N stands for the outward normal derivative on Γ.

The entries of these arrays depend on $\vec{\psi}$.

The z component of the incident electric field, $E_z^{(inc)}$, comes from the datum $\mathbf{E}^{(inc)} := \hat{\mathbf{z}}\ e^{i\mathbf{kx}}$, where $\mathbf{k}$ is the incident wavevector. The scattered electric field, $E_z^{(sc)}$ is a solution to the exterior boundary value (BV) problem for the scalar HELMHOLTZ equation (HE) subject to the SOMMERFELD radiation condition at infinity and to the DIRICHLET BC on $\partial\Omega$

$$(E_z^{(inc)} + E_z^{(sc)})\,|_{\partial\Omega} = 0\,. \tag{1.6}$$

Outside the circular cylinder of radius r_{max} circumscribed to the obstacle, the field $E_z^{(sc)}$ is represented by the converging series

$$E_z^{(sc)} = \sum_{\lambda} f_\lambda\, v_\lambda\,, \tag{1.7}$$

where $\{f_\lambda\}$ are the far field scattering coefficients.

The experimental data, which characterize this inverse problem, are the complex values of the scattering amplitude $S_A[\hat{\mathbf{x}}, \mathbf{k}]$, ideally known $\forall\ \hat{\mathbf{x}} \in S^1$, the circumference of unit radius. In practice they are given at uniformly or otherwise spaced points on S^1.

1.2 – The Reconstruction Algorithm

From $S_A[\hat{\mathbf{x}}, \mathbf{k}]$ one obtains $\vec{\varphi}^{(L)}$ i.e., the estimates of order L of the far field scattering coefficients $\{f_\lambda \mid \lambda \in \Lambda(L)\}$ by carrying out the following inner products, which involve the asymptotic counterpart of v_λ as $r \to \infty$, v_λ^{asympt}

$$\varphi_\lambda^{(L)} = \langle v_\lambda^{asympt}\,|_{S^1}\ S_A \rangle,\quad \lambda \in \Lambda(L) \tag{1.8}$$

If the assumption

$$\exists\,[\ \Re \mathbf{L}^{(L)}\ ]^{-1} \tag{1.9}$$

is met, then one can define the $\vec{\psi}$–dependent affine map

$$\mathbf{M}^{(L)}[.] := [\ \Re \mathbf{L}^{(L)}\ ]^{-1}\,(\,[.] + \tfrac{i}{4}\,\mathbf{h}^{(L)}) \tag{1.10}$$

i.e., the scalar $X_1^{(L)}$ – ABP of order L. It transforms $\vec{\varphi}^{(L)}$ into another vector of coefficients, $\vec{\xi}^{(L)}$ i.e.,

$$\vec{\xi}^{(L)} = \mathbf{M}^{(L)}\,[\,\vec{\varphi}^{(L)}\,]\,. \tag{1.11}$$

The latter appears in the approximate representation of $E_z^{(sc)}$ on Γ and in the definition of the objective function $B_{DV}^{(L)}$

$$B_{DV}^{(L)}\,[\,\vec{\psi}\,] := \frac{1}{2}\,\|\,E_z^{(inc)} + \sum_{\lambda \in \Lambda(L)} \xi_\lambda^{(L)}\, v_\lambda\,\|^2_{L^2(\Gamma[\vec{\psi}])}\,. \tag{1.12}$$

Shape reconstruction is restated as the search for $\vec{\psi}^{\,\star} \in \Psi_{ad}$ such that $B_{DV}^{(L)}[\,\vec{\psi}^{\,\star}\,] = \min$.

The minimization of $B_{DV}^{(L)}$ is carried out by means of a conjugate directions algorithm.

1.3 – Application to the Ipswich Data

Application of $X_1^{(L)}$ – ABP to the Ipswich data is slightly more complicated with respect to the algorithm outlined in Sect. 1.2, because the argument of S_A is given up to an unknown phase offset, which must also be identified by minimization.

The results obtained from inverting the **ips001/ips001vv.240** data set are shown by Fig. 1 and Tab. 1. Each of the 9 minimization runs is initialized by an ellipse such that the ratio $\eta := \psi_4^{(0)}/\psi_1^{(0)}$ is fixed: $\eta = 0.6$. The approximation order is $L = 5$, the unknown shape parameters are $I = 6$, the number of grid points on the perimeter is $n_p = 127$ and the maximum allowed number of main loop iterations is $N_{\text{main}} = 15$. The 9 reconstructed shapes are ranked by the final value of $B_{DV}^{(5)}$. The radius $r_\Gamma^{(0)}[\phi = = \pi/4]$ of the initial ellipse (labelled by r_0) is also listed. Thicker lines correspond to better results. One notices that 8 out of 9 runs accurately reconstruct the desired shape, a disk.

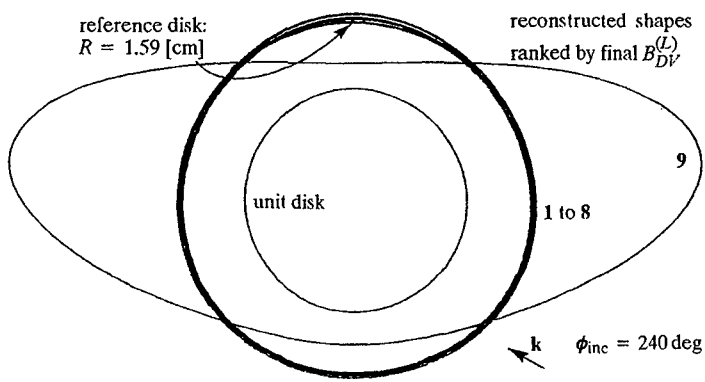

Figure 1. Shapes reconstructed from the **ips001/ips001vv.240** file. $L = 5, I = 6$, $n_p = 127$ and $N_{\text{main}} = 15$.

Table 1. Some numerical values related to runs **1**, **8** and **9** of Fig. 1.

Here r_0 denotes the radius of the initial shape at $\phi = \pi/4$. The best and worst results are labelled by **1** and **9** respectively.

1) ▬▬▬ r_0 = .571753D+00 N_{main} = 15; $B^{[5]}$ = .1041D+00 ; $\|\nabla B\|$ = .8770D+00

8) ——— r_0 = .174901D+01 N_{main} = 15; $B^{[5]}$ = .1066D+00 ; $\|\nabla B\|$ = .8804D+00

9) ——— r_0 = .152087D+01 N_{main} = 15; $B^{[5]}$ = .7990D+02 ; $\|\nabla B\|$ = .1881D+04

2 – JUSTIFICATION OF FORWARD AND BACKWARD PROPAGATION SCHEMES

$X_1^{(L)}$ – ABP has been used on a heuristic basis. The satisfactory numerical performance in inverse acoustics and to some extent in electromagnetics does not vouch for the well – posedness of the method. In fact, the determination of its properties is a major open problem. A few related results are listed below. Proofs are omitted for reasons of space.

2.1 – The Least Squares Boundary Coefficients

Given L, Γ, u and L, the problem of finding the vector of least squares boundary coefficients, $\mathbf{c}^{(L)}$ i.e., $\{ c_\lambda^{(L)} \mid \lambda \in \Lambda(L) \}$ such that

$$B_{DI}^{(L)} := \frac{1}{2} \left\| E_z^{(\mathrm{inc})} + \sum_{\lambda \in \Lambda(L)} c_\lambda^{(L)} v_\lambda \right\|_{L^2(\Gamma)}^2 = \min. \tag{2.1}$$

is well posed [B1, M1, R1]. Further properties of these coefficients are of interest, because they appear in the objective function of Eq. 1.12, although in a different role. The relation between $\{ c_\lambda^{(L)} \}$ and the $\{ f_\lambda \}$ of Eq. 1.7 comes as the following error bound.

THEOREM 2.1.

I) $\forall\, \epsilon > 0$, $\exists$ *at least an approximation order* $L[\epsilon]$ *and a vector of coefficients* $\mathbf{c}^{(L[\epsilon])}$ *such that*

$$B_{DI}^{(L[\epsilon])} < \epsilon^2 . \tag{2.2}$$

II) *Let an* $L[\epsilon]$ *be selected to comply with* INEQ. 2.2. *Let* $\rho >> r_{\max}$ *and* $C[\Gamma, \rho, k]$ *be a quantity, which depends on* Γ, ρ *and* k. *Then the corresponding vector* $\mathbf{c}^{(L[\epsilon])}$ *of least squares boundary coefficients is related to that of far field coefficients in Eq. 1.7 by the error bound*

$$|f_\lambda - c_\lambda^{(L[\epsilon])}|^2 < \frac{k^2 \epsilon^2}{\pi} C[\Gamma, \rho, k], \ \forall\, \lambda \in \Lambda(L[\epsilon]). \tag{2.3}$$

2.2 – The Forward Propagated Coefficients

With reference to Eq. 1.5, define the vector of $X_1^{(L)}$ – approximately forward propagated (AFP) coefficients

$$\mathbf{p}^{(L)} := \mathfrak{M}^{(L)} \cdot \mathbf{c}^{(L)} + \mathbf{b}^{(L)} . \tag{2.4}$$

One will notice that $\mathbf{M}^{(L)}$ of Eq. 1.10 is the inverse of this affine map $\mathbf{c}^{(L)} \mapsto \mathbf{p}^{(L)}$. A straightforward result is the following.

THEOREM 2.2. *Let* $n = 2$ *or* 3 *and* Ω *be a disk or, respectively a sphere of radius* R *i.e.,* $\Gamma = S_R^{n-1}$. *Then,* $\forall\, L \geq 0$

$$c_\lambda^{(L)} = f_\lambda = p_\lambda^{(L)}, \ \forall \lambda \in \Lambda(L) \tag{2.5}$$

i.e., the AFP scheme is consistent.

If the series in Eq. 1.7 converges (pointwise) on Γ as well, one says the Rayleigh hypothesis holds or that Ω is a Rayleigh obstacle, at least for the given $\mathbf{k}$. Another definition is needed.

Definition 2.1. An obstacle is of R–U class if it is a Rayleigh obstacle, on the surface of which the series of normal derivatives $\sum_{\mu} f_\mu \, \partial_N \, v_\mu$ converges uniformly.

A preliminary result about AFP is the following, where $\mathbf{b}$ and $\mathfrak{R}\mathbf{L}$ are the infinite dimensional counterparts of $\mathbf{b}^{(L)}$ and $\mathfrak{R}\mathbf{L}^{(L)}$, whereas $\mathbf{f} := \{f_\lambda\}$.

Theorem 2.3. *Let the obstacle be of R–U class. Assume* $\mathbf{f}, \mathbf{b} \in \ell_2$ *and* $\mathfrak{R}\mathbf{L} : \ell_2 \to \ell_2$ *is bounded. If the spectral radius* $r_\sigma[\mathfrak{R}\mathbf{L}]$ *of* $\mathfrak{R}\mathbf{L}$ *satisfies* $r_\sigma[\mathfrak{R}\mathbf{L}] < 1$, *then,* $\forall\, \mathbf{b} \in \ell_2$, *there exists a unique solution,* $\mathbf{f}$, *to* $\mathbf{f} = = \mathbf{b} + \mathfrak{R}\mathbf{L}\cdot\mathbf{f}$, *which is obtained by successive approximations, where t is the iteration index*

$$\mathbf{p}^{[t+1]} = \mathbf{b} + \mathfrak{R}\mathbf{L}\cdot\mathbf{p}^{[t]}, \, t = 0, 1, 2, \ldots \tag{2.6}$$

started with an arbitrary $\mathbf{p}^{[0]} \in \ell_2$.

Further work is needed to relate this last result to the finite – dimensional version, Eq. 2.4. This may establish the well posedness of AFP and, eventually, ABP. More specific conditions on Γ and k may be needed and their practical significance will have to be evaluated.

REFERENCES

[B1] R G Barantsev, V V Kozachek, Issledovanie Matrizy Rasseyaniya na Ob'ektach Slozhnoi Formy, *Vestnik Leningr Univers* # 7 71 – 77 (1968)

[C1] G F Crosta, The Backpropagation Method in Inverse Acoustics, in *Tomography, Impedance Imaging and Integral Geometry*, **LAM 30** (Edited by M Cheney, P Kuchment, E T Quinto) pp 35 – 68, AMS: Providence, RI (1994)

[C2] G F Crosta, A Shape Optimization Problem in Inverse Acoustics, in *Control and Optimal Design of Distributed Parameter Systems* (Edited by J Lagnese, D L Russel, L White) pp 1 – 23, Springer–Verlag: New York (1995)

[C3] G F Crosta, Scalar and Vector Backpropagation Applied to Shape Identification from Experimental Data: Recent Results and Open Problems to appear in *Inverse Problems, Tomography and Image Processing*, (Edited by A G Ramm) Plenum: New York, NY

[M1] R F Millar, The Rayleigh Hypothesis and a Related Least Squares Solution to Scattering Problems for Periodic Surfaces and Other Scatterers, *Radio Science* **8**, 785–96 (1973)

[MK1] McGahan, R. V., Kleinman, R. E., Special Session on Image Reconstruction Using Real Data, *IEEE Antennas and Propagation Magazine* **38** 39 – 40 (1996)

[R1] A G Ramm, *Scattering by Obstacles*, Reidel: Dordrecht, 1986

Analysis of Broad Wall Slots Excited by Tuning Screws

Tony Azar
Prof. Richard Coren
Drexel University
Philadelphia, PA

Geometric simplicity, and light weight make slot-antenna arrays attractive for many radar, broadcast, and communications applications. Since the work of Stevenson[1], Watson[2] and Oliner[3], slot arrays have been investigated by numerous researchers. With the development of fast computers, numerical analysis, and especially the method of moments, have been used to analyze these structures. Longitudinal, offset, and compound slots have been analyzed to a great degree of accuracy. One type of a non-radiating slot excited by tilted wires has recently been analyzed by Hashemi-Yeganeh [4]. Another type of non-radiating slot is the broad wall centered slot excited by tuning screws. This type of slot has several advantages. 1- elimination of cross polarization. 2 - ease and simplicity in changing the input impedance and radiation level. 3 - the possibility of using one waveguide for different frequency ranges and different radiation patterns. A disadvantage of these slots is their inherent narrow band. The advantages mentioned above make this type of antenna attractive for the broadcast industry where the band required for the TV channels is 6 MHz (approx. 1%). By clever mounting of the screw and the slot shorteners, one waveguide with one long slot in the center of its broad wall can be made to radiate at different channels and with different elevation patterns.

This paper presents a method of moments analysis of one unit element of this array. The basic goal is to determine the electric field distribution in the slot and the current distribution on the probe. From this, forward and backward scattering can be deduced and the input impedance can be obtained .

Figure 1 shows the geometry considered. We take the pairs (P_1,P'_1) and (P_2,P'_2) to be the field and source points on the surface of the probe and the slot respectively. One has to solve the following boundary conditions:

$$H^{\text{int ernal}}_{\text{tan gential}}\left(P_2; P_1', P_2'\right) = H^{\text{external}}_{\text{tan gential}}\left(P_2; P_1', P_2'\right) \tag{1}$$

$$E^{\text{int ernal}}_{\text{tan gential}}\left(P_1; P_1', P_2'\right) = 0 \tag{2}$$

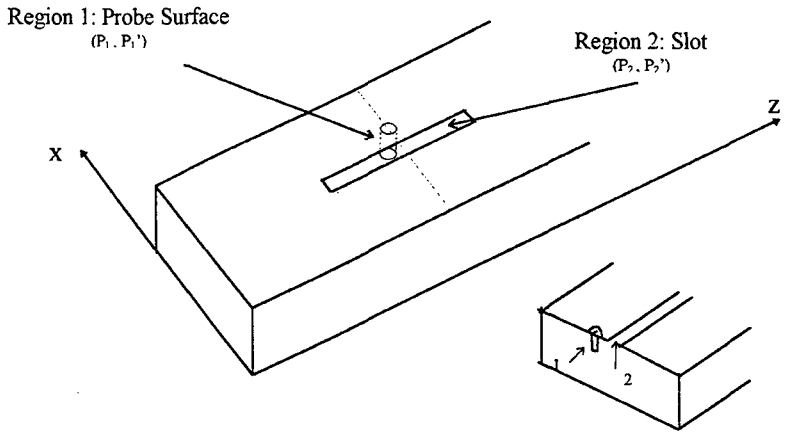

Figure 1

Each of the above equations consists of 3 parts : 1) The internal TE_{10} wave of known amplitude, 2) The self effect, 3) mutual effect of the post on the slot and the slot on the post. In expanded form equations (1) and (2) can be written as :

$$H_z^{Slot,\text{int}}(P_2; P_2') - H_z^{Slot,ext}(P_2; P_2') + H_z^{Post}(P_2; P_1') = -H_z^{inc}(P_2) \quad (3)$$

$$E_y^{slot}(P_1; P_2') + E_y^{Post}(P_1; P_1') = -E_y^{inc}(P_1) \quad (4)$$

With the following assumptions:
1- The upper broad wall has zero thickness
2- The slot ground plane has infinite extent
3- The E_z component in the aperture is neglected
4- The excitation is from a TE_{10} mode

It can be shown that the above equations take the form

$$H_z^{Slot,\text{int}}(x, y, z) = \frac{-2}{j\omega\mu\, ab} \sum_{m=0}^{\infty}\sum_{n=0}^{\infty} \varepsilon_{mn}^2 \frac{\cos(k_x x)\cos(k_y y)}{\gamma_{mn}}$$

$$\int_{slot} E_x(x', y', z')\cos(k_x x')\cos(k_y y')\left[k^2 + \gamma_{\text{mn}}^2 - 2\gamma_{mn}\delta(z - z')\right]e^{-\gamma_{mn}|z-z'|}ds' \quad (5)$$

where
$$\varepsilon_{mn} = \begin{cases} 1/2 & m = 0, n = 0 \\ 1/\sqrt{2} & m = 0, n \neq 0 \ \text{ or } \ m \neq 0, n = 0 \\ 1 & m \neq 0, n \neq 0 \end{cases} \quad (6)$$

$$H_z^{Slot,ext}(z) = \frac{-j}{2\omega\mu\pi} \iint_{x'z'} E_x(z')(k^2 + \partial^2 / \partial z^2)\frac{e^{-j\beta R}}{R}\, dx'\, dz' \quad (7)$$

$$H_z^{Post}(x, y, z) = \frac{2}{ab} \sum_{m=0}^{\infty}\sum_{n=0}^{\infty} \varepsilon_{mn}^2 \frac{\cos(k_x x)\cos(k_y y)}{\gamma_{mn}}$$
$$k_x \int_{v'} J_y(x', y', z')\sin(k_x x')\cos(k_y y')e^{-\gamma_{mn}|z-z'|}dv' \quad (8)$$

$$E_y^{Slot}(x, y, z) = \frac{j\omega\mu}{\gamma_{mn}^2 + k^2}\frac{\partial H_z}{\partial x} \quad (9)$$

$$E_y^{Post}(x, y, z) = \frac{j}{\omega\varepsilon\, ab} \sum_{m=1}^{\infty}\sum_{n=0}^{\infty} \frac{(2 - \delta_o)(k_y^2 - k^2)}{\gamma_{mn}} \sin(k_x x)\cos(k_y y)$$

$$\int_{v'} J_y(x', y', z')\sin(k_x x')\cos(k_y y')e^{-\gamma_{mn}|z-z'|}dv' \quad (10)$$

where
$$\delta_o = \begin{cases} 1 & ; \quad n = 0 \\ 0 & ; \quad n \neq 0 \end{cases} \quad (11)$$

$$H_z^{inc}(x, z) = j\cos(\frac{\pi x}{a})\, e^{-j\beta_{10} z} \quad (12)$$

$$E_y^{inc}(x,z) = \frac{\varpi\mu a}{\pi} \quad \sin(\frac{\pi x}{a})\, e^{-j\beta_{10}z} \tag{13}$$

where E_x is the field distribution in the slot and J_y the current distribution on the post

When applying the Method of Moments to:
the post we use Pulse functions for expansion and testing
the slot we use Pulse functions for expansion and delta function for testing
This yields the following matrix form

$$\begin{bmatrix} Y_{11} & Y_{12} \\ Y_{21} & Y_{22} \end{bmatrix} \cdot \begin{bmatrix} E_s \\ I_p \end{bmatrix} = \begin{bmatrix} h_s \\ h_p \end{bmatrix}$$

where
$Y_{11} = Y_i - Y_e$ = the field of the slot at the slot or the self coupling of the slot.
Y_{22} = the field of the post at the post or the self coupling of the post.
Y_{12} = the field of the slot at the post or the mutual coupling between the slot and the post.
Y_{21} = the field of the post at the slot or the mutual coupling between the post and the slot.
These are given by

$$Y_i = \frac{-4\,W_s^2}{j\omega\mu\, ab} \sum_{m=0}^{\infty} \sum_{n=0}^{\infty} \varepsilon_{mn}^2 \left(\frac{\cos(k_x x_s)\ \mathrm{sinc}(k_x W_s / 2)}{\gamma_{mn}} \right)^2 \begin{cases} (k^2 + \gamma_{mn}^2)\ \sinh(\gamma_{mn}\Delta z / 2)\, e^{-\gamma_{mn}|s-q|\Delta z} & ;\quad s \neq q \\ k^2 - (k^2 + \gamma_{mn}^2) e^{-\gamma_{mn}\Delta z/2} & ;\quad s = q \end{cases} \tag{14}$$

where s and q are integers and
W_s = width of slot ; $2L$ = length of slot
$D_z = 2L/Ns$; N_s = number of Pulses for expansion
x_s = location of slot along the x-axis

$$Y_e = \int_{x=0}^{W_s} (W_s - x) \left\{ (z_q - z_u)(1 + jkR_1) \frac{e^{-jkR_1}}{R_1^3} - (z_q - z_l)(1 + jkR_2) \frac{e^{-jkR_2}}{R_2^3} \right\} dx$$
$$+ k \int_{z=z_q-z_l}^{z_q-z_u} \left\{ je^{-jk\sqrt{z^2+W_s^2}} - kW_s \int_{x=0}^{W_s} \frac{e^{-jk\sqrt{x^2+z^2}}}{\sqrt{x^2+z^2}}\, dx \right\} dz \quad +2j\, \sin(k\Delta z / 2)\, e^{-jk|q-s|\Delta z} \tag{15}$$

where $z_q - z_u = (q - s - 0.5)\Delta z$; $R_1 = \sqrt{x^2 + (z_q - z_u)^2}$

$z_q - z_l = (q - s + 0.5)\Delta z$; $R_2 = \sqrt{x^2 + (z_q - z_l)^2}$ for $s \neq q$

and the above term is multiplied by : $\frac{1}{j\omega\mu\pi}$

$$Y_e = -\Delta z \int_{x=0}^{W_s} (W_s - x)(1 + jkR_3)\frac{e^{-jkR_3}}{R_3^3}\,dx + 2k^2 W_s \int_{x=0^+}^{W_s}\int_{z=0}^{\Delta z/2} \frac{e^{-jk\sqrt{x^2+z^2}} - 1}{\sqrt{x^2 + z^2}}\,dx\,dz \qquad (16)$$

$$-2k\int_{z=0}^{\Delta z/2}\left(jk\,e^{-jk\sqrt{W_s^2+z^2}} - kW_s \ln(W_s + \sqrt{W_s^2 + z^2})\right)dz$$

$$-k^2 W_s \Delta z\left(\ln(\Delta z / 2) - 1\right) + 2j\sin(k\Delta z / 2)$$

Where $R_3 = \sqrt{x^2 + (\Delta z / 2)^2}$ for $s = q$

and the above is multiplied by $\frac{1}{j\omega\mu\pi}$

$$Y_{22} = \frac{j8\Delta_y^2}{\omega\varepsilon ab}\sum_{m=1}^{\infty}\sum_{n=0}^{\infty}\frac{(2 - \delta_o)(k_y^2 - k^2)}{\gamma_{mn}^2}\cos(k_y y_i)\cos(k_y y_p)(1 - e^{-\gamma_{mn} t/2}) \cdot$$

$$\left[\frac{1}{k_x}\sin(k_x x_p)\sin(\frac{k_x W_p}{2})\,\mathrm{sinc}(\frac{k_y \Delta_y}{2})\right]^2 \qquad (17)$$

In analyzing Y_{22} we have assumed a flat strip of metal with a thickness t that later becomes the effective thickness of the post, and we assumed the post to be at z = 0 which is the center of the slot.

i and p are integers
W_p = width of post ; d = depth of post
$D_y = 2L/N_p$; N_p = number of Pulses for expansion
x_p = location of post along the x-axis

$$Y_{12} = \frac{4W_p W_s \Delta_y}{ab} \sum_{m=1}^{\infty} \sum_{n=0}^{\infty} \frac{\varepsilon_{mn}^2}{\gamma_{mn}^2} \cos(k_x x_s) \sin(k_x x_p) \operatorname{sinc}(k_x W_s / 2) \operatorname{sinc}(k_x W_p / 2) \operatorname{sinc}(k_y \Delta_y / 2)$$

$$\cos(n\pi) \cos(k_y y_p) \cdot \begin{cases} \sinh(\gamma_{mn} t / 2)\, e^{-\gamma_{mn}|z_q|} & ; \quad |z_q - z_p| \geq t / 2 \\ 1 - e^{-\gamma_{mn} t/2} \cosh(\gamma_{mn} z_q) & ; \quad |z_q - z_p| < t / 2 \end{cases} \tag{18}$$

$$\text{where } z_q = -L + (q - 0.5)\Delta_z$$

$$Y_{21} = \frac{8W_s \Delta_y}{ab} \sum_{m=1}^{\infty} \sum_{n=0}^{\infty} \frac{\varepsilon_{mn}^2}{\gamma_{mn}^2} \cos(k_x x_s) \sin(k_x x_p) \operatorname{sinc}(k_x W_s / 2) \sin(k_x W_p / 2) \operatorname{sinc}(k_y \Delta_y / 2)$$

$$\cos(n\pi) \cos(k_y y_i) \sinh(\gamma_{mn} \Delta_z / 2) \cdot \begin{cases} e^{+\gamma_{mn} z_s} & ; \quad s \leq N_s / 2 \\ e^{-\gamma_{mn} z_s} & ; \quad s > N_s / 2 \end{cases} \tag{19}$$

$$h_p = \frac{-2\omega\mu a^2 \Delta_y}{\pi^2} \sin\left(\frac{\pi x_p}{a}\right) \sin\left(\frac{\pi W_p}{2a}\right) \tag{20}$$

$$h_s = \frac{j2a}{\pi} \cos\left(\frac{\pi x_s}{a}\right) \sin\left(\frac{\pi W_s}{2a}\right) e^{-j\beta_{10} z_q} \tag{21}$$

The above equations were coded in MATLAB and a comparison between this MoM code and the commercial software HFSS was made. Figure 2 shows S_{11} and S_{12} for two different bands. The agreement is comparable to that found in other articles. A more accurate comparison (in terms of time) could not be made due to network limitation. However, it is noteworthy that our MoM code runs in a matter of minutes while HFSS requires hours. Only these two plots have been obtained at this time but other cases will be generated in the next few days.

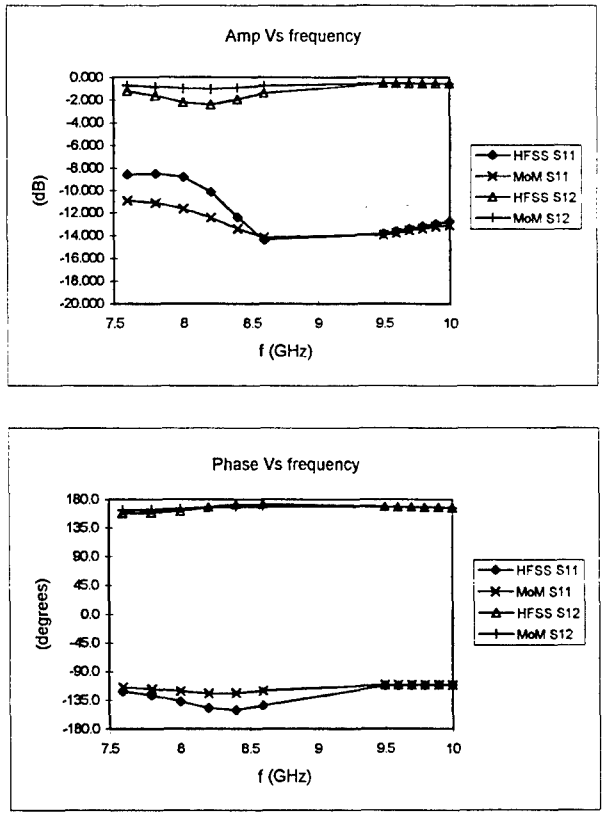

Figure 2 Amplitude and Phase of S_{11} and S_{12} for

Slot : Length = 16 mm Width = 1.6 mm
Location = a/2 (center of guide)

Post : depth = 4 mm Diam = 1.6 mm
Location = a/2 - 2.4 mm

Guide : a = 22.86 mm b = 10.16 mm

1. Stevenson, A. F. S.C.A.M. Ntional Research Council of Canada. "Theory of Slots in Rectangular Waveguides", (Parts I & II), 1944.

2. Watson W. H., "Resonant Slot", IEE Journal, Vol. 93, part 3A, pp. 747-77, 1946.

3. Oliner, A. A., "The Impedance Properties of Narrow Radiating Slots in the Broad Face of Rectangular Waveguide", IRE Trans., Vol. AP-5, p.p. 1-20, January 1957.

4. Hashemi-Yeganeh, S., "Analysis of Untilted Edge Slots Excited by Tilted Wires", IEEE Trans. AP, Vol. 38, No. 11, p.p. 1737, November 1990.

CLOSED-FORM EXPRESSION OF THE ARC-LENGTH OF THE TOROIDAL/HELICAL EQUILIBRIUM ORBIT

Ross A. Speciale

polytope@msn.com

ABSTRACT

An exact, closed-form mathematical expression has been found that gives the integrated path-length of a re-entrant, multiturn, toroidal/helical equilibrium orbit, as function of the azimuth angle, measured around the orbit axis.

The use of a multiturn, toroidal/helical equilibrium orbit is the distinctive characteristic of a recently proposed new type of High Power Microwave (HPM) amplifier, that synergistically combines the basic principles of the Relativistic Klystron Amplifier (RKA) with those of Electron Storage Rings.

The new type of High Power Microwave amplifier [1-2] is expected to attain much higher efficiencies, duty cycles, and spectral purity, because of its advanced design being based on most recent techniques of particle-beam dynamics.

The obtained closed-form expression gives the integrated orbit-path length as function of any arbitrary value of the azimuth angle, measured around the orbit axis, up to the total length of all the turns of the closed orbit. A previously developed approximate expression of the orbit length, based on a fourth-order power expansion of the integrand, has been found to be surprisingly accurate, having average relative error in the order of ± 0.005.

1 - GEOMETRY AND SYMMETRIES OF THE EQUILIBRIUM ORBIT.

The proposed re-entrant, multiturn, toroidal/helical electron "equilibrium-orbit" is defined, in Cartesian coordinates, by the parametric equation :

$$\hat{r}(\varphi,\theta) = x(\varphi,\theta)\cdot\hat{i} + y(\varphi,\theta)\cdot\hat{j} + z(\varphi,\theta)\cdot\hat{k} \qquad (1)$$

where φ is the azimuth angle around the torus axis, θ is the helical "wrapping angle" in-and-out of the "hole", around the "body" of the torus, and the three Cartesian components of the position-vector r are given by :

$$x = (R + r\cos\theta)\cos\varphi \qquad (2)$$

$$y = (R + r\cos\theta)\sin\varphi \qquad (3)$$

$$z = r\sin\theta \qquad (4)$$

while the linear relation between the angles φ , and θ is determined by the integer number n of re-entrant orbit turns :

$$\theta = \frac{n-1}{n}\varphi \qquad (5)$$

The integer n in (5) is the *minimum* number of turns around the torus axis that brings the re-entrant, multi-turn equilibrium orbit to close on itself, while it is $0 \le \varphi \le 2\,n\,\pi$.

The nominal equilibrium orbit, defined by the equations (1)-(5) , exhibits C_{n-1} rotation symmetry around the axis of the virtual torus surface, with an angular period of $2\pi/(n\text{-}1)$ radians, and C_n "rotation" symmetry around the center of the circular torus cross-section, with an angular period of $2\pi/n$ radians (a $\theta \rightarrow \theta + 2\pi / n$ mapping, with φ = constant).

Tests are being performed to determine whether this orbit is actually an Elliptic Curve.

A 3D representation of one such toroidal/helical orbit, with ratio $c = r/R = 0.2$, and the number of turns $n = 9$ is shown in Figure 1 . The location of a total of 120 electron bunches, spaced along the orbit by $9 \times 360^\circ / 120 = 27^\circ$, are shown there as small circles.

2 - APPROXIMATE EXPRESSION OF THE ORBIT LENGTH.

The rate of increase of the orbit-path length, with increasing azimuth angle φ , is given by the non-linear, periodic expression (Figure 2) :

$$\frac{ds}{d\varphi} = \sqrt{\left(\frac{dx}{d\varphi}\right)^2 + \left(\frac{dy}{d\varphi}\right)^2 + \left(\frac{dz}{d\varphi}\right)^2} = \qquad (6)$$

$$= R\sqrt{\left(1 + c\cos\theta\right)^2 + c^2\left(\frac{n-1}{n}\right)^2}$$

This expression can be approximated by a power-series expansion in the *"aspect ratio"* of the virtual torus surface, defined above as the ratio $c = r/R$ of the minor axis r to the major axis R.

A fourth-order approximation is given by the expressions :

$$\frac{ds}{d\varphi} = R\sqrt{(1+c\cos\theta)^2 + c^2\left(\frac{n-1}{n}\right)^2} \cong \tag{7}$$

$$\cong w_0 + w_1 c + w_2 c^2 + w_3 c^3 + w_4 c^4$$

where the w_i coefficients are given by :

$$w_0 = R \tag{8}$$

$$w_1 = R\cos\theta = R\cos\left(\frac{n-1}{n}\varphi\right) \tag{9}$$

$$w_2 = \frac{1}{2}R\left(\frac{n-1}{n}\right)^2 \tag{10}$$

$$w_3 = -\frac{1}{2}R\left(\frac{n-1}{n}\right)^2\cos\theta = \tag{11}$$

$$= -\frac{1}{2}R\left(\frac{n-1}{n}\right)^2\cos\left(\frac{n-1}{n}\varphi\right)$$

$$w_4 = \frac{R}{8n^2}\left(\frac{n-1}{n}\right)^2\left[4n^2\cos^2\theta - (n-1)^2\right] = \tag{12}$$

$$= \frac{R}{8n^2}\left(\frac{n-1}{n}\right)^2\left[4n^2\cos^2\left(\frac{n-1}{n}\varphi\right) - (n-1)^2\right]$$

Term-by-term integration of the power-expansion (7) leads to the corresponding approximate expression of the integrated orbit-path length given by :

$$s \cong \left(w_0 + w_2\, c^2\right)\int d\varphi + \int\left(w_1\, c + w_3\, c^3\right)d\varphi + \int w_4\, c^4\, d\varphi \;=$$

$$= h_1\,\varphi + h_2\,\sin\left(\frac{n-1}{n}\varphi\right) + h_3\,\sin\left(2\,\frac{n-1}{n}\varphi\right) \qquad (13)$$

where the coefficients h_1, h_2, and h_3, are expressed by :

$$h_1 = R\left\{1 + \frac{1}{2}\left(\frac{n-1}{n}\right)^2 c^2 + \frac{1}{4}\left(\frac{n-1}{n}\right)^2\left[1 - \frac{1}{2}\left(\frac{n-1}{n}\right)^2\right]c^4\right\} \qquad (14)$$

$$h_2 = R\,\frac{n}{n-1}\left[1 - \frac{1}{2}\,c^2\left(\frac{n-1}{n}\right)^2\right]c \qquad (15)$$

$$h_3 = \frac{1}{8}R\,c\,\frac{n-1}{n} \qquad (16)$$

3 - EXPRESSION OF THE CLOSED-FORM ORBIT-LENGTH INTEGRAL.

A closed-form expression of the integrated orbit-path length has been now obtained by exploiting the exceptional symbolic-integration capabilities of the *Mathematica 3.0* system.

The mathematical structure of the substantially complex result is expressed by :

$$s(\varphi) = \int_0^{\varphi}\frac{ds}{d\varphi} =$$

$$= \int_0^{\varphi}\sqrt{(1 + c\cos\theta)^2 + c^2\left(\frac{n-1}{n}\right)^2}\,d\varphi = \qquad (17)$$

$$= q(\theta)\left[T_1(\theta) + T_2(\theta)\right]$$

where the auxiliary functions $q(\theta)$, $T_1(\theta)$, and $T_2(\theta)$ are expressed by :

$$q(\theta) = \frac{n}{n-1}\frac{1+\cos\theta}{8\sqrt{\left(1+c\cos\theta\right)^2+c^2\left(\frac{n-1}{n}\right)^2}} \tag{18}$$

$$T_1(\theta) = 8\sin\theta\,\frac{\left(1+c\cos\theta\right)^2+c^2\left(\frac{n-1}{n}\right)^2}{\left(1+\cos\theta\right)^2} \tag{19}$$

$$T_2(\theta) = W_1(\theta)\left\{\chi_1 E(\varphi_E|m_1)+\chi_2 F(\varphi_E|m_1)+\chi_1\Pi(n_E;\varphi_E|m_2)\right\} \tag{20}$$

In the expression (20) of the second term $T_2(\theta)$ in the square brackets of equation (17), the functions F, E, and Π represent respectively the *Elliptic Integrals* of the *First* kind, identified as $F(\varphi \mid m)$, of the *Second* kind $E(\varphi \mid m)$, both with *"amplitude"* φ and *"parameter"* m, and the *Incomplete Elliptic Integral* $\Pi(n;\varphi \mid m)$ [3, 6,7].

The auxiliary functions $W_1(\theta)$, and $\varphi_E(\theta)$ are defined by the expressions :

$$W_1(\theta) = -i\,4\sec^2\left(\frac{\theta}{2}\right)\sqrt{\frac{\left(1+c\cos\theta\right)^2+c^2\left(\frac{n-1}{n}\right)^2}{1-c^2+c^2\left(\frac{n-1}{n}\right)^2+i\,2c^2\frac{n-1}{n}}} \tag{21}$$

$$\varphi_E(\theta) = i\sinh^{-1}\left[\sqrt{\frac{1-c^2+c^2\left(\frac{n-1}{n}\right)^2+i\,2c^2\frac{n-1}{n}}{\left(1+c\right)^2+c^2\left(\frac{n-1}{n}\right)^2}}\tan\left(\frac{\theta}{2}\right)\right] \tag{22}$$

while the complex constants χ_1, χ_2, χ_3, m_1, m_2, and n_E are given by :

$$\chi_1 = -\left[1 - c^2 + c^2 \left(\frac{n-1}{n} \right)^2 + i\, 2\, c^2 \frac{n-1}{n} \right] \tag{23}$$

$$\chi_2 = 2\left[1 - c + c^2 \left(\frac{n-1}{n} \right)^2 + i\, c^2 \frac{n-1}{n} \right] \tag{24}$$

$$\chi_3 = 4\,c \tag{25}$$

$$m_1 = \frac{\left\{ \left[1 - 6\left(\frac{n-1}{n}\right)^2 + \left(\frac{n-1}{n}\right)^4 \right] c^4 - 2\left[1 - \left(\frac{n-1}{n}\right)^2 \right] c^2 + 1 \right\} - i\, 4\, c^2 \frac{n-1}{n} \left[1 - c^2 + c^2 \left(\frac{n-1}{n}\right)^2 \right]}{\left[(1-c)^2 + c^2 \left(\frac{n-1}{n}\right)^2 \right] \left[(1+c)^2 + c^2 \left(\frac{n-1}{n}\right)^2 \right]} \tag{26}$$

$$m_2 = \frac{1 - c^2 + c^2 \left(\frac{n-1}{n} \right)^2 - i\, 2\, c^2 \frac{n-1}{n}}{1 - c^2 + c^2 \left(\frac{n-1}{n} \right)^2 + i\, 2\, c^2 \frac{n-1}{n}} \tag{27}$$

$$n_E = \frac{1 - c^2 + c^2 \left(\frac{n-1}{n} \right)^2 - i\, 2\, c^2 \frac{n-1}{n}}{(1-c)^2 + c^2 \left(\frac{n-1}{n} \right)^2} \tag{28}$$

The *"amplitude"* $\varphi_E(\theta)$, and the three *"parameters"* m_1, m_2, and n_E of the three *Elliptic Integrals* are all *complex*. The *Mathematica 3.0* system, however, correctly handles this situation, while performing *symbolic*, as well as *numerical* evaluations.

4 - TIMING BENCHMARKS.

The closed-form expression of the integrated orbit-path length, given by the above set of equations (17)-(28), was obtained by first performing a symbolic simplification upon the extremely complex initial formulation generated by the *"Integrate"* command [4].

This first computer-aided simplification was obtained by using the Mathematica 3.0 *"FullSimplify"* command [5]. The obtained first simplified expression, shown in Table I, was thereafter painstakingly further simplified by hand.

All the *Mathematica 3.0* symbolic processing was performed on a Pentium 166 MHz personal computer, having 128 Mb of 60-nanosecond RAM memory, a 2.1 Gb hard drive, and running the Windows 95 operating system.

The initial symbolic integration of the expression (6) was actually performed by *Mathematica 3.0* in less than a minute. It generated, however, an highly impractical, and extremely complex expression, extending across more than 20 pages.

Initial attempts at simplifying this obviously redundant expression, by issuing the *"FullSimplify"* command [5], were finally discontinued after three days of continuous processing, because of the escalating memory requirements having exceeded the available 128 Mb of RAM memory, and having forced the Windows 95 operating system to access the much slower virtual memory on the hard drive.

The first successful simplification of the initial 20-page closed-form expression was finally obtained, after a number of dismal failures, by a) substituting in (6) the symbol :

$$k \;=\; c^2\left(\frac{n-1}{n}\right)^2 \qquad (29)$$

to represent the constant term of the radicand, and b) by issuing an initial *<<Utilities`MemoryConserve` Mathematica* command [8].

The first acceptably simplified expression (shown in Table I), filling just a single page, was then obtained after three days of continuous Pentium 166 MHz processing.

Subsequent attempts at reintroducing the definition (29) of the symbol k , and at further refining the one-page computer-simplified expression thereafter, were again discontinued after four days of continuous processing, because of the operating system having again accessed virtual memory.

An occasional check of the dynamically-allocated swap-file, performed during these attempts, showed it had eventually exceeded 300 Mb in size.

Advantage was finally taken of rather obvious formal redundancies of the one-page expression in Table I, by painstakingly further refining the simplification process by hand, and by methodically verifying the correctness of every required step with *Mathematica*.

5 - NUMERICAL EVALUATIONS.

Numerical evaluations and graphic displays of the integrated orbit-path length, as expressed by set of equations (17)-(28), were generated again using the *Mathematica 3.0* system, and assuming the parameter-values $c = r/R = 0.2$, and $n = 9$, as in Figure 1 .

It was found that, notwithstanding the complex character of the various auxiliary functions and constants, the above given, further simplified expression of $S(\varphi)$ consistently evaluates to a real quantity, with its residual imaginary part being buried way down in the numerical noise with rms $\cong 10^{-15}$, and that the resulting values appear to be correct and physically significant (Figure 3). Direct comparison to the approximate expression, given above by equations (7)-(16), proved this fourth-order approximation to be surprisingly accurate, having average relative error of $\pm$ 0.005 (Figures 4-6). Graphic displays of the difference between the closed-form, exact expression of the integrated orbit-path length, and the fourth-order approximation show this difference to very closely depend on the wrapping angle θ as $0.0217 \times \mathrm{Sin}(2\theta)$, at least in the evaluated case of $c = 0.2$, and $n = 9$ (Figure 7).

This rather fortunate circumstance provides the possibility of further refining the accuracy of the fourth-order approximation, by appropriately tweaking the coefficient H_3 in its third term. Figures 8 and 9 show the extent of the accuracy improvement, obtained by applying such an ad hoc correction of the coefficient H_3 , in the case of $c = 0.2$, and $n = 9$. The possibility of using such a simple, and highly effective ad hoc correction of the coefficient H_3 actually makes the fourth-order approximation highly competitive, in view of the much longer numerical computation times required to numerically evaluate the exact expression (17)-(28).

The exact, closed-form expression of the orbit-path length, given by the above set of equations (17)-(28) , has indeterminate points at $\theta = (2\nu+1)\,\pi$ (where $\nu = 0, 1, 2 \ldots$), and assumes physically unacceptable negative values for $\pi < \theta < 2\pi$, $3\pi < \theta < 4\pi$, . . ; this numerical computation quirk can be, however, easily eliminated by adding a constant correction term to the obtained negative numerical values, the value of this term being dictated by the requirement of monotone continuity of the $s(\theta)$ function, as function of θ, across the θ-points corresponding to odd multiples of π .

The *Mathematica 3.0* system is, however, quite probably not the most efficient processing tool, if only high speed numerical evaluations are required, in which case the use of the FORTRAN Function Subprograms CELINT of type COMPLEX, and WELINT, of type COMPLEX*16, of the CERN MATHLIB Library [9-11] may be more appropriate.

6 - CONCLUSIONS.

An exact, closed-form mathematical expression has been given that expresses the integrated path-length of a re-entrant, multiturn, toroidal/helical equilibrium orbit, as function of the azimuth angle, measured around the orbit axis.

The use of a multiturn, toroidal/helical equilibrium orbit is the distinctive characteristic of a recently proposed new type of High Power Microwave (HPM) amplifier, that synergistically

combines the basic principles of the Relativistic Klystron Amplifier (RKA) with those of Electron Storage Rings. The new type of High Power Microwave amplifier [1-2] is expected to attain much higher efficiencies, duty cycles, and spectral purity, because of its advanced design being based on most recent techniques of particle-beam dynamics.

The given closed-form expression of the integrated orbit-path length has been obtained by symbolic integration performed with the *Mathematica 3.0* system [4-8], and thereafter aggressively simplified, through an unusually lengthy symbolic processing.

The symbolic simplification was further refined by hand, methodically verifying every step with *Mathematica 3.0* . Further, the performed numerical evaluations show a previously developed approximate expression of the integrated orbit-path length to be surprisingly accurate, and easily susceptible of further ad hoc accuracy enhancement. The obtained timing benchmarks show the numerical computation of the closed-form, exact expression of the integrated orbit-path length, performed by the *Mathematica 3.0* system, to require a much longer processing time than the one required by evaluation of the approximate expression.

7 - REFERENCES.

[1] Speciale R. A. ,"High Power Microwave Amplification by High-Intensity Relativistic Electron-Beam Storage Rings," Proceedings of the 12th Review of Progress in Applied Computational Electromagnetics, Monterey, California, March 18-22, 1996, pages 464-468.

[2] Speciale R. A. ,"Stability Analysis of Re-entrant Multi-Turn Toroidal/Helical Electron Orbits in Strong-Focusing Alternating-Gradient Magnetic Fields," Proceedings of the 13th Annual Review of Progress in Applied Computational Electromagnetics, Monterey, California, March 17-21, 1997, Vol. 1, pages 554-556.

[3] Abramowitz M. and Stegun I. A. , "Handbook of Mathematical Functions," National Bureau of Standards, Applied Mathematical Series - 55, Ninth Printing, November 1970, with corrections, U. S. Government Printing Office, Washington D. C. 20402.

[4] Wolfram S. , "The Mathematica Book," Third Edition, Cambridge University Press, 1996, ISBN 0-521-58888-X, pp. 79-80, 810-815, and 1116.

[5] Wolfram S. , "The Mathematica Book," Third Edition, Cambridge University Press, 1996, ISBN 0-521-58888-X, pp. 762, 783-784, and 1096.

[6] Wolfram S. , "The Mathematica Book," Third Edition, Cambridge University Press, 1996, ISBN 0-521-58888-X, pp. 753-754, and 1076.

[7] Wolfram S. , "The Mathematica Book," Third Edition, Cambridge University Press, 1996, ISBN 0-521-58888-X, p. 1077.

[8] Wolfram Research, "Mathematica Standard Add-On Packages," Edited by Emily Martin, Cambridge University Press, 1996, ISBN 0-521-58586-4, p. 483.

[9] Kölbig K. S. , "Function Subprograms CELINT and WELINT," CERN MATHLIB Library, Submitted 07.06.1992, Language : Fortran, CERN, Geneva, Switzerland.

[10] Burlich R. , "Numerical Calculation of Elliptic Integrals and Elliptic Functions, Numer. Math. 7 (1965), pp. 78-90.

[11] Burlich R. , "Numerical Calculation of Elliptic Integrals and Elliptic Functions III, Numer. Math. 13 (1969), pp. 305-315.

TABLE

FIRST CLOSED-FORM EXPRESSION OF THE ORBIT-PATH LENGTH
(as generated by the FullSimplify command)

```
FullSimplify[ % ]
```

$$\left((1+\text{Cos}[th])\sqrt{\frac{2+c^2+2k+4c\,\text{Cos}[th]+c^2\,\text{Cos}[2\,th]}{(1+\text{Cos}[th])^2}}\left(-\frac{1}{\sqrt{\frac{1-c^2+k+2\sqrt{-c^2k}}{(1+c)^2+k}}}\right.\right.$$

$$\left(4I\left[-\left(1-c^2+k+2\sqrt{-c^2k}\right)\text{EllipticE}\left[I\,\text{ArcSinh}\left[\sqrt{\frac{1-c^2+k+2\sqrt{-c^2k}}{(1+c)^2+k}}\,\text{Tan}\left[\frac{th}{2}\right]\right]\right],\right.\right.$$

$$\left.\frac{1-2c^2+c^4+2k-6c^2k+k^2+4(-1+c^2-k)\sqrt{-c^2k}}{((-1+c)^2+k)((1+c)^2+k)}\right]+$$

$$2\left(1-c+k+\sqrt{-c^2k}\right)\text{EllipticF}\left[I\,\text{ArcSinh}\left[\sqrt{\frac{1-c^2+k+2\sqrt{-c^2k}}{(1+c)^2+k}}\,\text{Tan}\left[\frac{th}{2}\right]\right]\right],$$

$$\left.\frac{1-2c^2+c^4+2k-6c^2k+k^2+4(-1+c^2-k)\sqrt{-c^2k}}{((-1+c)^2+k)((1+c)^2+k)}\right]+$$

$$4c\,\text{EllipticPi}\left[\frac{1-c^2+k-2\sqrt{-c^2k}}{(-1+c)^2+k},\right.$$

$$\left.I\,\text{ArcSinh}\left[\sqrt{\frac{1-c^2+k+2\sqrt{-c^2k}}{(1+c)^2+k}}\,\text{Tan}\left[\frac{th}{2}\right]\right],\ \frac{1-c^2+k-2\sqrt{-c^2k}}{1-c^2+k+2\sqrt{-c^2k}}\right]\Bigg)$$

$$\sqrt{\left(\frac{1}{(1+c)^2+k}\left(\left(1+c+k-\sqrt{-c^2k}\,(-1+\text{Cos}[th])+c\,\text{Cos}[th]+c^2\,\text{Cos}[th]\right)\text{Sec}\left[\frac{th}{2}\right]^2\right)\right)}$$

$$\left.\left.\sqrt{\left(\frac{1}{(1+c)^2+k}\left(\left(1+c+k+\sqrt{-c^2k}\,(-1+\text{Cos}[th])+c\,\text{Cos}[th]+c^2\,\text{Cos}[th]\right)\text{Sec}\left[\frac{th}{2}\right]^2\right)\right)}\right)+$$

$$\left.\left.(2+c^2+2k+4c\,\text{Cos}[th]+c^2\,\text{Cos}[2\,th])\,\text{Sec}\left[\frac{th}{2}\right]^4\text{Sin}[th]\right)\right)\Bigg/$$

$$\left(2\sqrt{2}\,\sqrt{2+c^2+2k+4c\,\text{Cos}[th]+c^2\,\text{Cos}[2\,th]}\,\sqrt{(2+c^2+2k+4c\,\text{Cos}[th]+c^2\,\text{Cos}[2\,th])\,\text{Sec}\left[\frac{th}{2}\right]^4}\right)$$

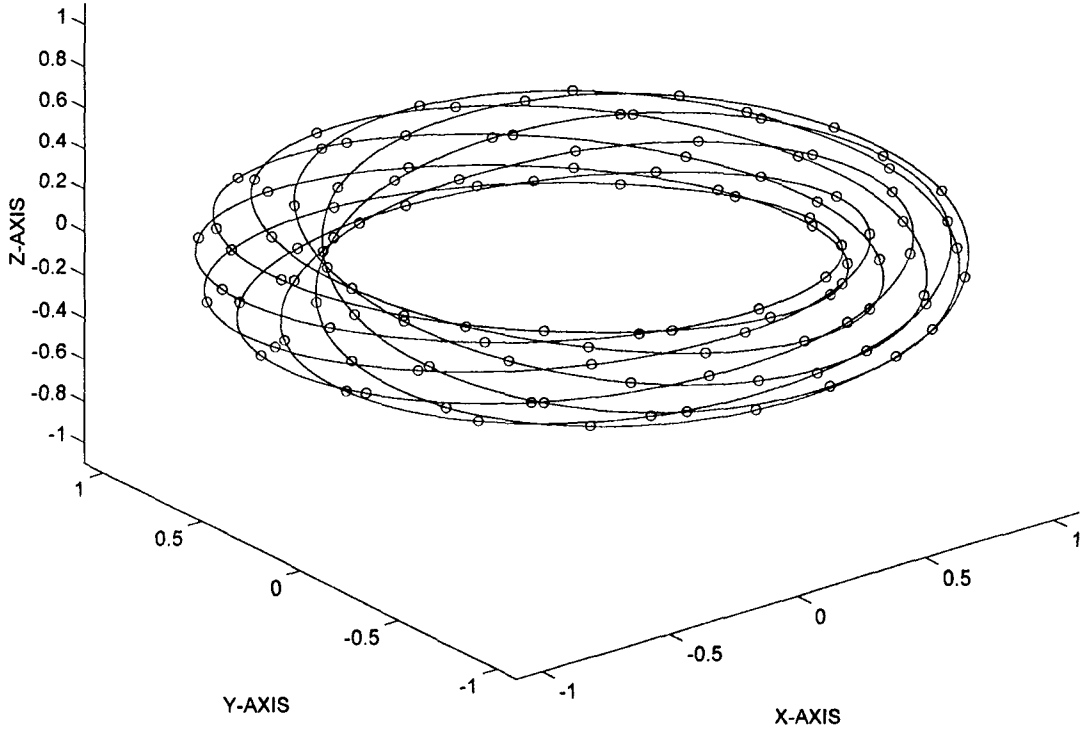

Figure 1 - 3 D Plot of the Nine Toroidal-Helical Electron Orbits : The 120 electron bunches are shown as small circles.

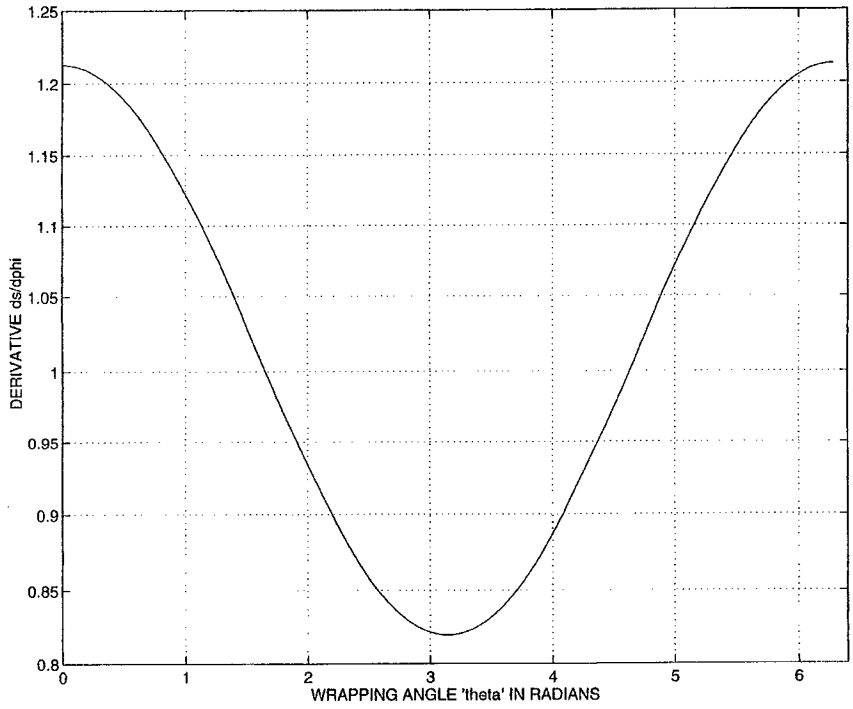

Figure 2 - Rate of Increase of the Orbit-Path Length as Function of the Wrapping Angle "theta" for c = r/R = 0.2 and n = 9.

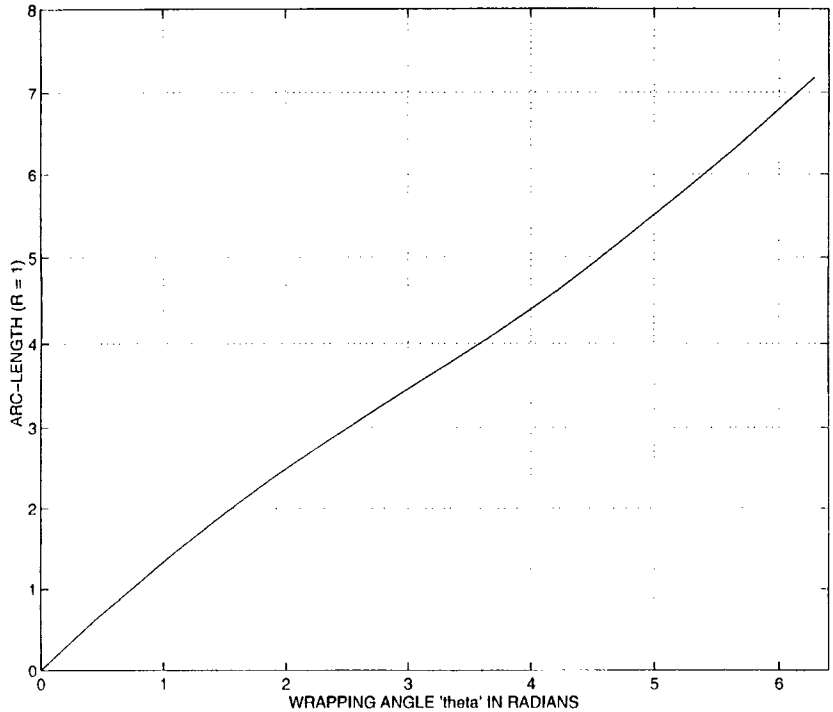

Figure 3 - Plot of the Closed-Form Expression of the Orbit-Path Length as Function of the Wrapping Angle "theta" (c = 0.2 and n = 9).

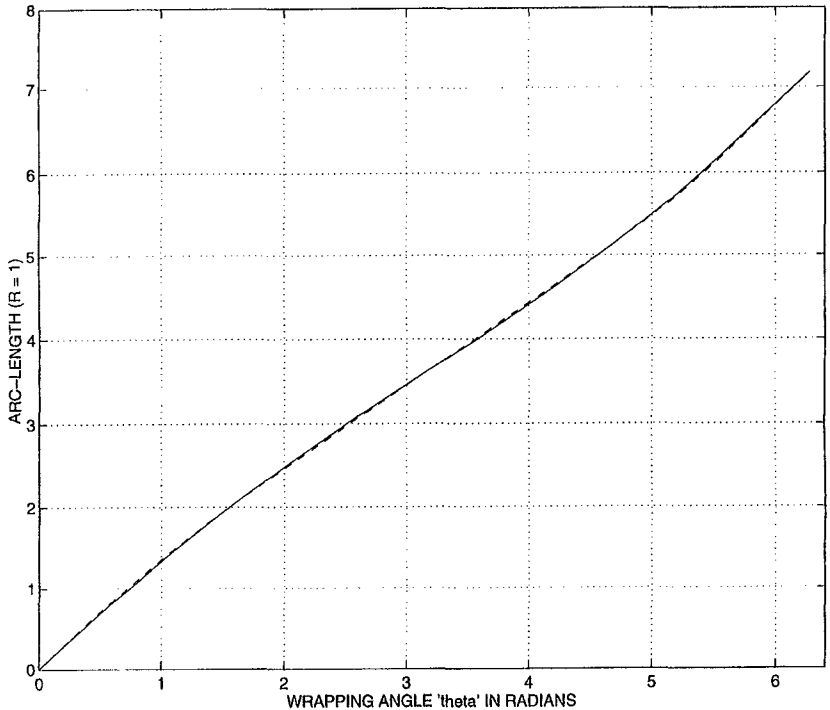

Figure 4 - Closed-Form (Solid) and Approximate (Dashed) Expressions of the Orbit-Path Length as Function of "theta" (c = 0.2 and n = 9).

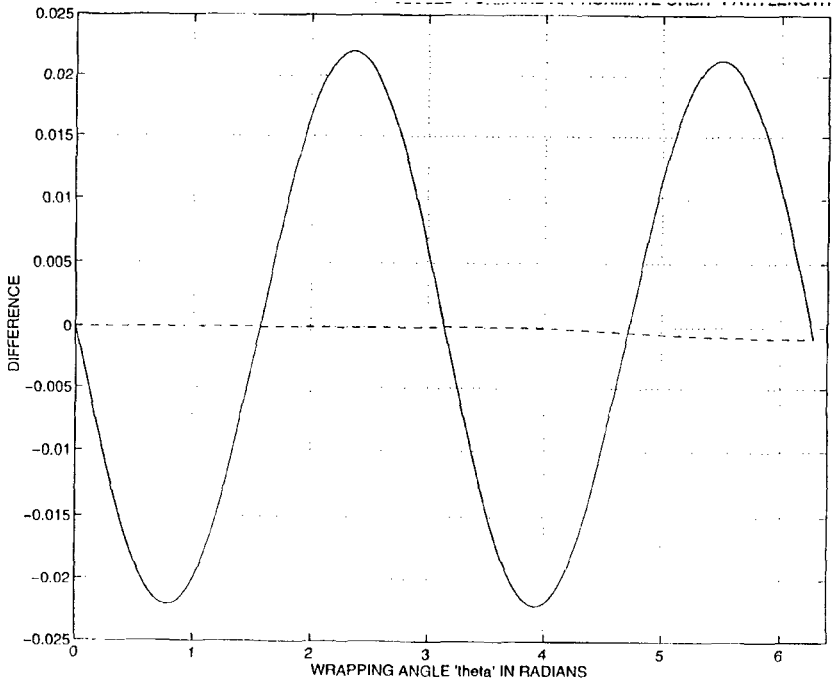

Figure 5 - Difference between the Closed-Form and the Approximate Expressions of the Orbit-Path Length (c = 0.2 and n = 9).

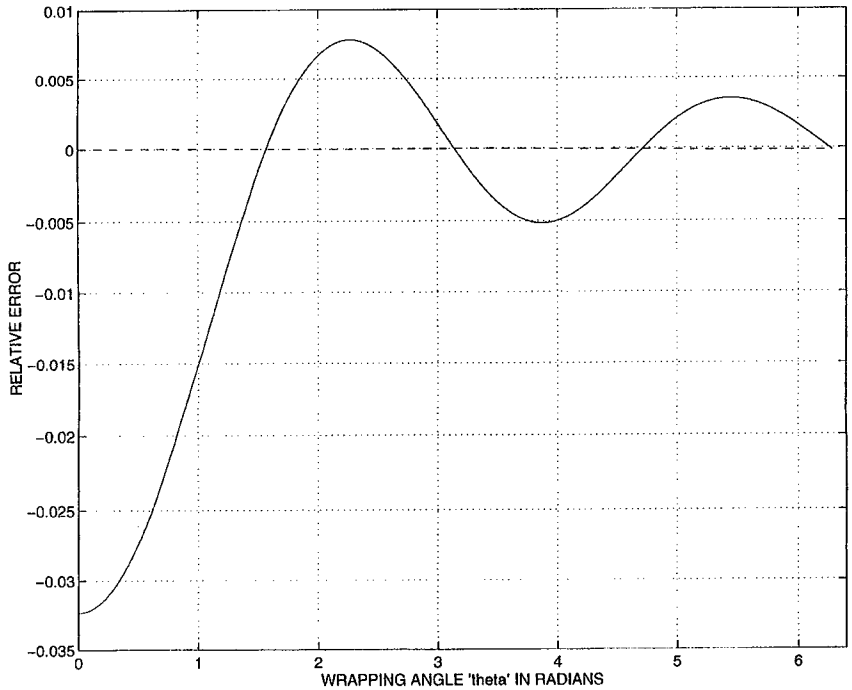

Figure 6 - Relative Error of the Approximate Expressions of the Orbit-Path Length as Function of "theta" (c = 0.2 and n = 9).

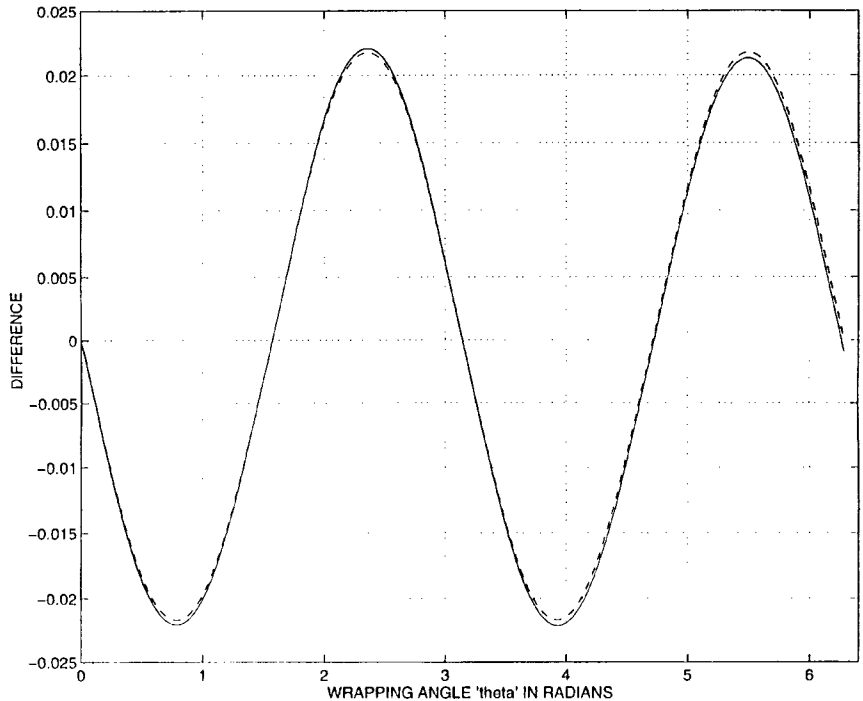

Figure 7 - Difference between the Closed-Form and Approximate Expressions (Solid) and Accuracy-Enhancing Term (Dashed).

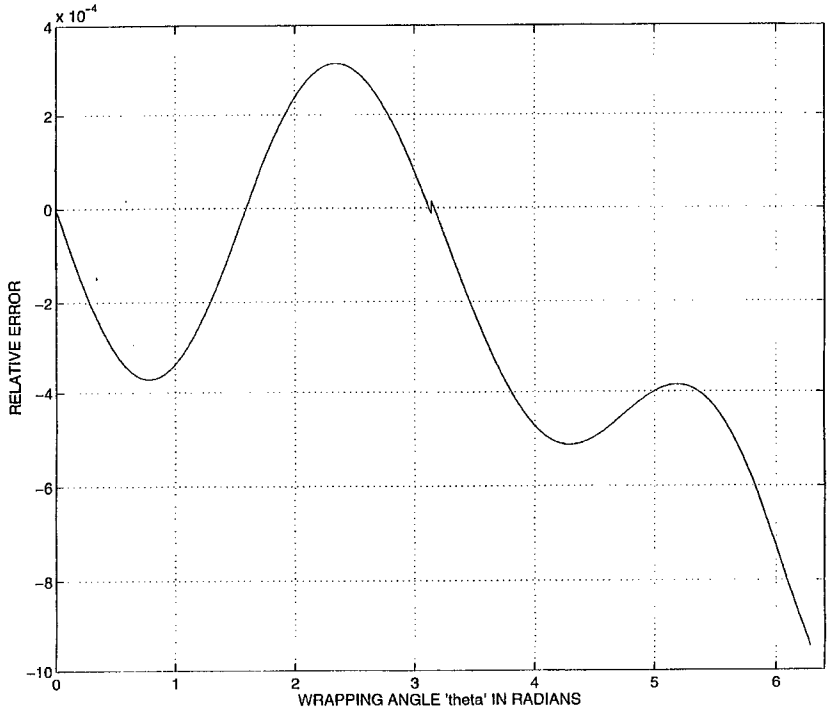

Figure 8 - Magnified Difference between the Closed-Form Expression and the Enhanced-Accuracy Approximate Expression.

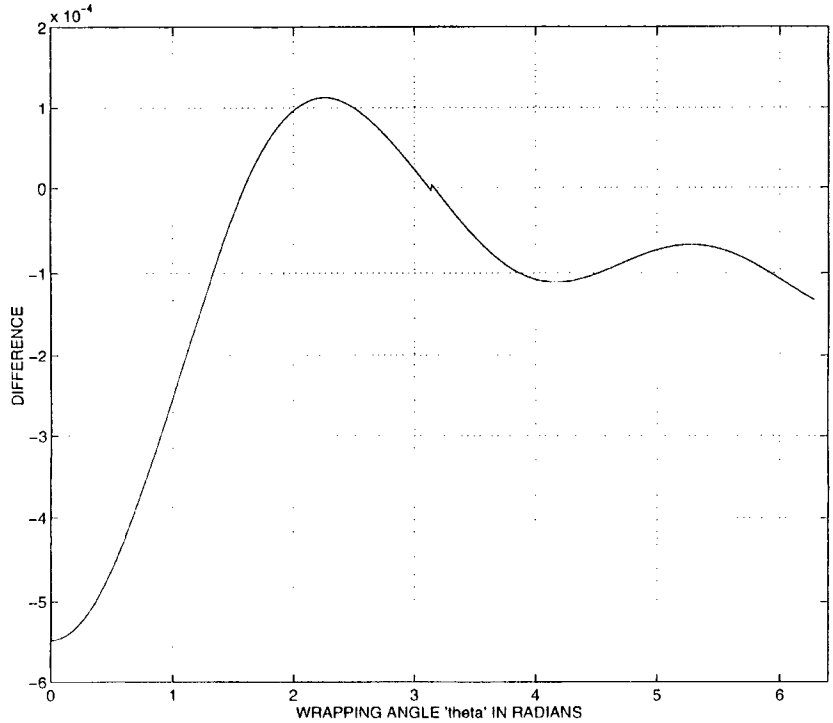

Figure 9 - Relative Error of the Enhanced-Accuracy Approximation with respect to the Closed-Form Expression (c = 0.2 and n = 9).

Asymptotic Techniques in Naval Ship Design

Mr. R. Routier, Naval Sea Systems Command, Washington, DC
Dr. R. Burkholder, The Ohio State University ElectroScience Laboratory, Columbus OH

Abstract

This paper discusses work NAVSEA, Ohio State University, and the Boeing Corporation are doing to allow surface ship designers to predict antenna pattern degradation due to ship structure, field strengths, radiation hazard (RADHAZ) levels, the effect of far-zone jammers, Multipath due to antenna-to-antenna coupling in complex scattering environments. It concentrates on work that is being done in the microwave and above frequency regime where asymptotic techniques can be used. This paper is not so much a prescription for how to perform Computational Electromagnetic (CEM) in ship design but rather a description of the techniques that are being tried, the present status of the work, and a presentation of some interim results.

Introduction

Numerical electromagnetics is difficult in almost all cases of interest. ACES papers and other professional journal articles routinely report new approaches and techniques for computing EM parameters but often the source or receptor of EM energy is fairly simple as is any geometry that might interact with this energy. Sometimes elementary sources and receptors of EM energy are useful in ship design computational electromagnetics, but complex geometries are a fact of life and it is often impossible to simplify ship geometries to the extent that is possible in other problems of practical interest. It is possible to simplify ship topside geometries when lower frequencies are being examined. For instance, at HF communication frequencies (2-30 Mhz) a wire grid model of the ship and its whip antennas can be developed and accurate antenna patterns and topside field strengths can be predicted using NEC. It is not necessary to model geometric details at these long wavelength frequencies. If the ship is too large, present matrix inversion techniques may not be adequate but the MoM technique still holds promise for handling these larger problems in the future. At radar frequencies (300 Mhz to 10 Ghz), NEC and MoM are inadequate if the whole ship must be considered in an analysis.

NAVSEA 03K/ElectroScience OSU/Boeing/GTRI and others have been working for several years to develop tools to predict antenna gain patterns, EM field strengths, and antenna-to-antenna coupling in the surface ship topside environment. The present state of this work is that some capability exists in each of these areas but large amounts of computer time are often needed and usually the geometry must be simplified. Computer time is not really an issue from a cost perspective. Millions of dollars can be saved by designing a ship properly in the first place and these savings justify any computer

expense needed to get good answers. Geometry simplification is another matter, however, because it is often unclear what geometry elements are important and what ones can be neglected. This paper concentrates on discussing what is being done to model electrically large aperture antennas while handling the whole ship geometry. It also mentions one approach to identifying and eliminating geometry elements that truly are unimportant. In all cases, we discuss only the use of ray techniques (Geometry Optic, Uniform Theory of Diffraction).

The Ray Tracing and Casting (RTC) Program

The Ray Tracing and Casting program was developed specifically to predict field strength levels anywhere on a ship topside when a radar or other microwave (or higher) frequency emitter is operating. It uses the asymptotic techniques of Geometric Optics and the Uniform Theory of Diffraction [1,2,3] as its theoretical basis and includes ray tracing approaches gleaned from the computer graphics community to allow relatively fast determination of ray paths when the geometry is complex [4]. This latter feature sets RTC apart from other ray based CEM codes; indeed, including efficient handling of tens of thousands of geometry elements was a primary reason RTC was developed rather than customizing an existing ray based code such as OSU's NEC/BSC. RTC also has a ray casting capability that is similar in spirit to the shooting and bouncing rays (SBR) approach [5] effectively used in certain CEM problems (cavity RCS prediction).

In ship design, RTC's ray casting capability is used to determine where the highest field levels are likely to be found in the topside environment. Rays are simply cast ("shot") from the source and allowed to reflect from whatever geometry they encounter up to a user-specified bounce level. Field levels are then estimated from the density of rays at any point of interest. Of course, only Geometry Optic contributions are included in this approach. Another application of ray casting is the quick determination of backscatter hot spots. Parallel rays are cast at the ship from an offboard location and allowed to bounce within the ship structure. Those that return to the source (those that have a final direction that is within some tolerance of being just opposite of the incoming direction) are saved and displayed. This technique is very effective at identifying "disjoint" corner reflectors that may not be noticed by a visual inspection of the topside geometry. Figure 1 shows an example of the results from this approach.

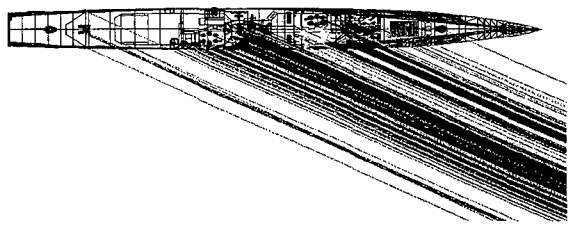

Figure 1. Ray Backscatter

Ray casting does not account for diffraction effects. To account for diffraction, it is necessary to use RTC's ray tracing mode (note: our use of the casting and tracing terminology differs from the computer graphics community's usage -- their ray tracing is our ray casting). In ray tracing, point-to-point propagation paths that satisfy Fermat's principle of stationary path length are found. RTC uses closed form algorithms to find reflection and diffraction points on planar surfaces and straight wedges and uses iterative algorithms to find reflection points on circular cylinders and non-uniform rational B-spline (NURBS) surfaces. RTC also finds curved surface diffraction paths associated with circular cylinders but ignores curved surface diffraction from more general shapes. RTC also ignores diffraction from curved wedges and diffraction from tips/corners. These limitations do not seem to be too severe in the shipboard geometries RTC was designed to handle.

The Generic Generalized Ray Expansion Antenna Model

Accurate modeling of radar antennas in a shipboard environment is a challenge. These antennas can have apertures tens of feet in size. It is clearly not reasonable to model such large antennas as point sources when other topside structure is in their near field. In 1997, a Generalized Ray Expansion (GRE) source model was added to RTC to allow proper modeling of large topside antennas. The GRE model has a strong theoretical foundation; it is based on the equivalence principle. In this model the antenna itself is replaced with a circumscribing bubble or "GRE surface" of convenient shape. Then, the fields that would exist on this imaginary surface in the presence of an antenna operating inside are determined and converted to equivalent surface currents. Finally, the GRE surface is discretized into patches small enough that topside structure near the antenna is in each patch's far field.

Figure 2 illustrates the details of the GRE source modeling technique. First, an equivalent planar aperture is defined as closely as possible to the physical aperture of the to-be-modeled antenna. This aperture will be allowed to tilt and rotate within the GRE

surface so it must be sized to fully contain this aperture for all possible antenna orientations. Next, aperture currents $\mathbf{J}_s$ and $\mathbf{M}_s$ are found such that the far field pattern of the aperture has the polarization, gain, horizontal and vertical beamwidths, and average sidelobe levels of the actual antenna. The entire GRE surface is divided into subapertures, two of which are shown in Figure 2. Equivalent surface currents for each subaperture are determined by:

$$\mathbf{J}_n(r_n)=\mathbf{u}_n \times \mathbf{H}(r_n)$$
$$\mathbf{M}_n(r_n)=\mathbf{E}(r_n) \times \mathbf{u}_n$$

where r_n is a point on the subaperture and $\mathbf{u}_n$ is the outward pointing unit surface normal vector at r_n and $\mathbf{E}(r_n)$, $\mathbf{H}(r_n)$ are the electric and magnetic fields radiated by the aperture currents $\mathbf{J}_s$, $\mathbf{M}_s$ while the antenna's equivalent aperture is oriented to point in a particular direction. Finally, in accordance with the equivalence principle, the aperture currents are removed and replaced by the GRE equivalent currents over the encapsulating surface.

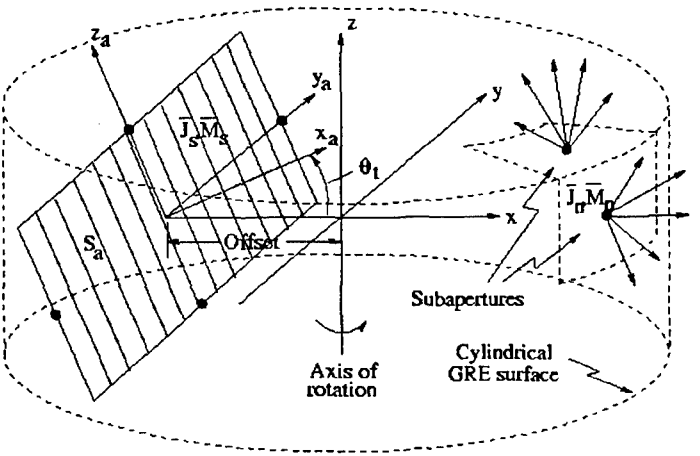

Figure 2. GRE Antenna Modeling

When this model is used to compute fields anywhere in or near the topside, each patch is treated as a separate but coordinated point source. Ray tracing is accomplished for each such point and the complex vector strength of each ray is accumulated at the observation point to arrive at a field strength prediction. The complex vector strength of rays leaving each patch are computed based on the angle of departure of the ray relative to the patch's normal and to the surface currents on the patch. These surface currents depend, of course,

on the orientation of the antenna's equivalent aperture as mentioned in the previous paragraph.

The version of the GRE model implemented in 1997 is termed the Generic GRE model. In this model the arbitrary GRE surface has been chosen as a cylinder that is roughly conformal to the volume swept out by the to-be-modeled antenna as it scans in azimuth and elevation. The whole reason for using the GRE surface instead of the antenna's aperture is that RTC can trace paths from patch centers to the observation point once yet be able to compute fields at the observation point for any orientation of the antenna. The strengths of the rays leaving the patches is dependent on the antenna pointing angle and must be recomputed each time a new antenna pointing angle is considered, but this is computationally inexpensive as compared to the ray tracing expense that now only needs to be incurred once.

Generic GRE Test Results

The Generic GRE antenna source model as implemented in RTC has not yet been validated against measurement data collected on a Naval ship. This is planned for 1998. However, a laboratory validation effort using a 2' diameter parabolic dish antenna and a simple geometry arrangement was accomplished as a proof of concept effort [6]. More recently, the proper integration of the Generic GRE model in RTC was verified by comparing RTC outputs to those generated by OSU's BSC program after installing the antenna model in that program. Figure 3 shows far field gain patterns (azimuth and elevation cuts) generated by RTC; BSC outputs were identical to plotting accuracy. A very large naval antenna (AN/SPS-49) was modeled in this test and the results look realistic.

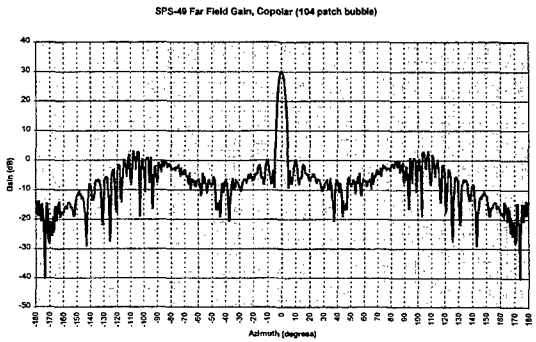

Figure 3a. AN/SPS-49 Azimuth Pattern

[Additional RTC output will be presented during the oral presentation of this paper.]

Future Plans

In addition to validating the Generic GRE source model predictions by comparing them to measurement data collected aboard a naval ship, two other efforts have been recommended to NAVSEA for sponsorship. Both are aimed at speeding up ray tracing which can require literally days of workstation CPU time. In the first, we would investigate methods for reducing ray tracing time by recognizing that traced paths from nearby patch centers to a common observation point location are likely to have much in common. Is there a way to simplify the path determination process for a second patch once the paths for a first patch have been found? This issue is discussed further in the next paragraph. The second effort being recommended to NAVSEA is the use of massively parallel computers. We believe such computers could take a brute force but time efficient approach to ray tracing a problem with hundreds of GRE bubble patches in a complex geometry setting.

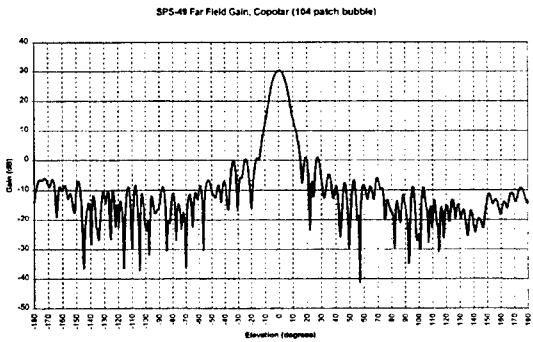

Figure 3b. AN/SPS-49 Elevation Pattern

Presently, RTC can very significantly reduce computation time required to find ray paths by automatically (if directed by the user) culling the geometry. In the culling process, RTC eliminates geometry elements that are not directly or indirectly (via surface reflections) visible to either the source or observer. This almost always eliminates more than half of the geometry elements and because the tracing processes is of order M^N where M is the number of geometry elements and N is the bounce level being sought, results in much reduced computation time. Although this technique does markedly reduce computation time, additional reductions are still needed to allow ship design engineers to get prediction results quickly. One thought that might be considered is to

perform full ray tracing on 50% (or 25%, or 10%) of the GRE patch centers and then only consider the geometry elements that "played" in these paths when looking for the paths associated with the remaining 50% (or 75%, or 90%) of the patch centers. Determining if this will work will require a certain amount of experimentation.

References

[1] G. L. James; Geometrical Theory of Diffraction for Electromagnetic Waves; Peter Peregrinus, Ltd.; 1980

[2] R. G. Kouyoumjian, P. H. Pathak; "A Uniform Geometrical Theory of diffraction for an Edge in a Perfectly Conducting Surface"; Proceedings of the IEEE, November, 1994

[3] P. H. Pathak, W. K. Burnside, R. J. Marhefka; "A Uniform GTD Analysis of the Diffraction of Electromagnetic Waves by a Smooth Convex Surface"; IEEE Transactions on Antennas and Propagation, September, 1980

[4] A. S. Glassner; "Space Subdivision for Fast Ray Tracing"; Computer Graphics and Applications, October 1994

[5] H. Ling, R. Chou, S. Lee; "Shooting and Bouncing Rays: Calculating the RCS of an Arbitrary Shaped Cavity"; IEEE Transactions on Antennas and Propagation, February, 1989

[6] Rockwell International; "Microwave EME Prediction, Interim Technical Report"; May 6, 1994 (Rockwell Reference Number: C89-794.090A1-I/601)

A BCG-FFT Solution of Scattering and Radiation by Large Finite Arrays of Microstrip Antennas

Chao-Fu Wang, Feng Ling and Jian-Ming Jin
Electromagnetics Laboratory and
Center for Computational Electromagnetics
Department of Electrical and Computer Engineering
University of Illinois at Urbana-Champaign
Urbana, Illinois 61801-2991

ABSTRACT

This paper presents a new fast full-wave analysis technique that can be used to analyze the scattering and radiation from finite arrays of microstrip antennas. The mixed potential integral equation (MPIE) describing microstrip problems is discretized in spatial domain by means of full-wave discrete image technique. With the help of a new algorithm to calculate the matrix-vector product, the resulting system is solved using biconjugate gradient (BCG) method in conjunction with FFT. Several numerical results illustrate that the proposed method is powerful for analyzing large finite arrays of microstrip antennas.

I. INTRODUCTION

A microstrip antenna array can be analyzed using two approaches. One approach is to approximate the array as an infinite array and, as a result, the analysis of the array is then reduced to the analysis of a single element using Floquet-type representation of field [1]-[3]. This approach is very efficient; however, it does not account for edge effects of a finite array, nor can it deal with the effect of the feed network. The other approach is to deal with the finite array directly. This approach is considerably more difficult because of the necessity of solving a large matrix equation, which requires a large computer memory and excessive computer time. In the past, finite arrays of print dipoles and rectangular microstrip patches have been studied by using the spectral domain moment methods [4]- [6]. A microstrip series-fed array has also been analyzed [7] using a full-wave discrete image technique that transforms a spectral domain formulation into the spatial domain without losing any full-wave information [8], [9].

A powerful numerical technique that can significantly reduce the memory requirement and computing time is to combine the conjugate gradient (CG) method with FFT. The resultant method is often referred to as the CG-FFT method that was first developed by Bojarski [10] and has been applied to many large electromagnetic problems. A much more accurate and efficient CG-FFT method can be achieved by using spatial discretization scheme and transferring the del operators from the Green's function to the expansion and testing functions [11], [12]. Realizing this fact, a full-wave analysis technique for microstrip structures has been proposed, which combines the CG-FFT method with the full-wave discrete image technique [13]. When a spatial domain discretization is used in the CG-FFT method, the efficiency of the method is primarily determined by the convergence of the CG algorithm. In many applications, the CG algorithm can be substituted by other iterative algorithm for a faster convergence. A commonly used alternative is the biconjugate gradient (BCG) algorithm [14]-[16]. The BCG algorithm is better suited for systems that are poorly conditioned than the CG algorithm, although it does not decrease the residual error

monotonically [17]. It is found that in the application dealt with in this paper, the BCG algorithm outperforms the CG algorithm significicantly.

In this paper, the authors present a new fast full-wave analysis technique that can be used to analyze large microstrip antenna arrays. We discretize the integral equation describing the micristrip problem by converting the spectral domain Green's functions into the closed-form spatial Green's functions by means of full-wave discrete image representations. In this procedure, the del opertors are transfered from the singular kernel to the expansion and testing functions. The BCG algorithm in conjunction with FFT is employed to solve the resulting system of equations. The radar cross section (RCS) and radiation pattern of microstrip antenna arrays are calculated using the reciprocity theorem. The numerical results illustrate that the proposed method is very powerful for solving the large microstrip antenna arrays.

II. MPIE AND DISCRETIZATION

For microstrip structures, the mixed potential integral equation (MPIE) yields a weaker singularity in its integrand than the electric field integral equation (EFIE). The MPIE can be written as

$$\hat{n} \times [j\omega\mu_0 \mathbf{A}(\mathbf{r}) + \nabla\Phi(\mathbf{r})] = \hat{n} \times \left[\mathbf{E}^i(\mathbf{r}) + \mathbf{E}^r(\mathbf{r})\right] \tag{1}$$

where $\mathbf{E}^i$ and $\mathbf{E}^r$ denote the incident electric field and the reflected field, respectively, and

$$\mathbf{A}(\mathbf{r}) = \frac{\mu_0}{4\pi} \iint_S \bar{\mathbf{G}}_A(\mathbf{r}, \mathbf{r}') \cdot \mathbf{J}(\mathbf{r}') ds' \tag{2}$$

$$\Phi(\mathbf{r}) = \frac{j}{4\pi\omega\varepsilon_0} \iint_S G_q(\mathbf{r}, \mathbf{r}') \nabla \cdot \mathbf{J}(\mathbf{r}') ds' \tag{3}$$

in which $\bar{\mathbf{G}}_A$ and G_q denote the Green's functions for the magnetic vector potential and the electric scalar potential, respectively.

The spatial domain Green's functions $\bar{\mathbf{G}}_A$ and G_q are the key to the discretization of the MPIE in spatial domain. The Green's functions G_a corresponding $\bar{\mathbf{G}}_A$ and G_q can be written in form of Sommerfeld integral:

$$G_{a,q}(\rho) = \int_{-\infty}^{+\infty} \tilde{G}_{a,q}(k_\rho) H_0^{(2)}(k_\rho \rho) k_\rho dk_\rho \tag{4}$$

Generally, this inverse Hankel transform cannot be solved analytically. Fortunately, a full-wave discrete image technique has been developed for rapid evaluation of this integral [8], [9]. The closed-form spatial Green's functions can be obtained from (4) by using the full-wave discrete image.

With the intend of computing the equation (1) via the FFT, we place the conducting surface of antenna in a rectangular area which is then divided into $M \times N$ small rectangulars whose side lengths are Δx and Δy along the x and y directions, respectively. Suppose $\mathbf{f}^x_{m,n} = f^x_{m,n}\hat{x}$ and $\mathbf{f}^y_{m,n} = f^y_{m,n}\hat{y}$ are vector basis functions in the x direction and y direction, respectively. $f^{x,y}_{m,n}$ represents the roof-top basis function. Expanding the surface current distribution $\mathbf{J}_s$ in a sequence of vector basis functions $\mathbf{f}^x_{m,n}$ and $\mathbf{f}^y_{m,n}$ as follows:

$$\mathbf{J}_s = \sum_{m,n} I^x_{m,n} \mathbf{f}^x_{m,n} + \sum_{m,n} I^y_{m,n} \mathbf{f}^y_{m,n} \tag{5}$$

and applying the Galerkin's testing procedure to (1) yields

$$\begin{bmatrix} \mathbf{G}_{xx} & \mathbf{G}_{xy} \\ \mathbf{G}_{yx} & \mathbf{G}_{yy} \end{bmatrix} \begin{bmatrix} \mathbf{J}_x \\ \mathbf{J}_y \end{bmatrix} = \begin{bmatrix} \mathbf{b}_x \\ \mathbf{b}_y \end{bmatrix} \tag{6}$$

where

$$\mathbf{G}_{xx} = [G_{xx}(m-m', n-n')], \qquad \mathbf{G}_{xy} = [G_{xy}(m-m', n-n')],$$
$$\mathbf{G}_{yx} = [G_{yx}(m-m', n-n')], \qquad \mathbf{G}_{yy} = [G_{yy}(m-m', n-n')],$$
$$\mathbf{b}_x = [\langle \mathbf{f}^x_{m,n}, \mathbf{E}^i(\mathbf{r}) + \mathbf{E}^r(\mathbf{r}) \rangle], \qquad \mathbf{b}_y = [\langle \mathbf{f}^y_{m,n}, \mathbf{E}^i(\mathbf{r}) + \mathbf{E}^r(\mathbf{r}) \rangle].$$

in which

$$G_{xx}(m-m', n-n') = \Gamma^x_a(m-m', n-n') + \Gamma_{xx}(m-m', n-n')$$
$$G_{xy}(m-m', n-n') = \frac{1}{\Delta x \Delta y} \sum_{i=0}^{1} \sum_{k=0}^{-1} (-1)^{i+k} \Gamma_q(m-m'+i, n-n'+k).$$
$$G_{yy}(m-m', n-n') = \Gamma^y_a(m-m', n-n') + \Gamma_{yy}(m-m', n-n'),$$
$$G_{yx}(m-m', n-n') = G_{xy}(n'-n, m'-m).$$
$$\Gamma_{xx}(m-m', n-n') = \frac{1}{(\Delta x)^2} \sum_{i=0}^{1} \sum_{k=0}^{-1} (-1)^{i+k} \Gamma_q(m-m'+i+k, n-n').$$
$$\Gamma_{yy}(m-m', n-n') = \frac{1}{(\Delta y)^2} \sum_{i=0}^{1} \sum_{k=0}^{-1} (-1)^{i+k} \Gamma_q(m-m', n-n'+i+k).$$
$$\Gamma^x_a(m-m', n-n') = \frac{j\omega\mu_0}{4\pi} \iint_S f^x_{m,n} ds \iint_S G_a f^x_{m',n'} ds',$$
$$\Gamma^y_a(m-m', n-n') = \frac{j\omega\mu_0}{4\pi} \iint_S f^y_{m,n} ds \iint_S G_a f^y_{m',n'} ds',$$
$$\Gamma_q(m-m', n-n') = \frac{j}{4\pi\omega\varepsilon_0} \iint_S \Pi_{m,n} ds \iint_S G_q \Pi_{m',n'} ds',$$

Here, $\Pi_{m,n}$ is the 2-D unit pulse function defined over $\{m,n\}^{th}$ small rectangular cell. So far, the discretization of MPIE in spatial domain is obtained.

III. BCG-FFT Solution

The linear system implied by (6) can be solved via a direct method or a CG iterative method. In order to analyze large finite arrays of microstrip antennas, we employ the BCG algorithm and FFT to reduce substantially the memory requirement and CPU time. The BCG algorithm employed here for solution of $Ax = b$, in which A is symmetric, can be found in [12], [17]. In this BCG algorithm, A is only involved in the matrix-vector product. For the problem considered here this product can be computed efficiently via FFT without a need to generate the square matrix.

In fact, it is observed that the relationship between $\bar{\mathbf{G}}_A$ and $\mathbf{J}$ is that of convolution from formulation (2). So we can get the following discrete convolution relationship:

$$\mathbf{G}_{xx}\mathbf{J}_x = DFT^{-1}\{G_{xx}(m,n)\} \cdot DFT\{J_x(m,n)\}\} \tag{7}$$
$$\mathbf{G}_{yy}\mathbf{J}_y = DFT^{-1}\{G_{yy}(m,n)\} \cdot DFT\{J_y(m,n)\}\} \tag{8}$$

It is also observed that the relationship between G_q and $\nabla \cdot \mathbf{J}$ is that of convolution from fomulation (3). So the following discrete convolution relatioship can be obtained:

$$\mathbf{G}_{xy}\mathbf{J}_y = [D_y(m,n) - D_y(m+1,n)], \mathbf{G}_{yx}\mathbf{J}_x = [D_x(m,n) - D_x(m,n+1)] \tag{9}$$

$$[D_x(m,n)] = \frac{1}{\Delta x \Delta y} DFT^{-1}\{\Gamma_{qx}(m,n)\}, [D_y(m,n)] = \frac{1}{\Delta x \Delta y} DFT^{-1}\{\Gamma_{qy}(m,n)\} \tag{10}$$

$$[\Gamma_{qx}(m,n)] = DFT\{\Gamma_q(m,n)\} \cdot DFT\{J_x(m,n) - J_x(m-1,n)\} \quad (11)$$

$$[\Gamma_{qy}(m,n)] = DFT\{\Gamma_q(m,n)\} \cdot DFT\{J_y(m,n) - J_y(m,n-1)\} \quad (12)$$

The matrix-vector product can be calculated efficiently via FFT by using formulations (7)–(12).

IV. NUMERICAL RESULTS AND CONCLUSION

In this section, the authors will present several numerical results to demonstrate the accuracy and efficiency of the above mentioned method. The numerical convergence is defined as $Err = \|\mathbf{r}_n\|^2/\|\mathbf{r}_0\|^2$. All computations were carried out on a DEC Alpha workstation.

In order to test the convergence behavior of the method, we first consider a typical problem, namely scattering of a normally incident plane wave from a rectangular microstrip patch antenna [18]: $10mm \times 15mm$ patch, $\varepsilon_r = 10.2$, width of substrate $h = 1.27mm$, $f = 3.12$ GHz. For given tolerance $Err < 10^{-6}$, the number of iterations vs. the number of unknowns for CG-FFT [13] and present method are given in Fig. 1(a). The CPU time per iteration vs. the number of unknowns for CG-FFT [13] and present method are given in Fig. 1(b). Fig. 1(a) and Fig. 1(b) show that the convergence behavior of the present method is better than that of the CG-FFT method.

As the second test case we consider the scattering from rectangular microstrip patch antenna. The monostatic RCS vs. frequency is given in Fig. 1(c) and is compared with the result of [19]. Two results agree very well. This example illustrates that the proposed method has a very good accuracy.

As the third test case we consider the radiation from a four-element series-fed micristrip antenna array shown in Fig. 2, which is fed at the left end [7]. The E-plane radiation pattern is given in Fig. 3 and is compared with measured data [7]. The comparison shows that the proposed method has also a very good accuracy even for solving antenna array problems.

The last test case we consider is the scattering and radiation from microstrip corporate fed planar arrays to test the capability of the proposed method. The 8×4 microstrip corporate fed planar array is given in Fig. 4(a). The current distribution on the 8×4 microstrip corporate fed planar array is given in Fig. 4(b). The radiation patterns of the microstrip corporate fed planar arrays are given in Fig. 5. The monostatic RCS of microstrip corporate fed planar arrays is given in Fig. 6. The radiation patterns of 16×8 and 16×16 microstrip corporate fed planar arrays are given in Fig. 7. The requirment of computational sources is listed in Table I.

Table I. CPU Time and Storage of DEC Alpha Workstation

Array	Number of Unknowns	CPU Time per Iteration	Number of Iterations	Computer Storage	Tolerance
8×8	118073	11.6 secs	313	18 Mb	10^{-3}
8×8	118073	11.6 secs	599	18 Mb	10^{-6}
16×16	495044	97.81 secs	425	65 Mb	10^{-3}
16×16	495044	97.81 secs	1070	65 Mb	10^{-6}

These results for microstrip corporate fed planar arrays show that the proposed method is powerful enough to be applied to analyze large electromagnetic problems and save on memory and CPU time.

ACKNOWLEDGMENTS

This work was supported by the Office of Naval Research under grant N00014-95-1-0848, the National Science Foundation under grant NSF ECE 94-57735, and a grant from AFOSR via the MURI Program under contract number F49620-96-1-0025.

The authors are indebted to Professor D. G. Fang at Nanjing University of Science and Technology, who taught them much about the discrete complex image method.

References

[1] D. M. Pozar and D. H. Schaubert, *IEEE Trans. Antennas Propagat.*, vol. 32, pp. 602-610, June 1984.

[2] D. M. Pozar and D. H. Schaubert, *IEEE Trans. Antennas Propagat.*, vol. 32, pp. 1101-1107, Oct. 1984.

[3] C. C. Liu, J. Shmoys, A. Hesel, J. D. Hanfling and J. M. Usoff, *IEEE Trans. Antennas Propagat.*, vol. 33, pp. 426-435, Apr. 1985.

[4] D. M. Pozar, *IEEE Trans. Antennas Propagat.*, vol. 33, pp. 1045-1053, Oct. 1985.

[5] D. M. Pozar, *IEEE Trans. Antennas Propagat.*, vol. 34, pp. 658-665, May 1986.

[6] A. S. King, and W. J. Bow, *IEEE Trans. Antennas Propagat.*, vol. 40, pp. 770-774, July 1992.

[7] K. L. Wu, M. Spenuk, J. Litva, and D. G. Fang, *IEE Proc.-H*, vol. 138, pp. 238-242, June 1991.

[8] D. G. Fang, J. J. Yang, and G. Y. Delisle, *IEE Proc.-H*, vol. 135, pp. 297-303, Oct. 1988.

[9] Y. L. Chow, J. J. Yang, D. G. Fang, and G. E. Howard, *IEEE Trans. Microwave Theory Tech.*, vol. 39, pp. 588-592, Mar. 1991.

[10] N. N. Bojarski, Air Force Avionics Lab. Technical Report AFAL-TR-71-75, Mar. 1971.

[11] A. P. M. Zwamborn and P. M. van der Berg, *IEEE Trans. Antennas Propagat.*, vol. 39, pp. 224-228, Feb. 1991.

[12] J. M. Jin and J. L. Volakis, *Electromagn.*, vol. 12, pp. 105-119, 1992.

[13] Y. Zhuang, K. L. Wu, C. Wu and J. Litva, *IEEE Trans. Antennas Propagat.*, vol. 44, pp. 102-109, Jan. 1996.

[14] C. Lanczos, *J. Res. Nat. Bur. Stand.*, vol. 45, pp. 255-282, 1950.

[15] R. Fletcher, in *Numerical Analysis Dundee* 1975, G. A. Watson, Ed. New York: Springer-Verlag, pp. 73-79, 1976.

[16] D. A. H. Jacobs, in *Sparse Matrices and Their Uses*, I. S. Duff, Ed. Berlin: Springer-Verlag, pp. 191-222, 1981.

[17] C. F. Smith, A. F. Peterson and R. Mittra, *IEEE Trans. Antennas Propagat.*, vol. 38, pp. 938-940, Jun. 1990.

[18] M. F. Catedra and M. Gago, *IEEE Trans. Antennas Propagat.*, vol. 38, pp. 1530-1536, Oct. 1990.

[19] S. A. Bokhari, J. R. Mosig and F. E. Gardiol, *Electromagn.*, vol. 14, pp. 19-32, 1994.

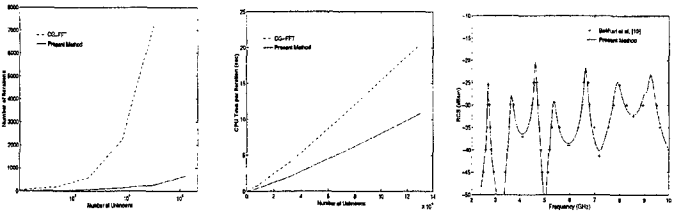

(a) (b) (c)

Figure 1: (a) The CPU time per iteration vs. the number of unknowns. (b) The number of iterations vs. the number of unknowns. (c) The RCS ($\sigma_{\theta\theta}$) vs. frequency for a rectangular microstrip patch antenna: 36.6 $mm \times 26.0$ mm, $\varepsilon_r = 2.17$, width of substrate $h = 1.58$ mm , $\theta^i = 60^o$, $\phi^i = 45^o$.

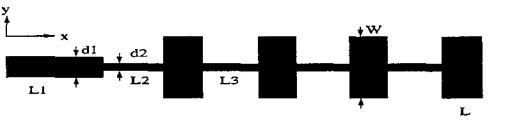

Figure 2: The geometry of a series-fed microstrip antenna array, $L = 10.08$ mm, $W = 11.79$ mm, $L_2 = 13.4$ mm, $L_3 = 12.32$ mm, $d_1 = 3.93$ mm, $d_2 = 1.3$ mm, $h = 1.5748$ mm , $\epsilon_r = 2.1$, $f = 9.42$ GHz.

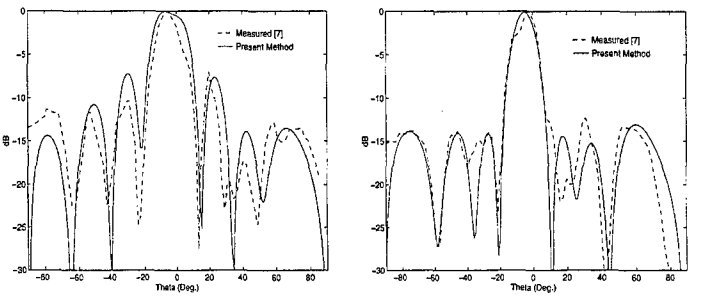

(a) (b)

Figure 3: The E-plane radiation patterns of a series-fed microstrip antenna arrays: (a) $L_1 = 23.6$ mm, (b) $L_1 = 14.6$ mm.

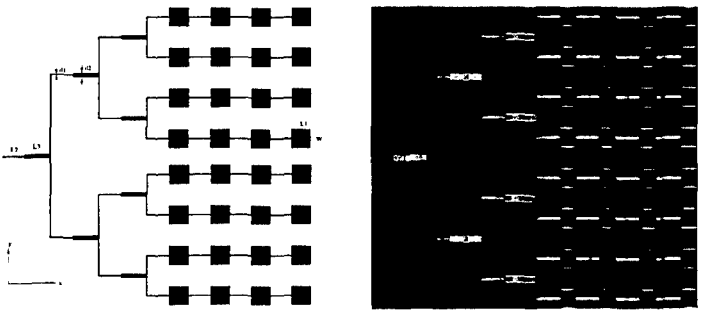

(a) (b)

Figure 4: (a) The geometry of an 8×4 microstrip corporated fed planar array. $L_1 = 10.08\ mm$, $L_2 = 12.32\ mm$, $L_3 = 18.48\ mm$, $W = 11.79\ mm$, $d_1 = 3.93\ mm$, $d_2 = 1.3\ mm$, the width of substrate $h = 1.59\ mm$, $\epsilon_r = 2.2, f = 9.42$ GHz. (b) The x-directed current distribution of the 8×4 microstrip corporated fed planar array .

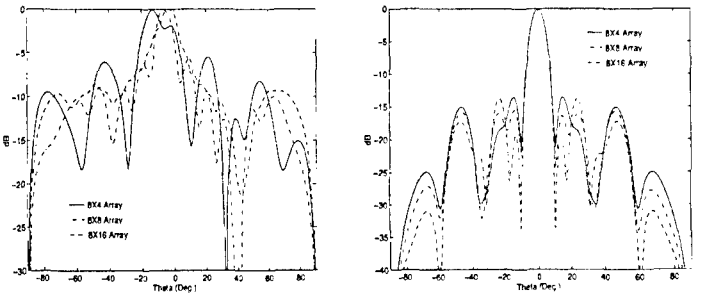

(a) (b)

Figure 5: Radiation patterns of an $8 \times N$ microstrip corporated fed planar arrays. (a) E-plane. (b) H-plane.

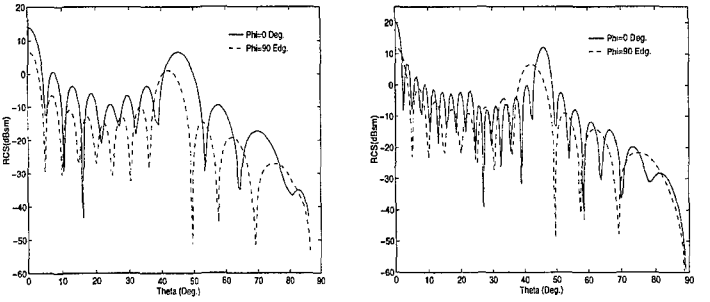

(a) (b)

Figure 6: RCS of microstrip corporated fed planar arrays. (a) 8×8 array. (b) 8×16 array

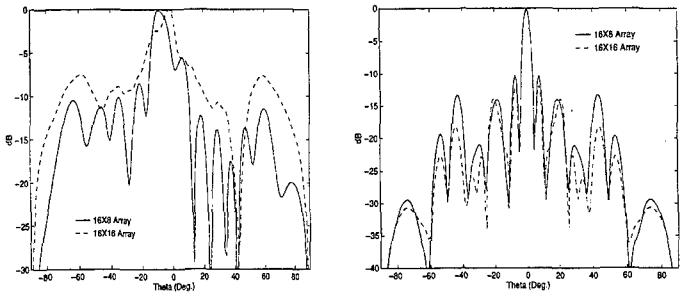

(a) (b)

Figure 7: Radiation patterns of 16×8 and 16×16 microstrip corporated fed planar arrays. (a) the E-plane. (b) H-plane.

Analytic Solution for Low-Frequency Electric Induction in an Equatorially Stratified Sphere

Trevor W. Dawson
Dept. Elec. & Comp. Eng., U. Victoria, P.O.Box 3055
Victoria, British Columbia, Canada V8W 3P6

Abstract

This paper considers the analytical solution to the problem of low-frequency induction, by quasi-uniform electric fields, in an equatorially stratified sphere having the particular conductivity distribution $\sigma(\varphi) = \sigma_0 e^{-\lambda \cos(p\varphi)}$, where $p \in \{1,2\}$ is a periodicity factor, σ_0 is a conductivity amplitude factor, and $\lambda > 0$ is a dimensionless conductivity contrast parameter. The resulting induced electric and current density fields are fully three-dimensional and exhibit interesting, yet physically reasonable, behaviour. Most noticeable are the deviations from the straight current paths that would be present in the absence of any conductivity gradient. This solution for electric excitation is supplementary to ones previously published for the quasi-static magnetic excitation, and so completes the solution for induction in the sphere by quasi-uniform electromagnetic sources.

1 Introduction

When the source frequencies are sufficiently low, the induction in compact isolated conductors can be considered in terms of separate contributions due to electric and magnetic sources [*Olsen*, 1994]. For the case of electric excitation, the electric field inside the conductor may be represented in terms of an unknown scalar potential using Stevenson's method [*Van Bladel*, 1985]. The applied electric field manifests itself through the surface boundary condition, which involves the induced zeroth-order surface charge density. The scalar potential contribution accounts for the effects of conductivity gradients and for currents due to surface charges. The resulting mathematical equations can give rise to a variety of numerical schemes, including the Scalar Potential Finite Difference (SPFD) method [*Dawson et al.*, 1997]. It is desirable to validate any numerical solution, preferably by comparison with an analytical solution. Suitable analytic solutions are relatively rare, particularly for fully three-dimensional problems. This paper presents such a solution for the case of a sphere having the particular function of equatorial angle

$$\sigma(\varphi) = \sigma_0 e^{-\lambda \cos(p\varphi)}, \tag{1}$$

where $p \in \{1,2\}$ is a periodicity factor, σ_0 is a conductivity amplitude factor, and $\lambda > 0$ is a dimensionless conductivity contrast parameter. This distribution has p conductivity maxima and minima as a function of equatorial angle φ, and a maximum conductivity contrast of $e^{2\lambda}$. The solution involves a Green's function which was previously derived for the case of arbitrary uniform magnetic excitation of the same sphere [*Dawson and Stuchly*, 1997; *Dawson*, 1997] . The result completes the solution for low-frequency induction in the equatorially stratified sphere by uniform quasi-static electromagnetic fields.

2 Analytic Solution

Under the quasi-static approximation, with a common $e^{i\omega t}$ factor dropped and in the absence of any applied magnetic field, the lowest-order electric field internal to the sphere has the representation [*Dawson and Stuchly*, 1997]

$$\boldsymbol{E}_1^i(\boldsymbol{u}) = i\omega \nabla \psi(\boldsymbol{u}) . \tag{2}$$

Here $\psi(\boldsymbol{u})$ is a scalar conduction potential to be determined as a solution to the differential equation

$$\boldsymbol{\nabla}\cdot[\sigma(\boldsymbol{u})\,\boldsymbol{\nabla}\psi(\boldsymbol{u})] = 0, \tag{3}$$

which follows from the requirement that the divergence of the current density be zero throughout the sphere interior. Specification of the problem is completed by imposition of the boundary condition

$$\sigma(\boldsymbol{u})\,\hat{\boldsymbol{n}}(\boldsymbol{u})\cdot\boldsymbol{\nabla}\psi(\boldsymbol{u}) = \rho_{s0}(\boldsymbol{u})\,, \tag{4}$$

where $\rho_{s0}(\boldsymbol{u})$ is the lowest-order charge density induced on the surface of the sphere by the applied external electric field.

The solution to the boundary value problem (2) and (3) can be expressed in terms of the same modified Green's function used for the case of magnetic excitation [*Dawson and Stuchly,* 1997] as

$$\psi(\boldsymbol{u}') = \oint\!\!\!\!\!\!\int_{\mathcal{B}} G_e\,(\boldsymbol{u}'|\boldsymbol{u})\,\rho_{s0}(\boldsymbol{u})\,da(\boldsymbol{u})\,. \tag{5}$$

Here $G_e\,(\boldsymbol{u}'|\boldsymbol{u})$ has the form of the expansion

$$G_e\,(\boldsymbol{u}'|\boldsymbol{u}) = \sum_{\varpi\in\{e,o\}}\sum_{m,n=0}^{\infty}{}' \left\{\hat{F}_m^{\varpi}(\varphi')\,\hat{F}_m^{\varpi}(\varphi)\,\hat{Q}_{mn}^{\varpi}(\theta')\,\hat{Q}_{mn}^{\varpi}(\theta)\,R_{\nu_{mn}^{\varpi}}(r'|r)\right\} \tag{6}$$

[*Dawson and Stuchly,* 1997] in eigenfunctions of the two angular coordinates, the prime indicating that the $m = n = 0$ term is to be omitted. The terms $\hat{F}_m^{\varpi}(\varphi')$ are the even and odd normalized eigenfunctions of the differential equation

$$F''(\varphi) + [\sigma'(\varphi)\,/\sigma(\varphi)]\,F'(\varphi) + \mu^2 F(\varphi) = 0. \tag{7}$$

Acceptable solutions of (7) are subject to a boundary condition of periodicity, which defines the equatorial eigenvalues μ_m^{ϖ}, $m = 0, 1, \ldots$, associated with even ($\varpi = e$) and odd ($\varpi = o$) eigenfunctions. In the case $p = 2$, the eigenfunctions additionally separate into π- and 2π-periodic classes. All are defined in terms of Fourier series. Eigenfunctions corresponding to different eigenvalues are orthogonal under a suitably defined inner product. Similarly, the terms $\hat{Q}_{mn}^{\varpi}(\theta)$ denote the normalized eigenfunctions of the ordinary differential equation

$$[\sin\theta\,Q'(\theta)]'/\sin\theta + \left(\nu\,(1+\nu) - \mu^2/\sin^2\theta\right)Q(\theta) = 0. \tag{8}$$

Boundary conditions of regularity at the sphere poles lead to the eigenvalues

$$\nu \in \{\,\nu_{mn}^{\varpi} \equiv \mu_m^{\varpi} + n \,|\, n = 0, 1, \ldots\}\,. \tag{9}$$

The functions

$$Q_{mn}^{\varpi}(\theta) = \sin^{\mu}\theta\,C_n^{(\mu+1/2)}(\cos\theta)\,,\ (n = 0, 1, \ldots)\,, \tag{10}$$

form a suitable set of unnormalized azimuthal eigenfunctions, in terms of the Gegenbauer [*Morse and Feshbach,* 1953; *Abromowitz and Stegun,* 1965] (ultraspherical) orthogonal polynomials. Pairs of eigenfunctions (10) of different azimuthal orders are again orthogonal under a suitably defined inner product.

The uniform electric excitation field of interest is

$$\boldsymbol{E}^e = E_x^e\hat{\boldsymbol{x}} + E_y^e\hat{\boldsymbol{y}} + E_z^e\hat{\boldsymbol{z}}, \tag{11}$$

where E_x^e, E_y^e and E_z^e are constants, and has the associated zeroth-order surface charge distribution

$$\rho_{s0}(\boldsymbol{u}) = 3\varepsilon_0\boldsymbol{E}^e\cdot\{\sin\theta\cos\varphi\,\hat{\boldsymbol{x}} + \sin\theta\sin\varphi\,\hat{\boldsymbol{y}} + \cos\theta\,\hat{\boldsymbol{z}}\} \tag{12}$$

[*Stratton,* 1941]. The surface integrals in the representation (5) for the potential can then formally be evaluated, leading to the solution

$$\psi(\boldsymbol{u}') = 3\varepsilon_0 a^2\boldsymbol{E}^e\cdot\sum_{\varpi\in\{e,o\}}\sum_{m,n=0}^{\infty}{}' \left\{\boldsymbol{W}_{mn}^{\varpi}\,\hat{F}_m^{\varpi}(\varphi')\,\hat{Q}_{mn}^{\varpi}(\theta')\,R_{\nu_{mn}^{\varpi}}(r'|r)\right\} \tag{13}$$

for the potential. The vector expansion coefficients have the form

$$\boldsymbol{W}^{\varpi}_{mn} \equiv U^{\varpi}_{m;x}\, V^{\varpi}_{m,n;x}\, \hat{\boldsymbol{x}} + U^{\varpi}_{m;y}\, V^{\varpi}_{m,n;y}\, \hat{\boldsymbol{y}} + U^{\varpi}_{m;z}\, V^{\varpi}_{m,n;z}\, \hat{\boldsymbol{z}}, \tag{14}$$

in terms of the equatorial contributions

$$U^{\varpi}_{m;x} = \int_{-\pi}^{+\pi} \hat{F}^{\varpi}_{m}(\varphi) \cos\varphi \, d\varphi, \qquad U^{\varpi}_{m;y} = \int_{-\pi}^{+\pi} \hat{F}^{\varpi}_{m}(\varphi) \sin\varphi \, d\varphi, \qquad U^{\varpi}_{m;z} = \int_{-\pi}^{+\pi} \hat{F}^{\varpi}_{m}(\varphi) \, d\varphi, \tag{15}$$

and the azimuthal contributions

$$V^{\varpi}_{m,n;x} = V^{\varpi}_{m,n;y} = \int_{0}^{\pi} \hat{Q}^{\varpi}_{mn}(\theta) \sin^2\theta \, d\theta, \qquad V^{\varpi}_{m,n;z} = \int_{0}^{\pi} \hat{Q}^{\varpi}_{mn}(\theta) \sin\theta\cos\theta \, d\theta. \tag{16}$$

The integrals (15) can be integrated either numerically, or semi-analytically in terms of the Fourier coefficients, while (16) can be evaluated analytically using properties of the Gegenbauer polynomials [*Abromowitz and Stegun*, 1965] and tabulated integrals [*Gradshteyn and Ryzhik*, 1965].

3 Field Examples

The examples pertain to a 1-m diameter sphere under exposure to 60-Hz, 1-V m^{-1} source fields. The contrast parameter in all cases is $\lambda = \ln\sqrt{50} \approx 1.956$, and the scale factor is chosen to be $\sigma_0 = \exp(-\lambda)$ S m^{-1}. The conductivity model is therefore

$$\sigma(\varphi) = 50^{-(1+\cos p\varphi)/2} \text{ S m}^{-1}, \tag{17}$$

with a maximum contrast of 50 : 1 and a maximum value of 1 S m^{-1}. The examples use 24 equatorial modes and 64 azimuthal modes. In the case $p = 1$, the conductivity has one minimum and one maximum as a function of φ, and these both lie in the plane $y = 0$. In contrast, in the case $p = 2$ there are two minima and two maxima as a function of φ. The minima both lie in the plane $y = 0$, while the maxima both lie in the plane $x = 0$.

The first example pertains to E_y excitation in the π periodic case. Figure 1 depicts normalized electric field (left panel) and current density (right panel) vectors in the horizontal near-equatorial plane $z = 35$ mm. The source vector is directed along the y-axis, and therefore parallel to the plane $x = 0$ containing the two conductivity maxima. The arrows are superimposed on a gray scale representation of the conductivity, with lighter shades being associated with higher conductivity values. If the sphere were uniform, the arrows in each panel would all be parallel and of the same length. The presence of the conductivity gradient leads to the preferential current flow in the regions of higher conductivity which is clearly visible in the right panel. The conservation of current in the sphere interior also results in the reduced electric field amplitude in the more highly conducting regions. Further information on the field distributions and amplitudes is presented in the gray scale plots of Figure 2. These are cross sections of the electric field (top row) and current density (bottom row) amplitudes, shaded by field amplitude according to the attached legends and using the indicated units. The current channeling by the higher conductivity is clearly illustrated in the lower left panel, as is the converse electric field behaviour in the top left.

The second example again involves E_y excitation, but for the case of a 2π periodic conductivity distribution. In this example, the source vector is parallel to the plane $x = 0$ containing the median conductivity values and separating the sphere into more highly ($x < 0$) and poorly ($x > 0$) conducting hemispheres. Figure 3 illustrates the resulting current flow in the horizontal near-equatorial plane $z = 35$ mm. The dominance of current flow in the more highly conducting hemisphere is immediately apparent in the right panel, as is the associated suppressed electric field in the left one. Figure 4 shows cross sections of the field amplitudes using the layout of Figure 2. The various panels reinforce the expected and reasonable nature of the resulting solution.

4 Closing Remarks

This paper has presented the analytical solution to the problem of low-frequency electromagnetic induction in an equatorially stratified sphere by applied quasi-uniform electric fields. The induced current density and electric field

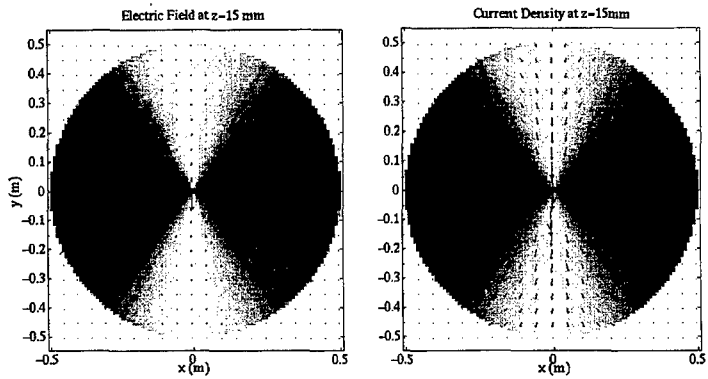

Figure 1: Representation of normalized electric field (left panel) and current density (right panel) vectors in the plane $z = 35$ mm for the π-periodic conductivity distribution in a 1-m diameter sphere, under excitation by a 60-Hz, 1-V m^{-1} electric source field directed along the y-axis (therefore parallel to the plane $x = 0$ containing the two conductivity maxima). The arrows are superimposed on a gray scale representation of the conductivity, with white denoting higher values. Coordinates are in meters.

are fully three-dimensional, and exhibit physically sensible behaviour. Linear combinations of these fields solve the problem for arbitrary uniform electric polarization. This solution for electric excitation is supplementary to previously published ones for low frequency magnetic excitation, and so completes the analytical solution to the problem of quasi-static uniform electromagnetic induction in the inhomogeneous spherical model. It is anticipated that the model and solution should prove particularly useful in the validation of three-dimensional low-frequency electromagnetic computer modelling codes.

Acknowledgment

This work was supported under the Natural Sciences and Engineering Research Council/BC Hydro/TransAlta Industrial Research Chair program.

References

[1] R. G. Olsen. Power-transmission electromagnetics. *IEEE. Antennas & Propagation Magazine*, **36**(6):7–16, December 1994.

[2] J. Van Bladel. *Electromagnetic Fields*. Hemisphere Publishing Corporation, Washington D.C., revised printing edition, 1985.

[3] Trevor W. Dawson, Kris Caputa, and Maria A. Stuchly. Influence of human model resolution on computed currents induced in organs by 60-hz magnetic fields. *Bioelectromagnetics Journal*, 18(7):478–490, 1997.

[4] Trevor W. Dawson and Maria A. Stuchly. An analytic solution for verification of computer models for low-frequency magnetic induction. *Radio Science*, 32(2):343–368, March-April 1997.

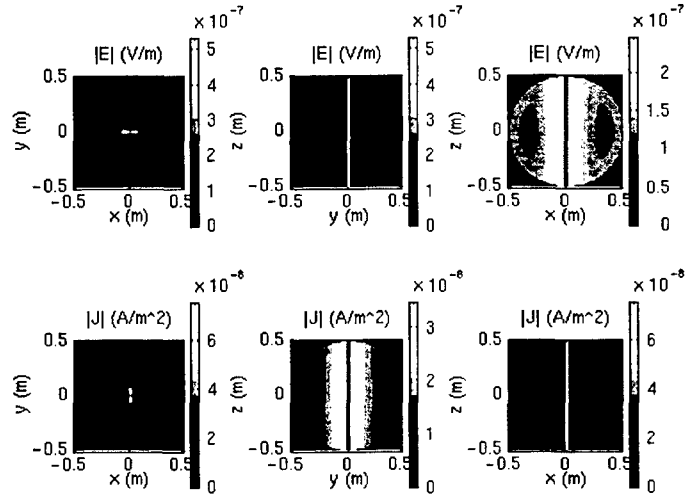

Figure 2: Magnitudes of the (top row) electric field (in volts per meter, as indicated in the legend bar) and (bottom row) current density (in amperes per square meter), under excitation by a 60-Hz, 1-V m^{-1} electric source field directed along the y-axis (and therefore parallel to the plane $x = 0$ containing the two conductivity maxima), for the π periodic conductivity distribution in a 1-m diameter sphere. The cross sections are taken in the planes (left column) $z = 35$ mm, (middle column) $x = 35$ mm, and (right column) $y = 35$ mm.

[5] Trevor W. Dawson. Analytic solution for low-frequency magnetic induction in an equatorially stratified sphere : Horizontal excitation. *Radio Science*, 1997. in press.

[6] Philip M. Morse and Herman Feshbach, editors. *Methods of Theoretical Physics*. McGraw-Hill Book Company, New York, 1953.

[7] Milton Abramowitz and Irene Stegun, editors. *Handbook of Mathematical Functions*. Dover Publications, Inc., New York, 1965.

[8] J. A. Stratton. *Electromagnetic Theory*. McGraw-Hill Book Company, New York, 1941.

[9] I. S. Gradshteyn and I. M. Ryzhik. *Tables of Integrals, Series and Products*. Academic Press, New York, 1965.

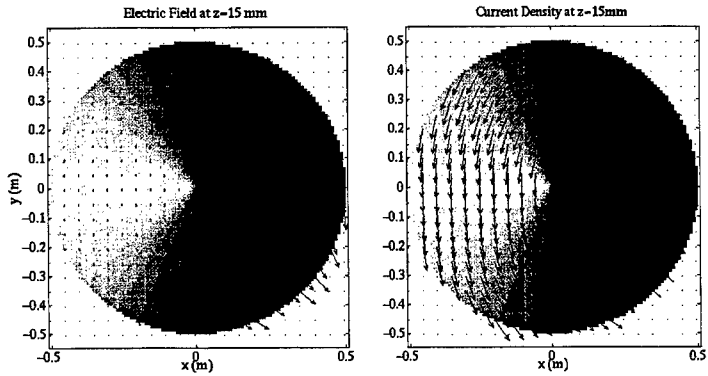

Figure 3: Similar to Figure 1, but for a 2π-periodic conductivity distribution.

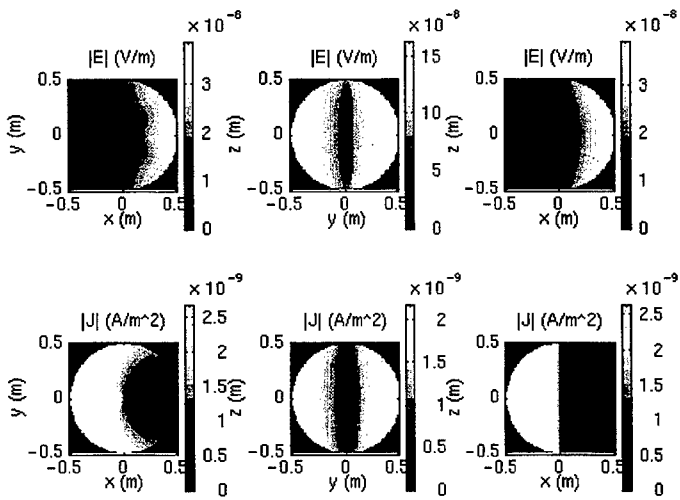

Figure 4: Similar to Figure 2, but for a 2π-periodic conductivity distribution.

Parallelizing Computational Electromagnetics Code using the Parallel Virtual Machine: Examples

Ed Skochinski, Sembiam Rengarajan
Department of Electrical and Computer Engineering
California State University, Northridge
Northridge, CA 91330-8346

Abstract

Oakridge National Labs' *Parallel Virtual Machine* (PVM) is used to parallelize computational electromagnetics codes in FORTRAN 77. We studied a Moment Method code in the spectral domain, a Physical Optics code, and Finite-Difference Time-Domain code. Though all problems are considered to be numerically intensive, the MoM and PO formulations displayed exceptionally parallel behavior, and produced 93% and 80% efficiencies, respectively, for 20 processors. A work-in-progress FDTD code and partitioning strategies are briefly discussed.

Introduction

The Parallel Virtual Machine, or PVM, is a group of function and subroutine calls which, under programmer control, enlist one or more computers to operate in parallel on a single problem [1]. With PVM, the task of discovering parallelism in a given problem and distributing the computations to independent processors is left entirely to the programmer.

PVM has a number of technical and economic features which make it a good product for use in scientific programming: it has interfaces for FORTRAN 77 as well as the C language, it runs on a wide variety of the most popular Unix workstations, and it frees the scientific programmer from having to know the low-level computer and data network details which underly its workings. Additionally, PVM is available *free* via the Internet, without any export restrictions, from Oakridge National Laboratory [2]. The environment used in this work was a collection of twenty-four HP 9000 712/80 workstations running HP-UX 10.20 and PVM version 3.3.11. All workstations were connected via ethernet, and the users' filesystem was shared using the Network File System (NFS).

In each case investigated, a master/slave technique was used, whereby a master program read in the problem definition and spawned several slave tasks. The master program then partitioned the program into pieces and doled out these pieces to each slave task. As the slaves completed

their pieces, they communicated their results back to the master. The master collected all the results from the slaves and either computed or presented the aggregate result.

To measure the performance of the parallelized code, each sequential program's execution time, T_s, was measured. Next, each parallel program's execution time, T_p, was measured for increasing number of processors, $P = 1..n$. The speedup factor, $S = T_s/T_p$, was calculated and plotted against P. For the highest values of P, the efficiency, $E = S/P$, is discussed.

For the spectral domain moment method and physical optics codes, the slave tasks did not have to communicate with each other. Therefore, a straight-forward loop-slicing technique was used to partition the problem into parallel pieces. The FDTD problem was somewhat more difficult, as its computations were interdependent. In this case, the problem was partitioned based upon geometry, and where each subsection of the overall geometry overlapped, slave-to-slave communication was used. A good technique for this problem is to choose a partitioning scheme that minimizes the slave-to-slave comminication.

1 A Spectral Moment Method Application

The Method of Moments, or MoM, is a widely used computational technique for solving a linear operator equation such as an integral equation subject to the boundary conditions [3]. The computational procedure involves populating an $n \times n$ matrix, $\mathbf{A}$, and obtaining a simultaneous set of solutions against the source column vector, $\mathbf{b}$. In the moment method, generally the fill time of the matrices is a substantial part of the overall computation time. Populating the matrices lends well to parallelization, whereas a parallel solution to a matrix equation involves a great deal of commnication and book-keeping compared to the computation involved.

The spectral domain MoM problem [4] permitted a partitioning whereby a single populate/solve spectral computation could be assigned to a single sequential processor. There was no immediate gain here other than avoiding parallelizing a trusted sequential matrix solver. Because the *total* solution required sampling various values (about 200) of the spectrum, each sample could be assigned to a separate processor and computed simultaneously. The spectral solution was formulated to avoid a massive moment matrix computation for 3D problems [4], and as a side-effect exposed an embarrassingly parallel algorithm (one where the computations are completely independent and the communications are minimal).

Figure 1 shows a linear speedup for up to 19 processors, without even hinting that the efficiency is beginning to fall off. At P=19, the efficiency is 93%, a very high mark. Each individual spectral computation consumed about 10 CPU seconds. The entire matrix population required only about 15 variables as parameters, of which only one, the spectral variable, changed for each different computation.

With a parallel workhorse, it was possible to quickly characterize and optimize various convergence criteria, such as integral equation tolerances, subdomain size, and where to truncate the spectrum.

2 Diffraction Analyses using Physical Optics Technique

The physical optics (PO) technique is popular for diffraction analyses of reflector antennas since such a computer code is robust [5]. In a typical PO computation, each reflector is divided up into

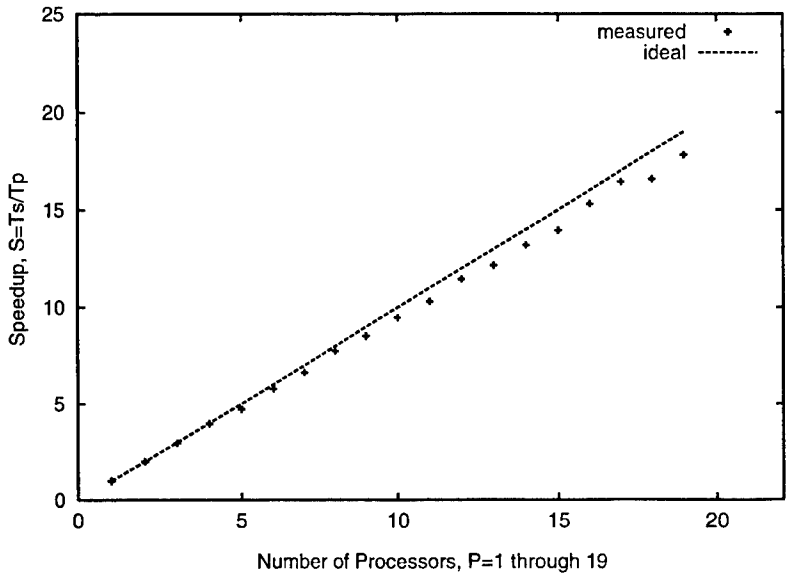

Figure 1: Speedup for the parallelized spectral-domain MoM program.

a large number of triangles such that the linear dimensions of each triangle is in the order of a half wavelength. The PO technique does not require the computation of currents interacting on the same surface, thus the fields on each triangle of one reflector may be computed independently. The program was used for diffraction analyses of multiple reflectors. A summation involving each triangular facet's current and the Green's function would yeild the field or current at a near-field point. For multiple reflectors, the output of one execution was fed as input to the next run. With a two-mirror test case, the first reflector's input data was approximately 20MB, describing a surface with some 90,000 triangles. The next reflector was divided up into about 20,000 triangles, for a total of 1.8×10^9 separate calculations!

The sheer magnitude of the problem, combined with the independent calculations, hint at a very parallelizable problem. Indeed, up to $P = 7$ in Figure 2, the performance is nearly ideal. But for increasing P, there is a definite trend with falling performances. At $P = 21$, the efficiency was only 80%. This disappointing behavior resulted from the 20MB of data which had to be transmitted to each parallel task. To reduce the effort in parallelizing the code, the program depended upon NFS to transmit the data: the slave program merely opened the file on every computer where it executed, and the data was read via the network. Unfortunately, the data is needed immediately, and all slaves read in the entire description *before* processing it in the exact same order.

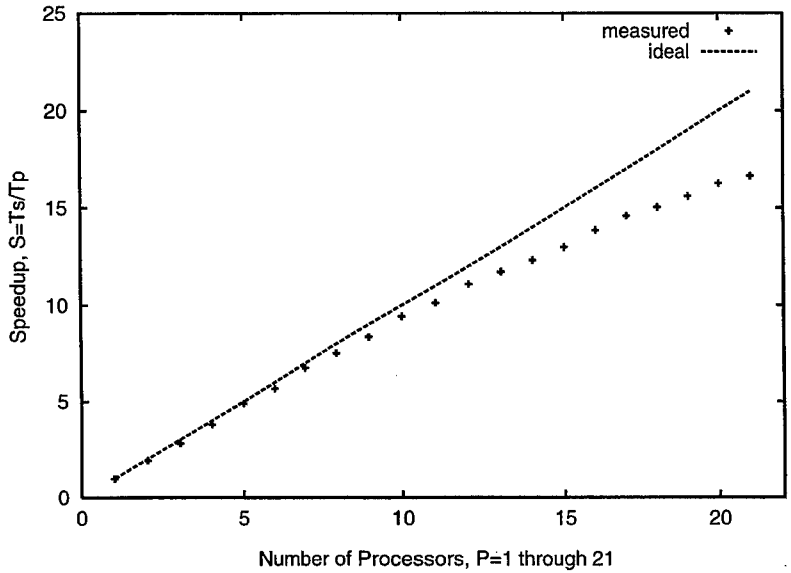

Figure 2: Speedup for the parallelized PO program.

The average transmission time for the 20MB of input data was nearly 20 seconds per processor. The ethernet connection was a shared resource, and all slaves read the input at the same time, competing for the same file server over the same network "wire." Unfortunately, as increasing numbers of processors cut the problem down to size, the communication time became increasingly significant. For $P = 1$, the 20 seconds taken in data transmission were insignificant compared to the $11\frac{1}{2}$ hours of computation. At $P = 21$, about 33 minutes of computation are expected, but no calculations were started until 400 seconds passed while the slaves loaded up the input data. The $6\frac{2}{3}$ minutes of communication accounted for a hefty 16% of the $41\frac{3}{4}$ minutes to solve the problem. The efficiency with $P = 21$ turned out to be only 80%: an additional 4% efficiency was lost due to master/slave communications overhead during the parallel computation. The only way to gain back some of the expected parallelism is to use a more sophisticated scheduling algorithm that permits computation and communication to overlap while reading the input data. Such an algorithm is being investigated and the results will be presented at the conference.

The program could compute the induced currents in two ways: 1) with a constant phase in each triangle, or 2) with a linear phase distribution in each triangle. Previous work has shown that for comparable accuracies, both methods require the same amount of computer time; however, the linear phase technique would require fewer triangles, and hence, less computer

storage and less data commucation time. PVM was used to investigate the two techniques.

3 Parallelizing Finite Difference Time Domain Code

Unlike the MoM and PO computations, FDTD requires the computational results of neighboring elements. The complete independence of the computations exploited in the previous examples does not occur. The problem space must be partitioned in such a way as to minimize the quantity of data communicated between tasks, or the number of commincations calls between tasks, with the latter approach being useful when the startup costs for task-to-task data transfers dominate the commuincations overhead.

A very modest 3D test geometry ($40 \times 40 \times 40$) was used for debugging, with T_s taking only 46 seconds. Because every eight time steps the entire volume of interest was reconstructed in the master from slave transmissions, the master and slaves were burdened by I/O intensive "snapshot" communications. In fact, a performance degradation was seen. Except for startup and snapshot updates, the slaves are entirely autonomous. For a run requiring a steady-state result, the slaves run to completion and update the master only once.

The test case was hardly a canditate for parallelization. A more realistic, large-scale computation with data quantity versus data transmissions comparisons will be presented at the conference.

Conclusions

PVM presents a very accessible tool for parallelizing programs. Fortunately, engineering problems tend to be somewhat brutish in their computing requirements, allowing a rather straightforward method of exploiting parallelism. With the increasing abundance of networked workstations in academic and industrial environments, formidable problems may now be within reach. A Windows 95 port of PVM is in the works, opening up the considerable power of today's PCs for parallel computation. An office PC or workstation that spends perhaps 16 hours of the day unused might now participate as a computational engine.

References

[1] Al Geist, Adam Beguelin, Jack Dongarra, Weicheng Jiang, Robert Mancheck, Vaidy Sunderam. *PVM 3 User's Guide and Reference Manual*, ORNL/TM-12187 (September, 1994), Oak Ridge National Laboratory, Oak Ridge, TN 37831.

[2] `http://www.epm.ornl.gov/pvm/`
This page contains links to online documentation and how to obtain the PVM distribution.

[3] R.F. Harrington. *Field Computations by Moment Methods, IEEE Press reprint ed.* Portland, OR: Book News, Inc., 1996.

[4] S.R. Rengarajan. *Mutual coupling between slots cut in rectangular cylindrical structures: Spectral domain technique.* Radio Science, Volume 31, Number 6, pp. 1651–1661, November–December 1996.

[5] W.A. Imbriale and R. Hodges. *Linear phase approximation in the triangular facet near-field physical optics computer program,* Applied Computational Electromagnetics Society Journal, Volume 6, Number 2, pp. 74–85, Winter 1991.

SAF Analysis Codes for Predicting the Electromagnetic Effectiveness of Antennas Enclosed in Composite Structures*

Barry J. Cown[1], John P. Estrada[1], and Ramses Routier[2]

(1) GEMTECH Microwaves, Inc. 1318 Chandler Court, Acworth, GA 30102
(2) NAVSEA, Code SEA-03K24 (EMENG), 2531 Jefferson Davis Highway, Arlington, VA 22242

A. INTRODUCTION

This paper describes the computer codes GRADM and GSCATT for predicting the electromagnetic effectiveness of antennas enclosed in composite structures. In particular, GRADM and GSCATT compute the antenna pattern performance and RCS, respectively, for enclosed antennas. The enclosed antennas may be of any type--horn, reflector, patch, spiral, phased array--for which the complex "free-space" pattern is known from measurements or numerical computations. GRADM and GSCATT are based on the near-field (NF) spectral analysis method known as the Spherical Angular Function (SAF) technique [1-7]. GRADM and GSCATT can be used in conjunction with the existing SAF codes GMULT, GLOSS and GCUPL to analyze antenna pattern performance, coupling, and RADHAZ for mixed composite/metallic topsides

This paper is organized as follows. Part B presents some background information concerning the Navy's progression toward integrated antenna/composite structures for ship topsides. The SAF analysis techniques implemented in GRADM and GSCATT are described in Part C. In part D, GRADM and GSCATT are applied to the analysis of the TAS antenna installed in the ATD mast. Concluding remarks are presented in Part E. Part F contains a list of references.

B. BACKGROUND

The progression toward increasing use of composite materials and structures for the topsides of Navy surface ships is well under way [8]. Current plans call for the increasing utilization of antennas that are either enclosed or embedded in multilayer composite structures, in contrast to present day topsides where antennas operate on mostly metallic topsides. This progression is necessary in order to meet the Navy's future war fighting requirements, especially for "littoral" warfare, where the electromagnetic effectiveness of the ships micro/millimeter wave antenna systems will increasingly be determined by the ability to satisfy stringent RCS requirements in addition to the usual requirements concerning antenna pattern performance, coupling, and RADHAZ

The progression toward antennas that are increasingly integrated with composite structures to both increase antenna performance and control topside RCS is illustrated by Figures B-1 through B-3.

* *Sponsored by the Naval Sea Systems Command (NAVSEA), Code SEA-03K24, Arlington, VA*

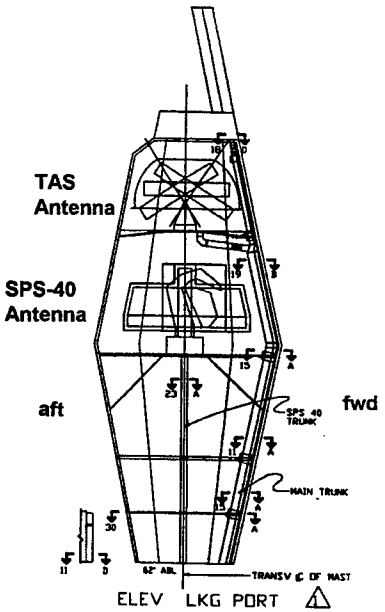

Figure B-1. ATD hexagonal composite mast and enclosed sensors (DD-963).

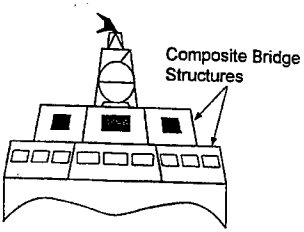

Figure B-2. Composite Bridge Concept with integrated sensor/comm antennas

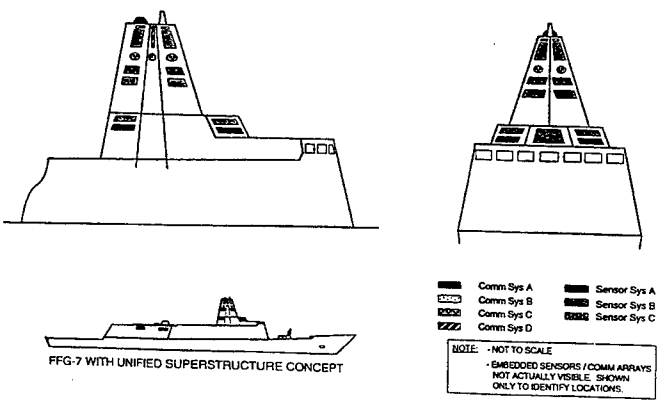

Figure B-3. Unified superstructure concept

Figures B-1 and B-2 depict situations where the antennas operate on mixed composite/metallic topsides. Figure B-1 shows the concept for the ATD hexagonal mast that encloses the TAS antenna and the SPS-40 antenna. Figure B-2 illustrates the composite bridge with embedded sensor and communication arrays. It is anticipated that the unified composite superstructure concept shown in Figure B-3 will be realized early in the next century.

C. SAF ANALYSIS TECHNIQUE FOR MULTIPLE SCATTERERS

The radiating near-field of an antenna or scattering object may be represented as a vectorial angular spectrum of outwardly propagating plane waves. This vectorial angular spectrum of plane waves is completely described by the Spherical Angular Function (SAF) for the antenna, and it is denoted as $\overline{F}(\theta,\phi)$, where (θ,ϕ) are the elevation and azimuth angles, respectively, in a standard vertically-oriented system of spherical coordinates. $\overline{F}(\theta,\phi)$ may be expressed directly in terms of the vectorial complex far-field electric field $\overline{E}_{ff}(\theta,\phi)$ as $\overline{F}(\theta,\phi) = r\{\exp[jkr]\}\overline{E}_{ff}(\theta,\phi)$, where $k = 2\pi/\lambda$, λ is the free-space wavelength, and r is the distance to the far-field pattern point

Consider the case depicted in Figure B-1 involving the TAS antenna enclosed in the ATD composite mast. The resultant total SAF for the antenna operating in the presence of the composite mast structural elements--ceiling, floor, other enclosed scattering objects, composite walls--is computed via the "Marching In Range Method", or MIRM for short. Assume the TAS antenna is pointing starboard. In the MIRM, the antenna SAF is propagated to the first scatterer (the ceiling), the scattered SAF is computed and added to the incident antenna SAF to obtain the total SAF. This total SAF is just the distorted SAF for the antenna operating in the presence of the first scatterer. This total SAF after this first step is then allowed to be incident on the second scatterer (the floor), the scattered SAF from the second scatterer is computed and added to the total SAF for the first scatterer to obtain the distorted total SAF for the antenna operating in the presence of the two scatterers. This distorted total SAF is then incident on the third scatterer, (the FSS wall), and the scattered SAF for this third scatterer is added to distorted total SAF incident on the third scatterer to obtain the final distorted total SAF. In general, this process is repeated N times if there are N scatterers This process can be expressed succinctly as

$$\overline{F}_N^{tot}(\theta,\phi) = \prod_{n=0}^{N} \overline{\overline{\Gamma}}_n\left(\theta,\phi|\theta',\phi'|\overline{R}_n\right) \bullet \overline{F}^a(\theta',\phi'), \tag{C-1}$$

where the SAF integral operator $\overline{\overline{\Gamma}}_n\left(\theta,\phi|\theta',\phi'|\overline{R}_n\right)$ is defined as

$$\bar{\bar{\Gamma}}_n\left(\theta,\phi|\theta',\phi'|\bar{R}_n\right) = \iint_{\Omega'} d\Omega' \exp\left\{j\left[\bar{k}(\theta,\phi) - \bar{k}(\theta',\phi')\right] \bullet \bar{R}_n\right\}\left\{\bar{\bar{I}} + \bar{\bar{S}}_n(\theta,\phi|\theta',\phi')\right\}, \quad \text{(C-2)}$$

where $\bar{\bar{S}}_n(\theta,\phi|\theta',\phi')$ is the plane-wave (PW) scattering dyad for the n^{th} obstacle, $\bar{R}_n$ is the vector distance from the antenna to the n^{th} obstacle, and where $\bar{k}(\theta,\phi)$ and $\bar{k}(\theta',\phi')$ are the wave vectors for the scattered and incident fields, respectively. $\bar{\bar{I}}$ is the identity dyad.

The canonical scatterers utilized by GRADM and GSCATT include flat polygonal composite or metallic plates as well as metallic finite circular cylinders, metallic finite elliptical cylinders, and metallic circular cone frusta. Trapezoidal and hexagonal shapes are particularly convenient for modeling the ATD mast structure. The PW scattering function for the flat composite or metallic polygonal panels is based on Physical Optics (PO) formulas for opaque polygonal plates and the Periodic Moment Method (PMM) code [9]. The PO formulas account for the shape of the panels and the PMM code is used to compute the PW transmission and reflection coefficients for the panels as a function of the PW incidence angle. We note that the PMM code is applicable to multilayer frequency selective surfaces as well as to multilayer dielectric panels.

The PW scattering dyad $S^{pp}(\theta,\phi|\theta',\phi')$ for a flat composite panel of any shape can be expressed in the PO approximation as

$$\bar{\bar{S}}^{pp}(\theta,\phi|\theta',\phi') = \begin{bmatrix} \chi_{\theta\theta} S(\theta,\phi|\theta',\phi') & 0 \\ 0 & \chi_{\phi\phi} S(\theta,\phi|\theta',\phi') \end{bmatrix} \quad \text{(C-3)}$$

where $S(\theta,\phi|\theta',\phi')$ is the PW scattering function for an opaque polygonal plate having the same shape as the composite panel, $\chi_{\theta\theta}$ is the PW scattering coefficient for the panel for vertical polarization, and $\chi_{\phi\phi}$ is the PW scattering coefficient for the panel for horizontal polarization. The PW scattering coefficients are equal to (1.0-PW transmission coefficients) for scattering into the forward hemisphere of the plate defined by positive values of $\bar{k}' \bullet \bar{n}$, where $\bar{k}'$ is a unit vector parallel with the incident wavevector and $\bar{n}$ is an outwardly-pointing unit vector perpendicular to the geometrically-shadowed side of the panel. For negative values of $\bar{k}' \bullet \bar{n}$, the PW scattering coefficient is equal to the PW reflection coefficient. Closed-form expressions exist in the literature for the PO approximation for PW scattering by opaque polygonal plates [10, 11] and these have been implemented in GRADM and GSCATT.

D. APPLICATION OF GRADM AND GSCATT TO THE DD-963 ATD MAST

In order to illustrate the application of GRADM and GSCATT to "real-world" topside problems, GRADM and GSCATT have been applied to the DD-963 ATD mast. In particular, GRADM was used to compute the pattern performance of the TAS antenna installed in the DD-963 ATD composite mast, and the results of this analysis are presented in Part D-1. GSCATT has been used to assess the resultant RCS due to the combined scattering from the ATD mast composite wall and a generic rectangular aperture antenna. The RCS analysis is presented in Part D-2. A sketch showing the antenna pointing directions for the GRADM and GSCATT computations presented herein is presented in Figure D-1.

We note that all of the physical dimensions for the ATD mast were estimated from sketches rather than detailed engineering drawings, and that the "free-space" TAS pattern used for the modeling is an idealized theoretical pattern. Accordingly, the results presented herein are primarily intended to be illustrative of the modeling capabilities of GRADM and GSCATT, and should not be construed as definitive assessments of the DD-963 ATD mast performance.

D-1. GRADM Analysis of TAS Pattern Performance

Plots of the TAS elevation pattern installed in the ATD mast are shown in Figures D-2 through D-4 for zero ship roll. Each figure compares the idealized free-space pattern with the installed patterns computed via GRADM for the indicated types of ceilings and floors, with and without the FSS wall. The main effect of the FSS wall at in-band frequencies is to provide some wide-angle filtering. All of the patterns are for the L-band operating frequency of the TAS.

Comparison of the installed patterns for the PEC (perfect electric conductor) ceiling and floor of Figure D-2 with the installed patterns for the absorbing ceiling, conducting floor of Figure D-3 shows that the absorbing ceiling significantly reduces the reflection lobes from the ceiling for elevation angles of ≥ 120 degrees. Hence, the absorbing ceiling is beneficial for RADHAZ and EMC performance.

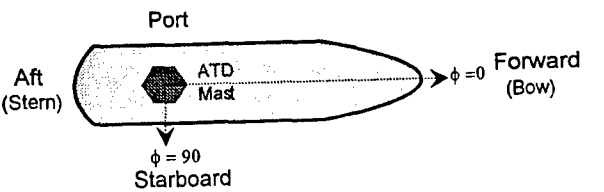

Figure D-1. Antenna azimuth pointing directions for GRADM and GSCATT computations.

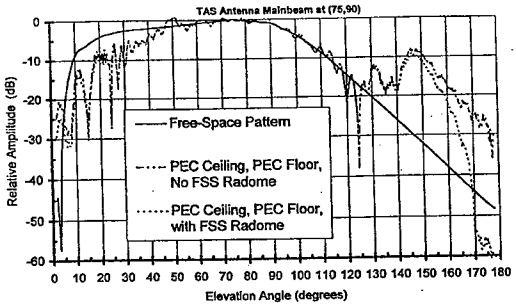

Figure D-2. Installed elevation pattern for the TAS pointed to starboard: conducting ceiling, conducting floor.

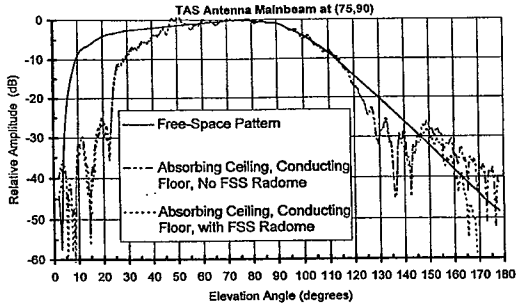

Figure D-3. Installed elevation pattern for the TAS pointed to starboard: absorbing ceiling, conducting floor.

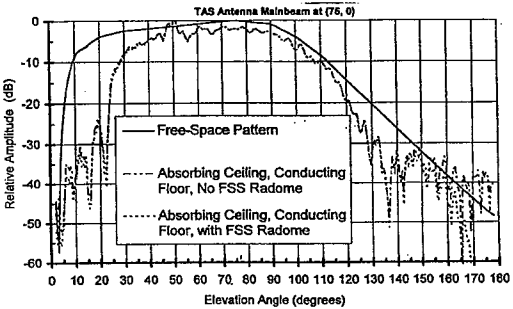

Figure D-4. Installed elevation pattern for the TAS pointed to the bow: absorbing ceiling, conducting floor, and blockage by the metallic cylindrical shroud.

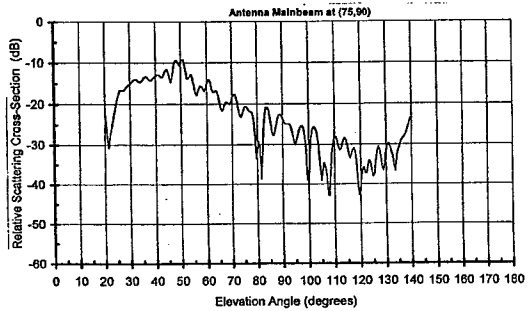

Figure D-5. Resultant bistatic RCS versus elevation angle for the generic antenna installed in the TAS compartment.

However, better coverage at the higher elevation angles is achieved for the conducting ceiling, conducting floor case due to stronger multiple reflections into the upper elevation angles.

Figure D-4 shows the computed elevation pattern when the TAS is pointed toward the bow at theta = 75°, phi = 0°. For this orientation, the TAS is blocked by a round metallic shroud enclosing the cable trunk and portable access ladder. Inspection of the computed TAS elevation pattern shown in Figure D-4 reveals that the cylindrical shroud causes about 1 dB to 2 dB of blockage over the central portion of the pattern compared to Figure D-3 where the TAS is pointed to starboard.

D-2. GSCATT Analysis of Resultant RCS

The dimensions of the rectangular aperture antenna enclosed in the ATD composite mast were chosen to be comparable to the TAS antenna aperture. However, in order to respect security guidelines, the parameters for the feed network and aperture distribution used for the illustrative RCS computations are deliberately chosen to be disparate from the actual TAS parameters.

It is well known that antenna scattering is comprised of two terms, the "antenna mode" scattering and the "structural mode" scattering [12]. The antenna mode scattering arises when a portion of the received power is re-radiated due to reflections in the feed network. The structural mode scattering modeled by GSCATT arises partly from "aperture rejection" of some of the incident field due to characteristic mode mismatches and partly from currents induced in the surrounding antenna physical structures. Forward and reverse marching in range accounts for contributions to the resultant RCS due to the reflected SAF of the FSS wall and the effects of the ceiling, floor, and FSS wall on the SAF scattered from the antenna. (The FSS wall has negligible effect on transmitted fields for in-band frequencies.)

A plot of the (normalized) resultant bistatic RCS for the generic antenna installed in the DD-963 mast are shown is Figure D-5 for the antenna pointed to starboard and an incident PW impinging perpendicular to the ATD mast wall from theta = 80°, phi = 90°. The bistatic RCS pattern shown is an elevation cut at phi = 90° for one particular choice of antenna load conditions. Families of monostatic and bistatic RCS patterns can be generated for user-specified load conditions and PW incidence angles.

D. CONCLUDING REMARKS

PW scattering dyads for flat polygonal panels composed of multilayer dielectric and/or frequency selective surfaces (FSS) have been derived by combining Physical Optics (PO) formulas for opaque polygonal plates and the Periodic Moment Method (PMM) code. The PO formulas account for the shape of the panels and the PMM code is used to compute the PW transmission and reflection coefficients for the panels as a function of the PW incidence angles. The PW dyads have been

implemented in the FORTRAN 77-compliant SAF computer codes GRADM and GSCATT for computing the pattern performance and resultant RCS performance, respectively, for antennas enclosed in composite masts. Current plans call for the development of advanced frequency-domain and time-domain computer models for efficient analysis of pattern and RCS performances of multifunction antenna arrays that are enclosed or embedded in planar and/or curved composite multilayer structures.

F. REFERENCES

1. Barry J. Cown, "Antenna Pattern Performance and Coupling in the Presence of Near-Field Shipboard Obstacles", Final Technical Report, GTRI, Prime Contract No. N00024-82-K-5329, July 1984.

2. Barry J. Cown, R. W. Cravey, and C. D. Papanicolopoulos, "Analysis of Antenna Coupling and Scattering Via Spherical Angular Functions", 1986 IEEE International Antenna and Propagation Symposium Proceedings, Philadelphia, PA, June 13-18, 1986.

3. B. J. Cown and C. E. Ryan, Jr., "Near-Field Scattering Measurements for Determining Complex Target RCS", *IEEE Trans. Ant. and Prop.*, Vol 37, No. 5, May 1989, pp. 576-585.

4. B. J. Cown, J. P. Estrada, Brian L Shirley, and C. E. Ryan, Jr., "Shipboard Near-Field Energy Determination", Final Technical Report, GMT-9101 and GTRI A-9275, Task SCEEE-NSWC/ 9C-0123 (Navy Prime Contract N6092C-87-D-A315-0123), September, 1992.

5. B. J. Cown and John P. Estrada, "SAF Analysis of Shipboard Antenna Performance, Coupling, and RADHAZ in Complex Near-Field Scattering Environments", IEEE Antennas and Propagation Symposium Proceedings, Newport Beach, CA, June 18-23, 1995, pp. 6-9.

6 B. J. Cown and J. P. Estrada, "SAF Analysis Codes for Computing Shipboard Antenna Pattern Performance, Antenna Coupling, and RADHAZ", 1997 ACES Symposium Proceedings, Monterey CA, March, 1997.

7. B. J. Cown and J. P. Estrada, " SAF Analysis Models for Antenna Performance, Coupling, RADHAZ, and RCS of Integrated Antenna/Composite Topsides", Final Technical Report, Phase I of SBIR Topic No. N97-051, Contract No. N00024-97-4105, November, 1997.

8. J. C. Logan, J. H. Meloling, L. C. Russell, D. F. Schwartz, "Interior Scattering Effects on the TAS Radar Performance for the AEM/S System", Technical Report 1713, Naval Command, Control, and Ocean Surveillance Center, RDT & E Division, San Diego, CA, May 1996.

9. L. W. Henderson, "Introduction to PMM, Version 4.0", Technical Report 725347-1, Contract No. SC-SP18-91-0001, July 1993.

10. William B. Gordon, "Far-Field Approximations to the Kirchoff-Helmholtz Representations of Scattered Fields", IEEE Trans. on Antennas and Propagation, July 1975, pp 590-592.

11. Shung-Wu Lee and Raj Mittra, "Fourier Transform of a Polygonal Shape Function and Its Application in Electromagnetics", IEEE Trans. on Antennas and Propagation, Vol. AP-31, No. 1, January 1983, pp 99-103.

12. R. C. Hansen, "Relationships Between Antennas as Scatterers and Radiators", Proc. of IEEE, Vol. 77, May 1989, pp 659-662.

SOME CONCENTRATED SOLUTIONS OF HELMHOLTZ EQUATION WITH NONLOCAL NONLINEARITY.

Yu.N.Cherkashin and V.A.Eremenko

Institute of Terrestrial Magnetism, Ionosphere and Radio Wave Propagation
IZMIRAN, Troitsk, Moscow region, 142092, Russia
e.mail: eva@top.izmiran.troitsk.ru
Phone: +7 095 3340278(work), +7 095 4302656(home),
Fax: +7 095 3340908,

Abstract

The nonlinear problem of the wave propagation is considered. It taken into account that the diffusion process transforms the interaction of the electromagnetic field with the environment. This phenomenon is described by the system of differential equations including. the equation for the perturbation of the dielectric permittivity. The mathematical problem is reduced to the eigen value problem for nonlinear integro-differential equation of Hartree type. The computational procedure is constructed.

1. Introduction

Recently there are many theoretical and experimental investigations concerning the nonlinear problem of the powerful wave beams propagation. Usually, these investigations are restricted by the local nonlinearity [1-3]. However, it is obviously such description is possible only in the case of negligible thermal conductivity, in the other words, when the wave beam size is much more than the scale of the thermal conduction. In the other case it is necessary to take into account the process of the thermal diffusion of the nonlinear perturbation from the wave field region [4].

2. Analysis

We will describe the wave field propagation in terms of Helmholtz equation for the electric field amplitude u

$$\Delta u + k^2 \cdot \varepsilon \cdot u = 0 \qquad (1)$$

where k is the wave number and ε is the dielectric permittivity. We will consider the propagation of the narrow shortwave beams. Thus we will construct the Helmholtz equation solution concentrated in the small vicinity of the ray trajectory. In this vicinity, we introduce the orthogonal coordinate system: ξ is the length of the trajectory arch; η is the distance along the orthogonal direction to the ray.

We represent the complex-valued function u in the terms of $u = v \cdot \exp(ik\psi)$, where v and ψ - are real functions. Instead (1), it is possible to write the equations:

$$\Delta v + k^2\left[\varepsilon - (\nabla\psi)^2\right]v = 0, \qquad div(v^2\nabla\psi) = 0$$

In this approach the derivatives along the trajectory are essentially less then the derivatives across the ray direction. Therefore, we can write in the main approximation:

$$\frac{\partial^2 v}{\partial y^2} + k^2\left[\varepsilon - \left(\frac{\partial\psi}{\partial x}\right)^2\right]v = 0, \qquad \frac{\partial\psi}{\partial y} = 0$$

The electric field heats the environment and creates the perturbation of the dielectric permittivity. Thus ε consists of the two parts: $\varepsilon = \varepsilon_r + \varepsilon_n$, ε_r being the regular part independent from wave field and ε_n being the perturbation caused by the electric field. For the ε_n, we can write the diffusion equation.

$$L^2 \cdot \frac{d^2\varepsilon_n}{d\eta^2} - \varepsilon_n + \alpha \cdot |u|^2 = 0$$

where L is the scale of the diffusion process, α is the nonlinear coefficient. We observe the small area near the ray and we can consider that L is constant in this area The diffusion equation for ε_n can be integrated in the frameworks of this assumption. Thus, we have get the simple expression for the nonlinear perturbation ε_n:

$$\varepsilon_n(\eta) = \frac{\alpha}{2L}\int_{-\infty}^{\infty}|u(t)|^2 \cdot \exp\left(-\frac{|\eta - t|}{L}\right)dt$$

Now, it is easy to see that we can reduce the problem of the nonlinear interaction in view of diffusion to the one nonlinear integro-differential equation of Hartree type. It is convenient to introduce the fundamental solution of the diffusion equation

$$G(x) = \frac{1}{2L}\exp\left(-\frac{|x|}{L}\right),$$

and the nondimensional variable (v_0 - is the maximum of $v(\eta)$.):

$$V=\frac{v}{v_0};\quad y=\left(k\cdot v_0\cdot\sqrt{\alpha}\right)\cdot\eta;\quad p=\alpha v_0^2\left[\left(\frac{\partial\psi}{\partial\xi}\right)^2-\varepsilon_r\right],$$

In these designations, we write the main equation.

$$\frac{d^2V}{dy^2}+V\cdot\int_{-\infty}^{\infty}V^2(t)\cdot G(y-t)dt=p\cdot V$$

It is easy to show that when L tends to 0, $G(x)$ tends to the Dirac delta function and we have the well known equation with the cubic nonlinearity. The classical soliton is the solution of this equation $v(y)=ch^{-1}(py)$ with $p=\sqrt{1/2}$. When $L\to\infty$, the problem becomes linear and not interesting for us.

Now, we can see that the wave amplitude V is described by the ordinary differential equation, because it depends on the longitudinal variable ξ just as on parameter. It is obviously that we have get the mathematical eigen value problem for the nonlinear integro-differential equation.

3. Numerical method

We can not hope to solve this problem by analytical methods. Therefore we constructed the computational approach which is based on the iterative algorithm. Any concentrated solution, for example soliton $\tilde{v}(y)=ch^{-1}(y)$, is used as the first approximation. Then, we determine the perturbation of the dielectric permittivity, that is we calculate the convolution

$$\tilde{v}(y)*G(y)=\int_{-\infty}^{\infty}\tilde{v}(t)G(y-t)dt$$

This procedure uses the fast Fouruer transformation. After that, we solve the linear problem for the eigen value p and the eigen function v for the second order differential operator with conditions: $v\to 0$ when $y\to\pm\infty$. This problem is solved by means of the iterations of p from interval (0,1) using the standard Runge-Kutta method. The solution v of this problem is used now as the second approximation. This procedure is continued until $\|v-\tilde{v}\|\geq\delta$, δ is the advance determined precession of the calculations. We used $\delta\approx 10^{-4}\div 10^{-5}$. This method is very quickly converge and it does not depends on the form of initial approximation.

4. Conclusions

The computational solution allow us to assert that the concentrated solution exist for any value of the diffusion scale. The concentrated solution have not any singularities for any value of $L\neq\infty$ and it looks like the soliton but more wide. The dependence of the wave amplitude v from

the cross variable y is represented in the Fig.1 (solid line) for the value $L=10$. The classical soliton $(L=0)$ is represented here by dotted line. Naturally, the diffusion process enlarges the soliton.

The dependence of eigen value p versus diffusion scale is represented in the Fig.2. We can see that the solution width which is determined by the value of p, is very slowly grow with growth of parameter L.

Acknowledgment

This investigation was supported by Russian Foundation of Base Research (96-05-65367)

References

1. G.S.Bochkarev, V.A.Eremenko, L.A.Lobachevsky at al. Nonlinear Interaction of Decameter Radio Waves at close Frequencies on oblique propagation. Journal of Atmos. and Terr.Phys. 1982, v.44, N 12.
2. S.Gotz and J.Herrmann. Soliton propagation in materials with sutarable nonlinearity. J.Opt.Soc. Am. B, 1991, v.8, N 11.
3. I.A.Molotkov and Yu.N.Cherkashin. Some Nonlinear Effects Wave Beams Propagation in the Ionosphere. Journal of Atmos. and Terr.Phys. 1994, v.56, N 11.
4. V.A.Eremenko and Yu.N.Cherkashin. Computational Modeling of Wave Plasma Interaction. 12th Annual Review of Progress in Applied Computational Electromagnetics. 1996, Conference proceedings.

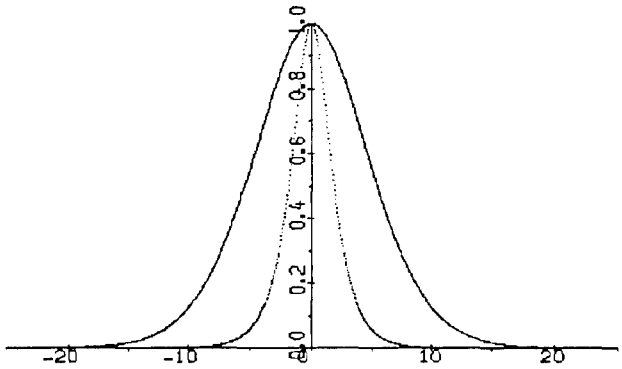

Fig.1. The dependence of wave amplitude versus across coordinate.

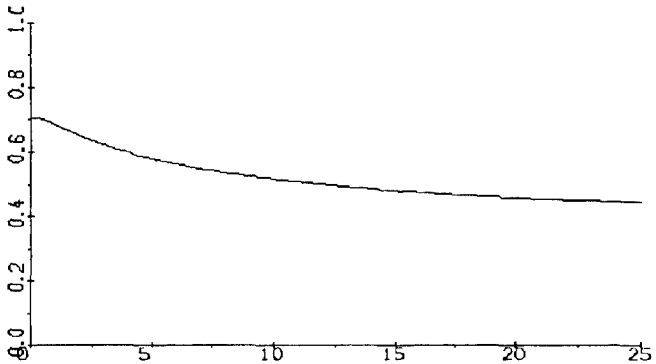

Fig.2. The dependence of eigen value versus diffusion scale.

Hysteresis and Eddy Currents in Ferromagnetic Media

János Füzi,
Electrical Engineering Dpt, "Transilvania" University, Brasov, Romania

Amalia Iványi,
Dpt. of Electromagnetic Theory, Technical University of Budapest, Hungary

Introduction

The paper deals with the computation of time-varying electromagnetic field in ferromagnetic and conductive media. A model is proposed, based on the static hysteresis characteristic of the given ferrous material described by the classical Preisach model [1] on one hand and the numerical computation of the electromagnetic field diffusion in the given geometry on the other. The classical Preisach model provides the relationship between magnetic field strength and magnetization or flux density at local level (a Preisach model is running in every spatial grid point). It is included in the governing equation system of the electromagnetic field, enabling eddy current simulation [2, 3] taking hysteresis into account. The static nature of the classical Preisach model is relaxed as dynamic effects appear during integration in time domain of the field governing equations. Integrating the flux density over the domain of interest, the total magnetic flux is obtained at every time step. Plotting it with respect to the source field strength at the border of the domain provides the dynamic characteristic of the given material in the given geometry. The method is implemented for toroidal and cylindrical geometry and its efficiency illustrated by the results of numerical examples, illustrating the frequency- and saturation-dependent skin-effect. The dependence of material characteristics (magnetic permeability and electric conductivity) on temperature is taken into account and a method for temperature-dependent electromagnetic field computation is proposed to reduce required memory and computing time.

Equations

For configurations in which the magnetic field strength **H** does not change its spatial orientation in time, the magnetization vector **M** can be assumed to be parallel to the field strength in isotropic media and its size can be determined by means of the classical Preisach model taking actual and past local values of field intensity into account. The toroidal geometry shown in Fig. 1 is considered. Due to cylindrical symmetry, the natural 3D problem becomes a 2D one, the co-ordinates to be considered being those of the cross-section of the core. The major hysteresis loop of the material is plotted on Fig. 2.

The field strength and eddy current density vectors have the following orientations:

$$\begin{aligned} \mathbf{H} &= \mathbf{u}_{\varphi} H(r, z, t) \\ \mathbf{J} &= -\mathbf{u}_r J_r(r, z, t) + \mathbf{k} J_z(r, z, t) \end{aligned} \tag{1}$$

and the divergence of field strength is zero due to geometry even in non-linear media:

$$\nabla \cdot \mathbf{H} = \frac{1}{r} \frac{\partial H(r, z, t)}{\partial \varphi} = 0. \tag{2}$$

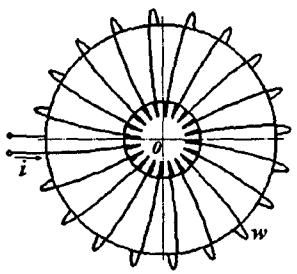

Figure 1. Geometrical configuration

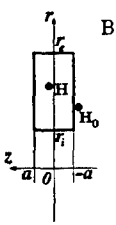

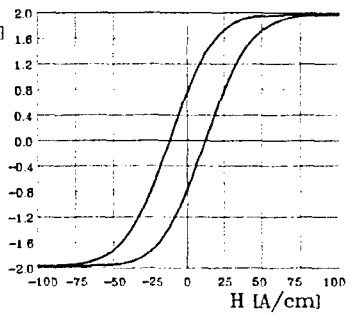

Figure 2. The major hysteresis loop

The source field, created on the surface of the core by the sinusoidal current i of a source coil:

$$H_0(r,t) = \frac{wi(t)}{2\pi r} \; ; \quad r \in [r_i, r_e]$$
$$H_0(r,t) = H_{0m}\frac{r_e + r_i}{2r}\sin(2\pi f t) \; ; \quad H_{0m} = \frac{wI\sqrt{2}}{\pi(r_e + r_i)} \; , \tag{3}$$

where H_{0m} stands for the magnitude of the source field along the mean radius of the core. Maxwell's equations with (1) and (2) lead to the differential equation of the magnetic field strength written in cylindrical co-ordinates:

$$\frac{\partial H}{\partial t} = \frac{\dfrac{\partial^2 H}{\partial r^2} + \dfrac{1}{r}\dfrac{\partial H}{\partial r} - \dfrac{H}{r^2} + \dfrac{\partial^2 H}{\partial z^2}}{\sigma\mu_0\left(1 + \dfrac{dM}{dH}\right)} \; , \quad r \in [r_i, r_e] \quad , \quad z \in [0,a] \quad , \quad t \geq 0 \; , \tag{4}$$

with the non-linear term dM/dH in the denominator (the slope of the transition curve of the magnetic characteristic corresponding to local history) computed by means of the classical Preisach model. The boundary conditions are:

$$\left.\begin{aligned} H(r,a,t) &= H_0(r,t) \\ \frac{\partial H}{\partial z}(r,0,t) &= 0 \end{aligned}\right\} \quad r \in [r_i, r_e]$$
$$\left.\begin{aligned} H(r_i,z,t) &= H_0(r_i,t) \\ H(r_e,z,t) &= H_0(r_e,t) \end{aligned}\right\} \quad z \in [0,a] \qquad ; \quad t \geq 0. \tag{5}$$

The solution in time domain of the equation system resulted from the formulation of (4) by finite difference is obtained by means of an alternating direction and fractional time-step method. The components of the induced eddy current density are computed like:

$$J_r = -\frac{\partial H}{\partial z} \quad ; \quad J_z = \frac{\partial H}{\partial r} + \frac{H}{r} \; . \tag{9}$$

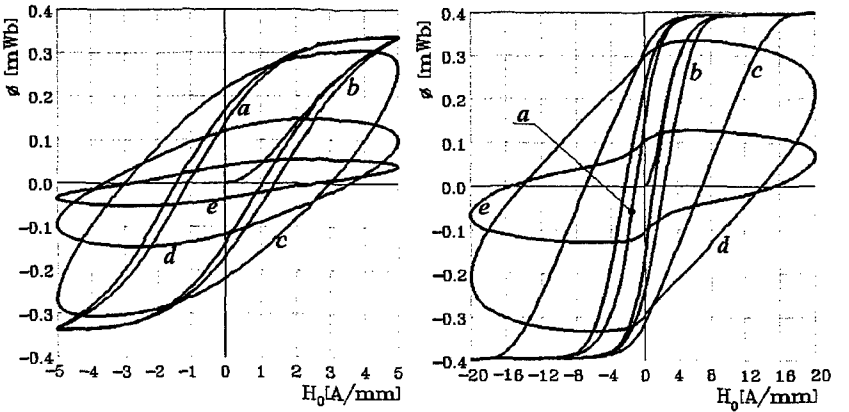

Figure 3. Steady-state magnetizing loops

Numerical results

Computations have been carried out for a core with interior radius $r_i = 10$ mm, exterior radius $r_e = 30$ mm and thickness $2a = 10$ mm (massive or made of 10 insulated sheets, 1 mm thick each) for source-field magnitudes $H_{0m} = 5000$ A/m and $H_{0m} = 20000$ A/m at frequencies:

a) $f \to 0$
b) $f = 50$ Hz, core of 10 sheets, 1 mm thick each
c) $f = 500$ Hz, core of 10 sheets, 1 mm thick each
d) $f = 50$ Hz, massive core
e) $f = 500$ Hz, massive core

The electrical conductivity of the material has been assumed to be $\sigma = 5 \cdot 10^6$ S/m. The dynamic loops from Fig. 3 have been plotted by integration of the resulting flux density over the torus cross-section. They illustrate the effects of frequency, saturation and geometry (thickness) on the dynamic behaviour of a given core. For two of the considered cases the distribution of the rms. values of magnetic field strength, flux density, radial and axial components of the induced eddy current density (also in steady-state operation) are plotted in Figs. 4 and 5.

The results illustrate the advantage of the proposed method, namely that it allows determination of field quantity distributions inside the ferromagnetic material, enabling for example thermal computation (by yielding the distribution of heat sources).

Accurate results can be expected for materials that can be considered homogeneous (thick medium-carbon steel parts with tiny domains) and at frequencies (variation rates of field quantities) where most of the dynamic effects are due to eddy currents. In the case of electrical steel sheets, especially grain-oriented ones, the effects of domain-wall dynamics are too important to be ignored. A hysteresis model that takes them into account is required to allow simulation with improved accuracy.

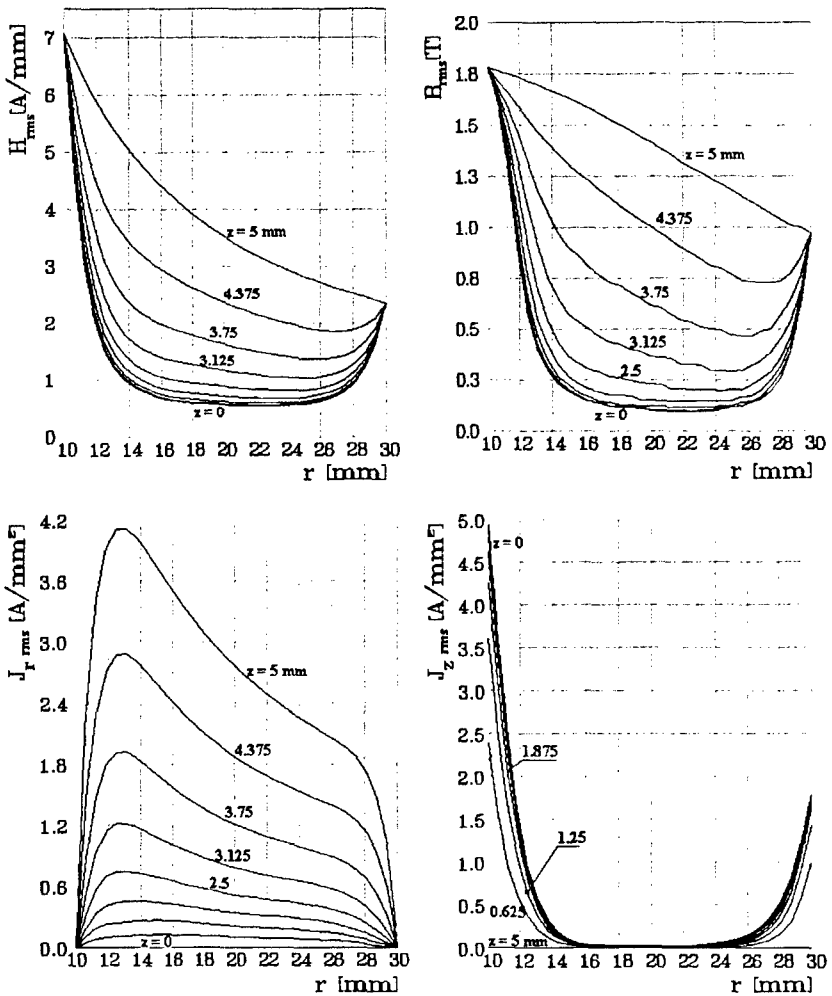

Fig. 4. Distribution of rms. values of electromagnetic field quantities obtained for: H_{0m} = 5000 A/m, f = 50 Hz, massive core

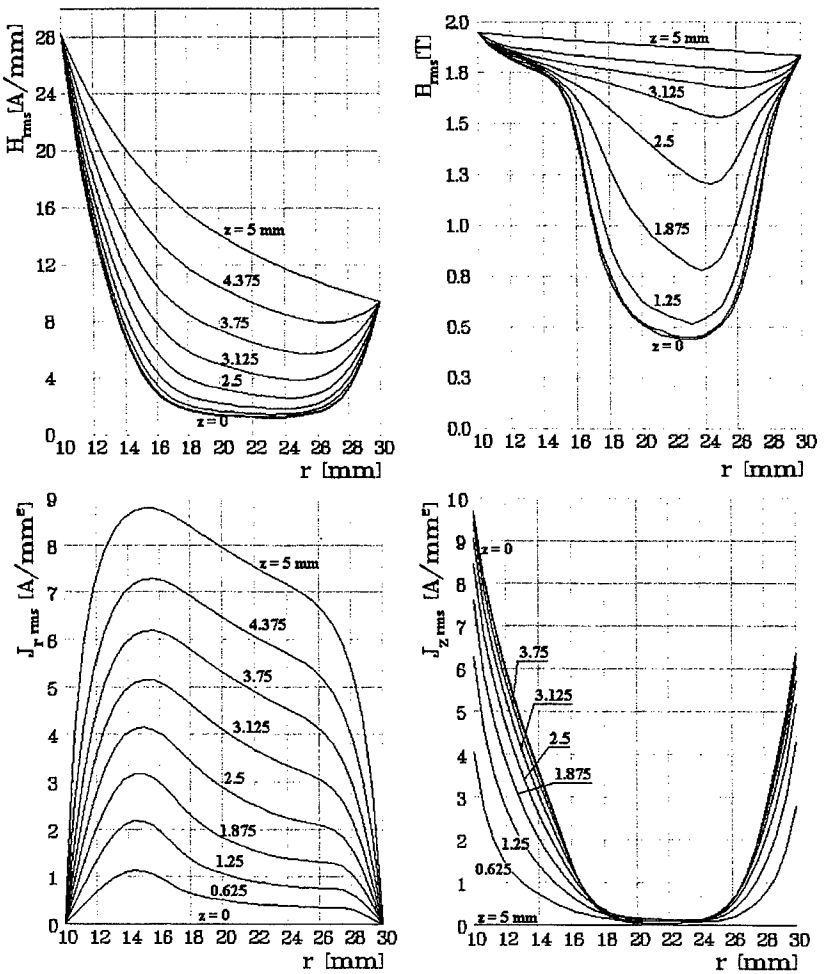

Fig. 5. Distribution of rms. values of electromagnetic field quantities obtained for: $H_{0m} = 20000$ A/m, $f = 50$ Hz, massive core

It can be observed how saturation leads to increase of penetration depth - the oversaturated outward layer becomes transparent (up to some extent) for the electromagnetic wave.

The effect of temperature

The variation of electric conductivity of medium carbon steel with respect to temperature can be analytically approximated by the function:

$$\sigma(\theta) = \frac{s_1}{\theta + s_2} + s_3\theta + s_4 \ . \tag{10}$$

with $s_1 = 2.38 \cdot 10^9$ S·K/m; $s_2 = 300$ K; $s_3 = 850$ S/m·K; $s_4 = -1.8 \cdot 10^6$ S/m. In Fig. 6 the circles stand for measured values and the line is plotted using equation (1).

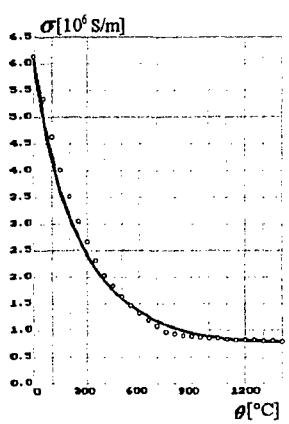

Figure 6. Electric conductivity of medium carbon steel with respect to temperature

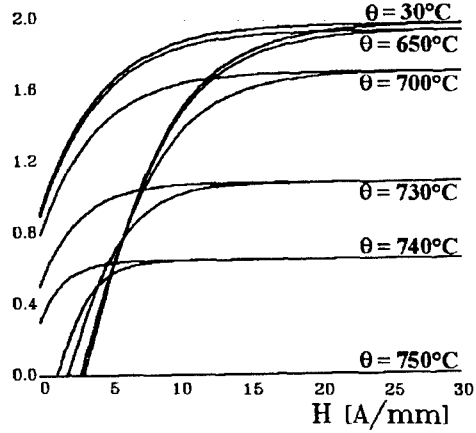

Figure 7. Major loops at several temperatures

The static magnetic characteristic is obtained using the distribution function [1]:

$$\mu(\alpha\ \beta) = e^{-\frac{(\alpha-\beta-c)^2}{a} - \frac{(\alpha+\beta)^2}{b}}, \qquad \alpha \in [-1,1]; \quad \beta \in [-1,1] \tag{11}$$

which for parameter values $a = 0.0224$, $b = 0.3162$ and $c = 0.232$ (obtained by means of a parameter identifying procedure [5]) yields the major hysteresis loop plotted in Fig. 7 for 30°C. The Preisach model for other values of temperature can be constructed by choosing parameters a, b, and c to fit the major hysteresis loops corresponding to the respective temperatures [4]. However, this way would result in a complex model, difficult to implement, needing very much computer memory. Massive economy of memory and increase of computing speed can be achieved using the same Everett-array for every temperature and appropriate scales for field strength and magnetization to approximate the major loops at the respective temperatures. While for room temperature the model is fitted for coercive intensity and remnant magnetization too, for higher temperatures these values are respected with a certain error. This is the price for the memory economy and computing speed enhancement mentioned above.

Field equations

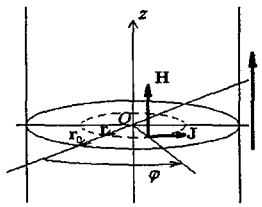

Figure 8. Geometrical configuration

For a cylindrical geometry (Fig. 8), with

$$\mathbf{H} = \mathbf{k}\,H(r,t) \quad ; \quad \mathbf{J} = \mathbf{u}_\varphi\,J(r,t)\,, \tag{13}$$

Maxwell's equations lead to:

$$\frac{\partial H}{\partial t} = \frac{1}{\sigma\mu_0\left(1+\dfrac{\partial M}{\partial H}\right)}\left[\frac{\partial^2 H}{\partial r^2} + \left(\frac{1}{r} - \frac{1}{\sigma}\frac{\partial\sigma}{\partial\theta}\frac{\partial\theta}{\partial r}\right)\frac{\partial H}{\partial r}\right], \tag{14}$$

$r \in [0, r_0]\,, t \geq 0$

with boundary conditions: $\dfrac{\partial H}{\partial r}(0,t) = 0$; $H(r_0,t) = H_{0m}\sin 2\pi f t$; $t \geq 0$. (15)

Results

A problem has been solved for: cylinder radius: $r_0 = 0.02$ m, source field magnitude: $H_{0m} = 50000$ A/m, source field frequencies: $f = 50$ Hz and $f = 2500$ Hz. The following temperature distributions have been considered: room temperature (**a**), given temperature distributions resulted during an inductive heating simulation in two different moments (**b** and **c** - Fig. 9).

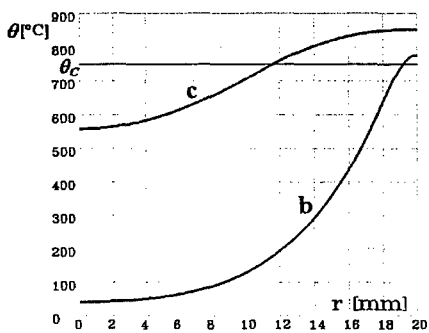

Figure 9. Temperature distributions

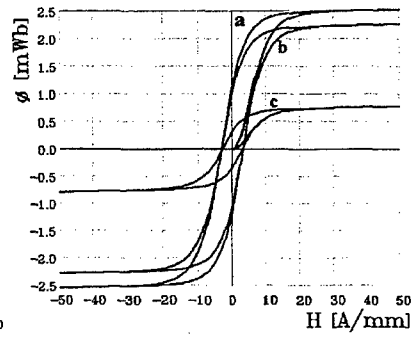

Figure 10. Static magnetic characteristics

Concerning the obtained results, the fact that on Fig. 11 the area of the hysteresis loops obtained for the temperature distribution **b** is greater than the ones obtained at room temperature (one would expect the opposite while an external layer is no longer ferromagnetic in case **b**) is due to the decrease of the electrical conductivity with the increase of temperature causing increase of the field penetration depth. Due to the reflection of the electromagnetic wave on the separation surface between the ferromagnetic core and the overheated (over Curie-temperature) external layer, the maximum value of the induced eddy current density rms. (Fig. 12) is not at the surface of the cylinder but in the vicinity of the mentioned separation surface (if it exists).

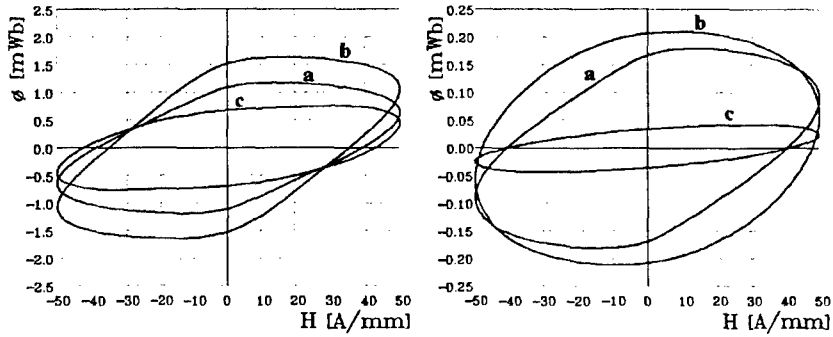

$f = 50$ Hz $f = 2500$ Hz.

Figure 11. Steady state magnetising loops for different temperature distributions

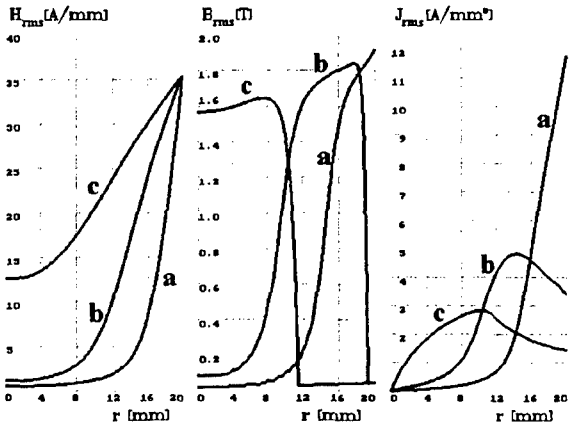

Figure 12. Distribution of field quantity rms. values at 50 Hz.

Conclusions

Different dynamic regimes of ferromagnetic cores can be simulated based on the static magnetic characteristic of the material, experimentally determinable at very low frequency (allowing the construction of accurate static hysteresis models, not affected by geometry and source-field frequency) and on the numerical computation of the time varying electromagnetic field.

References

[1] I.D. Mayergoyz, Mathematical Models of Hysteresis. Springer-Verlag, New-York, 1991.

[2] J. Füzi, Eddy Currents in Ferromagnetic Sheets Taking Magnetic Hysteresis Nonlinearities into Account, Periodica Polytechnica Budapest, Ser. El. Eng. 39 (2) (1995) 131-143.

[3] J.Füzi, A.Iványi: Eddy Currents in Ferromagnetic Cylinders Taking Hysteresis into Account, International Journal of Theoretical Electrotechnics 6 (1996) 54-61.

[4] J.Füzi, A.Iványi: Temperature Dependent Dynamic Hysteresis in Ferromagnetic Cylinders, Studies in Applied Electromagnetics and Mechanics, 11 (1997) 275-282.

[5] J.Füzi: Parameter Identification in Preisach Model to Fit Major Loop Data, Studies in Applied Electromagnetics and Mechanics, 11 (1997) 77-82.

Electrical Circuit Analysis Considering Hysteresis in Coil Cores

János Füzi,
Electrical Engineering Dpt, "Transilvania" University, Brasov, Romania

Introduction

Computer-aided engineering is a very useful tool in optimal design as it allows simulation of operation and tests prior to manufacturing the prototype. The accurate simulation of non-linear electromagnetic systems requires appropriate, comprehensive models, taking into account as many aspects of their behaviour as possible, along a reasonable effort in memory size and computer time. An important class of problems involves hysteretic processes, impelling the use of specific tools, named hysteresis models. The Preisach-model [1] is a numerical model of hysteresis, with its classical version relatively easy to implement and, completed with adequate field computing methods or circuit analysis algorithms, it is applicable in various problems involving ferromagnetic media. In this paper the Preisach model is used for the relationship between magnetic field strength at the surface of the core sheets and total magnetic flux through the cross section of the core, yielding the relationship between the current in the coil and the induced voltage. It is implemented in the circuit analysis program together with circuit equations to simulate circuit operation.

Circuit layout

The circuit plotted in Fig. 1 is considered, a transformer supplied from a sinusoidal voltage source with one-way rectifier load. The material of the core sheets is modelled by means of the classical Preisach model, operating on the Everett-surface plotted in Fig. 2.

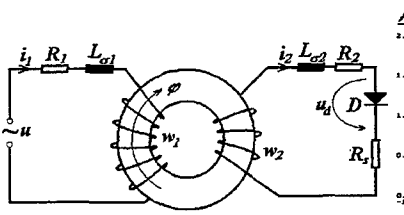

Figure 1. Circuit layout

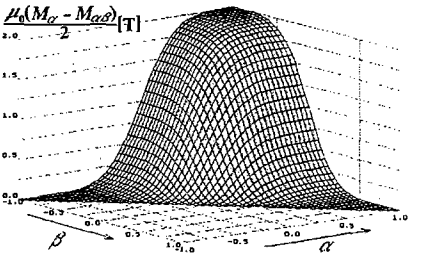

Figure 2. Everett integral surface

The numerical implementation of the classical Preisach model involves the discretization of a triangle (support of the Everett integral function) implying that exact values of output can be computed for multiples of input steps. The model is provided with an interpolation scheme based on the evolution of four models on exact input steps along transition curves starting at reversal points situated at exact step values and linear interpolation between their outputs [2].

Circuit equations

conducting diode:

$$\begin{cases} \dfrac{di_1}{dt} = \dfrac{1}{L_{\sigma 1}}\left(u(t) - R_1 i_1 - w_1 \dfrac{d\varphi}{dt}\right) \\ \dfrac{di_2}{dt} = \dfrac{1}{L_{\sigma 2}}\left(-(R_2 + R_S) i_2 - w_2 \dfrac{d\varphi}{dt}\right) \quad ; \quad i_2 > 0 \\ u_d = 0 \end{cases} \tag{1}$$

blocked diode:

$$\begin{cases} \dfrac{di_1}{dt} = \dfrac{1}{L_{\sigma 1}}\left(u(t) - R_1 i_1 - w_1 \dfrac{d\varphi}{dt}\right) \\ i_2 = 0 \quad ; \quad u_d < 0 \\ u_d = -w_2 \dfrac{d\varphi}{dt} \end{cases} \tag{2}$$

The source-field at the surface of the core sheets:

$$H_0(t) = \frac{w_1 i_1(t) + w_2 i_2(t)}{l} \tag{3}$$

To avoid the connection between the two differential equations in system (1) through the term $d\varphi/dt$, the following form can be applied:

$$\frac{d\varphi}{dt} = \frac{d\varphi}{dH_0}\frac{dH_0}{dt}, \text{ hence: } \quad \frac{d\varphi}{dt} = \lambda\left(w_1 \frac{di_1}{dt} + w_2 \frac{di_2}{dt}\right), \tag{4}$$

where:

$$\lambda = \frac{\mu_0 S}{l}\left(1 + \frac{dM}{dH}\right) \tag{5}$$

contains the non-linear term dM/dH, evaluated within each current computation step by means of the Preisach model. The current derivatives can be written explicitly:

conducting diode

$$\begin{cases} \dfrac{di_1}{dt} = \dfrac{\left(L_{\sigma 2} + w_2^2 \lambda\right)\left(u(t) - R_1 i_1\right) + w_1 w_2 \lambda\left(R_2 + R_S\right) i_2}{L_{\sigma 1} L_{\sigma 2} + \left(w_1^2 L_{\sigma 2} + w_2^2 L_{\sigma 1}\right)\lambda} \\ \dfrac{di_2}{dt} = -\dfrac{w_1 w_2 \lambda\left(u(t) - R_1 i_1\right) + \left(L_{\sigma 1} + w_1^2 \lambda\right)\left(R_2 + R_S\right) i_2}{L_{\sigma 1} L_{\sigma 2} + \left(w_1^2 L_{\sigma 2} + w_2^2 L_{\sigma 1}\right)\lambda} \quad ; \quad i_2 > 0 . \\ u_d = 0 \end{cases} \tag{6}$$

blocked diode:

$$\begin{cases} \dfrac{di_1}{dt} = \dfrac{u(t) - R_1 i_1}{L_{\sigma 1} + w_1^2 \lambda} \\ i_2 = 0 \quad ; \quad u_d < 0 . \\ u_d = -w_1 w_2 \lambda \dfrac{di_1}{dt} \end{cases} \tag{7}$$

If the leakage inductivities are zero, the circuit equations become:

conducting diode

$$\begin{cases} \dfrac{di_1}{dt} = \dfrac{\left(R_2 + R_S\right)\left(u(t) - R_1 i_1\right) + \lambda w_2^2 \dfrac{du}{dt}}{\left(w_1^2\left(R_2 + R_S\right) + w_2^2 R_1\right)\lambda} \\ i_2 = -\dfrac{w_2}{w_1}\dfrac{u(t) - R_1 i_1}{\left(R_2 + R_S\right)} \qquad ; \quad i_2 > 0 \\ u_d = 0 \end{cases} \tag{8}$$

blocked diode:

$$\begin{cases} \dfrac{di_1}{dt} = \dfrac{u(t) - R_1 i_1}{\lambda w_1^2} \\ i_2 = 0 \qquad ; \quad u_d < 0 \\ u_d = -\dfrac{w_2}{w_1}\left(u(t) - R_1 i_1\right) \end{cases} \tag{9}$$

Results

The following circuit parameters have been considered:

- windings: numbers: $w_1 = 360$, $w_2 = 90$; resistances: $R_1 = 1.8\ \Omega$, $R_2 = 0.2\ \Omega$; leakage inductivities (computation performed both with and without considering them): $L\sigma_1 = 10$ mH, $L\sigma_1 = 0.63$ mH.
- core: cross-section: $S = 1280$ mm^2; medium length: $l = 400$ mm.

The simulation has been performed starting with the moment of connection to the supply, in the following regimes:

with leakage inductivities

Case	f [Hz]	U_0 [V]	R_S [Ω]
A	50	80	0
B	50	170	5
C	200	350	0
D	200	350	5

without leakage inductivities

Case	f [Hz]	U_0 [V]	R_S [Ω]
E	50	80	0
F	50	154	5
G	200	80	0
H	200	350	5

The core magnetizing characteristics and the wave-forms of the currents and the flux through the core are plotted in Figs. 3 - 5.

At low frequency values the errors induced by ignoring dynamic effects are not very high. However, the accuracy of the model can be increased by use of the dynamic Preisach model instead of the classical one, which is static by nature, or by taking into account the effects of the global eddy currents induced in the core [3,4] and the so called anomalous effects caused by Bloch-wall dynamics. Eddy current simulation can be coupled with circuit analysis by considering $\lambda = \dfrac{1}{l}\dfrac{d\varphi}{dH_0}$ instead of (5), where the flux φ is obtained by integration over the core cross-section of the flux density resulting from the electromagnetic field computation in core sheets. However the price of the enhanced accuracy is the larger memory size and computing time required.

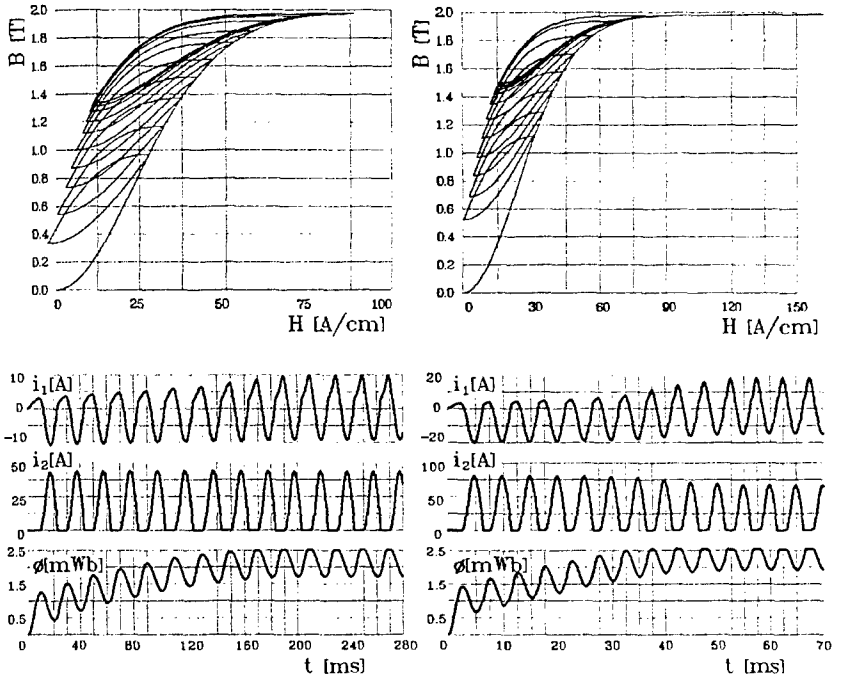

Figure 3. Track of core operation point and wave-forms of transformer in short-circuit ($R_S = 0$)

Conclusions

The operation of circuits involving ferromagnetic cores, such as transformers in power converter schemes, can be simulated with reasonable accuracy and high efficiency (relatively low memory requirement and high computing speed) by implementing a classical Preisach model in the circuit equation solving code.

The effects of saturation and hysteresis on the circuit operation can be well grasped as shown by the results of the considered numerical examples.

An interpolation procedure is required for output continuity of the Preisach model, so that artificial output jumps would not affect the stability of the circuit analysis algorithm.

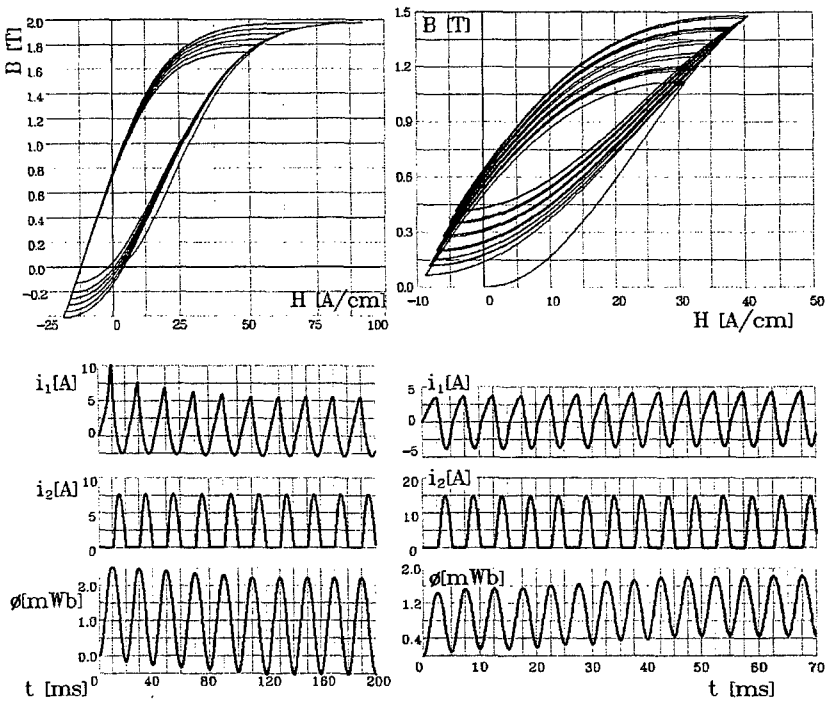

Case B Case D

Figure 4. Track of core operation point and wave-forms of loaded transformer

References

[1] I.D.Mayergoyz, *Mathematical Models of Hysteresis*, Springer-Verlag, New York, 1991.

[2] J.Füzi, A.Iványi, Zs.Szabó: Preisach Model with Continuous Output in Electrical Circuit Analysis. Journal of Electrical Engineering, Bratislava, Slovakia - 1997, vol.48, no.8/s (4th Japanese-Czech-Slovak Joint Seminar on Applied Electromagnetics), pp.18-21.

[3] E.Napieralska-Juszczak, R.Grzybowski, J.F.Brudny: Modelling of Losses Due to Eddy Currents and Histeresis in Converter Transformer During Failure. IEEE Magn. Vol.31, No.3, 1995, pp.1718-1721.

[4] J.Füzi: Dynamic Operation of Coils with Ferromagnetic Cores Taking Magnetic Hysteresis into Account. Applied Computational Electromagnetics Society Journal, Monterey USA-1997, vol.12, no.2, pp.96-101.

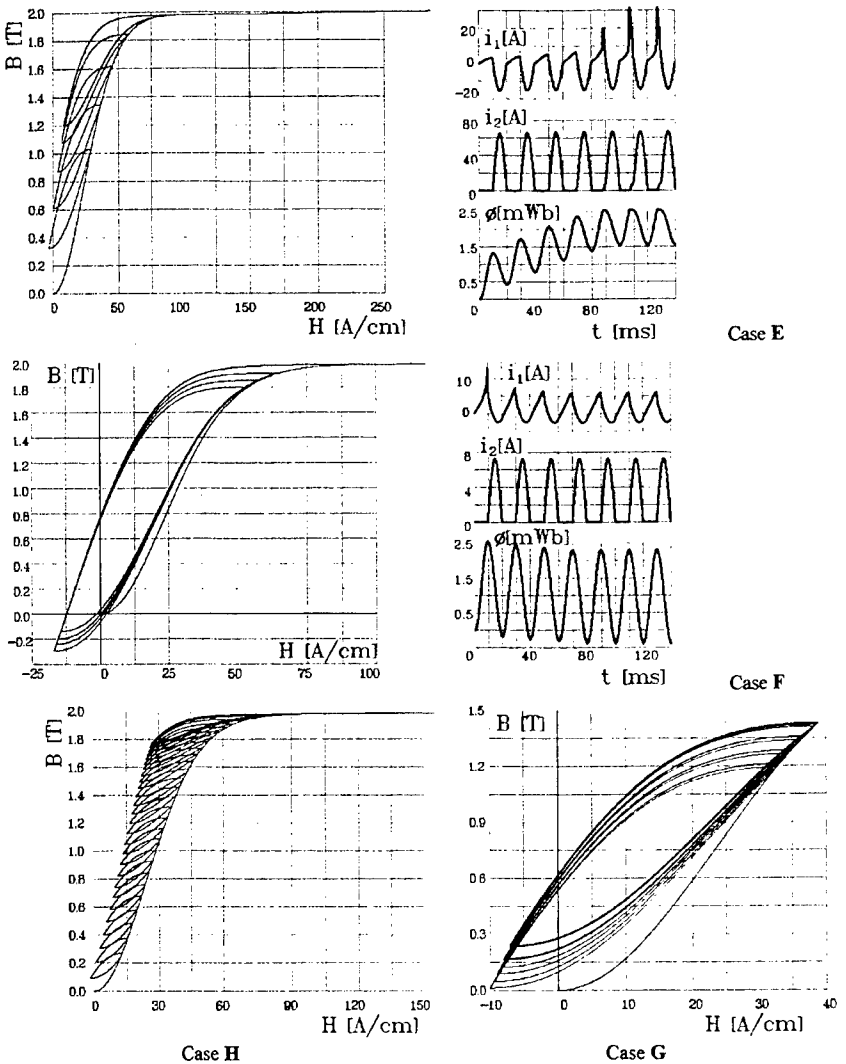

Figure 5. Track of core operation point and wave-forms of transformer without leakage inductivities

A Paradigm for Proving the Convexity Properties of Slowness Curves

Ali R. Baghai-Wadji[1]

Vienna University of Technology,
IAEE, 3592, Gußhausstraße 27-29, A-1040 Vienna, Austria, and,
Arizona State University,
Department of Mathematics, Tempe, AZ 85287, USA

Abstract: It is shown that the slowness curves for the fastest bulk acoustic waves in general anisotropic elastic media are strictly convex. The convexity is proven by showing that the number of intersection points of any arbitrary straight line in the slowness plane with slowness curves in question is either two or zero.

I Introduction

For modeling wave phenomena in various engineering and natural science applications it is often required to investigate the shape of slowness curves associated with transversal and longitudinal bulk acoustic waves [1]. Our recent numerical experiments have revealed that the *local-convexity* of "transversal" slowness curves may be positive or negative (see also [1]). However, we could not identify any concave region on "longitudinal" slowness curves. This work proves a generalization of this phenomenon.

Convention: In the wavenumber plane, we will interchangeably use polar- (k, θ) and cartesian- $(k_1 = k\cos\theta, k_2 = k\sin\theta)$ coordinate systems. Correspondingly, in the slowness (inverse velocity) plane, we will employ the coordinate systems (s, θ) and $(s_1 = s\cos\theta, s_2 = s\sin\theta)$. Thereby $s = k/\omega$, $s_1 = k_1/\omega$, and $s_2 = k_2/\omega$ with ω being the angular frequency.

Definition: In the slowness plane, let $s(\theta)$ be a closed curve, and L : $s_2 = as_1 + b$ $(a, b \in R)$ an arbitrary straight line. If the number of intersection points of L with $s(\theta)$ is either two or zero, $s(\theta)$ is called to be strictly convex (Fig. 1).

II Preparatory Considerations

For isotropic elastica the slowness curves degenerate into two concentric circles, and thus our claim is obvious. For general anisotropic elastica we may

[1]The author is presently on leave of absence with Motorola Inc., 8201 E. McDowell Rd., M.D. H1556, Scottsdale, AZ 85252. **phone:** (602) 441 2471, **fax:** (602) 441 7714, **email address:** abaghai@rs1.iaee.tuwien.ac.at

categorize the slowness curves $s_i(\theta)$ $(i = 1, 2, 3)$ as follows. (1) Slowness curves do not intersect. This is the usual case (Fig. 1). (2) Two outer slowness curves intersect. This is the case for strongly anisotropic materials. (3) Two inner slowness curves intersect, e.g. tellurium dioxide [1]. (Fig. 2). (4) Three slowness curves intersect. This hypothetical generalization is, however, consistent with physical realizability conditions. It is instructive to unify these categories by constructing $s_f(\theta)$, $s_s(\theta)$ and $s_i(\theta)$ $(-\pi \leq \theta < \pi)$ according to the rules in (1), (Figs. 1 and 2).

$$s_f(\theta) = \min\{s_1(\theta), s_2(\theta), s_3(\theta)\} \tag{1a}$$
$$s_s(\theta) = \max\{s_1(\theta), s_2(\theta), s_3(\theta)\} \tag{1b}$$
$$s_f(\theta) < s_i(\theta) < s_s(\theta). \tag{1c}$$

$s_f(\theta)$ and $s_s(\theta)$, respectively, correspond to the fastest and slowest bulk acoustic wave, and $s_i(\theta)$ refers to a bulk wave with an intermediate slowness. Note that $s_1(\theta)$, $s_2(\theta)$ and $s_3(\theta)$ are differentiable everywhere. However, $s_f(\theta)$, $s_i(\theta)$ and $s_s(\theta)$ do not possess this property at possible intersection points (the points a, b, c and d in Fig. 2).

Our motivation for introducing $s_f(\theta)$, $s_i(\theta)$ and $s_s(\theta)$, rather than working with slowness curves associated with (quasi-)longitudinal, (quasi-)transversal-vertical, and (quasi-)transversal-horizontal waves, has been to avoid possible ambiguities: For many materials the type of polarization alters, as we traverse the slowness curves $s_i(\theta)$ $(i = 1, 2, 3)$. However, the wave associated with, say, $s_s(\theta)$ is, irrespective its polarization, the slowest bulk wave, for any value of θ.

III On the Convexity of Slowness Curves

Convexity Theorem: Consider an anisotropic elastic medium characterized by the scalar mass density ρ, and the positive-definite elastic moduli matrix $\mathbf{C}$. Denote the associated slowness curves by $s_i(\theta)$, $(i = 1, 2, 3)$. Construct $s_f(\theta)$, $s_i(\theta)$ and $s_s(\theta)$. Assume an arbitrary straight line $L : s_2 = as_1 + b$ in the slowness plane. Denote the numbers of intersection points of L with $s_f(\theta)$, $s_i(\theta)$ and $s_s(\theta)$, respectively, by n_f, n_i and n_s. Then,

T1: $n_f + n_i + n_s \in [0, 2, 4, 6]$

T2: $s_f(\theta)$ is strictly convex $(n_f \in [0, 2])$

T3: $s_i(\theta)$ may possess concave regions with $n_i \in [0, 2, 4]$

T4: $s_s(\theta)$ may possess concave regions with $n_s \in [0, 2, 4, 6]$.

The Strategy for Proving the Convexity Theorem: Our reasoning shall be described in three steps. First we establish equations for the calculation of slowness curves, and deduce important properties. Then we rotate

the original (s_1, s_2) coordinates such that the $\bar{s}_1-$axis of the new $(\bar{s}_1, \bar{s}_2)$ system stands perpendicular to the line L (Fig. 1), and derive equations for the slowness curves in the $(\bar{s}_1, \bar{s}_2)$ coordinate system. Finally we pose and answer the following question. What is the maximum number of homogeneous plane waves whose slowness (propagation) vectors $\bar{\mathbf{s}}^{(1)} = (\bar{s}_1, \bar{s}_2^{(1)})$, $\bar{\mathbf{s}}^{(2)} = (\bar{s}_1, \bar{s}_2^{(2)})$, $\cdots$, $\bar{\mathbf{s}}^{(m)} = (\bar{s}_1, \bar{s}_2^{(m)})$ possess the common projection $\bar{s}_1$ on the $\bar{s}_1$-axis (Fig. 1)? Obviously, this question is equivalent to the following problem: What is the maximum number of intersection points of an $\bar{s}_1 = \text{const}$ line with the slowness curves? It turns out that this number is six.

1. Step: Construction of Slowness Curves: Consider governing equation (2a) and constitutive relation (2b) [1].

$$\underline{\underline{\nabla}}^T \tau = \rho \frac{\partial^2 \mathbf{u}}{\partial t^2} \tag{2a}$$

$$\tau = \mathbf{C}\, \underline{\underline{\nabla}} \mathbf{u} \tag{2b}$$

(The superscript T denotes transposition.) The components of the 6×1 vector τ are the stresses T_{11}, T_{22}, T_{33}, T_{23}, T_{13} and T_{12}. T_{ij} denotes the stress component in x_i-direction acting on a plane specified by the normal vector $\mathbf{n}_j$. Assume that there is no variation in x_3-direction $(\partial/\partial x_3 \equiv 0)$. Then the divergence operator $\underline{\underline{\nabla}}$ may be written in the form $\underline{\underline{\nabla}} = \mathbf{N}_1 \partial_{x_1} + \mathbf{N}_2 \partial_{x_2}$, with $\mathbf{N}_1 = [\mathbf{h}_1 \mathbf{h}_6 \mathbf{h}_5]$ and $\mathbf{N}_2 = [\mathbf{h}_6 \mathbf{h}_2 \mathbf{h}_4]$. $\mathbf{h}_i$ denotes a 6×1 unit vector whose ith component is unity [2-3]. Substituting (2b) into (2a) and invoking the proposed form for $\underline{\underline{\nabla}}$ we obtain the differential form in (3), which is diagonalized with respect to time.

$$\left[\mathbf{M}_{11} \partial_{x_1 x_1} + (\mathbf{M}_{12} + \mathbf{M}_{21}) \partial_{x_1 x_2} + \mathbf{M}_{22} \partial_{x_2 x_2}\right] \mathbf{u} = s_{\text{ref}}^2 \partial_{tt} \mathbf{u} \tag{3}$$

s_{ref} is a convenient reference slowness (here: $s_{\text{ref}}^2 = \rho / C_0$ with $C_0 = 10^{10} N/m^2$). The 3×3 matrices $\mathbf{M}_{ij}$ $(i, j = 1, 2)$ stand for $\mathbf{N}_i^T (\mathbf{C}/C_0) \mathbf{N}_j$. Let a homogeneous plane wave propagate in the $x_1 x_2-$plane. Let the mechanical displacement vector $\mathbf{u}$, associated with this wave, have the form $\mathbf{u} = \mathbf{a} \exp(j k_1 x_1) \exp(j k_2 x_2) \exp(-j \omega t)$ with arbitrarily-oriented polarization vector $\mathbf{a}$. Substituting this trial function into (3) we obtain the algebraic eigenvalue equation

$$\left[\mathbf{M}_{11} \cos^2\theta + (\mathbf{M}_{12} + \mathbf{M}_{21}) \sin\theta \cos\theta + \mathbf{M}_{22} \sin^2\theta\right] \mathbf{a} = (s_{\text{ref}}/s)^2 \mathbf{a} \tag{4}$$

for the slowness and the corresponding polarization vector. From (4) we may deduce the following properties.

P1: Given propagation angle θ, (4) leads to three positive (possibly degenerate) eigenvalues. This is particularly obvious for $\theta = 0, \pi$, and $\theta = \pi/2, 3\pi/2$, where the expression in the square bracket reduces to $\mathbf{M}_{11}$ and $\mathbf{M}_{22}$, respectively. However, $\mathbf{M}_{11}$ and $\mathbf{M}_{22}$, being among leading matrices of $\mathbf{C}/C_0$, are positive-definite. This property ensures the existence of three positive eigenvalues, leading to $s_1(\theta)$, $s_2(\theta)$ and $s_3(\theta)$. Therefore,

P2: the slowness curves are single-valued functions.

P3: Let θ_1 vary in the interval $[0, \pi)$, and define $\theta_2 = \theta_1 + \pi$. As $\cos^2\theta_1 = \cos^2\theta_2$, $\sin\theta_1\cos\theta_1 = \sin\theta_2\cos\theta_2$, and $\sin^2\theta_1 = \sin^2\theta_2$, (4) leads to the same slowness value for θ_1 and θ_2: the slowness curves are center symmetric and closed. Thus,

P4: n_f, n_i, and n_s are even numbers.

P5: Through the way of construction $s_f(\theta)$ is circumscribed in $s_i(\theta)$, and $s_i(\theta)$ is circumscribed in $s_s(\theta)$ (Fig. 2). Therefore, if an arbitrary straight line L intersects $s_f(\theta)$ then it also intersects $s_i(\theta)$ and $s_s(\theta)$. If L intersects $s_i(\theta)$ then it also intersects $s_s(\theta)$, but not necessarily $s_f(\theta)$. If L intersects $s_s(\theta)$, it may or may not intersect $s_i(\theta)$.

2. Step: An Appropriate Coordinate Rotation: Let $\mathbf{n}$ be the unit normal vector drawn from the origin onto the line L (the positive $\bar{s}_1-$direction in Fig. 1). Denote the angle between $\mathbf{n}$ and the positive s_1-axis by θ_0. Define a new coordinate system $(\bar{s}_1, \bar{s}_2)$ by rotating (s_1, s_2) counter-clockwise about the s_3-axis by θ_0, utilizing the matrix $\mathbf{R}$ given in (5). (The bar signifies variables in the new system.) Denote the spatial coordinates corresponding to $(\bar{s}_1, \bar{s}_2)$ by $(\bar{x}_1, \bar{x}_2)$.

$$\mathbf{R} = \begin{bmatrix} \cos\theta_0 & \sin\theta_0 & 0 \\ -\sin\theta_0 & \cos\theta_0 & 0 \\ 0 & 0 & 1 \end{bmatrix} \tag{5}$$

It can be shown that in the $(\bar{x}_1, \bar{x}_2)$ coordinate system we have

$$\left[\overline{\mathbf{M}}_{11}\partial_{\bar{x}_1\bar{x}_1} + (\overline{\mathbf{M}}_{12} + \overline{\mathbf{M}}_{21})\partial_{\bar{x}_1\bar{x}_2} + \overline{\mathbf{M}}_{22}\partial_{\bar{x}_2\bar{x}_2}\right]\bar{\mathbf{u}} = s_{\text{ref}}^2\partial_{tt}\bar{\mathbf{u}}. \tag{6}$$

where $\overline{\mathbf{M}}_{ij}$ stands for $\mathbf{R}\overline{\mathbf{N}}_i^T(\mathbf{C}/C_0)\overline{\mathbf{N}}_j\mathbf{R}^T$, with $\overline{\mathbf{N}}_1 = \cos\theta_0\mathbf{N}_1 + \sin\theta_0\mathbf{N}_2$ and $\overline{\mathbf{N}}_2 = -\sin\theta_0\mathbf{N}_1 + \cos\theta_0\mathbf{N}_2$. The 3×3 differential form in (6) is diagonalized with respect to time. Substituting $\bar{\mathbf{u}} = \bar{\mathbf{a}}\exp(j\bar{k}_1\bar{x}_1)\exp(j\bar{k}_2\bar{x}_2)\exp(-j\omega t)$ with $\bar{k}_1 = k\cos\bar{\theta}$, $\bar{k}_2 = k\sin\bar{\theta}$, and $\bar{\theta} = \theta - \theta_0$ we obtain

$$\left[\overline{\mathbf{M}}_{11}\cos^2\bar{\theta} + (\overline{\mathbf{M}}_{12} + \overline{\mathbf{M}}_{21})\sin\bar{\theta}\cos\bar{\theta} + \overline{\mathbf{M}}_{22}\sin^2\bar{\theta}\right]\bar{\mathbf{a}} = (s_{\text{ref}}/s)^2\bar{\mathbf{a}}. \tag{7}$$

Obviously, using (4) and (7) and varying $\bar{\theta}$ in $[0, 2\pi)$, and θ in $[\theta_0, 2\pi + \theta_0)$, respectively, result in the same slowness curves. However, the line L has a much simpler representation in $(\bar{s}_1, \bar{s}_2)$. $(\bar{L} : \bar{s}_i = \text{const.})$

3. Step: Equivalent Representations

Lemma 1: The 6×6 differential form in (8) is equivalent to the form in (6), [2-4]. Thereby, $\overline{\tau}_2/C_0$ stands for $\overline{\mathbf{M}}_{21}\partial_{\overline{x}_1}\overline{\mathbf{u}} + \overline{\mathbf{M}}_{22}\partial_{\overline{x}_2}\overline{\mathbf{u}}$, and $\mathbf{I}$ denotes the 3×3 identity matrix. Furthermore, $\overline{\mathbf{Q}}_{11} = -\overline{\mathbf{M}}_{22}^{-1}\overline{\mathbf{M}}_{21}$, $\overline{\mathbf{Q}}_{12} = \overline{\mathbf{M}}_{22}^{-1}$, $\overline{\mathbf{Q}}_{21} = \overline{\mathbf{M}}_{12}\overline{\mathbf{M}}_{22}^{-1}\overline{\mathbf{M}}_{21} - \overline{\mathbf{M}}_{11}$ and $\overline{\mathbf{Q}}_{22} = -\overline{\mathbf{M}}_{12}\overline{\mathbf{M}}_{22}^{-1}$.

$$\begin{bmatrix} \overline{\mathbf{Q}}_{11}\partial_{\overline{x}_1} & \overline{\mathbf{Q}}_{12} \\ s_{\mathrm{ref}}^2\mathbf{I}\partial_{tt} + \overline{\mathbf{Q}}_{21}\partial_{\overline{x}_1\overline{x}_1} & \overline{\mathbf{Q}}_{22}\partial_{\overline{x}_1} \end{bmatrix} \begin{bmatrix} \overline{\mathbf{u}} \\ \overline{\tau}_2/C_0 \end{bmatrix} = \partial_{\overline{x}_2} \begin{bmatrix} \overline{\mathbf{u}} \\ \overline{\tau}_2/C_0 \end{bmatrix} \tag{8}$$

The equivalence stated in this lemma implies that the homogeneous plane wave solution

$$\begin{bmatrix} \overline{\mathbf{u}} \\ \overline{\tau}_2/C_0 \end{bmatrix} = \begin{bmatrix} \overline{\mathbf{a}} \\ \overline{\mathbf{b}} \end{bmatrix} e^{j\overline{k}_1\overline{x}_1} e^{j\overline{k}_2\overline{x}_2} e^{-j\omega t} \tag{9}$$

substituted into (8) leads to (7) and thus to the same slowness curves. In (9) both $\overline{k}_1$ and $\overline{k}_2$ are real-valued. We recognize that the form in (8), which is diagonalized with respect to $\overline{x}_2$, suggests an alternative trial solution. Instead of $\exp(j\overline{k}_2\overline{x}_2)$ we choose $\exp(j\overline{k}_1\lambda\overline{x}_2)$, with a real- or complex-valued λ. The resulting trial functions correspond to homogeneous (λ: real) or inhomogeneous (λ: complex) plane waves, which propagate in different directions, possessing the common projection $\overline{k}_1$ on the $\overline{k}_1$-axis (Fig. 1). Substituting this type of trial function into (8) we obtain

$$\begin{bmatrix} \overline{\mathbf{Q}}_{11} & \overline{\mathbf{Q}}_{12} \\ (s_{\mathrm{ref}}/\overline{s}_1)^2\mathbf{I} + \overline{\mathbf{Q}}_{21} & \overline{\mathbf{Q}}_{22} \end{bmatrix} \begin{bmatrix} \overline{\mathbf{a}} \\ \overline{\mathbf{b}}/j\overline{k}_1 \end{bmatrix} = \lambda \begin{bmatrix} \overline{\mathbf{a}} \\ \overline{\mathbf{b}}/j\overline{k}_1 \end{bmatrix}. \tag{10}$$

Proof of T1: Since the coefficients in the enteries of the matrix in (10) are real-valued, the solutions for λ are either complex-conjugate pairs or real. Since the rank of the matrix (10) is six, the maximum number of real-valued λ possible is six. In other words, the maximum number of intersection points of an $\overline{s}_1 = \text{const}$ line with slowness curves possible is six (Fig. 1).

Proof of T2: Assume that an $\overline{s}_1 = \text{const}$ line intersects $\overline{s}_{\mathrm{f}}(\overline{\theta})$. Since $\overline{s}_{\mathrm{f}}(\overline{\theta})$ is circumscribed in $\overline{s}_{\mathrm{i}}(\overline{\theta})$, and $\overline{s}_{\mathrm{i}}(\overline{\theta})$ is circumscribed in $\overline{s}_{\mathrm{s}}(\overline{\theta})$, (**P5**), this line necessarily intersects $\overline{s}_{\mathrm{i}}(\overline{\theta})$ and $\overline{s}_{\mathrm{s}}(\overline{\theta})$. According to **P4** this line intersects each of the slowness curves at least at two points. Thus, the assumed $\overline{s}_1 = \text{const}$ line possesses minimally 6 intersection points with the slowness curves. However, since there are maximally six intersection points available, in accordance with **T1**, the following can be concluded. Any arbitrary straight line which intersects $s_{\mathrm{f}}(\theta)$, it intersects this curve at exactly two points. This proves the strict convexity of $\overline{s}_{\mathrm{f}}(\overline{\theta})$.

Proof of T3: Due to **P5** it is possible that an $\overline{s}_1 = \text{const}$ line intersects $\overline{s}_i(\overline{\theta})$ and thus $\overline{s}_s(\overline{\theta})$ without penetrating $\overline{s}_f(\overline{\theta})$. Thus, with reference to **T1** the following can be concluded: If an $\overline{s}_1 = \text{const}$ line intersects $\overline{s}_i(\overline{\theta})$, without intersecting $\overline{s}_f(\overline{\theta})$, then it has two or four intersection points with $\overline{s}_i(\overline{\theta})$, and exactly two intersection points with $\overline{s}_s(\overline{\theta})$.

Proof of T4: According to **P5** it is possible that an $\overline{s}_1 = \text{const}$ line intersects $\overline{s}_s(\overline{\theta})$ without intersecting $\overline{s}_i(\overline{\theta})$ and thus $\overline{s}_f(\overline{\theta})$. Therefore, with reference to **T1** the following can be concluded: If an $\overline{s}_1-$line intersects $\overline{s}_s(\overline{\theta})$, without intersecting $\overline{s}_i(\overline{\theta})$, then it has two or four or six intersection points with $\overline{s}_s(\overline{\theta})$.

The latter two proofs explain the possible existence of inflection points on $\overline{s}_i(\overline{\theta})$ and $\overline{s}_s(\overline{\theta})$. Our results can be stated in the following compact form.

Lemma 2: (n_f, n_i, n_s) takes on one of the following triples: $(0,0,0)$, $(0,0,2)$, $(0,0,4)$, $(0,0,6)$, $(0,2,2)$, $(0,4,2)$ and $(2,2,2)$.

It should be mentioned that waves in general *piezoelectric* media obey the stated convexity theorem and the lemma 2. Furthermore, all the results obtained here are *mutatis-mutandis* valid in three-dimensions.

Conclusion: It is proven that the slowness curves associated with the fastest bulk acoustic waves for general anisotropic elastic media are strictly convex.

References

[1] B. A. Auld, *Acoustic Fields and Waves in Solids*, second edition, Vol. I. Robert E. Krieger Publishing Company, Malabar, Florida, 1990.

[2] A. R. Baghai-Wadji, *Bulk Waves, Massloading, Cross-Talk, and Other Second-Order Effects in SAW-Devices* (a short-course manuscript). IEEE International Ultrasonics Symposium, San Antonio, Texas, Nov., 1996.

[3] ——, *Bulk Wave Analysis in Microacoustic Devices, Fundamentals, Modeling, and Applications* (a short-course manuscript). IEEE International Ultrasonics Symposium, Cannes, France, Nov., 1994.

[4] ——, *A Unified Approach for Construction of Green's Functions*. (Lecture Notes). Vienna University of Technology, Vienna, 1994.

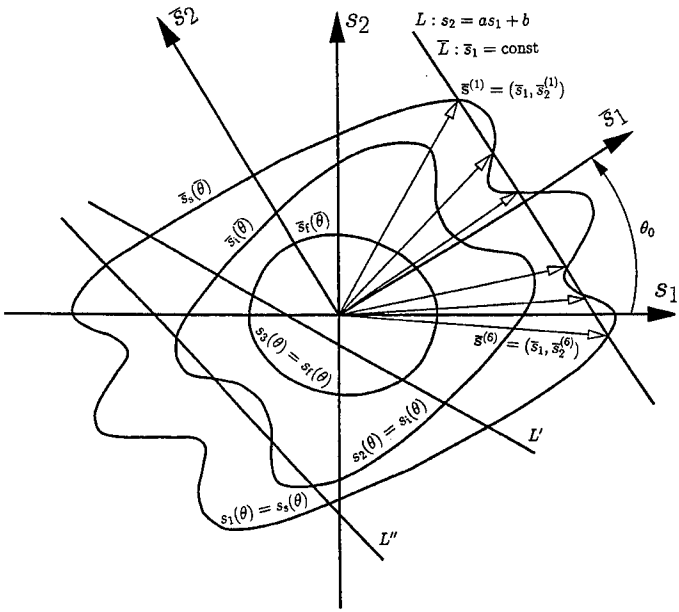

Figure 1: Three non-intersecting slowness curves are arbitrarily named $s_1(\theta)$, $s_2(\theta)$, and $s_3(\theta)$, and presented in the (s_1, s_2) coordinate system. $s_f(\theta)$, $s_i(\theta)$, and $s_s(\theta)$ are identified according to the rules (1) in the text. The line L is assumed to intersect $s_s(\theta)$ at six points. The original coordinate system is rotated counter-clockwise such that the $\bar{s}_1-$ axis of the new $(\bar{s}_1, \bar{s}_2)$ coordinate system has become perpendicular to $\bar{L}$. In the new system the slowness curves, and the line L, respectively, are named $\bar{s}_f(\theta)$, $\bar{s}_i(\theta)$, $\bar{s}_s(\theta)$ and $\bar{L}$. The six propagation vectors connecting the origin of the coordinate system to the $\bar{L} - \bar{s}_s(\theta)$ intersection points are seen to possess a common projection on the $\bar{s}_1-$axis. The lines L' and L'' provide an idea how a maximum number of six intersection points may be distributed among the slowness curves.

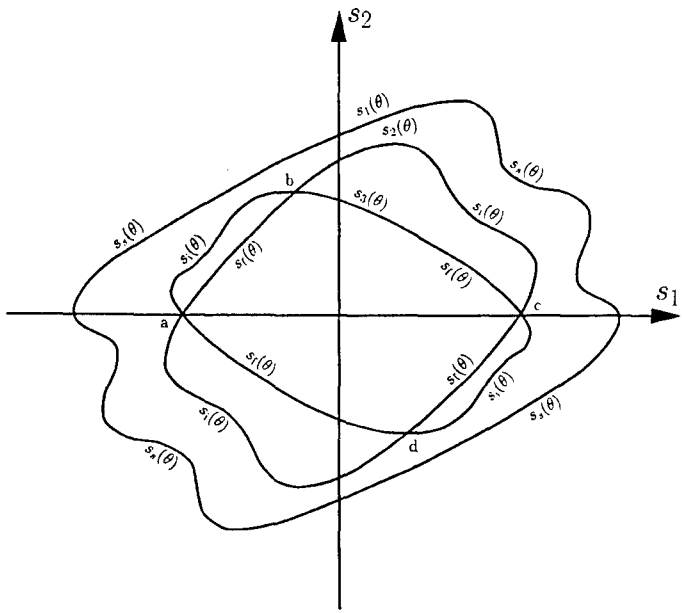

Figure 2: It is assumed that the inner slowness curves ($s_2(\theta)$ and $s_3(\theta)$) intersect at the points a, b, c, and d. Application of the rules (1) in the text results in $s_s(\theta)$, $s_i(\theta)$, and $s_f(\theta)$. The latter two curves are not differentiable at the points a, b, c, and d. It is seen that while $s_s(\theta)$ and $s_i(\theta)$ may possess concave regions, $s_f(\theta)$ is strictly convex everywhere.

On the Strict-Convexity of the Slowness Surfaces for the Fastest Bulk-Acoustic-Waves in Piezoelectric and Piezoelectromagnetic Media

Ali R. Baghai-Wadji[1]

Vienna University of Technology,
IAEE, 3592, Gußhausstraße 27-29, A-1040 Vienna, Austria, and,
Arizona State University,
Department of Mathematics, Tempe, AZ 85287, USA

Abstract: The two-dimensional (2-D) analysis of acoustic wave propagation in elastic media has revealed that the slowness curves for the fastest bulk acoustic waves are strictly convex [1]. The present work extends the validity range of this principle by analyzing 3-D wave propagation in piezoelectric and piezoelectromagnetic media. The arguments rely on firstly, the existence of a zero-radius slowness curve (surface) associated with piezoelectric media, and, secondly, the fact that the admissible slownesses are complex valued (with nonzero imaginary parts) outside any (closed) slowness surface. Based on these properties it is proven that the slowness surfaces for the fatsest bulk acoustic waves in general piezoelectric (piezoelectromagnetic) media are strictly convex.

I Introduction

It has been shown that the slowness curves for the fastest bulk acoustic waves propagating in purely elastic media are strictly convex [1]. The objective in this work is to prove the validity of this principle in piezoelectric (piezoelectromagnetic) media where a coupling between mechanical and electric (electromagnetic) fields takes place. The arguments rely on a number of facts which will next be listed. From these facts two fundamental properties are then inferred which are valid in general piezoelectric (and with adequate modifications in general piezoelectromagnetic) media.

(1) There exist five slowness surfaces associated with any piezoelectromagnetic medium [2].

(2) The three outer slowness surfaces describe the dispersion behavior of the bulk acoustic waves, and are predominantly characterized by the mechanical properties of the medium; i.e. stiffness constants and the mass density. (The piezoelectric effect causes an additional stiffening of the elastic medium.)

(3) The two inner slowness surfaces describe the dispersion behavior of the electromagnetic waves and are predominantly characterized by the

[1]The author is presently on leave of absence with Motorola Inc., 8201 E. McDowell Rd., M.D. H1556, Scottsdale, AZ 85252. **phone:** (602) 441 2471, **fax:** (602) 441 7714, **email address:** abaghai@rsl.iaee.tuwien.ac.at

electromagnetic properties of the medium.

(4) In existing piezoelectromagnetic materials the velocities of acoustic bulk waves are by five orders of magnitude slower than the electromagnetic space waves. Consequently the "radii" of the three outer slowness surfaces are 10^5 times larger than the "radii" of the electromagnetic slowness surfaces. Therefore, for physically realizable materials it is a reasonably good approximation to assume that the two inner (electromagnetic slowness) surfaces shrink to one point (the origin of the slowness plane); thereby constituting a (twofold degenerate) zero-radius slowness surface.

Constituting a zero-radius slowness surface establishes a *quasi-static* description of the piezoelectric effects which can be described as follows. Compared to the dynamic of acoustic wave phenomena, the propagation of electromagnetic disturbances is "instantaneous." Thereby, there is a curl-free electric field, which couples to the mechanical disturbances, and propagates at velocities typical for acoustic fields (a few 10^3 meters per second). Our discussion will be based on this interpretation of the quasi-static theory of piezoelectricity.

Preliminary Conclusions

Property 1: The quasi-static approximation in piezoelectric media implies the existence of a zero-radius slowness surface (**P1**).

Property 2: As we will see the admissible slowness values, in regions outside any closed slowness surface in the complex plane, are complex-valued with nonvanishing imaginary parts (**P2**).

In the next sections these properties will be discussed quantitatively by considering first the simplest physically realizable problem in which the piezoelectric coupling may take place. Then it will be shown that **P1** and **P2** hold true in general piezoelectric media. Finally an argument based on **P1** and **P2** will lead to the conclusion that the above-mentioned convexity property for piezoelectrica remains valid in piezoelectromagnetic media. (In the following discussion the familiarity with [1] is assumed.)

II Basic Equations

Adopting a quasi-static approximation for the electric field, the governing and constitutive equations in general piezoelectric media have the forms in (1) and (2), respectively [3].

$$\underline{\underline{\nabla}}^T \mathbf{T} = \rho \partial_{tt} \mathbf{u} \tag{1a}$$

$$\bar{\nabla}^T \mathbf{D} = 0 \tag{1b}$$

$$\mathbf{T} = \mathbf{C}\underline{\underline{\nabla}}\mathbf{u} + \mathbf{e}\vec{\nabla}\varphi \tag{2a}$$

$$\mathbf{D} = \mathbf{e}^T\underline{\underline{\nabla}}\mathbf{u} - \underline{\underline{\varepsilon}}\vec{\nabla}\varphi \tag{2b}$$

The symbols $\vec{\nabla}$, $\mathbf{D}$, $\mathbf{e}$, $\underline{\underline{\varepsilon}}$ and φ which have not been described in [1] have the following meanings: $\vec{\nabla}(= \mathbf{n}_1\partial_{x_1} + \mathbf{n}_2\partial_{x_2} + \mathbf{n}_3\partial_{x_3})$ is the divergence operator with $\mathbf{n}_i$ $(i = 1, 2, 3)$ referring to the 3×1 unit vector in the x_i direction; $\mathbf{D}$ represents the 3×1 dielectric displacement vector; $\mathbf{e}$ denotes the 6×3 piezoelectric matrix and $\underline{\underline{\varepsilon}}$ refers to the 3×3 positive definite permittivity matrix; φ stands for the scalar electric potential. In this work x_1 denotes the horizontal axis, x_3 the vertical axis, and x_2 is perpenticular to this plane. (This notation differs from the convention in [1], where x_1 and x_2, respectively, referred to the horizontal and vertical axes.)

II.1 Simplest Piezoelectric Problem

Under certain conditions [2], only the horizontal transversal component u_2 of the displacement vector $\mathbf{u}$ couples to the electric potential φ, forming a wave which propagates independently of any (u_1, u_3) elastic distorsion in the (x_1, x_3) sagittal plane. The analysis of this *shear horizontal piezoelectric* (u_2, φ) wave reveals a fact which is crucial to our arguments.

Consider an elastic medium built from Cadmium Sulfide with the following material parameters: $C_{11} = C_{22}$, C_{33}, $C_{44} = C_{55} = C_{66}$, C_{12}, $C_{13} = C_{23}$, $e_{13} = e_{23}$, e_{33}, $e_{51} = e_{42}$, $\varepsilon_{11} = \varepsilon_{22}$, ε_{33}; all other entries of $\mathbf{C}$, $\mathbf{e}$ and $\underline{\underline{\varepsilon}}$ are vanishingly small. Perform a (0°, 90°, 0°) crystal-rotation with reference to the (x_1, x_2, x_3) coordinate system. Assume that there is no variation in the x_2 direction ($\partial_{x_2} \equiv 0$). Under these conditions we find that the coupled equations (1) and (2) for u_1, u_2, u_3, and φ split into two systems for the pairs of variables (u_1, u_3) and (u_2, φ). In particular, for (u_2, φ) we find (the simplest piezoelectric problem):

$$\begin{bmatrix} C_{44} & e_{51} \\ e_{51} & -\varepsilon_{11} \end{bmatrix} \Delta \begin{bmatrix} u_2 \\ \varphi \end{bmatrix} = \begin{bmatrix} \rho & 0 \\ 0 & 0 \end{bmatrix} \partial_{tt} \begin{bmatrix} u_2 \\ \varphi \end{bmatrix} \tag{3}$$

with $\Delta(= \partial_{x_1x_1} + \partial_{x_3x_3})$. Note that (3) is a generalized differential eigenform for $[u_2, \varphi]^T$, and is diagonalized with respect to time. Similar to the discussion in [1] we next consider two special problems.

II.1.1 1st Special Problem

Assumptions: Consider a homogeneous plane wave which propagates in the (x_1, x_3) plane:

$$\begin{bmatrix} u_2 \\ \varphi \end{bmatrix} = \begin{bmatrix} U_2 \\ \Phi \end{bmatrix} \exp(jk_1x_1)\exp(jk_3x_3)\exp(-j\omega t)$$
$$= \begin{bmatrix} U_2 \\ \Phi \end{bmatrix} \exp[j(k_1/\omega)(\omega x_1)]\exp[j(k_3/\omega)(\omega x_3)]\exp(-j\omega t)$$
$$= \begin{bmatrix} U_2 \\ \Phi \end{bmatrix} \exp(js_1X_1)\exp(js_3X_3)\exp(-j\omega t). \quad (4)$$

This wave is characterized by the wavevector $\mathbf{k} = (k_1, k_3)$ and the angular frequency $\omega(\neq 0)$. In writing (4) the slownesses $s_i(= k_i/\omega)$ and the velocities $X_i(= \omega x_i)$ are introduced $(i = 1, 3)$.

Statement of the Problem: Using (4) calculate the slowness curves associated with (3).

Calculation of Slowness Curves: Substitute (4) into (3) to obtain

$$\begin{bmatrix} C_{44}s^2 + \rho & -e_{51}s^2 \\ -e_{51}s^2 & -\varepsilon_{11}s^2 \end{bmatrix} \begin{bmatrix} U_2 \\ \Phi \end{bmatrix} = 0. \quad (5)$$

(In obtaining (5) a $(s, \theta)-$polar coordinate system has been used: $s_1 = s\cos\theta$ and $s_3 = s\sin\theta$. Furthermore, both equations have been divided by ω^2, and use has been made from $s^2 = s_1^2 + s_3^2$.) For nontrivial solutions the determinant of this equation must vanish:

$$\det[\cdots] = 0 \Rightarrow s^2[1 - s^2/\tilde{s}_{\text{ref}}^2] = 0. \quad (6)$$

In this equation $\tilde{s}_{\text{ref}}$ stands for $(\rho/\tilde{C}_{44})^{1/2}$; thereby, the *stiffened* elastic modulus $\tilde{C}_{44}$ equals $C_{44} + e_{51}^2/\varepsilon_{11}$. (6) is the dispersion relation corresponding to (3), and leads to the twofold degenerate solutions $s = 0$ and $s = \tilde{s}_{\text{ref}}$.

Solution $s = 0$: This is the equation of a zero-radius slowness curve. In virtue of (5) this solution leads to a U_2 being zero, and to a Φ being arbitrary, i.e. $[U_2, \Phi]^T = [0, 1]^T$: the elastic and electric fields are decoupled. In the framework of our quasi-static theory we may interpret this result in the following way: The solution for Φ at $s = 0$ represents a field which propagates at an "infinite" velocity (zero slowness). However, since mechanical disturbances propagate at a finite velocity (see the next paragraph), U_2 must be zero at $s = 0$.

Solution $\tilde{s}_{\text{ref}}$: For the solution corresponding to $s = \tilde{s}_{\text{ref}}$ we obtain $[U_2, \Phi]^T = [1, e_{15}/\varepsilon_{11}]^T$. This means that for $e_{15} \neq 0$ (in a piezoelectric medium) the coupled field $[U_2, \Phi]^T$ propagates at the finite velocity $\tilde{v}_{\text{ref}} = 1/\tilde{s}_{\text{ref}}$. If $e_{15} = 0$ (in a nonpiezoelectric medium) U_2 decouples from Φ ($[U_2, \Phi]^T = [1, 0]^T$) and propagates at the slightly lower velocity $v_{\text{ref}} = 1/s_{\text{ref}}$ with $s_{\text{ref}} = (\rho/C_{41})^{1/2}$.

Conclusion: There are two slowness curves associated with (3), $s = 0$ and $s = \tilde{s}_{\text{ref}}$.

II.1.2 2nd Special Problem

Assumptions: Consider a wave which propagates with a real-valued wavenumber s_1 (slowness) in the x_1 direction:

$$u_2 = U_2 \exp(j s_1 X_1) \exp(j s_1 \lambda X_3) \exp(-j\omega t). \tag{7}$$

This wave may or may not be homogeneous depending on λ being real- or complex valued (with a nonvanishing imaginary part). Note that λ and the wavenumber (slowness) s_3 are related in the following form: $j s_3 X_3 = j s_1 (s_3/s_1) X_3 = j s_1 \lambda X_3$.

Statement of the Problem: Substitute (7) into (3), and calculate the associated real- or complex-valued λ.

Instead of using (3) we first construct an equivalent representation for (3). To this end we use the relationship

$$\begin{bmatrix} T_4 \\ D_3 \end{bmatrix} = \begin{bmatrix} C_{44} & e_{51} \\ e_{51} & -\varepsilon_{11} \end{bmatrix} \partial_{x_3} \begin{bmatrix} u_2 \\ \varphi \end{bmatrix}, \tag{8}$$

which derives from (2). Using this equation it can be shown that (3) transforms into the following equivalent equation which is diagonalized with respect to x_3 [2]

$$\begin{bmatrix} 0 & 0 & 1/\tilde{C}_{44} & e_{51}/(\varepsilon_{11}\tilde{C}_{44}) \\ 0 & 0 & e_{51}/(\varepsilon_{11}\tilde{C}_{44}) & -C_{44}/(\varepsilon_{11}\tilde{C}_{44}) \\ -C_{44}\partial_{x_1 x_1} - \rho\omega^2 & -e_{51}\partial_{x_1 x_1} & 0 & 0 \\ -e_{51}\partial_{x_1 x_1} & -\varepsilon_{11}\partial_{x_1 x_1} & 0 & 0 \end{bmatrix}$$

$$\times \begin{bmatrix} u_2 \\ \varphi \\ T_4 \\ D_3 \end{bmatrix} = \partial_{x_3} \begin{bmatrix} u_2 \\ \varphi \\ T_4 \\ D_3 \end{bmatrix}. \tag{9}$$

Upon substituting (7) into (9) we obtain a fourth order secular equation which splits into (10a) and (10b):

$$s_1^2 + (s_1\lambda)^2 = 0 \tag{10a}$$

$$s_1^2 + (s_1\lambda)^2 = \tilde{s}_{\text{ref}}^2 \tag{10b}$$

with the solutions

$$s_1\lambda = \pm j|s_1| \tag{11}$$

and

$$s_1\lambda = \begin{cases} \pm\sqrt{\tilde{s}_{\text{ref}}^2 - s_1^2} & s_1^2 \le \tilde{s}_{\text{ref}}^2 \\ \pm j\sqrt{s_1^2 - \tilde{s}_{\text{ref}}^2} & s_1^2 > \tilde{s}_{\text{ref}}^2. \end{cases} \tag{12}$$

(Note that (10a) represents the Laplace equation and (10b) the Helmholz equation.)

Remembering that s_1 and $s_1\lambda$ denote the components of the propagation vector in x_1 and x_3 directions, respectively, we may deduce the following facts.

F1: (12) describes a circular slowness curve with radius $\tilde{s}_{\text{ref}}$ for $s_1^2 \leq \tilde{s}_{\text{ref}}^2$.

F2: (12) results in $s_1\lambda \sim \pm j|s_1|$ for $s_1^2 >> \tilde{s}_{\text{ref}}^2$. ($a \sim b$ signifies that a asymptotically behaves the same as b.)

F3: From **F1** and **F2** we conclude that $s_1\lambda$ is real-valued for s_1 varying "inside" the slowness curve ($-\tilde{s}_{\text{ref}} \leq s_1 \leq \tilde{s}_{\text{ref}}$), and imaginary for s_1 "outside" the slowness curve ($s_1 < -\tilde{s}_{\text{ref}}$ and $s_1 > \tilde{s}_{\text{ref}}$).

F4: (11) states that $s_1\lambda$ is equal to $\pm j|s_1|$ *for any* s_1. We may rephrase this statement in the following form: $s_1\lambda$ is imaginary for s_1 "outside" a zero-radius slowness curve.

F5: The relationship between the $s = 0$ and $s = \tilde{s}_{\text{ref}}$ slowness surfaces can also be seen directly from (10). For $s_1^2 >> \tilde{s}_{\text{ref}}^2$ (10b) degenerates in (10a). This means that for every slowness value much larger than the characteristic slowness $\tilde{s}_{\text{ref}}$ the fields are asymptotically static. Thus, a field which is static (not asymptotically static) for *every* s_1, necessarily constitutes a characteristic slowness which is zero in magnitude.

Conclusion: Out of the four possible solutions two are always imaginary, (11). The remaining two solutions build a slowness curve $s = \tilde{s}_{\text{ref}}$. The strict convexity property of this (circular) slowness curve is trivial in this particular example.

III General Piezoelectric Media

In general piezoelectric media there are eight solutions, two of which behave the same as $\pm j|s_1|$ for $s_1 \to 0$. Generally these complex solutions substantially deviate from the lines $s_1\lambda = \pm j|s_1|$ for large values of s_1 (large as compared to the materials' cut-off slowness values). However, the fact that these solutions are complex (with strictly nonvanishing imaginary parts) for *arbitrary* s_1 remains valid, implying the existence of a zero-radius slowness surface in general piezoelectric media. Based on this fact, an argument similar to that presented in [1] leads to the conclusion that the slowness curves (surfaces), associated with the fastest bulk acoustic wave in piezoelectric media, are strictly convex. The generalization of the ideas developed in the previous section is quite straightforward, provided the basic piezoelectric equations can be diagonalized with respect to time, as well as, to a coordinate axis, say x_3 [2]. The appendices in this paper provide the results of these diagonalizations. The claim that these concepts are valid in three dimensions, is demonstrated by constructing the formulae in Appendix B.

IV General Piezoelectromagnetic Media

Similar statements can be made in general piezoelectromagnetic media. (For the diagonalization of the basic equations refer to [2].) In piezoelectromagnetic media, beside the fact that the slowness surface for the fastest bulk acoustic wave is strictly convex, the slowness surface for the fastest electromagnetic space wave is also strictly convex. Similar arguments as in [1] result in this conclusion.

Appendix A: Diagonalization of General Piezoelectric Equations with respect to Time

In Fourier domain we have the following representations:

$$\vec{\nabla} \Leftrightarrow jk\cos\theta\mathbf{n}_1 + jk\sin\theta\mathbf{n}_3 = jk\mathbf{n} \tag{13a}$$

$$\underline{\underline{\nabla}} \Leftrightarrow jk\cos\theta\mathbf{N}_1 + jk\sin\theta\mathbf{N}_3 = jk\mathbf{N} \tag{13b}$$

($\mathbf{N}_1$ and $\mathbf{N}_3$ are described in [1].) Substitute (2b) into (1b), and transform the result into Fourier domain to obtain (14).

$$\bar{\varphi} = \frac{(\mathbf{en})^T}{\mathbf{n}^T\underline{\underline{\varepsilon}}\mathbf{n}}\mathbf{N}\bar{\mathbf{u}} \tag{14}$$

Transform (2a) into Fourier domain, and substitute in the resulting equation for $\bar{\varphi}$ from (14) to obtain

$$\frac{\bar{\mathbf{T}}}{jk} = \tilde{\mathbf{C}}\mathbf{N}\bar{\mathbf{u}} \tag{15}$$

where the stiffened elastic constants

$$\tilde{\mathbf{C}} = \mathbf{C} + \frac{(\mathbf{en})(\mathbf{en})^T}{\mathbf{n}^T\underline{\underline{\varepsilon}}\mathbf{n}} \tag{16}$$

have been introduced. Transform (1a) into Fourier domain, use the expression for $jk\mathbf{N}$, and subtitute for $\bar{\mathbf{T}}$ from (15) to obtain

$$\left[\tilde{\mathbf{M}}_{11}\cos^2\theta + (\tilde{\mathbf{M}}_{13} + \tilde{\mathbf{M}}_{31})\sin\theta\cos\theta + \tilde{\mathbf{M}}_{33}\sin^2\theta\right]\bar{\mathbf{u}} = \frac{1}{\tilde{s}^2}\bar{\mathbf{u}} \tag{17}$$

where we have introduced the following quantities: $\tilde{\mathbf{M}}_{ij} = \mathbf{N}_i\tilde{\mathbf{C}}\mathbf{N}_j, i, j = 1, 3$. $s_{\text{ref}}^2 = \rho/C_0$ with $C_0 = 10^{10}N/m^2$. And, $\tilde{s} = s/s_{\text{ref}}$.

Appendix B: Diagonalization of General Piezoelectric Equations with respect to a Coordinate Variable ([4])

$$\mathcal{L}_{11} = -\mathbf{M}_{33}^{-1}\mathbf{M}_{32}\partial_{x_2} - \mathbf{M}_{33}^{-1}\mathbf{M}_{31}\partial_{x_1} \tag{18a}$$

$$\mathcal{L}_{12} = \mathbf{M}_{33}^{-1} \tag{18b}$$

$$\begin{aligned}\mathcal{L}_{21} = &-\left[\mathbf{M}_{22} - \mathbf{M}_{23}\mathbf{M}_{33}^{-1}\mathbf{M}_{32}\right]\partial_{x_2x_2} \\ &-\left[\mathbf{M}_{21} - \mathbf{M}_{23}\mathbf{M}_{33}^{-1}\mathbf{M}_{31}\right]\partial_{x_2x_1} \\ &-\left[\mathbf{M}_{12} - \mathbf{M}_{13}\mathbf{M}_{33}^{-1}\mathbf{M}_{32}\right]\partial_{x_1x_2} \\ &-\left[\mathbf{M}_{11} - \mathbf{M}_{13}\mathbf{M}_{33}^{-1}\mathbf{M}_{31}\right]\partial_{x_1x_1} + \underline{\underline{\rho}}\partial_{tt}\end{aligned} \tag{18c}$$

$$\mathcal{L}_{22} = -\mathbf{M}_{23}\mathbf{M}_{33}^{-1}\partial_{x_2} - \mathbf{M}_{13}\mathbf{M}_{33}^{-1}\partial_{x_1} \tag{18d}$$

$$\begin{bmatrix} \mathcal{L}_{11} & \mathcal{L}_{12} \\ \mathcal{L}_{21} & \mathcal{L}_{22} \end{bmatrix} \begin{bmatrix} \vec{\Psi} \\ \vec{\Gamma}_3 \end{bmatrix} = \partial_{x_3} \begin{bmatrix} \vec{\Psi} \\ \vec{\Gamma}_3 \end{bmatrix} \tag{19}$$

$$\mathbf{M}_{ij} = \begin{bmatrix} \mathbf{N}_i^T\mathbf{C}\mathbf{N}_j & \mathbf{N}_i^T\mathbf{e}\mathbf{n}_j \\ \mathbf{n}_i^T\mathbf{e}^t\mathbf{N}_j & -\mathbf{n}_i^T\underline{\underline{\varepsilon}}\mathbf{n}_j \end{bmatrix} \tag{20}$$

References

[1] A. R. Baghai-Wadji, *A Paradigm for Proving the Convexity Properties of Slowness Curves*. These Proceedings.

[2] A. R. Baghai-Wadji, *A Unified Approach for Construction of Green's Functions*. (Lecture Notes). Vienna University of Technology, Vienna, 1994.

[3] B. A. Auld, *Acoustic Fields and Waves in Solids*. New York: Wiley, 1973.

[4] A. R. Baghai-Wadji and Ch. Ringhofer, *A Survey of Numerical Techniques for Modeling the Massloading Effects in SAW Devices*. 1996 IEEE Ultrasonics Symp. Proceedings, Vol. 1, pp. 111-116.

Solving EMC Problems Using the FDTD Method

Franz Gisin[1]
Silicon Graphics Inc.
Mountain View, CA

Dr. Zorica Pantic-Tanner[2]
San Francisco State University
San Francisco, CA

Introduction

Commercial computers and other digital devices must be meet regulatory agency requirements that limits the amount of radio frequency energy they are allowed to radiate as a "by-product" of their primary "computational" function. Compliance with the limits set by regulatory agencies such as the FCC in the United States and the EC in Europe require the device under test be configured in a typical operational system configuration. A desktop computer or workstation test configuration includes not only the computer, but all associated peripheral devices such as keyboard, mouse, monitor, printer, and modem that connect to the computer. An example of such a test configuration is shown in Figure 1.

It is rather obvious from Figure 1 that any attempts to completely model such a system using currently available modeling tools is nearly impossible. Usually not all engineering information is available to the manufacturer since many of the peripheral devices and internal subassemblies are manufactured by someone else. And even if all information were available, different test configurations such as placing the printer to the right of the monitor rather than left of the monitor will probably produce a different emission profile. If modeling the entire system is not practical, then only two options are available: 1) forget modeling and revert back to the "build it - test it - figure out what's wrong with it - fix it - retest" method; and 2) model only a portion of the system. Option 1 is still widely used today because in the option 2 method one has to successfully convert the system level specification (for example, radiated emission limits in units of dBμV/M) into units that are applicable to the portion of the system that is being modeled (for example, maximum allowable length, in cm, of enclosure aperture "seams" along mating shield enclosure pieces). Success is also dependent on how well the person doing the modeling knows the system and the modeling tool being used.

This paper describes how one common problem within the EMC community (system clock harmonics leaking through apertures in the enclosure) was addressed using the FDTD method.[3] Using the principles outlined herein, other modeling tools such as MOM and FEM can be used with success.

Allocating the Allowable Noise Budget

When modeling only a portion of a complex system, one must assign some "values" to the modeling results. With most emission limits being of the "not to exceed" form, one must do a good job of allocating the allowable noise budget (that region underneath the limit) to different parts of the system. How much of the maximum allowable emission level (the limit) should be allocated to leakage from apertures? How much should be allocated to leakage from cables? What are the cost tradeoffs between leakage from apertures and from interconnect cables (e.g. is it more cost effective to build "water-tight" enclosures and then buy cheaper cables or vice versa)?

One way to visualize this problem is to break up the EMC aspects of the system into a transfer function model similar to the one shown in Figure 2. A number of sources within the system generate noise. The noise from these sources can propagate out of the system via a number of paths including conduction, cross-talk, radiation into internal enclosure cavities, leakage through apertures, etc. The total radiation

[1] Franz Gisin, EMC Manager, Visual Systems Group, Silicon Graphics Inc., 2011 North Shoreline Blvd, Mountain View, CA, 94043, Tel: (650) 933-8789, Fax: (650) 933-8789, e-mail: gisinf@engr.sgi.com.

[2] Dr. Zorica Pantic-Tanner, Director - Director, School of Engineering, San Francisco State University, 1600 Holloway Ave, San Francisco, CA 94132, Tel: (415) 338-7739, Fax: (415) 338-0525, e-mail: zpt@sfsu.edu.

[3] LC FDTD software supplied by Cray Research Inc. The LC web site is http://www/cray.com/lc/.

from all these sources and paths cannot exceed the allowable limit. By visualizing the system in this way, "noise source/propagation" pairs that naturally lend themselves to modeling become apparent For example, the impact of changing one of the noise sources (e.g. a higher speed CPU upgrade) becomes readily apparent. Viewed in this larger context, proper interpretation of the modeling results also becomes easier.

A Practical Example

Consider the case where radiation from a digital clock circuit leaks out of the enclosure via an aperture such as a thin seam. Questions such as how large can the aperture be, is orientation of the source with respect to the aperture important, does the shape of the aperture play a dominant role, is gasketing required, what about future processor speed upgrades, etc., often get asked during the development phases of an enclosure design. To answer these questions, one can use the transfer function model concept described earlier to conceptually define a simple block consisting of an electromagnetic field input, $e(t)$, an electromagnetic field output, $c(t)$, and the transfer function of the aperture itself, $g(t)$. The output, $c(t)$, is equal to the convolution of the input, $e(t)$, and the transfer function, $g(t)$. See Figure 3.

$$c(t) = e(t) \otimes g(t) = \int_{-\infty}^{+\infty} e(\tau)g(t-\tau)d\tau \qquad \text{(Eqn 1)}$$

In our example, the input electromagnetic field impinging on the inner side of the aperture, $e(t)$, is dependent on the spectral content of the digital clock circuitry that generates the noise. For many computer systems this source of noise can take on a broad range of values. A typical example is the personal computer enclosure owned by one of the authors. Since it was first purchased several years ago, the CPU board has been upgraded 3 times, starting out with a 286 and finishing up with a 486. The enclosure has the capability of accepting a Pentium class processor sometime in the future (a similar philosophy, where the enclosure design is not changed as often as the circuitry inside the enclosure, is used by many computer manufacturers).

One way to get around the problem of not knowing the exact spectral content of the source is to concentrate on the transfer function, $g(t)$, instead of the output, $c(t)$.[4] Since most regulatory agency limits are specified in the frequency domain, and the FDTD method is a time domain process, one can simply take the Fourier transform of the transfer function described by Eqn 1. Convolution in the time domain becomes multiplication in the frequency domain, in which case the transfer function of the aperture, $G(\omega)$, as a function of frequency can be simply calculated by taking the output, $C(\omega)$, and dividing it by the input, $E(\omega)$.

$$c(t) = e(t) \otimes g(t) \Rightarrow C(\omega) = E(\omega) \bullet G(\omega) \Rightarrow G(\omega) = {C(\omega)}/{E(\omega)} \qquad \text{(Eqn 2)}$$

Both $C(w)$ and $E(w)$ are complex because of the time retardation associated with the emission (electromagnetic wave) propagating through space. Since one is primarily interested in the magnitude of the leakage through the aperture (e.g. home much of the energy on the inside of the aperture leaks through the aperture), one can take the absolute value of $|C(w) / E(w)|$ to arrive at the final answer, $|G(w)|$

$$|G(\omega)| = \left|\frac{C(\omega)}{E(\omega)}\right| = \frac{|C(\omega)|}{|E(\omega)|} \qquad \text{(Eqn 3)}$$

[4] "Introduction to Continuous and Digital Control Systems", Robert Saucedo and Earl E. Schiring. The MacMillan Company, 1968.

One can go also compare $|G(w)|$ for different configurations, for example, taking the ratio of two different transfer functions. In this case, one can simplify the computations by just taking the ratio of the output values obtained for each case (see Eqn 4). This ratio is also known as the "Insertion Loss" if the ratio is compared to a measured value when the nothing is present (in this case, no shield).

$$\frac{\left|G(\omega)_1\right|}{\left|G(\omega)\right|_2} = \frac{\left|C(\omega)_1\right|}{\left|E(\omega)\right|} \Big/ \frac{\left|C(\omega)_2\right|}{\left|E(\omega)\right|} = \frac{\left|C(\omega)_1\right|}{\left|C(\omega)_2\right|}$$

$$20Log_{10}\frac{\left|G(\omega)_1\right|}{\left|G(\omega)\right|_2} = 20Log_{10}\left|C(\omega)_1\right| - 20Log_{10}\left|C(\omega)_2\right| \qquad \text{(Eqn 4)}$$

A few comments are in order at this point. First, the whole issue of what the source waveform looks like (or might look like sometime in the future) was "conveniently" defined away by concentrating on the transfer function rather than the actual value of the electromagnetic energy on the outside of the aperture. The source waveform shape no longer becomes important as long as it contains enough energy in the frequency range of interest to produce reliable results. In the FDTD case, the trapezoidal waveshapes normally used by EMC engineers to model digital logic clocks can now be replaced by a Gaussian pulse that has a smoother frequency roll off better suited for FDTD analysis purposes.[5] Secondly, a fair amount of latitude can be taken in how one generates the electromagnetic wave that impinges on the aperture. It is not necessary to model the complex multi-layer printed circuit board that typical clock circuits are mounted on. And finally, if one has actual test data from a system that is "similar" to the one being analyzed, one can use it as a reference point, in which case comparing the transfer functions of different shapes/sizes of the aperture produces delta values that can be added to the actual measured values to predict the final outcome. Depending on the circumstances, other simplifications can be made to make the modeling problem less complicated while still producing useable results. It is important to note that a good understanding of the system being analyzed and the strengths/weaknesses of the particular modeling method used can help one determine which simplifications can be made without significantly degrading the calculated results.

Modeling Results

Figure 4 shows the basic structure of the modeling environment. The boundary of the FDTD simulation space contains a small vertically oriented source (left side in Figure 4) and four sets of electric field probes (E_x, E_y, E_z, and E_{mag}) positioned at six locations within the space. The structures under study are to be located within the rectangular space between the six probe measurement locations. Shown in Figure 4 is the vertical ground plane with one horizontal slot that forms the basis for subsequent studies.

Figures 5 and 6 show the time results of aperture leakage for aperture length to width ratios of 70:12, 70:6, and 70:2. Referring to this Figure, one can see that as the aperture width decreases, the resonant frequency becomes sharper (e.g. the Q of the slot goes up). This can pose problems in situations where the slot width cannot be very accurately controlled. Examples where this can occur include conductively coated plastics (mechanical tolerances on enclosure shield pieces are difficult to control), and using metal finishes that are not very conductive. In either case, random slots are created in the enclosure that allow radiation to occur at different frequencies depending on where the adjacent metallic pieces end up mating at any given time.

[5] "Finite Difference Time Domain Methods for Electromagnetics", Karl S. Kunz and Raymond J. Luebbers, pp 33-36, CRC Press, 1993.

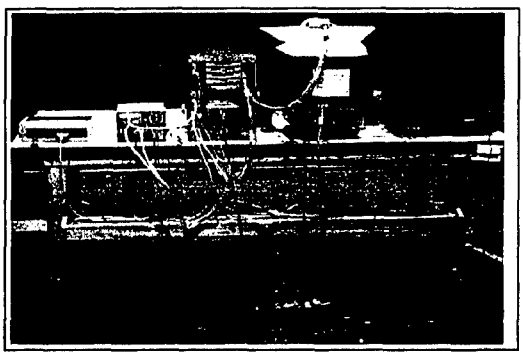

Figure 1:
Typical Radiated Emission Test Configuration

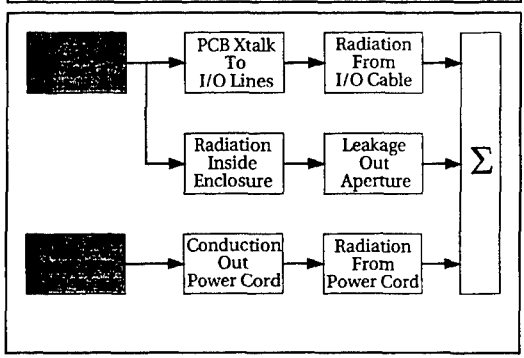

Figure 2:
Transfer Function Model of System Level EMC

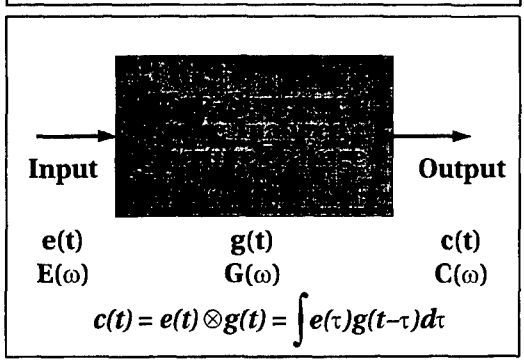

Figure 3:
Transfer Function of Aperture Leakage

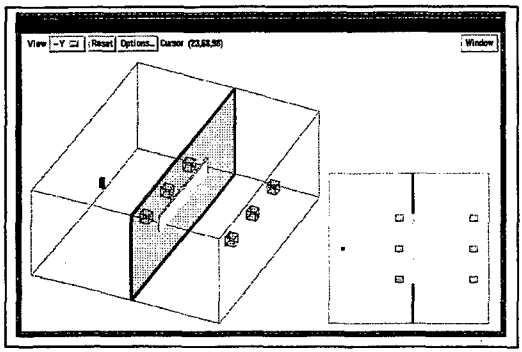

Figure 4:
FDTD Modeling Space

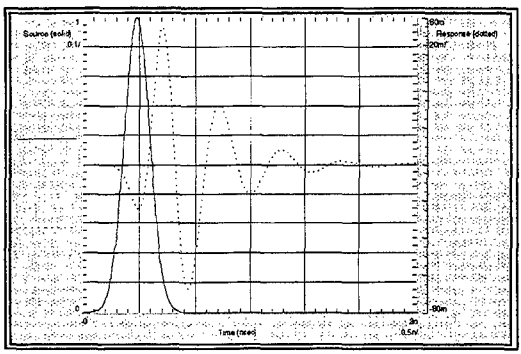

Figure 5:
Time Domain Response to a Gaussian Pulse

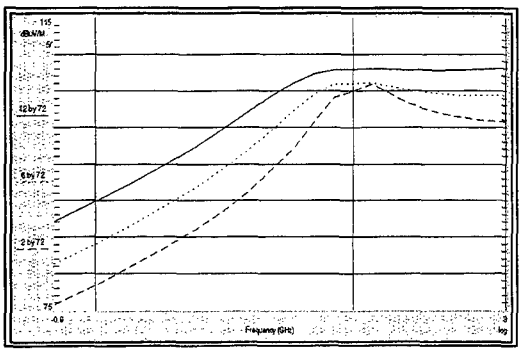

Figure 6:
Freq. Domain Response of Different Slot Widths

SESSION 5:

TLM MODELING AND APPLICATIONS

Chairs: W.J.R. Hoefer and P. Russer

A Hybrid Time Domain TLM-Integral Equation Method for Solution of Radiation Problems

Luca Pierantoni, Stefan Lindenmeier and Peter Russer

Technische Universität München, Lehrstuhl für Hochfrequenztechnik
Arcisstrasse 21, D-80333, München, Germany; phone: +49 89 289 23378
fax: +49 89 289 23365, e-mail: lindenmr@hft.e-technik.tu-muenchen.de

Abstract

Radiation phenomena are central problems in many topics such as EMP (E.M. Pulse), EMC (E.M. Compatibility) and EMI (E.M. Interference), inverse scattering, microwave imaging and radar target identification. Because of that the analysis of radiation problems in time domain is of increasing practical interest. In these problems we have to deal with interacting objects of arbitrary shape separated by large distances in free space or in open site.
In this contribution we present a novel hybrid Transmission Line Matrix-Integral Equation (TLMIE) method in which the efficient Integral Equation method (I.E.) is combined with the very flexible Transmission Line Matrix (TLM) method, for the solution of radiating problems. This method works in time domain for efficient solution of transient interferences. For the analysis of many radiation problems the Method of Moments (MoM) is a common tool. Its efficiency is related to the geometry of the given structure. Especially in the case of different combined dielectric structures the Method of Moments presents increasing analytical and computational problems. On the other hand the TLMIE Method is applicable very easily to a large variety of problems for structures of nearly arbitrary shape. We apply our hybrid method on a typical EMC problem of the radiation from apertures in metallic enclosures, fixed by a dielectric slab. The numerical results of the TLMIE method are then compared with results obtained by the pure TLM method.

Introduction

In many radiation problems we have to deal with transient phenomena in response to an impulse excitation. The presence of these impulsive fields provides a great amount of e.m. disturbance against wich an equipment should be immune. These problems demonstrate the importance of an accurate prediction of the e.m. near and far field surrounding the object. For this purpose a great number of numerical methods have been developed [4,6,8,9,10].
The numerical methods are suited for the evaluation of the field related to very arbitrary shape [1,2] but, because of the problem of the memory, this works only efficiently in a local or limited context. On the other hand, the I.E. method, in connection with the Method of Moment approach, permits us to evaluate the fields in large free space region, because it reduces the complexity of a field problem by one dimension [3]. The disadvantage of the I.E. or MoM approach is that the efficiency is related to the complexity and the number of the structures.
In this paper we describe a novel hybrid method of numerical electromagnetic field analysis, combining the Transmission Line Matrix method (TLM) with the Integral Equation (I.E.) method. With that the TLMIE method has got the high flexibility of a space discretizing method and the efficiency of the Integral Equation method for the analysis of large homogeneous regions. The TLMIE method is applicable for the analysis of

EMC problems and it makes possible the efficient computation of complex structures which are coupled by their far fields.
In the TLMIE method the near field of radiating structures is computed by TLM/FDTD, the far field properties are modeled by the Integral Equation method. The space of the entire problem is subdivided into subregions to which the different methods are applied. By this way the modeling of complex structures is simplified by segmentation. At the boundary interfaces of these subregions the transverse e.m. field is expanded by means of subdomain basis functions, as in the TLM or the FDTD scheme [4,5]. The expanded fields on the interfaces are then related to each other by the Green's functions. By using the continuity of the fields and taking into account the orthonormal properties of the expanding and testing functions, respectively, we derive a matrix system whose solution provides the unknown expanding coefficients of the e.m. field. The TLMIE method is demonstrated by studying a typical EMC problem regarding the radiation from a rectangular aperture in a shielded metallic box [6].
Apertures are widely used in many electromagnetic applications such as antennas, but just due to their radiating characteristics, they are also sources of interferences with respect to other equipments [6]. In particular, the interferences exist in the case of a realistic equipment which consists of a metallic box with a rectangular aperture, partially filled with a dielectric slab. The cavity is fed by an arbitrary distribution of electric and magnetic dipoles inside the box. For such equipments, it is very important to achieve an accurate computation of the e.m. field surrounding the metallic enclosure and, in particular, it is essential to compute the box resonances, aperture resonances and, most of all, resonances due to the interaction between sources and apertures [6,9,10]. These resonant frequencies are dominant in the far field interaction with other devices. In the present contribution we apply the hybrid method for studying the radiation from the metallic box described above, in view to an accurate prediction of the e.m. near and far field, surrounding the box. In the further derivation we apply the TLM-method for the calculation of the near field. The Finite Difference method can be applied in an analoguous way.

Theory

In the following we consider a general physical situation. We define a closed region which contains a structure with complex geometry and the open free-space region around the closed region. The regions are separated by the surface S. We define the closed region as the TLM-region because it is discretized by the TLM method. This TLM-region is coupled to the open region by means of the Green`s function in the time domain. Inside the TLM-region there are present sources. The field which is excited by the given sources produces an incident tangential field ${}^{TLM}\boldsymbol{E}_t^{inc}(r,t)$ and ${}^{TLM}\boldsymbol{H}_t^{inc}(r,t)$ at the interface S. This field is calculated by the TLM algorithm. By applying the continuity of the tangential fields on the interface, we derive the following integral equations as also shown in [7]:

$$\boldsymbol{E}_t(r,t)={}^{TLM}\boldsymbol{E}_t^{inc}(r,t)+\boldsymbol{E}_t^{r}(r,t) \qquad \text{(EFIE)} \qquad (1)$$

$$\boldsymbol{H}_t(r,t)={}^{TLM}\boldsymbol{H}_t^{inc}(r,t)+\boldsymbol{H}_t^{r}(r,t) \qquad \text{(MFIE)} \qquad (2)$$

The fields $\boldsymbol{E}_t(r,t)$, $\boldsymbol{H}_t(r,t)$ represent the unknown total fields at the interface. The fields $\boldsymbol{E}_t^r(r,t)$, $\boldsymbol{H}_t^r(r,t)$ represent the tangential radiated fields. The radiated field is derived as in [7] from the total tangential fields via the free space Green´s functions. With that the equations (1) and (2) are written in a compact matrix form:

$$\boldsymbol{E}_t(r,t)={}^{TLM}\boldsymbol{E}_t^{inc}(r,t)+\tilde{C}_e(r,r',t-\tau)\boldsymbol{E}_t(r',\tau)+\tilde{C}_h(r,r',t-\tau)\boldsymbol{H}_t(r',\tau) \qquad (3a)$$

$$\boldsymbol{H}_t(r,t)={}^{TLM}\boldsymbol{H}_t^{inc}(r,t)+\tilde{D}_e(r,r',t-\tau)\boldsymbol{E}_t(r',\tau)+\tilde{D}_h(r,r',t-\tau)\boldsymbol{H}_t(r',\tau) \qquad (3b)$$

where the matrices $\tilde{C}_e$, $\tilde{C}_h$, $\tilde{D}_e$, $\tilde{D}_h$ represent operators involving integral and differential operations, according to the form of the radiated field of equations (1) and (2). The vectors **r** and **r**´are the destination and source position vectors, respectively. The points **r**' are defined on the radiating interface. The integral equations (3a,3b) have a time-retardation feature $\tau=(r-r')/c$ that allows us to solve them in an iterative way. Since the variable τ in the integral equations (3) is always less than t, the unknown field $E_t(r,t)$ and $H_t(r,t)$ is the sum of the known incident field and an integral that is also known from the past history of the same fields. With that we derive the basis for solving integral equations by iterative methods, [7]. Now we discretize the I.E. by expanding the tangential fields with an appropriate set of functions, in time and in space; the subdomains of such functions are due to the TLM mesh.

$$\boldsymbol{E}_t(\boldsymbol{r},t)=\sum_{m'=1}^{M}\sum_{n'=0}^{N}\boldsymbol{E}_\varphi(\boldsymbol{r}_{m'},t_{n'})\Phi(\boldsymbol{r},\boldsymbol{r}_{m'},t,t_{n'})=\sum_{m'=1}^{M}\sum_{n'=0}^{N}\boldsymbol{E}_\varphi(\boldsymbol{r}_{m'},t_{n'})P(\boldsymbol{r}-\boldsymbol{r}_{m'})T(t-t_{n'}) \tag{4a}$$

$$\boldsymbol{H}_t(\boldsymbol{r},t)=\sum_{m'=1}^{M}\sum_{n'=0}^{N}\boldsymbol{H}_\psi(\boldsymbol{r}_{m'},t_{n'})\Psi(\boldsymbol{r},\boldsymbol{r}_{m'},t,t_{n'})=\sum_{m'=1}^{M}\sum_{n'=0}^{N}\boldsymbol{H}_\psi(\boldsymbol{r}_{n'},t_{n'})Q(\boldsymbol{r}-\boldsymbol{r}_{m'})T(t-t_{n'}) \tag{4b}$$

In eqs. (4) Φ and Ψ denote surface pulse functions of rectangular type, being equal to unity for $\boldsymbol{r}$ on the elementary surface centred at $\boldsymbol{r}_{m'}$. P and Q are time-pulse functions, being equal to unity for t in the time interval centered at $t_{n'}$. We consider M elementary subdomains and N time steps. $\boldsymbol{E}_\varphi$ and $\boldsymbol{H}_\psi$ are the unknown expanding coefficients. Following the Method of Moments, as in [7], we choose the weighting functions

$$W_{mn}(\boldsymbol{r},\boldsymbol{r}_m,t,t_n)=\delta(t-t_n)\delta(\boldsymbol{r}-\boldsymbol{r}_m)\quad\text{with}\quad t_n=n\Delta t \tag{5a}$$

$$\left\langle W_{mn}(\boldsymbol{r},\boldsymbol{r}_m,t,t_n),\Phi(\boldsymbol{r},\boldsymbol{r}_{m'},t,t_{n'})\right\rangle=\int_{-\infty}^{+\infty}dt\iint_S P(\boldsymbol{r}-\boldsymbol{r}_{m'})T(t-t_{n'})\delta(t-t_n)\delta(\boldsymbol{r}-\boldsymbol{r}_m)dS=\delta_{nn'}\delta_{mm'}. \tag{5b}$$

For obtaining a matrix system we give numbers to the coordinates of the fields: m, m', m'' are numbers of the discrete coordinates $\boldsymbol{r}$, $\boldsymbol{r}_{m'}$, $\boldsymbol{r}_{m''}$ and n, n', n'' are numbers of the discrete time steps t, $t_{n'}$, $t_{n''}$. Now, by inserting eq. (4) in (3) and taking the symmetric product with eq. (5a), we derive:

$$\boldsymbol{E}_\varphi(m,n)={}^{TLM}\boldsymbol{E}_t^{inc}(m',n)+\sum_{m'=1}^{M}\sum_{n'=1}^{n}\left\{\tilde{\boldsymbol{K}}_e^E(m,m';n-n')\boldsymbol{E}_\varphi(m',n')+\tilde{\boldsymbol{K}}_h^E(m,m';n-n')\boldsymbol{H}_\psi(m',n')\right\} \tag{6a}$$

$$\boldsymbol{H}_\psi(m,n)={}^{TLM}\boldsymbol{H}_t^{inc}(m',n)+\sum_{m'=1}^{M}\sum_{n'=1}^{n}\left\{\tilde{\boldsymbol{K}}_e^H(m,m';n-n')\boldsymbol{E}_\varphi(m',n')+\tilde{\boldsymbol{K}}_h^H(m,m';n-n')\boldsymbol{H}_\psi(m',n')\right\} \tag{6b}$$

The equations (6) constitute an equation system whose solution permits us to recover iteratively the expanding coefficients of the field. The matricies $\boldsymbol{K}$ involve all the integral and differential operations of the Green's function formulation of the radiated field, which are discretized and evaluated on each elementary subdomain of number m, for every time-step n. The same equations show that, for every cell of number m, the expanding coefficients at time n can be directly computed from the incident field at the same time and the past history of the tangential field in all the cells. This process is called marching-on-in-time method [7]. With that the hybrid method is devided into the following steps: The TLM program starts with the excitation of the fields in the TLM-regions. From that the absorbing boundary conditions on the surface S are derived by the Integral Equation Method. After that the total field at the surface S is derived from the incident field and the past history of the same total field.

Results

We consider a typical EMC-problem which is depicted in Fig.1. We have a metallic box with a rectangular aperture, where the field is excited by an electric dipole **J**. In the following we assume ideal conducting walls. We consider the following physical situation: the cavity is partially filled with dielectric material. We analyze a box of dimension a=100 mm, b=335 mm, c=160 mm, with an aperture of 225x10 mm, referring to Fig.1. We consider an y-directed electric dipole, placed at x=284 mm, z=110 mm and centred in y=50 mm, having a gaussian evolution in the time domain, with amplitude E_{ys} .We partially fill the box by means of a dielectric slab, placed from the bottom of the box up to 30 mm, in the y-direction, as shown in Fig.1.
We place the aperture in the plane z=0. An incident field coming from the source region inside the box impinges on the slot S, producing an equivalent distribution of sources; this, in turns, produces a radiating field to the free-space region. The solution of the problem consists of finding out the distribution of the tangential total field on the surface of the interface where the continuity of the fields is applied. This surface divides all the space in two regions: an internal limited region, where the field is evaluated by the TLM algorithm and an external extended region, where the field is evaluated by means of the free space Green's function. The choice of this separating surface is very important: it can be coincident or not with a physical one. If we choose the slot as the separating surface, as in Fig.1, we apply the continuity of the field (1), (2), providing the integral equations. Then we discretize the field by (4a), (4b) and solve iteratively the matrix system (6a), (6b), finding out the expanding coefficient for the tangential field. After that we choose another separating surface as interface: for example a surface surrounding the slot from five sides, as depicted in Fig.1 with $S=S_2$. In this latter case we have got a more extended surface, but we avoid the problems related to the presence of the field singularities. We analyze our equipment just with this interface $S= S_2$. whose front plane is placed at a distance of 10 mm from the slot.
Now the continuity of the e.m. field is defined on S_2, as well as the domain of the integral equations (1), (2), (3). For a self-consistant comparison, we evaluate the E_y field (normalized with respect to E_{ys}), at a distance of 50 mm far from the slot, in the normal direction in respect to the plane of the slot in two ways: In a first case the fields are calculated by means of the hybrid method, as above described. In the second case the fields are calculated by the pure TLM method. The latter is possible by enlarging the 3-D spatial domain of the TLM despite of a great waste of memory, and by applying absorbing boundary conditions; the dimension of the TLM cell is dl=0.5 mm.

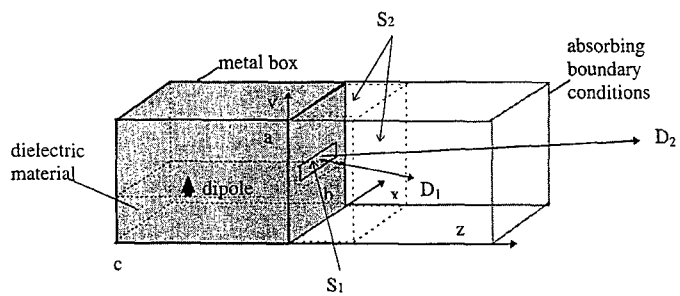

Fig. 1. A metallic box with a rectangular aperture, fed by a vertical electric dipole.

In Fig.2 we compare the E_y field (normalized with respect to E_{ys}), of the hybrid method and the pure TLM method, in the time domain. We use the interface surrounding the slot, whose front plane is placed at a distance of 10 mm from the slot, in a normal direction with respect to the plane of the slot. We consider the ceramics (ε_r=10.8). as a dielectric material. In Fig.3 the same comparison is shown in frequency domain, after a FFT. In both cases we observe a very good agreement between the pure TLM method and the hybrid TLMIE method.

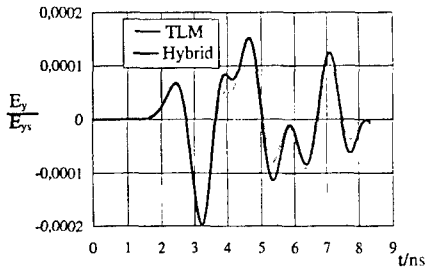

Fig.2. Time evolution of the electric field at a distance of 50 mm from the slot. The interface of the TLMIE method is 10 mm far from the slot. Dielectric: Ceramics (ε_r=10.8). TLM: gray-curve; TLMIE: black-curve.

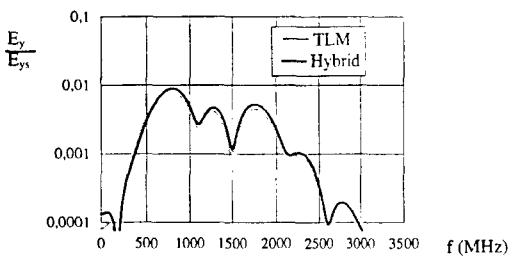

Fig.3. Comparison of the spectra of the electric fields: Ceramics (ε_r=10.8). TLM: gray-curve; TLMIE: black curve.

Now we evaluate the far field with the hybrid method, in order to investigate the behaviour of the radiated emission in real EMC situations. In Fig.4 we report the Ey field in the frequency domain, evaluated at a distance of 1 m far from the box. The curves corresponding to the partially filled box are compared with respect to the corresponding ones of the empty box. In the case of the partially filled box the field amplitude decreases, because a part of the energy is now more confined into the dielectric slab. We note, indeed, the presence of a main resonance around 800 MHz, which can be source of relevant interference to other devices.

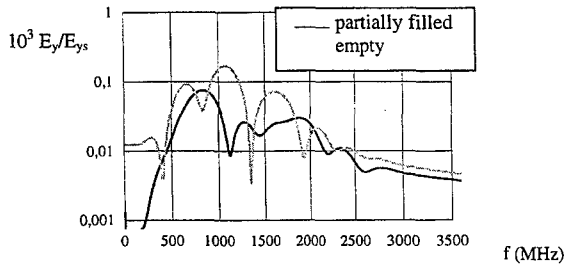

Fig4. Spectrum of the far-field at the distance of 1m far from the slot (Hybrid Method). Dielectric: Ceramics (ε_r=10.8). Empty box: gray-curve; partially filled box: black-curve.

Conclusions

In this contribution we present the development of the hybrid Transmission Line Matrix-Integral Equation (TLMIE) method combining the advantages of both methods. The TLM method is very flexible for modeling general structures with arbitrary shape. The Integral Equation method allows to incorporate the treatment of large free space regions. The general purpose of such a hybrid method is to analyze and predict the radiation phenomena involved in many important practical situations, such as EMC and EMI problems. As an application we consider the radiation from an aperture in a metallic enclosure, partially filled by a dielectric slab. The near field results which are calculated by the TLMIE method are compared with results calculated by the pure TLM method, showing very good agreement.

References

[1] P.B. Johns, "A Symmetrical Condensed Node for the TLM-Method", IEEE Trans. Microwave Theory Tech., vol. MTT-35, no. 4, Apr. 1987, pp. 370-377

[2] K. S. Yee, "Numerical solution of initial boundary value problems involving Maxwell's equations in isotropic media," IEEE Trans. Antenna Propagat., Vol.14, pp. 302-307, May 1966.

[3] R.F. Harrington, „Field Computation by Moment methods".

[4] T.Mader, H.D.Brüns, "EFIE Analysis of Arbitrary Metallic Structures in the Area of EMC", 9th International Symposium and Technical Exhibition on EMC, paper 17D5.

[5] M.Krumpholz and P.Russer, "A Field Theoretical Derivation of TLM", IEEE Trans. Microwave Theory Tech., vol. MTT-42, no. 9 Sept. 1994, pp. 1660-1668.

[6] G.Cerri, R. De Leo and V. Mariani Primiani, "Theoretical and Experimental Evaluation of the Electromagnetic Radiation From Apertures in Shielded Enclosures", IEEE Trans. on EMC, vol. 24, no.4, Nov.1992, pp. 423-432.

[7] Johnson J.H. Wang " Generalized Moment Methods in Electromagnetic", John.Wiley and sons, 1991.

[8] C. R. Cockrell, "The input admittance of the rectangular cavity-backed slot antenna", IEEE Trans. Antennas Propagation, vol. AP-24. no.3, pp. 288-294, May 1976.

[9] B. Audone and M. Balma, "Shielding effectivness of apertures in rectangular cavities", IEEE Trans. Electromagnetic Compatibility, vol. 31. no.1, pp. 102-106, Feb. 1989.

[10] R.F. Harrington and J.R. Mautz, "Computational methods for transmission of waves through apertures", Electromagnetic Scattering, P.L.E. Uslenghi, Ed. New York Academic, 1978, pp. 429-470.

Comparison of Symmetric Condensed TLM, Yee FDTD and Integer Lattice Gas Automata Solutions for a Problem Containing a Sharp Metallic Edge

Neil Simons[1], Riaz Siushansian[2], Joe LoVetri[2], Greg Bridges[3], Michel Cuhaci[1]

[1]Directorate of Antennas and Integrated Electronics
Communications Research Centre
Ottawa, Canada, K2H 8S2

[2]Department of Electrical and Computer Engineering
Faculty of Engineering Science
The University of Western Ontario
London, Canada, N6A 5B9

[3]Department of Electrical and Computer Engineering
University of Manitoba
Winnipeg, Canada, R3T 2N2

Abstract:

A comparison of Yee Finite Difference Time Domain (FDTD), Symmetric Condensed Transmission Line Matrix (TLM) and Integer Lattice Gas Automata (ILGA) solutions is provided for a cavity containing a metallic fin. Differential equation based numerical methods are known to produce inaccurate results for this type of problem, due to the rapid spatial variation in the field distribution in the vicinity of the singularity at the edge of the metal fin. This problem is relevant to the analysis of structures of practical interest such as microstrip and coplanar waveguides. It is determined that the TLM method requires fewer computational cells than Yee FDTD or ILGA to achieve the same accuracy. The computational requirements of each method are not included in the present investigation. Therefore, a statement is not made regarding which method achieves a given accuracy with the smallest computational resources. Surprisingly accurate results are obtained from the ILGA given the low computational cost required to update each cell, and the limited precision used for field variables.

I: Introduction

The Finite Difference Time Domain (FDTD) and the Transmission Line Matrix (TLM) methods are numerical techniques capable of determining an approximate solution of the time-dependent Maxwell's equations in the presence of complex environments [1], [2]. The Integer Lattice Gas Automata (ILGA) approach is a new approach for solving EM field problems. The ILGA strategy is based on the combination of algorithms which use low-precision integer variables with special-purpose computational hardware [3-5].

In this paper we investigate the relative accuracy of the Yee FDTD, symmetric-condensed TLM [6], and ILGA approaches for problems which contain sharp metallic edges. The specific problem we examine is a perfectly conducting cavity with metal fins. The cross-section of the geometry of the problem is inset within Fig. 1. This cross-section lies in the x-y plane. The boundaries are perfectly conducting, with free space material assumed within the cavity (ε_o, μ_o, σ=0). We consider the specific case: $a=32mm$, $b=16mm$ and various gap sizes, d. The problem is

effectively two-dimensional due to the placement of magnetic walls on the minimum and maximum surfaces in the x-y plane. However, in the case of the TLM and FDTD methods the three-dimensional algorithms are applied. This specific geometry has been previously investigated [7-9]. The methods are known to shift the frequency domain characteristics of the solutions due to their inability to accurately model the rapid spatial variation of the field distribution in the vicinity of the metal fin. Although the geometry of this problem is simple, it isolates the errors caused by the metallic edge, referred to as *coarseness error*, from other sources of error. Dispersive errors have been investigated in [10], where a comparison of different finite-difference algorithms is provided.

Numerical methods have been proposed for overcoming the inaccuracies described above. In [7], the structure was analyzed for a few different mesh sizes, and the resultant solutions extrapolated to the limit of an infinitely fine mesh. In [8], a local mesh modification scheme is provided which eliminates the error from the solution. In [9], a comparison of local mesh modifications and mesh refinement using a graded mesh are presented. Other approaches include the use of an unstructured mesh in order to increase the physical discretization in the region surrounding the metallic edge. This allows the second-order approximation to be applied over shorter physical lengths, and therefore obtain a more accurate fit to the field distribution. The FDTD [11] and TLM [12] methodologies are compatible with unstructured meshes. Higher-order algorithms would more accurately predict the rapidly varying field distribution [13-16].

Given the significant errors obtained for typical discretizations in the TLM, FDTD and ILGA solutions, an opportunity exists to compare their relative accuracy for problems containing sharp field discontinuities. The purpose of this paper is therefore to quantitatively determine the relative accuracy of the methods.

II: A Benchmark Solution

In order to obtain benchmark solutions for the resonant frequency for various gap sizes, we analyze the problem using the TLM and FDTD methods on increasingly fine meshes. We consider cubic mesh sizes of Δl= 1.0, 0.5, 0.25, and 0.125mm for both the x and y directions. The simulations for these mesh sizes were run for 8000, 16000, 32000, and 64000 time steps, respectively. The FDTD algorithm is run at the limit of stability. For each gap size, and for each method, the predictions for b/λ versus cell size (where λ is the wavelength corresponding to the first resonance of the cavity) are fit to a linear function. The *y-intercept* of these linear functions is an estimate of the solution for $\Delta l \to 0$, an infinitely-fine discretized problem. Shih and Hoefer have utilized a similar strategy [7]. These estimated values are provided in Table I. We select the benchmark solution to the problem as the average of the TLM and FDTD estimates. For the two specific gap sizes common to both our investigation and that of Shih and Hoefer [7], our benchmark solution is identical to that provided by the Transverse Resonance Method [7]. Data in [7] is only provided to four decimal places.

Table I: TLM and FDTD Prediction of b/λ for $\Delta l \to 0$ and the Benchmark Solution for various Gap Sizes.

Gap Size, d(mm)	TLM ($\Delta l \to 0$)	FDTD ($\Delta l \to 0$)	Benchmark Solution
4	0.192791	0.192794	0.192792
6	0.210921	0.210648	0.210784
8	0.224782	0.224959	0.224870
10	0.235851	0.236001	0.235926
12	0.243742	0.243806	0.243774

In Fig. 1, the percent difference of the solutions from the benchmark for b/λ are provided versus gap size for $\Delta l = 0.5mm$. Error decreases as gap size increases because the problem approaches that of a simple two-dimensional waveguide cross section. For the case of a simple two-dimensional waveguide cross-section, the error in the TLM and FDTD solutions is due only to dispersive errors. The inverse of the discretization ratio, $\lambda/\Delta l$ is always greater than 64 in our calculations, and therefore these errors are minimal [17].

In the ILGA simulations in addition to the dispersion errors an additional damping is observed. The damping is similar to the effect of viscosity in a fluid. For sinusoidal plane waves with a wavenumber k the damping is of the form e^{-kvt}. The value of damping factor v has been determined numerically to vary from $0.4\Delta l^2/\Delta t$ for a traditional single-bit HPP LGA [4], to $0.006\Delta l^2/\Delta t$ for the four-bit per direction ILGA model utilized in the present investigation.

III: Comparison of FDTD, TLM and ILGA Solutions

We now compare the FDTD, TLM, and ILGA solutions with the benchmark solution in order to determine the Δl required by the methods in order to achieve the same accuracy. In Fig. 1, the percent difference of the solutions from the benchmark are provided versus Δl for two gap sizes (d=4.0mm and 12.0mm). As expected, the curves appear to intersect the point (0,0), indicating the error reduces to zero as $\Delta l \rightarrow 0$. For any given Δl considered, TLM is more accurate than FDTD and ILGA, i.e., the percent error in the TLM solution is always less than that of the FDTD or ILGA solution. The curves for the errors versus cell size appear to be linear for all three methods. The slopes of the curves in Fig. 1 can be used to provide a relative measure of accuracy for the methods since the slopes represent the increase in solution error for a given increase in Δl. Table II contains the slopes of the curves of Fig. 1 (as well as for gap sizes of 6.0, 8.0, and 10.0mm not shown in Fig. 1). The slopes are greater for the FDTD method, indicating a larger increase in solution error for the same increase in Δl. The ratio of the slopes is equivalent to $\Delta l_{FDTD}/\Delta l_{TLM}$, the ratio of cell sizes required by each method to obtain the same accuracy of solution. The average value of $Slope_{FDTD}/Slope_{TLM}$ is approximately 1.5 indicating that 1.5 times more FDTD cells are required to achieve the same accuracy as TLM. The ILGA data points of Fig. 1 indicate that the ILGA requires approximately twice the discretization as the FDTD method, and therefore approximately three times the discretization as TLM.

Table II: Slopes of the lines of Fig. 1 (as well as for gap sizes of 6.0, 8.0, and 10.0 mm not shown in Fig. 1).

Gap Size, d(mm)	Slope (TLM)	Slope (FDTD)	Slope (FDTD)/ Slope (TLM)
4	0.3282	0.4788	1.46
6	0.2573	0.3422	1.33
8	0.1671	0.2601	1.56
10	0.1196	0.1893	1.58
12	0.0802	0.1233	1.54

IV: Discussion/Conclusions

A comparison of the accuracy of TLM, FDTD and ILGA algorithms for the analysis of a perfectly conducting cavity possessing sharp metallic edges has been presented. The shift in resonant frequency observed in the solutions to this problem is due to the inability of the methods to accurately model the rapid spatial variation in the field distribution in the vicinity of the singularity at the edge of the strip. We obtain a benchmark solution with which to compare our calculations by extrapolating the solutions on meshes of different cell size to the limit of an infinitely fine mesh.

The FDTD and ILGA meshes must be approximately 1.5 and 3.0 times as fine, respectively, as the TLM mesh (per spatial dimension of the problem) in order to achieve the same accuracy as TLM. Although the ILGA requires 3.0 times as many cells as the TLM algorithm, the relatively simple computational requirements make it an attractive approach (simple table look-up computation rather than floating point operations). Future work can compare the computational requirements of the three methods (memory and cpu time) to achieve the same accuracy based on our determination of the relative meshing requirements.

---

[1] K. S. Kunz and R. J. Luebbers, **The Finite Difference Time Domain Method for Electromagnetics**, CRC Press, 1993.

[2] C. Christopoulos, **The Transmission Line Modelling Method (TLM),** Piscataway, NJ: IEEE Press, 1993.

[3] N. R. S. Simons, G. Bridges, D. Cule, M. Zhang, M. Cuhaci, "Sources of Error within Lattice Gas Automata Simulation of Electromagnetic Field Problems", *ACES'97*, Monterey CA, vol. II, pp. 1465, 1997.

[4] G. Doolen (ed.), **Lattice Gas Methods for Partial Differential Equations**, Santa Fe Inst. (Addison-Wesley), 1990.

[5] N. Margolus, "CAM-8: a computer architecture based on cellular automata", in: **Pattern Formation and Lattice Gas Automata**, (ed: R. Kapral, A. Lawniczak) American Mathematics Society (Fields Institute Series), 1995.

[6] P. B. Johns, "A Symmetrical Condensed Node for the TLM Method," *IEEE Transactions on Microwave Theory and Techniques*, vol. 35, no. 4, pp. 370-377, 1987.

[7] Y-C. Shih, W. J. R. Hoefer, "The Accuracy of TLM Analysis of Finned Rectangular Waveguide", *IEEE Transactions on Microwave Theory and Techniques*, vol. 28, no. 7, pp. 743-746, July 1980.

[8] J. L. Herring, W. J. R. Hoefer, "Improved Correction for 3-D TLM Coarseness Error", *Electronics Letters*, vol. 30, no. 14, pp. 1149-1150, July 7, 1994.

[9] J. L. Herring, W. J. R. Hoefer, "Accurate Modelling of Zero Thickness Septa with the Symmetric Condensed Node", *First International Workshop on Transmission Line Matrix (TLM) Modelling - Theory and Applications*, pp. 237-240, 1995.

[10] K. L. Shlager, J. G. Maloney, S. L. Ray and A. F. Peterson, "Relative Accuracy of Several Finite-Difference Time-Domain Methods in Two and Three Dimensions," *IEEE Transactions on Antennas and Propagation*, vol. AP-41, no. 12, pp. 1732-1737, December 1993.

[11] S. D. Gedney, F. Lansing, "Explicit Time-Domain Solution of Maxwell's Equations Using Nonorthogonal and Unstructured Grids", *Chapter 11 in:* A. Taflove, **Computational Electrodynamics: The Finite-Difference Time-Domain Method**, Artech House, pp. 70-71, 1995.

[12] N. R. S. Simons and J. LoVetri, "Derivation of Two-Dimensional TLM Algorithms on Arbitrary Grids Using Finite Element Concepts", *First International Workshop on Transmission Line Matrix (TLM) Modelling - Theory and Applications*, pp. 47-54, 1995.

[13] J. Fang and K. K. Mei, "A Higher Order Finite Difference Scheme for the Solution of Maxwell's Equations in the Time Domain," Proceeding of the 1989 URSI Radio Science Meeting, San Jose, California, 1989.

[14] T. Deveze, L. Beaulieu and W. Tabbara, "A Fourth Order Scheme for the FDTD Algorithm Applied to Maxwell's Equations," *1992 IEEE AP-S International Symposium*, Chicago Illinois, pp. 346-349, 1992.

[15] N. R. S. Simons and A. Sebak, "Fourth-Order in Space and Second-Order in Time TLM Model", *IEEE Transactions on Microwave Theory and Techniques*, vol. 43, no. 2, pp. 437-444, February 1995.

[16] G. Haussmann and M. Piket-May, "FDTD M24 Dispersion and Stability in Three Dimensions", *13th Annual Review of Progress in Applied Computational Electromagnetics*, Monterey CA., pp. 82-89, 1997.

[17] A. Taflove, **Computational Electrodynamics: The Finite-Difference Time-Domain Method**, Artech House, pp. 99, 1995.

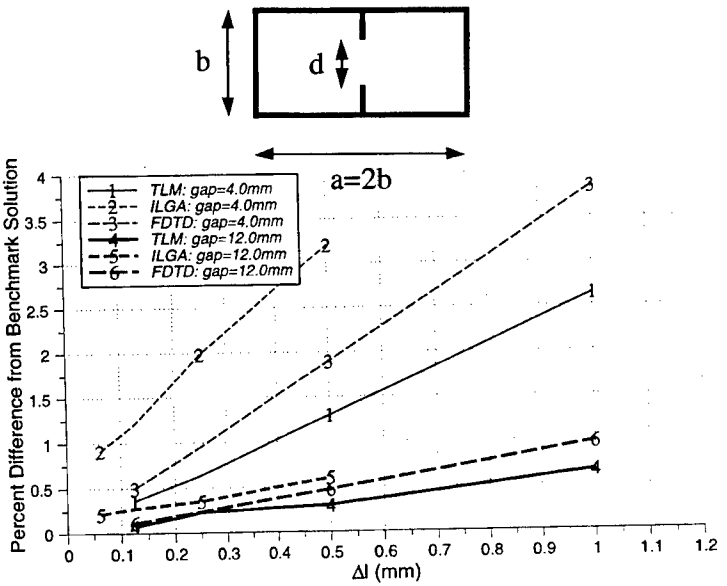

Figure 1: Comparison of the percent difference of TLM, FDTD, and ILGA solutions for b/λ from the benchmark solutions versus mesh discretization, Δl. Curves are provided for gap sizes, d of 4.0mm and 12.0mm.

Some observations on stubs, boundaries and parity effects in TLM models

Donard de Cogan (ddc@sys.uea.ac.uk), **Cai Kun***
School of Information Systems, University of East Anglia, Norwich NR4 7TJ (UK)

Introduction

To a large extent TLM is still strongly dependent on its roots. We as users tend to start from the algorithms as they were originally defined and to develop them from that point. However unwilling we may be some element of change has been forced upon us. We believe that there are much wider implications which affects both lossless and lossy formulations. As TLM approaches maturity it is important to stand back and re-examine it in a slightly more sceptical manner. For instance, more attention needs to be focused on the use of alternative stubs and their correct placement. In this paper we look at three specific aspects: spurious effects, time-step changes and the scalar pml.

Spurious effects

Anomalous 'jumps-to-zero' are observed in many numerical models for spatial propagation in the time domain. The occurrence is dependent on the initial conditions in a system. Single-shot excitation is a primary requirement, as the contributions of successive inputs in continuous or band-limited excitation may mask the effect. In the case of multiple excitation a saw-tooth diffusion profile can be observed if there are an odd number of excitations at a single point or at an odd number of adjacent points. Boundaries are known to play a part; they can either accommodate or inhibit the effect. Many of these anomalies are not normally observed in two-dimensional lossless algorithms because of band limiting, but they frequently observed in one-, two- and three-dimensional lossy TLM, where $0 < \rho < 1$.

When lossy TLM nodes are used to model diffusion phenomena there is an element of choice about the positioning of the transmission line and the associated resistance which is represented as a lumped electrical component. We can have the node centre positioned at the join between two resistors and such arrangements are called 'link-line' nodes (figure 1(a)). The alternative is to have the resistors as the links to adjacent nodes and such arrangements are called link-resistor nodes (figure 1(b)).

We can demonstrate 'jumps-to-zero' and saw-tooth effects using a one-dimensional link-line TLM model. We start with a sample which has a single unit magnitude injection to left and to right at time $t = 0$. This is allowed to propagate for 10 iterations with $\rho = \tau = 0.5$. The output in figure 2(a) clearly shows jumps-to-zero. We could reduce both the time and space discretisations by a factor 2. In order to achieve the same injection conditions as previously we now have to inject inputs of magnitude 1/4 to left and right in each of two adjacent nodes during the first two time-steps. The reflection and transmission coefficients are now $\rho = 1/3$ and $\tau = 2/3$. The simulation is run for 20 iterations and the results are shown in figure 2(b). We can proceed further by reducing the space and time-discretisations of the original problem by a factor 3. This means that injections of 1/9 are input to left and right at three adjacent nodes during three iterations. The reflection and transmission coefficients are $\rho = 1/4$ and $\tau = 3/4$ and there are 30 iterations. In this case the output (figure 2(c))

has a saw-tooth profile. This process of magnification can be continued when it will be observed that every even sub-division yields a smooth profile. Of course, the saw-tooth profile becomes finer as the level of odd-subdivision is increased.

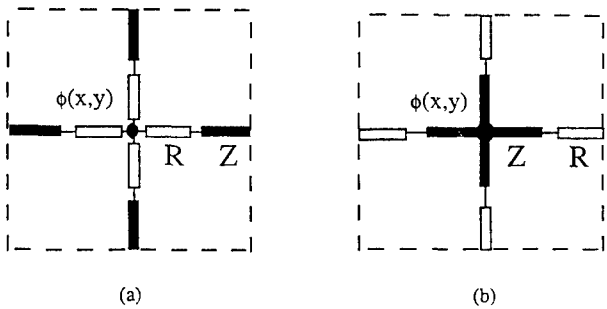

Figure 1. (a) a link-line node (b) a link-resistor node

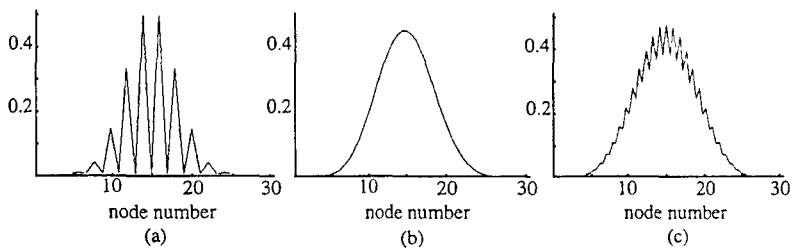

Figure 2. Diffusion simulation showing concentration as a function of nodal position using a one-dimensional link-line TLM model divided into 20 nodes: (a) single shot injection after 10 iterations, (b) $\Delta x \rightarrow \Delta x/2$, $\Delta t \rightarrow \Delta t/2$, (c) $\Delta x \rightarrow \Delta x/3$, $\Delta t \rightarrow \Delta t/3$

We can now review some observations concerning these anomalies in TLM models. Even if there is a single-shot initial excitation 'jumps-to-zero' will not be observed if:

- link-resistor nodal formulations are used (lossy TLM only)
- the excitation point is located between two link-line nodes (lossy TLM only)
- a boundary is placed between two nodes (applies to lossy and lossless TLM)
- conventional ($\Delta x/2$) stubs are used (applies to lossy and lossless TLM nodes)

Spurious modes, ATLM, sampling and redundancy

The question of mesh parity has been addressed by Russer [1]. Since states of even and odd parity are independent of each other, their interconnection may cause the propagation of spurious solutions. This has led to the suggestion of ATLM, the computation of states with even parity (sample every $2\Delta t$). States with odd parity can be obtained by interpolation. Pulko et al [2] have noted that

observations made at Δt in a link-line lossy mesh of nodal length Δx represent a significant redundancy. There is no loss of accuracy if the same mesh is sampled at intervals of $2\Delta t$. This is quite distinct from a mesh of length $2\Delta x$ sampled at $2\Delta t$. These observations are consistent with the work of Enders and de Cogan [3] on two-dimensional random-walk models where it is noted that the propagation space comprises two separate sub-systems with identical equations of motion, but different initial conditions.

The behaviour of scattering processes can also be interpreted in terms of sampling. In the link-line node the signals travelling a distance Δx, are sampled at time intervals Δt and are coincidentally scattered at the same locations. In a one-dimensional link-resistor node the signals are sampled at the centre of the node. They then travel a distance $\Delta x/2$ during time $\Delta t/2$, where they undergo scattering at the interface between transmission line and resistors. The transmitted and reflected pulses then arrive at locations (x-1), x and (x+1) after another time $\Delta t/2$, where sampling again takes place. Thus the network is sampled at intervals Δt with scattering events occurring at distances $\Delta x/2$ from the sample point. This could be interpreted as a network with fundamental mesh distance $\Delta x/2$ sampled at Δt which is the equivalent of the Pulko system with all redundancy removed. In two-dimensional link-resistor nodes there is one scattering event at the node centre with reflection coefficient $\rho_{node} = -1/2$ and $\tau_{node} = 1/2$. There are 4 separate scattering events at the resistor links with $\rho_{link} = R/(R+Z)$ and $\tau_{link} = Z/(R+Z)$. Sampling occurs at the node centre at intervals, Δt, but scattering events occur at distances $\Delta x/2$.

Stubs and boundaries

The ATLM scheme has been proposed to avoid the propagation of spurious modes. Pulko's suggestion of sampling at alternate time-steps in a link-line lossy TLM network avoids 'jumps-to-zero' and reduces computational load. However, it is believed that these principles have wider implications than have been appreciated up to now. A boundary placed at the interface between nodes forces a mixing between the meshes of a lossless or link-line lossy TLM model. If boundaries are to be located between nodes then a link-resistor network should be used in lossy TLM formulations. Otherwise the boundary should be located at a distance Δx from the node, so that its response is returned to the mesh with the correct parity. Similarly, the location and timing of an excitation may be important.

Conventional TLM stubs of length $\Delta x/2$ will return a signal to the node after a time interval Δt. This will give rise to mixing in lossless networks. In lossy meshes the positioning of the stub is also significant. Mesh mixing will normally occur if it is placed between the resistors. For this reason a stub of length Δx is recommended. On the other hand it is possible to use a conventional half-length stub so long as it is located at the centre of a transmission line. By this means link-resistor formulations can be successfully sampled at intervals Δt and link-line formulations at intervals $\Delta t/2$.

Time-step changes in TLM models

On 12 April 1988 one of the authors (DdeC) penned a note to Peter Johns with a suggestion that time-step changes should be implemented at the node and not, as is conventional at the half-steps between iterations. His response was not encouraging and the matter was left in abeyance until recently. The normal method of time-step change which is described in reference [4] takes the scattered pulses and transforms them into the new time frame at the middle of the link transmission lines. The conservation of nodal voltage and line current yields

$$\begin{bmatrix} {}^{s}V'_1 \\ {}^{s}V'_2 \end{bmatrix} = \frac{1}{2} \begin{bmatrix} (1 + \frac{\Delta t'}{\Delta t}) & (1 - \frac{\Delta t'}{\Delta t}) \\ (1 - \frac{\Delta t'}{\Delta t}) & (1 + \frac{\Delta t'}{\Delta t}) \end{bmatrix} \begin{bmatrix} {}^{s}V_1 \\ {}^{s}V_2 \end{bmatrix} \qquad (1)$$

This immediately introduces a mixing between the interlaced meshes. A time-step transformation which takes place at the node does not and is consistent with the ATLM approach. On the other hand, the conventional approach is ideally suited for a link-resistor formulation. It is clear that is is effectively operating at the node centre of this type of mesh and will not lead to anomalies.

Stubs and the scalar PML

At the 1997 ACES Meeting de Cogan and Chen [5] proposed what was effectively a scalar absorbing node. This involved a set of special lossy nodes which could be placed around the periphery of a lossless region. The requirements were that the lossy nodes had to be both matched and distortionless. It was shown that these conditions could not be achieved without the inclusion of a stub. The results which were presented indicated the existence of dispersion which frequency limited the application of this boundary. However, it must be remembered that the open-circuit stub which was used is an approximation to a capacitance and any formulation will be troubled by an error inductance due to the line. We now believe that there is no reason (except convention amongst TLM modellers) why an infinitely long stub should not be used. Such a stub would have $\rho_{St} = 0$ and would have no error inductance or capacitance.

Recent work has confirmed this observation. A boundary consisting of distortionless matched nodes with 'infinite' stubs was found to introduce no dispersion effects. However it was noted that the return signal was very sensitive to the precise coincidence of the matching and distortionless conditions. An input pulse of magnitude 1000 was allowed to traverse a one-dimensional lossless mesh before interacting with a string of absorbing nodes each with $Z_{St} = 0.1$ ($\rho_{St} = 0$), R = 0.99602 and r = 0.004149. The return signal was inverted with magnitude 2×10^{-2} and displayed no dispersion. However when the node was defined with greater resolution (R = 0.99602447204 and r = 0.00414872477) the sign of the return signal was a perfect copy of the original, but with an amplitude of 1.75×10^{-13}.

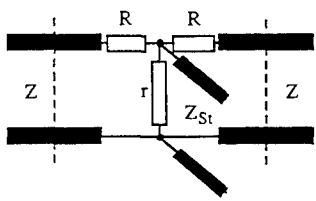

Figure 3. A lossy node with shunt resistance and stub for distortionless matching to a lossless line.

We now have a broad-band attenuation network which can be treated as a filter whose output can be given by F V_{in}. At present, this is placed between nodes so that the incident pulses in a one-dimensional formulation are given by:

$$ {}_{k+1}{}^{i}V_L(x) = F_L(x)\, {}_{k}{}^{s}V_R(x-1) \qquad {}_{k+1}{}^{i}V_R(X) = F_R(x)\, {}_{k}{}^{s}V_L(x+1) \qquad (2) $$

There are similar expressions for two and three-dimensional formulations. This is identical to the empirical approach used by O'Connor [6] whereby a scalar factor, F is gradually changed from unity to zero to obtain total absorption of signals.

Conclusion

These observations have been drawn from the wider field of TLM but are important in electromagnetic modelling. Excitations, storage elements (stubs), time-step changes and boundaries

should not lead to mixing between meshes of different parity and we have proposed schemes which would ensure this. Our distortionless, absorbing network still resides at the mid-point between lossless nodes, but as it is perfectly matched, there is no spurious return signal and therefore no mode mixing.

References

1. P. Russer, *On the field theoretical foundations of the transmission line matrix method* Proc. First International Workshop on Transmission Line Matrix (TLM) Modelling - Theory and Applications, University of Victoria (BC), August 1995 pp 3 - 12

2. S.H. Pulko, A.J. Wilkinson and M. Gallagher, *Redundancy and its implications in TLM diffusion models* Int. Jnl. Numerical Modelling **6** (1993) 135 - 144

3. P. Enders and D. de Cogan, *Discrete Modelling of Transport Processes in Two Spatial Dimensions* Int. Jnl. of Numerical Modelling **5** (1992) 121 - 129

4. S.H. Pulko, A. Mallik, R. Allen and P.B. Johns, *Automatic timestepping in TLM routines for the modelling of thermal diffusion processes* Int. Jnl. of Numerical Modelling **3** (1990) 127 - 136

5. D. de Cogan and Z. Chen, *Towards a TLM description of an open-boundary condition* Proceedings of 13th Annual Review of Progress in Applied Computational Electromagnetics (ACES-97), Naval Postgraduate School, Monterey CA March 17-21 1997 pp 655 - 660

6. W. O'Connor (Department of Mechanical Engineering, University College, Dublin) *private communication*

Modelling of dispersive media in TLM using the propagator approach

Jürgen Rebel and Peter Russer

Lehrstuhl für Hochfrequenztechnik an der Technischen Universität München

Abstract

In this paper a new approach for modelling dispersive media with the Transmission Line Matrix (TLM) method is presented. The updating relations for a dielectric node are derived utilizing the so called propagator approach. A perturbed TLM process yields the solution for the discretized coupled Maxwell and Polarization equations. Canonical stability criteria are provided by the propagator approach. Experimental results for a TEM parallel plate waveguide, partially filled with a model dispersive dielectric are presented and validate the approach.

1 Introduction

A growing interest in modelling dispersive and non-reciprocal media with TLM has become apparent [1, 2, 3, 4, 5].
In FDTD, three types of approaches can be distinguished for treating dispersive media. First, an implementation of a discrete convolution of the dispersion relation [6]. Second, methods that discretize a differential equation which relates $\mathbf{D}(t)$ and $\mathbf{E}(t)$ [7]. Third, Z-transform methods [8].
In TLM, approaches are the modification of John's scattering matrix by Dawson's method or state space representations which lead to adaptive matrix elments via a time dependent equivalent conductance [3, 1, 4]. A major problem with these techniques is that the involved TLM processes easily become unstable and their practical use is hence limited. Furthermore, the modelling of dispersive media in this way lacks mathematical rigor.
With the development of the so called propagator approach Hein has created a powerful framework for the synthesis of TLM algorithms [9, 10]. So far, this concept has been applied to the modelling of ferrites by developing a TLM solution for the coupled Bloch-Maxwell equations, for non-orthogonal TLM grids and superconducting bounderies [2, 9, 10, 11].
In this paper, we apply this concept to the modelling of dispersive media, whose frequency dependence is described by a Debye model. The derivation is similar to the analysis presented in [2] , but we have abstained from incorporating a non-orthogonal mesh.

2 The propagator approach

2.1 The discrete propagator

In the following we work in the Hilbert Space $\mathcal{H}_v$ over $\mathcal{R}^n$, which is defined in [12]. The center of a node is located at position l, m, n. Wave pulses are at the node at normed time k and at the cell boundary at times $k \pm \frac{1}{2}$. The complete time evolution of the whole TLM system can be described by [12]

$$|b>= \mathbf{TS}|a> \qquad |a>= \mathbf{\Gamma}|b> \tag{1}$$

$\mathbf{S}$ denotes the nodal scattering operator, $\mathbf{T}$ is the time shift operator, and $\mathbf{\Gamma}$ the connection operator which handels the exchange of the quantities at the cell boundaries with the surrounding cells.
Hein [9] has shown, that the time evolution of a single TLM cell can locally be described by

$$_k\mathbf{b} = \mathbf{\Psi}_k\mathbf{a} \tag{2}$$

where ${}_k\mathbf{a}$ and ${}_k\mathbf{b}$ are the vectors of incident and reflected wave pulses at the node. The same relation is valid for the wave pulses at the boundaries at times $k \pm \frac{1}{2}$, i.e. all indices k are replaced by $k \pm \frac{1}{2}$. $\mathbf{\Psi}$ is the so called *discrete* propagator which is defined as

$$\mathbf{\Psi} = \mathbf{S} \sum_{\mu=1}^{\infty} (\mathbf{PS})^{\mu-1} \mathbf{QT}^{\mu} \tag{3}$$

with $\mathbf{P}$ and $\mathbf{Q}$ being the projectors into the stub and link subspaces. For this approach, it is essential that the quantities of the stub subspace are *non-observable* from outside.
A complete TLM system $(\mathbf{\Gamma}, \mathbf{\Psi}_\zeta)$ can thus be characterized by the connection operator $\mathbf{\Gamma}$ and a family of cell dependent reflection operators $\mathbf{\Psi}_\zeta$ [2, 10]. $\mathbf{\Psi}_\zeta$ describe essentially different types of nodes (more precisely, they describe the time evolution of different types of nodes with scattering operators $\mathbf{S}_\zeta$).

2.2 Connection to finite difference equations

A system of partial differential equations may be written in operator notation as

$$\mathcal{L}\mathbf{u} = 0 \tag{4}$$

where $\mathcal{L}$ is the differential operator. After discretization, a set of finite difference equations with linear and real valued difference operators $\mathbf{\Delta}$ and $\mathbf{F}_\mu$ (which may be functions of the spatial shift operators, for example) may be written in Hilbert Space formulation as

$$\mathbf{\Delta T}_h |\mathbf{F}> = \sum_{\mu=0}^{\infty} \mathbf{F}_\mu \mathbf{T}^{\mu} |\mathbf{F}> \tag{5}$$

The operators $\mathbf{\Delta}$ and $\mathbf{F}_\mu$ will be specified in section 3.2. $\mathbf{T}_h$ denotes the time shift operator which decrements k by $\frac{1}{2}$. $|\mathbf{F}>$ represents the state vector of the finite difference system.
The idea behind the propagator approach is, that a TLM system $(\mathbf{\Gamma}, \mathbf{\Psi}_\zeta)$ generates solutions to these finite difference equations. Hence, the responses of the TLM process (1) have to fulfill the finite difference equations at *every* time step for the same initial values. From this identity at every time step, the scattering parameters of $\mathbf{S}$ can be derived *uniquely* . As a consequence, the discrete propagator relation needs to be written in a canonical representation where all the finite-difference relations are decoupled. This is achieved by an orthonormal transformation $\mathbf{D}$ (which leaves the scattering response of the discrete propagator unchanged). Hence the scattering operator written in matrix form takes the canonical form

$$\tilde{\mathbf{S}} = \mathbf{DSD}^{-1} = \begin{bmatrix} \mathbf{S}_E & & & \\ & -\mathbf{Id}_{3\times3} & & \\ & & \mathbf{S}_H & \\ & & & \mathbf{Id}_{3\times3} \end{bmatrix} \tag{6}$$

$\mathbf{Id}$ denotes the identity operator written as identity matrix in matrix form. These identity blocks are a consequence of the "parcel twines " lemma and can be viewed as an explicit consequence of the divergence conditions of Maxwell's equations [10] (In the following we shall not distinguish between operators and their associated matrices).
$\mathbf{S}$ denotes the representation of $\tilde{\mathbf{S}}$ in the "normal" TLM world, which has the structure of John's original matrix [1]. Details to the transformation $\mathbf{D}$ can be found in [9, 11], and its origin will be sketched in a later section of this paper. In order to derive the nodal scattering parameters, the blocks $\mathbf{S}_E$ and $\mathbf{S}_H$ (both are 6×6 matrices) can be decomposed into four blocks using the relation $\mathbf{Id} = \mathbf{Q}_j + \mathbf{P}_j$ (j denoting E or H). $\mathbf{Q}_j$ and $\mathbf{P}_j$ are the respective projectors into the link and stub subspaces of $\mathbf{S}_j$. The decomposition of $\mathbf{S}_j$ results in

$$\mathbf{S}_j = \underbrace{\mathbf{Q}_j\mathbf{S}\mathbf{Q}_j}_{\mathbf{K}_j} + \underbrace{\mathbf{Q}_j\mathbf{S}\mathbf{P}_j}_{\mathbf{L}_j} + \underbrace{\mathbf{P}_j\mathbf{S}\mathbf{Q}_j}_{\mathbf{M}_j} + \underbrace{\mathbf{P}_j\mathbf{S}\mathbf{P}_j}_{\mathbf{N}_j} \tag{7}$$

[1] In the following, the skew is omitted, if it is clear in which representation a matrix is given

In order to get simple relations, the process (2) is started with a Dirac pulse $\mathbf{a}_0$ at time $k = -\frac{1}{2}$ and the response of the system for the respective subspaces is calculated for time k to:

k	${}_{k\pm\frac{1}{2}}\mathbf{b}$ (cell boundary)	${}_{k}\mathbf{b}$ (node centre)
0	0	$\mathbf{K}_j\mathbf{a}_0$
1	$\mathbf{K}_j\mathbf{a}_0$	$\mathbf{L}_j\mathbf{M}_j\mathbf{a}_0$
≥ 2	$\mathbf{L}_j\mathbf{N}_j^{k-2}\mathbf{M}_j\mathbf{a}_0$	$\mathbf{L}_j\mathbf{N}_j^{k-1}\mathbf{M}_j\mathbf{a}_0$

2.3 Perturbed TLM processes

If the finite difference scheme described by equation (5) would be dependent on a large number of past values, e g. due to the evaluation of a discrete convolution in time, it would take the form

$$\mathbf{\Delta T}_k|\mathbf{F}'> = \sum_{\mu=0}^{\infty} \mathbf{F}_\mu \mathbf{T}^\mu |\mathbf{F}'> + \mathbf{G}\left[\sum_{\mu=0}^{\infty} \mathbf{T}^\mu |\mathbf{F}'>\right] \tag{8}$$

The operator $\mathbf{G}[..]$ can possibly be nonlinear (this is the reason, why the infinite sum as *a whole* is taken as its argument). Clearly, a TLM system with different reflection operators $\mathbf{\Psi}'_\zeta$ may generate solutions to this finite-difference equation, as the connection operator $\mathbf{\Gamma}$ remains unchanged. It can be shown, that there exists a necessary condition for the existence of solutions to (8) generated by the dashed TLM system $(\mathbf{\Gamma}, \mathbf{\Psi}'_\zeta)$, which relates $\mathbf{\Psi}'_\zeta$ and $\mathbf{\Psi}_\zeta$. Hence, the dashed TLM system generates solutions to finite difference equation (8), iff a real valued casual operator ${}_k\mathbf{D}[..]$ exists, satisfying

$${}_k\mathbf{D}\left[\sum_{\mu=0}^{\infty} \mathbf{T}^\mu |\mathbf{F}'>\right] = \mathbf{\Psi}' - \mathbf{\Psi} \tag{9}$$

The operator ${}_k\mathbf{D}[..]$ may be dependent upon time, which is indicated by the index k. The relation between $\mathbf{\Psi}$ and $\mathbf{\Psi}'$ implies that the undashed system $(\mathbf{\Gamma}, \mathbf{\Psi}_\zeta)$ can *also* generate solutions to the "perturbed" finite difference equations (8) in a so called "truncated" process if equation (9) is rearranged. This means, in addition to the normal scattering, another vector $\mathbf{d}$ is updated at every time step. Details are provided in references [2, 10].

3 Discretization of the coupled Maxwell - Polarization equations

We have seen how nodal scattering parameters can *directly* be derived from finite difference equations. In this section we are going to discretize the coupled Maxwell - Polarization equations along lines, similar to the discretization procedure of the coupled Bloch - Maxwell equations [2]. We have restricted ourselves to the use of a graded mesh and the modelling of anisotropic behaviour along the principle axes.

3.1 The coupled Maxwell - Polarization equations

In integral formulation, Maxwell's equations take in nonmagnetic dielectrics the following form

$$\int_{\partial A} \mathbf{H} \cdot d\mathbf{l} = \int_A \left(\sigma \mathbf{E} + \varepsilon_0 \varepsilon_\infty \frac{\partial}{\partial t}\mathbf{E}\right) \cdot d\mathbf{A} + \frac{\partial}{\partial t}\int_A \mathbf{P} \cdot d\mathbf{A} \tag{10}$$

$$-\int_{\partial A} \mathbf{E} \cdot d\mathbf{l} = \mu_0 \frac{\partial}{\partial t}\int_A \mathbf{H} \cdot d\mathbf{A} \tag{11}$$

Anisotropic ohmic loss along the principal axes is considered by $\sigma = Diag(_x\sigma, _y\sigma, _z\sigma)$. ε_0 is the permittivity of free space. The permittivity for $\omega \to \infty$ is given by $\varepsilon_\infty = Diag(_x\varepsilon_\infty, _y\varepsilon_\infty, _z\varepsilon_\infty)$. For Debye dielectrics with anisotropy

along the axes, the polarization current density can be described by

$$\frac{\partial \mathbf{P}}{\partial t} = \underbrace{\begin{bmatrix} -\frac{1}{x\tau_0} & 0 & 0 \\ 0 & -\frac{1}{y\tau_0} & 0 \\ 0 & 0 & -\frac{1}{z\tau_0} \end{bmatrix}}_{\mathbf{U}} \mathbf{P} + \underbrace{\begin{bmatrix} \frac{\varepsilon_0 \chi_x'}{x\tau_0} & 0 & 0 \\ 0 & \frac{\varepsilon_0 \chi_y'}{y\tau_0} & 0 \\ 0 & 0 & \frac{\varepsilon_0 \chi_z'}{z\tau_0} \end{bmatrix}}_{\mathbf{V}} \mathbf{E} \tag{12}$$

Where $\chi_i' = {}_i\varepsilon_s - {}_i\varepsilon_\infty$, $(i = x, y, z)$. Along each axis, the respective differential equation of (12) describes the frequency dependence of orientational polarization, which is given by

$${}_i\varepsilon_r(\omega) = \frac{{}_i\varepsilon_s - {}_i\varepsilon_\infty}{1 + j\omega_i\tau_0} \qquad (i = x, y, z) \tag{13}$$

The complete Debye model for the permittivity is of course given by [13]

$${}_i\varepsilon_{Debye}(\omega) = {}_i\varepsilon_\infty + {}_i\varepsilon_r(\omega) = {}_i\varepsilon' - j_i\varepsilon'' \qquad (i = x, y, z) \tag{14}$$

(the constant part of the Debye permittivity ${}_i\varepsilon_\infty$ is already accounted for in Maxwell's equations). $\mathbf{U}$ and $\mathbf{V}$ become tensors, when the dielectric is fully anisotropic. A special solution of (12) is given by the convolution integral

$$\mathbf{P} = e^{t\mathbf{U}} \int_0^t e^{-\theta\mathbf{U}} \mathbf{V}\mathbf{E}(\theta)d\theta = Diag\left(e^{-\frac{t}{i\tau_0}} \int_0^t e^{\frac{\theta}{i\tau_0}} \frac{\varepsilon_0 \chi_i'}{i\tau_0} \mathbf{E}_i(\theta)d\theta \right) \qquad (i = x, y, z) \tag{15}$$

Substituting (15) into expression (12) yields the polarization current density in the following form

$$\frac{\partial \mathbf{P}}{\partial t} = Diag\left(-\frac{1}{i\tau_0} e^{-\frac{t}{i\tau_0}} \int_0^t e^{\frac{\theta}{i\tau_0}} \frac{\chi_i'}{i\tau_0} \mathbf{E}_i(\theta)d\theta + \frac{\varepsilon_0 \chi_i'}{i\tau_0} \mathbf{E}_i(t) \right) \qquad (i = x, y, z) \tag{16}$$

3.2 The discretization of Maxwell's equations

The discretization of Maxwell's equations is accomplished by finite integration in space and finite differencing in time. In the following, the procedure is exemplified at the x-component of Ampère's law and Fig.1 shows the integration paths.

The electric and magnetic fields are related to the wave amplitudes in the following way, i.e. the cell boundary mapping of [12] , shown for ports 11 and 12

$$\begin{aligned} {}_{k-\frac{1}{2}}a^{11}_{l,m,n-\frac{1}{2}} + {}_{k-\frac{1}{2}}b^{11}_{l,m,n-\frac{1}{2}} &:= \int_{p^{11}} \mathbf{E} \cdot dl \qquad {}_{k-\frac{1}{2}}a^{12}_{l,m-\frac{1}{2},n} + {}_{k-\frac{1}{2}}b^{12}_{l,m-\frac{1}{2},n} := \int_{p^{12}} \mathbf{E} \cdot dl \\ {}_{k-\frac{1}{2}}a^{11}_{l,m,n-\frac{1}{2}} - {}_{k-\frac{1}{2}}b^{11}_{l,m,n-\frac{1}{2}} &:= -z_0 \int_{p^9} \mathbf{H} \cdot dl \qquad {}_{k-\frac{1}{2}}a^{12}_{l,m-\frac{1}{2},n} - {}_{k-\frac{1}{2}}b^{12}_{l,m-\frac{1}{2},n} := -z_0 \int_{p^{10}} \mathbf{H} \cdot dl \end{aligned} \tag{17}$$

z_0 is the characteristic impedance of free space. The cell boundary is completely equivalent to the interpretation of total quantities $\mathbf{u}, \mathbf{i}$ used in [2, 10, 11]. Nodel fields are evaluated as the aritmethic mean of the tangential fields, i.e.

$${}_kE^x_{l,m,n} = \frac{1}{4}\left({}_{k-\frac{1}{2}}E^x_{l,m-\frac{1}{2},n} + {}_{k-\frac{1}{2}}E^x_{l,m,n+\frac{1}{2}} + {}_{k-\frac{1}{2}}E^x_{l,m,n-\frac{1}{2}} + {}_{k-\frac{1}{2}}E^x_{l,m,n+\frac{1}{2}} \right) \tag{18}$$

The polarization current term $\frac{\partial}{\partial t}\int_A \mathbf{P} \cdot dA$ has to be discretized seperately due to the time integral. Hence, the discretization of Ampère's law looks as follows,

$$\begin{aligned} \oint_{\partial A_x} \mathbf{H} \cdot dl = &\left({}_{k-\frac{1}{2}}a^5_{l,m-\frac{1}{2},n} + {}_{k-\frac{1}{2}}b^5_{l,m-\frac{1}{2},n} \right) + \left({}_{k-\frac{1}{2}}a^6_{l,m,n-\frac{1}{2}} + {}_{k-\frac{1}{2}}b^6_{l,m,n-\frac{1}{2}} \right) + \\ &\left({}_{k-\frac{1}{2}}a^{11}_{l,m,n-\frac{1}{2}} + {}_{k-\frac{1}{2}}b^{11}_{l,m,n-\frac{1}{2}} \right) + \left({}_{k-\frac{1}{2}}a^{12}_{l,m+\frac{1}{2},n} + {}_{k-\frac{1}{2}}b^{12}_{l,m+\frac{1}{2},n} \right) \\ &= \left({}_{k-\frac{1}{2}}\tilde{a}^1_{i,m-\frac{1}{2},n} + {}_{k-\frac{1}{2}}\tilde{b}^1_{l,m-\frac{1}{2},n} \right) \end{aligned} \tag{19}$$

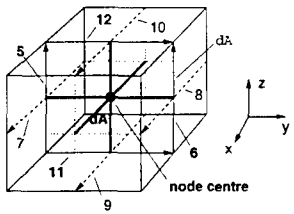

Figure 1: TLM cell with the finite integration path along port vectors 5, 6, 11, and 12 (the port labelling scheme of [12] is used)

The transition from normal to skewed wave amplitudes shows the origin of the transformation $\mathbf{D}$. The loss and displacement currents at the right hand side of (10) become at infinitesimal mesh width, with second order accuracy

$$\sigma_x \int_{A_x} \mathbf{E} \cdot dA_x + \varepsilon_0 \frac{\partial}{\partial t} \int_{A_x} \mathbf{E} \cdot dA_x = \sigma E^x_{l,m,n}(t) \cdot dA_x + \varepsilon_0 \frac{\partial}{\partial t} E^x_{l,m,n}(t) \cdot dA_x + o(u^2 + v^2) \tag{20}$$

Using a centered difference time discretization, this yields

$$\sigma_x \int_{A_x} \mathbf{E} \cdot dA_x + \varepsilon_0 \frac{\partial}{\partial t} \int_{A_x} \mathbf{E} \cdot dA_x \simeq \sigma_x \frac{vw}{8u} \left[{}_k E^x_{l,m,n} + {}_{k-1} E^x_{l,m,n} \right] + \frac{\varepsilon_0}{\tau} \frac{vw}{4u} \left[{}_k E^x_{l,m,n} - {}_{k-1} E^x_{l,m,n} \right] \tag{21}$$

Applying this procedure to all six scalar equations of (10) and (11) will result in the discretized Maxwell's equations of the following form ($\mathbf{Q}_E$ and $\mathbf{Q}_H$ are matrices with a 1 on the principal diagonal at row 1-3 and 10-12, respectively, and otherwise zero)

$$\mathbf{Q}_E \left({}_{k-\frac{1}{2}}\tilde{\mathbf{a}} - {}_{k-\frac{1}{2}}\tilde{\mathbf{b}} \right) = \frac{\sigma}{2} \mathbf{W} \mathbf{Q}_E \left[\mathbf{Id} + \mathbf{T} \right] \left({}_k\tilde{\mathbf{a}} + {}_k\tilde{\mathbf{b}} \right) + \frac{\varepsilon_0}{\tau} \mathbf{W} \mathbf{Q}_E \left[\mathbf{Id} - \mathbf{T} \right] \left({}_k\tilde{\mathbf{a}} + {}_k\tilde{\mathbf{b}} \right) \tag{22}$$

$$\mathbf{Q}_H \left({}_{k-\frac{1}{2}}\tilde{\mathbf{a}} + {}_{k-\frac{1}{2}}\tilde{\mathbf{b}} \right) = \frac{\mu_0}{\tau} \mathbf{W} \mathbf{Q}_H \left[\mathbf{Id} - \mathbf{T} \right] \left({}_k\tilde{\mathbf{a}} - {}_k\tilde{\mathbf{b}} \right) \tag{23}$$

Whereby a diagonal matrix $\mathbf{W}$ comprising the geometrical scaling factors along each axis was introduced:

$$\mathbf{W} = Diag \left(\frac{vw}{4u}, \frac{uw}{4v}, \frac{uv}{4w} \right) \tag{24}$$

To establish a connection to section 2.2, we want to identify the operators $\mathbf{F}_\mu$,

$$\mathbf{F}_0 = \begin{bmatrix} \frac{\sigma}{2}\mathbf{W}\mathbf{Q}_E + \frac{\varepsilon_0}{\tau}\mathbf{W}\mathbf{Q}_E & 0 \\ 0 & \frac{\mu_0}{\tau}\mathbf{W}\mathbf{Q}_H \end{bmatrix} \quad \mathbf{F}_1 = \begin{bmatrix} \frac{\sigma}{2}\mathbf{W}\mathbf{Q}_E - \frac{\varepsilon_0}{\tau}\mathbf{W}\mathbf{Q}_E & 0 \\ 0 & -\frac{\mu_0}{\tau}\mathbf{W}\mathbf{Q}_H \end{bmatrix} \quad \mathbf{F}_{2,\ldots\infty} = \mathbf{0} \tag{25}$$

$\mathbf{\Delta}$ and the state vector $|\mathbf{F}>$

$$\mathbf{\Delta} = \begin{bmatrix} 0 & \mathbf{Q}_E \\ \mathbf{Q}_H & 0 \end{bmatrix} \qquad |\mathbf{F}> = \begin{bmatrix} |\tilde{\mathbf{a}}> + |\tilde{\mathbf{b}}> \\ |\tilde{\mathbf{a}}> - |\tilde{\mathbf{b}}> \end{bmatrix} \tag{26}$$

3.3 The discretized polarization current

The discretization of the polarization current density runs completely analogue to the derivation in reference [2] for the gyromagnetic current density, so that we only give the results here. The nodal electric field ${}_k\mathbf{E}^{l,m,n}$, changing its value at times k, is a step function of time. Since the beginning of the TLM process, there have been μ time steps. Performing the integration in time in equation (16) and using a centered difference approximation for the time derivative, equation (16) yields

$$\left. \frac{\Delta \mathbf{P}}{\Delta t} \right|_\mu = \mathbf{A} \cdot \left({}_{\mu+\frac{1}{2}}\mathbf{E}_{l,m,n} - {}_{\mu-\frac{1}{2}}\mathbf{E}_{l,m,n} \right) + \mathbf{B} \cdot \mathbf{\Lambda}_{\mu-1} \left[\mathbf{T}^{\mu-\eta}_{\mu+\frac{1}{2}} \mathbf{E}_{l,m,n} \right] \tag{27}$$

with matrices

$$\mathbf{A} = Diag\left(-\frac{\varepsilon_0}{\tau}\chi_i'\left(e^{-\frac{\tau}{2_i\tau_0}}-1\right)\right) \qquad \mathbf{B} = Diag\left(-\frac{2}{\tau}i\tau_0\sinh-\frac{\tau}{2_i\tau_0}\right) \qquad (i=x,y,z) \tag{28}$$

and the casual operator

$$\mathbf{\Lambda}_\mu\left[\mathbf{T}^{\mu-j}_{\mu+\frac{1}{2}}\mathbf{E}_{l,m,n}\right] = \sum_{j=0}^{\mu}\lambda_j\cdot\mathbf{T}^{\mu-j}_{\mu+\frac{1}{2}}\mathbf{E}_{l,m,n} \tag{29}$$

with

$$\lambda_j = Diag\left(\left\{\begin{array}{ll}\frac{\varepsilon_0\chi_i'}{i\tau_0}e^{-\frac{\tau}{i\tau_0}} & \text{for } j=0\\ e^{-\frac{\mu\tau}{i\tau_0}}(e^{-\frac{\tau}{i\tau_0}}-\frac{\varepsilon_0\chi_i'}{i\tau_0}) & \text{for } j>0\end{array}\right.\right) \qquad (i=x,y,z) \tag{30}$$

Now, we can write down the finite difference approximation for the polarization current

$$\varepsilon_0\frac{\partial}{\partial t}\int_{\partial A}\mathbf{P}\cdot dA \simeq \mathbf{WA}\,Q_E\left[\mathbf{Id}-\mathbf{T}\right]\left({}_k\tilde{\mathbf{a}}+_k\tilde{\mathbf{b}}\right)+\mathbf{WB}\mathbf{\Lambda}_{\mu-1}\left[\mathbf{Q}_E\mathbf{T}^{\mu-j}\left({}_k\tilde{\mathbf{a}}+_k\tilde{\mathbf{b}}\right)\right] \tag{31}$$

Adding this to the right side of equation (22), the completely discritized general Ampère's law looks like

$$\mathbf{Q}_E\left({}_{k-\frac{1}{2}}\tilde{\mathbf{a}}-_{k-\frac{1}{2}}\tilde{\mathbf{b}}\right)=\mathbf{X}_1\mathbf{Q}_E\left({}_k\tilde{\mathbf{a}}+_k\tilde{\mathbf{b}}\right)+\mathbf{X}_2\mathbf{Q}_E\left({}_{k-1}\tilde{\mathbf{a}}+_{k-1}\tilde{\mathbf{b}}\right)+\mathbf{WB}\mathbf{\Lambda}_{m-1}\left[\mathbf{Q}_E\mathbf{T}^{\mu-j}\left({}_k\tilde{\mathbf{a}}+_k\tilde{\mathbf{b}}\right)\right] \tag{32}$$

with the matrices

$$\mathbf{X}_1=\mathbf{W}\left(\sigma+\mathbf{A}+\frac{\varepsilon_0}{\tau}\mathbf{Id}\right) \qquad \mathbf{X}_2=\mathbf{W}\left(\sigma-\mathbf{A}-\frac{\varepsilon_0}{\tau}\mathbf{Id}\right) \qquad \mathbf{X}_3=\mathbf{W}\frac{\mu_0}{\tau} \tag{33}$$

Inserting the responses of the TLM process started with a Dirac pulse into equations (32) and (23) in connection with (33) yields for Ampère's and Faraday's law:

$$\begin{array}{lcl}\mathbf{K}_E &=& \mathbf{X}_2^{-1}\mathbf{Q}_E-\mathbf{Q}_E\\ \mathbf{L}_E &=& \mathbf{Id}\\ \mathbf{M}_E &=& -\mathbf{L}_E^*\mathbf{X}_2^{-1}\mathbf{K}_E-\mathbf{L}_E^*\mathbf{X}_1^{-1}\mathbf{X}_2(\mathbf{Q}_E+\mathbf{K}_E)\\ \mathbf{N}_E &=& -\mathbf{L}_E^*\left(\mathbf{X}_1^{-1}+\mathbf{X}_1^{-1}\mathbf{X}_2\right)\mathbf{L}_E\end{array} \tag{34}$$

$$\begin{array}{lcl}\mathbf{K}_H &=& \mathbf{Q}_H\left(\mathbf{Id}-\mathbf{X}_3^{-1}\right)\\ \mathbf{L}_H &=& -\mathbf{Id}\\ \mathbf{M}_H &=& -\mathbf{L}_H^*\mathbf{Q}_H\left((\mathbf{X}_3)^{-2}-\mathbf{X}_3^{-1}\right)\\ \mathbf{N}_H &=& \mathbf{P}_H\left(\mathbf{Id}-\mathbf{X}_3^{-1}\right)\end{array} \tag{35}$$

* denotes the adjoint operator or the transpose matrix, respectively (for details on $\mathbf{L}_j$ and $\mathbf{P}_j$ see e.g. [11]). Applying the deflection lemma as exemplified in reference [2] yields the TLM algorithm for a dielectric node in canonical representation with the so called deflection matrices $\mathbf{S}_{Dj}(j=1..5)$

$$\begin{array}{lcl}{}_{k+\frac{1}{2}}\tilde{\mathbf{b}} &=& \mathbf{S}_{k-\frac{1}{2}}\tilde{\mathbf{a}}+_{k-\frac{1}{2}}\tilde{\mathbf{d}}\\ \left({}_k\tilde{\mathbf{a}}+_k\tilde{\mathbf{b}}\right) &=& {}_{k-\frac{1}{2}}\tilde{\mathbf{a}}+_{k+\frac{1}{2}}\tilde{\mathbf{b}}\\ {}_{k+\frac{1}{2}}\tilde{\mathbf{d}} &=& \mathbf{S}_{D1k-\frac{1}{2}}\tilde{\mathbf{d}}-\mathbf{S}_{D2}\left({}_k\tilde{\mathbf{a}}+_k\tilde{\mathbf{b}}\right)-\mathbf{S}_{D3k-\frac{1}{2}}\tilde{\mathbf{m}}\\ {}_{k+\frac{1}{2}}\tilde{\mathbf{m}} &=& \mathbf{S}_{D4}\left({}_k\tilde{\mathbf{a}}+_k\tilde{\mathbf{b}}\right)+\mathbf{S}_{D5k-\frac{1}{2}}\tilde{\mathbf{m}}\end{array} \tag{36}$$

$$\begin{array}{lcl}\mathbf{S}_{D1} &=& -\left(\mathbf{X}_1^{-1}-\mathbf{X}_1^{-1}\mathbf{X}_2^{-1}\right)\\ \mathbf{S}_{D2} &=& \mathbf{X}_1^{-1}\mathbf{W}e^{t\mathbf{U}}\mathbf{V}\\ \mathbf{S}_{D3} &=& \mathbf{V}^{-i}\mathbf{S}_{D2}\\ \mathbf{S}_{D4} &=& \left(e^{t\mathbf{U}}-\mathbf{Id}\right)\mathbf{V}\\ \mathbf{S}_{D5} &=& e^{t\mathbf{U}}\end{array} \tag{37}$$

The evaluation of the time step runs completely analogue to the way presented in reference [2].

4 Numerical results

We have derived a TLM algorithm for the treatment of dispersive media whose frequency dependent behaviour can be described by a Debye model. In order to verify the validity of the approach, a simple test structure was investigated (see Fig. 2). An infinite parallel plate TEM waveguide was partially filled with a dispersive model dielectric. The static dielectric constant of the model medium was ${}_z\varepsilon_s = 65$ (for simplicity, ${}_z\varepsilon_\infty$ was set to 1) its

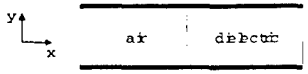

Figure 2: TEM parallel plate waveguide, partially filled with dispersive dielectric.

relaxation time was $\tau_0 = 1.0 * 10^{-}13s$. The structure was modelled by a one-dimensional chain of nodes, 30 for free space and 70 for the dielectric. A Gaussian pulse of the form $\mathbf{E}_y(k\tau) = \mathbf{E}_{y0}e^{-\frac{(k\tau-t_0)^2}{T^2}}$ was launched onto the air-dielectric interface and the transient fields calculated.
From these data, the complex reflection coefficient was evaluated. Magnitude and phase were then compared to the exact values given by the analytical expressions

$$|R_{ana}| = \left|\frac{1-\sqrt{\varepsilon_r(\omega)}}{1+\sqrt{\varepsilon_r(\omega)}}\right| \tag{38}$$

$$\varphi_{ana} = \frac{\varepsilon''(\omega)}{\varepsilon'(\omega)} \tag{39}$$

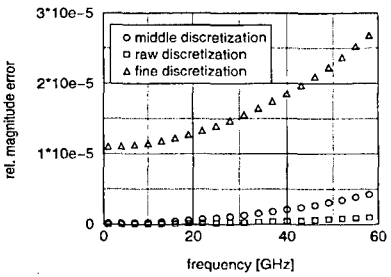

Figure 3: Relative amplitude error between solution obtained by equation (38) and a TLM simulation.

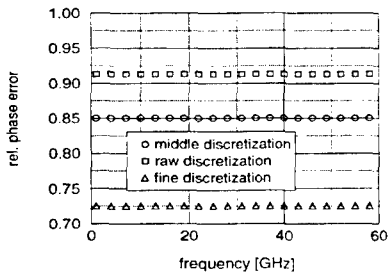

Figure 4: Relative phase error between solution ontained by equation (39) and a TLM simulation

discretization	u (cell size)	τ (time step)	T (pulse width)
coarse	1.4 μm	$0.2 * 10^{-}14$ s	25 τ
middle	0.7 μm	$1.0 * 10^{-}15$ s	50 τ
fine	0.35 μm	$0.5 * 10^{-}15$ s	100 τ

Table 1: The simulation parameters

In Fig. 3 the relative error $\frac{||R_{ana}|-|R_{sim}||}{|R_{ana}|}$ between the magnitude of the reflection coefficient obtained from the TLM simulation, $|R_{sim}|$, and the exact values calculated using formula (39) is shown. Apparently, excellent agreement is found between the analytical and simulated solution, as the relative error is extremely small. Surprisingly, the error increases with finer discretization. In Contrast, Fig. 3 shows the relative phase error $\frac{|\varphi_{ana}-\varphi_{sim}|}{|\varphi_{ana}|}$ between the analytical solution given by equation (40) and the simulation.
The deviation of the TLM solution from the analytical solution is quite significant but can be explained as follows: In the analytical case, the interface between the two media is *exactly* defined. In the TLM mesh, the interface

is *supposed* to be at the middle of two nodes. As the dispersion characteristics of the nodes at either side of the interface differ considerably, one does not know where to assume the exact interface plane. That this is indeed the case, can be seen when the relative phase errors for three different discretizations specified in Table 1 are compared. The finer the discretization, the lower is the relative phase error, as the interface between the two media is better localized in the simulation.

5 Conclusions

We have shown that the propagator concept can be applied to the modelling of dispersive media in TLM, whose frequency dependence is described by the Debye model. The accuracy of the approach is excellent and the advantages of the approach are fully exploited. Even for relative permittivities of arbitrary value (tested up to $\varepsilon_s \simeq 100$), the process remains absolutely stable due to the canonical stability criteria. Work is in progress to extend the approach to the modelling of dispersive media whose frequency characteristics can be described by a Lorentz model.

6 Acknowledgement

The authors are indepted to Steffen Hein who elucidated the implications of the propagator approach in many fruitful discussions. Moreover, we would like to thank our collegues M. Aidam and T. Mangold for numerous support in computational matters.

References

[1] J.F. Dawson, "Improved magnetic loss for TLM", Electron. Lett., Vol. 29, pp. 467-468, 1993

[2] S. Hein, "TLM numerical solution of Bloch's equations for magnetized gyrotropic media", Appl. Math. Modelling, Vol. 21, pp. 221-229, 1997

[3] M.I. Sobhy, R. Ng, R.J. Langley and J. Batchelor, "Using TLM to simulate ferrite and dispersive media", Proc. 2nd Int. Workshop on Transmission Line Matrix (TLM) Modelling, Munich, pp. 246-255, 1997

[4] L. de Menezes, W.J.R. Hoefer,"Modeling of General Constitutive Relationships in SCN TLM", IEEE Trans. on Microwave Theory and Techniques, Vol. 44, No. 6, pp. 854-861, 1996

[5] J. Huang and K. Wu, "A Unified TLM Model for Wave Propagation of Electrical and Optical Structures Considering Permittivity and Permeability Tensors", IEEE Trans. on Microwave Theory and Techniques, Vol. 43, No. 10, pp. 2472-2477, 1995

[6] F. Hunsberger,R. Luebbers, and K.S. Kunz, "Finite-Difference Time- Domain Analysis of Gyrotropic Media - I: Magnetized Plasma", IEEE Trans. on Antennas and Propagation, Vol. 40, No. 12, pp. 1489-1495, 1992

[7] P.G. Petropoulos, "Stability and Phase Error Analysis of FD-TD in Dispersive Dielectrics", IEEE Trans. on Antennas and Propagation, Vol. 42, No. 1, pp. 62-69, 1994

[8] D.M. Sullivan, "Z-Transform Theory and the FDTD-Method", IEEE Trans. on Antennas and Propagation, Vol. 44, No. 1, pp. 28-34, 1996

[9] S. Hein, "Consistent finite-difference modelling of Maxwell's equations with lossy symmetrical condensed TLM node", Int. J. Num. Modelling, Vol. 6, pp. 207-220, 1993

[10] S. Hein, "Synthesis of TLM algorithms in the propagator integral framework", Proc. 2nd Int. Workshop on Transmission Line Matrix (TLM) Modelling, Munich, pp. 1-11, 1997

[11] S. Hein, "Finite-difference time-domain approximation of Maxwell's equations with nonorthogonal condensed TLM mesh", Int. J. Num. Modelling, Vol. 7, pp. 179-188, 1994

[12] P. Russer, M. Krumpholz, "A field theoretical derivation of TLM", IEEE Trans. on Microwave Theory and Techniques, Vol. 42, No. 4, pp. 1660-1668, 1994

[13] P. Robert, "Electric and Magnetic Properties of Materials", Artech House, 1988

Characterization of Quasiplanar Structures Using the TLM Method

Oliver Pertz, Ulf Müller and Adalbert Beyer

Gerhard-Mercator Universität Duisburg, Department of Electromagnetic Theory and Engineering, Bismarckstr. 81, 47048 Duisburg, Phone +49 203 3791055, email Pertz@uni-duisburg.de

Abstract

In the last years the importance of quasiplanar structures made it necessary to find efficient simulation tools. Under certain circumstances the amount of memory and CPU time needed for the simulation can be reduced significantly. In this paper a simplified TLM algorithm is used to simulate longitudinally homogeneous or periodic waveguides. In the first part of this paper a brief explanation of the theory is given. The algorithm is used to simulate some structures of interest, e.g. an inset dielectric waveguide structure.

Theoretical Background

The characterization of waveguides by numerical simulation tools requires discretization elements sufficiently dense for the description of the metalization. Because of the required memory amount a transient analysis becomes almost impossible. In the case of a longitudinally homogeneous or periodic waveguide the simulation requirements can be reduced.

If losses are neglected, the vectors of the electric and magnetic field strength can be expressed as [1]

$$\mathbf{E} = \mathbf{E}_1 \, e^{j\beta z} + \mathbf{E}_2 \, e^{-j\beta z}, \tag{1}$$

$$\mathbf{H} = \mathbf{H}_1 \, e^{j\beta z} + \mathbf{H}_2 \, e^{-j\beta z}, \tag{2}$$

assuming propagation along the z-direction. Thus, two waves in positive and negative z-direction respectively contribute to the electric and magnetic fields. The TLM-simulation can then be reduced to a simple layer of nodes discretizing the transverse plain. The voltages at the gate can be calculated by

$${}_{n+1}u_2^+(i,j) = e^{j\beta\Delta z} \, {}_n u_9^-(i,j), \tag{3}$$

$${}_{n+1}u_4^+(i,j) = e^{j\beta\Delta z} \, {}_n u_8^-(i,j), \tag{4}$$

$${}_{n+1}u_9^+(i,j) = e^{j\beta\Delta z} \, {}_n u_2^-(i,j), \tag{5}$$

$${}_{n+1}u_8^+(i,j) = e^{j\beta\Delta z} \, {}_n u_4^-(i,j) \tag{6}$$

if a symmetrical condensed node (SCN) is used. + and − indicate the incoming and outgoing waves respectively.

The properties of the grid and the field solution of equation (1) yield the simulation of standing waves [2]. During the simulation the propagation constant β is given as simulation input and the corresponding frequencies can be calculated from the resulting time signal. Each frequency corresponding to one propagation constant represents a propagating mode.

When looking at equation (3) one can easily see that the TLM grid requires complex descriptors. Thus, two TLM networks are necessary describing real and imaginary parts of the voltages. The networks are coupled by a modified exchange algorithm. The scattering does not lead to a further coupling. Under certain conditions it is possible to implement this algorithm with two networks with the number of relevant voltages halved in each network. This can be proven starting with Maxwell's equations

$$\mathbf{rot}\,\mathbf{H} = \mathbf{J}_c + \frac{\partial \mathbf{D}}{\partial t}, \tag{7}$$

$$\mathbf{rot}\,\mathbf{E} = -\frac{\partial \mathbf{B}}{\partial t}. \tag{8}$$

Assuming that $\mathbf{H}_2$ and $\mathbf{E}_2$ can be set to zero and considering material isotropy the above equations can be simplified. As final result it can be shown that

$$u_2 = u_9^* \text{ and} \tag{9}$$

$$u_4 = u_8^* \tag{10}$$

must be valid. In this case the simulation effort can be reduced to one half of the original algorithm.

Another important class of waveguides are periodic waveguides. "Periodic" usually means periodic boundary conditions, e.g. in a rectangular waveguided which is capacitively loaded periodically. Periodic waveguides have the property that they have certain frequency bands where wave propagation is possible and frequency bands between them, where a wave cannot propagate [3].

The problem of periodic waveguides can be solved similarly to the problem of homogeneous waveguides. With the help of Floquet's theorem a field ansatz

$$\mathbf{E} = \mathbf{E}_1\, e^{\gamma z} + \mathbf{E}_2\, e^{-\gamma z}, \tag{11}$$

$$\mathbf{H} = \mathbf{H}_1\, e^{\gamma z} + \mathbf{H}_2\, e^{-\gamma z} \tag{12}$$

can be derived, in which damping is considered too. The field coefficients $\mathbf{E}_1, \mathbf{E}_2, \mathbf{H}_1$ and $\mathbf{H}_2$ are periodic functions.

The SCN voltages at the gates can be calculated by

$$ {}_{n+1}u_2^+(i,j,k) = e^{j\beta N_p \Delta z}\, {}_nu_9^-(i,j,k+N_p), \tag{13} $$

$$ {}_{n+1}u_4^+(i,j,k) = e^{j\beta N_p \Delta z}\, {}_nu_8^-(i,j,k+N_p), \tag{14} $$

$$ {}_{n+1}u_9^+(i,j,k+N_p) = e^{j\beta N_p \Delta z}\, {}_nu_2^-(i,j,k), \tag{15} $$

$$ {}_{n+1}u_8^+(i,j,k+N_p) = e^{j\beta N_p \Delta z}\, {}_nu_4^-(i,j,k). \tag{16} $$

where $P = N_p \cdot \Delta z$ is the periodicity of the structure. The index k can be set to zero in the simulation, but the further simplification similar to the simplifications for longitudinally homogeneous waveguides can only be done in some limited cases [4] and will not be presented here.

Results

As an example for longitudinally homogeneous waveguide an inset dielectric guide was simulated according to Fig. 1. Fig. 2 and fig. 3 show the transverse component of the electric and magnetic

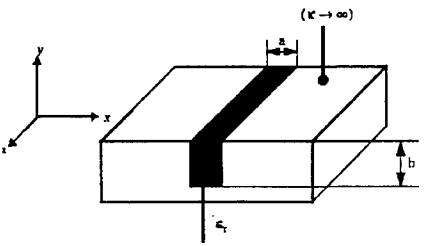

Figure 1: Inset dielectric waveguide used for the simulation.

fields respectively. The parameter used in this simulation were $h/a = 1.5$, $a = 10.16$ mm and $\epsilon_r = 2.08$. The simulation results are compared with measurements by Rozzi et al. [5] in Fig. 4. Simulation results and measurements are very close together. The precision of the measurement is limited, since the permittivity of the used dielectric material has a tolerance of one percent. Fig. 5 shows the tangential magnet field component on the contour of the inset dielectric guide for the base wave type at a discrete time step during simulation. The tangential magnetic field component corresponds to a surface current on the contour.

For periodic waveguides we present two results for the calculation in this paper. The first example is a capacitively loaded rectangular waveguide according to Fig. 6 with $a = 22.56$ mm. $b =$

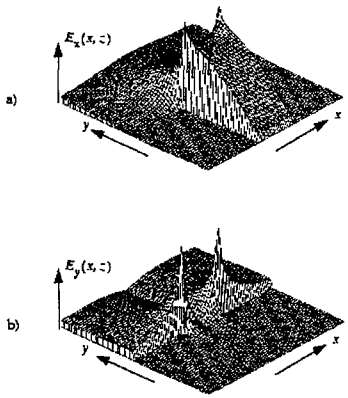

Figure 2: Electric fieldstrength in a transverse plain of the inset dielectric waveguide according to Fig. 1: a) x-component and b) y-component.

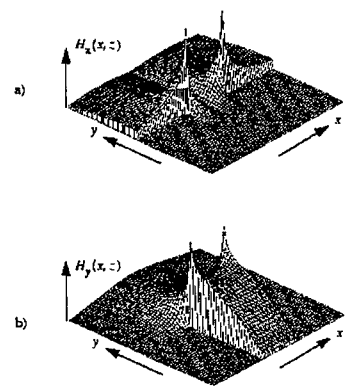

Figure 3: Same plot as in Fig. 2, but with magnetic fieldstrength.

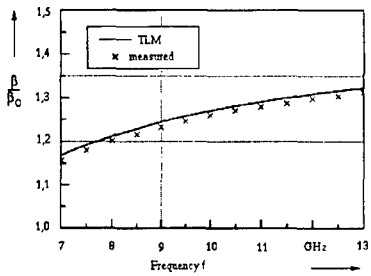

Figure 4: Dispersion diagram of an inset dielectric waveguide for the X-band. Calculated values compared to measurement results [5].

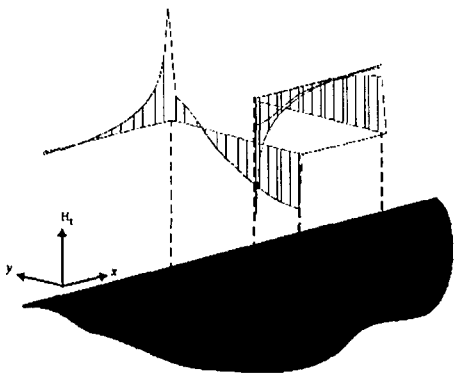

Figure 5: Tangential magnetic fieldstrength on the contour of an inset dielectric waveguide as shown in Fig. 1.

5.08 mm, $d = 3.81$ mm and $P = 2$ mm. The simulation results are compared with the analytical result for this structure. Fig. 7 shows the dispersion diagram. The stop bands (dotted region) and pass bands can be seen. Simulation results and analytical calculations show excellent agreement.

A second example calculated was a capacitively loaded coplanar waveguide. Simulation results

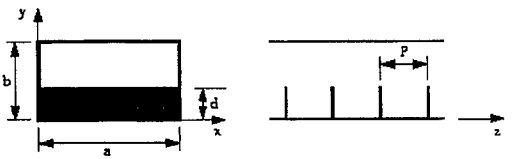

Figure 6: Capacitively loaded rectangular waveguide.

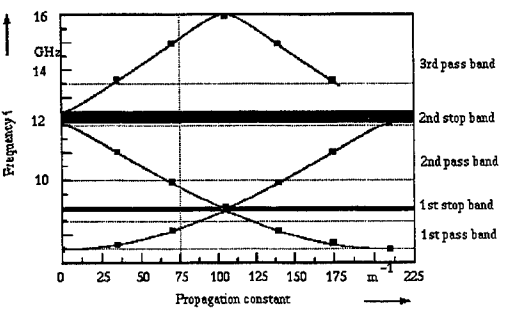

Figure 7: Dispersion diagram of a periodic capacitively loaded rectangular waveguide (symbols: TLM simulation, lines: analytical solution in [3]).

for phase velocity over frequency [4] are compared to measurements by [6] (Fig. 8). In this case measurement and simulation show fair agreement.

Conclusion

In this paper we have shown that the TLM method is a powerful method to simulate longitudinally homogeneous or periodic waveguides. A simplified simulation algorithm was proposed and the theory was explained. Simulation results for homogeneous and for periodic waveguides were presented which underline that the method can be used successfully.

In future the algorithm will be used for simulating more complicated structures. By comparing the results to measurements or, where measurements are not available, to other methods like Finite Difference Time Domain method (FDTD) the algorithm will be verified.

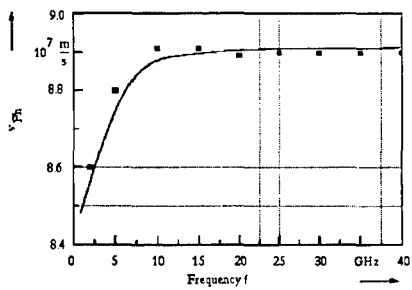

Figure 8: Phase velocity of a wave on a periodically capacitively loaded coplanar waveguide (line: simulation after [4], symbols: measurement according to [6]).

References

[1] M. Walter, "Untersuchungen zur Simulation der Methodik der TLM-Simulation für längshomogene Leitunsstrukturen," Master's thesis, Gerhard Mercator Universit"at, 1995.

[2] S. Hofschen, *Analyse planarer Wellenleiter und MMIC-Komponenten mir der Methode der zweidimensionalen Finiten-Differenzen im Zeitbereich.* PhD thesis, Gerhard Mercator Universit"st Duisburg, 1996.

[3] R. E. Collins, *Field theory of guided waves.* New York: IEEE Press, 1991.

[4] M. Walter, "Anwendung der TLM Methode auf längsperiodische Leitungsstrukturen der Mikrowellen- und Millimeterwellentechnik," Master's thesis, Gerhard Mercator Universit"at Duisburg, 1996.

[5] T. Rozzi and S. J. Hedges, "Rigorous analysis and network modeling of the inset dielectric guide," *IEEE Trans. Microwave Theory Tech.*, vol. 35, pp. 823–834, September 1987.

[6] R. Spickermann and N. Dagli, "Millimetre wave colpanar slow-wave structures on GaAs suitable for use in electro-optic modulators," *Electronics Letters*, vol. 29, pp. 272–273, March 1993.

Generation of Lumped Element Equivalent Circuits from Time-Domain Scattering Signals

T. Mangold, P. Russer
Institut für Hochfrequenztechnik, Technische Universität München,
Arcisstraße 21, D-80333 München, Germany

Abstract

We present a general method for the generation of lumped element equivalent circuits for linear passive reciprocal distributed microwave components from time domain scattering signals. The method is based on a field theoretical analysis of the distributed multiport circuit in time domain. For this purpose the three-dimensional Transmission-Line-Matrix method is used. A canonical representation of the multiport admittance matrix $\mathbf{Y}(p)$ allows to generate an equivalent circuit directly after specifying the frequency range of validity. Topology as well as the parameters of the lumped element equivalent circuit are given by the method. A distributed four-port microwave circuit was modeled and the applicability of the generated circuit model in transient spice simulations could be demonstrated.

1 Introduction

Electromagnetic full-wave analysis in time domain can be used for an efficient broadband modeling of distributed circuit components. The Transmission-Line-Matrix (TLM) method [1] and the Finite Difference Time Domain method (FDTD) [2] have proven their ability to handle general structures. Because of high computational effort and practical limitations in problem size, only critical distributed circuit elements are modeled by full-wave analysis. Complete system simulations are usually performed by network-oriented CAD-tools like Spice [3]. Frequency domain simulations allow the use of lookup tables to incorporate the results of full-wave analysis with network-oriented methods. Network-oriented methods in time domain, especially transient spice simulations, require the existence of lumped element equivalent circuits to include distributed elements. There are different ways to combine full-wave and network-oriented analysis methods. Besides other methods as for example general system identification techniques, lumped element equivalent circuits exhibit the advantage of compactness, easy implementation in existing circuit simulators, applicability in frequency domain as well as in time domain, and exact representation of fundamental circuit properties like passivity, stability and reciprocity. The main problem in getting a lumped element model for a distributed microwave circuit is to find a network topology which is able to reproduce the transmission characteristics of a distributed multiport circuit. Empirical techniques may lead to most compact models, which may also offer a direct mapping between model parameters and geometric dimensions. But they need a lot of creativity and experience, cannot be automated and lack for a mathematical formulation. A systematic method for the generation of lumped element equivalent circuits for lossless microwave circuits has been given in [4].

In this paper, we extend this approach to lossy structures and propose a straight forward general method for computer aided generation of lumped element equivalent circuits for linear passive reciprocal multiports from time domain scattering signals.

2 Theory

The described method is based on a canonical representation of a multiport admittance matrix $\mathbf{Y}(p)$. Knowing the location and amplitudes of a number of N poles α_n of a linear reciprocal lossless multiport its admittance matrix can be expressed in form of a Foster matrix [5]. This representation allows to generate an equivalent circuit model directly after specifying the desired frequency range of validity for the model. We extend this canonical description to linear lossy reciprocal multiports. An admittance matrix of this type may be represented by

$$\mathbf{Y}(p) = \mathbf{A}^{(0)} + \sum_{n=1}^{N} \underbrace{\left(\frac{A_0^{(n)}}{p-\alpha_n} + \frac{A_0^{(n)*}}{p-\alpha_n^*} \right)}_{Y^{(n)}} \cdot \mathbf{A}^{(n)} + \mathbf{A}^{(\infty)} p \,. \tag{1}$$

$\mathbf{A}^{(n)}$ are real, symmetric and positive semidefinite matrices, $A_0^{(n)}$ are complex constants and α_n denote stable poles with $\mathrm{Re}\{\alpha_n\} \leq 0$. The proof is given for two-ports in [6] and holds also for multiports. A representation of $\mathbf{Y}(p)$ in terms of a summation corresponds to a shunt connection of circuit sections with identical network topology but different parameter values. Each section consists of a scalar frequency dependent factor $Y^{(n)}$ related to the location of a single pole α_n and a constant matrix $\mathbf{A}^{(n)}$ related to the amplitudes of this pole α_n observable at the different ports of a circuit.

Cauer has shown that every constant matrix $\mathbf{A}^{(n)}$ can be realized by a network of ideal transformers and $M \leq \dim(\mathbf{A}^{(n)})$ one-port admittances [7]. Replacing all constant one-port admittances by simple one-port networks with a frequency dependent behavior equal to $Y^{(n)}$ enables us to find a lumped element circuit for a given admittance matrix $\mathbf{Y}^{(n)} = Y^{(n)}\mathbf{A}^{(n)}$. The basic compact n-port subcircuit resulting from Cauers method consists of R, G, L, C and ideal transformers as depicted in Fig. 1. It contributes a rank one admittance matrix

$$\begin{aligned} \mathbf{Y}_i^{(n)} &= Y_i^{(n)} \mathbf{k}_i^{(n)} = \\ &= \frac{G_i^{(n)} + pC_i^{(n)}}{p^2 L_i^{(n)} C_i^{(n)} + p(G_i^{(n)} L_i^{(n)} + R_i^{(n)} C_i^{(n)}) + 1 + R_i^{(n)} C_i^{(n)}} \cdot \begin{pmatrix} 1 & k_{i1} & \cdots & k_{iN} \\ k_{i1} & (k_{i1})^2 & \cdots & k_{i1}k_{iN} \\ \vdots & \vdots & \ddots & \vdots \\ k_{iN} & k_{iN}k_{i1} & \cdots & (k_{iN})^2 \end{pmatrix} . \end{aligned} \tag{2}$$

After decomposing all matrices $\mathbf{A}^{(n)}$ of (1) into sums of rank 1 matrices, these compact lumped element circuits can be used to realize all summands in (1). For a matrix of dimension three this decomposition looks like

$$\mathbf{A}^{(n)} = K_1^{(n)} \begin{pmatrix} 1 & k_{11} & k_{12} \\ k_{11} & (k_{11})^2 & k_{11}k_{12} \\ k_{12} & k_{11}k_{12} & (k_{12})^2 \end{pmatrix} + K_2^{(n)} \begin{pmatrix} 0 & 0 & 0 \\ 0 & 1 & k_{21} \\ 0 & k_{21} & (k_{21})^2 \end{pmatrix} + K_3^{(n)} \begin{pmatrix} 0 & 0 & 0 \\ 0 & 0 & 0 \\ 0 & 0 & 1 \end{pmatrix} . \tag{3}$$

Connecting all compact multiport elements associated with a certain pole α_n leads to multiport elements (shown in Fig. 2) realizing full rank matrices of the form $Y^{(n)}\mathbf{A}^{(n)}$. The parameter values of a specific lumped element subcircuit can be obtained from

$$Y_i^{(n)} = Y^{(n)}\mathbf{A}^{(n)} = Y^{(n)} K_i^{(n)} \,. \tag{4}$$

For a subcircuit with given indices (n, i) the parameter values of R, G, L and C can be found to be

$$\begin{aligned} \frac{1}{L} &= 2\mathrm{Re}\{\gamma\} \quad , \quad C = \frac{2\mathrm{Re}\{\gamma\}}{\frac{1}{LC}} \\ \frac{R}{L} &= \frac{\mathrm{Re}\{\gamma\alpha_n^*\}}{\mathrm{Re}\{\gamma\}} - 2\mathrm{Re}\{\alpha_n\} \quad , \quad \frac{G}{C} = \frac{\mathrm{Re}\{\gamma\alpha_n^*\}}{\mathrm{Re}\{\gamma\}} \end{aligned} \tag{5}$$

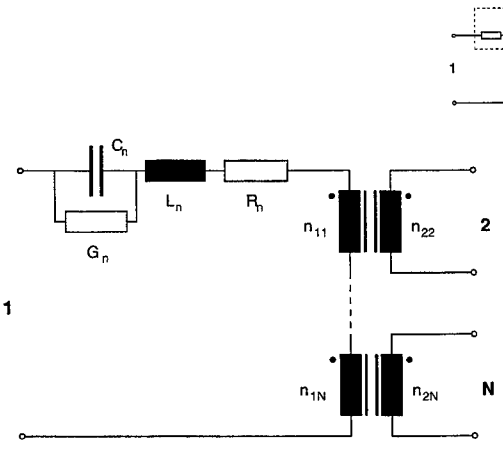

Figure 1: A compact rank 1 n-port element

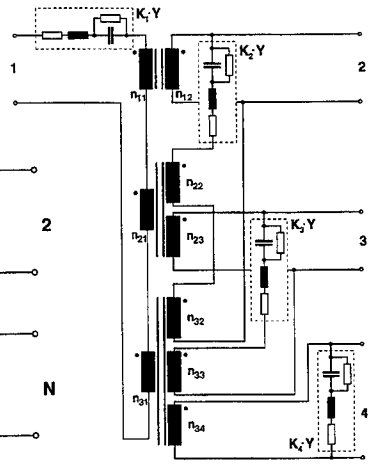

Figure 2: A full rank four-port element

with

$$\frac{1}{LC} = |\alpha_n|^2 - \frac{R}{L}\frac{G}{C} \quad , \quad \gamma = A_0^{(n)} K_i^{(n)} \tag{6}$$

These expressions are valid for the general case and degenerate to even simpler formulas for $\alpha_n = 0, \mathrm{Re}\{\alpha_n\} = 0$ or $\alpha_n = \infty$. The turns ratios of transformers are defined by the matrix elements $k_{ij}^{(n)}$. For a four-port circuit the following relationships apply:

$$\begin{aligned} k_{11} &= -\frac{n_{11}}{n_{12}} \quad , \quad k_{12} = -\frac{n_{21}}{n_{23}} \quad , \quad k_{13} = -\frac{n_{31}}{n_{34}} \\ k_{21} &= -\frac{n_{22}}{n_{23}} \quad , \quad k_{22} = -\frac{n_{32}}{n_{34}} \quad , \quad k_{31} = -\frac{n_{33}}{n_{34}} \end{aligned} \tag{7}$$

3 Model Generation

The theory described above gives a straight forward way to generate a lumped element circuit model for a given admittance matrix in form of (1). To make use of this synthesis method a parameter set of equation (1) approximating admittance values in generic description has to be found. Dividing this problem into subsequent steps reduces the complexity of the task and ensures convergence.

Electromagnetic Full-wave Analysis

Starting with a three-dimensional electromagnetic full-wave analysis of a distributed multiport we obtain input/output signal pairs related to each other by the impulse response functions of reflection and transmission between the ports. For this we use the time domain TLM scheme with Symmetrical Condensed Nodes [1]. To reduce the computational effort an irregularly graded mesh is used [8]. Further, this technique provides an efficient

way for exact boundary positioning. Free space boundaries are modeled by terminating the mesh with a constant, matched impedance.
TLM time responses $s(n)$ are separated from spurious parts by utilizing system identification techniques. Deembedding is done by shifting all obsevation points located outside of the near field region of the modeled discontinuity into virtual ports located at the geometrical edges of the distributed structure. This has to be done with respect to the dispersive transmission properties of all connecting transmission lines.

Extraction of Pole Locations

The main principle of our proposed method is to separate the extraction of admittance function pole locations α_n from the extraction of pole amplitudes $a_{ij}^{(n)}$ and $A_0^{(n)}$. Therefore we use a steepest-ascent search algorithm applied to the admittance matrix Laplace transform $\mathbf{Y}(p)$ numerically calculated from time domain scattering signals. The scattering parameters for a certain frequency point p are given by

$$S_{ij}(p) = \frac{\sum_{n=1}^{N} s_i(n)_{out} e^{-pnT}}{\sum_{n=1}^{N} s_j(n)_{in} e^{-pnT}} \tag{8}$$

Time domain scattering signals are well suited for numerical transformations, because they are limited in bandwidth as well as in time duration. Even lossless structures result in short time series due to the loading of resonant structures by their connecting transmission-line impedances. The required multiport admittance matrix $\mathbf{Y}(p)$ can be determined from its corresponding scattering matrix $\mathbf{S}(p)$.

$$\mathbf{Y}(p) = (\mathbf{q} + \mathbf{S}(p)\mathbf{q})^{-1} \cdot (\mathbf{q}^{-1} - \mathbf{S}(p)\mathbf{q}^{-1}) \tag{9}$$

$\mathbf{q}$ is a diagonal matrix containing the square roots of all port impedances. Reasonable starting values for a gradient based pole extraction working on single elements of $\mathbf{Y}(p)$ can be taken from contour plots of the admittance function Laplace transforms. A typical contour plot is shown in Fig. 3. Choosing all local maxima in the Fourier transform ($\mathrm{Re}(p) = 0$) of all admittance functions $y_{ij}(p)$ within the specified frequency range results in the extraction of all dominant poles. Any additional poles and trial solutions converging towards them can be found easily. Choosing a certain number of poles controls the accuracy and complexity of the generated lumped element circuit model.

Extraction of Pole Amplitudes

After all necessary poles α_n have been determined, their locations are fixed. Matrix elements $a_{ij}^{(n)}$ associated with the amplitudes of the poles can now be calculated by fitting (1) to the supposed admittance values obtained from (9). Solving these $(N+2)$ dimensional complex optimization problems has to be done with respect to the valid parameter space. To describe strictly passive multiports with R, L, C and G greater equal zero we have to map this restricted parameter space onto the parameter space of (1). In addition to the already mentioned restriction of real, symmetric and positive semidefinite matrices $\mathbf{A}^{(n)}$ and stable poles α_n located within the half plane $\mathrm{Re}\{\alpha_n\} \leq 0$ the following set of relations must be fulfilled:

$$\mathrm{Re}\left\{A_0^{(n)}\right\} > 0 \quad , \quad \left|\arg\left\{A_0^{(n)}\right\}\right| \leq \left|\arg\{-j\alpha_n\}\right| \quad , \quad \mathrm{Im}\left\{A_0^{(n)}\right\} \cdot \mathrm{Im}\{\alpha_n\} \geq 0 \tag{10}$$

Ensuring positive semidefinite matrices $\mathbf{A}^{(n)}$ can be achieved by forcing all eigenvalues of $\mathbf{A}^{(n)}$ to be greater or at least equal zero at every step of the fitting procedure. The solution will converge, if redundant degrees of freedom in (1) are eliminated. Therefore all complex parameters $A_0^{(n)}$ are fixed in their absolut value according to

$$\left|A_0^{(n)}\right| = 1 \quad . \tag{11}$$

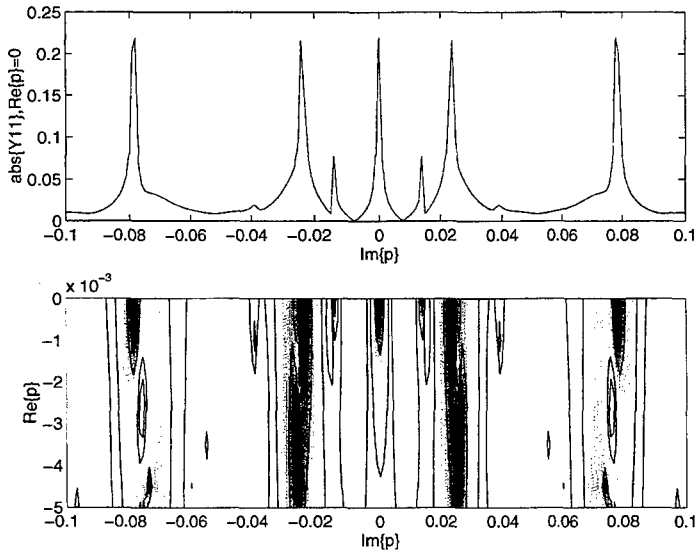

Figure 3: Laplace transform of Y_{11}

The convergence of the fitting process is not dependent on starting values and trivial assumptions can be made. Variable parameters $a_{ij}^{(n)}$ occur in linear terms and their contribution to the overall error is localized in frequency by their frequency dependent, but constant coefficients $Y^{(n)}$. This property results in a good convergence and the global minimum of the used error function can be found quickly. As an error function a weighted l_1-norm is used. A Least-Square error minimization of admittance parameters would lead to a bad approximation of scattering or transient behavior for the modeled distributed circuit. Sensitive admittance levels would end up with a large relative error compared to insensitive levels.

When a valid parameter set of (1) has been found, the generation of an equivalent lumped element circuit is straight forward. After all matrices $\mathbf{A}^{(n)}$ have been decomposed according to (3), lumped element parameters are calculated from (7), (5) and (6). To store the network topology and parameters of the generated equivalent circuit model a spice netlist is generated automatically.

4 Example

To demonstrate the versatility of the proposed method a distributed four-port circuit has been modeled. The geometry of the multichip module transmission-line crossing is shown in Fig. 4. It is placed on a ceramics MCM substrate ($\epsilon = 9.8$). The dielectric filling separating the two conducting layers is polyimid ($\epsilon = 3.3$). A conductor width of 58μm gives a line impedance of 50Ω for the microstrip lines at the ports of the circuit. Remaining geometrical dimensions can be found in [9]. As a result of the symmetry of the discontinuity only two TLM

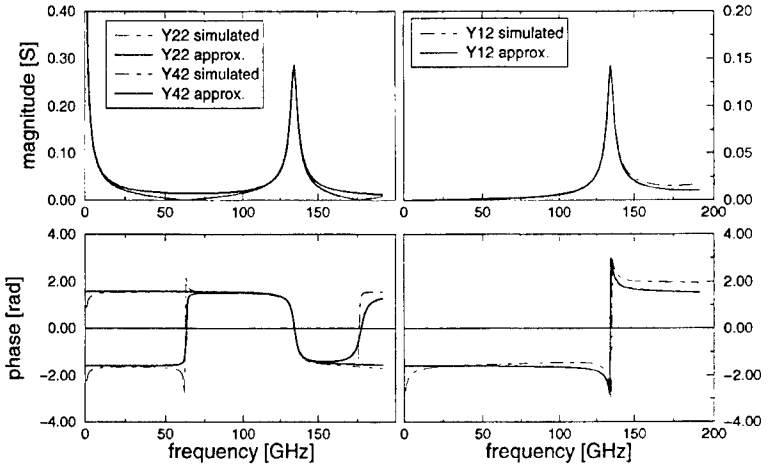

Figure 5: Admittance parameters of the MCM crossing

simulations are needed to describe the circuit completely. The frequency range of validity for the model to be generated was specified to be 0GHz – 150GHz. We took three poles for the model generation and the resulting lumped element equivalent circuit is built out of a shunt connection of three blocks shown in Fig. 2. A comparison of admittance parameters is shown in Fig. 5. Since the main application of lumped element equivalent circuit models is located in the area of transient network-simulation, we compared the original TLM simulation with a transient spice-simulation of the generated circuit model. Results for an input signal exceeding the bandwidth of the generated circuit model by a factor of two are shown in in Fig. 6. Though there is an expected difference between lumped element model and full-wave analysis, the stability and low-pass behavior of the lumped element equivalent circuit can be seen. More comparable results have been achieved after a TLM simulation with an input signal limited to the bandwidth of the circuit model was made. Then a good agreement between TLM- and Spice-simulation can be seen (Fig. 7). Remaining deviations are mainly caused by the fact, that a minimization of admittance approximation errors doesn't minimize the approximation error for scattering parameters. Increasing the number of poles up to six

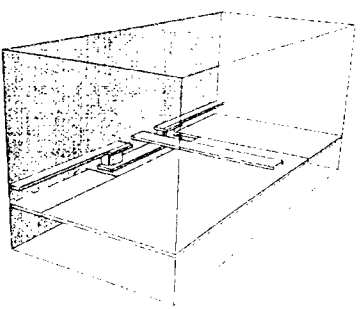

Figure 4: Multichip module transmission-line crossing: computational domain used to calculate the impulse response functions for one of the two different transmission directions

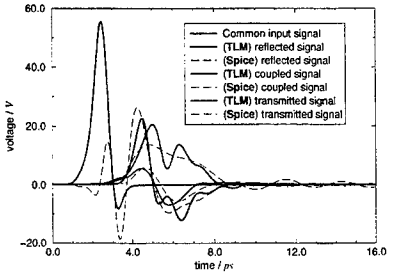

Figure 6: Comparison between full-wave analysis (TLM) and network simulation (Spice): bandwidth of input signal $B \approx 280\text{GHz} \leftrightarrow$ bandwidth of the original TLM simulation used for model generation

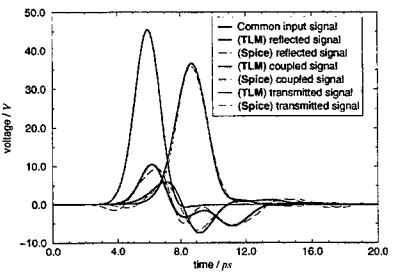

Figure 7: Comparison between full-wave analysis (TLM) and network simulation (Spice): bandwidth of input signal $B \approx 140\text{GHz} \leftrightarrow$ bandwidth of the equivalent circuit model

didn't increase the complexity of the model significantly. Originated in the symmetry of the structure, a mayor part of the matrices $\mathbf{A}^{(n)}$ reduces to rank one or two simplifying the equivalent circuit model considerably.

5 Conclusion

We have presented a method for generation of lumped element equivalent circuits for distributed microwave components based on time domain scattering signals. It can be applied to linear reciprocal multiports and produces topology as well as parameters of a model. A distributed four-port microwave circuit has been modeled and the applicability of the generated lumped element equivalent circuit in transient spice simulations has been demonstrated. The question of which error function to be used cannot be answered in general. Depending on the application of a model an appropriate choice is needed to get best results.

Acknowledgment

This work has been financially supported by the German Federal Ministry of Education, Science, Research and Technology (BMBF).

References

[1] W.J.R. Hoefer. The transmission line matrix (tlm) method: Theory and applications. *IEEE Trans. Microwave Theory Tech*, 33:882–893, 1985.

[2] K.S. Yee. Numerical solution of boundary value problems involving maxwell's equations in isotropic media. *IEEE Trans. Antennas and Propagation*, 14(5):302–307, May 1966.

[3] T. Quarles, A.R. Newton, D.O. Pederson, and A. Sangiovanni-Vincentelli. Spice3 version 3f3 user's manual. Department of Electrical Engineering and Computer Sciences, University of California, Berkeley, Ca, 94720, may 1993.

[4] P. Russer, M. Righi, C. Eswarappa, and W. Hoefer. Lumped element equivalent circuit parameter extraction of distributed microwave circuits via tlm simulation. *IEEE MTTS-Digest*, pages 887–890, 1994.

[5] V. Belevitch. *Classical network theory*. Holden-Day.

[6] Rolf Unbehauen. *Synthese elektrischer Netzwerke und Filter*. R. Oldenbourg Verlag, München, 1988.

[7] W. Cauer. Ideale transformatoren und lineare transformationen. *Elektr. Nachr. Techn.*, 9:157–174, 1932.

[8] D.A. Al-Mukhtar and J.E. Sitch. Transmission-line matrix method with irregularly graded space. *Proc. IEE*, 128(6):299–305, 1981.

[9] T. Mangold and P. Russer. Modeling of multichip module interconnections by the tlm method and system identification. *Proc. of the 27th Europ. Microwave Conf.*, 1997. to be published.

TLM Analysis of an Optical Sensor

Ronald R. DeLyser, University of Denver, Denver, CO

1 Introduction

Numerical analysis of optical sensors at microwave frequencies is essential in order to compliment measurements and to determine vulnerability of internal components. Micro-Stripes 3.0, produced by Kimberly Communications Consultants Ltd. and marketed by Sonnet Software, Inc., was used for the analysis of a Celestron-8 telescope and a satellite optical sensor. In the past, the Finite Element Method [1] was used to analyze the Celestron-8, and the Finite Difference Time Domain Method [2] was used to analyze the satellite optical sensor. This paper addresses only the Micro-Stripes analysis of the optical sensor.

Micro-Stripes uses the Transmission-Line Matrix (TLM) technique [3] [4] in the time domain for the analysis of full three-dimensional high-frequency structures and antennas. Post-processing is done to obtain fields, S-parameters, far-field radiation patterns and other outputs. Full control is provided over the model mesh where a dense mesh can be specified in regions where high potential gradients exist, and less dense meshes where electromagnetic activity is relatively low. The mesh can be graded to reflect local material and geometry and neighboring cells may have relative size ratios that may exceed ten or more. The geometric models are created from flexible primitives such as cylinders, cones, spheres, bricks, arbitrary 2D shapes and prisms, and boolean combinations of primitives and subsets of primitives.

Micro-Stripes is first used to obtain the time-domain impulse response for a given structure, and then in post-processing, extracts high-resolution frequency-domain results. Resonances or other frequencies of interest are then chosen for analysis by doing the radiation problem. A band limited pulse is used for the excitation at a point located inside the sensor. The frequencies of interest are specified and a virtual surface is defined for the calculation of equivalent surface currents. These currents are written to a file for post processing. Patterns can then be generated at the pre-determined frequencies. The outputs for a particular run are then any cut pattern that is defined to the post processor, or a 3-D plot of the entire pattern at the specified frequencies. Field quantities can also be recorded at points and slices in the problem space.

2 The Models

A number of models were analyzed, representing varying degrees of fidelity. The two models discussed here are shown in Figures 1 and 2[1]. The models used for scattering response had two planes of symmetry and a ground plane flush with the plane just outside the cavity lens. The excitation was a plane wave incident on boresight. This excitation is indicated in the figures with a large rectangle. The light areas are metal; the dark areas are a Germanium lens (towards

[1]Details of the sensor geometry and the assumptions made to create the simulation model are presented in [2].

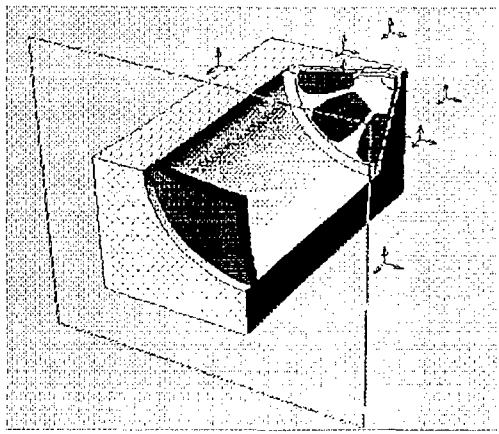

Figure 1: Model of the sensor without toroids.

the front of the figure) and Germanium filters. Thermopile detectors in the sensor are mounted on a Mylar substrate just below the Germanium filters (towards the back of the figure). The orthogonal arrows indicate simulation field point sensors.

The table below shows relevant data for the simulations. Micro-Stripes was run on an IBM PC with a 133 MHz Pentium processor and 128 MBytes of RAM. There is a reference to "graded cells" in the table. The capability exists to change the cell size in different regions. For this model as for the full models, a 0.5 mm cell size was chosen for the regions with the Mylar and Germanium materials and a 1.0 mm cell size for the air regions. This technique resulted in doubling the frequency response with an approximate three times increase in RAM usage. However, if a regular mesh of 0.5 mm cells were specified, the RAM usage would increase 8 fold with no greater frequency response than with the graded mesh.

Model		RAM (MBytes)	Time (hrs)	Steps/Highest frequency
1	Figure 1	12.7	3.75	10,000/8 GHz
2	Figure 1 with graded cells	32.6	23	20,000/16 GHz
3	Figure 2, Scattering	83.4	62	20,000/16 GHz
4	Figure 2, Radiation	59.1	41	20,000/8 GHz

Another technique used to conserve RAM was to put a ground plane flush with the top of the sensor. This addition did not affect the response in the cavities for the scattering problems. However, it does eliminate the need to provide "pad cells" for the radiation boundaries for all but the top area of the problem space. The TLM method requires approximately 1/3 of the

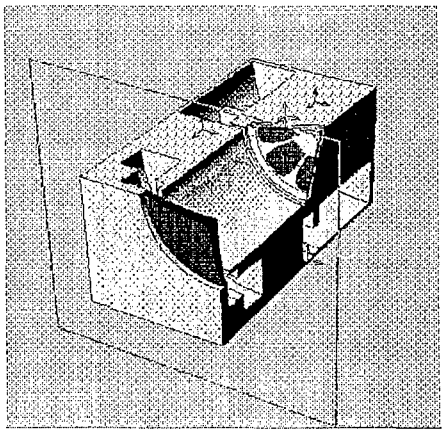

Figure 2: Geometry of the full sensor model.

largest dimension of a radiating aperture or structure to be left as free space in the model. This can triple the amount of RAM usage if the full structure is modeled surrounded by the radiation boundary conditions.

3 The Scattering Problem

Results for the simple model of Figure 1 with the graded mesh for two locations in the sensor are shown in Figures 3 and 4. Comparison of these results with the FDTD results reported in [2] show that the Micro-Stripes results have a "smoother" frequency response but the low frequency resonances are similar and the higher frequency response, on average, is the same. The full model scattering problem results are shown in Figures 5 and 6. The results compare favorably to the FDTD results reported in [2]. Also notice that the smooth nature of the results presented for the simplified model without the toroids is now gone. The spikes in the response with the toroids indicates that this is due to their inclusion in this model. The toroids are resonating at the frequencies of these spikes and are extracting energy from the main cavity.

4 The Radiation Problem

Only the full model was used for the radiation problem. The resonances at 3.55 GHz, 4.85 GHz and 6.56 GHz were investigated by doing the radiation problem with a point source located at one of the detector locations in the xz plane. Both x and y polarizations of the source were used

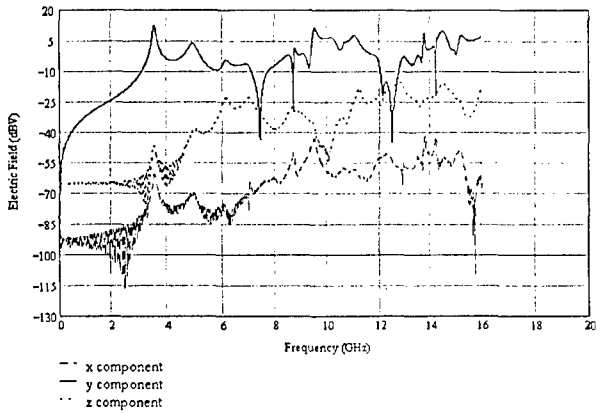

Figure 3: Center of the cavity region for sensor model 2.

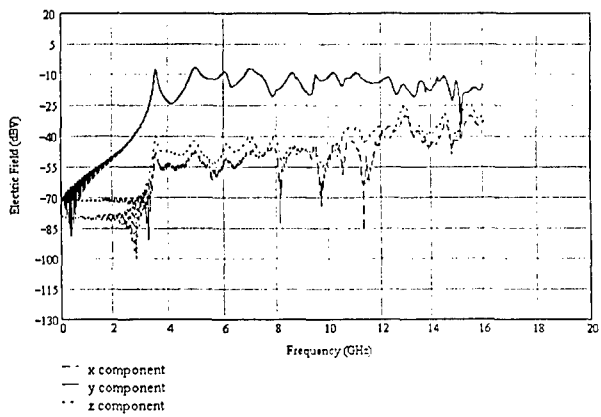

Figure 4: Detector location for sensor model 2.

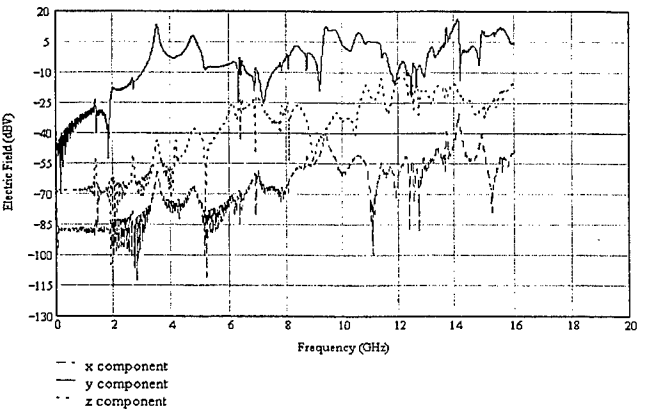

Figure 5: Large cavity region of the full sensor model.

so that comparisons with FDTD data [2] could be made. The resonances from that data were at 3.58 GHz, 4.82 GHz and 6.57 GHz. The differences between the TLM and FDTD simulations are use of symmetry and a ground plane in the plane of the lens for TLM, and no symmetry or ground plane for FDTD. A slice sensor was placed just below the lens and point sensors at the same locations as for the scattering problem.

Only the data at 4.85 GHz are presented here[2]. First, the 3-D radiation plots in Figures 7 and 8 are presented. The RMS total (all polarizations) electric field is plotted with a linear scale with the z axis pointing up and the x axis toward the front. Figures 9 and 10 show field plots just below the lens for the sensor at 4.85 GHz for both x and y polarizations. The data pictured has "bubbles" whose sizes are proportional to the field intensity. As presented in the Micro-Stripes generated figures, the slice sensor data is taken from an FFT of the time history of the points over the specified surface.

5 Conclusions

Micro-Stripes is a versatile and self-contained program. It is a time domain code which makes it computationally efficient for large open cavities; it has the capability of using graded meshes, modeling regions with fine details with a fine grid and regions with large objects with a coarse grid; it can be used with closed and open problems with and without symmetry; it can do both radiation and scattering problems; it has geometry and mesh creating capabilities; and it has

[2]Details of the entire study are in preparation for publication and can be obtained from the author.

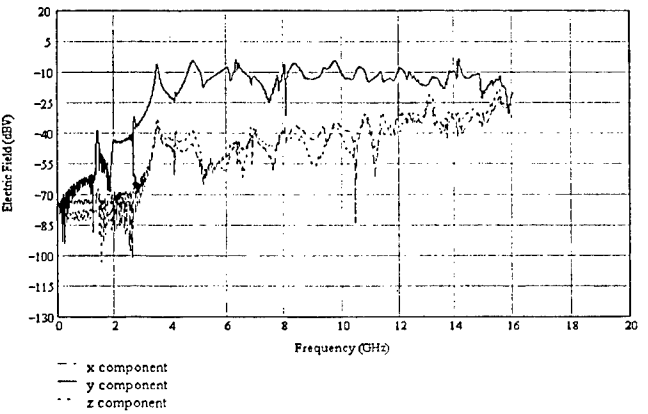

Figure 6: Detector location for the full sensor model.

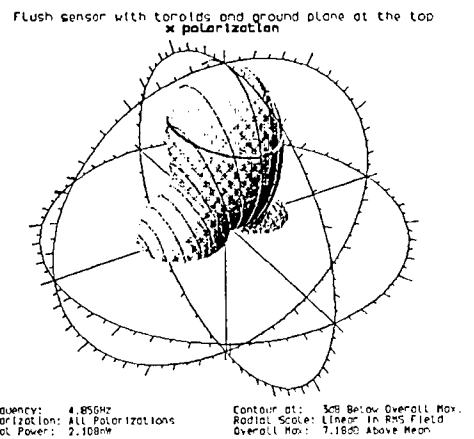

Figure 7: Full pattern radiation plot for the sensor at 4.85 GHz, x polarization.

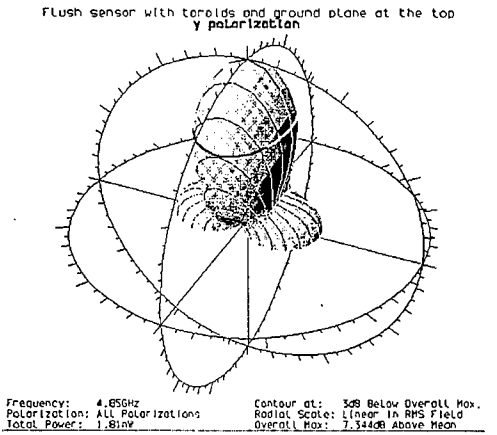

Figure 8: Full pattern radiation plot for the sensor at 4.85 GHz, y polarization.

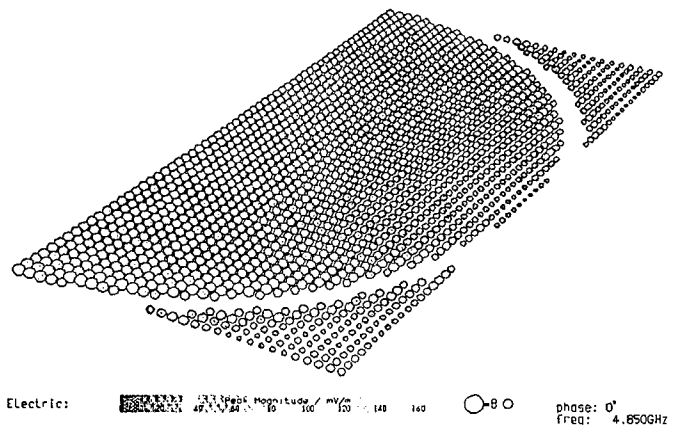

Figure 9: RMS electric field just below the lens at 4.85 GHz, x polarization.

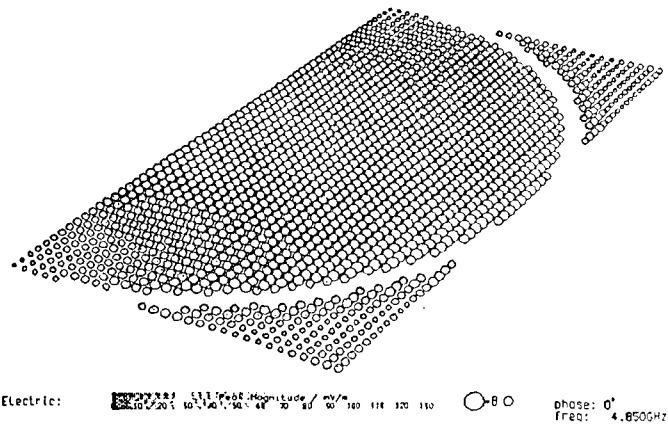

Figure 10: RMS electric field just below the lens at 4.85 GHz, y polarization.

extensive post-processing capabilities, including time to frequency domain conversion, temporal and spacial field visualization, scattering parameter calculations, and three dimensional radiation plots.

References

[1] R. R. DeLyser and H. Pohle, "Finite Element Method Analysis of the Celestron-8 Telescope," *The Twelfth Annual Review of Progress in Applied Computational Electromagnetics*, Naval Postgraduate School, Monterey, CA, 18-22 March, 1996.

[2] R. R. DeLyser, "Computational Evaluation of an Optical Sensor using the Finite Difference Time Domain Method," The Thirteenth Annual Review of Progress in Applied Computational Electromagnetics, Naval Postgraduate School, Monterey, CA, 17-21 March, 1997.

[3] P. B. Johns and R. L. Beurle, "Numerical solution of two-dimensional scattering problems using a transmission-line matrix", *Proc. IEE*, 1971, Vol. 118, No. 12, pp 1203-1208.

[4] C. Christopoulos, "The Transmission-Line Modeling Method", IEEE Press, Oxford University Press, 1995.

TLM Modeling and TDR Validation of Soil Moisture Probe for Environmental Sensing

Giampaolo Tardioli, Mario Righi, Lucia Cascio, Wolfgang J.R. Hoefer
and Ronald McFarlane*

NSERC Industrial Research Chair in RF Engineering.
Department of Electrical and Computer Engineering, University of Victoria,
Victoria, B.C. V8W 3P6, CANADA
*ESI Environmental Sensors Inc., 100-4243 Glanford Ave., Victoria B.C. V8Z 4B9, CANADA

Abstract

In this paper we present the application of the Transmission Line Matrix (TLM) method to the modeling of soil moisture probes for environmental sensing. The moisture probe, including the feeding coax and the coax-to-device transition, is modeled in TLM and measured using a Time Domain Reflectometer. The obtained results are validated with measurements. The time domain full-wave method is then adopted for the design of new optimized probe configurations, with enhanced propagation characteristics.

Introduction

TDR techniques are widely used in areas such as remote sensing, device and cable testing and measurements [1]. The time domain characteristics of the propagation of an electromagnetic wave through a guiding structure are measured, and information regarding electrical and geometrical properties of the structure are extracted from the inspection of the reflected waveforms. In this paper we focus on the characterization of soil moisture probes [2]-[3]. They consist of an open transmission line immersed in an unknown medium (such as soil of unknown moisture content). An electromagnetic pulse is injected and propagates along the line. The propagation characteristics of the wave in this guiding structure are affected by the dielectric constant surrounding the line, and the parameters of the unknown medium can be extracted therefrom.

For example, an increase in the soil moisture content around the probe leads to higher soil permittivity which results in a wave propagating slower in the transmission line. The typical pattern of the reflected waveform represents a signature for that specific soil and can be related to soil properties.

The development of sophisticated electromagnetic modeling techniques allows the characterization of the measurement setup as a whole, thus using the E/M time domain CAD tool as a virtual TDR instrument. The coaxial feed lines, the transition to the transmission line, and details of probe construction can all be included in the simulation.

There are many advantages to electromagnetic modeling:

- The possibility of quickly testing the instrument in a variety of media conditions without expensive on-site measurements.
- The possibility of quickly testing new ideas and device geometries avoiding costly prototypes.
- The possibility of sampling the field inside and around the probe, without perturbing it, a feature not available in a real measurement.
- The possibility of exploring the effects of localized impurities (air or water pockets) on the probe performance.

All of these advantages result in a significant cost reduction in the development of sensing devices. The characteristics of a full wave analysis are particularly useful in the design of novel sensor configurations with optimum sensitivity. This is achieved by maximizing the interaction of the wave with the soil.

Modeling

The test structure under consideration is shown in figure 1a. It is composed of two metallic plates supporting a TEM wave. The metalling plates are kept in place by a dielectric separator. The transmission line is fed from a 50 Ω coaxial line (the detail of the transition is shown in figure 1b). A layer of aluminum foil connects the two brass plates at the far end of the probe, thus providing a short circuit.

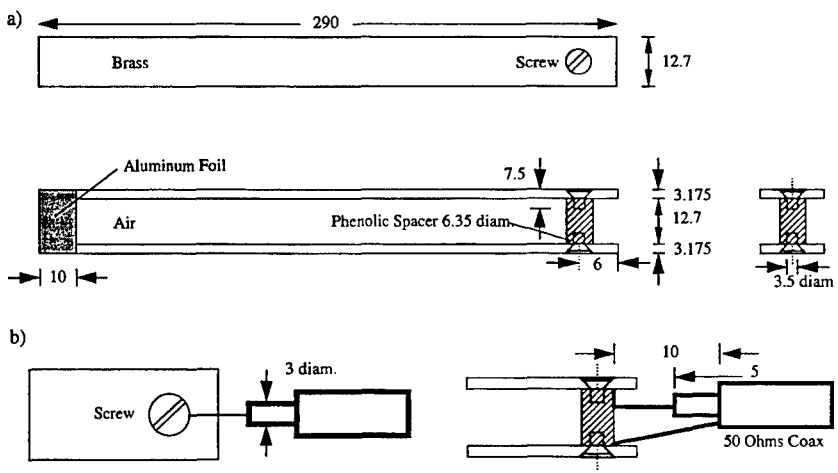

Fig. 1 Geometry of the soil moisture probe. All dimensions are in mm. a) probe, b) detail of the coax-to-probe transition.

The whole setup has been discretized with a uniform TLM mesh of size 16 by 18 by 135 cells. The cell size is 3.175 mm with a corresponding time step of 5.29 ps. The node used is the Symmetrical Condensed Node (SCN) [4]. The computational domain is terminated with single reflection coefficient boundary conditions. The same conditions are applied to the termination of the coaxial feeding line. The brass electrodes, as well as the aluminum short circuit have been modeled as perfect electric conductors.

Results

A step signal with a rise time of approximately 0.2 ns was injected in the feeding coaxial line. The waveform is shown in figure 2.

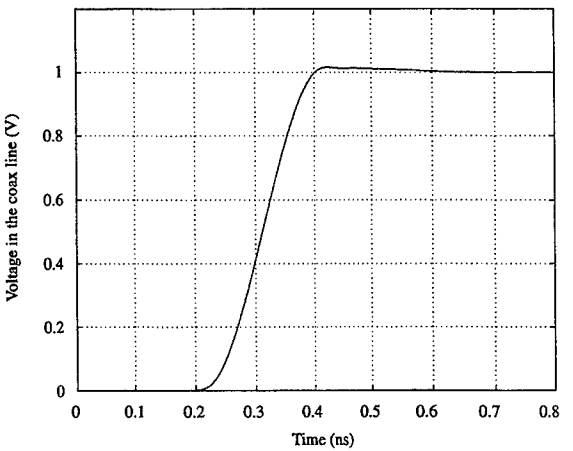

Fig. 2 Excitation waveform.

In order to accurately validate the simulated results, measurements have been performed under well defined conditions (probe immersed in air). Figure 3 shows the total voltage at the feeding coaxial line normalized to the incident voltage.

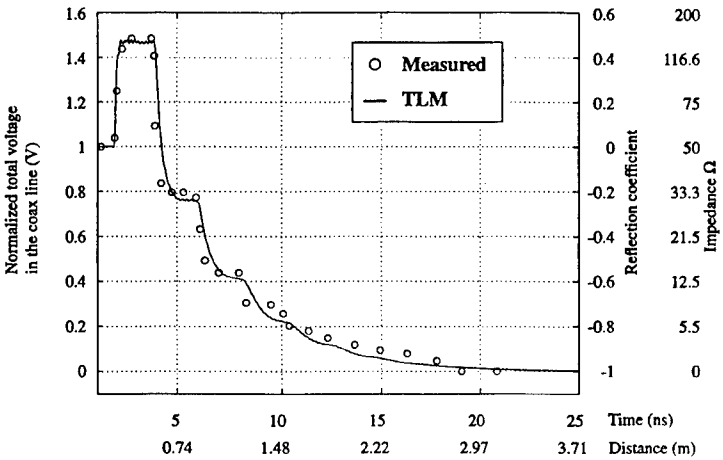

Fig. 3 Comparison of simulated results and measurements for the probe in air.

The TLM simulation requires only a few minutes on a high-end Pentium PC, thus making the simulation competitive with actual measurements in terms of time. Memory requirements are less than 4 MBytes. The measurements have been performed on a Tektronix 1502C TDR.

The agreement shown in figure 3 is excellent. Both timing and amplitude of the signal at the coaxial line have been accurately predicted. The simulated results appear to be slightly lower than the measured ones after 5 ns; this is believed to be due to the losses in the metallic conductors, that have not been included in the simulation. Nevertheless the simulated results are sufficiently accurate to predict measurements within the margin of experimental error.

By assuming an average propagation speed of the wave in the structure equal to V_p=f c (where c is the speed of light in vacuum and f=0.99 an empirical factor characteristic of the TDR), we can relate travel time to distance along the path of the wave. The distance scale is reported below the time scale for convenience. On the vertical scale the total normalized voltage at the coaxial port is reported along with the corresponding reflection coefficient and impedance. In this way the impedance of the transmission line in different sections can be traced. For example, the first reflection (encountered at about 1.5 ns) is related to the mismatch between the coax cable and the parallel plate transmission line in air. From the mismatch the impedance of the parallel plate transmission line can be easily obtained.

In a second test the probe has been partially immersed in water. The results are shown in figure 4. The step towards lower impedances at 3 ns (when the signal encounters the water) is clearly visible. These

two extreme conditions indicate to the designer the type of signals that must be expected from the actual probe.

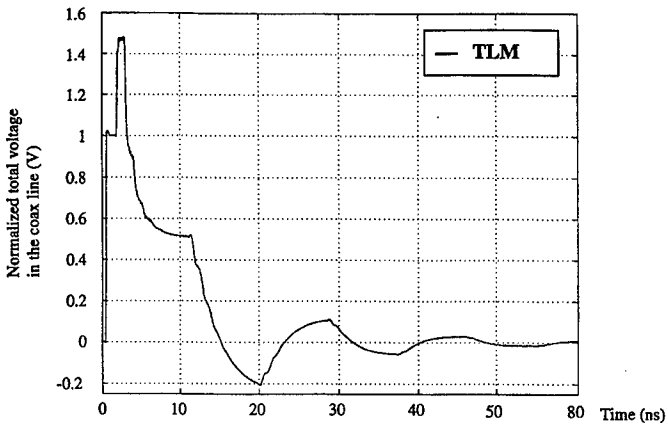

Fig. 4 Simulated results for the probe partially immersed in water.

A Novel Class of Probes

A critical factor in the design of a probe is its sensitivity. Highly sensitive probes are achieved by optimizing the wave interaction with the soil as much as possible. This can be accomplished in several ways:

- by creating a longer electrical path for the electromagnetic wave in the soil.
- By shaping the electrodes so as to maximize the field penetration into the soil, without significant radiation loss.

These guidelines have been implemented in a novel probe configuration significantly more complex than the one previously described. The new probe presents eight electrodes distributed around a dielectric rod. A schematic representation of such a probe is shown in figure 5.

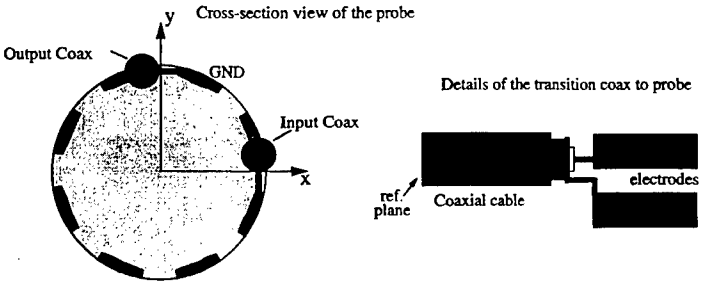

Fig. 5 Schematic representation of the novel probe configuration.

Connections between the electrodes at the extremities of the probe provide an electrical path which is four times the geometrical length of the probe. With the two-port configuration both reflected and transmitted signals can be monitored, thus yielding more information in a single measurement cycle.

The realization of prototypes can be both time-consuming and expensive. For this reason the TLM method has been used to characterize the virtual probe. Input and output are still on 50 Ω coaxial cables. The electrodes have been optimized to produce the highest sensitivity. This was achieved by maximizing the percentage of the wave that travels in the soil. With this configuration as much as 50% of the electromagnetic wave energy propagates in the soil. This optimization requires the knowledge of the electromagnetic field in the soil; this information is readily available in a TLM simulation.

Different conditions can be rapidly considered and the response of the probe predicted (from dry to wet soil with different losses). In addition the perturbation of the soil as a consequence of the probe presence can be taken into account. The time domain waveforms at the input and output coaxial lines for one of the considered cases (uniform dry soil) are shown in figure 6.

Conclusion

We have presented the characterization of soil moisture probes for environmental sensing with the TLM method. The model can account for the entire probe, including the coaxial feeds. In this way, the actual operation of the probe as a time-domain reflectometer can be simulated in all detail. The results compare well with measurements. The use of a full wave tool allows rapid testing and optimization of new configurations, thus facilitating the design and shortening the development time.

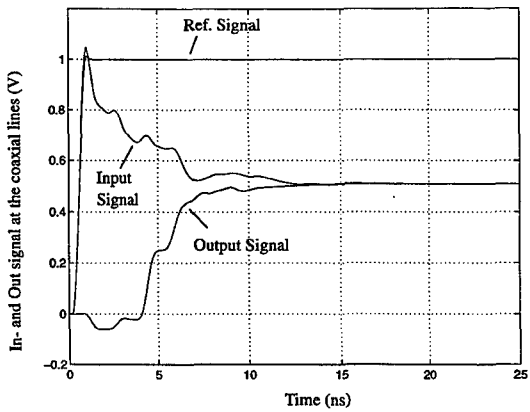

Fig. 6 Time domain waveforms at the input and output coaxial lines of the enhanced probe.

Acknowledgments

The authors wish to acknowledge the financial support and the scientific input on soil moisture probes provided by Dr. Clarke Topp, of Agriculture Canada, Ottawa, Canada.

References

[1] Edmund K. Miller, *Time-Domain Measurements in Electromagnetics*, New York, Van Nostrand Reinhold, 1986

[2] Bin Xiao, "Moisture Content Measurements Using Time-Domain Techniques", M.Sc. Thesis, University of Victoria, 1994.

[3] J.H. Knight, P.A. Ferre, D.L. Rudolph, R.G. Kachanoski, "A Numerical Analysis of the Effects of Coating and Gaps upon Relative Permittivity Measurement with Time Domain Reflectometry", *Water Resources Research*, vol. 33, no. 6 pp. 1455-1460, June 1997.

[4] C. Christopoulos, *The Transmission-Line Modeling Method*, IEEE Press Oxford University Press, 1995.

TLM Analysis of the Celestron-8 Telescope

Ronald R. DeLyser, University of Denver, Denver, CO

1 Introduction

Numerical analysis of optical sensors at microwave frequencies is essential in order to compliment measurements and to determine vulnerability of internal components. Micro-Stripes 3.0, produced by Kimberly Communications Consultants Ltd. and marketed by Sonnet Software, Inc., was used for the analysis of a Celestron-8 telescope and a satellite optical sensor. In the past, the Finite Element Method [1] was used to analyze the Celestron-8, and the Finite Difference Time Domain Method [2] was used to analyze the satellite optical sensor. This paper addresses only the Micro-Stripes analysis of the Celestron-8 telescope.

Micro-Stripes uses the Transmission-Line Matrix (TLM) technique [3] [4] in the time domain for the analysis of full three-dimensional high-frequency structures and antennas. Post-processing is done to obtain fields, S-parameters, far-field radiation patterns and other outputs. Full control is provided over the model mesh where a dense mesh can be specified in regions where high potential gradients exist, and less dense meshes where electromagnetic activity is relatively low. The mesh can be graded to reflect local material and geometry and neighboring cells may have relative size ratios that may exceed ten or more. The geometric models are created from flexible primitives such as cylinders, cones, spheres, bricks, arbitrary 2D shapes and prisms, and boolean combinations of primitives and subsets of primitives.

Micro-Stripes is first used to obtain the time-domain impulse response for a given structure, and then in post-processing, extracts high-resolution frequency-domain results. Resonances or other frequencies of interest are then chosen for analysis by doing the radiation problem. A band limited pulse is used for the excitation at a point located inside the sensor. The frequencies of interest are specified and a virtual surface is defined for the calculation of equivalent surface currents. These currents are written to a file for post processing. Patterns can then be generated at the pre-determined frequencies. The outputs for a particular run are then any cut pattern that is defined to the post processor, or a 3-D plot of the entire pattern at the specified frequencies. Field quantities can also be recorded at points and slices in the problem space.

2 The Model

A drawing and the simulation model of the Celestron-8 are shown in Figures 1 and 2. All of the models used for scattering response had two planes of symmetry. The excitation was a plane wave incident on the aperture. This excitation is indicated in Figure 2 with the large rectangle. Two models were created. One with the Plexiglass window in the aperture and glass behind the primary mirror (these are shown as dark areas in Figure 2), and one without those features. The table below shows relevant data for the Celestron-8 simulations. This software was run on an IBM PC with a 133 MHz Pentium processor and 128 MBytes of RAM. There is a reference to "graded cells" in the table. The capability exists in Micro-Stripes to change the cell size in different regions.

Another technique used to conserve RAM was to put a ground plane flush with the aperture of the model. This should not affect the response in the cavities for the scattering problems. It does eliminate the need to provide "pad cells" for the radiation boundaries for all but the top area of the problem

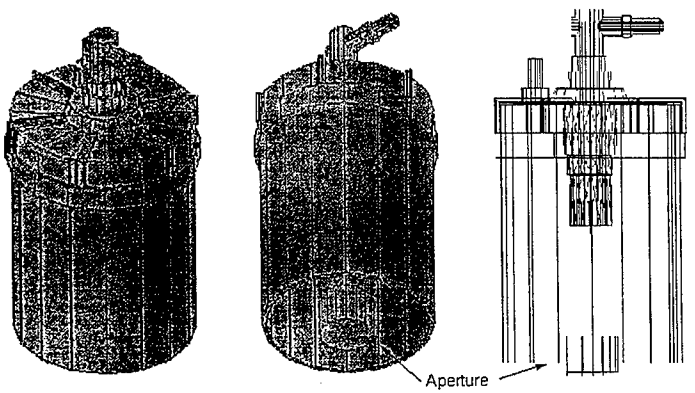

Figure 1: The Celestron-8 telescope.

space. The TLM method requires approximately 1/3 of the largest dimension of a radiating aperture or structure to be left as free space in the model. This can triple the amount of RAM usage if the full structure is modeled surrounded by the radiation boundary conditions. Compare, for example, models 1 and 2 of the table. The run time for these models differs by a factor of six. Comparisons of the results for these two models follows.

	Model	RAM (MB)	Time (hrs)	Steps/Frequency
1	Plane wave excitation - no materials	120	58	10,000/15 GHz
2	as for 1 but with ground	41.6	10	10,000/15 GHz
3	as for 1 but with materials	90	24	10,000/8 GHz
4	Probe excitation (radiation, graded cells)	83.2	51	15,000/2 GHz

3 The Scattering Problem Results

Model 1 (without the materials) gave the results shown in Figure 3 along with measured results from [5]. For those measurements, a sensor was placed in the location of the eye-piece for the telescope and transmission to that sensor from a radiating source was measured. For a radiation measurement, a probe was inserted into the large central cavity region of the telescope and S_{11} data taken. Thus Figure 3 refers to these locations as points where simulation data was taken. Notice that the low frequency measured data, even though it is taken at the location of the eyepiece, corresponds to simulation data at the location of the probe. This can be explained by the fact that isolation of the receiving sensor from the large cavity region could not be assured. Note also that the characteristic high pass filter response of the small cylinder leading to the eyepiece is evident in the "Eye piece location" data.

Model 2, similar to Model 1, was generated and analyzed. The only difference is that Model 2 had a ground plane flush with the window to the Celestron-8. As shown in the table, this reduces computational

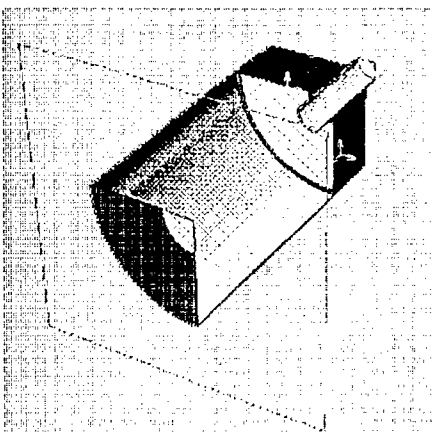

Figure 2: Cutaway view of the Celestron-8 model.

resources substantially. But is the model still valid? Figures 4 and 5 show the comparisons of the results of the two models for locations at the eyepiece and at the probe.

Particular attention should be given to the "Difference" data. It is only large for regions of the data that have large negative going spikes or where the data varies rapidly with changing frequency. Otherwise, the data plots for the two models basically lie on top of each other. This was expected since the ground plane should not significantly affect the response inside the cavity. This is then a useful modeling technique for the scattering problem that will conserve computational resources.

The absence of the materials for Models 1 and 2 extended the frequency response to 15 GHz. The response of Model 3 (with the materials) was limited to 8 GHz and was not substantially different from those models without the materials. This was to be expected since the dielectric constants for the glass and Plexiglass are relatively low (< 4).

4 The Radiation Problem Results

The geometry for the Celestron-8 radiation model is as reported above with the exception that a large region of absorber was used to fill the region outside the telescope below the plane of the Plexiglass window. For the 234 mm diameter aperture of the Celestron-8, the far field is at 730 mm so that the problem size is substantially greater than for the scattering problem[1]. This technique of filling a large region with absorber backed by metal[2] reduces the problem size significantly and only removes the

[1]Subsequent to this study it was learned that placement of absorbing boundaries for radiation problems need not be in the far field, but nearly 1/3 of the largest dimension (as it is for the scattering problem) of a radiation source. In this case, that was 1/3 the diameter of the aperture.

[2]The metal cells are "dead cells" because the fields are zero there.

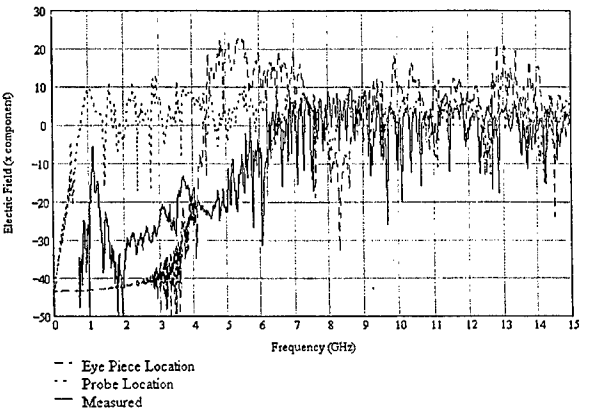

Figure 3: Response for the simplified model of the Celestron-8.

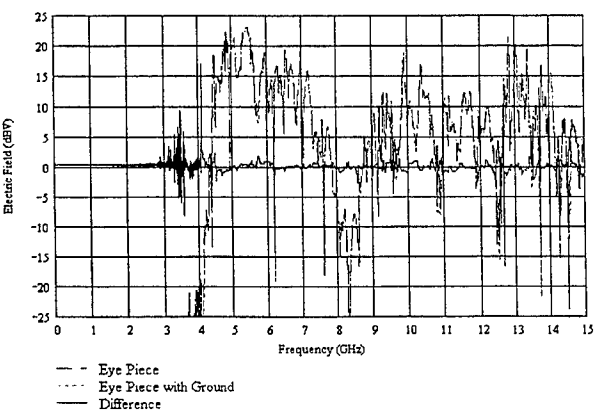

Figure 4: Results for Models 1 and 2 at the eyepiece location.

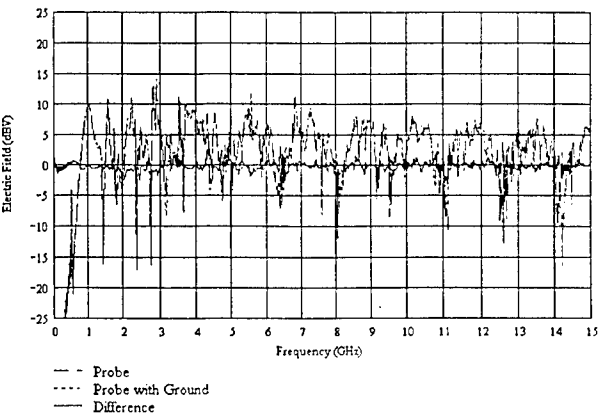

Figure 5: Results for Models 1 and 2 at the probe location.

portion of the radiation pattern below the plane of the Plexiglass window. An equivalent surface is also defined so that far field calculations can be done based on equivalent sources on that surface.

The resonances at 1.00 GHz, 1.43 GHz, 1.63 GHz and 1.77 GHz were investigated by doing the radiation problem with a dipole source located at the probe location in the xz plane, the plane of symmetry. As a comparison, previous data generated using FDTD and reported in [6] show the resonance frequencies are at 1.02 GHz, 1.45 GHz, 1.61 GHz and 1.76 GHz. A slice sensor was placed at the aperture of the model in order to view the electric fields there. The 3-D radiation plot for 1.63 GHz[3] are shown in Figure 6. The RMS total (all polarizations) electric fields are plotted with a linear scale with the z axis (boresight) up and the x axis toward the front. Unfortunately, no measured data exists to compare with the numerical results. This is fertile ground for testing in the future.

The field plot for the plane of the aperture is shown in Figure 7. The data pictured has "bubbles" whose sizes are proportional to the field intensity. As presented in the Micro-Stripes generated figures, the slice sensor data is taken from an FFT of the time history of the points over the specified surface.

5 Conclusions

Micro-Stripes is a versatile and self-contained program. It is a time domain code which makes it computationally efficient for large open cavities; it has the capability of using graded meshes, modeling regions with fine details with a fine grid and regions with large objects with a coarse grid; it can be used with closed and open problems with and without symmetry; it can do both radiation and scattering problems; it has geometry and mesh creating capabilities; and it has extensive post-processing

[3]Details of the entire study are in preparation for publication and can be obtained from the author

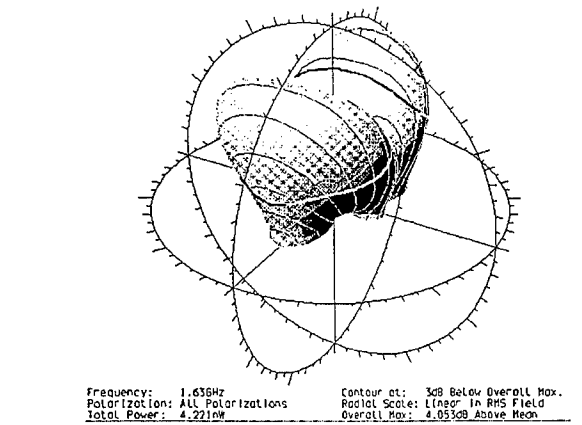

Figure 6: Radiation for the probe excited Celestron-8 telescope - 1.63 GHz.

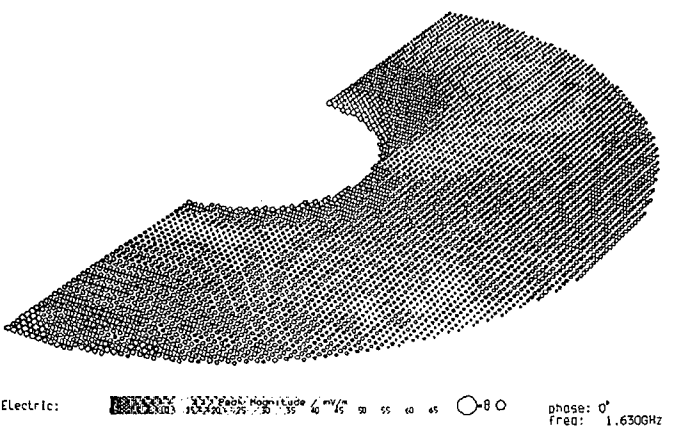

Figure 7: RMS value of the total electric field in the plane of the aperture- 1.63 GHz.

capabilities, including time to frequency domain conversion, temporal and spacial field visualization, scattering parameter calculations, and three dimensional radiation plots.

References

[1] R. R. DeLyser and H. Pohle, "Finite Element Method Analysis of the Celestron-8 Telescope," *The Twelfth Annual Review of Progress in Applied Computational Electromagnetics*, Naval Postgraduate School, Monterey, CA, 18-22 March, 1996.

[2] R. R. DeLyser, "Computational Evaluation of an Optical Sensor using the Finite Difference Time Domain Method," The Thirteenth Annual Review of Progress in Applied Computational Electromagnetics, Naval Postgraduate School, Monterey, CA, 17-21 March, 1997.

[3] P. B. Johns and R. L. Beurle, "Numerical solution of two-dimensional scattering problems using a transmission-line matrix", *Proc. IEE,* 1971, Vol. 118, No. 12, pp 1203-1208.

[4] C. Christopoulos, "The Transmission-Line Modeling Method", IEEE Press, Oxford University Press, 1995.

[5] R. R. DeLyser and Peyman Ensaf, "Quality Factor Evaluation of Complex Cavities," Final Report, Summer Research Extension Program, Sponsored by Phillips Laboratory, December, 1995.

[6] Ronald R. DeLyser, "FEM and FDTD Analysis of the Celestron-8 Telescope and a Satellite Sensor," Final Report, Contract F29650-96-W-0172, December, 1996.

NEAR- TO FAR FIELD TRANSFORMATION VIA PARABOLIC EQUATION

A.N.Kurokhtin, Yu.V.Kopylov, and A.V.Popov,
IZMIRAN, Russia
A.V.Vinogradov, Lebedev Physical Institute, Russia

Introduction

It is well known that the scattered wave produced by a dielectric object of diameter D propagates, in the short-wave limit, within a cone of angular width $\theta \sim \lambda / D$. At large distances $R >> 4D^2 / \lambda$ (Fraunhofer zone) it forms a modulated spherical wave

$$E_s \sim F(\vartheta,\varphi)\frac{e^{ikR}}{R} \qquad (1)$$

The diffraction pattern, $F(\vartheta,\varphi)$, depending on the wave number $k = 2\pi / \lambda$, the object shape and dielectric properties, is the subject of interest for many applications, from radars to diffraction-limited optics. This work is focused on field calculations for X-ray and EUV optics. In this spectral range, due to condition $|\varepsilon - 1| << 1$, an efficient numerical method can be applied which is based on the Leontovich-Fock parabolic wave equation [1,2]. It adequately describes spatial field distribution inside X-ray optical elements, such as zone plates, as well as in free space up to the focal spot or image position. However, it is not sufficient for some important applications where the knowledge of the far field pattern $F(\vartheta,\varphi)$ in Eq.(1) is really needed. Our first example is dark field X-ray microscopy [3] where scattering by small gold label particles is used to enhance spatial resolution. Another example is point diffraction interferometry [4]. In this case, diffraction by a pinhole is used to produce a reference spherical wave for at-wavelength testing the performance of EUV optical elements and systems. In both applications, the wave field is studied at very large distances where even the validity of the parabolic equation is not evident, not speaking of the computational difficulties that grow up considerably.

Here, we suggest a new numerical approach which allows one to minimize computational resources by transferring the near field (Fresnel diffraction) data to the Fraunhofer zone. The method is based on the Malyuzhinets transversal diffusion principle [5] combining the original Leontovich-Fock parabolic equation [6] with the formalism of ray coordinates. We demonstrate that Malyuzhinets' parabolic equation written in spherical coordinates perfectly suits the problem of calculating the radiation patterns of typical X-ray and EUV scatterers.

1. Parabolic wave equation.

Parabolic wave equation (PWE) governs the slowly varying amplitude $u(x,y,z)$ of a paraxial wave packet

$$E(x,y,z)=u(x,y,z)e^{ikz} \qquad (2)$$

After substituting (2) into the scalar wave equation, one obtains an exact relationship

$$\frac{\partial^2 u}{\partial z^2} + 2ik\frac{\partial u}{\partial z} + \frac{\partial^2 u}{\partial x^2} + \frac{\partial^2 u}{\partial y^2} + k^2(\varepsilon - 1)u = 0 \tag{3}$$

Leontovich's approximation - see [5, 6], consists in neglecting the first term $\frac{\partial^2 u}{\partial z^2}$ and leads to the well known PWE

$$2ik\frac{\partial u}{\partial z} + \frac{\partial^2 u}{\partial x^2} + \frac{\partial^2 u}{\partial y^2} + k^2(\varepsilon - 1)u = 0 \tag{4}$$

Its validity conditions are roughly expressed by two criteria [1]

$$|\varepsilon - 1| << 1, \qquad z << \frac{4\lambda}{\theta^4} \tag{5}$$

where $\varepsilon(x,y,z)$ is dielectric permittivity and θ is the angular spectral width of the wave packet. In our case of a single localized scatterer, θ coincides with the polar angle $\vartheta = \arctan r/z$ of the radius vector r pointing from the scatterer to the observation point $(r\cos\varphi, r\sin\varphi, z)$. So the second condition in (5) determines a spatial domain

$$r << (4\lambda)^{1/4} z^{3/4} \tag{6}$$

where the parabolic approximation holds.

In order to calculate the diffraction pattern $F(\vartheta, \varphi)$ one has to propagate the scattered field into the Fraunhofer zone $z >> 4D^2/\lambda \equiv z_F$ inside the cone $0 < \vartheta < \theta \sim \lambda/D$ where the main lobes are enclosed. Substituting $r \approx \theta z$ in to the inequality (6) gives an estimate of the maximum distance $z_{PE} \approx 4D(D/\lambda)^3$ where the PWE can be used for the field calculation inside the whole diffraction cone. As can be easily seen

$$z_{PE} \approx z_F\left(\frac{D}{\lambda}\right)^2 \tag{7}$$

so, for large scatterers $(D >> \lambda)$ we have $z_{PE} >> z_F$, which means that basically the diffraction pattern can be extracted from the solution of the PWE (4). Still, at least three weak points of the straightforward PWE application for this purpose are to be emphasized:

(i) Actually, numerical integration of the PWE (4) is performed in a cylinder of radius $A >> \theta z_F \sim 4D$ whereas the scattered field is formed in a considerably smaller volume starting at the scatterer and being smoothly transformed into the diffraction cone $\vartheta \le \lambda/D$. Therefore, a major part of the computational work is performed in a nonphysical domain.

(ii) The scattered wave goes down with distance whereas the background associated with the incident wave and the numerical errors remain constant which greatly reduces the accuracy.

(iii) Even if the above difficulties are overcome, the resulting solution is not satisfactory from the theoretical point of view as the asymptotic behavior of the PWE (4) does not have the form (1).

2. Angular diffusion approach.

The shortcomings of the standard PWE approach can be got over by using the generalization of the parabolic equation suggested by Malyuzhinets in his classical paper [5]. According to Malyuzhinets, short-wave diffraction can be understood as transversal diffusion of the complex wave amplitude along the curved wave fronts defined in geometric optics. In our case, the wave fronts of the scattered field in the Fraunhofer zone are spheres. Therefore, the adequate theory of

wave propagation from near zone to the Fraunhofer zone has to describe wave diffusion along spherical, not plane wave fronts. Mathematically, that means that the wave field has the form

$$E = e^{ikz} + U(R,\vartheta,\varphi)\frac{e^{ikR}}{R} \tag{8}$$

where e^{ikz} represents the plane incident wave, and the scattered component is sought as a spherical wave modulated by a slowly varying function $U(R,\vartheta,\varphi)$. In free space it satisfies the following exact equation

$$\frac{\partial^2 U}{\partial R^2} + 2ik\frac{\partial U}{\partial R} + \frac{1}{R^2\sin\vartheta}\frac{\partial}{\partial\vartheta}\left(\sin\vartheta\frac{\partial U}{\partial\vartheta}\right) + \frac{1}{R^2\sin^2\vartheta}\frac{\partial^2 U}{\partial\varphi^2} = 0\ . \tag{9}$$

Neglecting the first term $\frac{\partial^2 U}{\partial R^2}$ yields

$$2ik\frac{\partial U}{\partial R} + \frac{1}{R^2\sin\vartheta}\frac{\partial}{\partial\vartheta}\left(\sin\vartheta\frac{\partial U}{\partial\vartheta}\right) + \frac{1}{R^2\sin^2\vartheta}\frac{\partial^2 U}{\partial\varphi^2} = 0\ . \tag{10}$$

This new PWE is a particular case of general Malyuzhinets transversal diffusion equation [5]. We will call it the angular diffusion equation (ADE).

The main advantage of Eq.(10), as compared with the standard PWE (4), is that its solution tends at $R\to\infty$ to some limiting function: $U(R,\vartheta,\varphi)\to U(\infty,\vartheta,\varphi)$, which gives the right asymptotic form (1) with $F(\vartheta,\varphi) = U(\infty,\vartheta,\varphi)$. On the other hand, it is evident that this approximation can't be helped failing at small radii R. To estimate its applicability limit we construct a complete set of ADE solutions corresponding to spherical harmonics:

$$U_l^m(R,\vartheta,\varphi) = C_l\exp\left[i\frac{l(l+1)}{2kR}\right]Y_l^m(\vartheta,\varphi) \tag{11}$$

that are to be compared with the exact wave harmonics - solutions of Eq.(9):

$$U_l^m(R,\vartheta,\varphi) = \sqrt{R}e^{-ikR}H^{(1)}_{l+\frac{1}{2}}(kR)Y_l^m(\vartheta,\varphi)\ , \tag{12}$$

In the problem of short-wave diffraction $\lambda << D$, we are actually interested in comparing the short-wavelength asymptotics $(kR>>1,\ l\sim 1/\theta = D/\lambda >> 1)$ of the solutions (11) and (12). In this region, the Debye approximation can be used:

$$H_\nu^{(1)}(\rho)\sim\sqrt{\frac{2}{\pi}}\left(\rho^2-\nu^2\right)^{-\frac{1}{4}}\exp i\left(\sqrt{\rho^2-\nu^2}-\nu\arccos\nu/\rho-\pi/4\right) \tag{13}$$

that holds for $\rho = kR >> 1$, $\nu = l+\frac{1}{2} >> 1$ but $\nu/\rho \le 1$. For $\nu << \rho$ (which means $D<<R$), no matter small or large ν is, the Debye formula can be simplified by expanding the exponent in powers of ν/ρ :

$$H_\nu^{(1)}(\rho)\sim\sqrt{\frac{2}{\pi\rho}}\exp i\left[\rho+\frac{\nu^2}{2\rho}+\frac{\nu^4}{24\rho^3}-\frac{\pi}{2}\left(\nu+\frac{1}{2}\right)\right] \tag{14}$$

Substitution into Eq.(12) yields

$$U_l^m \approx C_l\exp\left[i\left(\frac{\nu^2}{2\rho}+\frac{\nu^4}{24\rho^3}\right)\right]Y_l^m(\vartheta,\varphi) \tag{15}$$

In terms of $\rho = kR$, $\nu = l + 1/2$, ADE harmonics (11) take the form

$$U_l^m = C_l \exp\left(i\frac{\nu^2 - 1/4}{2\rho}\right) Y_l^m(\vartheta,\varphi) \tag{16}$$

We see that Eqs.(15) and (16) are equivalent if $\nu^4 / 24\rho^3 << 1$, which gives the lower validity limit of the angular diffusion equation:

$$R >> \frac{D}{2\pi\sqrt[3]{24}}\left(\frac{D}{\lambda}\right)^{1/3}. \tag{17}$$

This estimate shows that the ADF holds in a vast spatial domain containing both the Fraunhofer $\left(R > \frac{4D^2}{\lambda}\right)$ and Fresnel $\left(2D\sqrt{\frac{D}{\lambda}} < R < \frac{4D^2}{\lambda}\right)$ diffraction zones. Only a small vicinity of the scatterer must be treated with another method. Hence, a hybrid approach arises: to use standard PWE (4) for field calculations in a narrow cylinder containing the scattering object:

$$0 < z < R_0 \sim D\left(\frac{D}{\lambda}\right)^{1/3}, \qquad 0 < r < A \sim D \tag{18}$$

and change to ADE (10) in a cone $0 < r \le \frac{\lambda}{D} z$ for greater distances $z \ge R_0$. On this way we get rid of the limitations inherent in both methods while retaining and combining their advantages. One can expect this will be an efficient computational method to propagate the wave field from the scatterer to the far zone.

3. Numerical implementation of hybrid PWE-ADE approach.

For the practical implementation of the hybrid PWE-ADE approach proposed in Section 2, some further transformations of Eq.(10) are helpful. First, as far as we are interested in relatively narrow axially symmetric diffraction patterns $\theta \sim \lambda/D << 1$, the coefficients of Eq.(10) can be simplified by substitution $\sin\vartheta \to \vartheta$ and eliminating the azimuthal derivative $\frac{\partial^2 U}{\partial\varphi^2}$. Second, change of variables

$$t = \frac{1}{R_0} - \frac{1}{R} \tag{19}$$

removes the range-dependent coefficients:

$$2ik\frac{\partial U}{\partial t} + \frac{1}{\vartheta}\frac{\partial}{\partial\vartheta}\left(\vartheta\frac{\partial U}{\partial\vartheta}\right) = 0 \tag{20}$$

and maps the computation domain $R_0 < R < \infty$ onto finite interval $0 < t < \frac{1}{R_0}$. Moreover, Eq.(20) has the form of the standard PWE (4) written in cylindrical coordinates - see [1]. So, finally, it is natural to introduce scaled variables

$$r = R_0\vartheta, \qquad z = z_0 + R_0^2 t; \qquad U(\vartheta,t) = u(r,z) \tag{21}$$

having the dimension of length. This substitution does not alter the differential equation (20):

$$2ik\frac{\partial \tilde{u}}{\partial z}+\frac{1}{r}\frac{\partial}{\partial r}\left(r\frac{\partial \tilde{u}}{\partial r}\right)=0 \qquad (22)$$

Now Eq.(22), which can be called modified angular diffusion equation (MADE), totally coincides with the free-space, axially symmetric form of Eq.(4).

We integrate Eq.(22) in a cylinder $0<r<R_0\theta$ where $\theta \sim \lambda / D$ is the angular width of the diffraction pattern. The initial values $\tilde{u}(z_0,r)$ are supplied by the solution of PWE (4), solved in a cylinder $0<r<A$, $0<z<R_0$ enclosing the scattering object. The integration domains of Eqs.(4) and (22) can be matched by taking

$A = R_0\theta, \qquad z_0 = R_0$.

To match the wave fields, we have to equate the paraxial Ansatz (2) with the spherical scattering model (8):

$$u(r,z)e^{ikz} = e^{ikz} + U(R,\vartheta)\frac{e^{ikR}}{R} \ . \qquad (23)$$

Hence, the following initial condition arises

$$\tilde{u}(r,R_0) = R_0\left[u\left(r,R_0-\frac{r^2}{2R_0}\right)-1\right]\exp(ik\frac{r^2}{2R_0}) \qquad (24)$$

describing transition from plane wave fronts of the PWE method to spherical fronts of the scattered field. Note the phase correcting exponent and shift in arguments of the PWE and ADE solutions.

For large radii R_0, we can neglect small difference in the arguments of u and $\tilde{u}$. With this approximation, the initial condition (24) takes the simplest form

$$\tilde{u}(r,R_0) \approx R_0\left[u(r,R_0)-1\right]\exp(-ik\frac{r^2}{2R_0}) \qquad (25)$$

which has a clear physical interpretation: transition from PWE (4) to the modified ADE (22) is equivalent to inserting a thin microlens (quadratic phase corrector) focused at the scattering object (its position $z_0 = R_0$ coincides with the focal length $f = R_0$). Fig.1 outlines the idea of the hybrid PWE - MADE approach:

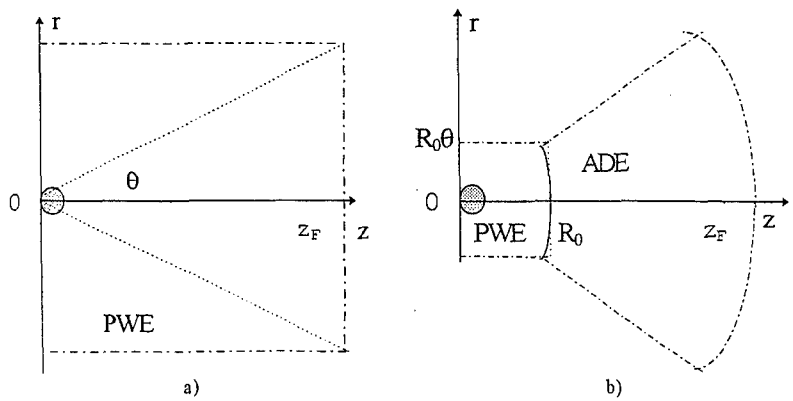

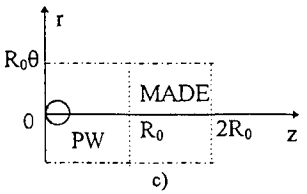

Fig.1. Scheme of direct PWE (a), hybrid PWE-ADE (b) and PWE-MADE (c) calculation.

(a) Ordinary PWE (4) requires a large cylindrical computational domain in order to cover the scattering cone $0 < \vartheta < \theta$ up to the Fraunhofer zone $z \geq z_F$. (b) The use of ADE reduces it to a horn-like region with rather narrow neck $0 < z < R_0$, $0 < r < R_0\theta$. (c) ADE to MADE transform maps it onto a finite-length cylinder $0 < z < 2R_0$, $0 < r < R_0\theta$ with a focusing lens at $z = R_0$ compensating the wavefront mismatch.

The identity of the modified ADE (22) with the original PWE (4) simplifies construction and analysis of the numerical algorithm. First, we can use the same mesh steps both in the near field $0 < z < R_0$ and "compressed" far zone $R_0 < z < 2R_0$ (the estimates for Δz and Δr have been given in [1]). Note that constant steps Δz for MADE, in virtue of (19) and (21) , correspond to increasing with distance radial steps

$$\Delta r \approx \frac{R^2}{R_0^2}\Delta z, \tag{26}$$

which allows one to reach the infinity in a finite number of steps (opposite to the famous Achilles and tortoise sophism). Second, there is no problem of boundary conditions - the best choice is to consider the surrounding cylindrical border $r = A = R_0\theta$ as a nonreflecting wall and apply the nonlocal transparency condition suggested in [1]

$$\frac{\partial u}{\partial r}(A,z) \approx -\sqrt{\frac{2k}{\pi i}}\int_0^z \frac{\partial u}{\partial \zeta}(A,\zeta)\frac{d\zeta}{\sqrt{z-\zeta}}. \tag{27}$$

For the case of scattering by an aperture in a dielectric screen extending beyond the computational domain, Eq.(27) must be replaced by its modified form

$$\frac{\partial u}{\partial r}(A,z) = -\sqrt{\frac{2k}{\pi i}}\int_0^z \frac{\partial}{\partial \zeta}\left\{u(A,\zeta)\exp\left[i\frac{k}{2}\int_\zeta^z(\varepsilon-1)d\zeta\right]\right\}\frac{d\zeta}{\sqrt{z-\zeta}} \tag{28}$$

taking into account refraction of the outgoing waves.

To illustrate the performance of the computational algorithms considered in Section 1 and 3 we present examples of simulated wave fields and diffraction patterns produced by dielectric objects illuminated by synchrotron radiation beams.

References

1. Yu.V.Kopylov, A.V. Popov, A.V.Vinogradov. Application of the Parabolic Wave Equation to X-Ray Diffraction Optics, Optics Communications, V.118, pp. 619-636 (1995).

2. Yu.V.Kopylov, A.V.Popov. Diffraction Phenomena Inside Thick Fresnel Zone Plates, Radio Science, V.31, No. 6, pp. 1815-1822 (1996).

3. H.N.Chapman, J.Fu, C.Jacobsen, S.Williams. Dark-Field X-Ray Microscopy of Immunogold-Labeled Cells, JMSA, V.2 No 2, pp. 53-62, (1996).

4. K.A.Goldberg et al. At-wavelength Testing of Optics for EUV, SPIE 2437, p. 30 (1995).

5. G.D.Malyuzhinets. Progress in Understanding Diffraction Phenomena, Soviet Physics (Uspekhi), V.69, pp.312-334 (1959, in Russian).

6. V.A.Fock. Electromagnetic Diffraction and Propagation Problems. Pergamon, 1965.

SESSION 6:

FREQUENCY-DOMAIN FAST ALGORITHMS

Chairs:J. Song and W.C. Chew

Recent advances in the numerical solution of integral equations applied to EM scattering from terrain

Peter Cullen † and Conor Brennan.
Dept. of Electrical Engineering.
Trinity College Dublin.
e-mail: pcullen@tcd.ie
† Author to whom correspondence should be addressed

ABSTRACT

Three efficient integral equation (IE) schemes are presented in the context of EM scattering from terrain. These schemes offer dramatic computational savings over standard IE solution methods. The underlying solution strategy underpinning each of the quick methods is explored and made explicit. Results are presented yielding excellent agreement with published measured data

I. INTRODUCTION

The modelling of UHF radio wave propagation over undulating terrain has evolved dramatically over the last 40 years, all the while satisfying the conflicting requirements of accuracy and computational efficiency as effectively as possible given the computational resources of the period. Given the almost unenumerable parameter space governing UHF propagation over terrain, as well as the massive scale of the problem, simplifying approximations must be made in order to render the computation tractable. The advances of the last 4 decades have seen a successive relaxation of these approximations as the computational tools become more sophisticated. Thus we see the simple single knife edge physical optics diffraction models of the 1950's [1], possibly with empirical corrections (such as that of Okamura Hata) give way to multiple knife edge diffraction models and models that incorporate the Geometric Theory of Diffraction (GTD) [2]. GTD requires that dominant ridge features be modelled as canonical shapes (wedges,cylinders) and applies the appropriate high frequency asymptotic solutions. Thus a more accurate propagation model is achieved including reflections and a more rigorous diffraction mechanism. Extensions to 3D are possible as are the incorporation of roughness effects. The adoption of the parabolic equation (PE) model [3], originally developed by the underwater acoustics community [4], allows for great freedom in modelling terrain profile, propagation medium anomalies (ducts etc.), and variation of terrain electric constants (via an impedance boundary condition). The factoring out of a fast phase term allows the solution to be marched forward in large range steps, the necessary assumption of forward propagation not being overly restrictive in the case of grazing incidence.

The high accuracy of the integral equation (IE) method was demonstrated by Hviid *et al*[5], as indeed was its main disadvantage, namely tremendous computational burdens. Of course the accuracy and slowness are conflicting features of the same computational aspect, that is the fact that all multiple scattering effects (both forward and backward) can be calculated with this method, yielding full wave solutions. Other features include a compact problem formulation (only the terrain surface need be discretised, and the presence of the free space Green's function ensures rigorous compliance with the radiation condition at infinity), incorporation of dielectric rough terrain and a straightforward extension to 3D (as yet unachieved due to lack of computational resources). The work of the Trinity College Dublin propagation group over the last few years has concentrated on efficient IE solution schemes, in an attempt to render feasible the implementation of IE propagation models on a modest computational resource such as a HP workstation. In this paper we outline three schemes used by ourselves in this regard; the Fast Far Field / Green's Function Perturbation method (FAFFA/GFPM)[6] [7] [8], the Natural Basis Set (NBS)[9][10][11], and the Tabulated Interaction Method (TIM)[12]. The three, seemingly disparate, methods have a common solution strategy which we discuss in section IV before closing with some results in section V.

II. IE PROPAGATION MODEL

As stated in the introduction simplifying approximations must be made in order to implement deterministic propagation model. The severity of these approximations determine the potential accuracy of the numerical solution. Our integral equation model assumes a two dimensional problem, the terrain is invariant in one direction and a line source irradiates the surface. Terrain heights are taken at regular range intervals, the intervening terrain modelled by a straight line segment. A further simplification of the formulation is had by assuming the surface to be perfectly reflecting, an approximation which proves extremely reasonable given the grazing incidences involved in most propagation problems. These assumptions, desirable for the numerical efficiency they facilitate, are by no means necessary and can be relaxed as required by utilising accordingly more sophisticated integral equations than that presented below.

Assuming a TM^z polarised line source with time variation $e^{j\omega t}$ assumed and suppressed we write the 2D Electric Field Integral Equation (EFIE) for a perfectly conducting surface

$$\frac{\beta\eta}{4}\int_C J(\rho')H_0^{(2)}(\beta|\rho-\rho'|)\,d\rho' = E^i(\rho) \qquad (1)$$

where E^i is the incident electric field J the unknown surface current, β the radiation wavenumber, η the impedance of the propagation medium (we employ the free space value of 377 ohms) and ρ,ρ' are as indicated in Figure 1.

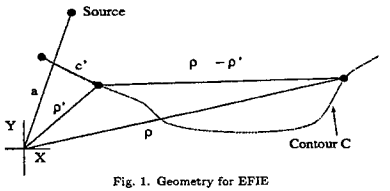

Fig. 1. Geometry for EFIE

The integration contour is along the terrain surface C. To convert the EFIE to a matrix equation we expand J in terms of a set of basis functions

$$J(\rho) = \sum_{n=1}^{N} a_n g_n(\rho) \tag{2}$$

Applying point matching (collocation) at the N points $\rho_1 \ldots \rho_N$ (one on the centre of each basis group) leads to the matrix equation

$$ZJ = V \tag{3}$$

Applying the conceptually simple pulse basis functions with equisized domains of size Δs results in the following system.

$$Z_{mn} = \frac{\beta\eta}{4} H_0^{(2)}(\beta|\rho_m - \rho_n|)\,\Delta s \tag{4}$$

$$Z_{mm} \simeq \Delta s \frac{\beta\eta}{4}\left(1 - j\frac{2}{\pi}\ln(K\Delta s)\right) \tag{5}$$

$$J_n = a_n \tag{6}$$

$$V_m = E^i(\rho_m) \tag{7}$$

where K is a constant equal to $\frac{1.781\beta}{4e}$. The necessity to model accurately the quickly varying phase of J requires that we use a pulse basis function every $\frac{\lambda}{4}$ at least resulting in a Z matrix of huge size (typically of order 10^5). This matrix cannot be stored let alone inverted. A solution of (3) can still be had,however, by employing an iterative scheme such as 'forward/backward' [13], [14] or a Conjugate Gradient Solver which do not require the explicit storage of the impedance matrix Z but rather calculate elements as required. While tractable, the huge computational times associated relegates these IE solutions to the status of reference solutions for the other, quicker, deterministic models discussed above. Below we outline work performed by ourselves which expedites dramatically these IE methods, rendering them, we feel, feasible deterministic tools in their own right.

III. Three Efficient Solution Schemes

• FAFFA / GFPM

Iterative solutions offer us the potential to solve equation (3) even using simple pulse basis functions though at a considerable $O(N^2)$ computational burden. This is due to the need to perform the sum

$$\sum_{n=1}^{N} Z_{mn} J_n$$

independently for each collocation point ρ_m.

To speed up the iterative process we must speed up the matrix-vector multiplies described above. To achieve this aim we group together points, each group having a designated group centre. Now for a point ρ_m in a group j with centre ρ_M, we write

$$\sum_{n=1}^{N} Z_{mn} J_n = \sum_{i \in FF_j} F^i_{Mm} \sum_{n \in i} Z_{Mn} J_n + \sum_{i \in NF_j} \sum_{n \in i} Z_{mn} J_n \tag{8}$$

where F^i_{Mm} are constants to be derived later. The first i summation is over groups deemed to be in j's far-field, in practice groups which are not near neighbours of j. NF_j stands for j's near field and the second i summation is thus over near-neighbour groups (and j itself).
Noting that the far-field summations $\sum_{n \in i, i \in FF_j} Z_{Mn} J_n$ can be reused for each point ρ_m in group j and that similar approximations exist for each group indicates the key computational advantage of this scheme. To derive the constants F^i_{Mm} we introduce the far field approximation to the Hankel function

$$H_0^{(2)}(x) \simeq \sqrt{\frac{2}{\pi x}} e^{-j(x - \frac{\pi}{4})}, x \to \infty \tag{9}$$

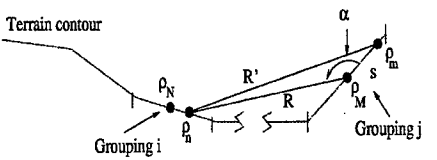

Fig. 2. Groupings in FAFFA scheme

Referring to Fig. 2, we apply the cosine rule to the quantities R, R', α and s to write (assuming R' is sufficiently large to enable us to use the above far field approximation)

$$Z_{mn} = Z_{Mn} A_{nMm} e^{-j\phi_{nMm}} \tag{10}$$

where

$$A_{nMm} = \left(1 + \frac{s^2 - 2Rs\cos\alpha}{R^2}\right)^{-\frac{1}{4}} \tag{11}$$

$$\phi_{nMm} = \beta R\left(\left(1 + \frac{s^2 - 2Rs\cos\alpha}{R^2}\right)^{\frac{1}{2}} - 1\right) \tag{12}$$

We cannot make the identification

$$F^i_{Mm} = A_{nMm} e^{-j\phi_{nMm}}$$

as both A and ϕ depend on n through their dependence on R and α and we demand that F^i_{Mm} be independent of n.
However if we define

$$A^i_{Mm} = A_{NMm} \tag{13}$$

$$\phi^i_{Mm} = \phi_{NMm} \tag{14}$$

where ρ_N is the centre of group i we can use equation (8) with

$$F^i_{Mm} = A^i_{Mm} e^{-j\phi^i_{Mm}} \tag{15}$$

These 'shifting functions' differ slightly from those presented by Lu and Chew [6], in being more accurate, though at slightly higher computational cost. Both variants coincide as the group separation distance becomes appreciably large. Indeed, the TIM discussed later uses Lu and Chew's shifting functions in conjunction with several more approximations peculiar to problems of this type to produce an exceptionally fast scheme.

As the computational saving depends on the amount of 'recycling' achieved by equation (8) one would imagine that making groups as large as possible would offer the maximal efficiency. However the necessity to perform exactly the near-field summations illustrates the naivety of this approach as the larger the groups the larger the near-field summation. Of primary concern is the efficient calculation of a groups self-interaction. To do so we note that physically we expect terrain to be locally quite smooth. Height variations, while very important globally, tend to occur slowly with range. This observation suggests the Green's Function Perturbation Method (GFPM) to be a suitable candidate for calculating an observation domain's self interaction. Noting that we can denote a points position on the contour C either with reference to a fixed origin, resulting in the vector ρ or as a function of arclength along the contour itself resulting in the parameter c (See Fig. (1) prompts us to approximate the EFIE of equation 1 by

$$E^i(c) = \frac{\beta\eta}{4}\int_C H_0^{(2)}\left(\beta\left(c-c'\right)\right) J(c')dc' \qquad (16)$$

where replacing the Euclidean distance $|\rho - \rho'|$ that appears in equation (1) by the arclength $(c - c')$ yields an integral that we note is convolutional in form. This suggests a fast solution to equation (16) by utilising the Fast Fourier Transform, namely

$$\frac{\beta\eta}{4}J = \mathcal{F}^{-1}\left(\frac{\mathcal{F}E^i}{\mathcal{F}H_0^{(2)}}\right) \qquad (17)$$

where $\mathcal{F}$ and $\mathcal{F}^{-1}$ represent the Fourier transform and its inverse respectively.

Applying this to the problem of efficiently calculating the self-interaction of a large group (j, say) involves writing a reduced EFIE as

$$E^i(\rho) = \frac{\beta\eta}{4}\int_{\rho'\notin j} H_0^{(2)}\left(\beta\left|\rho-\rho'\right|\right) J(\rho')d\rho' + \frac{\beta\eta}{4}\int_{c'\in j} H_0^{(2)}\left(\beta\left(c-c'\right)\right) J(c')dc' \qquad (18)$$

for $\rho \in j$ or

$$\hat{E}^i(\rho) = \frac{\beta\eta}{4}\int_{c'\in j} H_0^{(2)}\left(\beta\left(c-c'\right)\right) J(c')dc' \qquad (19)$$

where

$$\hat{E}^i(\rho) = E^i(\rho) - \frac{\beta\eta}{4}\int_{\rho'\notin j} H_0^{(2)}\left(\beta\left|\rho-\rho'\right|\right) J(\rho')d\rho' \qquad (20)$$

Equation (19) is now in a form amenable to a solution via a FAFFA/GFPM hybrid. $\hat{E}^i$ can be efficiently calculated using the Fast Far Field approximation and equation (19) can then be efficiently solved using the GFPM.

The GFPM is an exact method of solution for a flat plate, where the Euclidean distance and arclength between two discretisation points coincide, and so we expect it to give good results when the scatterer deviates only slowly from such a flat segment as is the case for the large groups in question here (due to the locally smooth nature discussed earlier). This does not preclude the addition of small scale random roughness to the profile a topic discussed in [8], which also discusses how further efficiencies can be had by a more careful aggregation of field contributions from scattering groups which possess a similar angular relationship with the receiving group.

• The Natural Basis Set

The Natural Basis Set (the basis set arising in the High Frequency Panel Method of [11]) is a set of complex valued basis functions over large domains whose value at a point is the normalised incident field at that point. In particular, for a point ρ_m in the j^{th} domain the j^{th} basis function g_j takes the value

$$g_j(\rho_m) = \frac{E^i(\rho_m)}{|E^i(\rho_m)|} \qquad (21)$$

and is zero for points outside the domain. Explicitly for a line source and a domain sufficiently far away to use the far field approximation to the Hankel function

$$g_j(\rho_m) = \exp\left(-j\beta\left|a-\rho_m\right| - \frac{\pi}{4}\right) \qquad (22)$$

where $|a - \rho_m|$ is the distance from the line source to the point ρ_m (See Fig. 1).

The success of the method lies in the fact that the basis functions accurately model the fast varying phase of the current leaving only a slowly varying residual to be calculated via a moment method. Thus far less basis functions are required with a subsequent reduction in the size of the Z matrix. Evidence to suggest why is this particular basis function should describe the current so accurately for massive smooth scatterers is produced in [9] where several different techniques are examined (Born Series [15], the Nussenzveig-Fock correction [16], the Parabolic Equation method (to which it bears a conceptual similarity in the sense that in both cases fast moving approximate solutions are factored out) and the GFPM) each suggesting this structure for J. Also explored in [9] are methods to reduce the matrix fill time associated with this basis.

A legitimate question is the relationship of the Natural Basis to the, also complex valued, directional basis functions of Canning [17] which lead to very sparse matrices. Canning postulates a complete basis set on each domain, each basis radiating in a specific direction, hence covering every angle $\alpha \in [0, 2\pi]$ and potentially covering any interaction between domains. Most of the subsequent matrix entries are very small and can be neglected leaving us with a sparse matrix whose entries correspond to interactions between basis functions that radiate towards each other. In a sense Cannings functions pick out the actual physical interactions that occur on the scatterer. The Natural Basis Set would seem, in comparison, somewhat incomplete as it has only one basis function per domain and so cannot achieve the same angular coverage. However for domains far away from the source the

Natural Basis Set can be shown to radiate in almost exclusively a forward direction (tangential to the surface) which is sufficient to describe the interactions between domains on a massive smooth scatterer (due to the slow height variations with range of typical terrain profiles). Nearer the source the basis is also well equipped as in this area we expect the Kirchhoff current to be a good approximation, a current whose phase variation is within a constant of that of the Natural Basis.

With these observations in mind it is perhaps unsurprising that the Natural Basis achieves its greatest efficiencies for quite flat terrain, its performance degrading as the terrain profile becomes more hilly (See Section V for numerical examples). It should be however stressed that even for these tougher problems it still offers large computational savings over traditional basis functions.

• Tabulated Interaction Method

The final method we present is that of the Tabulated Interaction Method which conceptually breaks the scatterer into large groups and postulates that all these groups interact in the form of plane waves. This postulation was derived from observing the behaviour of the FAFFA shifting functions A and ϕ when $R \to \infty$

$$A_{NMm} \rightarrow 1 \tag{23}$$

$$\phi_{NMm} \rightarrow \exp(-j\beta s \cos\alpha) \tag{24}$$

This behaviour still holds even for R smaller because of the local smoothness of typical terrain profile assures us that $\alpha \simeq \pi$ for near neighbours and so

$$\phi_{NMm} \simeq \exp(j\beta s)$$

and, discounting the amplitude shift A_{NMm} which is of secondary importance, our plane wave postulation holds even in the nearfield. This coupled with the observation that over these localised groups the incident field can also be approximated locally as a plane wave leads us to conclude that any current that lies on a group is excited by plane waves.

What makes this tremendously interesting is the fact that, with our terrain model, we can make our groups identical in structure, namely PEC segments of fixed length. By examining the behaviour of such a group under a variety of plane wave incidences, using an IE to tabulate the current induced and its far field scatter pattern, we have precise knowledge of the scattering properties of **every** group in the problem for the range of incident fields it is likely to encounter.

The far field scatter pattern is defined as (see Fig.3)

$$\sum_{n\in i} J_n \exp(j\beta s_2 \cos\theta) \tag{25}$$

We use this far-field scatter to write

$$\sum_{n\in i} Z_{mn} J_n = F_{Mm}^{i(TIM)} \sum_{n\in i} J_n \exp(j\beta s_2 \cos\theta) \tag{26}$$

where

$$F_{Mm}^{i(TIM)} = Z_{MN} \exp(\beta s_1 \cos\alpha) \tag{27}$$

In this fashion we obviate the need to perform the summations of equation (8) inherent in the FAFFA/GFPM method. Fields scattered from one group to the centre of another can easily be interpolated from the tabulated data.

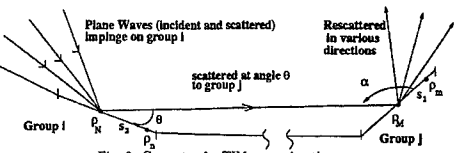

Fig. 3. Geometry for TIM approximation

IV. Comparison of the 3 schemes

The three schemes outlined in the last section have an underlying similarity and it would be perhaps enlightening to pursue this idea briefly in this section. The massive $O(N^2)$ computational burden encountered by a conventional moment method solution using pulse basis functions, is as stated previously, due to the independent calculation of

$$\sum_{n=1}^{N} Z_{mn} J_n$$

for each discretisation (collocation) point. The three schemes all succeed via a grouping together of discretisation points (into the groupings of the FAFFA and TIM, and the large basis domains of the NBS). What is inherently similar about all three methods is the approximation of fields scattered to points in a group (domain) in terms of fields scattered to the group centre. Where they differ is the manner in which this approximation is made. This concept is explicitly visible in equation (8) where the fields scattered to point ρ_m from group i is written as

$$\sum_{n\in i} Z_{mn} J_n = F_{Mm}^{i} \sum_{n\in i} Z_{Mn} J_n$$

that is F_{Mm}^{i} times the field scattered to the centre point ρ_M. The same interpretation can be put on the TIM scheme. What is perhaps not so obvious is the interpretation of the NBS in this light. To do so we will write a forward solution using the NBS and its large basis domains in terms of a solution using much smaller pulse basis functions. Indeed, the large domains of the NBS could be thought of as a grouping of many smaller pulse basis functions of size Δs , similar to the groupings inherent in the FAFFA and TIM schemes. Consider a point ρ_m in a natural basis domain j with collocation point (group centre) ρ_M. The current at ρ_m is equal to the value of the j^{th} basis function at ρ_m multiplied by the amplitude coefficient a_j. That is

$$J_m = a_j g_j(\rho_m) \tag{28}$$

$$= J_M \frac{g_j(\rho_m)}{g_j(\rho_M)} \tag{29}$$

Now let Z_{ij}^{NBS} denote an impedance matrix entry using the Natural Basis Set.

We can write

$$Z_{ij}^{NBS} = \sum_{n\in i} g_i(\rho_n) \frac{\beta\eta}{4} H_0^{(2)}(\beta|\rho_n - \rho_M|)\,\Delta_s \tag{30}$$

$$= \sum_{n\in i} g_i(\rho_n) Z_{Mn} \quad (31)$$

where Z_{Mn} is a matrix entry obtained using normal pulse basis functions.

Employing a forward scattering Natural Basis solution (i.e. approximating Z^{NBS} as a lower triangular matrix) we obtain for the j^{th} coefficient, a_j

$$Z^{NBS}_{jj} a_j = V_M - \sum_{i<j} Z^{NBS}_{ij} a_i \quad (32)$$

$$\sum_{l\in j} a_j g_j(\rho_l) Z_{Ml} = V_M - \sum_{i<j}\sum_{n\in i} g_i(\rho_n) a_i Z_{Mn} \quad (33)$$

$$\sum_{l\in j} J_l Z_{Ml} = V_M - \sum_{i<j}\sum_{n\in i} Z_{Mn} J_n \quad (34)$$

Thus

$$J_M Z_{MM} + \sum_{l\in j, l\neq M} Z_{Ml} J_l = V_M - \sum_{i<j}\sum_{n\in i} Z_{Mn} J_n \quad (35)$$

$$J_m \frac{g_j(\rho_M)}{g_j(\rho_m)} Z_{MM} = V_M - \sum_{i<j}\sum_{n\in i} Z_{Mn} J_n - \sum_{l\in j, l\neq M} Z_{Ml} J_l \quad (36)$$

Noting that Z_{MM} equals Z_{mm} (as the discretisations are equisized)

$$J_m Z_{mm} = \frac{g_j(\rho_m)}{g_j(\rho_M)} \left(V_M - \sum_{i<j}\sum_{n\in i} Z_{Mn} J_n - \sum_{l\in j, l\neq M} Z_{Ml} J_l \right) \quad (37)$$

$$J_m Z_{mm} = F^{(NBS)}_{Mm} \left(V_M - \sum_{i<j}\sum_{n\in i} Z_{Mn} J_n - \sum_{l\in j, l\neq M} Z_{Ml} J_l \right) \quad (38)$$

where

$$F^{(NBS)}_{Mm} = \frac{g_j(\rho_m)}{g_j(\rho_M)} \quad (39)$$

$$= \frac{\exp(-j\beta(|a-\rho_m|))}{\exp(-j\beta(|a-\rho_M|))} \quad (40)$$

What we should note from this analysis is the similar treatment of fields from other groups in both the FAFFA and the NBS. Both schemes calculate the fields scattered to the group centre, ρ_M and then distribute this information to other points in the group via some shifting function. The fact that the NBS uses the same shift $F^{(NBS)}_{Mm}$ for fields coming from all domains while the FAFFA 'tailors' its shifts F^{i}_{Mm} by incorporating information about the geometrical relationship between the groups (in the form of R and α) would seem to indicate that the FAFFA (and indeed the TIM) is a more robust scheme, an indication borne out by some numerical experiments in [18]. This homogeneity of shifting function coupled with it's application in the near field areas leads to the NBS performing far more efficiently than the FAFFA for a certain class of problem, namely massive relatively flat scatterers, with a corresponding decline in it's efficiency when applied to more mountainous terrain. We close this section by explicitly writing formulae for forward scattering solutions using the three schemes indicating the different shifting functions of each scheme. We stress that these formulae are only intended to show the similarity between the schemes. They are not intended as a definitive implementation of the techniques.

FAFFA:

$$J_m Z_{mm} = V_m - \sum_{i\in FF_j} F^{i}_{Mm} \sum_{n\in i} Z_{Mn} J_n - \sum_{i\in NF_j} \sum_{n\in i} Z_{mn} J_n \quad (41)$$

This is the basic FAFFA scheme, without the GFPM improvement of section III.

NBS:

$$J_m Z_{mm} = F^{(NBS)}_{Mm} \left(V_M - \sum_{i<j}\sum_{n\in i} Z_{Mn} J_n - \sum_{l\in j, l\neq M} Z_{Ml} J_l \right) \quad (42)$$

TIM:

$$J_m Z_{mm} = \hat{V}_m - \sum_{i<j} F^{i(TIM)}_{Mm} \sum_{n\in i} J_n \exp(j\beta s_2 \cos\theta) - \sum_{n\in j, n\neq m} Z_{mn} J_n \quad (43)$$

where $\hat{V}_m$ is the approximate incident field at ρ_m (assuming that the incident field is locally planar over each group).

V. Results and discussion

To illustrate the concepts introduced in this paper we now present a comparison of the methods presented versus published measured data [5]. The terrain profile (Fig. 4) is taken from Northern Denmark and was sampled once every 50m. The transmitting antenna was situated 10.4 metres over the leftmost point and fields were calculated 2.4 metres above the terrain. The chosen frequency was 970MHz, which used 5 pulse basis functions per wavelength, leads to roughly 178,000 unknowns. All the models assumed forward scattering. Fig. 5 shows the measured data versus

- A slow $O(N^2)$ reference solution
- A solution using the basic FAFFA with group sizes equal to 50m. The near field was restricted to each group's self interaction.
- A FAFFA/GFPM hybrid solution using groups 200m in length and a simple geometrical procedure to aggregate fields scattered to group centres before distribution to other points in the group. The near field again was restricted to the observation domain's self-interaction.
- A solution obtained using the Natural Basis Set with a domain size of 250m.
- A TIM solution using groups 50m in size.

The following table compares computation times (in seconds on a Power PC) between the methods.

Solution scheme	Computation time
Reference model	100857
FAFFA	42
FAFFA/GFPM	18
Natural Basis	3
TIM	3

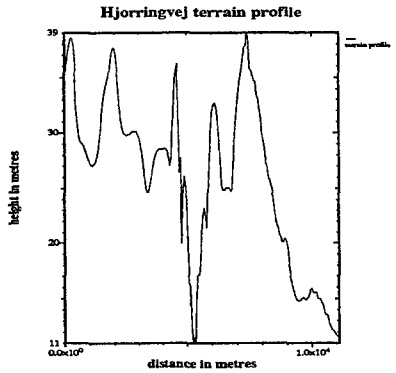

Fig. 4. Hjorringvej terrain profile

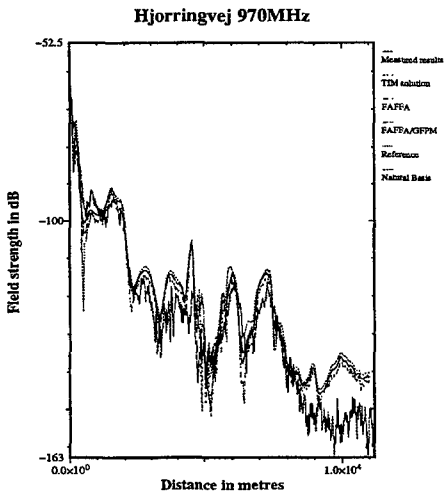

Fig. 5. Fields over profile Hjorringvej at 970MHz

We now present results of numerical experiments conducted with more challenging mountainous terrain (Fig.6). Unfortunately the absence of measured data for this profile prevents us from comparing our results with measurements. However, we would expect the slow reference solution to give good agreement with experimental data and so we should demand good agreement between our quick solution schemes and this reference solution. A source radiating at 970 MHz was assumed 52.0 metres above the leftmost point and all models assumed forward scattering. Fig. 7 shows

- A slow $O(N^2)$ reference solution
- A solution using the FAFFA with groups equal in size to 5m, and the near field restricted to each group's self interaction.
- A FAFFA/GFPM hybrid solution with groups 20m in length and a similar field aggregation procedure as in the last example. The near field again was restricted to the group's self-interaction.
- A solution obtained using the Natural Basis Set with a domain size of 1.25m.
- A TIM solution with a group size of 5m.

Solution scheme	Computation time
Reference model	12600
FAFFA	509
FAFFA/GFPM	426
Natural Basis	819
TIM	49*

* This time can be reduced further to around 10 seconds using improvements to the basic TIM scheme. These improvements are outlined in [19].

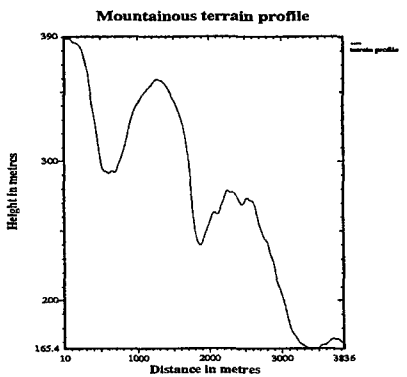

Fig. 6. Mountainous terrain profile

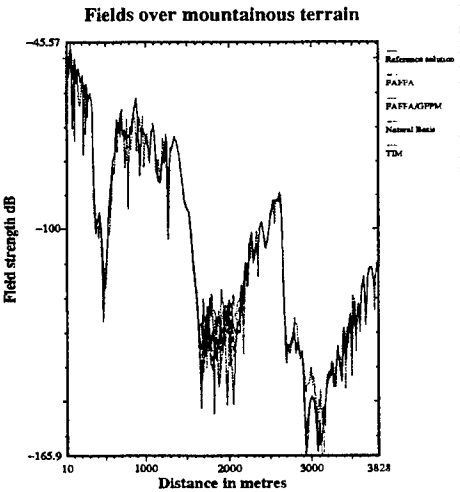

Fig. 7. Fields over mountainous terrain at 970MHz

We see how the FAFFA and FAFFA/GFPM are in good agreement with the slow reference solution and still offer considerable computational savings (though the physical extent of the groupings had to be much smaller because of the mountainous nature of the terrain). The Natural Basis, while still accurate, is now much slower than the other two fast schemes. This is hardly surprising as it uses one simple phase shift (based on the phase of the incident radiation) to account for scattering from all areas of terrain, ignoring the geometrical considerations inherent in the FAFFA and FAFFA/GFPM. Hence it must use very small groupings to compensate for this inaccuracy with correspondingly slower computation times. This contrasts with the previous example where the flatter terrain produced a greatly reduced spread of angular interaction, a situation exploited to great effect by the Natural Basis. Once again the TIM performs best, giving good agreement with the reference solution.

VI. Conclusions

Three efficient solutions of the matrix equations that arise when applying an IE formulation to the problem of UHF propagation over irregular terrain have been presented. Two schemes, the FAFFA/GFPM and TIM expedite iterative solutions of the matrix equation that arises using pulse basis functions, while a third, the NBS, uses complex valued basis functions defined over large domains to produce a matrix equation of significantly lower order than that using pulse functions. A common solution strategy can be demonstrated by examining how a forward scattering solution using the NBS relates to one using pulse basis functions. The NBS is seen to expedite the pulse basis solution in a manner similar to the two other schemes. Numerical results are presented which show excellent agreement with published measured data. A further numerical study over mountainous terrain illustrate the relative regions of applicability of the schemes.

VII. Acknowledgments

The authors would like to thank TELTEC Ireland for financial assistance and Prof Anderson of Aalborg University for providing the measured data.

References

[1] K. Bullington,'Radio Propagation Fundamentals' Bell Syst. Tech. J. pp 593-626 1957.

[2] R. J. Luebbers,'Finite Conductivity Uniform GTD versus Knife Edge Diffraction in prediction of Propagation Path Loss' IEEE Trans. Ant. Prop. Vol. 32 No 1 pp 70-76.

[3] M.F. Levy, 'Parabolic Equation modelling of propagation over irregular terrain' Electron Lett Vol. 26, pp 1153-1155.

[4] F. D. Tappert,'The Parabolic Equation Method' Chapter V of 'Wave Propagation and Underwater Acoustics' edited by Keller and Papadakis. Springer-Verlag 1977.

[5] J Hviid et al, 'Terrain-Based Propagation Model for Rural Area - An Integral Equation Approach' IEEE Trans. Ant. Prop. Vol. 43, pp 41-46

[6] C.C. Lu and W.C. Chew,'Far Field Approximation for calculating the RCS of large objects' Micro. Opt. Tech. Lett, Vol. 8, No. 5, pp. 238-240.

[7] D. Moroney and P. Cullen,'The Green's Function Perturbation Method for the solution of Electromagnetic Scattering Problems' Progress in Electromagnetic Research PIER97[11 B] PIER 15 221-252 1997 USA Jan 97.

[8] C Brennan and P. J. Cullen, 'A high speed adaptive methodology for calculating UHF propagation loss over terrain' 8th IEEE International Symposium on Personal, Indoor and Mobile Radio Communications. Helsinki September 1997.

[9] D. Moroney, Computational Methods for the Calculation of Electromagnetic Scattering from Large-Scale Perfect Electrical Conductors. PhD Thesis, University of Dublin, Trinity College, 1995.

[10] Aberegg and Peterson,'Integral Equation Asymptotic Phase Method to Two-Dimensional Scattering' IEEE Trans. Antennas and Prop. Vol 43 No.5 May 1995

[11] Richard M James,'A Contribution to Scattering Calculation for Small Wavelengths - The High Frequency Panel Method' IEEE Trans. Ant. Prop. Vol 38 No 10, October 1990.

[12] C. Brennan and P. Cullen,'Tabulated Interaction Method for UHF terrain propagation problems' Accepted for publication in the IEEE Trans Ant. Prop.

[13] Holliday *et al*,'Forward Backward : A new method for computing low grazing angle scattering ' IEEE Trans Ant. Prop Vol.44 No.5

[14] Kapp and Brown,'A new numerical method for rough surface scattering calculations ' IEEE Trans Ant Prop Vol 44 No.5

[15] E.G.Liszka and J.J.McCoy,'Scattering at a rough boundary - Extensions of the Kirchhoff Approximation' J. Acoust. Soc. Am. Vol.71 No.5 pp 1093-1100. 1982.

[16] H.M Nussenzveig,'High Frequency Scattering by an Inpenetrable Sphere' Ann Phys Vol.34 pp 23-95 1965

[17] F.X. Canning,'Interaction Matrix Localisation (IML) permits solution of larger scattering problems' IEEE Trans. Magnetics Vol 27, No 5, 1991.

[18] P. Cullen and C. Brennan,'Efficient techniques for the Computation of UHF Grazing incidence scattering' ICEEA97, Torino, Italy, September 1997.

[19] C.Brennan and P. Cullen,'Multilevel TIM applied to UHF propagation over irregular terrain' Submitted for publication to the IEEE Trans. Ant. and Prop

Solution of Combined-Field Integral Equation Using Multi-Level Fast Multipole Algorithm for Scattering by Homogeneous Bodies

X. Q. Sheng, J. M. Jin, J. M. Song, W. C. Chew, and C. C. Lu
Center for Computational Electromagnetics
Department of Electrical and Computer Engineering
University of Illinois at Urbana-Champaign
Urbana, Illinois 61801-2991

ABSTRACT

In this paper, we present an accurate method of moments (MoM) solution of the combined-field integral equation (CFIE) using the multi-level fast multipole algorithm (MLFMA) for scattering by large, three-dimensional, arbitrarily-shaped, homogeneous objects. We first investigate several different MoM formulations of CFIE and propose a new formulation, which is both accurate and free of interior resonance. We then employ MLFMA to significantly reduce the memory requirement and computational complexity of the MoM solution. Numerical results are presented to demonstrate the accuracy and capability of the proposed method. The method can be extended in a straightforward manner to scatterers composed of different homogeneous dielectric and conducting objects.

I. INTRODUCTION

The calculation of electromagnetic scattering from arbitrarily-shaped three-dimensional homogeneous or layered homogeneous dielectric bodies has been of considerable current interest owing to the wide application of materials in a variety of radar targets. Analytical solutions are available for only very limited geometries such as a sphere and a spheroid. For dielectric objects having an arbitrary shape, one has to resort to some approximate numerical techniques based on either integral or differential equations. The integral equation approach is often preferred for homogeneous or layered homogeneous objects because it limits the discretization of the unknown quantity to the surface of the object and the discontinuous interfaces between different materials.

One of widely uesd formualtions for scattering by three-dimensional dielectric bodies is the so-called PMCHW formulation, which is found to be free of interior resonance and yields accurate and stable solutions. However, this formulation cannot produce a matrix equation which can be considered as a constraint for the field outside the object. As a result, the PMCHW formulation cannot be combined with other methods such as the finite-element method (FEM) for scattering by inhomogeneous objects.

Another popular formulation for scattering by three-dimensional dielectric bodies is to combine EFIE and MFIE linearly to form a combined-field integral equation (CFIE). Although the CFIE formulation has been used extensively for conducting and impedance bodies, few researchers have applied it to the analysis

of scattering by three-dimensional dielectric bodies. Rao and Wilton claimed the first use of CFIE for this problem [4]. In their approach, $\mathbf{J}$ is expanded in terms of the Rao-Wilton-Glisson [3] (RWG) vector basis functions ($\mathbf{g}_i$) and $\mathbf{M}$ is expanded in terms of another set of basis functions ($\hat{n} \times \mathbf{g}_i$) that are orthogonal to the RWG functions. The resulting EFIE and MFIE are then converted into matrix equations using line testing functions, and a combined EFIE and MFIE is then solved for an approximate numerical solution of $\mathbf{J}$ and $\mathbf{M}$. Although Rao and Wilton argued that it is advantageous for a stable numerical procedure to use two sets of spatially orthogonal basis functions $\mathbf{g}_i$ and $\hat{n} \times \mathbf{g}_i$ to represent $\mathbf{J}$ and $\mathbf{M}$, representing $\mathbf{M}$ in terms of $\hat{n} \times \mathbf{g}_i$ actually violates the property of $\mathbf{M}$ at the edges of dielectric because $\hat{n} \times \mathbf{g}_i$ requires the continuity of the $\mathbf{M}$ component tangential to the edge. Since $\mathbf{M}$ is related to the electric field by $\mathbf{M} = \mathbf{E} \times \hat{n}$, this, in turn, requires the surface tangential electric field normal to the edge to be continuous across the edge from one patch to another, which is not true if the two patches are not in the same plane.

In this paper, we first consider the MoM solution of CFIE for scattering by three-dimensional dielectric bodies. We use the RWG basis functions to expand both $\mathbf{J}$ and $\mathbf{M}$ and then use the RWG functions as the testing functions to convert EFIE and MFIE into matrix equations. By combining the resultant EFIE and MFIE in a traditional manner, we obtain four different formulations. We show that none of these formulations can yield accurate solutions and at the same time are immune to the problem of interior resonance. We then propose a new formulation of CFIE which, like the PMCHW formulation, produces accurate MoM solutions and is free of interior resonance. We then apply the multi-level fast multipole algorithm (MLFMA) [5] to the new formulation to significantly reduce the memory requirement and computational complexity of the MoM solution.

II. FORMULATION AND ANALYSIS

Consider the problem of electromagnetic wave scattering by an arbitrarily-shaped and homogeneous body characterized by a permittivity ϵ_2 and a permeability μ_2 and immersed in an infinite and homogeneous medium having a permittivity ϵ_1 and a permeability μ_1. Introducing equivalent electric and magnetic currents, $\mathbf{J}$ and $\mathbf{M}$, on the surface of the homogeneous body, which are related to the surface fields by $\mathbf{J} = \hat{n} \times \mathbf{H}$ and $\mathbf{M} = \mathbf{E} \times \hat{n}$, respectively, and applying the equivalence principle to the exterior fields, we obtain an electric-field integral equation (EFIE)

$$Z_1 \mathbf{L}_1(\mathbf{J}) - \mathbf{K}_1(\mathbf{M}) = \mathbf{E}^i \tag{1}$$

and a magnetic-field integral equation (MFIE)

$$Z_1 \mathbf{K}_1(\mathbf{J}) + \mathbf{L}_1(\mathbf{M}) = Z_1 \mathbf{H}^i \tag{2}$$

where $Z_1 = \sqrt{\mu_1/\epsilon_1}$, $(\mathbf{E}^i, \mathbf{H}^i)$ denote the incident fields, and the operators $\mathbf{L}_1$ and $\mathbf{K}_1$ are defined as in [1]

Equations (1) and (2) can be discretized by first expanding $\mathbf{J}$ and $\mathbf{M}$ as

$$\mathbf{J} = \sum_{i=1}^{N_S} \mathbf{g}_i J_i \tag{3}$$

$$\mathbf{M} = \sum_{i=1}^{N_S} \mathbf{g}_i M_i \tag{4}$$

where N_S denotes the total number of edges on S and $\mathbf{g}_i$ denotes the RWG vector basis functions [3]. Substituting (6) and (7) into (1) and using $\mathbf{g}_i$ as the testing function, we obtain the TE formulation (short

for $\hat{t} \cdot \mathbf{E}$ where $\hat{t}$ denotes a unit vector tangential to S). Similarly, from (2) we obtain the TH formulation (short for $\hat{t} \cdot \mathbf{H}$). Alternatively, we may choose $\hat{n} \times \mathbf{g}_i$ as the testing function and obtain from (1) the NE formulation (short for $\hat{n} \times \mathbf{E}$) and from (2) the NH formulation (short for $\hat{n} \times \mathbf{H}$). Theoretically, any of TE, TH, NE, and NH can be used to provide a matrix relation between $\{J\}$ and $\{M\}$, which can be written as

$$[P_1]\{M\} + [Q_1]\{J\} = \{b\}. \tag{5}$$

However, it is well known that each of them suffers from the problem of interior resonance and fails to produce accurate solution at and near frequencies corresponding to the resonant frequencies of the cavity formed by covering S with a perfect electric or magnetic conductor and filling it with the exterior medium. To eliminate this problem, one has to combine an equation from EFIE with another equation from MFIE to obtain a combined equation [2]. For example, one can combine TE with TH to obtain the TETH formulation or TE with NH to obtain the TENH formulation. One can also combine NE with NH to obtain the NETH formulation or NE with NH to obtain the NENH formulation. The combined matrix equation can still be written in the form of (5).

Equation (5) cannot be solved unless another relation between $\{J\}$ and $\{M\}$ is specified. Such a relation can be derived by applying the equivalence principle to the interior fields, and doing so we obtain an EFIE

$$Z_2\mathbf{L}_2(\mathbf{J}) - \mathbf{K}_2(\mathbf{M}) = 0 \tag{6}$$

and an MFIE

$$Z_2\mathbf{K}_2(\mathbf{J}) + \mathbf{L}_2(\mathbf{M}) = 0 \tag{7}$$

where $Z_2 = \sqrt{\mu_2/\epsilon_2}$ and the operators $\mathbf{L}_2$ and $\mathbf{K}_2$ are defined similarly to $\mathbf{L}_1$ and $\mathbf{K}_1$, provided that all the subscripts are changed from "1" to "2." Equations (6) and (7) can be discretized in the same manner as for (1) and (2), resulting in the corresponding TETH, TENH, NETH, and NENH formulations, which provide a matrix relation

$$[P_2]\{M\} + [Q_2]\{J\} = \{0\}. \tag{8}$$

Equation (8) can be combined with (5) to form a complete set of linear algebraic equations for $\{J\}$ and $\{M\}$. Although the CFIE for a homogeneous scatterer has been solved by a number of researchers using different expansion or testing functions, it has not been solved before using the RWG functions as both the expansion and testing functions, as is done in this section. Therefore, it is not clear which of the four formulations (TETH, TENH, NETH, and NENH) can yield accurate solution and is immune to the problem of interior resonance. For this, we consider the inner products $\langle \mathbf{g}_i, \mathbf{L}(\mathbf{g}_j)\rangle$ and $\langle \mathbf{g}_i, \mathbf{K}(\mathbf{g}_j)\rangle$, which arise in the TE and TH formulations. Apparently, both terms in $\mathbf{L}(\mathbf{g}_j)$ contribute to $\langle \mathbf{g}_i, \mathbf{L}(\mathbf{g}_j)\rangle$; however, when $i = j$ both terms in $\mathbf{K}(\mathbf{g}_j)$ do not contribute to $\langle \mathbf{g}_i, \mathbf{K}(\mathbf{g}_j)\rangle$, and moreover, when $\mathbf{g}_i$ and $\mathbf{g}_j$ are in the same plane the second term in $\mathbf{K}(\mathbf{g}_j)$ does not contribute $\langle \mathbf{g}_i, \mathbf{K}(\mathbf{g}_j)\rangle$ even if $i \neq j$. Therefore, the $\mathbf{K}(\mathbf{g}_j)$ is not well tested by $\mathbf{g}_i$. Next, we consider the inner products $\langle \hat{n} \times \mathbf{g}_i, \mathbf{L}(\mathbf{g}_j)\rangle$ and $\langle \hat{n} \times \mathbf{g}_i, \mathbf{K}(\mathbf{g}_j)\rangle$ encountered in the NE and NH formulations, and in this case we find that when $i = j$ or when $\mathbf{g}_i$ and $\mathbf{g}_j$ are in the same plane the second term in $\mathbf{K}(\mathbf{g}_j)$ does not contribute to $\langle \hat{n} \times \mathbf{g}_i, \mathbf{K}(\mathbf{g}_j)\rangle$; however, the first term always has a dominant contribution. Furthermore, when $i = j$ the first term in $\mathbf{L}(\mathbf{g}_j)$ has no contribution to $\langle \hat{n} \times \mathbf{g}_i, \mathbf{L}(\mathbf{g}_j)\rangle$. This suggests that $\mathbf{g}_i$ is not a good testing function for $\mathbf{K}(\mathbf{g}_j)$ and $\hat{n} \times \mathbf{g}_i$ is not a good testing function for $\mathbf{L}(\mathbf{g}_j)$. Therefore, in the TE formulation, M is not well tested, while in the TH formulation, J is not well tested. Similarly, J is not well tested in the NE formulation, while M is not well tested in the NH formulation. As a result, in the TENH formulation M is not well tested and in

the THNE formulation **J** is not well tested. Therefore, both TENH and NETH would fail to produce the correct solution.

III. NUMERICAL RESULTS

To verify the analysis above, we consider the problem of plane-wave scattering by a dielectric sphere. The sphere has a diameter of $1\lambda_0$ and a relative permittivity $\epsilon_r = 4$. Figure 1 shows the bistatic radar cross section (RCS) of the sphere, obtained using the four formulations and the exact Mie series or the PMCHW formulation. It is observed that both TENH and NETH produce completely incorrect results. This observation agrees well with our analysis. Among the two remaining formulations, TETH produces a very good result since both **J** and **M** are well tested, whereas NENH is rather inaccurate. However, our analysis above shows that $\hat{n} \times \mathbf{g}_i$ is a good testing function for $\mathbf{K}(\mathbf{g}_j)$ and the inaccuracy of NENH must be rooted in other causes. Further numerical experiment reveals that the matrix equation produced by NENH is a very ill-conditioned matrix. As a result, a small error introduced in the discretization can render the final solution meaningless.

It is apparent that among the four formulations, only TETH yields the most accurate solution. Unfortunately, because of its improper combination, TETH suffers from the problem of interior resonance and this is demonstrated clearly in Fig. 2, where the bistatic RCS is given for a sphere having a diameter of $0.888\lambda_0$ and a relative permittivity $\epsilon_r = 4$. The size of the sphere corresponds to the first resonant frequency of the air-filled spherical cavity. It is well known that CFIE removes the interior resonance by combining EFIE and MFIE in such a manner that the resultant integral operators correspond to that for a cavity with a resistive wall. The proper combinations are TENH and NETH; however, neither of them produces accurate solution, as demonstrated earlier. Both TETH and NENH are the improper combinations in the sense that the combined integral operators do not correspond to those for a resistive cavity, and therefore, they still experience the interior resonance. However, because of the numerical discretization error, the singularity (resonance) of the TE (or NE) equation does not coincide exactly with that of the TH (or NH) equation. As a result, the bandwidth of the incorrect solution is extremely narrow (less than 1%), compared to those resulting from either EFIE or MFIE (about 10%).

To obtain a formulation that is both accurate and free of the interior resonance, we should find a proper combination among TE, TH, NE, and NH, which tests both **J** and **M** well and contains a true CFIE. Based on the analysis described above, we find that any of the following combinations, TENENH, TENETH, THNHNE, and THNHTE, satisfies both requirements. Figure 3 shows the RCS of a dielectric sphere obtained using TENENH and TENETH, along with the results obtained using PMCHW and Mie. Good results are obtained both away and at the frequency of interior resonance. Note that THNHNE and THNHTE are the dual formulations of TENENH and TENETH, respectively, and their validity is expected by duality, which is also verified numerically.

To enhanced the solution of the TENENH formulation, MLFMA is implemented. Several representative results are given in Fig. 4 for a sphere whose diameter varies from $1\lambda_0$ to as large as $6\lambda_0$. The results are compared to those obtained using the Mie series and good agreement is observed. The memory requirement and the total CPU time on one processor of an SGI Power Challenge (R8000) are given in Fig. 5.

IV. CONCLUSION

In this paper, we studied a variety of CFIE formulations for scattering by three-dimensional arbitrarily-shaped homogeneous objects using the RWG functions as both the expansion and testing functions. We have shown that, due to the deficiency of the RWG functions as the testing functions, among the four CFIE formulations (namely, TETH, TENH, NETH, and NENH), only TETH can test both the equivalent electric and magnetic currents well and thus yield accurate solution. However, because of its improper combination, TETH suffers from the problem of interior resonance.

Based on the analysis, we then proposed new formulations (namely, TENENH, TENETH, THNHNE, and THNHTE) that have a good accuracy and are free of interior resonance. These formulations can be derived using two approaches. The first approach formulates the CFIE as a linear combination of the two tangential components of EFIE and MFIE (that is, CFIE = EFIE + $\hat{n}\times$ EFIE + MFIE + $\hat{n}\times$ MFIE) and then uses the RWG $\mathbf{g}_i$ as the testing functions. Since both $\mathbf{J}$ and $\mathbf{M}$ are already well tested in the first two terms (EFIE + $\hat{n}\times$ EFIE), one can neglect either MFIE or $\hat{n}\times$ MFIE for the sake of efficiency. The other term, $\hat{n}\times$ MFIE or MFIE, is needed to remove the problem of interior resonance. The resulting formulation is TENENH or TENETH, depending on the neglected term. Similarly, since both $\mathbf{J}$ and $\mathbf{M}$ are also well tested in the last two terms (MFIE + $\hat{n}\times$ MFIE), one can neglect either EFIE or $\hat{n}\times$ EFIE and the resulting formulation is THNHNE or THNHTE. The second approach formulates the CFIE as a linear combination of EFIE and MFIE (CFIE = EFIE + MFIE) and then uses $\mathbf{g}_i + \hat{n} \times \mathbf{g}_i$ as the testing functions. Again, one of the four terms can be dropped for the sake of efficiency, resulting in one of the four formulations described above.

Having identified the accurate and reliable CFIE formulations, we then applied MLFMA to significantly reduce the memory requirement and computational complexity of their MoM solutions. Numerical results were presented to demonstrate the accuracy and capability of the proposed method. The method can be extended in a straightforward manner to scatterers composed of different homogeneous dielectric and conducting objects.

References

[1] A. J. Poggio and E. K. Miller, "Integral equation solutions of three dimensional scattering problems," in *Computer Techniques for Electromagnetics*. Oxford, UK: Permagon, 1973, ch-4.

[2] R. F. Harrington, "Boundary integral formulations for homogeneous material bodies," *J. Electromagn. Waves Appl.*, vol. 3, no. 1, pp. 1–15, 1989.

[3] S. M. Rao, D. R. Wilton, and A. W. Glisson, "Electromagnetic scattering by surfaces of arbitrary shape," *IEEE Trans. Antennas Propagat.*, vol. AP-30, pp. 409–418, May 1982.

[4] S. M. Rao and D. R. Wilton, "*E*-field, *H*-field, and combined field solution for arbitrarily shaped three-dimensional dielectric bodies," *Electromagnetics*, vol. 10, no. 4, pp. 407–421, 1990.

[5] J. M. Song and W. C. Chew, "Multilevel fast-multipole algorithm for solving combined field integral equations of electromagnetic scattering," *Microwave Opt. Tech. Lett.*, vol. 10, no. 1, pp. 14-19, Sept. 1995.

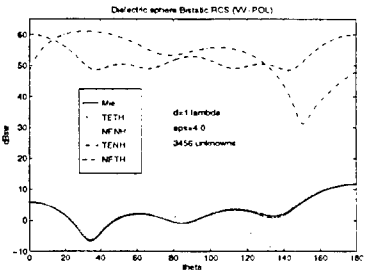

Figure 1: Bistatic RCS of a dielectric sphere.

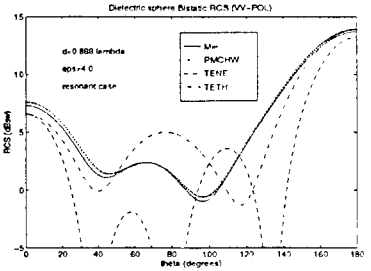

Figure 2: Bistatic RCS of a dielectric sphere.

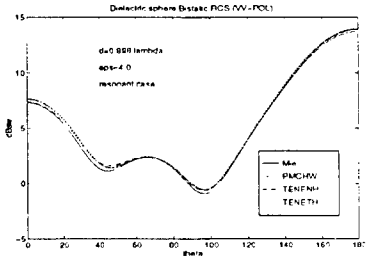

Figure 3: Bistatic RCS of a dielectric sphere.

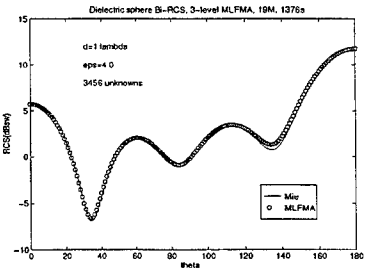

(a)

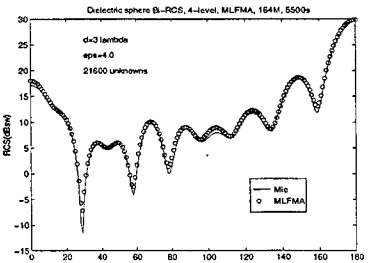

(b)

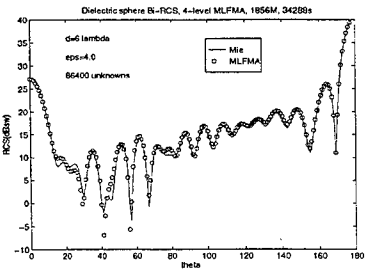

(c)

Figure 4: Bistatic RCS of a dielectric sphere in the E plane.

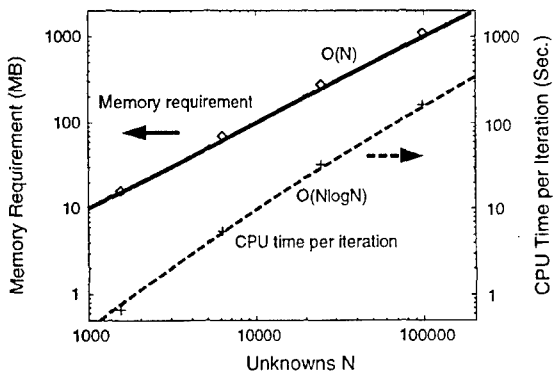

Figure 5: Memory requirement and CPU time per iteration as functions of the number of unknowns for MLFMA solution of scattering from a dielectric sphere.

Comparisons of FMM and AIM Compression Schemes in Finite Element – Boundary Integral Implementations for Antenna Modeling

K. Sertel, D. S. Filipoviç, S. Bindiganavale and J. L. Volakis
Radiation Laboratory
Department of Electrical Engineering and Computer Science
The University of Michigan
Ann Arbor, MI 48109-2122

Abstract

In this paper we consider implementations of the FMM and AIM compression schemes to speed-up the solution time associated with finite element-boundary integral systems. Of particular interest is the analysis of cavity backed antennas which may possess fine details as is the case with slot arrays, spirals, log-periodic and other broadband antennas. In those cases, the computational demand for the boundary integral is large in comparison to that of the finite element volume subsystem and therefore a fast integral method is attractive for speeding-up the iterative solution algorithm. We will present the CPU improvement using AIM and FMM with particular emphasis on the capability of each method to handle these types of antenna problems.

1 FE-BI Formulation for Cavity-Backed Antennas

Consider a cavity-backed antenna recessed in a ground plane as depicted in Figure 1. This class of configurations have been modeled using the finite element method [1, 2, 3] very successfully. The most rigorous of the implementations is to employ the finite element method to model the interior volume below the cavity and the boundary integral for truncating the finite element mesh on the antenna/cavity aperture [1, 2].

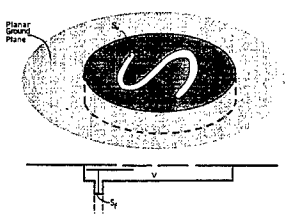

Figure 1: Geometry of a cavity-backed annular slot antenna in a ground plane

To develop the necessary linear equations, a standard approach is to begin with the weighted residual equation

$$\iiint_V \{(\nabla \times \mathbf{T}) \cdot \bar{\mu}_r^{-1} \cdot (\nabla \times \mathbf{E}) - k_0^2 \mathbf{T} \cdot \bar{\epsilon}_r \cdot \mathbf{E}\}\, dV + \iiint_{V_s} \mathbf{T} \cdot \left(-ik_0 Z_0 \mathbf{J}^i + \nabla \times \bar{\mu}_r^{-1} \cdot \mathbf{M}^i\right) dV - ik_0 Z_0 \iint_{S_o} \mathbf{T} \cdot (\mathbf{H} \times \hat{n})\, dS = 0 \quad (1)$$

where $\mathbf{E}$ and $\mathbf{H}$ denote the electric and magnetic fields. $\bar{\epsilon}_r$ and $\bar{\mu}_r$ are the relative tensor permittivity and permeability of the cavity filling (possibly inhomogeneous), S_0 represents the non-metallic portions of the aperture and S_f denotes the junction opening to the feeding structures. As usual, $\mathbf{T}$ represents an appropriate testing/weighting function to be specified later. The volume V_s refers to the volume occupied by the impressed sources $\mathbf{J}_i$ and $\mathbf{M}_i$. Note that the latter integral refers to $\mathbf{H}$ on the antenna aperture S_o and over the feed opening. Here, the unit normal $\hat{n}$ is directed outward from the boundary surfaces S_o.

To solve (1) for $\mathbf{E}$, we require knowledge of $\mathbf{H}$ over S_o. In the context of the FE-BI method, the relation between $\mathbf{H}$ and $\mathbf{E}$ is determined by the boundary integral equation

$$\mathbf{H} = \mathbf{H}^{go} - 2ik_0 Y_0 \iint_{S_o} \bar{\mathbf{G}}(\mathbf{r}, \mathbf{r}') \cdot (\hat{z} \times \mathbf{E}(\mathbf{r}'))\, dS' \quad (2)$$

where $\bar{\mathbf{G}}$ is the electric dyadic Green's function of the first kind such that $\hat{n} \times \bar{\mathbf{G}} = 0$ is satisfied on the metallic platform. For the cavity recessed in a ground plane, $\bar{\mathbf{G}}$ becomes the half space dyadic Green's function

$$\bar{\mathbf{G}} = \left(\bar{\mathbf{I}} - \frac{1}{k_0^2} \nabla \nabla'\right) \frac{e^{ik_0 R}}{4\pi R} \quad (3)$$

with $\mathrm{R} = |\mathbf{r} - \mathbf{r}'|$ and $\bar{\mathbf{I}}$ is the unit dyad. For this problem, $\mathbf{H}^{go}$ is equal to the sum of the incident and ground plane reflected fields for scattering computations and zero for antenna analysis.

To construct a linear set of equations from Eq. (1) and Eq. (2), we must first tessellate the volume and introduce expansions for each of the tessellation elements. For this application, the chosen tessellation elements can be of constant depth but must be more adaptable for surface modeling. The edge-based prismatic elements presented in [2, 3] allow for this type of flexibility while at the same time provide for meshing simplifications.

Choosing prisms as the tessellation elements (see Figure 2), the field is expanded within the cavity volume as

$$\mathbf{E}^e = \sum_{j=1}^{9} E_j^e \mathbf{W}_j^e = [\mathbf{W}]_e^T \{E^e\} \quad (4)$$

where $[\mathbf{W}]_e = [\{W_x\}, \{W_y\}, \{W_z\}]$ and $\{E^e\} = \{E_1^e, E_2^e, \ldots, E_9^e\}^T$ are specified explicitely in [3]. On the aperture, since the top and bottom faces of the prism are triangles, these reduced to

$$\mathbf{E}^t(\mathbf{r}) = \sum_{i=1}^{3} E_i^t \mathbf{S}_i^t(\mathbf{r}) = [S]_t^T \{E^t\} \quad (5)$$

where $[S]_s = [S_x, S_y]$ and

$$\mathbf{S}_i = \frac{l_i}{2A^e} \hat{z} \times (\mathbf{r} - \mathbf{r}_i) \quad (6)$$

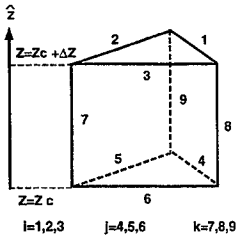

Figure 2: Right angled prism

Here, $\mathbf{r}$ and $\mathbf{r}_i$ refer to the position vector within the triangle and at the ith node of the triangular face. The parameters l_i and A^e denote the length of the ith edge of the triangle and its area, respectively.

To generate a linear system for E_j^e, (4) and (5) are substituted into (1) and (2) and Galerkin's method (setting $\mathbf{T} = \mathbf{W}$) is employed to yield the assembled system

$$[\mathcal{A}]\begin{Bmatrix} \{E^V\} \\ \{E^S\} \end{Bmatrix} + \begin{bmatrix} [0] & [0] \\ [0] & [\mathcal{B}] \end{bmatrix}\begin{Bmatrix} \{E^V\} \\ \{E^S\} \end{Bmatrix} = \begin{Bmatrix} \{b^V\} \\ \{b^S\} \end{Bmatrix}. \tag{7}$$

In this system, $\{E^V\}$ denotes the field unknowns within the volume enclosed by S_o, whereas $\{E^S\}$ represents the corresponding unknowns on the boundary S_o. The excitation column $\{b^V\}$ are due to internal sources and $\{b^S\}$ is associated with incident field excitations (for scattering).

2 Fast Integral Algorithms

The FE-BI system (7) is partly sparse and partly dense. More specifically $[\mathcal{A}]$ is sparse, whereas $[\mathcal{B}]$ is dense. Thus, although $[\mathcal{B}]$ is much smaller in rank than $[\mathcal{A}]$, it is usually responsible for most of the CPU and memory when an iterative algorithm is used for the solution of (7). To alleviate the CPU and memory requirements, fast integral methods have recently been introduced to perform the matrix-vector product $[\mathcal{B}]E^S$ much faster and with much less memory. Two of these approaches are the adaptive integral method (AIM) and the fast multipole method (FMM). Both FMM and AIM reduce the CPU time and memory requirement from $O(N^2)$ down to $O(N^\alpha)$ where $\alpha \leq 1.5$. The main feature of AIM and FMM is the decomposition of the matrix as

$$[\mathcal{B}] = [\mathcal{B}]^{near} + [\mathcal{B}]^{far} \tag{8}$$

based on some threshold distance referred to as the near-zone radius. The matrix $[\mathcal{B}]^{near}$ contains the interactions between elements separated less than the threshold distance, whereas $[\mathcal{B}]^{far}$ contains the remaining interactions. The elements of $[\mathcal{B}]^{near}$ are evaluated without approximation. However, the product $[\mathcal{B}]^{far}E^S$ is evaluated in an approximate manner leading to a much faster execution[4]. Below we describe how the evaluation of $[\mathcal{B}]^{far}E^S$ is done for each of the fast algorithms.

2.1 AIM Algorithm

Application of AIM requires that the aparture is immersed in a regular rectangular grid. The fields of each interior edge is then re-expressed using a new expansion based on delta sources located at the nodes of the uniform AIM grid. For the m^{th} edge, this new expansion has the form

$$\mathbf{e}_m = \sum_{q=1}^{M^2} \delta(x - x_{mq})\delta(y - y_{mq})[\Lambda_{mq}^x \hat{x} + \Lambda_{mq}^y \hat{y}] \tag{9}$$

where $\mathbf{r}_{mq}$ are the position vectors of M^2 points on the square surrounding the center of the edge and $\delta(x)$ is the usual Dirac delta function. The coefficients $\Lambda_m^{x,y}$ are suitably chosen so that the new expansion is equivalent to the original representation using triangular elements. A similar expansion is used for the divergence of the basis functions

$$e_m^d = \sum_{q=1}^{M^2} \delta(x - x_{mq})\delta(y - y_{mq})\Lambda_{mq}^d \tag{10}$$

To find a relation between the $\Lambda_m^{x,y}$ and I_n coefficients, we equate moments of the two expansions up to order M. Specifically, we set

$$\mathbf{M}_{q_1,q_2}^m = \mathbf{F}_{q_1,q_2}^m \tag{11}$$

where

$$\begin{aligned} \mathbf{M}_{q_1,q_2}^m &= \int_{-\infty}^{\infty}\int_{-\infty}^{\infty} \mathbf{e}_m (x - x_a)^{q_1}(y - y_a)^{q_2} dx dy \quad for \;\; 0 \le q_1, q_2 \le M \\ &= \sum_{q=1}^{M^2} (x_{mq} - x_a)^{q_1}(y_{mq} - y_a)^{q_2}[\Lambda_{mq}^x \hat{x} + \Lambda_{mq}^y \hat{y}] \quad with \;\; q = q_1 + q_2 \end{aligned} \tag{12}$$

$$\mathbf{F}_{q_1,q_2}^m = \int_{-\infty}^{\infty}\int_{-\infty}^{\infty} \mathbf{f}_m (x - x_a)^{q_1}(y - y_a)^{q_2} dx dy \tag{13}$$

Similarly, by equating moments of the divergence of the basis $\nabla_s \cdot \mathbf{J}_s$ with the new expansion (10), we establish a relation between Λ_m^d and I_n. That is, we set

$$D_{q1,q2}^m = H_{q1,q2}^m \tag{14}$$

where

$$D_{q_1,q_2}^m = \int_{-\infty}^{\infty}\int_{-\infty}^{\infty} e_m^d (x - x_a)^{q_1}(y - y_a)^{q_2} dx dy = \sum_{q=1}^{M^2} (x_{mq} - x_a)^{q_1}(y_{mq} - y_a)^{q_2}\Lambda_{mq}^d \tag{15}$$

$$H_{q_1,q_2}^m = \int_{-\infty}^{\infty}\int_{-\infty}^{\infty} \nabla_s \cdot \mathbf{f}_m (x - x_a)^{q_1}(y - y_a)^{q_2} dx dy \tag{16}$$

Eqs. (11) and (14) give three $M^2 \times M^2$ systems yielding the equivalence coefficients as the solution.

Using the equivalent expansions to represent the currents everywhere, the resulting impedance matrix will be of the form

$$[\mathcal{B}]_{AIM}^{total} = \sum_{i=1}^{3} [\Lambda]_i [G] [\Lambda]_i^T \tag{17}$$

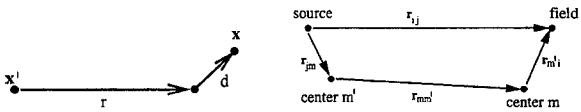

Figure 3: The geometry constructions used in FMM formulations, illustrating the relation between source point, field point and the group centers.

where $[\Lambda]_i$ are the sparse matrices containing the coefficients of the expansion (9) and (10) whereas $[G]$ is the Toeplitz matrix whose elements are the free space Green's function evaluated at the grid points. The speed-up of AIM is achieved by taking advantage of the Toeplitz property of $[G]$.

Using (17),$[\mathcal{B}]$ can be written as

$$[\mathcal{B}] \simeq [\mathcal{S}] + \sum_{i=1}^{3} [\Lambda]_i [G] [\Lambda]_i^T \tag{18}$$

where $[\mathcal{S}] = [\mathcal{B}]^{near} - [\mathcal{B}]^{near}_{AIM}$ is a sparse matrix corresponding to the difference between the near field interactions computed by moment method and AIM. Basically, the Toeplitz property of the Green's function enables use of the FFT to accelerate the computation of the matrix-vector product. In the computation of the matrix-vector product, the initial step of transforming the currents from the original MoM grid onto the uniform AIM grid is comparable to the grouping operation of the FMM. While the FMM relies on grouping to reduce the number of scattering centers, the sequence of operations in AIM can be interpreted as a realignment of scattering centers onto a regular grid.

2.2 Fast Multipole Method

The FMM [7, 8, 9] is based on two elementary identities. One of them is the expansion [5] of the scalar Green's function appearing in moment matrix elements as

$$\frac{e^{ik|\mathbf{r}+\mathbf{d}|}}{|\mathbf{r}+\mathbf{d}|} = ik \sum_{l=0}^{\infty} (-1)^l (2l+1) j_l(kd) h_l^{(1)}(kr) P_l(\hat{d} \cdot \hat{r}). \tag{19}$$

Here j_l is the spherical Bessel function, $h_l^{(1)}$ is the spherical Hankel function of the first kind, P_l is the Legendre polynolmial, and $d < r$ is the condition for the validy of the expansion. In the FMM formulations, where the source point is denoted by $\mathbf{x}'$ and the observation point by $\mathbf{x}$, $\mathbf{r}$ will be chosen to be close to $\mathbf{x} - \mathbf{x}'$ so that $\mathbf{d}$ will be small as depicted in Fig. 3. The second identity is the expansion of the product $j_l P_l$ appearing in Eq. (19) as a sum of propagating plane waves

$$4\pi i^l j_l(kd) P_l(\hat{d} \cdot \hat{r}) = \int d^2\hat{k} e^{i\mathbf{k}\cdot\mathbf{d}} P_l(\hat{k} \cdot \hat{r}). \tag{20}$$

Using this, the expansion (19) can be rewritten as

$$\frac{e^{ik|\mathbf{r}+\mathbf{d}|}}{|\mathbf{r}+\mathbf{d}|} = \frac{ik}{4\pi} \int d^2\hat{k} e^{i\mathbf{k}\cdot\mathbf{d}} \sum_{l=0}^{\infty} (2l+1) h_l^{(1)}(kr) P_l(\hat{k} \cdot \hat{r}), \tag{21}$$

where the orders of summation and integration are interchanged. The speed-up of FMM is derived from the observation that the sum

$$T_L(kr, \hat{k}\cdot\hat{r}) = \sum_{l=0}^{L}(2l+1)h_l^{(1)}(kr)P_l(\hat{k}\cdot\hat{r}) \tag{22}$$

is independent of kd and thus can be computed for various values of kr which can be reused thus eliminating the need for recomputation of the time consuming sum. The number of terms, $L+1$, kept for approximating the sum depends on the maximum value of kd, and the desired accuracy.

Noting that the direct path from the source to the field point can be decomposed into three parts (see Fig. 3) as, where

$$\mathbf{r}_{ji} = \mathbf{r}_{jm} + \mathbf{r}_{mm'} - \mathbf{r}_{im'}. \tag{23}$$

The Green's function can be rewritten as

$$\begin{aligned} 4\pi\overline{\mathbf{G}}(\mathbf{r}_j, \mathbf{r}_i) &= \left[\bar{\mathbf{I}} - \frac{1}{k^2}\nabla\nabla'\right]\frac{e^{ikr_{ji}}}{r_{ji}} \\ &\approx \int d^2\hat{k}\left[\bar{\mathbf{I}} - \frac{1}{k^2}\nabla\nabla'\right]e^{i\mathbf{k}\cdot(\mathbf{r}_{jm}-\mathbf{r}_{im'})}T_L(kr_{mm'}, \hat{k}\cdot\hat{r}_{mm'}) \\ &= \int d^2\hat{k}\left[\bar{\mathbf{I}} - \hat{k}\hat{k}\right]e^{i\mathbf{k}\cdot(\mathbf{r}_{jm}-\mathbf{r}_{im'})}T_L(kr_{mm'}, \hat{k}\cdot\hat{r}_{mm'}), \end{aligned} \tag{24}$$

and the matrix entries become

Using the above equations, a matrix entry is approximated by

$$\begin{aligned} B_{ij} &= 2\int_s ds\tilde{\mathbf{S}}_i(\mathbf{r})\cdot\int_{s'} ds'\left[\tilde{\mathbf{S}}_j(\mathbf{r}') + \frac{1}{k^2}\nabla'\cdot\tilde{\mathbf{S}}_j(\mathbf{r}')\nabla\right]\frac{e^{ikR}}{R} \\ &\approx \frac{ik}{2\pi}\int d^2\hat{k}\mathbf{V}_{fmj}(\hat{k})\cdot T_L(kr_{mm'}, \hat{k}\cdot\hat{r}_{mm'})\mathbf{V}^*_{sm'i}(\hat{k}), \end{aligned} \tag{25}$$

with

$$\begin{aligned} \mathbf{V}_{sm'i}(\hat{k}) &= \int_S ds' e^{i\mathbf{k}\cdot\mathbf{r}_{im'}}\left[\bar{\mathbf{I}} - \hat{k}\hat{k}\right]\cdot\tilde{\mathbf{S}}_i(\mathbf{r}_{im'}), \\ \mathbf{V}_{fmj}(\hat{k}) &= \int_S ds e^{i\mathbf{k}\cdot\mathbf{r}_{jm}}\left[\bar{\mathbf{I}} - \hat{k}\hat{k}\right]\cdot\tilde{\mathbf{S}}_j(\mathbf{r}_{jm}) \end{aligned} \tag{26}$$

in which $\tilde{\mathbf{S}}_i$ and $\tilde{\mathbf{S}}_j$ denote the expansion and testing functions for the unknown magnetic surface current density, which are the well known RWG [6] basis functions for the finite element basis functions used, and * denotes complex conjugation.

To realize the FMM speed-up the computational domain is divided into M groups. The total memory storage needed is $O(N^2/M) + O(KN) + O(KLM^2)$ where K is the number of wavevector directions used in the numerical evaluation of the outermost integral in Eq. (25). Using the proportionalities $K \propto L^2$, $D^2 \propto N/M$, and $L \propto D$, this expression can be simplified to $C_1(N^2/M) + C_2(NM\sqrt{N/M})$, where C_1 and C_2 are machine- and implementation-dependent constants. The coefficient C_2 is so small compared to C_1 and thus the memory is dominated by the $O(N^2/M)$ term.

The CPU requirement of the FMM is $O(NM) + O(N^2/M)$[8, 9]. This can be minimized by choosing $M = \sqrt{N}$ and the result is an $O(N^{1.5})$ algorithm. The memory required for the FMM also becomes $O(N^{1.5})$. In numerical practice, both the operation cost and the memory requirement of the FMM is less than those of standart MoM formulation for problem sizes larger than 1000, which makes the FMM more suitable for the solution of large problems.

3 Results and Comparisons

Before we show the CPU trend and memory savings of AIM and FMM for antenna modeling, it is important to first show validation results. Fig. 4 shows FE-BI results for a 4 element slot array computed with AIM and FMM compression schemes. As seen, both approaches yield the same patterns. In comparison to the uncompressed FE-BI method AIM compression yields a 25% speed-up even though the BI unknowns are only 248, i.e. very small to realize benefits from the fast integral method. We are currently testing the performances of AIM and FMM algorithms. At the meeting we will present results and comparisons for FE-BI implementations with AIM and FMM compressions for large BI systems. We will contrast AIM and FMM on the basis of CPU time and memory savings acquired by employing each method.

References

[1] J.L. Volakis,T. Özdemir and J. Gong "Hybrid Finite Element Methodologies for Antennas and Scattering", IEEE Trans. Antenna Propagat., pp. 493-507, March 1997

[2] J.Gong, J.L. Volakis and H.T.G. Wang, "Efficient Finite Element Simulation of Slot Antennas Using Prismatic Elements", Radio Sci., Vol. 31, No. 6, pp. 1837-1844, Nov-Dec. 1996

[3] T. Özdemir and J. L. Volakis, "Triangular Prisms for Edge-Based Vector Finite Elements Analysis" IEEE Trans.Antennas Propagat., pp. 788-797, May 1997

[4] E. Bleszynski, M. Bleszynski, and T. Jaroszewicz, "AIM: Adaptive Integral Method for Solving Large-Scale Electromagnetic Scattering and Radiation Problems" Radio Science, pp. 1225-1251, Sep.-Oct. 1996

[5] M. Abramowitz and I. A. Stegun, "Handbook of Mathematical Functions", National Bureau of Standards, 1972

[6] S. M. Rao, D. R. Wilton, and A. W. Glisson, "Electromagnetic Scattering by Surfaces of Arbitrary Shape", IEEE Trans.Antennas Propagat., pp. 409-418, May 1982

[7] R. Coifman, V. Rokhlin, and S. Wandzura, "The Fast Multipole Method for the Wave Equation: A Pedestrian Prescription", IEEE Antennas and Propagation Magazine, Vol. 35, pp. 7-12, June 1993

[8] W. C. Chew, J. Jin, C. Lu, E. Michielssen, and J. M. Song, "Fast Solution Methods in Electromagnetics", IEEE Trans. Antenna Propagat., Vol. 45, No. 3, pp. 533-543, March 1997

[9] S. S. Bindiganavale and J.L. Volakis, "Comparison of Three FMM Techniques for Solving Hybrid FE-BI Systems", IEEE Antennas and Propagation Magazine, Vol. 39, No. 4, pp. 47-59, August 1993

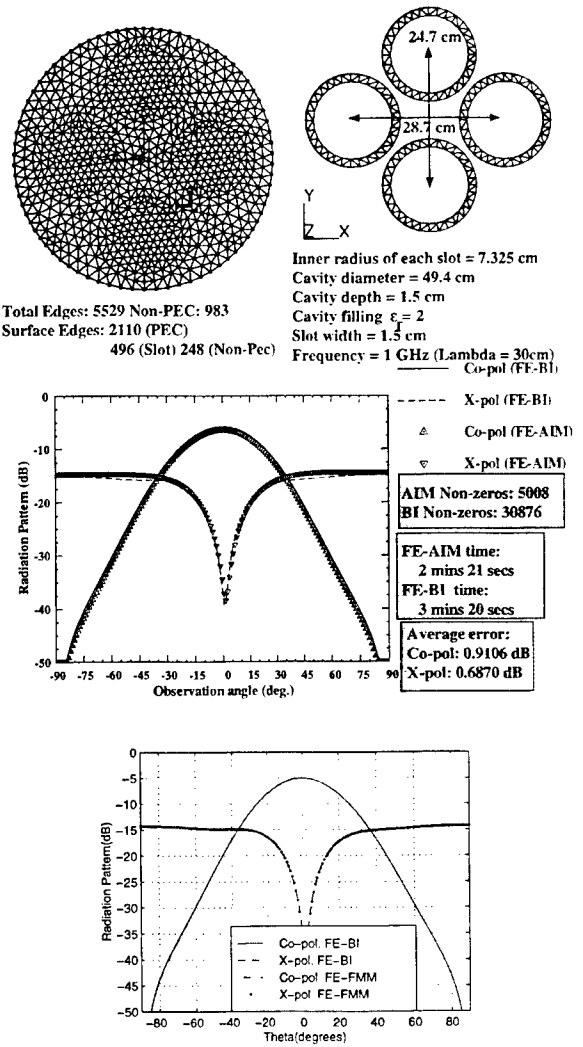

Figure 4: Validations of AIM and FMM algorithms

High-order Nyström discretization for faster, more accurate scattering calculations

Lawrence S. Canino, John J. Ottusch*, Mark A. Stalzer,
John L. Visher, and Stephen M. Wandzura

Hughes Research Laboratories
3011 Malibu Canyon Road, Malibu, CA 90265-4799
e-mail: ottusch@hrl.com

Abstract

Time-harmonic scattering problems can be solved faster and more accurately by using a high-order, point-based (Nyström) discretization. The distinguishing feature of our method is the implementation of local corrections to the quadrature rules in the vicinity of the kernel singularity. Enhanced by local corrections, the new algorithm has the simplicity and speed advantages of the traditional Nyström method, but also enjoys the advantages of high-order convergence for controlling solution error.

1 Introduction

Several different methods are available for discretizing boundary integral formulations of Maxwell's equations, of which the method of moments is the most common. In this method, the source distribution on the boundary is approximated as the sum over elemental source distributions (expansion functions) whose amplitudes are unknown. The N unknown amplitudes are determined by the requirement that they satisfy the N equations formed by taking moments of the boundary integral equation using N testing functions. When the same basis functions are used for expansion and testing, the method is called a Galerkin method. As far as method of moments scattering codes are concerned, it is hard to do better than a Galerkin code using high-order basis functions, if the objective is to compute accurate cross sections with the fewest unknowns. We have convincingly demonstrated this fact in recent years [1][2] using our own high-order Galerkin code called FastScat™.

The Nyström method is an alternative technique for discretizing an integral equation. In the Nyström method, the source distribution is sampled at a finite set of points judiciously distributed over the surface, and the value of the source at each of these points is determined by the requirement that the boundary integral equation hold true at each point. In its simplest form it is a low-order method, but it can be made high-order by applying a quadrature correction technique described by Strain [3]. In its high-order realization, a Nyström discretization can be as unknown-efficient as a high-order Galerkin discretization. A high-order Nyström discretization has several advantages over a high-order Galerkin discretization, however, one of which is that the setup phase of the computation (i.e. filling the impedance matrix) proceeds much more rapidly. The underlying reason is that the Nyström method does not require evaluation of a double integral to fill each impedance matrix element, but rather requires nothing more than a kernel evaluation to fill most matrix elements and $\mathcal{O}(N)$ single integrations and some low-rank linear algebra to fill the others (specifically, the near interactions). The upshot is that cross section computations obtained with a high-order Nyström code are more accurate and can be obtained in less time than those produced by well-tuned, low-order method of moments codes.

2 Nyström method

2.1 Conventional Nyström method

The traditional Nyström method is a simple and efficient mechanism for discretization of integral equations with non-singular kernels. Suppose we have the following integral equation

$$\phi(\mathbf{x}) = \int_S ds'\, G(\mathbf{x}-\mathbf{x}')\,\psi(\mathbf{x}') \tag{1}$$

and a quadrature rule for integrating a function $f(\mathbf{x})$ over the region S

$$\int_S ds\; f(\mathbf{x}) = \sum_{n=1}^{N} \omega_n f(\mathbf{x}_n)\,. \tag{2}$$

Such a quadrature rule will be provided by Gauss-Legendre or Gauss-Jacobi rules on a parameterization of S, so that the weights ω_n will be the products of the elementary weights w_n with the Jacobian of the parameterization:

$$\omega_n = \sqrt{g(u_n)}\,w_n \tag{3}$$

$$\mathbf{x}_n = \mathbf{x}(u_n)\,, \tag{4}$$

where u_n are the abscissae of the elementary rule, $\mathbf{x}(u)$ is the mapping function of the surface S, and $g(u)$ is the determinant of the mapping metric. The extension to patched parameterization is straightforward.

Since the Nyström discretization of a function on S is simply the tabulation of the function at the quadrature points $\mathbf{x}_n$,

$$\psi_n = \psi(\mathbf{x}_n)\,, \tag{5}$$

we can discretize integral Eq. (1) simply by making a matrix out of the kernel:

$$\phi_m = \sum_{n=1}^{N} \omega_n G(\mathbf{x}_m - \mathbf{x}'_n)\,\psi_n \tag{6}$$

This discretization has an error of the same order as the underlying quadrature rule. In other words, if the surface S is smooth, ϕ and $G(\mathbf{x}-\mathbf{x}')$ are regular functions, and a high-order quadrature rule is used, then the solution to Eq. (6) represents a high-order approximation to the exact solution.

The kernels $G(\mathbf{x}-\mathbf{x}')$ that arise in boundary integral formulations of wave scattering are not regular functions, however. Instead, they have singularities (or even hypersingularities) at short distances. With such kernels it is often not even possible to make a matrix out of the kernel because its value is undefined when $\mathbf{x}=\mathbf{x}'$. Even if the kernel were finite at vanishing separation, a singular[1] kernel would spoil the high-order discretization properties of the above prescription.

2.2 High-order Nyström method for singular kernels

We have adapted the Nyström method to handle singular kernels, without sacrificing high-order convergence, by incorporating Strain's method [3] for obtaining high-order quadrature rules for singular functions. The essence of the method is that by computing convolutions of the kernel with a suitable set of testing functions, it is possible to determine how to adjust the quadrature rule so that it is just as accurate near the singularity as far from it. The beauty of the method is that these quadrature rule modifications are required only in the vicinity of the singularity, hence the name local corrections.

Conceptually, local corrections may be viewed as adjustments to the quadrature weights (at the original set of sample points) that are required to make the quadrature rule high-order accurate when the (singular) function $G(\mathbf{x}-\mathbf{x}')$ is included in the integrand. In practice, since quadrature weights and discretized kernel terms always enter into the quadrature rule as product pairs, one can equally well "locally correct" the discretized representation of kernel and keep the original quadrature weights. This is the preferred approach because the modified representation of the kernel has no infinities.

[1] A function is singular in the mathematical sense where the function or any of its derivatives is undefined

We can write the "corrected" matrix representation of the kernel as

$$\widetilde{G}_{mn} \equiv \begin{cases} L_{mn} & \text{when } \mathbf{x}'_n \in D_m \\ G(\mathbf{x}_m - \mathbf{x}'_n) & \text{otherwise} \end{cases}, \tag{7}$$

where L_{mn} is a (sparse) matrix of local corrections whose entries are non-negligible only for source points $\mathbf{x}'_n$ within a small domain D_m centered on the field point $\mathbf{x}_m$. For $|\mathbf{x}_m - \mathbf{x}'_n|$ sufficiently large (i.e., outside the local correction domain D_m), $G(\mathbf{x}_m - \mathbf{x}'_n)$ is a smoothly varying function of position and the underlying quadrature rule provides a high-order approximation to the desired integral. Close to the singularity, on the other hand, the singular nature of the kernel spoils the high-order behavior of the underlying quadrature rule, and it becomes necessary to use locally corrected values for the kernel instead of $G(\mathbf{x}_m - \mathbf{x}'_n)$ in order to achieve high-order convergence.

The underlying quadrature rule is exact for integration of a certain class of functions (typically polynomials). The local corrections are chosen to make convolution of the singular kernel with the same class of functions exact. They are obtained by solving the linear system

$$\sum_n \omega_n L_{mn} f^{(k)}(\mathbf{x}_m - \mathbf{x}'_n) = \int_S ds'\, G(\mathbf{x}_m - \mathbf{x}')\, f^{(k)}(\mathbf{x}_m - \mathbf{x}'), \tag{8}$$

which represents K constraints (one for each testing function $f^{(k)}$) on J local correction coefficients (one for each of J source points in the vicinity of the m^{th} field point). The integral over S can be obtained by oversampling the region of integration until the result has converged to the desired accuracy. The non-zero components of the m^{th} row of the local correction matrix are obtained by inverting the (small) system of equations above, either by LUD if $J = K$ or singular value decomposition if $J \neq K$. Computing local corrections is the most time consuming step of the precomputation phase. Fortunately, it needs to be done only once at every sample point.

2.3 Advantages of a high-order Nyström discretization

- *More accurate results.* Conventional codes use RWG [4] basis functions to represent the source distribution on a flat-faceted surface model. These constitute low-order methods. Our code uses a high-order Nyström discretization on an exact or high-order (e.g., bi-cubic spline) model of the surface. As a consequence thereof, our code can compute more accurate answers with the same or fewer unknowns than the conventional codes. Fewer unknowns translates into a lower requirement for computer memory.

- *Practical accuracy estimation.* Another benefit of using a high-order discretization is that error estimation becomes practical [5]. This is an indispensable asset for a scattering code since computed results without meaningful accuracy estimates are of limited utility. The fact that such estimates are usually very difficult to obtain with low-order codes may explain why they so infrequently accompany reported results, but it does not make them any less important. Error estimation becomes practical with a high-order code because a substantially more accurate reference solution can be computed at a modest additional cost in computer resources.

- *Faster precomputation.* Unlike conventional method of moments codes, which require N^2 numerical double integrations (where N is the number of discretized sources on the surface) to fill the impedance matrix, a high-order Nyström code requires nothing more than kernel evaluations to fill in most of the matrix (specifically, the far interactions), and the rest is filled in by means of local corrections (each of which involves a small number of adaptive integrations and a low-rank matrix inversion). As a result, the precomputation phase of a high-order Nyström calculation is generally much less time consuming, an advantage that grows as the number of unknowns applied to the problem increases.

- *Elimination of multi-patch, parametric basis functions.* Conventional method of moments scattering codes require basis functions that are continuous (in the surface parameterization) across patch boundaries to facilitate differentiation. Implementing such multi-patch basis functions in a high-order code is complicated and inconvenient. No such requirement applies to a code using a point-based discretization. In the Nyström case, continuity of the source distribution drops out as a natural consequence of accurately solving the integral equation rather than by being built into the elemental sources. [A further note is in order regarding use of basis functions that are not explicitly continuous across patch boundaries. The error caused by not

enforcing continuity is comparable to the error of the underlying discretization. In the case of a low-order discretization (e.g., RWG basis functions on flat patches), continuity enforcement pays off because the error in the underlying discretization is already significant. In the case of a high-order discretization, where the error due to the underlying discretization can more easily be made insignificant, the situation is reversed. Thus, for high-order codes, whether Galerkin or Nyström, the benefits of enforcing continuity between patches do not outweigh the inconveniences.]

- *More amenable to fast solution algorithms.* Implementation of a fast method that requires segregation of the discretized scatterer into groups (such as the fast multipole method (FMM) [6] or adaptive integral method (AIM) [7]) is simpler and more natural with a point-based discretization. When a Galerkin implementation with overlapping basis function domains is employed, the fast algorithm is either more complicated (because multi-patch basis functions must be split apart) or less efficient (because the groups must overlap). A Galerkin implementation that uses high-order basis functions (even those confined to single patches) cannot achieve optimum efficiency from the FMM because high-order basis functions are used to their greatest advantage on patches larger than a wavelength, whereas optimum use of the FMM favors groups smaller than a wavelength. In a Nyström discretization, the groups consist of individual sample points on the surface, so no such grouping restrictions apply.

- *Iterative solver memory reduction.* With the Nyström method, the memory requirement for an iterative solver using the full impedance matrix can be reduced from $\mathcal{O}(N^2)$ (storing the full impedance matrix) to $\mathcal{O}(N)$ (storing only the sparse local correction matrix). This is practical because reconstruction of the unsaved portions of the impedance only requires evaluations of the kernel, which are fast. If the FMM is used to represent the far interactions, the storage requirement goes from $\mathcal{O}(N^{5/4})$ in the single-stage case to $\mathcal{O}(N \log(N))$ in the multi-level case.

- *Symmetry exploitation.* When basis functions are used, it is more complicated to reflect geometrical symmetries in the matrix representation. It may be necessary to explicitly consider basis function transformation properties and to provide special treatment for some variables (e.g., the coefficients of basis functions whose domains intersect reflection planes). In the Nyström case, the representation of symmetries is much simpler.

3 High-order convergence

Achieving high-order convergence is the key to computing accurate cross sections efficiently and obtaining practical accuracy estimates. In this section, we demonstrate that our Nyström code (FastScat) achieves high-order convergence[2] to the correct cross section for a PEC sphere.

A sphere is the ideal surface to use for benchmarking a high-order 3*d* vector code because it is uniformly smooth and because the accuracy of computed results can be determined unambiguously by comparison to the Mie series solution. We chose to present data for a $\frac{1}{4}\lambda$−radius sphere because it is in the regime of small discretization scales and small errors that the high-order convergence behavior is most clearly illustrated. With larger spheres, the error in the computed cross section is actually lower for the same unknown density (because each patch is flatter), but the asymptotic convergence behavior is the same.

A $\frac{1}{4}\lambda$−radius sphere was meshed into triangular patches each of which corresponds to a segment of an ideal sphere. The coarsest meshing of the sphere consists of 20 identical triangular patches, formed by mapping the triangles of an inscribed icosahedron onto the surface of the sphere. Finer meshes were generated by dividing each of the 20 triangles into n^2 nearly-identical subtriangles, where n ranged from 2 up to 10. The distribution of Nyström quadrature points on each patch was determined by high-order triangle rules [8][9] that used 1, 3, 6, or 15 sample points per patch depending on the rule. The number of testing functions used for computing local corrections was always chosen to match the number of sample points.

Solutions for the bistatic cross section of the $\frac{1}{4}\lambda$−radius sphere were computed using the MFIE with the various discretizations and compared against the Mie series solution. Figure 1 contains log-log plots of maximum relative

[2]The order of convergence of a numerical method relates to the rate at which the error in the computed solution decreases as the discretization scale decreases. For small enough discretization scales Δ, the error in the solution computed by an n^{th}-order method scales as Δ^n.

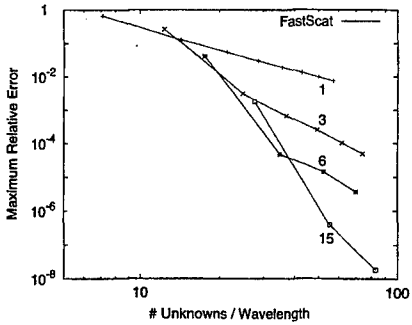

Figure 1: Log-log plot of maximum relative error vs. unknown density for bistatic scattering from a $\frac{1}{4}\lambda$-radius PEC sphere in $\theta\theta$ polarization using the MFIE. Points obtained with different meshings, but the same method order, are connected by lines. FastScat data points are connected by solid lines and are labeled by the number of sample points per patch.

error[3] vs. unknown density for FastScat calculations performed with four different Nyström quadrature orders. Lines connect data points corresponding to different meshings but the same order quadrature rule. Each line is labeled by the number of sample points per patch used by the rule. Note that for a given Nyström order, refining the mesh always improves the accuracy of the solution. Note also that with enough unknowns, the data approach a linear trend line whose slope increases as the Nyström order increases. This is the signature of a high-order method.

4 Computational Performance

With high-order convergence behavior established in the limit of very small errors, it is worthwhile to show how our high-order Nyström code performs in a "practical accuracy" regime. We provide two examples. The first is bistatic scattering from PEC spheres with radii ranging from 0.9λ to 3.6λ. The second is monostatic scattering from a 10 inch $\times$ 2 inch EMCC ogive at 9 GHz. This is a problem for which the exact answer is not known (although inexact experimental data [10] is available for comparison purposes) and error assessments can only be made by comparison to solutions computed with sufficiently refined discretizations.

We can evaluate the accuracy of the FastScat calculations on spheres of different sizes by comparing the computed results to Mie series solutions. We present data for bistatic scattering from $r = 0.9\lambda$, 1.8λ, and 2.7λ PEC spheres. Our computations used a dense matrix fill, an LUD solver, and the MFIE formulation. Unknowns were distributed with an average density of about 7.7 unknowns/wavelength in all three cases. The smallest sphere was patched as described in the previous section using an inscribed icosahedron mapped to an exact sphere. The $r = 1.8\lambda$ and 2.7λ spheres were patched by dividing each of these patches into 4 and 9 subtriangles, respectively. In all cases, we used a high-order triangle quadrature rule that puts 15 sample points (i.e., 30 unknowns) on each patch.

The second demonstration problem involves computing of the monostatic cross section of an ogive at 9 GHz. A plot comparing the FastScat result to the measured data is given in Figure 2. The measured data have been shifted to correct (apparent) calibration errors both in amplitude and angle. There are actually two measured data curves shown, each of which corresponds to half of the full 360 degree scan around the ogive target. The two halves should be identical and symmetric about 90 degrees; the fact that they are not puts a lower bound on the

[3] Maximum relative error is defined as the maximum value of $\left|\frac{\sigma(\theta)}{\sigma_{ref}(\theta)} - 1\right|$.

Radius (λ)	# Unknowns	Setup Time (sec)	Total Time (sec)	RMS Error (dB)
0.9	600	74	110	0.35
1.8	2400	539	3281	0.26
2.7	5400	1953	33689	0.10

Table 1: FastScat performance computing the bistatic cross section of PEC spheres of increasing size.

the measurement error at each observation angle. At some angles, such as near the tips, the error is actually much worse.

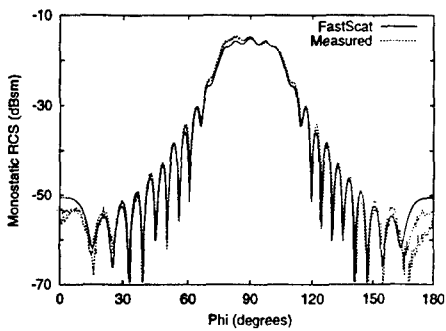

Figure 2: Monostatic cross section of ogive at 9 GHz in $\theta\theta$ (VV) polarization. Solid line — FastScat result; Dashed lines — 360° worth of measured data.

The correct cross section (for an ogive target that exactly matches the ogive model) is much closer to the FastScat result. The FastScat result was computed by first creating an ideal model of an ogive, meshing it with 108 patches, and then computing the cross section using the MFIE, a 15 point per patch quadrature rule, and an LUD solver. A total of 3240 unknowns were used. To estimate the accuracy of this solution, we compared it to a substantially more accurate solution obtained with a finer discretization, namely one that used 232 patches and 6960 unknowns. Over the whole range of angles (dips included) the RMS error of the original solution turns out to be 1.0 dB; near broadside incidence the error is less than 0.08 dB and near the tips it is less than 0.7 dB.

5 Acknowledgments

We are grateful to Drs. Vladimir Rokhlin and Leslie Greengard for considerable guidance regarding the use of high-order Nyström discretizations in scattering calculations.

The United States Government is authorized to reproduce and distribute reprints for government purposes notwithstanding any copyright notation hereon.

References

[1] L. R. Hamilton, J. J. Ottusch, M. A. Stalzer, R. S. Turley, J. L. Visher, and S. M. Wandzura, "FastScat benchmark data," In *Proc. 1994 HAVE FORUM Symposium*, volume I, pages 255–268, Wright Patterson AFB, OH 454-7523, February 1995, Wright Laboratory, WL–TR–95–6003.

[2] L. Canino, L. Hamilton, J. J. Ottusch, R. Ross, J. Visher, and S. Wandzura, "FastScat performance on EMCC benchmark cases," In *Presentations of Electromagnetic Code Consortium Annual Meeting*, Rome, NY, May 1996.

[3] J. Strain, "Locally-corrected multidimensional quadrature rules for singular functions," *SIAM Journal of Scientific Computing*, 16(4):992–1017, July 1995.

[4] S. M. Rao, D. R. Wilton, and A. W. Glisson, "Electromagnetic scattering by surfaces of arbitrary shape," *IEEE Transactions on Antennas and Propagation*, AP-30(3):409–418, May 1982.

[5] L. R. Hamilton, J. J. Ottusch, M. A. Stalzer, R. S. Turley, J. L. Visher, and S. M. Wandzura, "Accuracy estimation and high-order methods," In *11th Annual Review of Progress in Applied Computational Electromagnetics*, volume II, pages 1177–1184, Monterey, CA, March 1995, Applied Computational Electromagnetics Society.

[6] R. Coifman, V. Rokhlin, and S. Wandzura, "The fast multipole method: A pedestrian prescription," *IEEE Antennas and Propagation Society Magazine*, 35(3):7–12, June 1993.

[7] E. Bleszynski, M. Bleszynski, and T. Jaroszewicz, "AIM: adaptive integral method for solving large-scale electromagnetic scattering and radiation problems," *Radio Science*, 31(5):1225–51, Sep-Oct 1996.

[8] J. N. Lyness and D. Jespersen, "Moderate degree symmetric quadrature rules for the triangle," *Journal of the Institute of Mathematics and its Applications*, 15:19–32, 1975.

[9] L. R. Hamilton, M. A. Stalzer, R. S. Turley, J. L. Visher, and S. M. Wandzura, "Fast multipole methods for scattering computation," Annual contract report, Hughes Aircraft Company Research Laboratories, August 1993, AFOSR Contract No. F49620-91-C-0064.

[10] H. T. G. Wang, M. L. Sanders, and A. Woo, "Radar cross section measurement data on low-cross-section targets (Part 1. Almond, ogive, and double ogive)," Technical Memorandum NWC TM 7002, Naval Air Warfare Center Weapons Division, China Lake, October 1991, Limited Distribution Document.

Large Scale Computing with the Fast Illinois Solver Code —Requirements Scaling Properties †

JIMING SONG[1,2] AND WENG CHO CHEW[1]

[1]CENTER FOR COMPUTATIONAL ELECTROMAGNETICS
DEPARTMENT OF ELECTRICAL AND COMPUTER ENGINEERING
UNIVERSITY OF ILLINOIS, URBANA, IL 61801

[2]DEMACO, INC.
100 TRADE CENTRE DR., CHAMPAIGN, IL 61820

1. Introduction

We have witnessed the rapid progress of computational electromagnetics recently, due to its increased importance. Computational electromagnetics problems are generally solved by differential equation solvers as well as integral equation solvers [1].

Differential equation solvers solve for the field in a problem: the field permeates the whole of space in general, and hence the number of unknowns needed to model the problem correctly is generally large. Differential equation solvers have caught on in popularity recently, because of their associated sparse matrices.

On the contrary, integral equation solvers solve for induced currents in a problem: the current resides only on the support of the body, and hence, the number of unknowns is generally small. But integral equation solvers yield dense matrices which are more costly to solve. Hence, the popularity of integral equation solvers has been impeded until recently.

The recent advent of fast algorithms in computational electromagnetics has permitted the solution of integral equations with an unprecedented number of unknowns. This is the consequence of the development of the fast multipole algorithms (FMA) [2,3], and the multilevel fast multipole algorithms [4,5]. Such algorithms allow a matrix-vector multiplication to be performed in $O(N \log N)$ operation or less for many scattering problems. Moreover, the memory requirements of these methods are $O(N \log N)$, or almost matrix free. Using the fast matrix-vector multiplications in an iterative solver, problems for integral equations involving millions of unknowns have been solved recently [6-9].

These fast solvers calculate the action of a matrix on a vector (or an operator on a function) without generating every element of the matrix. Therefore, the generation and the storage of the matrices are avoided, yielding an algorithm which is almost matrix free.

The Fast Illinois Solver Code (FISC) is a recently developed code to tackle such large scale computing and scattering problems using the multilevel fast multipole algorithm (MLFMA). Very large problems have been solved with FISC involving as much as 2 million unknowns [9].

† This work was supported by the Office of Naval Research under grant N00014-95-1-0872, the National Science Foundation under grant NSF ECS 93-02145, and AFOSR under a MURI grant F49620-96-1-0025. The computer time was provided by the NCSA at the University of Illinois, Urbana-Champaign, and the ASC MSRC.

Meanwhile, much empirical data on the solutions to large scale problem are generated.

One important empirical data is on how the number of iterations (N_{iter}) scales as the number of unknowns in a scattering problem. The application of iterative solvers to integral equation is less matured than to differential equation solvers due to the aforementioned reason. While much knowledge has been derived on how N_{iter} scales as the number of unknowns N increases for differential equation solvers [1,10], much less knowledge is available for how N_{iter} scales as N for integral equation solvers. We hope that by providing the empirically derived data from numerical experiments, we will motivate the more mathematically inclined to arrive at theory on how one can predict the scaling property of N_{iter} for these problems.

In this paper, FISC requirements about memory and CPU time are discussed. Some empirically derived formulas and charts are given. Examples used to get these conclusions are also plotted. FISC is designed to compute the RCS of a target described by a triangular facet file. The problem is formulated by the method of moments (MoM), where the RWG (Rao, Wilton, and Glisson) [11] basis functions are used. The resultant matrix equation is solved iteratively by the conjugate gradient (CG) method where the multilevel fast multipole algorithm (MLFMA) is used to speed up the matrix-vector multiply in CG. Both complexities for the CPU time per iteration and memory requirements are of $O(N\log N)$, where N is the number of unknowns.

2. Scaling of Memory Requirements

FISC solves surface integral equation, and the surface is described by a facet model. The RWG basis function [11] is assigned to each interior edge. The total number of unknowns (N) is the number of interior edges, which is about one and a half (1.5) times the number of triangular facets. In most cases, average edge length (a) should be about 0.1λ, where λ is the wavelength. Therefore, the number of unknowns (N) can be expressed as:

$$N \simeq 350S\left(\frac{0.1\lambda}{a}\right)^2, \tag{1}$$

where S is the total surface area in the unit of square wavelength (λ^2) and a is the average edge length. For a given target, N is proportional to the square of the frequency. If the facet size is refined to half, N increases by a factor 4.

Each single precision complex number needs 8 bytes. Hence, for a full matrix, the memory needed in the unit of MB is:

$$MEM_{\text{full}} = 8\left(\frac{N}{1000}\right)^2 \simeq 0.98S^2\left(\frac{0.1\lambda}{a}\right)^4. \tag{2}$$

The memory needed for a full matrix is proportional to the fourth power of the frequency, and increases a lot if a finer facet model (smaller a) is used.

FISC memory requirement (using MLFMA [5]) can be empirically approximated as:

$$MEM_{\text{FISC}} \simeq 0.75S\left[0.2 + 0.8\left(\frac{0.1\lambda}{a}\right)^2\right]. \tag{3}$$

It increases linearly as the number of unknowns increases, and is proportional to the square of the frequency only. If the facet size is refined by half, FISC only needs about 3 times more memory, not 16 as for the case of a full matrix. The complexity of the memory requirement for MLFMA is $O(N\log N)$ or $O(S\log S)$. But for the problems we have tested (up to 2 million unknowns), the linear term in the memory requirement (storage for near interaction elements in MoM matrix and the radiation pattern for each basis) is dominant.

In Figure 1, we plot FISC memory requirement as a function of surface area with 3 different discretization densities.

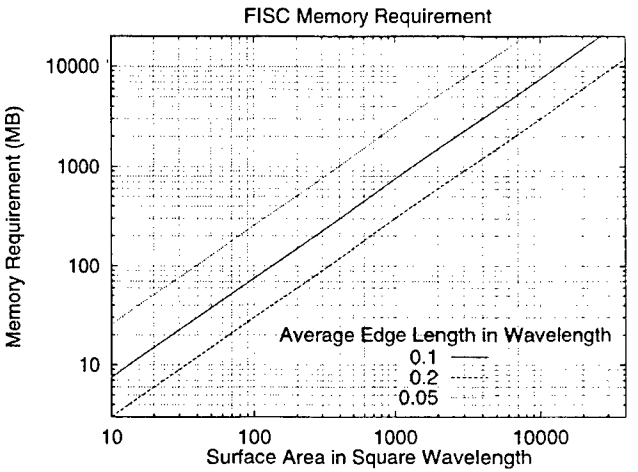

Figure 1. FISC memory requirement as a function of surface area with 3 different discretization densities.

3. CPU Time Scaling

We divide the total CPU time into two parts: set-up (matrix filling) time and solution time. The set-up time is for one frequency point, and is not a function of numbers of incident angles, observation angles, and polarization. If a full matrix is used, the set-up time is proportional to N^2, where N is the number of unknowns.

If LUD (LU Decomposition) is used to solve the full matrix, it needs $O(N^3)$ operations to perform LUD, and then $O(N^2)$ for each incident angle. If an iterative solver with full matrix is used, the CPU time for each incident angle is proportional to $N_{\text{iter}}N^2$, where N_{iter} is the number of iterations.

We have tested FISC on different machines and systems, like SUN Sparc workstations, SGI workstations (R4400 and R10000), SGI Power Challenge Array, SGI CRAY Origin2000,

and DEC Alpha workstations. Since the peak performance is not very accurate for comparing different machines, we will use the LINPACK benchmark and our numerical test results to compare different machines for FISC CPU requirement. (An extensive listing of the performance of different computer systems is available from the *netlib* repository at Oak Ridge National Laboratory. This database can be accessed on the World Wide Web at the address "http://www.netlib.org/index.html".)

The test problem is the electromagnetic scattering problem from a sphere with a 1 m radius at 450 MHz. The surface area is $28\lambda^2$, and is discretized to 6,272 facets, which leads to $N = 9,408$. The FISC solution time given in the following table is for one incident angle.

LINPACK Benchmark and FISC Testings

Machine	Peak Performance (Mflops)	LINPACK Benchmark (Mflops)	FISC CPU Time Set-up (Sec.)	FISC CPU Time Solution (Sec.)
SUN Sparc10	40	10	1,264	557
SGI Indy (100MHz, R4600PC)	?	15	927	332
SGI Extreme (250MHz)	?	40	336	124
DEC Alpha (250 4/266)	500	119	262	64
1 CPU of SGI Power Challenge (R8000, 90 MHz)	360	126	311	54
1 CPU of SGI CRAY Origin2000 (R10000)	390	140	114	34

FISC CPU time requirement given in this paper is based on one CPU of SGI CRAY Origin2000.

Since the number of near interaction elements in the MoM matrix is a constant for a basis in MLFMA, the set-up (filling MoM matrix for near interactions) time T_{fill} in the unit of second for one CPU of SGI CRAY Origin2000 can be empirically approximated as:

$$T_{\text{fill}} \simeq 5S \tag{4}$$

where S is the surface area in the unit of square wavelength. The set-up time is proportional to the problem size linearly. But the matrix-filling time for a full matrix is proportional to N^2.

The solution time T_{solve} in the unit of second for each angle can be approximated as:

$$T_{\text{solve}} \simeq 0.05S\log(S)(S^{1/4} + I_{\text{open}}S^{1/2})\log\left(\frac{1}{\epsilon}\right)\frac{0.1\lambda}{a}\left(\frac{1}{r_{\min}}\right)^{1/2}, \tag{5}$$

where S is the surface area in the unit of square wavelength, I_{open} is 1 for open targets, and 0 for closed targets, ϵ is the relative residual error for iterative solvers, a is the average edge length, and $r_{\min}$ is the minimum aspect ratio (the aspect ratio is always less than one).

In (5), we use the fact that the CPU time per matrix-vector multiply using MLFMA is $O(N\log N)$ or $O(S\log S)$. For closed targets, CFIE (combined field integral equation) [12] is used to reduce the number of iterations. The number of iterations needed for CFIE increases slowly when the problem size increases, and can be approximated by $O(N^{1/4})$ or $O(S^{1/4})$.

But for open targets, only EFIE (electric field integral equation) can be used. It converges much slower than CFIE for the same problem size where the number of iterations needed is proportional to $N^{1/2}$ or $S^{1/2}$. CFIE is mandatory for closed surfaces, because it removes the nonuniquess problem at the internal resonant frequencies of the closed structure. In addition, it provides a second kind integral equation which is well-known to be better conditioned compared to the first kind integral equation offered by EFIE [13].

When $\epsilon = 0.01$, $a = 0.1\lambda$, and $r_{\min} \simeq 1$, the solution time T_{solve} can be simplified as:

$$T_{\text{solve}} \simeq 0.1S\log(S)(S^{1/4} + I_{\text{open}}S^{1/2}). \tag{6}$$

In Figure 2, we plot 3 curves as a function of S. The first curve (solid line) is for set-up time calculated using Equation (4), and the second and third curves (dash lines) are for the solution time calculated using equation (6) with I_{open} equals to 1 (EFIE for open target), and 0 (CFIE for closed target), respectively.

Therefore, the total CPU time for FISC can be written as:

$$T_{\text{total}} = N_{\text{freq}}(T_{\text{fill}} + N_{\text{inc}}N_{\text{pol}}T_{\text{solve}}), \tag{7}$$

where N_{freq} is the number of frequency points, N_{inc} is the number of incident angles, and N_{pol} is the number of polarizations. Since the previous solution with phase correction is used as the initial guess for the next incident angle in FISC, the CPU time in the second part of Equation (7) increases slower as the number of incident angles increases. When the Advanced Feature 1 (approximation of bistatic RCS to monostatic RCS) is used, the number of incident angles used for iterative solutions can be further reduced. For example, 30 incident angles were used to calculate the monostatic RCS of VFY218 at 1 GHz from 0 to 180 degrees with 900 points. Similarly, the Advanced Feature 2 (frequency interpolation) can be used to reduce the number of frequency points.

4. FISC Scaling Results

In this section, FISC numerical results used to get the approximated FISC requirements scaling are given. In Figure 3, we plot the estimated FISC memory requirement calculated using Equation (3) and the memory used from our tests. In Figure 4, we plot the estimated FISC set-up time [Eq.(4)] and solution time [Eq.(6)], the set-up time used, the solution time used [normalized to Eq.(6)]. These FISC results come from spheres with electric different size, VFY218 at different frequencies, bi-cones, closed cylinders, trihedrons, etc.

5. Summary

The scaling properties of the CPU and memory requirements of the fast Illinois solver code (FISC) are given. This code is developed with an iterative solver based on the multilevel fast multipole algorithm (MLFMA) applied to solve a surface integral equation.

The number of unknowns scales approximately as the surface area of the scatterer, or $N \simeq 350S\left(\frac{0.1\lambda}{a}\right)^2$, where S is the target surface area in the unit of square wavelength, and a is the average edge length.

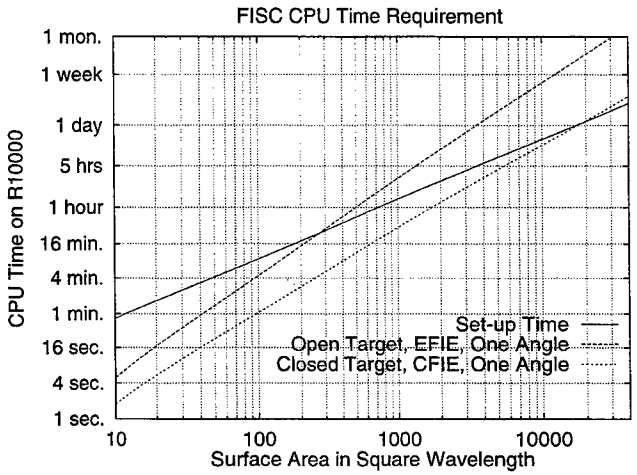

Figure 2. FISC CPU time (set-up time and solution time) requirement as a function of surface area. The solid line is for set-up time calculated using Equation (4), and the dash lines are the solution time calculated using equation (6) with I_{open} equals to 1 (EFIE for open target, long dash line), and 0 (CFIE for closed target, short dashed lines), respectively.

The memory requirement scales approximately as the number of unknowns, and hence, the surface area of the scatterer. The memory requirement is approximately $0.75S\left[0.2+0.8\left(\frac{0.1\lambda}{a}\right)^2\right]$ MB of memory.

If one CPU of SGI CRAY Origin2000 is used, for each frequency, FISC needs the set-up time $T_{\text{fill}} \simeq 5S$ (seconds), and solution time $T_{\text{solve}} = 0.1S\log(S)(S^{1/4} + I_{\text{open}}S^{1/2})$ (seconds) for each angle. This formula is true for non-resonant structures.

CFIE is *de rigueur* for scatterers with closed surfaces. It yields a formulation with second kind integral equation with better condition numbers, and hence requiring a smaller number of iterations. The number of iterations required, N_{iter} scales as $N^{1/4}$ in this case.

For scatterers with open surfaces, our only choice is to use EFIE which is a first kind integral equation with worse condition number than a second kind integral equation. The number of iterations required, N_{iter} scales as $N^{1/2}$ in this case.

The scaling properties of N_{iter} at this point is empirically derived via numerical experimentation of very large scale computing problems. It calls for a more theoretical analysis to arrive at these scaling properties.

In addition, FISC uses a triangular facet model with complete connectivities and good aspect ratio. Furthermore, two advanced features in FISC can be used to reduce the total CPU time for multiple incident angles and/or multiple frequencies.

References

[1] W. C. Chew, J. M. Jin, C. C. Lu, E. Michielssen, and J. M. Song, "Fast solution methods in electromagnetics," *IEEE Trans. Ant. Propag.*, vol. 45, no. 3, pp. 533-543, March 1997.

[2] V. Rokhlin, "Rapid solution of integral equations of scattering theory in two dimensions." *J. Comput. Phys*, vol. 36, no. 2, pp. 414-439, 1990.

[3] R. Coifman, V. Rokhlin, and S. Wandzura, "The fast multipole method for the wave equation: A pedestrian prescription," *IEEE Antenna Propagat. Mag.*, vol. 35, no. 3, pp. 7-12, June 1993.

[4] C. C. Lu, and W. C. Chew, "A multilevel algorithm for solving a boundary integral equation of wave scattering," *Micro. Opt. Tech. Lett.*, vol. 7, no. 10, pp. 456-470, July 1994.

[5] J. M. Song and W. C. Chew, "Multilevel fast-multipole algorithm for solving combined field integral equations of electromagnetic scattering, " *Micro. Opt. Tech. Lett.*, vol. 10, no. 1, pp. 14-19, Sept. 1995.

[6] J. M. Song, C. C. Lu, W. C. Chew, and S. W. Lee, "Fast Illinois Solver Code (FISC)," *13th Annual Review of Progress in Applied Computational Electromagnetics*, vol. 2, pp. 966-973, Monterey, California, March 1997.

[7] *User's Manual for FISC (Fast Illinois Solver Code)*, Center for Computational Electromagnetics, University of Illinois at Urbana-Champaign and DEMACO, Inc., Champaign, Illinois, January 1997.

[8] J.M. Song, C.C. Lu, and W.C. Chew, "MLFMA for electromagnetic scattering from large complex objects," *IEEE Transactions on Antennas and Propagation*, vol.45, no.10, pp.1488-1493, October 1997.

[9] J.M. Song, C.C. Lu, W.C. Chew, and S.W. Lee, "Fast Illinois Solver Code (FISC)" *IEEE Antennas and Propagation Magazine*, submitted for publication.

[10] O. Axelsson and V.A. Barker, *Finite Element Solution of Boundary Value Problems: Theory and Computation.* Academic Press, New York, 1984.

[11] S. M. Rao, D. R. Wilton, and A. W. Glisson, "Electromagnetic scattering by surfaces of arbitrary shape," *IEEE Transactions on Antennas and Propagation*, vol. 30, no. 3, pp. 409-418, May 1982.

[12] J.R. Mautz and R.F. Harrington, "H-Field, E-Field, and Combined Field Solutions for Conducting Bodies of Revolution," *Arch. Elektron. Übertragungstech (AEÜ)*, vol. 32, no. 4, pp. 159-164, April 1978.

[13] G. C. Hsiao and R. E. Kleinman, "Error analysis in numerical solution of acoustic integral equations," *Int. J. Numer. Meth. Engg.*, vol. 37, pp. 2921-2933, 1994.

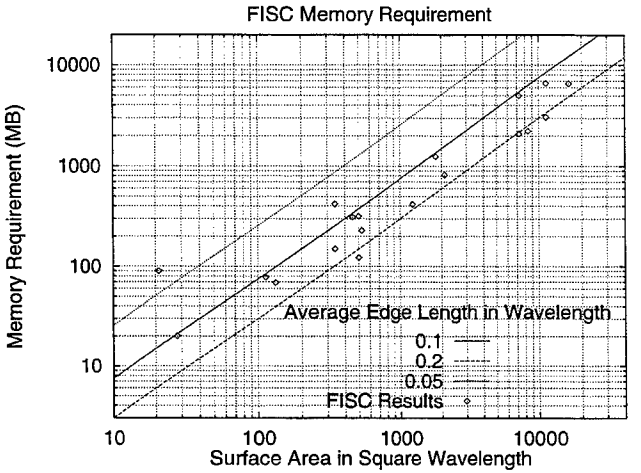

Figure 3. Estimated memory requirement as a function of surface area (lines) and the memory used running FISC (points).

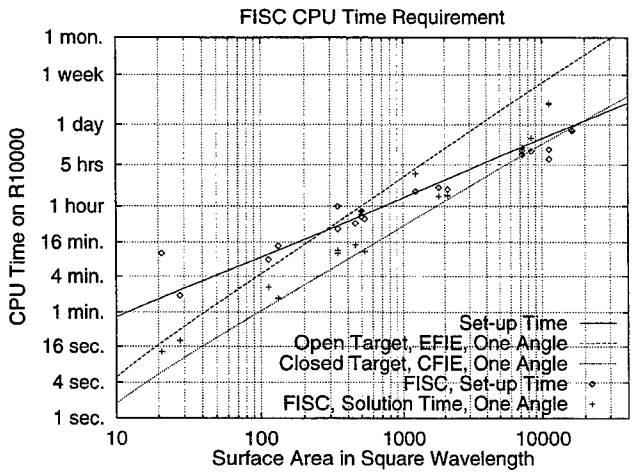

Figure 4. Estimated set-up time and solution time requirement as a function of surface area (lines) and the CPU time used running FISC (points).

A Fast Technique for Determining Electromagnetic and Acoustic Wave Behavior in Inhomogeneous Media

Michael A. Jensen
Department of Electrical and Computer Engineering
Brigham Young University
Provo, UT 84602
Tel: (801) 378-5736 Fax: (801) 378-6586

I. Introduction

Determining the behavior of electromagnetic and acoustic fields in inhomogeneous domains is a difficult yet important problem. Generally, a moment method solution of the volume integral equation is used [1] since the radiation condition is automatically satisfied and multiple excitations can be efficiently accommodated. The difficulty with this approach is the computational and storage requirements associated with the technique, which can become excessive when simulating electrically large structures.

This paper presents a technique, known as the Recursive Greens Function Method (RGFM), for efficiently solving the scalar wave equation in inhomogeneous domains. The technique is derived from a one-dimensional formulation which was originally applied to optical waveguide analysis [2] [3], and it is very similar to the Nested Equivalence Principle Algorithm (NEPAL) [4]–[5] and the nested dissection approach for finite element analysis [6]. The approach uses a recursive formulation to construct the domain Greens function from known Green's functions on subdomains. Surface integral solution techniques are then used to compute the fields interior or exterior to the inhomogeneous medium for any source configuration. If only exterior fields are required, the algorithm has asymptotic computational complexities of $O(N^{3/2})$ and $O(N^2)$ in two- and three-dimensions respectively and a storage requirement of $O(N)$.

The paper presents a brief derivation of the algorithm and discusses its efficient implementation. Results of its application to several configurations found in electromagnetic and acoustic analyses are then shown. Where possible, results are compared to exact solutions or to results obtained from a moment method (MOM) solution of the volume integral equation. These comparisons demonstrate the excellent computational resource utilization and accuracy of the method.

II. Green's function construction

The problem consists of an incident wave $\phi^{inc}(\mathbf{r})$ illuminating a finite-sized inhomogeneous region Ω^i embedded in an otherwise homogeneous space Ω^o, as implied in Figure 1. The boundary between the two regions is denoted as $\partial\Omega^i$. The field propagating in either region satisfies the general Helmholtz equation

$$\left\{\nabla \cdot \rho^{-1}(\mathbf{r})\nabla + \rho^{-1}(\mathbf{r})k^2(\mathbf{r})\right\}\phi^{\gamma}(\mathbf{r}) = 0 \tag{1}$$

where $\gamma = i, o$ for $\mathbf{r} \in \Omega^{i,o}$ and $k(\mathbf{r})$ is the spatially varying wavenumber. If $\mathbf{r} \in \Omega^o$, $k(\mathbf{r}) = k_o$, the homogeneous-space wavenumber. The term $\rho(\mathbf{r})$ is defined as

$$\rho(\mathbf{r}) = \begin{cases} 1 & \text{transverse magnetic (TM) fields} \\ \epsilon_r(\mathbf{r}) & \text{transverse electric (TE) fields} \\ m(\mathbf{r}) & \text{(mass density) for acoustic fields.} \end{cases} \tag{2}$$

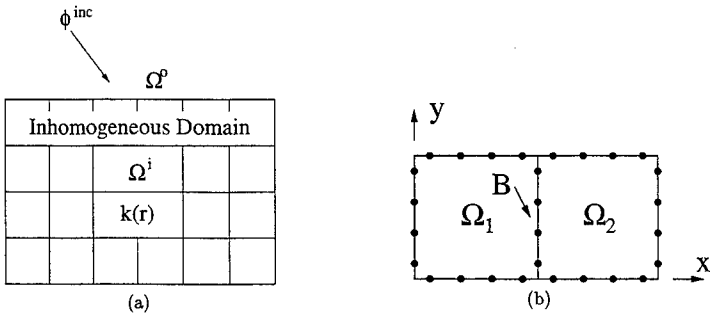

Figure 1: (a) Inhomogeneous domain Ω^i embedded in the otherwise homogeneous space Ω^o along with the divisions required for the RGFM. (b) Two adjacent sections to be combined into a single section using the RGFM.

Consider now the Green's function $G^\gamma(\mathbf{r},\mathbf{r}')$ which is a solution to the equation

$$\left\{\nabla\cdot\rho^{-1}(\mathbf{r})\nabla+\rho^{-1}(\mathbf{r})k^2(\mathbf{r})\right\}G^\gamma(\mathbf{r},\mathbf{r}')=-\delta(\mathbf{r}-\mathbf{r}') \tag{3}$$

where $\delta(\cdot)$ represents the Dirac delta function. Knowledge of G^γ allows construction of ϕ^γ using integral equation formulations [1]. However, for the inhomogeneous domain Ω^i, construction of this Green's function generally requires a costly solution of a volume integral equation. To avoid this problem, we first divide the domain Ω^i into N subdomains Ω_p, $1\le p\le N$, as implied in Figure 1(a). Within Ω_p, we assume that $k(\mathbf{r})=k_p$ and $\rho(\mathbf{r})=\rho_p$ remain constant so that the Greens function G_p on Ω_p can be constructed analytically. To simplify the algorithm formulation, we will assume that G_p satisfies homogeneous Neumann boundary conditions on $\partial\Omega_p$.

To begin, consider the situation depicted in Figure 1(b) where G_1 and G_2 are known on two adjacent domains Ω_1 and Ω_2 separated by the boundary $B=\Omega_1\cap\Omega_2$. Let G_{pq} be defined such that

$$G_{pq}(\mathbf{r},\mathbf{r}')=G^c(\mathbf{r},\mathbf{r}')\qquad \mathbf{r}\in\Omega_p,\mathbf{r}'\in\Omega_q \tag{4}$$

where $p,q\in[1,2]$ and where $G^c(\mathbf{r},\mathbf{r}')$ represents the Greens function for the combined region $\Omega=\Omega_1\cup\Omega_2$. First, we recognize that G_{pp} and G_p satisfy the same differential equation but satisfy different conditions at B. Therefore, their first argument dependence must differ only by a homogeneous solution of Eq. (3). Similarly, G_{pq}, $p\neq q$, must be a homogeneous solution of Eq. (3) in its first argument. These homogeneous solutions can be constructed from the subdomain Green's functions, resulting in the expressions

$$G_{pp}(\mathbf{r},\mathbf{r}') = G_p(\mathbf{r},\mathbf{r}')+\int_B d\mathbf{r}''G_p(\mathbf{r},\mathbf{r}'')A_{pp}(\mathbf{r}'',\mathbf{r}') \tag{5}$$

$$G_{pq}(\mathbf{r},\mathbf{r}') = \int_B d\mathbf{r}''G_p(\mathbf{r},\mathbf{r}'')A_{pq}(\mathbf{r}'',\mathbf{r}')\qquad p\neq q \tag{6}$$

where the A_{pq} represent unknown functions.

With these representations, we now enforce continuity of the normal derivatives of G_{pq} at the interface B. Using the forms in Eqs. (5) and (6) leads to

$$\lim_{\mathbf{r}_p\to\mathbf{r}_B}\int_B d\mathbf{r}''\frac{1}{\rho_p}\frac{\partial}{\partial n}G_p(\mathbf{r}_p,\mathbf{r}'')A_{pq}(\mathbf{r}'',\mathbf{r}')=\lim_{\mathbf{r}_q\to\mathbf{r}_B}\int_B d\mathbf{r}''\frac{1}{\rho_q}\frac{\partial}{\partial n}G_q(\mathbf{r}_q,\mathbf{r}'')A_{qq}(\mathbf{r}'',\mathbf{r}') \tag{7}$$

where $p \neq q$, $\mathbf{r}_B \in B$, and n represents the coordinate normal to B. Note that this expression has used the boundary condition $\partial G_q(\mathbf{r}_B, \mathbf{r}')/\partial n = 0$. Since the derivatives within the integrands involve the situation where the source point $\mathbf{r}''$ is on the interface as the observation point approaches B we must use the jump condition [7] in conjunction with the Neumann boundary condition. For the geometry in Figure 1(b), this condition provides the expression

$$\lim_{\mathbf{r}_p \to \mathbf{r}_B} \frac{1}{\rho_p} \frac{\partial}{\partial n} G_p(\mathbf{r}_p, \mathbf{r}'') = \pm \delta(y_B - y'') \delta(z_B - z'') \tag{8}$$

where + and − are used for $p = 1$ and 2 respectively. Substitution of these results into Eq. (7) results in $A_{pq}(\mathbf{r}_B, \mathbf{r}') = -A_{qq}(\mathbf{r}_B, \mathbf{r}')$ for $p \neq q$. Using this result in Eqs. (5) and (6) and enforcing the continuity of the G_{pq} across B leads to the expression

$$G_q(\mathbf{r}_B, \mathbf{r}') = -\int_B d\mathbf{r}'' \left[G_p(\mathbf{r}_B, \mathbf{r}'') + G_q(\mathbf{r}_B, \mathbf{r}'') \right] A_{qq}(\mathbf{r}'', \mathbf{r}'). \tag{9}$$

To solve Eq. (9) for A_{qq}, we project the $\mathbf{r}$ and $\mathbf{r}'$ dependence of G_p and G_q and the $\mathbf{r}'$ dependence of A_{qq} onto basis sets complete on either $\partial\Omega_p$ or $\partial\Omega_q$, and the $\mathbf{r}''$ dependence of A_{qq} onto a basis complete on B. For simplicity, we assume the basis functions are of compact support. With this representation, let $\mathbf{g}_p$ represent the matrix of coefficients for the series representing the function G_p, with $\overline{\mathbf{g}}_p$ representing the matrix of elements for which $\mathbf{r}, \mathbf{r}' \in B$ and $\hat{\mathbf{g}}_p$ representing the elements with $\mathbf{r} \in B$ and $\mathbf{r}' \in \partial\Omega_p$. Then solution of Eq. (9) results in

$$\mathbf{a}_{qq} = -(\overline{\mathbf{g}}_p + \overline{\mathbf{g}}_q)^{-1} \hat{\mathbf{g}}_q = -\mathbf{T}\hat{\mathbf{g}}_q. \tag{10}$$

Inserting $\mathbf{a}_{qq}$ into discrete forms of Eqs. (5) and (6) results in the matrix expressions

$$\mathbf{g}_{pp} = \mathbf{g}_p - \hat{\mathbf{g}}_p^t \mathbf{T} \hat{\mathbf{g}}_p \qquad \mathbf{g}_{pq} = \hat{\mathbf{g}}_p^t \mathbf{T} \hat{\mathbf{g}}_q \tag{11}$$

where t denotes a transpose.

This final result completely specifies G_{pq} and therefore G^c in terms of G_1 and G_2. Consider now that the entire domain in Figure 1(a) initially consists of N unit cells. Each pair of adjacent cells can be combined using the procedure outlined above to form $N/2$ new Green's functions. These new Greens matrices can be combined in pairs, and the procedure recursively repeats itself to form a single Greens matrix for the domain. Boundary fields can be obtained by MOM solution of a *surface* integral formulation. To obtain external fields only, then Green's function values where the source and observation points lie on the boundary must be computed, resulting in storage costs of $O(N)$ and computational requirements of $O(N^{3/2})$ and $O(N^2)$ for two- and three-dimensional domains, respectively. If internal fields are desired, then values for the observation point interior to the domain must also be generated and stored, resulting in computational complexities of $O(N^2)$ and $O(N^{7/3})$ and storage requirements of $O(N^{3/2})$ and $O(N^{4/3})$ for two- and three-dimensions, respectively.

III. Computational examples

A. Circular Cylinders

We first apply the RGFM to examine scattering from a circular cylinder with two layers in the radial direction ($\epsilon_r = 1.5$ for $\rho <= 0.2\lambda$ and $\epsilon_r = 3.0$ for $0.2\lambda \leq \rho \leq 0.4\lambda$), as indicated in the inset of Figure 2(a). The curves in Figure 2(a) compare the bistatic scattering width from the eigenfunction series solution with that obtained using the RGFM and volume MOM. For these latter two cases, the geometry is modeled using a 16×16 grid with a stair-stepped approximation to the cylindrical surfaces. For this geometry, the RGFM results agree favorably, although there is some error in the forward- and

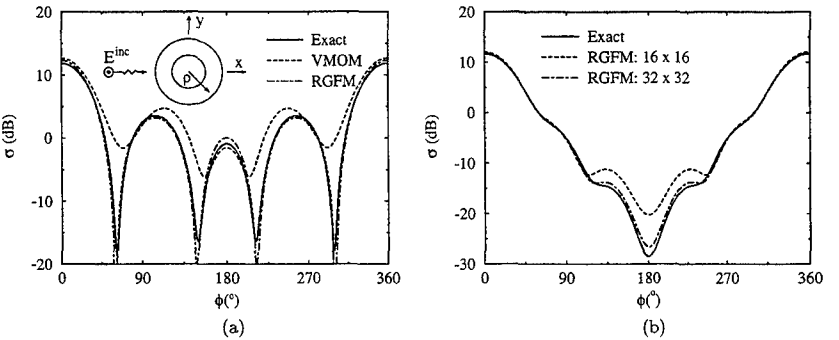

Figure 2: (a) Bistatic scattering width (TM case) for a two-layer circular cylinder with $\epsilon_r = 1.5$ for $\rho \leq 0.2\lambda$ and $\epsilon_r = 3.0$ for $0.2\lambda \leq \rho \leq 0.4\lambda$. (b) Bistatic scattering width (TE case) for the two-layer circular cylinder studied in Figure 2(a).

back-scattered directions which is likely due to the stair-step discretization of the surface. The error in the results from the volume MOM indicate that this method has more difficulty in accurately representing the field behavior for this structure.

Figure 2(b) illustrates the scattering from the same two-layer circular cylinder for a TE incident field. In this case, the RGFM results for two different grid sizes – 16×16 and 32×32 – are compared to those generated with the exact eigenfunction solution. Because the back-scattered fields are very weak for this case, a higher grid resolution is required in order to obtain high accuracy in this region. However, with this increased grid resolution, the RGFM results agree very well with the exact solution.

To investigate the RGFM effectiveness in computing fields internal to the structure, we apply it to the case of a simple homogeneous cylinder of radius $a = 0.8\lambda$ and permittivity $\epsilon_r = 3.0$. For the case of a $+x$-traveling incident TM plane wave, the fields computed using the exact series solution and the RGFM are plotted in Figures 3(a) and (b), respectively. As can be seen, the two results are in excellent agreement. This example serves the illustrate the RGFM accuracy in computing internal fields, a result which proves useful in many studies including inverse scattering and biomedical applications.

B. Synthetic Seismograms

The RGFM can also be used to compute seismograms for acoustic pulse scattering. Consider the geometry shown in Figure 4, which depicts a square inclusion embedded in an otherwise homogeneous medium. Two different cases are considered: 1) all four regions in Figure 4 are identical, and 2) the four regions have different material properties, as indicated in the figure caption. In this case, the surrounding medium has a velocity of 2 km/s and a density of 2000 kg/m^3. A line source excitation emits a pulse whose shape is given by

$$s(t) = -\frac{(t - t_o)}{2\sigma^2} \exp\left[-\frac{(t - t_o)^2}{2\sigma^2}\right] \tag{12}$$

where $\sigma = 2.5$ ms and $t_o = 4\sigma$. This pulse contains no zero frequency components, has a bandwidth of approximately 256 Hz, and possesses a dominant frequency of 68 Hz (29 m dominant wavelength). 64 receivers are used to record the scattered signal. Figures 5(a) and (b) illustrate the synthetic seismograms for each of the two cases described. As can be seen, the seismograms for the two inclusions are similar,

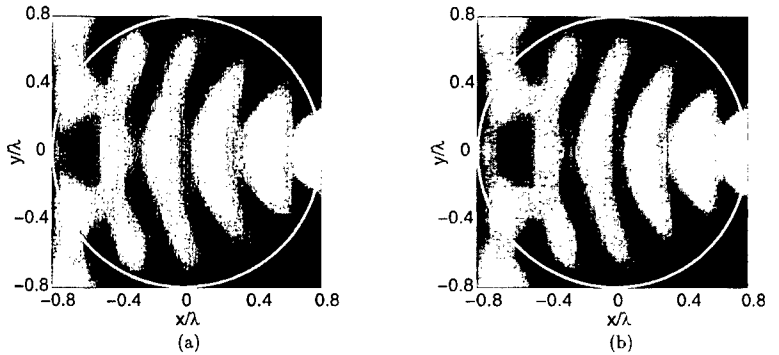

Figure 3: Internal (and near) fields for a homogeneous circular cylinder of radius $a = 0.8\lambda$ and permittivity $\epsilon_r = 3$ computed using (a) the eigenfunction series solution and (b) the RGFM.

although the inhomogeneous domain results in a noticeably stronger late-time return due to the strong reflection from the last interface.

IV. Conclusions

We have presented a novel numerical technique for analysis of the electromagnetic behavior of inhomogeneous dielectric domains. The methodology allows efficient construction of the Green's function for the domain which can subsequently be used in surface integral formulations for the fields. Numerical results show that the RGFM faithfully constructs the Green's function for inhomogeneous domains and provides highly accurate results for scattering from various cylindrical structures.

References

[1] W. C. Chew, *Waves and Fields in Inhomogeneous Media*, Van Nostrand Reinhold, New York, 1990.

[2] K. B. Kahen, "Analysis of distributed-feedback lasers using a recursive Green's functional approach", *IEEE J. of Quantum Electron.*, vol. 29, no. 2, pp. 368–373, Feb. 1993.

[3] J. D. Freeze, M. A. Jensen, and R. H. Selfridge, "A unified Green's function analysis of complicated DFB lasers", *IEEE J. Quantum Electron.*, vol. 33, pp. 1253–1259, Aug. 1997.

[4] W. C. Chew and C.C. Lu, "The use of Huygens' equivalence principle for solving the volume integral equation of scattering", *IEEE Trans. Antennas Propag.*, vol. 41, pp. 897–904, Jul. 1993.

[5] C. C. Lu and W. C. Chew, "The use of Huygens' equivalence principle for solving 3-D volume integral equation of scattering", *IEEE Trans. Antennas Propag.*, vol. 43, pp. 500–507, May 1995.

[6] A. George, "Nested dissection of a regular finite element mesh", *SIAM J. Numer. Anal.*, vol. 10, pp. 345–363, Apr. 1973.

[7] J. Mathews and R. L. Walker, *Mathematical Methods of Physics*, pp. 272–273, Benjamin, New York, 1970.

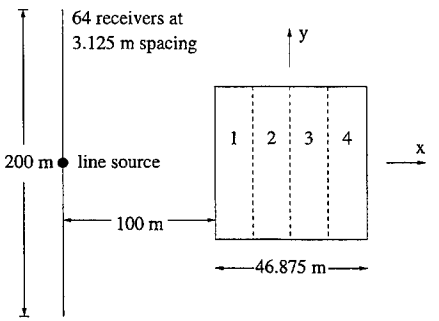

Figure 4: Geometry for computing synthetic seismograms using the RGFM. In the first case, regions 1–4 are identical, with $c = 2.8$ km/s and $\rho = 2800$ kg/m^3. In the second case, the regions have parameters $c_1 = 2$ km/s, $\rho_1 = 3200$ kg/m^3, $c_2 = 2.3$ km/s, $\rho_2 = 2800$ kg/m^3, $c_3 = 2.8$ km/s, $\rho_3 = 2400$ kg/m^3, $c_4 = 6.3$ km/s, $\rho_4 = 2000$ kg/m^3. The surrounding medium has parameters $c_s = 2$ km/s and $\rho_s = 2000$ kg/m^3.

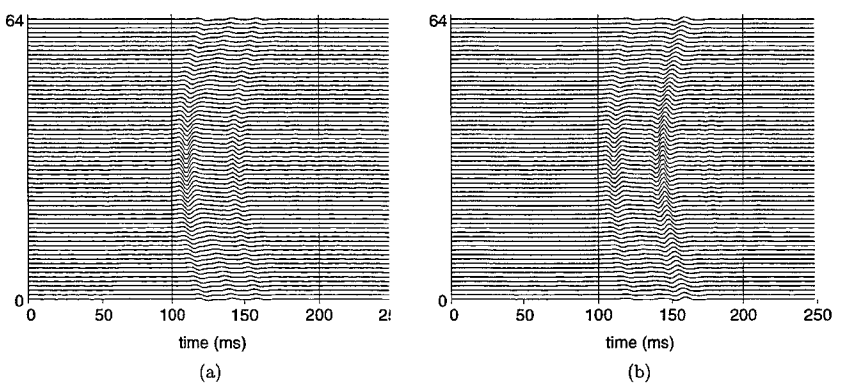

Figure 5: Synthetic seismograms for the square inclusion shown in Figure 4 for the two cases described.

Rapid Analysis of Perfectly Conducting and Penetrable Quasi-Planar Structures with the Steepest Descent Fast Multipole Method

Vikram Jandhyala, Eric Michielssen,
Balasubramaniam Shanker, and Weng C Chew
Center for Computational Electromagnetics
Dept. of Electrical and Computer Engineering
1406 West Green St.
University of Illinois at Urbana-Champaign
Urbana Il 61801
Email: vikram@decwa.ece.uiuc.edu

Abstract

The applicability of the steepest descent fast multipole method (SDFMM) to the analysis of scattering and radiation from a large class of quasi-planar structures, including rough surfaces, gratings, and microstrip antennas, is demonstrated in this paper. The SDFMM was first devised for the fast solution of scattering from perfectly conducting rough surfaces. Here, the technique is extended and applied to the analysis of scattering and radiation from arbitrarily shaped, multi-region penetrable and perfectly conducting quasi-planar structures. This technique promises to open the door to accurate full-wave electromagnetic analysis of much larger and more complex problems than is possible with prevailing techniques.

1 Introduction

The analysis of electromagnetic scattering and radiation by perfectly conducting and penetrable quasi-planar structures is a topic of fervent current interest. The study of rough surface scattering has applications in remote sensing, long-range communications, and surface physics. Simulation of gratings is necessitated in the design of diffractive optical elements and quantum well infrared photodetectors. The prediction of radiation and scattering from microwave circuits and multilayered patch antennas is essential in the design of communication systems. The analysis of electromagnetic phenomena involving large-scale quasi-planar structures requires efficient and accurate numerical techniques. The most popular approach for analyzing scattering and radiation from such structures relies on integral equation formulations and method of moments (MoM) based solution techniques, although finite difference time domain and finite element methods are also employed. Unlike the latter two techniques which require discretization of the entire volume of the structure under study, surface integral equation techniques utilize basis functions only on interfaces between homogeneous regions, thereby reducing the number of unknowns.

The application of the MoM to solve surface integral equations leads to a matrix equation involving a dense matrix. For large problems, solution of the MoM equations using direct inversion is impractical due to the large CPU time and memory requirements associated with this procedure. The iterative solution of the MoM system is also a time consuming process, with both the number of operations per iteration and the memory cost associated with storing the matrix scaling as $O(N^2)$, where N is the dimension of the system. To expedite the iterative solution of electromagnetic scattering problems, researchers have exploited the underlying structure of the Green's function kernel and have developed techniques that facilitate the fast computation of MoM matrix-vector products.

We have recently reported on the development of the steepest descent-fast multipole method (SDFMM) [1] for the analysis of scattering from perfectly conducting rough surfaces. The SDFMM, a numerically rigorous technique, exploits the quasi-planarity of rough surfaces, to reduce the computational costs per iteration and memory requirements to $O(N)$. In this paper, the SDFMM is extended to the more general and complex problem of scattering and radiation by arbitrarily shaped quasi-planar structures comprised of multiple homogeneous regions with penetrable or perfectly conducting interfaces.

A combined field integral equation (CFIE) formulation [2] is utilized, and terms arising in an MoM matrix-vector product are cast in the form of discrete inhomogeneous plane-wave expansions arising from the representation of the pertinent Green's function along steepest descent paths and from the use of the FMM. As opposed to the electric current-based formulation for analyzing perfectly conducting surfaces reported earlier in Ref.[1], both electric and magnetic surface currents need to be incorporated into the multilevel formulation, and independent fast multipole

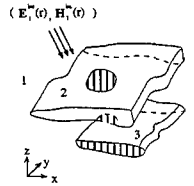

Figure 1: A multi-region quasi-planar structure excited from free-space. Two other homogeneous regions are shown. Interfaces are either penetrable or perfectly conducting (striped). The structure is quasi-planar, i.e., its lateral x-y dimensions are much larger than its extent in the z- direction.

and steepest descent representations are required for each region. Furthermore, identification of independent basis functions and enforcement of appropriate boundary conditions are incorporated through another matrix transformation. The SDFMM permits the solution of scattering and radiation from extremely large and complex structures within realistic times. These include large microstrip patch arrays with finite substrates and ground planes modeled using 90,000 or more MoM basis functions, and dielectric rough surfaces modeled using as many as 190,000 MoM basis functions.

2 Integral Equation Formulation for Scattering by Penetrable and Perfectly Conducting Quasi-Planar Structures

To formulate integral equations for analyzing scattering and radiation from multi-region penetrable or PEC structures, we follow the approach outlined in Ref.[2]. Throughout this paper, a temporal dependency of $e^{-i\omega t}$ is assumed and suppressed. A finite multi-region quasi-planar structure is shown in Fig. 1. For the purpose of illustration, three homogeneous regions are shown, with region 1 being free-space. The formulation and implementation permit an arbitrary number of regions R_T. The interface between any two regions can be a penetrable boundary, a perfectly conducting boundary, or a segmented combination. In general, incident electric and magnetic fields $\mathbf{E}_q^{inc}(\mathbf{r})$ and $\mathbf{H}_q^{inc}(\mathbf{r})$ excite the structure from region q, and equivalent electric and magnetic surface currents $\mathbf{J}_q(\mathbf{r})$ and $\mathbf{M}_q(\mathbf{r})$ are impressed on the surfaces bounding each region q, $q = 1, .., R_T$. In what follows, ϵ_q and μ_q represent the permittivity and permeability, respectively, of region q. Also, $k_q = \omega\sqrt{\epsilon_q\,\mu_q}$, and $\eta_q = \sqrt{\frac{\mu_q}{\epsilon_q}}$. The scattered fields produced in each region can then be written as:

$$\mathbf{E}_q^{scat}(\mathbf{r}) = L_q\mathbf{J}_q(\mathbf{r}) - K_q\mathbf{M}_q(\mathbf{r}) \tag{1a}$$

$$\mathbf{H}_q^{scat}(\mathbf{r}) = K_q\mathbf{J}_q(\mathbf{r}) + \frac{1}{\eta_q^2}L_q\mathbf{M}_q(\mathbf{r}) \tag{1b}$$

where the operators L_q and K_q are defined by

$$L_q\mathbf{X}(\mathbf{r}) = \int_{S_q} ds' \left(-i\omega\mu_q\ \mathbf{X}(\mathbf{r}') + \frac{-i}{\omega\epsilon_q}\ \nabla\nabla'\cdot\mathbf{X}(\mathbf{r}')\right)\ g_q(\mathbf{r},\mathbf{r}'), \tag{1c}$$

$$K_q\mathbf{X}(\mathbf{r}) = \int_{S_q} ds'\mathbf{X}(\mathbf{r}')\times\nabla g_q(\mathbf{r},\mathbf{r}'), \tag{1d}$$

and $g_q(\mathbf{r},\mathbf{r}')$ is the scalar Green's function

$$g_q(\mathbf{r},\mathbf{r}') = \frac{e^{ik_q|\mathbf{r}-\mathbf{r}'|}}{4\pi|\mathbf{r}-\mathbf{r}'|}\,. \tag{1e}$$

The overall CFIE can be obtained by enforcing constraints on the fields and currents. Specifically, one equates tangential components of total electric and magnetic fields across a penetrable interface, and enforces zero total electric field on a perfectly electrically conducting (PEC) boundary. An independent set of currents is obtained by introducing the constraints that equivalent currents are equal and opposite across a penetrable interface, and that magnetic current is zero on a PEC surface. The enforcement of these constraints will be discussed in the next section.

The solution of the constrained CFIE yields the electric and magnetic surface current densities $\mathbf{J}_q(\mathbf{r})$ and $\mathbf{M}_q(\mathbf{r})$. Once the current densities have been obtained, radar cross sections (RCSs) can be computed.

3 The Steepest Descent–Fast Multipole Method

To solve the constraint-imposed version of (Eqn.(1)), the unknown current densities $\mathbf{J}_q(\mathbf{r})$ and $\mathbf{M}_q(\mathbf{r})$ are approximated in terms of linear combinations of a set of basis functions $\mathbf{j}_{q,n}, n = 1, ..., N_q$ as

$$\mathbf{J}_q(\mathbf{r}) \cong \sum_{n=1}^{N_q} I_{q,n}^1 \, \mathbf{j}_{q,n}(\mathbf{r}) \ , \tag{2a}$$

$$\mathbf{M}_q(\mathbf{r}) \cong \sum_{n=1}^{N_q} I_{q,n}^2 \, \mathbf{j}_{q,n}(\mathbf{r}) \ . \tag{2b}$$

The total number of possible basis functions N equals $2\sum_{q=1}^{R_T} N_q$. Let the number of independent basis functions be N_{ind}. Substituting the expansions into the CFIE, testing the equations with functions $\mathbf{f}_{q,m}, m = 1, ..., N_q$, and introducing the constraints, we arrive at the following full-rank matrix equation [2]

$$\bar{\mathbf{A}}\bar{\mathbf{Z}}\bar{\mathbf{A}}^T\mathbf{I}_{ind} = \bar{\mathbf{A}}\mathbf{V} \ . \tag{3}$$

The Rao-Wilton-Glisson (RWG) basis is chosen for both $\mathbf{j}_{q,n}$ and $\mathbf{f}_{q,m}$. Here, the MoM matrix $\bar{\mathbf{Z}}$ possesses dimensions of $N \times N$ and has the form

$$\bar{\mathbf{Z}} = \begin{bmatrix} \bar{\mathbf{L}}_1 & -\bar{\mathbf{K}}_1 & \mathbf{0} & \mathbf{0} & \dots \\ \bar{\mathbf{K}}_1 & \frac{\epsilon_1}{\mu_1}\bar{\mathbf{L}}_1 & \mathbf{0} & \mathbf{0} & \dots \\ \mathbf{0} & \mathbf{0} & \bar{\mathbf{L}}_2 & -\bar{\mathbf{K}}_2 & \dots \\ \mathbf{0} & \mathbf{0} & \bar{\mathbf{K}}_2 & \frac{\epsilon_2}{\mu_2}\bar{\mathbf{L}}_2 & \dots \\ \dots & \dots & \dots & \dots & \dots \end{bmatrix} , \tag{4a}$$

with the entries of the submatrices given by

$$\bar{\mathbf{L}}_q(m,n) = \langle \mathbf{f}_{q,m}, L_q \mathbf{j}_{q,n} \rangle \ , 1 \le m, n \le N_q, \tag{4b}$$

$$\bar{\mathbf{K}}_q(m,n) = \langle \mathbf{f}_{q,m}, K_q \mathbf{j}_{q,n} \rangle \ , \ 1 \le m, n \le N_q \ . \tag{4c}$$

Also, a vector of coefficients $\mathbf{I}$ of length N is defined by

$$\mathbf{I} = \begin{bmatrix} \mathbf{I}_1^1 \\ \mathbf{I}_1^2 \\ \mathbf{I}_2^1 \\ \mathbf{I}_2^2 \\ \cdot \\ \cdot \end{bmatrix} , \tag{5}$$

with the vector of independent coefficients $\mathbf{I}_{ind}$, of length N_{ind}, related to $\mathbf{I}$ as

$$\mathbf{I} = \bar{\mathbf{A}}^T\mathbf{I}_{ind} \ . \tag{6}$$

The excitation vector $\mathbf{V}$ of length N is given by

$$\mathbf{V} = \begin{bmatrix} \mathbf{V}_1^E \\ \mathbf{V}_1^H \\ \mathbf{V}_2^E \\ \mathbf{V}_2^H \\ \cdot \\ \cdot \end{bmatrix} , \tag{7a}$$

where

$$V_q^E = \langle \mathbf{f}_{q,m}, \mathbf{E}_q^{inc}(\mathbf{r}) \rangle \ , 1 \leq m \leq N_q \ , \tag{7b}$$

$$V_q^H = \langle \mathbf{f}_{q,m}, \mathbf{H}_q^{inc}(\mathbf{r}) \rangle \ , 1 \leq m \leq N_q . \tag{7c}$$

In the special case where the incident field is purely in region 1 (free-space), only the first two subvectors if $\mathbf{V}$ are non-zero. The rectangular matrix $\bar{\mathbf{A}}$ of dimensions $N_{ind} \times N$ is a sparse matrix that is used to enforce boundary conditions on fields, and relate dependent variables to dependent ones, as in [2,3].

An iterative solution of Eqn.(3) is expensive, since both the CPU time per iteration and the memory scale as $O(N^2)$. For large scale problems, one needs to develop efficient fast algorithms to alleviate the computational burden. To this end, the SDFMM is introduced, based on our earlier work on electric field integral equations for perfectly conducting surfaces [1]. The key differences between the penetrable surface problem considered here and our previous work are that (i) both electric and magnetic currents feature in the equations, (ii) both electric and magnetic fields need to be evaluated in a multilevel manner, and (iii) each homogeneous region requires a different Green's function and therefore has to be treated separately.

In a single level implementation of the multi-region SDFMM, the quasi-planar structure is embedded in a block, which is then subdivided into smaller blocks in the x- and y- directions. A matrix element is classified as a near-field element if the corresponding basis and testing functions reside in blocks which are separated by less than a pre-specified number of blocks. All other elements are termed far-field elements. This classification is used to formally decompose the impedance matrix $\bar{\mathbf{Z}}$ as

$$\bar{\mathbf{Z}} = \bar{\mathbf{Z}}' + \bar{\mathbf{Z}}'' \tag{8}$$

where $\bar{\mathbf{Z}}'$ and $\bar{\mathbf{Z}}''$ contain near- and far-field interactions, respectively.

In the SDFMM, the action of $\bar{\mathbf{Z}}'$ on a vector is computed classically. However, the product of $\bar{\mathbf{Z}}''$ with a vector is computed indirectly and rapidly, without ever generating the matrix. This procedure is briefly summarized here. The three-dimensional dynamic scalar Green's function $g_q(\mathbf{r},\mathbf{r}')$ is first expressed in a contour integral form, using the Sommerfeld identity. This integral can be evaluated efficiently through a steepest descent path integration. Moreover, a Hankel function appearing in the integrand is expanded in the spectral domain using the addition theorem. This overall steepest-descent fast multipole expansion can be used to efficiently represent terms arising in the product of $\bar{\mathbf{Z}}''$ with a trial vector in the following manner [4]

$$\begin{aligned} \langle \mathbf{f}_{q,m}, L_q \, \mathbf{j}_{q,n} \rangle \ = \ & \frac{i}{16\pi^2} \sum_{j=1}^{n_{sd,q}} \sum_{j'=1}^{P_q} w_{jq}^{sd} w_{j'q}^{fmm} \ k_{pq}^{(j)} \int_S d\mathbf{r} \ \mathbf{f}_{q,m} e^{i\mathbf{k}_q^{(j)} \cdot (\mathbf{r} - \mathbf{r}_t)} \\ & \mathcal{T}_{jj'q}(\mathbf{r}_t - \mathbf{r}_s) \ \left(\bar{\mathbf{I}} - \frac{\mathbf{k}_q^{(j)} \mathbf{k}_q^{(j)}}{k_q^2} \right) \int_S d\mathbf{r}' \ \mathbf{j}_{q,n} e^{i\mathbf{k}_q^{(j)} \cdot (\mathbf{r}_s - \mathbf{r}')} \ , \end{aligned} \tag{9}$$

and

$$\begin{aligned} \langle \mathbf{f}_{q,m}, K_q \, \mathbf{j}_{q,n} \rangle \ = \ & -\frac{1}{16\pi^2} \sum_{j=1}^{n_{sd,q}} \sum_{j'=1}^{P_q} w_{jq}^{sd} w_{j'q}^{fmm} \ k_{pq}^{(j)} \int_S d\mathbf{r} \ (\mathbf{f}_{q,m} \times \mathbf{k}_q^{(j)}) e^{i\mathbf{k}_q^{(j)} \cdot (\mathbf{r} - \mathbf{r}_t)} \\ & \mathcal{T}_{jj'q}(\mathbf{r}_t - \mathbf{r}_s) \int_S d\mathbf{r}' \ \mathbf{j}_{q,n} e^{i\mathbf{k}_q^{(j)} \cdot (\mathbf{r}_s - \mathbf{r}')} \ . \end{aligned} \tag{10}$$

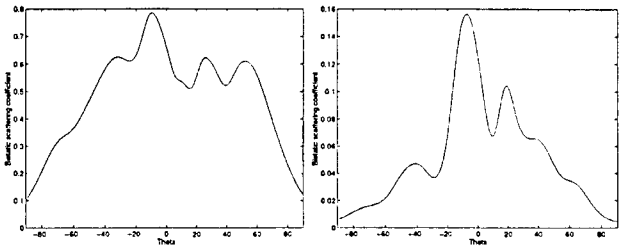

Figure 2: (a): Co-polarized scattering coefficient. (b) : Cross-polarized scattering coefficient.

Here, $k_q^{(j)}$ are complex wavenumbers,and $n_{s\delta,q}$ and $w_j^{s\delta,q}$ are the number of points and integration weights associated with integration along the steepest descent path of the Sommerfeld integral representation of the free-space Green's function [1]. Source and testing block centers are denoted by $\mathbf{r}_s$ and $\mathbf{r}_t$, respectively. The translation operator $\mathcal{T}_{jj'q}(\mathbf{r}_t - \mathbf{r}_s)$, integration weights $w_{j,q}^{fmm}$, and number of harmonics P_q are analogous to those defined in well-known fast multipole algorithms. While computing a matrix-vector product, source and observation terms can be grouped independently (through their plane-wave spectra) rather than by individually combining the effect of single source-observer interactions. Furthermore, plane-wave spectrum information at different levels is recycled, as in standard FMMs. These steps result in substantial CPU time and memory savings.

In a multilevel SDFMM, the rough surface is recursively divided into blocks, by hierarchically partitioning a block (the *parent*) at a coarse level into four blocks (the *children*) at a finer level. Plane-wave expansions are shifted to centers of parent blocks, and incoming spectra are shifted to centers of child blocks. Such an operation is termed an FMM tree traversal. Distinct translation operators and steepest descent rules are utilized at each FMM level. For an R_T region problem, R_T separate FMM trees and tree-traversals are necessitated. Moreover, it can be shown that the effect of both the electric and the magnetic surface currents in a particular region can be accounted for through a single tree formation and traversal. Also, magnetic fields at the observer locations are obtained through transforming each plane-wave component of the computed electric field. Earlier, we have rigorously shown that the computational complexity and memory requirements of the SDFMM when applied to the analysis of scattering from perfectly conducting rough surfaces are $O(N)$ [1]. This proof can easily be extended to the present problem. In effect, the SDP integral representation of the Sommerfeld integral reduces the original three- dimensional problem to a quasi-two-dimensional volumetric one, with the ensuing improvement in computational complexity.

4 Simulation Results

In this section, several numerical results are presented which demonstrate the efficacy of the SDFMM in analyzing scattering and radiation from penetrable and PEC quasi-planar structures. The computing platform used is a single R8000 processor on an SGI Power Challenge, with 2 Gbytes of RAM and an average in-program throughput of 60 MFlops. A TFQMR iterative solver is used with both the SDFMM and the MoM.

The first example involves a Monte-Carlo simulation over an ensemble of 50 PEC rough surfaces, and illustrates the utility of the SDFMM in solving multiple moderately sized problems rapidly. Each Gaussian surface is of size $5.9\lambda \times 5.9\lambda$ with λ being the free-space wavelength, has a root mean square height of 0.5λ and a correlation length of 1.5λ. The number of MOM unknowns associated with each problem is $N_{ind} = 10,325$. The overall solution for all 50 problems using the SDFMM requires 52 CPU hours. Figure 2 depicts the non-coherent portion of the bistatic scattering coefficient, for a Gaussian beam incident at an angle $\theta = -10°$. The phenomenon of backscattering enhancement associated with rough surfaces is clearly observable in both the co- and cross-polarized scattering coefficients.

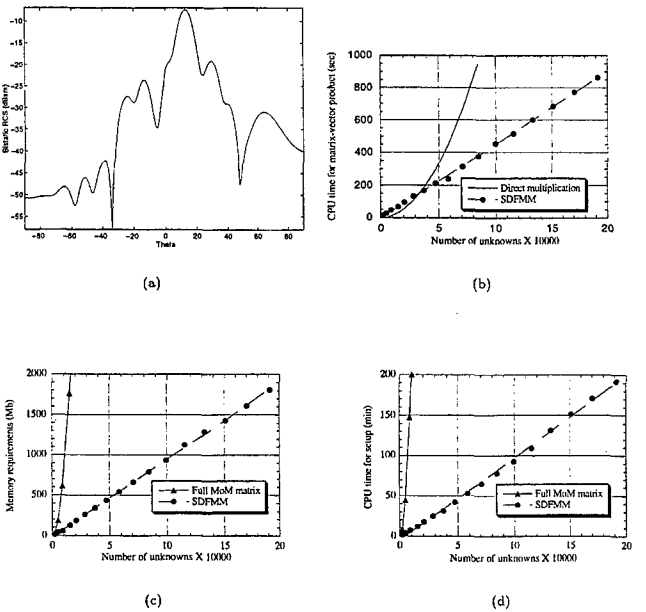

Figure 3: (a): Copolarized bistatic RCS. (b): CPU time for a matrix-vector product. (c): Memory requirements. (d): Setup time.

Scattering from dielectric rough surfaces is studied in the next example. Here, a very large rough surface, possessing an area of $162\lambda^2$, a root mean square height of 0.4λ, and a correlation length of 1.5λ is analyzed using the SDFMM. The number of MoM basis functions is $N_{ind} = 151,046$. The surface is an interface between free-space and a homogeneous region with $\epsilon_r = 2$. A Gaussian beam is incident from the free-space side at an angle of $\theta = -10°$. The bistatic RCS, including a specular peak, is shown in Fig. 3(a). The CPU time and memory requirements of the SDFMM are examined by applying it to progressively larger dielectric rough surface problems. The rough surfaces have the same statistics and material as the above example. Fig. 3(b) depicts the CPU time required for a matrix-vector product. The CPU time required for direct matrix-vector multiplication, in a standard iterative solution of an MoM system of equations, scales as $O(N^2)$. The SDFMM, on the other hand, requires CPU time proportional only to $O(N)$. A standard iterative MoM solution entails storage of the entire MoM matrix. This leads to prohibitively large $O(N^2)$ memory requirements, as can be seen from Fig. 3(c). With 2 Gbytes of memory, the largest solvable problem would have approximately $N_{ind} = 16,000$ unknowns. The SDFMM has far more economical memory requirements, scaling as $O(N)$. A problem involving $N_{ind} = 191,000$ unknowns was accomodated in 1.8 Gbytes of memory.

The overall CPU time required to solve the integral equation consists of two dominant portions. One is proportional to the product of the cost of a matrix-vector and the number of iterative steps required. The second is the initial setup time, which in the case of a standard MoM is the matrix-fill time, while for the SDFMM, it is the matrix-fill time for the near-field part $\tilde{\mathbf{Z}}'$ and the inhomogeneous plane-wave projection generation time for the far-

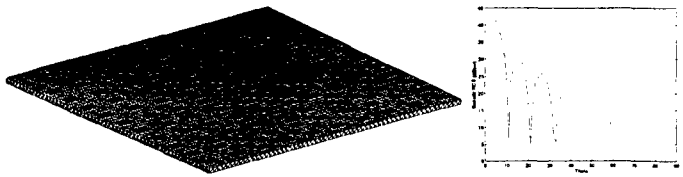

(a) (b)

Figure 4: (a) 10×10 microstrip array with a finite substrate and ground plane. (b) Bistatic RCS ($\theta\theta$) for a normally incident plane wave.

field portion. As shown in Fig. 3(d), the setup time rises extremely steeply, with an $O(N^2)$ growth for the standard MoM, and is as high as 200 minutes for a moderately sized 10,000 unknown problem. The SDFMM has a far more gradual $O(N)$ growth. The speedup and memory savings become dramatic as the problem size increases; for an $N_{ind} = 191,530$ unknown case, a standard iterative MoM solution would entail practically impossible CPU time requirements of 80 minutes per matrix-vector product, 1,200 hours for matrix fill, and would require 325 Gbytes of memory. The SDFMM correspondingly needs only approximately 14 minutes for a matrix-vector product, 3 hours for setup, and 2 Gbytes of memory.

Finally, we apply the multi-region SDFMM to analyze scattering from a large microstrip patch array (Fig. 4(a)). The overall dimensions of the finite substrate ($\epsilon_r = 2.17$) are $6.1\lambda \times 6.1\lambda \times 0.05\lambda$. The 10×10 microstrip array, the substrate, and the finite ground plane below the substrate are modeled using a total of $N = 92,280$ MoM basis functions, with $N_{ind} = 41,952$. The bistatic RCS for a normally incident plane wave is depicted in Fig. 4(b)).

5 Conclusions

A new multilevel algorithm, the SDFMM, has been shown to permit the rapid analysis of scattering and radiation from multi-region penetrable and PEC quasi-planar structures with $O(N)$ time and memory requirements. Due to the dramatic speedup and memory savings possible, it is expected that the SDFMM will become a useful tool in a variety of applications, including microwave circuit and optical component design, rough surface analysis, and the analysis of rough surfaces and infrared detectors.

References

[1] V. Jandhyala, E. Michielssen, B. Shanker, and W. Chew. "A combined steepest descent –fast multipole algorithm for the fast analysis of three-dimensional scattering by rough surfaces." Tech. Rep. CCEM-3-97, Center for Computational Electromagnetics, University of Illinois, Urbana, March 1997.

[2] L. Medgyesi-Mitschang, J. Putnam, and M. Gedera, "Generalized method of moments for three-dimensional penetrable scatterers," *J. Opt. Soc. Am. A*, vol. 12, pp. 1383–1398, April 1994.

[3] E. Yip and B. Dembart, "Matrix assembly in fmm-mom codes," Tech. Rep ISSTECH-97-002, The Boeing Company, Seattle, WA, January 1997.

[4] V. Jandhyala, B. Shanker, E. Michielssen, and W. Chew, "A fast algorithm for the analysis of scattering by dielectric rough surfaces," Tech. Rep. CCEM-17-97, Center for Computational Electromagnetics, University of Illinois, Urbana, July 1997.

Iterative Solution Strategies in Adaptive Integral Method (AIM)

E. Bleszynski[+], M. Bleszynski[++], and T. Jaroszewicz[+++]
[+]Boeing Space, Information and Defense Group, Seal Beach, CA 90740-7644
[++] Rockwell Science Center, P.O. Box 1085, Thousand Oaks, CA 91360
[+++] Monopole Research, 2725 Glendon Ave, Los Angeles, CA 90064

Abstract

We describe some aspects of an iterative solution strategy implemented in the AIM solver, which reduces memory and disk space requirements.

1. Introduction

With the advent of fast algorithms for solving Maxwell's equations in the integral form, the issue of establishing effective multiple right hand sides (m.r.h.s.s.) iterative procedures is becoming increasingly important. The most frequently used iterative methods, the minimum-residual (MINRES) algorithms, create a set of Krylov subspaces, over which residual norms are minimized simultaneously for a number of r.h.s.s. For problems of tens or hundreds thousands of unknowns and many r.h.s.s the resulting high dimensions of Krylov subspaces may lead to prohibitively high memory requirements.

Although the total computational time is minimal when the entire Krylov subspace is stored in memory ("long sequence" iterative strategies), we may be forced, when the resources are limited, to trade the storage space for the computation time. In this case it is necessary to develop an approach which would allow to restart iterations with a possibly small loss of the computation time. We refer to such methods as "short sequence" iterative strategies. We describe here such a solution strategy currently implemented in the AIM solver [1].

2. Choice of minimum number of right-hand sides and Nyquist theorem

While in the "long sequence" iterative method implemented in AIM we are essentially free to choose any set of r.h.s.s, that choice becomes essential for a satisfactory performance of the "short sequence" algorithm. In this case it is advantageous to reduce the number of r.h.s.s to the mimimum set necessary to reconstruct all the solutions in the required

angular range. We discuss now how to determine a "minimal" vector basis in the solution space such that all other solutions in the considered angular span can be expressed, with the desired accuracy, as linear combinations of the basis solutions.

We start with the observation that, for sufficiently smooth objects, solutions (i.e., currents on the object surface) are of finite bandwidth: they do not oscillate more rapidly than the incident wave. Under such circumstances, the solution on the object of size L can be represented by its values at $N_{\mathrm{Nyq}} \sim 2L/\lambda$ discrete points with the spacing $\lambda/2$ in the direction of the oscillations (the Nyquist theorem). Equivalently, the solution can be represented by its discrete Fourier transforms, in which the wave number spacing is $\Delta q \sim 2\pi/L$ and the maximum wave number value $q_{\max} \sim (L/\lambda)\,\Delta q = 2\pi/\lambda \equiv k$, is equal to the incident wave number k. Now, a solution induced by a wave incident at an angle α (Fig. 1) displays, in the direction of L, an oscillatory pattern corresponding to the wave number $q = k \sin\alpha$. Hence, the resolution $\Delta q \sim 2\pi/L$ in the wave number corresponds to the angular resolution $\Delta\alpha \sim \Delta q/k$, i.e.,

$$(\Delta\alpha)_{\mathrm{Nyq}} \sim \lambda/L \; . \tag{1}$$

We refer to this quantity as the "Nyquist angular spacing". The arguments just given suggest that in order to obtain a minimal set of solutions it is necessary to choose a set of incident waves with the Nyquist angular spacing.

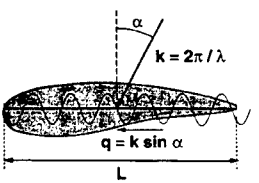

Fig. 1: A schematic representation of a solution with the wave number q induced by an incident wave of the wave number k.

To make the above reasoning more quantitative, we consider a system of N linear equations for s right hand sides

$$A\,x_p = b_p \; , \qquad p = 1, \ldots, s \; , \tag{2}$$

with a complex $N \times N$ matrix A and complex N-component vectors x_p and b_p.

We assume that the right-hand sides b_p represent incident plane waves with wave vectors in a certain angular range Ω. We further denote by $\mathcal{X}$ the space spanned by the full set of s solutions, $\mathcal{X} = \text{span}(x_1, x_2, \ldots, x_s)$, and by $\mathcal{X}_n$ the space spanned by a certain n-element ($n \leq s$) subset of solutions, $\mathcal{X}_n = \text{span}(x_{i_1}, x_{i_2}, \ldots, x_{i_n})$, such that the set of vectors $x_p \in \mathcal{X}$ can be approximated with the required tolerance δ by its orthogonal projection $\Pi_{\mathcal{X}_n}$ on the space $\mathcal{X}_n$, in the sense that

$$\sum_{p=1}^{s} \|x_p - \Pi_{\mathcal{X}_n} x_p\|^2 \equiv \sum_{p=1}^{s} \|x_p - x_{p,n}\|^2 \leq \delta^2 \sum_{p=1}^{s} \|x_p\|^2 \,. \tag{3}$$

The relevant practical question now becomes: what is, for the given tolerance δ, the *minimum* dimension n of all the spaces $\mathcal{X}_n$ satisfying the condition (3)? We refer to it as the "critical dimension" $n_c(\mathcal{X}, \delta)$ for the given problem.

Clearly, the rigorous answer to this question can only be obtained a posteriori, i.e., after the solutions have been found. The angular resolution estimate, Eq.(1), suggests that

$$n_{c,\,\text{Nyq}}(\mathcal{X}) \sim \frac{\Omega}{(\Delta\alpha)_{\text{Nyq}}} \sim \frac{\Omega L}{\lambda} \,. \tag{4}$$

This estimate can only serve as a rough first guess, especially since the "object size" L is not precisely defined. We propose, however, another, more reliable (and computationally inexpensive) phenomenological estimate, which we developed and successfully tested in conjunction with the mGCR (multiple right hand sides Generalized Conjugate Residuals) algorithm, described in Appendix A.

The procedure consists of solving an auxiliary, significantly simpler problem of finding the minimum dimension of subspaces $\mathcal{B}_n$ approximating the corresponding set $\mathcal{B}$ of right-hand sides $\{b_1, b_2, \ldots, b_s\}$ in the sense of Eq.(3), i.e.,

$$\sum_{p=1}^{s} \|b_p - \Pi_{\mathcal{B}_n} b_p\|^2 \leq \delta^2 \sum_{p=1}^{s} \|b_p\|^2 \,. \tag{5}$$

The physical justification for the validity of such a procedure is based on the observation that, especially for large problems, solutions are qualitatively similar to the right hand sides. (This is particularly true when the physical optics approximation is valid, since then the currents on the illuminated surfaces are proportional to the incident fields.)

We observe now that subspaces $\mathcal{B}_n$ satisfying the condition (5) can be constructed by using the mGCR algorithm with the tolerance δ and with the impedance matrix A replaced by the identity matrix I. Indeed, in this case the vectors u and v spanning the variational

spaces $\mathcal{U}_n$ and $\mathcal{V}_n$ are identical, and they are linear combinations of the right-hand sides, i.e., the space $\mathcal{U}_n = \mathcal{V}_n$ is also identical to $\mathcal{B}_n$. The conditions (5) and (A.2), with the definition (A.1), are then equivalent.

Thus, the mGCR algorithm, after reaching the prescribed tolerance δ in some number $n_{\rm it}$ of iterations, finds a $n_{\rm it}$-dimensional subpace $\mathcal{B}_{n_{\rm it}}$ spanned by a subset of right-hand side vectors, such that all the right-hand sides $b_p \in \mathcal{B}$ can be approximated with the accuracy δ by vectors in $\mathcal{B}_{n_{\rm it}}$. We have verified by numerical analysis (modifying the algorithm selecting r.h.s.s in the mGCR method) that $n_{\rm it}$ is a good estimate of the *minimum* (critical) dimension $n_{\rm c}(\mathcal{B}, \delta)$ of *all* spaces $\mathcal{B}_n$ satisfying the condition (5).

The evidence accumulated in the course of our analysis indicates that the critical dimension $n_{\rm c}(\mathcal{B}, \delta)$ depends almost entirely on the *geometrical* problem size, and exhibits a weak, approximately logarithmic, increase with the decreasing tolerance (due to an exponential fall-off of the residual norm for a large number of iterations). Our findings can be summarized in a simple semi-empirical formula

$$n_{\rm c}(\mathcal{B}, \delta) \simeq \Omega \left(\frac{L}{\lambda} + c \, \log_{10} \frac{1}{\delta} \right) , \tag{6}$$

where Ω is in radians, L is the effective object size, and c is a problem-dependent constant of order 1. For large problems the tolerance-dependent term is of marginal relevance, the essential component being the term proportional to the angular span and the object size.

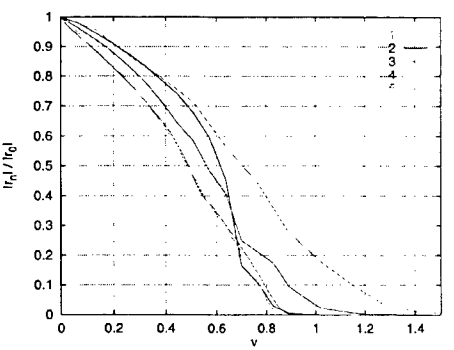

Fig. 2: Convergence histories (with $A = I$) for a variety of problems, plotted as functions of the rescaled number of iterations ν.

Fig. 2 shows a more systematic analysis of convergence histories for a wide variety of systems, as functions of the rescaled number of iterations $\nu = \frac{\lambda}{\Omega L} n$. According to Eq.(6), if the exponential tails of the convergence curves are disregarded, all the convergence histories, plotted as functions of ν, should fall close to a single universal curve; indeed, we find this feature in Fig. 2, where the problems 1 through 5 are:

1. a $5\,\lambda \times 2\,\lambda$ plate positioned in (x, y) plane, $N = 2,930$, $\theta_i = 90°$, $0° \leq \phi_i \leq 90°$;
2. a $10\,\lambda \times 10\,\lambda$ plate positioned in (x, y) plane, $N = 29,800$, $\phi_i = 0°$, $0° \leq \theta_i \leq 90°$;
3. the almond-shaped body of length about $5\,\lambda$, $N = 9,978$, $\theta_i = 90°$, $0° \leq \phi_i \leq 180°$;
4. VFY218 fighter at 500 MHz, about $25\,\lambda$ long, $N = 98,967$, $\theta_i = 90°$, $0° \leq \phi_i \leq 180°$;
5. VFY218 fighter at 1000 MHz, about $50\,\lambda$ long, $N = 318,911$, $\theta_i = 90°$, $0° \leq \phi_i \leq 90°$.

The actual critical dimensions n_c for these system range from about $n_c = 8$ to about $n_c = 160$. In all cases we took as L the maximum object size.

To summarize, the numerical evidence supports the estimate (6) for the minimum set of right hand side required and is consistent with the simpler estimate (4) based on the Nyquist angular resolution.

In the following Section we return to the problem of multiple-right-hand-side solution strategies with "short iterative sequences". As we shall see, the concept of the minimum dimension of the solution space is in this case of particular relevance.

3. Short iterative sequences

For large problems (several tens of thousand unknowns), storing the full iterative sequence may not be possible. It is also less advantageous than for smaller problems. The physical reason behind this observation is that the solution spaces corresponding to nonoverlapping sets of right-hand sides become more and more orthogonal as the space dimensions increase; therefore, availability of solutions for one set of right-hand sides provides little advantage in solving for another set.

Such circumstances require us to devise an efficient method for terminating and restarting iterations. In what follows we describe a method which we implemented and verified in conjunction with the mGCR algorithm:

(i) We select a set of right-hand sides, b_p, $p = 1, \ldots, s$, and apply to them the mGCR algorithm as described in the Appendix A. We perform no more than some predetermined number n of iterations, determined by the available memory.

(ii) We store on the disk the obtained set of approximate solutions solutions $x_{p,k}$ (where $k \leq n$ is the actual number of iterations), and the corresponding residuals $r_{p,k} = b_{p,k} - A\,x_{p,k}$. The residuals are a by-product of the mGCR algorithm, and require no additional

computation. The sets of vectors $u \in \mathcal{U}_k$ and $v \in \mathcal{V}_k$ (which have been stored in memory) are discarded.

(iii) If the required tolerance δ has not been achieved, we repeat the iterative process for the same as before set of r.h.s.s, with the initial s-dimensional variational spaces $\mathcal{U}_s$ and $\mathcal{V}_s$ constructed, respectively, from the vectors $x_{p,k}$ and $y_{p,k} \equiv b_{p,k} - r_{p,k} = A\, x_{p,k}$.

The process continues until all the solutions have been obtained, with the prescribed tolerance.

In order for the approach described above to be efficient, certain conditions have to be met:

1. First, the directions of the incident waves representing the right-hand sides should be spaced approximately as dictated by Nyquist theorem. If their angular spacing is larger than the critical spacing, the variational space constructed from the solutions and residuals is too small to restart the iterative process with no loss of accuracy.

2. Secondly, the sets of r.h.s.s should not be too large, because then the vectors spanning the solution space are so dissimilar as to diminish the gain due to solving simultaneously for many r.h.s.s. In addition, for a given maximum length n of iterative sequences, a large set of r.h.s.s may require an excessive number of restarts. Although it is difficult to give here a precise prescription for the size of the r.h.s.s set, a general guideline is about 10 vectors, assuming the Nyquist angular spacing.

We discuss now the application of the above procedure to a test case of an almond-shaped body [2], five wavelengths long, discretized with $N = 9,978$ unknowns. The almond is positioned in the (x, y) plane, and the set $\mathcal{B}$ of the right-hand sides is defined by the cut $0° \leq \phi_i \leq 180°$, $\theta_i = 90°$.

Fig. 3a shows the convergence history for a set of 19 r.h.s.s with the angular spacing $\Delta\phi_i = 10°$, divided into 4 sets. We made here sufficient allocation to store the entire iterative sequence for each set of r.h.s.s. As expected, the total number of iterations is considerably larger than in the "long sequence" case, with the full spaces $\mathcal{U}$ and $\mathcal{V}$ retained (300 compared to 155). On the other hand, the dimension of the variational space to be stored has been reduced from 155 to 82.

Fig. 3b shows a similar convergence history, but with the length of iterative sequences limited to 45 iterations. This limitation necessitates several restarts and each of the convergence curves becomes a "zig-zag" line. Since the angular spacing of r.h.s.s. is sufficiently small, we observe, within each r.h.s. set, no increase of the relative residual norm due to the restart. However, the convergence slows down after restarts and the total number of iterations becomes larger than in Fig. 3a (359 compared to 300). On the other hand, the maximum allocation for the variational space decreased from the dimension of 82 to 52.

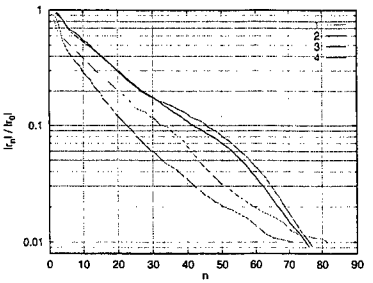

Fig. 3a: Convergence history for 19 r.h.s.s with $\Delta\phi_i = 10°$, partitioned into 4 sets, indicated by the numbers $1, \ldots, 4$. The storage is sufficient obtain solutions for each set in one sequence.

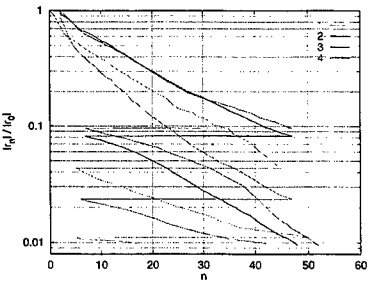

Fig. 3b: Convergence history in a problem similar to that of Fig. 3a, but with the iterative sequence length limited to 45, and thus with restarts in each r.h.s. set.

Finally, we checked that the 19 solutions with the angular spacing $\Delta\phi_i = 10°$ are, indeed, sufficient to reproduce all the solutions in the range $0° \leq \phi_i \leq 180°$ with an arbitrarily fine resolution: if the minimum solution set (together with the corresponding residuals) is used to generate the initial variational space, no further iterations are necessary to obtain all the remaining solutions.

The above examples illustrate some of the trade-offs in the speed of solution and the required storage. For problems larger than shown here, however the "short" iterative sequence strategy is usually more advantageous (and often remains the only possibility).

Appendix A. Multiple right-hand-side GCR algorithm (mGCR)

We describe here briefly a multiple right-hand-side variant [6] of the Generalized Conjugate Residual (GCR) method [3, 4], used in AIM.

The GCR method for a single right-hand side problem $A\,x = b$ belongs to the class of minimum-residual algorithms. In these algorithms x_n (the n-th approximation to the solution x) is found by minimizing the l_2 norm of the residual $r_n \equiv b - A\,x_n$ over $x_n \in \mathcal{U}_n$, where $\mathcal{U}_n = \mathrm{span}(b, A\,b, \ldots, A^{n-1}\,b)$ is the n-th Krylov subspace. The defining features of GCR are that the space $\mathcal{U}_n$ and a related space $\mathcal{V}_n = A\mathcal{U}_n$ are built by constructing two sequences of vectors spanning those spaces, $\{u_k\}$ and $\{v_k\}$, such that the vectors v_k are orthonormal, and $v_k = A\,u_k$. In terms of these vectors $x_n = \sum_{k=1}^{n} u_k\,v_k^{\mathrm{H}}\,b$. Equivalently, since $u_k = A^{-1}\,v_k$, we have $x_n = A^{-1}\sum_{k=1}^{n} v_k\,v_k^{\mathrm{H}}\,b \equiv A^{-1}\,\Pi_{\mathcal{V}_n}\,b$, where $\Pi_{\mathcal{V}_n}$ is the projection on the subspace $\mathcal{V}_n$.

In the actual GCR algorithm a new vector u_{n+1} is added to the space $\mathcal{U}_n$ by first taking $u'_{n+1} = r_n$, computing $v'_{n+1} = A\,u'_{n+1}$, and then orthonormalizing v'_{n+1} relative to the previous vectors and simultaneously transforming u'_{n+1} to preserve their relation.

The mGCR generalization of GCR to multiple right-hand sides (a set of problems $A\,x_p = b_p$, $p = 1, \ldots, s$) involves just one new element: in every iteration step the new vector u'_{n+1} is taken as the residual $r_{p,n} \equiv b_p - A\,x_{p,n}$ having the *largest norm*. As before, the n-th approximation to any solution x_p is constructed as $x_{p,n} = A^{-1}\,\Pi_{\mathcal{V}_n}\,b_p$. This procedure minimizes the norm of each residual $r_{p,n}$ separately, which is equivalent to minimizing the "total residual norm" squares, *defined* as

$$|r_n|^2 \equiv \sum_{p=1}^{s} \|r_{p,n}\|^2 = \sum_{p=1}^{s} \|b_p - A^{-1}\,\Pi_{\mathcal{V}_n}\,b_p\|^2 \ . \tag{A.1}$$

By construction, the norms $|r_n|$ constitute a monotonically (although not sharply) decreasing sequence, $|r_1| \geq |r_2| \geq \ldots$. The iterations are stopped as soon as the residual norm satisfies the convergence criterion

$$|r_n|^2 \leq \delta^2 \sum_{p=1}^{s} \|b_p\|^2 \ , \tag{A.2}$$

where δ is the desired tolerance.

References

1. E. Bleszynski, M. Bleszynski, and T. Jaroszewicz, "AIM: Adaptive integral method for solving large-scale electromagnetic scattering and radiation problems". *Radio Science*. Vol. 31, pp. 1225-1251, 1996.
2. A.C. Woo, H.T.G. Wang, M.J. Schuh, and M.L. Sanders, "Benchmark Radar Targets for the Validation of Computational Electromagnetic Programs", *IEEE Trans. on Antennas and Propagation Mag.*, Vol. 35, pp. 84-89, 1993.
3. H.C. Elman, "Iterative methods for large, sparse, nonsymmetric systems of linear equations", Ph.D. thesis and Res. Rep. #229, Department of Computer Science, Yale University, New Haven, CT, 1982.
4. S.C. Eisenstat, H.C. Elman, and M.H. Schultz, "Variational iterative methods for nonsymmetric systems of linear equations", *SIAM J. Numer. Anal.*, Vol. 20, pp. 345-357, 1983.
5. Y. Saad and M.H. Schultz, "GMRES: a generalized minimal residual algorithm for solving nonsymmetric linear systems", *SIAM J. Sci. Stat. Comput.*, Vol. 7, pp. 856-869, 1986.
6. P. Soudais, "Iterative solution of a 3-D scattering problem form arbitrary shaped multidielectric and multiconducting bodies", *IEEE Trans. on Antennas and Propagation*, Vol. AP-42, pp. 954-959, 1994.

A Fast Moment Method Matrix Solver

Francis X. Canning
Kevin Rogovin
Rockwell Science Center
1049 Camino Dos Rios
Thousand Oaks, CA 91360

1. Abstract.

This paper follows the spirit of ACES having roots in NEC. We present results which are especially relevant to NEC, but which also have a broader application. We present a method for computing electromagnetic solutions faster when a frequency domain integral equation is being used. This method will apply to certain other integral equations as well. In particular, we assume the moment method matrix has already been computed, and we find more efficient ways to store it and to invert it. That is, we have a matrix solver which is more efficient than the standard one. This is accomplished by finding and using hidden structure which occurs in all moment method matrices.

This hidden structure in moment method matrices is quite simple to compute with existing linear algebra methods. Blocks of the moment method matrix are considered as matrices in their own rite. We use only blocks which do not cross the main diagonal of the moment method matrix. Examining these blocks using Singular Value Decomposition routines shows that they do not have a full rank. In fact, to single precision accuracy they can be approximated by very low rank matrices. Often, their rank is one hundred times smaller than their dimension. Thus, the low rank approximation requires significantly less storage. When the whole matrix is assembled from a near diagonal part plus low rank blocks, taken as a whole it still has full rank.

2. Algorithm.

A previous paper has described the overall algorithm[1]. Thus, we will briefly outline the algorithm, and then proceed to describe some new numerical results. Figure 1 shows a five level decomposition of the matrix. The largest blocks will be called level one blocks and the smallest level five block. There are sixteen level five blocks above the diagonal and another sixteen below. All of the level one through level five blocks will be stored

using low rank decompositions. The center part of the matrix is as wide as three level five blocks. This part of the matrix will not be decomposed. Storage will be allocated for the actual matrix elements for this near diagonal part.

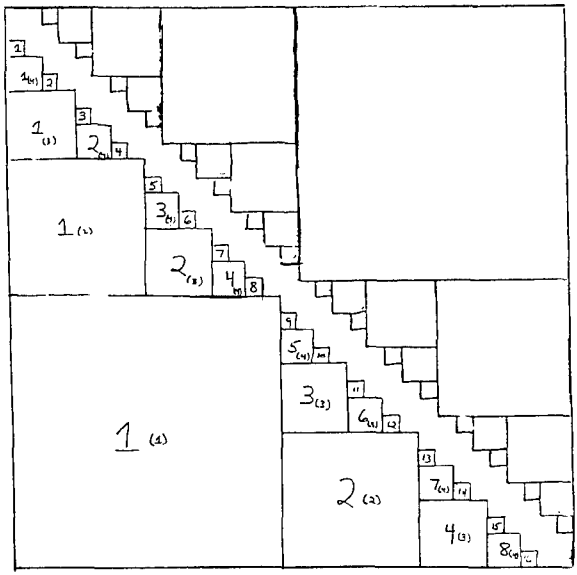

Figure 1
Block Structure for Five Levels

This structure appears to be very regular, but the underlying matrix need not be. The structure is transpose symmetric, but the actual matrix elements need not be. Also, imagine stretching Figure 1 in the horizontal direction. This could be done so that certain blocks are wider, and hold more matrix elements. Any such stretching is allowed, provided that it is done both horizontally and vertically at the same time. That is, the structure must remain symmetric. Thus, there is no restriction on the number of matrix elements. If we had required that all of the blocks were the same size, that would have created the restriction that N must be exactly divisible by $(2^L + 1)$ when the matrix is N by N, and there are L levels.

The algorithm that will be used has two parts. The first is to find the low rank decomposition of each block, and then replace that block by a sparse representation. The second is to find a sparse representation of the LU factorization of the matrix. The low rank approximations to each block on each level, levels 1 through L, are found using Lanczos bi-diagonalization with complete Householder re-orthogonalization. To find this for a rank k approximation, we must multiply that block (sub-matrix) times a vector k times and must also multiply the Hermitian conjugate of the block times a vector k times. The computational time to do this will be called MD, for the mnemonic Multiply-Decompose. All of the other time to compute the decomposition will be called OD, for the mnemonic Other-Decompose (or Orthogonalize-Decompose, since nearly all of this "other" time will be in orthogonalization). In performing the second part, one factors the matrix, while retaining the sparse storage format. In doing so, several operations must be performed. Dot products of vectors from the representations of blocks below the diagonal are taken with vectors from representations of blocks above the diagonal. The time to do this will be called Dot. The rest of the time for the interaction of two blocks is to calculate the sparse representation and this time will be called Rep. The center part of the matrix is three level L blocks wide. Whenever the exact center of these blocks is involved the time for calculation will be called Diag. If one of the blocks on either side of it is involved (and the center block is not also involved) then the time for that calculation will be called OffD. The time to multiply the original (full) matrix times a vector will be called Mult, and the time to compute one solution using the sparse LU factored matrix will be called Solve. With all of these conventions, we can now look at actual execution times.

3. Numerical Results.

The problem we consider is scattering by a flat rectangular plate. The plate is 11 cells wide and 186 cells long. This represents 5 points per wavelength. Because of two polarizations and the restriction that the normal component of the current is zero at an edge, the number of unknowns is N=3895. The problem is run on a Sun Ultra, which would require about 16,000 seconds to perform the standard LU factorization. There is enough memory available so that page faults are not a factor (except possibly for the Mult time for L=7). The results are shown in Table 1 below. Notice that the time "Dot", to calculate dot products, is negligible for any number of levels. From Table 1 we see that the rank of each block, in the top right corner or the lower left corner, varies from 8 to 34. In deciding when to terminate the low rank decomposition algorithm, we used the rule that three

digits of accuracy were needed. However, if say five digits were required then the ranks would only have been slightly higher. If we had wanted full single precision accuracy then the decomposition would have to have been calculated using a higher precision.

The low rank of these off-diagonal blocks is crucial to the success of this method. It creates one slight issue in using an existing moment method matrix. One would like the unknowns numbered so that, as much as is possible, if two unknowns are numbered far apart the physical points they correspond to must be separated in space. One way to achieve this is to pick the longest dimension of the scatterer, and to sort unknowns according to their location in that direction. It was obvious how to do this with the plate. For a model of a boat, we sort unknowns according to their distance from the bow. Similar methods have been used in the past with differential equation solvers to reduce the bandwidth of the matrix which results there.

Table 1
Execution times for 1 to 7 Levels for 11 by 186 cell Flat Plate

Levels	MD	CD	Dot	Rep	Diag	OffD
L=2	112	6	0	30	1994	1313
L=3	229	14	0	58	655	452
L=4	390	18	5	65	174	152
L=5	499	32	21	78	59	72
L=6	740	58	52	126	63	70
L=7	902	100	156	250	101	115

Levels	Mult	Solve	Total	k-TopR	k-BottomL
L=2	6	5	3455	8	8
L=3	7	2	1408	13	12
L=4	6	1	804	16	15
L=5	6	1	761	22	21
L=6	8	1	1109	28	29
L=7	17	2	1624	34	34

Notice that as the number of levels increased from 2 to 5 the time necessary to deal with the near diagonal parts of the matrix decreased. This is to be expected since the width of the diagonal part decreases as the number of levels increases. However, by L=7 there is a slight increase, even though these times are still over 100 times smaller than the time for the standard full LU factorization. This slight increase is because the factored form becomes more complicated as more levels are involved.

As more levels are used the significant increase in time is for the decomposition itself. This time is dominated by the time for the multiplication of the blocks times a vector, MD. The "Total" column gives the total for all of the parts of the factorization. This does not include the solve time. The minimum "Total" time results from a compromise number of levels; small for MD and OD time and large for Diag and OffD times. However, the exact choice is not critical. For example, any choice from L=3 to L=7 would give a total time within a factor of two of the best choice, L=5. All of these choices are over 10 times faster than full LU decomposition.

The Mult time is given for comparison, since it should equal the time it would take for each solve if one used the full LU decomposition rather than the sparse one we are using for "Solve" times. Notice that we have a direct solver, and it beats the N^2 time per RHS of the standard full LU decomposition.

The choice we used here of five points per wavelength is probably unrealistic. Fortunately, as more points per wavelength are used we generally have an increasingly large advantage over LU factorization. Also, the advantage is believed to increase with problem size. This method has been applied to other problems, including a model of a boat generated by NEC. It was found there also that a compact representation of the matrix is possible.

4. Storage Required.

The original moment method matrix is a full matrix, requiring storage for N^2 complex numbers. However, the first part of the algorithm reduces this to a sparse matrix. The storage needed for the diagonal part when there are L levels is

$$3\,N^2 / (2^L + 1) \qquad (1)$$

The storage needed for the off-diagonal blocks will depend on the rank of these blocks relative to their full rank. To simplify matters, assume that for every block, its rank as a fraction of its dimension is f. That is, each block will have a rank k when that block is (k/f) by (k/f). In that case, the storage required for the off-diagonal blocks will be

$$2f\,N^2\,[(2^L + 1) - 3]/(2^L + 1) \qquad (2)$$

The total of these two numbers will be smaller than

$$N^2 \{ [3/(2^L + 1)] + 2f\} \qquad (3)$$

and we see that factors of twenty or greater in storage savings are easily attainable. This form of compression is especially useful since the compressed form can be used as is, and doing so is much more efficient than using the original full form.

When the sparse LU factorization is computed the amount of storage required will increase slightly. However, the increase is always small. It was shown in [1] the the ratio of storage needed for the factored form to that needed for the original matrix will generally be less than 2:1. Thus, the factored form will still be sparse, and there will be a large savings in storage over standard methods.

5. Conclusions.

A method has been presented for more efficiently dealing with the matrix which results from any number of moment method computer codes. For large problems, dealing with the matrix is generally the bottleneck in their solution. Efficiencies were found both for the execution time to factor the matrix and for the storage it requires. The best part of this is that this method can be added to existing computer programs with little effort. The only complication is that the unknowns must be numbered intelligently. However, this can be done after the fact. All that is needed is that in addition to the matrix, one must have access to the coordinates in space associated with each unknown. A long direction is chosen, and the unknowns are sorted according to their coordinate along that direction. This can be automated. What results is a better matrix solver for moment method problems. Its use is nearly transparent to the user. These are all highly desirable attributes. The result of all of this is that existing computer programs will be able to run in less time with less memory, with little need for intervention by the user.

6. Reference.

1. F. X. Canning and Kevin Rogovin, "Fast Direct Solution of Standard Moment Method Matrices," submitted to IEEE Antennas and Propagation Society Magazine.

Vector parabolic equation technique for the RCS calculations

A.A. Zaporozhets and M.F. Levy
Rutherford Appleton Laboratory, Chilton, Didcot, OX11 0QX, UK

Introduction

We compute the Radar Cross Section (RCS) of a perfectly conducting object with the recently developed vector parabolic equation technique [1]. The size of the object ranges from a few wavelengths to tens and even hundreds of wavelengths, whilst the calculations can still be performed on a personal computer. The key idea is that instead of treating all the points of the computation domain simultaneously, the solution is marched through the domain plane by plane. The method has been validated on simple canonical shapes and tested on complex targets.

Parabolic equation technique for EM scattering calculations

Parabolic equation (PE) techniques have been widely used to solve various types of wave propagation problems. They provide an efficient solution for long-range propagation of the acoustical waves in the ocean or electromagnetic waves in the atmosphere [2, 3]. More recently they have been applied to scattering problems, and in particular to RCS calculations [4 -6]. The basics of the PE approach are given below.

In all that follows, we assume *exp(-iωt)* time-dependence of the fields. Working with Cartesian coordinates (x,y,z), we introduce the reduced function associated with a scattered field component ψ

$$u(x,y,z) = \exp(-ikx)\psi(x,y,z) \qquad (1)$$

The reduced function is slowly varying in range for energy propagating close to the paraxial direction. The scalar wave equation in terms of u is then factored as

$$\left\{\frac{\partial u}{\partial x} + ik(1-Q)\right\}\left\{\frac{\partial u}{\partial x} + ik(1+Q)\right\}u = 0 \qquad (2)$$

where k is the reference wave number and the pseudo-differential operator Q is defined by

$$Q = \sqrt{\frac{1}{k^2}\frac{\partial^2}{\partial y^2} + \frac{1}{k^2}\frac{\partial^2}{\partial z^2} + n^2(x,y,z)}, \qquad (3)$$

n is refractive index of the media. The first term in Eq.2 represents energy propagating in the forward paraxial cone (increasing x), and the other the backward propagating energy (decreasing x). The outgoing parabolic equation for u is

$$\frac{\partial u}{\partial x} = -ik(1-Q)u \qquad (4)$$

The great advantage of Eq.4 is that it can be marched in range, getting the solution at range $x+\Delta x$ from that at range x and suitable boundary conditions on the scattering object and at the outer boundaries of the integration domain, as shown in Fig. 1.

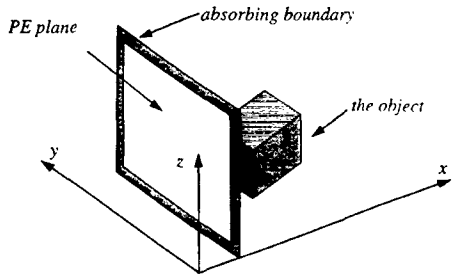

Fig.1. PE computational domain. The solution is marched plane by plane along the x-axis with the corresponding boundary condition on the object surface and absorbing condition at the outer boundaries.

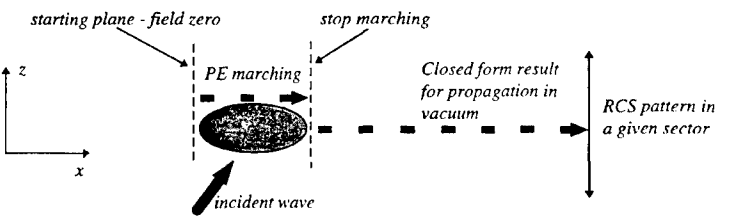

Fig.2. RCS computation with the parabolic equation method.

The recipe for scattered far-field calculation is the following (see Fig.2). We start just before the object setting the field on the PE plane to zero (this initial condition will be explained in the next paragraph). The scattered field is marched plane by plane, while the incident energy is fed though non-homogeneous boundary condition on the object [6]. As soon as we pass the object, the closed form formulae for propagation in vacuum can be used [6], which gives the scattering pattern in a given sector. The main limitation is that the square-root operator can only be defined in a paraxial cone, so that a single PE run can only give a partial image of scattering phenomena. It is possible to overcome this restriction by carrying out several "rotated" PE runs to cover all scattering angles of interest.

A consequence of solving for the scattered field is that the initial field for the marching algorithm should be zero. The object is the source of the scattered field; in a spherical coordinate system the

scattered field has outgoing component only. Since the integration starts on a transverse plane just before the scatterer, the scattered field there cannot have any forward propagating components. Indeed the reduced function u is zero until the boundary of the scatterer is reached, at which point the non-homogeneous boundary conditions introduce the scattering sources into the marching solution.

Now we discuss the electromagnetic scattering case, where the object is a perfect electric conductor. We can solve for the electric field only, since the magnetic field can be obtained through the curl equation if required. Follow the derivation of equation 4, we obtain the vector parabolic for the electric field from the vector wave equation. Basically, the vector PE is a combination of 3 scalar PEs for each Cartesian component of the electric field.

For a perfect conductor, the tangential electric field must be zero on the object, so the boundary condition for the total field is:

$$\left[\vec{n}(P)\times\vec{E}(P)\right]=0 \qquad (5)$$

where P is a point on the surface of the scatterer and $\vec{n}=(n_x,n_y,n_z)$ is the outer normal to the surface at P. In terms of the PE reduced scattered field, these conditions become non-homogeneous:

$$\left[\vec{n}(P)\times\vec{u}(P)\right]=-e^{-ikx}\left[\vec{n}(P)\times\vec{E}^i(P)\right] \qquad (6)$$

where E^i is the incident electric field. Eq.6 corresponds to three equations for scalar components. These equations are not independent, but form a system of rank 2. Hence we need another equation to ensure unicity of the solution. This is provided by the divergence-free condition. Enforcing the divergence-free condition on the object boundary ensures a well-determined system of equations, and it can be shown that the PE solution is then divergence-free everywhere.

If the scattering object is not a perfect conductor, boundary conditions of surface impedance type must be used. In that case one must solve simultaneously for both **E** and **H** components, which results in a system of six coupled scalar parabolic equations.

Implementation

In the rest of this paper, we assume a homogeneous background medium, taking n constant equal to 1. In this work, we use the simplest approximation of Eq.3, which is obtained with first order Taylor expansions of the square-root and the exponential. This yields the well-known Standard Parabolic Equation (SPE)

$$\frac{\partial u}{\partial x}=\frac{i}{2k}\left(\frac{\partial^2 u}{\partial y^2}+\frac{\partial^2 u}{\partial z^2}\right) \qquad (7)$$

The SPE is a narrow-angle approximation which is very accurate at angles within 15 degrees or so of the paraxial direction. Because of the simplicity of the SPE, boundary conditions on the scatterer are relatively easy to incorporate, which we found particularly useful for 3-dimensional electromagnetic applications where coding can become quite intricate. We should state here that the narrow-angle approximation is only accurate when energy scattered by the object does not undergo large changes in direction. This can break down for non-convex objects, as shown in [6]. There is no doubt that wide-

angle schemes [7] could improve accuracy when the modelling of deep-shadow diffraction is important.

The finite-difference scheme has been described in [6]. Scattering objects are discretized on a rectangular grid, keeping track of the normal along the surface of the scatterer. The grid spacing is fixed in the transverse (y-z) plane, but adaptive in range. Since the non-homogeneous boundary conditions contain an exponential term in x on the right hand side (see Eq.6 for example), accurate representation of phase variations require smaller grid spacing as the angle between the paraxial and incident directions increases. Typical range steps are $1/10^{th}$ of a wavelength or less. For domain truncation in the transverse plane, we selected the Perfectly Matched Layer technique [8], which has recently been adapted for paraxial methods [9].

Typical integration times for a single rotating PE run on a 133 MHz Pentium are of the order of a few minutes for three-dimensional simulations of forward scatter. Timings increase with the angle between paraxial and incident directions, and can reach several hours for backscatter calculations. If bistatic RCS results are required at scattering angles encompassing several narrow-angle sectors, an appropriate number of runs is carried out and the scattering pattern is constructed by using the relevant results in each sector.

Examples

We now look at scattering by perfectly conducting spheres. The vector PE solution is compared to the theoretical solution given by Mie expansions [10]. Fig. 3 shows the full bistatic scattering pattern for a sphere of radius 5 wavelength, assuming a wavelength of 0.1m (frequency 3 GHz). Both the vector PE and the theoretical results are shown. For each plane, the full pattern required seven PE runs covering angular sectors of 30° each. The forward PE run took under 5 minutes on a 133 MHz Pentium machine. Since the larger scattering angles require finer grids, computation times increase as the paraxial direction moves towards 180°. The longest execution time was 2 hours. The complete execution time was about 6 hours per plane pattern. Agreement with the theoretical results is excellent for this case.

Next we consider the ogive, which is one of the well-known test cases for scattering algorithms [11]. Fig. 4 shows the monostatic backscatter RCS of the ogive computed as a function of azimuthal angle for the case of VV polarisation. The frequency of the incident wave is 9 GHz. The measured data was extracted from graphs published in [11]. The 0° angle corresponding to incidence on the tip. Although the PE results follows the measured data, they are not very accurate. When the ogive is viewed from the side (90° azimuth), the model behaves well, but the error increases substantially as incidence moves towards the sharp tip of the ogive where the creeping wave dominates. The source of the errors is discussed after the figures.

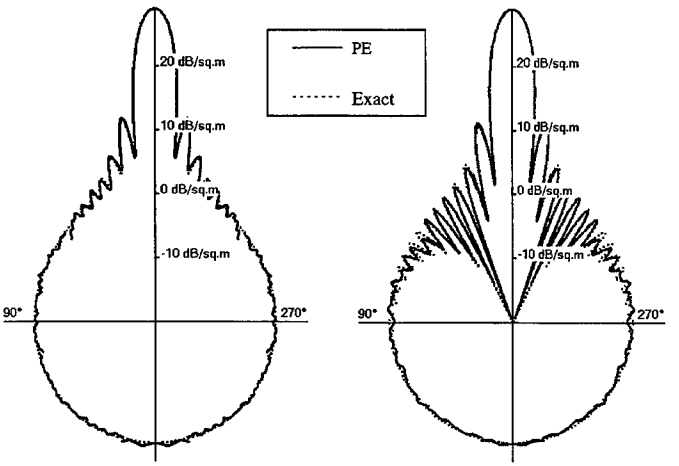

Fig. 3. Total bistatic RCS for perfectly conducting sphere of radius 5λ (0.5 m at 3GHz) from 7 rotated vector PE runs, a) horizontal plane pattern, b) vertical plane pattern.

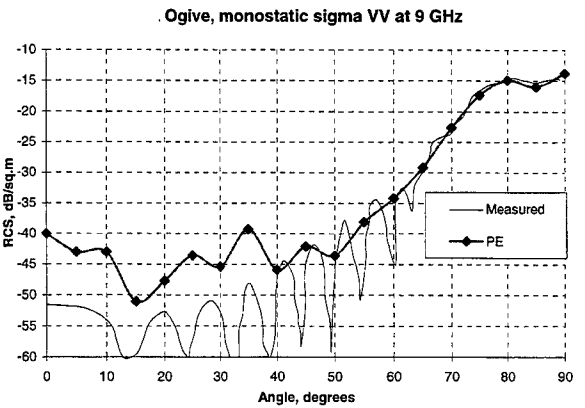

Fig. 4. Monostatic backscatter RCS for the ogive [11].

The parabolic equation technique essentially assumes that the currents on the object surface originate from two sources: the incident field and the contribution from the part of the object we have passed. In this sense the approach should be very accurate for the forward scatter calculation, since we start from the illuminated part of the object where the field has highest intensity and carry this contribution to the shadow region. The worst case is the backscatter calculation, since we have no information about the sources located in the illuminated side until we pass them. The error should be small for smooth objects and increases for the objects with sharp edges, like the ogive tip. It might be possible to correct this problem with some iterative approach.

Acknowledgment

This work was carried out with the support of the Radiocommunications Agency of the Department of Trade and Industry and of the Engineering and Physical Sciences Research Council of the United Kingdom.

References

[1] A.A. Zaporozhets and M.F. Levy, "Bistatic RCS calculations with the vector parabolic equation method", submitted to *IEEE Trans. Antennas Propagat.*

[2] G.D. Dockery and J.R. Kuttler, "An improved impedance-boundary algorithm for Fourier split-step solutions of the parabolic wave equation", *IEEE Trans. Antennas Propagat.*, vol. 44, pp. 1592-1599, Dec. 1996.

[3] F.B. Jensen, W.A. Kuperman, M.B. Porter and H. Schmidt, *Computational Acoustics*, New York: AIP Press, 1994.

[4] M.F. Levy and P-P. Borsboom, "Radar cross-section computations using the parabolic equation method", *Electron. Letters*, vol. 32, pp. 1234-1236, June 1996.

[5] M.F. Levy, P-P. Borsboom, A.A.Zaporozhets and A.Zebic-Le Hyaric, "RCS calculations with the parabolic wave equation", *AGARD Conf. Proc. No 583*, paper 5, Oct. 1996.

[6] M.F. Levy and A.A. Zaporozhets, "Target scattering calculations with the parabolic equation method", to appear in *Journal of the Acoustical Society of America.*

[7] M.D. Collins, "A split-step Padé solution for the parabolic equation method", *J. Acoust. Soc. Am.*, vol. 94, pp. 1736-1742, Apr. 1993.

[8] J.-P. Bérenger, "A perfectly matched layer for the absorption of electromagnetic waves", *J. Comp. Phys.*, vol. 114, pp. 185-200, Oct. 1994.

[9] C. Vassalo and F. Collino, "Highly efficient absorbing boundary conditions for the beam-propagation method", *J. of Lightwave Technology*, vol 14, pp. 1570-1577, June 1996.

[10] J.J. Bowman, T.B.A. Senior and P.L.E. Uslenghi, *Electromagnetic scattering by simple shapes*, revised ed., New York: Hemisphere Publishing Corporation, 1987.

[11] H.T.G. Woo, M.J. Schuh and M.L. Sanders, "Benchmark radar targets for the validation of computational electromagnetics programs", *IEEE Antennas and Propagat. Magazine*, Vol. 35, pp. 84-89, Feb. 1993.

SESSION 7:

ELECTROMAGNETICS IN BIOLOGICAL AND MEDICAL APPLICATIONS

Chairs: C. Furse and M.A. Stuchly

EM Interaction Evaluation of Handset Antennas and Human Head: A Hybrid Technique

Kang W. Kim and Yahya Rahmat-Samii
Department of Electrical Engineering
University of California, Los Angeles
Los Angeles, CA 90095-1594
E-mail: rahmat@ee.ucla.edu
Work: (310) 206-3847, 206-4801
FAX: (310) 206-8495

Abstract

An efficient hybrid technique, which combines the eigenfunction expansion method (EEM) and the method of moments (MoM), has been developed to critically assess the electromagnetic interactions between handset antennas and a human head, especially the effects of very thin layers (e.g skin) and high frequencies (e.g. 30 GHz). The developed technique is based on the exact scattering solution of infinitesimal dipoles in the presence of a multi-layered, lossy dielectric spherical head. This technique allows to simulate a variety of antennas or antenna arrays. This paper presents mathematical formulations of the technique, validation tests together with results of antenna-head interactions at 900 MHz and 30 GHz.

1. Introduction

Today's wide-spread use of personal communication systems (e.g. cellular phones) necessitates better understanding of electromagnetic (EM) interactions between various types of antennas and a human body. Recently, considerable improvements toward the understanding of EM interactions in personal communications have been achieved by numerical computations employing various methodologies (see Fig. 1) such as Finite-Difference Time-Domain (FDTD) method [1]-[4], the Method of Moments (MoM), and the Eigenfunction Expansion Method (EEM) [5]-[8]. However, the popular numerical techniques such as FDTD have severe limitations in dealing with the effects of thin skin layers (~1 mm) and high operating frequencies (e.g. 30 GHz) due to huge computer memory and excessive computation time. On the other hand, the EEM can be used to investigate these effects without limitations of computer resources. This approach, however, requires a prior knowledge of the antenna current distribution.

To accurately and efficiently evaluate antenna-head interactions in personal communications, a hybrid technique, which combines EEM and MoM, has been implemented [7]-[8]. With this hybrid technique, the dyadic Green's functions for the scattered field from a multi-layered sphere are obtained using EEM, and then the current distribution on the antenna is determined by applying MoM to the electric field integral equation. The hybrid technique is very efficient since unknowns are limited only to the surface of the antenna. This technique allows to study a variety of antennas or antenna arrays used in personal communications.

Using this hybrid technique, the effects of thin biological layers (e.g. skin) and high frequencies (e.g. 30 GHz) are investigated. Also, systematic and parametric studies on EM interactions between

various handset antennas and a multi-layered spherical head have been performed. In addition, this technique is based on the canonical solution, which can be used to validate other numerical techniques.

2. Scattered Field through Dyadic Green's Functions

The eigenfunction expansion method (EEM) in this paper is based on the exact scattering solution of infinitesimal dipoles. The total electric field at any observation location can be decomposed into the incident field and the scattered field. For the calculation of the incident field, the closed-form analytical expression is used for efficient computations; the scattered field is expressed as a series expansion of the spherical vector wave functions. Figure 2 illustrates the geometry of a multi-layered sphere consisting of N regions with the corresponding constitutive parameters. For example, infinitesimal dipoles are assumed to be oriented in the x-direction and located outside of the multi-layered sphere.

The total electric field can be expressed through dyadic Green's function [9] as

$$\mathbf{E}(\mathbf{r}) = -j\omega\mu_1 \iiint \overline{\mathbf{G}}_e^{(p1)}(\mathbf{r}, \mathbf{r}') \bullet \mathbf{J}(\mathbf{r}') dv' \tag{1}$$

where $\overline{\mathbf{G}}_e^{(p1)}(\mathbf{r}, \mathbf{r}')$ is the dyadic Green's function for each region, and μ_1 is the permeability for Region 1. In the superscript of $\overline{\mathbf{G}}_{es}^{(p1)}(\mathbf{r}, \mathbf{r}')$, p denotes for the p-th region and 1 is used for the source region.

For an infinitesimal electric dipole located at $\mathbf{r}' = (r_0, \theta_0, \phi_0)$ with a current moment $\mathbf{c} = Il\hat{\mathbf{x}}$, the electric field can be obtained from (1) as

$$\mathbf{E}(\mathbf{r}) = -j\omega\mu_1 Il \cdot \overline{\mathbf{G}}_e(\mathbf{r}, \mathbf{r}') \bullet \hat{\mathbf{x}} \tag{2}$$

Using the dyadic Green's function for the scattered field in Region p $(a_p \le r \le a_{p-1})$ where $p = 1, 2, \ldots, N$, the scattered electric field can be obtained as

$$\mathbf{E}_{(p)}^s(\mathbf{r}) = -\left(\frac{\omega\mu_1 Il}{4\pi} \cdot \beta_1\right) \sum_{n=1}^{\infty} \sum_{m=0}^{n} (2-\delta_{m0}) \frac{(2n+1)(n-m)!}{n(n+1)(n+m)!} \cdot \tag{3}$$
$$\left\{ \begin{array}{l} \left(A_{n,p} \mathbf{M}_{\substack{e \\ o}mn}^{(4)}(\beta_p) + C_{n,p} \mathbf{M}_{\substack{e \\ o}mn}^{(1)}(\beta_p) \right) \left[\mathbf{M}_{\substack{e \\ o}mn}^{(4)'}(\beta_1) \bullet \hat{\mathbf{x}} \right] \\ + \left(B_{n,p} \mathbf{N}_{\substack{e \\ o}mn}^{(4)}(\beta_p) + D_{n,p} \mathbf{N}_{\substack{e \\ o}mn}^{(1)}(\beta_p) \right) \left[\mathbf{N}_{\substack{e \\ o}mn}^{(4)'}(\beta_1) \bullet \hat{\mathbf{x}} \right] \end{array} \right\}$$

where $\beta_p = \omega\sqrt{\mu_p \varepsilon_p}$ and δ_{m0} is the Kronecker delta function. $\mathbf{M}_{\substack{e \\ o}mn}^{(i)}$ and $\mathbf{N}_{\substack{e \\ o}mn}^{(i)}$ are the even or odd spherical vector wave functions, which are solutions of the source-free vector wave equation $\nabla \times \nabla \times \mathbf{E} - \beta^2 \mathbf{E} = 0$ [9]. $A_{n,N} = B_{n,N} = 0$ in the above equation to avoid infinite field at the origin.

The expansion coefficients $A_{n,p}$, $B_{n,p}$, $C_{n,p}$, and $D_{n,p}$ in (3) are obtained by applying boundary conditions to the tangential electric and magnetic fields at the dielectric interfaces ($r = a_p$).

3. Hybridization of the EEM and MoM

To accurately account for EM interactions between antennas and the multi-layered sphere, the hybridization of the eigenfunction expansion method (EEM) and the method of moments (MoM) has been performed. By the hybridization, the current distribution on the antenna can be determined efficiently. The unknowns are limited only to the surface of the antenna since the scattered dyadic Green's function is provided by EEM.

The electric field integral equation (EFIE) for any antenna in the presence of a multi-layered dielectric sphere can be written as

$$\mathbf{E}(\mathbf{r}) = \mathbf{E}^i(\mathbf{r}) + \mathbf{E}^s(\mathbf{r}) = \mathbf{E}^i(\mathbf{r}) - j\omega\mu\iiint \overline{\mathbf{G}}_e^{(11)}(\mathbf{r}, \mathbf{r}') \bullet \mathbf{J}(\mathbf{r}')dv' \tag{4a}$$

$$\hat{\mathbf{n}} \times \mathbf{E}(\mathbf{r}) = 0 \text{ on the surface of the antenna} \tag{4b}$$

where $\mathbf{E}^i(\mathbf{r})$ is the incident field due to the localized source (modeled as a delta gap or a magnetic frill), $\mathbf{E}^s(\mathbf{r})$ is the scattered field due to the induced current on the antenna, and $\overline{\mathbf{G}}_e^{(11)}(\mathbf{r}, \mathbf{r}')$ is the dyadic Green's function for the region outside the sphere (Region 1).

In this treatment, a thin wire dipole antenna oriented in the x-direction is considered. On the surface of the thin wire, tangential components of the electric field vanishes; i.e.,

$$E_x = E_x^i + E_x^s = 0 \tag{5}$$

The tangential field can approximately be evaluated along the center of the thin wire, while the induced current is confined on the surface of the wire (thin wire approximation).

We obtain

$$\begin{aligned} -E_x^i = E_x^s &= E_x^{s,fs} + E_x^{s,sob} \\ &= -j\omega\mu\iint \hat{\mathbf{x}} \bullet \overline{\mathbf{G}}_{e0}(\mathbf{r}, \mathbf{r}') \bullet \hat{\mathbf{x}} J_x(\mathbf{r}')dv' - j\omega\mu\iiint \hat{\mathbf{x}} \bullet \overline{\mathbf{G}}_{es}^{(11)}(\mathbf{r}, \mathbf{r}') \bullet \hat{\mathbf{x}} J_x(\mathbf{r}')dv' \end{aligned} \tag{6}$$

where $E_x^{s,fs}$ is the field due to induced current through free-space propagation, $E_x^{s,sob}$ the field due to scattering from the multi-layered sphere; $\overline{\mathbf{G}}_{e0}(\mathbf{r}, \mathbf{r}')$ the free-space dyadic Green's function, and $\overline{\mathbf{G}}_{es}^{(11)}(\mathbf{r}, \mathbf{r}')$ the dyadic Green's function for scattered field, which is provided by EEM. The above equation can be solved for the unknown current coefficients on the surface of antenna by applying the method of moments—e.g. applying a pulse basis function and point-mating technique.

4. Numerical Implementation and Validation Tests

The computer code for the hybrid technique has been implemented in FORTRAN using double precision variables, and extensively verified using various methods including: 1) limiting cases when the problem reduces to simpler cases; 2) series convergence tests; 3) the decaying electric field inside the lossy dielectric sphere; 4) boundary conditions at the dielectric interfaces; 5) plane wave incidence (comparison with the results in the literature); 6) comparison of the radiated field between an analytical $\lambda/2$ dipole antenna and a simulated $\lambda/2$ antenna which uses finite number of infinitesimal dipoles; 7) comparison of scattered far-field radiations with FDTD. All the results obtained using the code agree self-consistently and also with the literature data for the plane wave incidence [6]. In this paper, however,

we will only discuss the series convergence tests and the comparison of radiation patterns with FDTD.

For numerical validation tests presented in this section, the dielectric sphere is assumed lossy and homogeneous with the relative permittivity 49 and the conductivity 1.9 S/m—i.e. $\varepsilon_{r2}=49-j\ 1.9/(\varepsilon_0\omega)$—at operating frequency 1.5 GHz. The radius of the sphere is assumed 10 cm.

4.1 Series Convergence Tests

As can be seen in (3), the scattered field is expressed as an infinite sum of spherical vector wave functions. In practice, however, the required number of series terms at each field point is determined if the ratio between the q-th term and the sum up to q terms is less than a specified error. Figures 3(a)–(b) plot the number of n series terms for field convergence when an infinitesimal dipole is located at 2 cm away from the surface of the lossy dielectric sphere. As we can see in Fig. 3(a), converged results have been obtained with 40~100 series terms near the sphere surface, and with fewer terms (≤ 20 terms) away from the sphere surface. In the case that a dipole is located further away from the surface of the sphere, fewer n series terms are requires for convergence. When the operating frequency is increased, the electrical size of the sphere becomes larger, and more n series terms are needed for a specified convergence test as illustrated in Fig. 3(b). At 15 GHz, ~40 terms are needed outside the sphere whereas inside the sphere ~80 terms are needed. More series terms are needed for 30 GHz. Similar effects can be observed when the size of the sphere is increased at a fixed frequency.

For each n, all the m series terms from 0 to n have to be summed up except special cases when infinitesimal dipoles are on the z-axis—i.e., in these cases, only $m = 0$ or 1 is non-trivial. The m series terms are related to the angular functions (i.e. associated Legendre functions). An alternative technique which avoids the m summation has also been developed; this technique requires axis rotations to match the orientation of infinitesimal dipoles on the z-axis.

4.2 Comparison with FDTD results

Far-field radiation patterns of a $\lambda/2$ antenna in the presence of a homogeneous dielectric sphere are compared with those obtained by the FDTD method. A $\lambda/2$ antenna is located at 2 cm away from the surface of the sphere. For FDTD, the dimension of a cubical cell size is 2 mm, and the sphere is simulated as a combination of cubes. In Fig. 4, the far-field pattern (in the x-z plane) obtained using the hybrid technique is compared with that obtained using the FDTD method. These radiation patterns agree very well except minor differences in the direction of the sphere. The difference in the radiation patterns may be accounted for by considering the minor differences associated with modeling the dielectric sphere. In the FDTD case, the dielectric sphere is modeled with cubical cells which does not allow smooth surfaces.

5. Antennas and Human Head Interactions

5.1 Human Head Model

A six-layered, lossy dielectric sphere is used to simulate the biological tissues of a human head. Identified biological tissues include skin, fat, bone, dura, cerebrospinal fluid (CSF), and brain. The radius of each layer of the spherical head was taken from [5]. The electrical parameters (permeability and conductivity) of the biological tissues at 900 MHz and 30 GHz are shown in Table 1. The electrical parameters of the tissues at 900 MHz are taken from [4]. At 30 GHz, these parameters are obtained using the multiple Cole-Cole dispersion equation and the corresponding parameters in [12].

5.2 EM Interactions at 900 MHz

Let's assume that the operating frequency is 900 MHz and a $\lambda/2$ dipole antenna is located at 2 cm

away from the surface of the sphere. The current distribution on the antenna is obtained by applying the hybrid technique. The far-field gain patterns are shown in Fig. 5(a). As can be seen in the figure, the far-field patterns are significantly changed in the presence of the spherical head. The gain with the spherical head is slightly enhanced (~0.28 dB) in the θ=0 direction, but dropped by 2.28 dB toward the spherical head direction.

Next, Fig. 5(b) shows the unaveraged and 1-g averaged specific absorption rate (SAR) distributions inside the spherical head along the z-axis. In this case the maximum SAR lies along the z axis. The 1-g averaged SAR distribution is obtained by moving-average over a $1.1\times1.1\times1.1$ cm^3 cube with eleven 1 mm cells per each side of the cube. With the unaveraged SAR distribution, the main SAR peak occurs at the cerebrospinal fluid (CSF) layer just outside of the brain region: the second peak occurs at the skin layer. With the 1-g averaged SAR distribution, still there are two SAR peaks, but the peaks are much lower than those of the unaveraged SAR: e.g., with 1 W of the delivered power, 4.5 W/kg with the 1-g averaged SAR near the CSF layer vs. 11.2 W/kg with the unaveraged SAR. Also, we observe that the SAR peak locations are shifted, due to averaging process, from those of the unaveraged SAR. The reason of occurring peak SARs at skin and CSF layer is the following: the electric field distribution inside the sphere exponentially decays (with small glitches) from the surface of the sphere due to tangential field continuity (see Fig. 6(b)). However, SAR, which is obtained by the product of the conductivity and the square of the electric field, peaks at the biological layers that possess high conductivity such as the skin and CSF layers.

A three-dimensional surface plots of the SAR distribution in the x-z plane is shown in Fig. 6(a). As can be seen in the figure, SAR peak lies along the z-axis. In the figures, it is interesting to observe small ripples near the center of the brain region due to the focusing effect of the sphere. These ripples may be more conspicuous when the head–antenna separation distance is increased. When antenna is moved far away from the sphere to simulate the plane wave, sometimes the hot spots occur near the center of the brain. A contour plot of the electric field intensity in the x-z plane is shown in Fig. 6(b). The numbers in the contour plots designate contour lines for 20 $\log_{10}$ |**E**|.

5.3 Effect of High Operating Frequency: e.g. Ka-band

To accommodate vast amount of multi-media data, applications of wideband operation at high operating frequencies (e.g. Ka-band) has been proposed. In general, as the frequency becomes higher, the permittivity of the biological tissue decreases, but the conductivity of the tissue increases. For example, at 30 GHz, the conductivities of the tissues become much higher than those at 900 MHz (see Table 1). In this example, a half-wave dipole antenna is assumed to be located at 2 cm away from the surface of the spherical head. In Fig. 7, the 1-g averaged SAR distribution is compared with the unaveraged SAR. As can be seen in the figure, at 30 GHz, the power deposition is highly localized near the surface ($\leq$ 1 mm) of the sphere with very high unaveraged peak SAR (~457 W/kg at the skin). In this case, the role of the skin layer becomes dominant. In the figure, it is noted that the 1-g averaged peak SAR is only 10.6 W/kg at the skin layer, which is significantly lower than the unaveraged peak SAR. The reason is that, at 30 GHz, SAR is highly localized at the skin layer, and the averaged SAR is significantly lowered in the process of averaging over a $1.1\times1.1\times1.1$ cm^3 volume. Also, note that the non-trivial 1-g averaged SAR is extended to ~7 mm from the surface of the spherical head, while the non-trivial unaveraged SAR is localized to the skin layer (~1 mm from the surface).

The total power absorption of the antenna delivered power at 30 GHz is much lower than that at 900 MHz: i.e. 14.7% at 30 GHz and 43.9% at 900 MHz. The power deposition, however, is localized to

a very small region, resulting in a high peak SAR near the skin layer.

6. Conclusions

An accurate and efficient hybrid technique, combining the EEM and MoM, has been used to study EM interactions with a variety of antennas in personal communications. In this paper, with the hybrid technique, EM interactions between antennas and a six-layered spherical head have been performed. Summaries of important results are as follows: In the presence of the six-layered spherical head, the antenna radiation patterns may be significantly modified from those of free-space patterns. The unaveraged SAR peaks occurred at CSF and skin layers at 900 MHz, while with 1-g SAR averaging, the peak positions are shifted. Also, the 1-g averaged SAR peak is significantly lower than the unaveraged SAR peak. At 30 GHz, total power absorption is much smaller, but power deposition is highly localized (≤1 mm), resulting into a very high unaveraged peak SAR (457 W/kg); peak SAR with 1-g averaging is much lower (10.6 W/kg). In this case, the role of the skin layer becomes very important.

References

[1] M.A Jensen and Y. Rahmat-Samii, "EM Interaction of Handset Antennas and a Human in Personal Communications," *Proc. IEEE*, Vol. 83, No. 1, pp. 7-17, Jan. 1995

[2] O.P. Gandhi, G. Lazzi, C.M. Furse, "Electromagnetic Absorption in the Human Head and Neck for Mobile Telephones at 835 and 1900 MHz," *IEEE Trans. Microwave Theory Tech.*, Vol. 44, pp. 1884-1897, Oct. 1996

[3] M. Okoniewski, M.A. Stuchly, "A Study of the Handset and Human Body Interaction," *IEEE Trans. Microwave Theory Tech.*, Vol. 44, pp. 1855-1864, Oct. 1996

[4] V. Hombach, K. Meier, M. Burkhardt, E. Kühn, N. Kuster, "The Dependence of EM Energy Absorption Upon Human Head Modeling at 900 MHz," *IEEE Trans. Microwave Theory Tech.*, Vol. 44, pp. 1865-1873, Oct. 1996

[5] N.C. Skaropoulos, M.P. Ioannidou, D.P. Chrissoulidis, "Induced EM Field in a Layered Eccentric Spheres Model of the Head: Plane-Wave and Localized Source Exposure," *IEEE Trans. Microwave Theory Tech.*, Vol. 44, pp. 1963-1973, Oct. 1996

[6] A.R. Shapiro, R.F. Lutomirski, H.T. Yura, "Induced Fields and Heating Within a Cranial Structure Irradiated by an Electromagnetic Plane Wave," *IEEE Trans. Microwave Theory Tech.*, Vol. MTT-19, pp. 187-196, Feb. 1971

[7] H.-O. Ruoss, U. Jakobus, and F.M. Landstorfer, "Efficient EM analysis of hand-held mobile telephones close to human head using modified method of moments," *Electron. Lett.* Vol. **31** (12), pp.947-948, June 1995

[8] K.W. Kim and Y. Rahmat-Samii, "Antennas and Humans in Personal Communications: An Engineering Approach to the Interaction Evaluation," Proceedings of the IEEE Engineering in Medicine and Biology Society, Chicago, pp. 2488-2491, October, 1997

[9] Chen-To Tai, *Dyadic Green Functions in Electromagnetic Theory*, 2nd Edition, IEEE PRESS Series on Electromagnetic Waves, IEEE PRESS, New York, 1994

[10] C. A. Balanis, *Antenna Theory: Analysis and Design*, John Wiley & Sons, 1997

[11] J.C. Lin and O.P. Gandhi, "Computational Methods for Predicting Field Intensity," Chapter 9 in *Handbook of Biological Effects of Electromagnetic Fields*, 2nd Edition, Edited by C. Polk and E. Postow, CRC Press, 1996

[12] S. Gabriel, R.W. Lau, and C. Gabriel, "The Dielectric Properties of Biological Tissues: III. Parametric Models for the Dielectric Spectrum of Tissues," *Phys. Med. Biol.* **41**, 2271-2293, November 1996

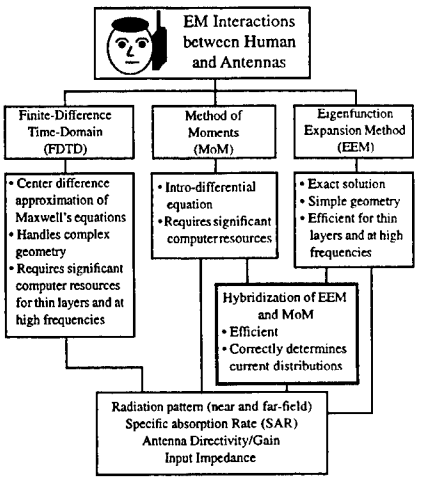

Figure 1 Various numerical approaches for study of EM interactions between human and antennas.

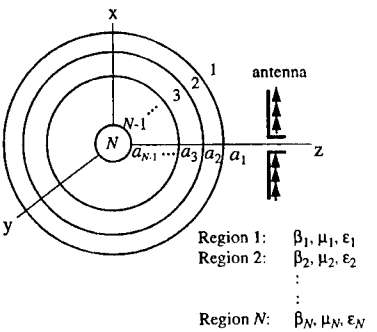

Figure 2 A multi-layered, lossy dielectric sphere radiated by an antenna.

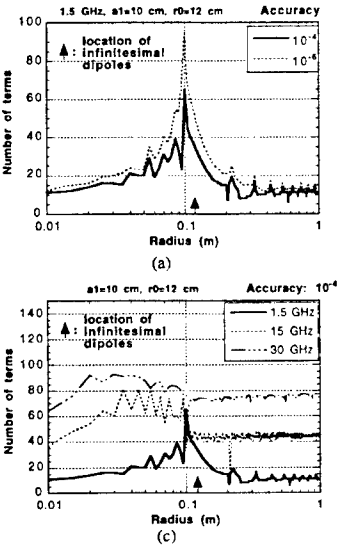

Figure 3 The number of n series terms required for convergence within a specified error (a) at 1.5 GHz and (b) at frequencies 1.5, 15, and 30 GHz. An infinitesimal dipole is located at r=12 cm.

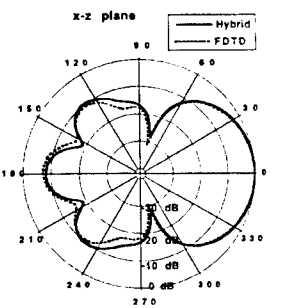

Figure 4 Comparison of normalized radiation patterns obtained with the hybrid technique and FDTD.

Table 1 Electrical parameters of a six-layered head model at 900 MHz and 30 GHz; a_p (cm) is the radius, ε_r the permittivity, σ the conductivity, and ρ ($\times 10^3$ kg/m^3) is mass density of each spherical layer.

Biological Tissues	a_p	900 MHz		30 GHz		ρ
		ε_r	σ	ε_r	σ	
skin	9.00	40.7	0.65	15.52	27.10	1.01
fat	8.90	10.0	0.17	5.91	5.33	0.92
bone	8.76	20.9	0.33	6.12	7.21	1.81
dura	8.35	40.7	0.65	15.52	27.10	1.01
CSF	8.30	79.1	2.14	30.72	57.81	1.01
brain	8.10	41.1	0.86	17.62	27.18	1.04

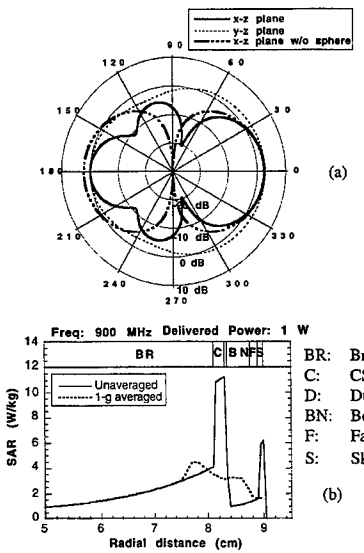

Figure 5 (a) Gain patterns of a $\lambda/2$ antenna with and without a six-layered spherical head. (b) SAR distribution—1-g averaged and unaveraged—along the z axis. Operating frequency of antenna is 900 MHz

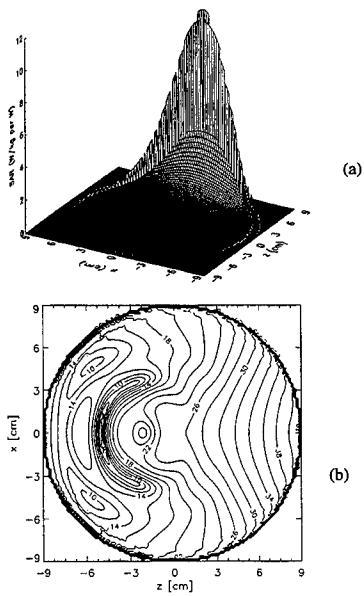

Figure 6 (a) A 3-D surface plot of the SAR distribution inside the six-layered spherical head in the x-z plane, (b) a contour plot of the electric field distribution (log scale) in the x-z plane.

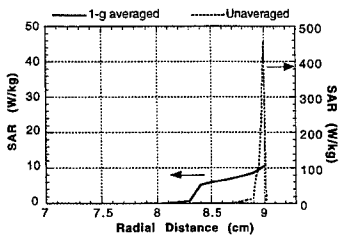

Figure 7 Comparison of the 1-g averaged SAR and unaveraged SAR at 30 GHz along the z-axis. The antenna delivered power is 1W.

Comparison of RGFM and FDTD for Electromagnetic-Tissue Interaction Problems

Michael A. Jensen
Department of Electrical and Computer Engineering
Brigham Young University
Provo, UT 84602
Tel: (801) 378-5736 Fax: (801) 378-6586

I. Introduction

Determining the behavior of electromagnetic fields within and around biological media is a topic which has received steadily increasing attention. Accurate, efficient modeling of complex tissue configurations illuminated by local or distributed sources facilitates the design of antennas for wireless communications [1], allows determination of specific absorption rates within tissue for different exposure scenarios [2], and aids in the optimal design of MRI coils for medical imaging [3]. Several different numerical tools exist which can accommodate the material and geometrical complexities associated with biological tissue, with the Finite Difference Time Domain (FDTD) technique being very widely used due to its flexibility in modeling very general configurations as well as its efficient numerical implementation.

Recently, a new technique has been introduced, known as the Recursive Green's Function Method (RGFM), which shows potential as a viable alternative for analyzing field interactions with biological tissues. This technique uses a recursive formulation to construct the Green's function for an inhomogeneous domain, and subsequently uses a moment method (MOM) solution of a surface integral equation formulation to obtain the fields on the scatterer. To date, the technique has been applied to scalar problems, and therefore is suitable for analyzing two-dimensional configurations. Like the FDTD approach, it easily accommodates very general material and geometrical complexities and provides good numerical efficiency for single frequency or narrow band simulations.

The paper presents a comparison of the RGFM and FDTD approaches when applied to the simulation of two-dimensional biological tissue configurations. A brief summary of each technique highlights their similarities and differences. Several examples are used to compare the two methods in terms of computational accuracy as well as computational resource requirements.

II. FDTD Methodology

The FDTD technique [4] is a widely used numerical approach based upon straightforward discretizations of the integral and differential operators in Maxwell's time-domain equations. Based upon this discretization in space and time, a time-stepping algorithm has been developed in which the magnetic and electric vector fields are computed over the entire spatial grid at each discrete time interval. Because this time stepping approach is explicit, the algorithm does not require a costly linear system solution and is therefore highly efficient from a computational standpoint. The spatial domain is discretized into small rectangular parallelepiped unit cells, and spatially varying material profiles are easily accommodated by simply assigning different material parameters to each cell in the grid.

Because the FDTD technique is based directly upon Maxwell's equations, it includes no information concerning radiation conditions. Therefore, to allow simulation of open structures such as those considered in this paper, artificial absorbing boundary conditions (ABCs) must be used to truncate the computational grid. In this implementation, a perfectly matched layer (PML) ABC [5] is used with quadratically varying electric and magnetic conductivities in an 8 cell layer surrounding the configuration under consideration. In all cases, the PML conductivities are chosen to achieve a reflection coefficient of 10^{-5} at normal incidence. A buffer layer is included between the simulation geometry and the PML, and therefore the computational domain used in the FDTD simulation is somewhat larger than the region containing the inhomogeneous structure. Exact grid sizes used in the following comparisons are given for each configuration.

One obvious advantage of the FDTD technique is its ability to provide the time-domain response of a system to an arbitrary excitation. If the data is Fourier transformed in time, the result is a broad-band frequency response obtained with one simulation. It should be recognized however that this requires storage of the fields over the region of interest at a sample rate at least as high as the Nyquist rate for the highest significant frequency component in the input time-domain waveform. This can clearly lead to significant storage requirements. Furthermore, if only a narrow-band or single-frequency response is required, the user must either perform the transient simulation and discard the unwanted data, or must use a single frequency excitation and step in time until the transient response of the system has decayed to a negligible level. This can imply unnecessary computational time, particularly when the domain includes high-Q dielectrics.

III. RGFM Methodology

The RGFM [6], [7] is a frequency domain technique which solves the generalized scalar Helmholtz equation for the Green's function on an inhomogeneous domain. Much like the FDTD method, the RGFM models the domain by discretizing it into small rectangular cells with each cell being assigned dielectric material parameters. Since the medium is homogeneous within each cell, the Green's function for each cell can be obtained in closed form. Using a formulation based upon differential equation theory, these Green's functions are efficiently combined to construct the Green's function for the entire inhomogeneous domain. This Green's function can then be used in a surface integral equation solution via the MOM to obtain the electric or magnetic fields. Since the integral equation formulation includes the radiation condition, the domain is restricted to the region of inhomogeneity.

This methodology gains its efficiency by selectively computing only required Green's function values. For example, for most scenarios, the integral equation formulation requires knowledge of the Green's function for source points on the domain boundary only. Furthermore, if only fields exterior to the domain are required, then Green's function values for observation points restricted to the boundary are required. This case results in an RGFM asymptotic computational complexity of $O(N^{3/2})$, where N is the number of cells in the domain. This is in contrast to a complexity of $O(N^3)$ associated with a traditional volume integral equation approach. The storage costs are $O(N)$. If fields internal to the domain are required, then values at observation points within the region must also be computed and stored, resulting in computational and storage complexities of $O(N^2)$ and $O(N^{3/2})$ respectively.

Unlike the FDTD technique, the RGFM can only provide data at a single frequency and is therefore relatively costly for wide-band response simulations. However, once the MOM matrix has been computed and factored for the surface integral equation solution, it can be utilized in any single-frequency source configuration. This results in a very efficient technique for examining the system behavior in response

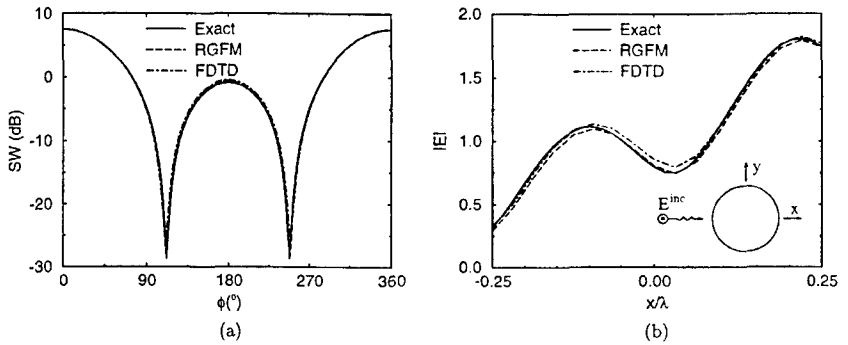

Figure 1: (a) Bistatic scattering width and (b) internal electric field magnitude along the x axis for a circular cylinder with $\epsilon_r = 3$ and radius $\lambda/2$ computed using the RGFM, FDTD, and exact solution algorithms.

to a variety of sources.

IV. Computational examples

In the following computations, the FDTD and RGFM methodologies are compared in terms of accuracy and computational requirements for different biological tissue configurations. To limit the amount of data presented, simulations are restricted to transverse magnetic (TM) illuminations. Similar comparisons have been performed for transverse electric (TE) illuminations, and similar conclusions can be drawn for either scenario. In each case, the cylinder is centered at the origin and the incident plane wave travels in the $+x$-direction, as shown in the inset of Figure 1(b).

A. Low Permittivity Circular Cylinder

Before conducting a comprehensive comparison of the two techniques, we first test the performance of each method without adding the complexities of high dielectric constants or conductivities associated with biological tissue. This test is accomplished by simulating a plane wave incident upon a homogeneous cylinder with relative permittivity of $\epsilon_r = 3$ and no loss. The cylinder diameter is $\lambda/2$, where λ is the free-space wavelength. In the RGFM and FDTD computations, a 16×16 grid is used to model the cylinder, with a stair-step representation of the cylindrical surface. The FDTD uses an additional buffer layer of 8 cells between the cylinder and the PML.

Figure 1(a) illustrates the bistatic scattering width for this configuration computed using the FDTD and RGFM methods. Also included for comparison is the result obtained from the exact eigenfunction series solution. Excellent agreement exists between the results, indicating that the algorithms are functioning as intended. Figure 1(b) represents the electric field magnitude internal to the cylinder along the x axis. As can be seen, both methods faithfully predict the correct field distribution internal to the domain.

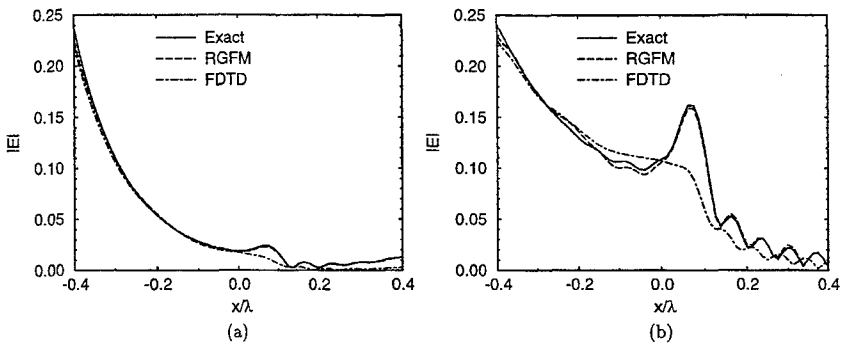

Figure 2: Internal electric field magnitude along the x axis at frequencies of (a) 1 GHz and (b) 2 GHz for a circular cylinder with $\epsilon_r = 58$, $\sigma = 1.21$ S/m, and radius 0.4λ computed using the RGFM, FDTD, and exact solution algorithms.

B. Homogeneous Circular Cylinder

As a first test case, we consider a cylinder similar to that studied in Figure 1 but with a permittivity of $\epsilon_r = 58$, a conductivity of $\sigma = 1.21$ S/m, and a radius of 0.4λ. Both the FDTD and RGFM use a 64×64 grid to represent the geometry in order to maintain approximately 10 cells per internal wavelength. The FDTD uses a 16 cell buffer layer between the cylinder and the PML. To ensure that the fields had attained a steady state condition in the FDTD simulation, runs which stepped for 5, 10, and 15 sinusoidal cycles were performed. It was determined that the transient response had died down to a negligible level by 10 cycles, a computation which required 225 seconds on a Hewlett-Packard HP C180 workstation with 250 MB of core memory. Experimentation with the buffer layer between the cylinder and the PML as well as the PML thickness also demonstrated that the stated grid dimensions provided a reasonably accurate computational scenario. The RGFM computation required a total of 466 seconds, with 362 seconds for the Green's function construction and 104 seconds for the MOM solution. This indicates that for this moderately-sized geometry, the computational resources required for the two algorithms are very similar. Naturally, as the grid sizes increase, the computational and storage efficiency of the FDTD method will make it superior in terms of computational resource utilization.

Figures 2(a) and (b) depict the internal electric field for this geometry along the x axis at frequencies of 1 and 2 GHz respectively. Excellent agreement between the three results can be observed, particularly at 1 GHz. At the higher frequency, the FDTD shows some difficulty in representing the rise in field near the center of the cylinder, but is reasonably accurate over the remainder of the curve. It is interesting to note that at the higher frequency of 2 GHz, the imaginary part of the relative permittivity due to the conductivity of $\sigma = 1.21$ S/m is smaller, resulting in a less pronounced decay of the fields within the structure.

C. Two-Layer Circular Cylinder

As a second example, we consider the case of a two layer inhomogeneous cylinder, as depicted in the inset of Figure 3(a). The geometry has material parameters of $\epsilon_r = 8$, $\sigma = 0.105$ S/m for $\rho \leq 0.2\lambda$, and

$\epsilon_r = 58, \sigma = 1.21$ S/m for $0.2\lambda \leq \rho \leq 0.4\lambda$. Four different frequencies are considered: 100 MHz, 500 MHz, 1 GHz, and 2 GHz. Figures 3(a)–(d) show the internal field along the x axis for these four frequencies. Good agreement can be observed for all three methods, with the FDTD result again departing from the exact solution as the frequency increases. It is noteworthy that for all cases, the RGFM result shows excellent agreement with the exact result.

V. Conclusions

We have presented a comparison of the performance of two techniques – the FDTD and the RGFM methods – for computing the behavior of fields within inhomogeneous biological tissues. The results show that both methods provide relatively accurate representations of the fields, with the FDTD results proving to deviate slightly from the exact solutions as the frequency of operation is increased. Also, for the grid sizes used, both methods have very similar computational resource requirements. However, it is clear that for larger grid sizes the FDTD method will provide superior computational efficiency.

References

[1] M. A. Jensen and Y. Rahmat-Samii, "EM interaction of handset antennas and a human in personal communications", *Proc. of the IEEE*, vol. 83, pp. 7–17, 1995.

[2] P. J. Dimbylow and O. P. Gandhi, "Finite-difference time-domain calculations of SAR in a realistic heterogeneous model of the head for plane-wave exposure from 600 MHz to 3 GHz", *Phys. Med. Biol.*, vol. 36, pp. 1075–1089, 1991.

[3] J. M. Jin, J. Chen, H. Gan, W. C. Chew, R. L. Magin, and P. J. Dimbylow, "Computation of electromagnetic fields for high-frequency magnetic resonance imaging applications", *Phys. Med. Biol.*, vol. 41, pp. 2719–2738, 1996.

[4] A. Taflove, *Computational Electrodynamics: The Finite-Difference Time-Domain Method*, Artech House, Inc., Boston, MA, 1995.

[5] D. S. Katz, E. T. Thiele, and A. Taflove, "Validation and extension to three dimensions of the berenger pml absorbing boundary condition for FD-TD meshes", *IEEE Micro. and Guided Lett.*, vol. 4, pp. 268–270, 1994.

[6] J. D. Freeze and M. A. Jensen, "The recursive green's function method for surface integral equation analysis of inhomogeneous media of maxwell's equations", in *1997 IEEE AP-S Intl. Symposium Digest*, Montreal, Canada, July 13-18 1997, vol. 4, pp. 2342–2345.

[7] J. D. Freeze, M. A. Jensen, and R. H. Selfridge, "A unified Green's function analysis of complicated DFB lasers", *IEEE J. Quantum Electron.*, vol. 33, pp. 1253–1259, 1997.

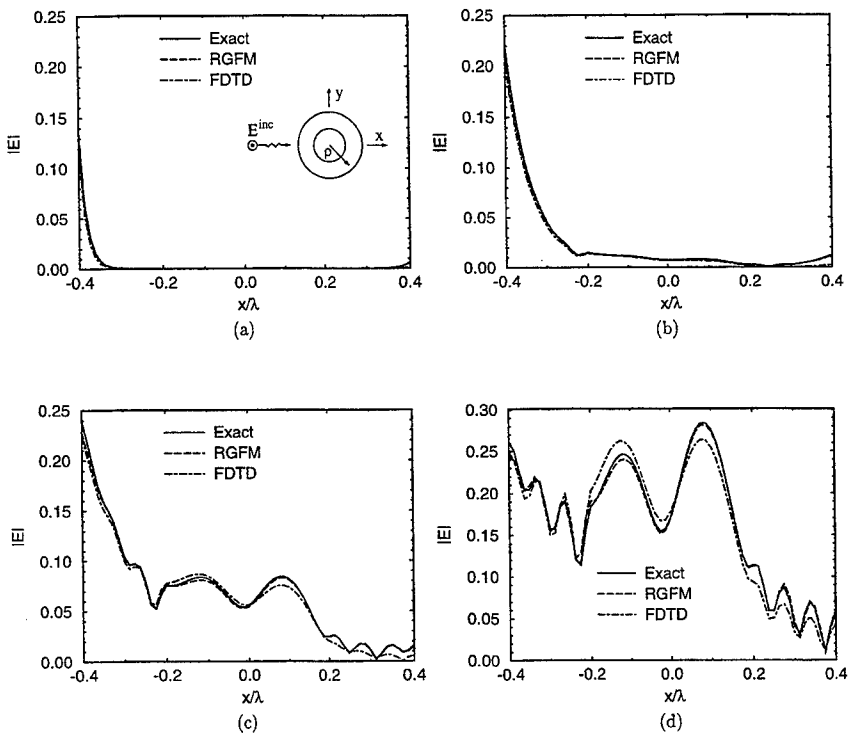

Figure 3: Internal electric field magnitude along the x axis at (a) 100 MHz, (b) 500 MHz, (c) 1 GHz, and (d) 2 GHz for a circular cylinder with $\epsilon_r = 8$, $\sigma = 0.105$ S/m for $\rho \leq 0.2\lambda$, and $\epsilon_r = 58$, $\sigma = 1.21$ S/m for $0.2\lambda \leq \rho \leq 0.4\lambda$ computed using the RGFM, FDTD, and exact solution algorithms.

Isolated vs. *in situ* Human Heart Dosimetry under Low Frequency Magnetic Exposure

Trevor W. Dawson, K. Caputa and Maria A. Stuchly
Dept. Elec. & Comp. Eng., U. Victoria, P.O.Box 3055
Victoria, British Columbia, Canada V8W 3P6

Abstract

Numerical modelling is used to estimate the electric fields and currents induced in the human heart and associated major blood vessels by low-frequency external magnetic fields. The modelling is accomplished using a scalar-potential finite-difference code applied to a 3.6-mm resolution voxel-based model of the whole human body. The main goal of the present work is a comparison between the induced field levels in the heart located *in situ* and in isolation. This information is of value in assessing any health risks due to such fields, given that some existing protection standards consider the heart as an isolated conducting body. It is shown that the field levels differ significantly between these two scenarios. Consequently, data from more realistic and detailed numerical studies are required for the development of reliable standards.

1 Introduction

Induced current density is used in several guidelines as a basis for setting source level limits for human exposure to extremely low frequency (ELF) electric and magnetic fields. These limits are based on known properties of excitable tissues in strong fields [*WHO*, 1984]. However, they do not account for recently-published weak field effects [e.g., *Luben*, 1991], which are less well-established for use in guideline development. In attempts to relate induced fields to source levels, geometrically simple homogeneous isotropic conducting bodies, such as ellipsoids, spheroids, spheres or simple loops, are often used to represent the human body or its parts. Despite their common reliance on a current density upper limit of 10 mA m^{-2}, widely disparate magnetic flux limits are published in various guidelines [*Bailey, et. al.*, 1997]. The variations are largely due to the model size, which is based on the chosen body part (e.g. upper torso vs. heart). Organ location within the body also plays a crucial role [*Reilly*, 1992], and must be accounted for in any realistic modelling.

Anatomically-derived high-resolution voxel-based body models and effective computer codes are now available for detailed dosimetric calculations for human exposure to low-frequency magnetic fields [*Dawson and Stuchly*, 1997; *Dawson et. al.*, 1997]. These tools are used here for a quantitative numerical dosimetric comparison between the human heart located within the body (*in situ*) or in isolation. The electric fields and current densities induced by uniform magnetic fields of three orthogonal orientations are modelled in both scenarios, and the differences are evaluated. The induced fields are 2–3 times greater for the *in situ* case, for all three source orientations. The computed values pertain to 60 Hz, but can be scaled to higher (up to 100 kHz) frequencies using the frequency and tissue conductivity ratios. The associated error should be below 5%.

The data provided herein are anticipated to be of use in setting health protection guidelines based on the induced current thresholds.

2 Methods

The full-body model used is fully described elsewhere [*Dawson et al.*, 1997]. It consists of a total of 1 736 873 voxels with 3.6-mm edges, with an approximate height and mass of 1.77 m and 76 kg. The heart model is a subset

consisting of heart tissue and associated blood (smaller features cannot be resolved at the 3.6-mm level). The heart model has a bounding box spanning $36 \times 32 \times 32$ voxels, or 12.96 cm $\times$ 11.52 cm $\times$ 11.52 cm. Figure 1 shows

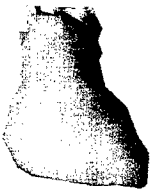

Figure 1: A smoothed view of the external surface of the voxel-based heart model.

an idealized external view of the model, and Table 1 lists the conductivity values used for its two homogeneous

Table 1: Heart component conductivity values.

Blood	0.7 Sm^{-1}	Muscle	0.1 Sm^{-1}

components.

The scalar-potential finite-difference (SPFD) method used for the numerical calculations is based on Stevenson's method [*Van Bladel,* 1985]. For magnetic excitation, the internal electric field has the representation

$$\boldsymbol{E}^{\mathrm{i}}(\boldsymbol{x}) = -i\omega \left\{ \boldsymbol{A}_0(\boldsymbol{x}) + \nabla\psi(\boldsymbol{x}) \right\}. \tag{1}$$

Here the static limit of the applied magnetic field is described in terms of a vector potential as $\boldsymbol{B}_0^{\mathrm{e}}(\boldsymbol{x}) = \nabla \times \boldsymbol{A}_0(\boldsymbol{x})$, and $\psi(\boldsymbol{x})$ is a scalar potential to be determined. The divergence of the associated conduction current vanishes, leading to the differential equation

$$\nabla \cdot [\sigma(\boldsymbol{x})\, \nabla\psi(\boldsymbol{x})] = -\nabla \cdot [\sigma(\boldsymbol{x})\, \boldsymbol{A}_0(\boldsymbol{x})] \tag{2}$$

and boundary condition

$$\sigma(\boldsymbol{x})\, \hat{\boldsymbol{n}}(\boldsymbol{x}) \cdot \nabla\psi(\boldsymbol{x}) = -\sigma(\boldsymbol{x})\, \hat{\boldsymbol{n}}(\boldsymbol{x}) \cdot \boldsymbol{A}_0(\boldsymbol{x}). \tag{3}$$

The numerical implementation is based on a finite difference approximation of (2) [*Dawson et al.,* 1997]. Discrete values for the scalar potential are defined at voxel vertices. They are related by a sparse system of linear equations, which is amenable to solution using the Conjugate Gradient Method [*Dawson et al.,* 1997]. Data for both the *in situ* and isolated heart scenarios were computed under excitation by three orthogonal 60-Hz, 1-μT magnetic source orientations, for a total of six basic sets. The source orientations with respect to the upright body model are B_x (left-to-right), B_y (back-to-front) and B_z (foot-to-head). The *in situ* field values are subsets of previously-described whole-body data [*Dawson et al.,* 1997], using only those voxels corresponding to the isolated heart model. The isolated heart data were computed separately, treating the isolated composite heart model as a distinct smaller conductor. The final data are in one-to-one voxel-wise correspondence between the two heart models.

3 Results and Discussion

Figure 2 shows the amplitudes of the electric field (top row) and current density (bottom row) in a horizontal cross section, through the mid-plane of the 17^{th} voxel layer from the bottom of the heart in isolation (left column) and *in situ* (right column). The source is directed from left to right. The electric field patterns in the top row differ significantly between the two scenarios, and the peak values in the *in situ* case are approximately a factor of two greater than in the isolated heart. In the bottom row, the direct impact of the highly conducting blood is to

make the current density distribution appear more similar between the two scenarios, but there still are obvious differences; moreover, the peak values indicated in the *in situ* case (lower right) are approximately 2.5 times greater than the corresponding values for the isolated heart (lower left).

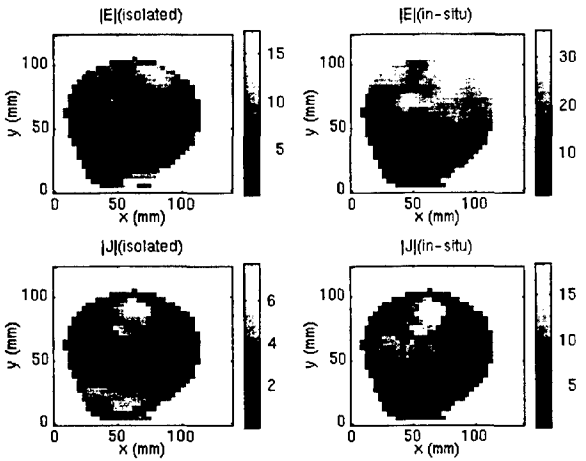

Figure 2: Amplitudes of the electric field (top row) and current density (bottom row) in a central horizontal cross section through the heart in isolation (left column) and *in situ* (right column) under excitation by a 60-Hz, 1-μT source directed from left to right with respect to the upright human body. Electric field and current density units are microvolts per meter and microamperes per square meter, respectively.

In order to quantify the differences between the two heart scenarios, three global scalar measures of electric field amplitude are compared for the various tissue groups (heart, blood and composite). These measures are the average, root-mean-square, and variance, whose values for a vector field $\boldsymbol{F}$ are defined by

$$\mathrm{Avg}\{\boldsymbol{F}\} \equiv \frac{1}{N}\sum_i |\boldsymbol{F}_i|, \qquad \mathrm{Rms}\{\boldsymbol{F}\} \equiv \sqrt{\frac{1}{N}\sum_i |\boldsymbol{F}_i|^2}, \tag{4}$$

and

$$\mathrm{Var}\{\boldsymbol{F}\} \equiv \sqrt{\frac{1}{N-1}\sum_i \left(|\boldsymbol{F}_i| - \mathrm{Avg}\{\boldsymbol{F}\}\right)^2} \quad \left(\approx \sqrt{\mathrm{Rms}\{\boldsymbol{F}\}^2 - \mathrm{Avg}\{\boldsymbol{F}\}^2}\right). \tag{5}$$

In each case the summation index i ranges over all N voxels in the appropriate tissue group.

The left column of Figure 3 shows the above measures for the electric field, with the average, variance and root-mean-square values in the top, middle and lower panels respectively. Each panel depicts the results for both heart model scenarios by tissue group, scenario, and source orientation. The data within each tissue group are presented in sets of three bars, corresponding to the three source orientations according to the accompanying legend. Heart tissue groups are designated as blood (B), heart tissue (H) and composite (H+B), and the scenarios as *in situ* (sit) and isolated (iso).

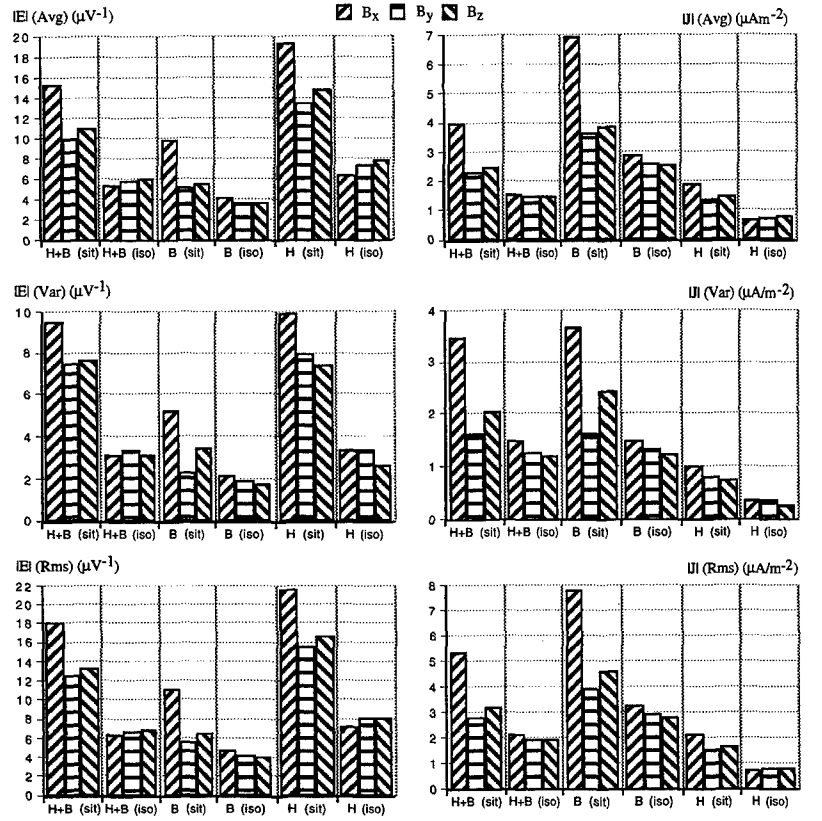

Figure 3: Average (top row), variance (middle row) and root mean square (bottom row) values of the electric field (left column, in microvolts per meter) and current density amplitude (right column, in microamperes per square meter) for the tissue groups in the two scenarios and under three orthogonal excitation directions. The labels 'H' and "B' refer to the voxels coded as 'heart' and 'blood' respectively, while 'H+B' refers to the composite heart model. The isolated and *in situ* cases are labelled as '(iso)' and '(sit)', respectively. All sources are 60 Hz at 1 μT.

For all three measures, it is evident that the heart model in isolation somewhat resembles a sphere, in that the induced field levels in the composite tissue group do not vary significantly over the three source orientations. This is in contrast to the *in situ* case, in which the effects of the whole-body current distribution lead to significantly higher levels in all three measures, as well as to a much greater dependence on source orientation.

It is also from evident from Figure 3 that the *in situ* measures all exceed their corresponding isolated heart values. This is clarified in Table 2, which gives numerical values of the ratios of the various *in situ* electric field

Table 2: Ratios between the *in situ* and isolated values of the various scalar measures for the electric field magnitudes.

	B_x			B_y			B_z		
Tissue	Avg	Var	Rms	Avg	Var	Rms	Avg	Var	Rms
Composite	2.83	3.07	2.89	1.72	2.23	1.86	1.83	2.46	1.98
Blood	2.41	2.47	2.42	1.41	1.24	1.38	1.54	1.96	1.63
Heart	3.03	2.98	3.02	1.84	2.38	1.94	1.92	2.76	2.03

measures to their associated isolated values. These ratios range from a minimum of 1.24 (for the variance in the blood under back-to-front excitation) to a maximum of 3.07 (for the variance in the composite tissue under left-to-right excitation). It is also clear from this table that the ratios are most typically in the range of 1.5—3 times greater for the *in situ* case.

For comparison with the model results, Table 3 gives analytic values of these measures for an isolated homo-

Table 3: Comparison of analytic electric field measures in a homogeneous spherical approximation with numerical values obtained from the voxel-based isolated heart. The first column defines the field measure, with its analytical value for a homogeneous sphere of radius a (in meters) in an external field of strength B_0 (in Tesla) and frequency f (in Hertz) given in the second column, where the constant $C = \pi B_0 f a$. The values in the third column (in microvolts per meter) pertain to the particular case of a sphere of radius 0.06 m in a 1-μT, 60-Hz magnetic field. The values in the final column are the corresponding approximate numerical values for the isolated heart model, read from the 'H+B (iso)' portions of the left column of Figure 3.

Measure	Homogeneous Sphere		Heart (iso)
$\text{Avg}\{\boldsymbol{E}\} = \frac{1}{V}\int_V \lvert\boldsymbol{E}\rvert\, dV$	$(3\pi/16)\,C$	$= 6.662$	≈ 6
$\text{Var}\{\boldsymbol{E}\} = \sqrt{\frac{1}{V}\int_V (\lvert\boldsymbol{E}\rvert - \text{Avg}\{\boldsymbol{E}\})^2\, dV}$	$\sqrt{2/5 - (3\pi/16)^2}\,C$	$= 2.604$	≈ 3
$\text{Rms}\{\boldsymbol{E}\} = \sqrt{\frac{1}{V}\int_V \lvert\boldsymbol{E}\rvert^2\, dV}$	$\sqrt{2/5}\,C$	$= 7.153$	≈ 7

geneous sphere. The third column gives values for a sphere of radius 0.06 m, as used in several standards. The half-widths of the present heart model bounding box are 0.0648 m, 0.0576 m and 0.0576 m, and so roughly conform to the spherical approximation. These measures can be compared to the composite isolated heart values plotted in Figure 3. There it is evident that the average, variance and root-mean-square values are approximately 6, 3 and 7 μV m^{-1}, as indicated in the final column of Table 3, roughly independent of source orientation. These values are in reasonable agreement with the analytical values given in Table 3. Thus, use of a spherical model of the heart is perhaps not inappropriate, if the goal is to model the heart in isolation. This is clearly not a good approximation for the *in situ* case, however.

The corresponding global scalar measures for the current density amplitude are depicted in the right column of Figure 3. In all cases, the overall levels are again higher for the *in situ* scenario.

The degree to which the *in situ* modeling enhances the current density magnitudes in the heart over the isolated scenario is emphasized in Table 4, which gives the ratios of the various *in situ* measures to their corresponding isolated values. The ratios for the blood and heart are the same as for the electric field (Table 4), since each is modelled as a homogeneous conductor. These ratios range from a minimum of 1.24 (for the variance in the blood under back-to-front excitation) to a maximum of 3.03 (for the average in the heart muscle under left-to-right excitation). As was the case for the electric field measures, modelling the heart in isolation typically underestimates the induced current levels by a factor of 1.5—3.

Table 4: Ratios between the *in situ* and isolated values of the various scalar measures for the current density magnitudes.

	B_x			B_y			B_z		
Tissue	Avg	Var	Rms	Avg	Var	Rms	Avg	Var	Rms
Composite	2.55	2.36	2.46	1.53	1.30	1.44	1.65	1.71	1.68
Blood	2.41	2.47	2.42	1.41	1.24	1.38	1.54	1.96	1.63
Heart	3.03	2.98	3.02	1.84	2.38	1.94	1.92	2.76	2.03

4 Conclusions

This work has presented a numerical dosimetric comparison of quasi-uniform low frequency magnetic induction in the human heart located *in situ* and in isolation. The identical heart model was used in both scenarios. Being anatomically-derived, the model is realistic to within the limitations of the 3.6-m resolution. Using a variety of field measures, it has been shown that the induced electric field and current density levels are consistently about 1.5–3 times greater for the *in situ* case, for all orientations of the uniform magnetic source fields. Although based on a single geometric realization of a particular human body model, the data presented indicate the need for highly realistic numerical modelling in the development of viable protection standards for human exposure to low-frequency magnetic fields. In particular, it is clearly inadequate to base protection standards on simple geometric models of critical human body components considered in isolation.

Acknowledgment

This work was supported by EPRI contract No. WO 2966-14.

References

[1] World Health Organization. *Environmental Health Criteria 35: Extremely Low Frequency (ELF) Fields.* World Health Organization, Geneva, Switzerland, 1984.

[2] R. A. Luben. Effects of low-energy electromagnetic fields (pulsed and dc) on membrane transduction processes in biological systems. *Health Physics*, 61:15–28, 1991.

[3] William H. Bailey, Steave H. Su, T. Dan Bracken, and Robert Kavet. Summary and evaluation of guidelines for occupational exposure to power frequency electric and magnetic fields. *Health Physics*, 73(3):433–453, September 1997.

[4] J. Patrick Reilly. *Electrical Stimulation and Electropathology.* Cambridge University Press, New York, NY, 1992.

[5] Trevor W. Dawson and Maria A. Stuchly. An analytic solution for verification of computer models for low-frequency magnetic induction. *Radio Science*, 32(2):343–368, March-April 1997.

[6] Trevor W. Dawson, Kris Caputa, and Maria A. Stuchly. Influence of human model resolution on computed currents induced in organs by 60-hz magnetic fields. *Bioelectromagnetics Journal*, 18(7):478–490, 1997.

[7] S. Gabriel, R. W. Lau, and C. Gabriel. The dielectric properties of biological tissues: Ii. measurements in the frequency range 10 Hz to 20 GHz. *Phys. Med.Biol.*, **41**:2251–2269, 1996.

[8] J. Van Bladel. *Electromagnetic Fields.* Hemisphere Publishing Corporation, Washington D.C., revised printing edition, 1985.

Faster than Fourier -- Ultra-Efficient Time-to-Frequency Domain Conversions for FDTD Applied to Bioelectromagnetic Dosimetry

Cynthia M. Furse
Department of Electrical and Computer Engineering
Utah State University
Logan, Utah 84322-4120
E-mail: furse@alpha.ece.usu.edu
Phone: (435) 797-2870
Fax: (435) 797-3054

Abstract

Two highly efficient methods of computing magnitude and phase from time-domain data have been developed. These methods, based on solution of linear equations, are found to be equally accurate and more efficient than Fourier transform methods (DFT and FFT) for limited numbers of frequencies. These methods provide a significant savings in computation time and storage requirements for FDTD simulations which require a large number of time-to-frequency domain conversions. The effectiveness of these methods are demonstrated for analysis of a millimeter-resolution human model underneath a 60-Hz power line and calculation of coupling of a cellular telephone to the human head.

1. Introduction

Many applications of the finite-difference time-domain (FDTD) method require conversion of time-domain field data to magnitude and phase (frequency-domain data) over large regions of the model. Applications include bioelectromagnetic dosimetry calculations of the human body for analysis of cellular telephones [1-4], power lines [5,6], and other EM-safety studies [7,8], radar cross section calculations [9], and calculations of S-parameters [10]. For multiple-frequency calculations, this has traditionally been accomplished with either the Fast Fourier transform (FFT) [11-12] or the Discrete Fourier transform (DFT) [13-14]. For single-frequency calculations, this has been done with either of the Fourier transform methods.

Fourier transform calculations provide an accurate time-to-frequency domain conversion, however their computational requirements are very high. The DFT requires approximately as much time as the FDTD calculations themselves, and FFT computations are even more expensive, particularly when a limited number of frequencies are of interest [15]. Desampling has been used to minimize these computational requirements [14]. Of even greater concern for many calculations is the computer memory required for the complete simulation. The Fourier transform methods require approximately as much computer storage as the FDTD simulation itself for each frequency of interest. This quickly limits the size of models which can be analyzed over any broad frequency range.

A third problem which plagues Fourier transform computations is that they are very difficult to use for low frequency simulations, where the sampling resolution of the wave form is very high. For single-frequency (CW) simulations, the Fourier transform calculations must be made over a full half-cycle of the converged sine wave. This requires at least an additional half-cycle of FDTD calculations, which can be difficult or impossible for low frequency calculations, and which increases the cumulative error inherent in the finite-difference calculations .

This paper presents two methods that overcome these limitations and have the added advantage that they are extremely simple to program. Both methods are based on the solution of linear equations. The first method, for use with single-frequency analysis, is significantly more efficient than Fourier transform methods, and can be applied effectively for an extremely broad frequency range from the low kHz to high GHz and beyond. This method has the added advantage that for many applications, it can be applied with virtually no memory or computational requirement (beyond the FDTD requirements themselves).

The second method is an extension of the first method, and can be used for multi-frequency analysis. Theoretically, this method minimizes computational and memory requirements for any simulation. However, computer round-off errors limit this method, somewhat, so trade-off curves are presented which show that this multi-frequency extension is the most efficient method for up to about 30 frequencies, and that the single-frequency method is preferable for larger numbers of frequencies.

These two methods are presented below.

2. Two Equations - Two Unknowns Method

A simple, direct method for solving for the magnitude and phase of sine wave in the time-domain is based on writing two equations in two unknowns (magnitude and phase) for the time-domain fields, and then solving them directly for the magnitude and phase. At a given location in space, we can write

$$\begin{aligned} A \sin(\omega t_1 + \theta) &= q_1 \\ A \sin(\omega t_2 + \theta) &= q_2 \end{aligned} \tag{2}$$

where A is the magnitude, θ is the phase angle, and ω ($= 2 \pi F_i$) is the angular frequency. At two times, t_1 and t_2, the values q_1 and q_2 are obtained from the FDTD simulation. Therefore, these equations can be solved for the unknowns, A and θ, to give direct relationships for these values:

$$\begin{aligned} \theta &= \tan^{-1}\left[\frac{q_2 \sin(\omega t_1) - q_1 \sin(\omega t_2)}{q_1 \cos(\omega t_2) - q_2 \cos(\omega t_1)}\right] \\ A &= \left|\frac{q_1}{\sin(\omega t_1 + \theta)}\right| \end{aligned} \tag{3}$$

This new method provides dramatic savings in computer time and memory over the traditional methods of peak detection or Fourier transformation shown in Table 1. These savings are obtained because both the peak detection and Fourier transform methods require calculations to be made over the last half cycle of the simulation, and the two-equation method requires only a single calculation.

The choice of t_1 and t_2 depends on the simulation. For most FDTD simulations, the spatial resolution Δx, is on the order of λ / 10 to λ / 100. For these simulations, t_1 and t_2 can be the last two time steps of the simulation. For higher-resolution simulations, the time resolution is also high ($\Delta t = \Delta x/2c$), so q_1 and q_2 are nearly equal if t_1 and t_2 are so close. This results in errors due to numerical round-off when calculating A and θ. For these simulations, it is better to choose t_1 to be a few time steps (say, 50) before the end of the simulation, and t_2 to be the final time step. Optimized sample spacings can be found using the method described in Section 3 below. In this case, the number of frequenies is 1, and the condition number of the matrix as a function of sample spacing is indicative of the resultant accuracy of the solution.

The equations in (3) can be programmed one of two ways, depending on t_1 and t_2. The first is to store (or output to disk) the value of q_1 at time step t_1, and then when the final time step, t_2, is reached, the values of A and θ can be calculated. This is necessary if t_1 and t_2 are not subsequent time steps. An alternate method of eliminating the memory requirement can be used when t_1 and t_2 are taken to be the last two time steps. For the final time step, q_1 is stored in a single location (not an array), then q_2 is calculated from the FDTD algorithm, then A and θ are calculated and output to disk. This is then repeated for each location.

This method provides accurate magnitude and phase calculations for simulations with clean, sine wave output. Noise and dc offsets will cause errors. Ramped sine excitations known not to cause a dc offset should be used [16] or a

pulse with a very smooth turn-on [17]. Ramped sine excitations have also been observed to reduce or eliminate numerical noise in FDTD simulations [18].

The computational requirements for this method are shown in Table 1. For comparison, computational requirements for the FDTD algorithm itself and for the Fourier transform methods are also included. These requirements are also plotted in Figure 1, for a particular example. Values for the FFT are not plotted, because it has already been shown [15] to be less efficient than the DFT.

3. N-Equations N-Unknowns

The two-equations 2-unknowns method can be extended to multiple frequencies. In this case, N-equations are solved for N-unknowns (amplitude and phase at each frequency of interest). This requires samples at N time steps and results in the following equations for two frequencies:

$$\begin{aligned} A_1 \sin(\omega_1 t_1 + \theta_1) + A_2 \sin(\omega_2 t_1 + \theta_2) &= q_1 \\ A_1 \sin(\omega_1 t_2 + \theta_1) + A_2 \sin(\omega_2 t_2 + \theta_2) &= q_2 \\ A_1 \sin(\omega_1 t_3 + \theta_1) + A_2 \sin(\omega_2 t_3 + \theta_2) &= q_3 \\ A_1 \sin(\omega_1 t_4 + \theta_1) + A_2 \sin(\omega_2 t_4 + \theta_2) &= q_4 \end{aligned} \qquad (4)$$

This can be extended to multiple frequencies:

$$q_i = \sum_{n=1}^{N} A_n \sin(\omega_n t_i + \theta_n) \quad i = 1,2,3,\ldots,2N \qquad (5)$$

Using trigonometric identities on the sine function, this can be broken into a matrix equation which can be solved for functions ($A_n\cos(\theta_n)$) of A_n and θ_n .

$$\begin{bmatrix} \sin(\omega_1 t_1) & \cos(\omega_1 t_1) & \sin(\omega_2 t_1) & \cos(\omega_2 t_1) & \ldots & \sin(\omega_N t_1) & \cos(\omega_N t_1) \\ \sin(\omega_1 t_2) & \cos(\omega_1 t_2) & \sin(\omega_2 t_2) & \cos(\omega_2 t_2) & \ldots & \sin(\omega_N t_2) & \cos(\omega_N t_2) \\ \vdots & \vdots & \vdots & \vdots & & \cdots & \cdots \\ \sin(\omega_1 t_N) & \cos(\omega_1 t_N) & \sin(\omega_2 t_N) & \cos(\omega_2 t_N) & \ldots & \sin(\omega_N t_N) & \cos(\omega_N t_N) \end{bmatrix} \begin{bmatrix} A_1\cos(\theta_1) \\ A_1\sin(\theta_1) \\ A_2\cos(\theta_2) \\ A_2\sin(\theta_2) \\ \vdots \\ A_N\cos(\theta_N) \\ A_N\sin(\theta_N) \end{bmatrix} = \begin{bmatrix} q_1 \\ q_2 \\ \vdots \\ q_N \end{bmatrix}$$

A standard matrix solution method such as Gaussian elimination via Linpack is used to obtain the vector of functions, and the unknowns A_n and θ_n are found from these functions.

This specific solution method requires a multi-frequency source in the form of (5), which does not utilize methods such as sine wave ramping to prevent high frequency transients or dc offsets. These specialized ramps could be included in the source type, and the same solution method could be followed. This would change the specifics of the matrix above. In practice, this was not found to be necessary, as the human dosimetry models have not shown themselves to be highly susceptible to either spurious transients or dc offsets.

In theory, the method above provides an exact conversion from time to frequency domain. In practice, however, the matrix can be ill-conditioned. This happens when the cosine and sine samples become very close together so that they are numerically indistinguishable. In particular, this occurs when the time samples (t_1, t_2, t_3, etc.) are too close together, when a very large number of frequencies are involved, or when the frequencies are too close together. There is a also a problem when their relative magnitudes are several orders of magnitude different. This paper discusses each of these problems and the efficiency tradeoffs for solving them. In practice, this method, which we will call "N-equations N-unknowns" or (NENU) is the most efficient method of converting from time to frequency domain data for up to about 30 frequencies, which covers most of the applications of FDTD to-date.

As an example of the application of the NENU method, solutions were computed for 25 different frequencies, as a function of the spacing of the time samples ($t_2 = t_1 + n\Delta t$). The frequencies are evenly-spaced from 0.1 to 1 MHz, and have equal magnitudes. The time resolution Δt is $\Delta x / 2c$, where Δx is the spatial resolution of the FDTD grid. And $\Delta x = \lambda_{min} / 20$. In the first case (Figure 2a), the amplitudes and phases are computed using the simple Ax=b form, where the matrix A and vector b are given above. The vector x is computed using standard Gaussian-elimination solution of the matrix equation. The magnitudes and phases are computed from the vector x. Errors of less than 1% are obtained when samples are spaced at least 7 samples apart. In the second case (Figure 2b), the x vector is computed using the Singular Value Decomposition and related psuedo-inverse. This method provides a significant improvement in solutions of ill-conditioned matrices. Using SVD provides accurate calculations (less than 1% error) for all time sample spacing. This enables calculations of magnitude and phase of 25 frequencies using the last 50 converged time steps of the FDTD simulation.

Figure 3 shows the significance of the advantage of using SVD for these calculations. When the number of frequencies evenly-spaced from 0.1 to 1MHz is increased to 100, the SVD can provide calculations with less than 1% error for sample spacings greater than 4, whereas the direct method without SVD is far more sporadic and requires at least a spacing of 21 samples. Furthermore it should be noted that merely increasing the sample spacing beyond this minimum does not necessarily improve the solution.

4. Conclusions and Summary

Figure 1 shows the relative cost of the Fourier transform, 2E2U and NENU methods. For up to 30 frequencies, the NENU method is most efficient. The cost of taking the pseudo-inverse of the matrix for this method eventually outstrips the cost of the additional FDTD simulations required in the 2E2U method, and after 30 frequencies the 2E2U method is more efficient. Both of these methods are more efficient than the DFT method.

Memory and storage are tradeoffs for these methods. As noted in Table 1, the DFT must store a complex value (equal to 2 real values) for every location and parameter of interest. The 2E2U can completely eliminate this requirement if the sampling resolution is sufficient to allow computation of magnitude and phase from the final two time steps of the simulation. The NENU method must store the matrix which is $(2\ NF)^2$ where NF is the number of frequencies for each location and parameter of interest. These values would generally be written to disk, with final solution being done as a post-processing step, but this may be prohibitively expensive for some applications.

References

[1] O. P. Gandhi, G. Lazzi, and C. M. Furse, "Electromagnetic Absorption in the Human Head and Neck for Mobile Telephones at 835 and 1900 MHz," *IEEE Transactions on Microwave Theory and Techniques*, Vol. 44, October 1996, pp. 1884-1897

[2] M. Okoniewski, M.A. Stuchly, "A Study of the Handset Antenna and Human Body Interaction," *IEEE Transactions on Microwave Theory and Techniques*, Vol. 44, October 1996, pp. 1855-1864

[3] M. A. Jensen and Y. Rahmat-Samii, "EM Interaction of Handset Antennas and a Human in Personal Communication," *Proc. IEEE*, Vol. 83, pp. 7-17, 1995.

[4] P. J. Dimbylow and S. M. Mann, "SAR Calculations in an Anatomically Based Realistic Model of the Head for Mobile Communication Transceivers at 900 MHz and 1.8 GHz," *Physics in Medicine and Biology*, Vol. 39, pp. 1537-1553, 1994.

[5] O.P. Gandhi, J.Y. Chen, "Numerical Dosimetry at Power Line Frequencies Using Anatomically-Based Models," *Bioelectromagnetics Supplement* 1992, pp. 43-60

[6] C. M. Furse, J. Y. Chen, and O. P. Gandhi, "Calculation of Electric Fields and Currents Induced in a Millimeter-Resolution Human Model at 60 Hz Using the FDTD Method," to appear in *Bioelectromagnetics*.

[7] R.A. Hart , O.P. Gandhi, "Endogenous electric fields and current densities in an anatomical model of the human body due to the electrical activity of the beating heart," *submitted to IEEE Transactions on Biomedical Engineering 1997*

[8] O. P. Gandhi, Y. G. Gu, J. Y. Chen, and H. I. Bassen, "Specific Absorption Rates and Induced Current Distributions in an Anatomically Based Human Model for Plane-Wave Exposure," Health Physics, Vol. 63, pp. 281-290, 1992.

[9] A. Taflove, K. Umashankar, "Review of FD-TD Numerical Modeling of Electromagnetic Wave Scattering and Radar Cross Section," *Proc. IEEE*, Vol.77, pp. 682-698, May 1989

[10] T. Shibata, T. Hayashi, T. Kimura, "Analysis of Microstrip Circuits Using Three-Dimensional Full-Wave Electromagnetic Field Analysis in the Time Domain," *IEEE Trans. Microwave Theory and Techniques*, June 1988, pp. 1064-1070

[11] J.C. Olivier, "Mutual Coupling Between Waveguide Apertures Mounted on a Common Conducting Surface Using a Time- and Fourier-Gated Pulsed FDTD Method," *IEEE Trans. Microwave Theory and Techniques*, Feb. 1993, pp. 290-297

[12] A.C. Cangellaris, M. Gribbons, G. Sohos, "A Hybrid Spectral/FDTD Method for the Electromagnetic Analysis of Guided Wave Structures," *IEEE Microwave and Guided Wave Letters*, Oct. 1993, pp. 375-377

[13] C.M. Furse, S.P. Mathur, O.P. Gandhi, "Improvements to the Finite-Difference Time-Domain Method for Calculating the Radar Cross Section of a Perfectly Conducting Target," *IEEE Trans. Microwave Theory and Techniques*, Vol. MTT-38, No. 7, July 1990, pp. 919-927

[14] Z. Bi, Y.Shen, K.Wu, J.Litva, "Fast Finite-Difference Time-Domain Analysis of Resonators Using Digital Filtering and Spectrum Estimation Techniques," *IEEE Trans. Microwave Theory and Techniques*, pp. 1611-1619, 1992

[15] C.M. Furse, O.P. Gandhi, "Why the DFT is faster than the FFT for time-to-frequency domain conversion," *IEEE Microwave and Guided Wave Letters* , Vol. 6, No. 10, 1995, pp. 326-328

[16] C.M. Furse, D.H. Roper, D.N. Buechler, D.A. Christensen, C.H. Durney, "The Problems and Treatment of DC Offsets in FDTD Simulations," submitted to *IEEE Transactions on Antennas and Propagation*

[17] D.S. Katz, E.T. Thiele, A. Taflove, "Validation and Extension to Three Dimensions of the Berenger PML Absorbing Boundary Condition for FD-TD Meshes," *IEEE Microwave and Guided Wave Letters* , 4(8), pp. 268- 270, August, 1994

[18] Buechler DN, Roper DH, Christensen DA, Durney CH (1995): Modeling sources in the FDTD formulation and their use in quantifying source and boundary condition errors. To appear in *IEEE Trans. Microwave Theory and Techniques* 43(4).

Table 1: Computational Requirements for Time-to-Frequency Conversion Methods

	Multiplications or Divisions	Additions or Subtractions	Number of FDTD simulations	Real Storage Locations
FDTD only	$9\ (N_{FDTD})(N_{xyz})$	$8\ (N_{FDTD})(N_{xyz})$		$7\ (N_{xyz})$
DFT	$(2^{**})\ (N_{FDTD})(N_{Pxyz})\ (N_P)(N_F)$	$2\ (N_{FDTD})(N_{Pxyz})\ (N_P)(N_F)$	N_F (CW FDTD)	$2(N_P)\ (N_F)\ (N_{Pxyz})$
FFT (Radix 2: N_{FDTD} must be 2^n)	$(2^{**})\ (N_{FDTD}/2)\ \log_2(N_{FDTD})\ (N_{Pxyz})\ (N_P)$	$(N_{FDTD}/2)\ \log_2(N_{FDTD})\ (N_{Pxyz})\ (N_P)$	1 (pulsed FDTD)	$2(N_P)\ (N_{Pxyz})\ (N_{FDTD})$
2E2U (storing t_1)	$4\ (N_P)(N_{Pxyz})$	$4\ (N_P)(N_{Pxyz})$	N_F (CW FDTD)	$(N_P)\ (N_{Pxyz})$
2E2U (no storage -- use last two time steps)	$4\ (N_P)(N_{Pxyz})$	$4\ (N_P)(N_{Pxyz})$	N_F (CW FDTD)	0
NENU	$9(N_{\Delta FDTD})(N_{xyz}) + 8(N_{Pxyz})(N_P)(N_F)\ (N_F\text{-}1/2)(N_F\text{+}1/2)/3 + 8(N_{Pxyz})(N_P)(N_F)\ (N_F\text{-}1/2)$	$8(N_{\Delta FDTD})(N_{xyz}) + 8(N_{Pxyz})(N_P)(N_F)\ (N_F\text{-}1/2)(N_F\text{+}1/2)/3$	1 (pulsed FDTD)	$(2N_F)^2\ (N_{Pxyz})\ (N_P)$

		Values used in Figure 1
N_{FDTD}	= # of FDTD time steps	= 2000
N_{xyz}	= # of FDTD cells	= 100 x 100 x 100
N_F	= # of frequencies of interest	
N_P	= # of parameters of interest	= 6 (all **E** and all **H**)
N_{Pxyz}	= # of FDTD cells of interest	= 100 x 100 x 100

$N_{\Delta FDTD}$ = additional FDTD time steps required (depends on simulation)

** Complex multiplications are given the weight of approximately 2 real multiplications

Table 1: Computational Requirements for Time-to-Frequency Conversion Methods

	Multiplications or Divisions	Additions or Subtractions	Number of FDTD simulations	Real Storage Locations
FDTD only	$9\,(N_{FDTD})(N_{xyz})$	$8\,(N_{FDTD})(N_{xyz})$		$7\,(N_{xyz})$
DFT	$(2^{**})\,(N_{FDTD})(N_{Pxyz})$ $(N_P)(N_F)$	$2\,(N_{FDTD})(N_{Pxyz})$ $(N_P)(N_F)$	N_F (CW FDTD)	$2(N_P)$ (N_F) (N_{Pxyz})
FFT (Radix 2: N_{FDTD} must be 2^n)	$(2^{**})\,(N_{FDTD}/2)$ $\log_2(N_{FDTD})\,(N_{Pxyz})$ (N_P)	$(N_{FDTD}/2)$ $\log_2(N_{FDTD})\,(N_{Pxyz})$ (N_P)	1 (pulsed FDTD)	$2(N_P)$ (N_{Pxyz}) (N_{FDTD})
2E2U (storing t_1)	$4\,(N_P)(N_{Pxyz})$	$4\,(N_P)(N_{Pxyz})$	N_F (CW FDTD)	(N_P) (N_{Pxyz})
2E2U (no storage -- use last two time steps)	$4\,(N_P)(N_{Pxyz})$	$4\,(N_P)(N_{Pxyz})$	N_F (CW FDTD)	0
NENU	$9(N_{\Delta FDTD})(N_{xyz}) +$ $8(N_{Pxyz})(N_P)(N_F)$ $(N_F-1/2)(N_F+1/2)/3$ $+ 8(N_{Pxyz})(N_P)(N_F)$ $(N_F-1/2)$	$8(N_{\Delta FDTD})(N_{xyz}) +$ $8(N_{Pxyz})(N_P)(N_F)$ $(N_F-1/2)(N_F+1/2)/3$	1 (pulsed FDTD)	$(2\,N_F)^2$ $(N_{Pxyz})\,(N_P)$

		Values used in Figure 1
N_{FDTD}	= # of FDTD time steps	= 2000
N_{xyz}	= # of FDTD cells	= 100 x 100 x 100
N_F	= # of frequencies of interest	
N_P	= # of parameters of interest	= 6 (all **E** and all **H**)
N_{Pxyz}	= # of FDTD cells of interest	= 100 x 100 x 100

$N_{\Delta FDTD}$ = additional FDTD time steps required (depends on simulation, approximately 7)

** Complex multiplications are given the weight of approximately 2 real multiplications

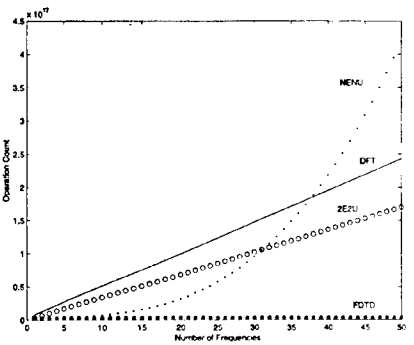

Figure 1: Computational requirements of the FDTD algorithm and associated time-to-frequency domain conversions for the parameter values indicated below Table 1.

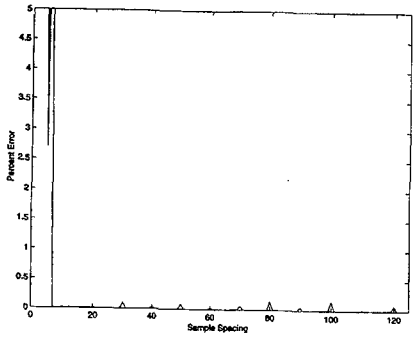

(a) Direct Method Ax=b

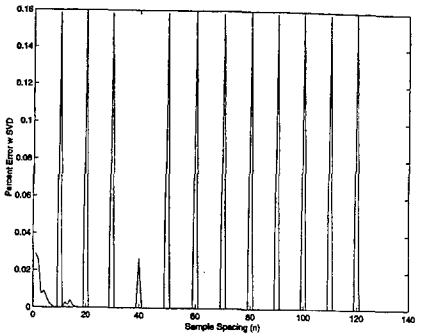

(b) Using Singular Value Decomposition

Figure 2: Maximum error in the calculation of magnitude for 25 frequencies evenly-spaced between 0.1 and 1 MHz for various time spacing between the samples.

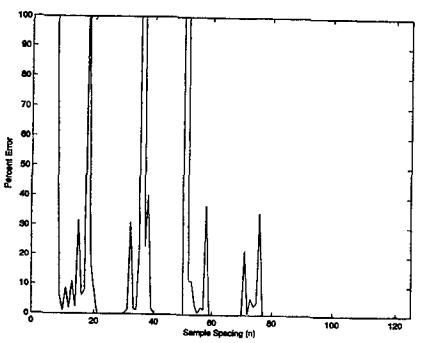

(a) Direct Method Ax=b

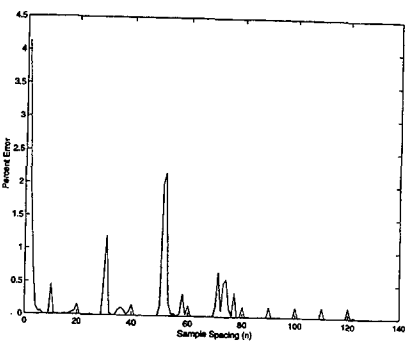

(b) Using Singular Value Decomposition

Figure 3: Maximum error in the calculation of magnitude for 100 frequencies evenly-spaced between 0.1 and 1 MHz for various time spacing between the samples.

Modelling of Antennas in Close Proximity to Biological Tissues Using the TLM Method

J.Paul, C.Christopoulos and D.W.P.Thomas

Numerical Modelling Group, Department of Electrical and Electronic Engineering
University of Nottingham, University Park, Nottingham, NG7 2RD, United Kingdom
Fax: +44 (0)115 9515616, Email: jdp@eee.nott.ac.uk

Abstract

The interaction of antennas in close proximity with materials can be analysed using transmission-line modelling (TLM). A common example of this situation is the hand-held mobile phone, where the transmitting antenna is close to the users head. In this paper, TLM is used to calculate both the absorption in the head and the effect of the head on the antenna input impedance. Although this is essentially a frequency domain problem, the frequency dependence of biological materials can be described efficiently in the time-domain, allowing the same model to be used for both continuous and transient wave excitations.

1 Introduction

The measured frequency dependence of biological materials can be described by an extension of the standard Debye equation for a single relaxation [1] to include multiple relaxations and a dc conductivity term [2]. The finite-difference time-domain (FDTD) method has been used for the modelling of biological tissues at a single frequency using constant material parameters [3] and extended to include frequency dependence in [4] and [5]. The effect of the head on mobile phone antennas was studied in [6], and the induced current and specific absorption rate (SAR) in the head was discussed in [7]. The cubical, homogeneous head phantom, irradiated by a dipole examined in this paper is based on the canonical model of the COST244 group [8], [9]. Recently, new data has appeared on the frequency dependence of biological tissues [10] and these are used as the material parameters for this study. As is well known in FDTD, the recursive convolution method is an efficient technique for the inclusion of frequency dependent material behaviour in the time domain [11]. Although the recursive convolution method has been previously applied to TLM in [12] and [13], the approach presented here is based on $\mathcal{Z}$-transform methods and leads to a formulation requiring minimal backstorage. This technique was recently applied to the modelling of absorbing materials [14] and extended here for the description of biological tissues in the time-domain.

2 Formulation

Material Parameters From Gabriel's recently published data [10], it has been observed that the measured relative permittivity ε_r of biological media can be described over the range 10-10000 MHz using a Debye susceptibility function χ_e with two relaxations and a static conductivity term σ_e.

$$\varepsilon_r = \frac{\sigma_e}{s\,\varepsilon_0} + 1 + \chi_e = \frac{\sigma_e}{s\,\varepsilon_0} + \varepsilon_\infty + \frac{\chi_0}{1 + s\,\tau_0} + \frac{\chi_1}{1 + s\,\tau_1} \tag{1}$$

In equation (1), s is the Laplace variable, ε_∞ is the optical relative permittivity, χ_0 and χ_1 are the susceptibilities and τ_0 and τ_1 are the relaxation times. Fig. 1 compares the modelled relative permittivity of brain grey matter with the data of reference [10]. The estimated parameters for two types of bone and two types of brain tissue are tabulated below along with the parameters for average bone and brain material used in the simulations of head-antenna interaction.

Tissue Type	ε_∞	χ_0	τ_0 (sec)	χ_1	τ_1 (sec)	σ_e (S m^{-1})
Cortical Bone	5	25	5×10^{-9}	7.5	20×10^{-12}	0.03
Cancellous Bone	6	65	5×10^{-9}	14	20×10^{-12}	0.09
Average Bone	5.5	45	5×10^{-9}	10.8	20×10^{-12}	0.06
White Matter	18	130	5×10^{-9}	20	15×10^{-12}	0.13
Grey Matter	20	250	4×10^{-9}	32	15×10^{-12}	0.23
Average Brain	19	190	4.5×10^{-9}	26	15×10^{-12}	0.18

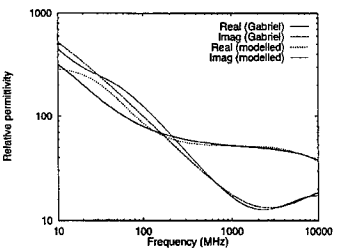

Figure 1: Relative permittivity of brain grey matter

The material properties of biological media are included in the TLM algorithm using the dual of the technique developed in [14] for magnetic media. Dielectric behaviour is described in the Ampere-Maxwell equation, ie

$$\nabla \times \underline{H} = \underline{J}_{ef} + \sigma_e * \underline{E} + \varepsilon_0 \frac{\partial \underline{E}}{\partial t} + \varepsilon_0 \frac{\partial}{\partial t}(\chi_e * \underline{E}) \tag{2}$$

where $\underline{H}$ is the magnetic field (A m^{-1}), $\underline{J}_{ef}$ is a free electric current density (A m^{-2}), σ_e is the electric conductivity (S m^{-1}), $\underline{E}$ is the electric field (V m^{-1}), ε_0 is the permittivity of free-space (F m^{-1}) and $*$ denotes a time domain convolution.

1-D Model For the 1-D case with propagation along x, the electric field polarized in y and the magnetic field polarized in z, equation (2) becomes

$$-\frac{\partial H_z}{\partial x} = J_{cfy} + \sigma_c * E_y + \varepsilon_0 \frac{\partial E_y}{\partial t} + \varepsilon_0 \frac{\partial}{\partial t}(\chi_e * E_y) \tag{3}$$

Using regular space-steps $\Delta x = \Delta y = \Delta z = \Delta\ell$, equation (3) is normalized using the

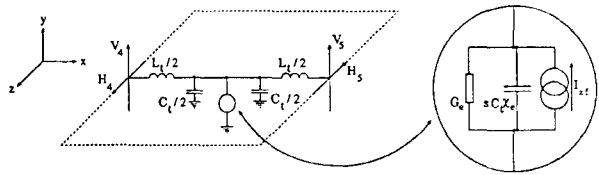

Figure 2: 1-D shunt node

field-circuit equivalences, $E_y = -V_y/\Delta\ell$, $H_z = -I_z/\Delta\ell$ and $J_{cfy} = -I_{yf}/\Delta\ell^2$. The finite difference approximation of the spatial derivative leads to the circuit model of Fig. 2 (cf Fig. 4), with

$$I_4 + I_5 = I_{yf} + G_e * V_y + C_t \frac{\partial V_y}{\partial t} + C_t \frac{\partial}{\partial t}(\chi_e * V_y) \tag{4}$$

where the electric conductance is $G_e = \sigma_e\ \Delta\ell$ and the transmission-line capacitance is $C_t = \varepsilon_0\ \Delta\ell$. The magnetic fields H_4 and H_5 of Fig. 2 are represented by the currents I_4 and I_5 of equation (4). For solution as a physical circuit, in equation (5) the currents I_4 and I_5 are converted to the orthogonal voltages V_4 and V_5 using $V = I\ \eta_0$. The free current is normalized using $i_{yf} = I_{yf}\ \eta_0$ and the conductance is normalized using $g_e = \sigma_e\ \eta_0\ \Delta\ell$ where η_0 is the intrinsic impedance of free-space. Finally, the Laplace transform is applied, $\partial/\partial t \rightarrow s = \bar{s}/\Delta t$, where $\bar{s}$ is the normalized Laplace variable, Δt is the time-step and the speed of propagation in the 1-D model is the speed of light in free-space, ie $c = \Delta\ell/\Delta t$,

$$V_4 + V_5 = i_{yf} + g_e(s)\, V_y + \bar{s}\, V_y + \bar{s}\, \chi_e(s)\, V_y \tag{5}$$

The transmission-line equivalent circuit of Fig. 3 and equation (6) describe the update of the total field V_y in terms of the incident voltages (V_4^i and V_5^i) and the free-source i_{yf},

$$2(V_4 + V_5)^i - i_{yf} = (2 + g_e(s) + \bar{s}\, \chi_e(s))\, V_y = 2V_y^r \tag{6}$$

Using z as the time shift operator, the discrete model is obtained using the bilinear $\mathcal{Z}$-transform, $\bar{s} \rightarrow 2(1 - z^{-1})/(1 + z^{-1})$ applied to equation (6) yielding (7), the transmission coefficient $t_{ey}(z)$ describing the update of V_y from V_y^r,

$$\frac{V_y}{V_y^r} = \frac{2}{2 + g_e(s) + \bar{s}\, \chi_e(s)} \quad \longrightarrow \quad \frac{2}{2 + g_e(z) + 2\left(\frac{1 - z^{-1}}{1 + z^{-1}}\right) \chi_e(z)} = t_{ey}(z) \tag{7}$$

Neglecting the free-sources, the update equations are

$$\begin{bmatrix} V_y \\ i_z \end{bmatrix}^r = \begin{bmatrix} V_4 + V_5 \\ V_5 - V_4 \end{bmatrix}^i \quad , \quad \begin{bmatrix} V_y \\ i_z \end{bmatrix} = \begin{bmatrix} t_{ey}\, V_y^r \\ t_{mz}\, i_z^r \end{bmatrix} \quad , \quad \begin{bmatrix} V_4 \\ V_5 \end{bmatrix}^r = \begin{bmatrix} V_y - i_z - V_5^i \\ V_y + i_z - V_4^i \end{bmatrix} \tag{8}$$

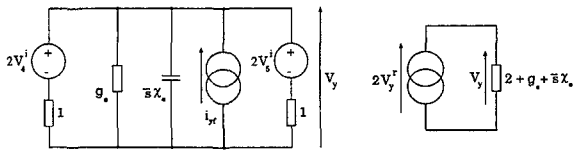

Figure 3: 1-D shunt transmission-line equivalent

From a dual analysis of the Faraday-Maxwell equation [14], in equation (8) the transmission coefficient $t_{mz} = -1$ for a non-magnetic material.

Extending equation (1) to a dielectric material with a number (N) of relaxations and an optical susceptibility $\chi_\infty = \varepsilon_\infty - 1$, the frequency-domain and $\mathcal{Z}$-domain electric susceptibilities are

$$\chi_e(s) = \chi_\infty + \sum_{i=1}^{N} \frac{\chi_{ei}}{1 + s\,\tau_{ei}} \longrightarrow \chi_\infty + \sum_{i=1}^{N} \frac{\chi_{ei}(1 - \beta_{ei})}{1 - z^{-1}\,\beta_{ei}} \quad , \quad \beta_{ei} = e^{-\frac{\Delta t}{\tau_{ei}}} \tag{9}$$

The update of V_y in equation (8) is modified to

$$V_y = t_{ey}\, V_y^r = T_{ey}\, V_y^r + S_{ey}\, z^{-1} \tag{10}$$

$$S_{eyi} = \alpha_{ei}\, V_y + \beta_{ei}\, S_{eyi}\, z^{-1} \quad , \quad i = 1 \ldots N \tag{11}$$

$$S_{ey} = T_{ey}\, V_y^r + \kappa_{ey}\, V_y + \sum_{i=1}^{N} S_{eyi} \tag{12}$$

where the coefficients are

$$T_{ey} = \frac{2}{y_t} \quad , \quad \kappa_{ey} = -\frac{q + g_e - q\,\chi_\infty}{y_t} \quad , \quad \alpha_{ei} = \frac{q\,\chi_{ei}\,(1 - \beta_{ei})^2}{y_t} \tag{13}$$

$$y_t = q + g_e + q\,\chi_\infty + q\sum_{i=1}^{N} \chi_{ei}\,(1 - \beta_{ei}) \tag{14}$$

where $q = 2$ for the 1-D case. Thus in a discrete TLM system describing an Nth order Debye material, $N + 1$ backstores for each electric field component are required.

3-D Model The basic element of the 3-D TLM method is the symmetrical condensed node (SCN) [15] shown in Fig. 4. Note that unlike FDTD in TLM the electric and magnetic fields are solved at the same point (ie at the node centre) and at the same time. Neglecting the free sources, following a similar analysis to the 1-D node of previous section applied to the 3-D TLM cell leads to the iteration procedure (cf equation (8)),

$$\begin{bmatrix} V_x \\ V_y \\ V_z \\ i_x \\ i_y \\ i_z \end{bmatrix}^r = \begin{bmatrix} V_0 + V_1 + V_2 + V_3 \\ V_4 + V_5 + V_6 + V_7 \\ V_8 + V_9 + V_{10} + V_{11} \\ V_6 - V_7 - V_8 + V_9 \\ V_{10} - V_{11} - V_0 + V_1 \\ V_2 - V_3 - V_4 + V_5 \end{bmatrix}^i \quad , \quad \begin{bmatrix} V_x \\ V_y \\ V_z \\ i_x \\ i_y \\ i_z \end{bmatrix} = \begin{bmatrix} t_{ex}\, V_x^r \\ t_{ey}\, V_y^r \\ t_{ez}\, V_z^r \\ t_{mx}\, i_x^r \\ t_{my}\, i_y^r \\ t_{mz}\, i_z^r \end{bmatrix} \quad , \quad \begin{bmatrix} V_0 \\ V_1 \\ V_2 \\ V_3 \\ V_4 \\ V_5 \\ V_6 \\ V_7 \\ V_8 \\ V_9 \\ V_{10} \\ V_{11} \end{bmatrix}^r = \begin{bmatrix} V_x - i_y - V_1^i \\ V_x + i_y - V_0^i \\ V_x + i_z - V_3^i \\ V_x - i_z - V_2^i \\ V_y - i_z - V_5^i \\ V_y + i_z - V_4^i \\ V_y + i_z - V_7^i \\ V_y - i_z - V_6^i \\ V_z - i_z - V_9^i \\ V_z + i_z - V_8^i \\ V_z + i_y - V_{11}^i \\ V_z - i_y - V_{10}^i \end{bmatrix} \tag{15}$$

For a node describing free-space, it follows that the electric transmission coefficients $t_{ex} = t_{ey} = t_{ez} = 0.5$ and the magnetic transmission coefficients $t_{mx} = t_{my} = t_{mz} = -0.5$. The wire nodes of the dipole are modelled by setting the electric transmission coefficient in the wire direction to zero, eg for a z directed wire, $t_{ez} = 0$. This formulation leads to a scattering matrix for the wire node which is identical to that shown in [16]. The biological tissue is modelled using the same process as for the 1-D case detailed in the previous section, with the coefficient $q = 4$ in equations (13) and (14).

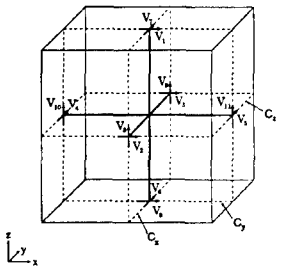

Figure 4: Symmetrical condensed node (SCN)

3 Results

Reflection Coefficient As an initial validation of the 1-D and 3-D models discussed in this paper, the reflection coefficient of an interface consisting of 0.5 cm of average bone over an infinite half space of average brain tissue was calculated using space step $\Delta\ell = 0.1$mm and is compared in Fig. 5 with the analytic solution found using classical boundary matching methods [17]. The line had a total length in x of 2500 cells and the program was iterated for 65536 time-steps.

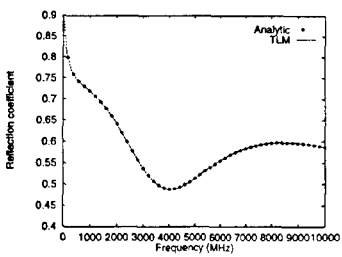

Figure 5: Reflection coefficient of an air-bone-brain interface

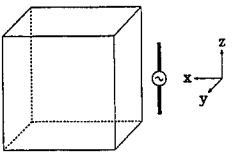

Figure 6: 3-D model of an antenna-head interaction

Antenna-Human Head Interaction The geometry of the antenna-human head interaction is based on the COST244 canonical model g1s1f1s1 [8] and is shown in Fig. 6. The space step for the simulation was 0.5cm, the head was modelled as a cube of average brain tissue with 20cm sides, the dipole antenna had a computational tip to tip length of 12.5cm (ie 25 cells) and was placed 1.5cm from the head. The problem space was truncated with a perfectly matched layer absorbing boundary condition [18] of 5 cells in depth. The overall size of the problem space in cells was $80 \times 60 \times 60$ cells.

The dipole input impedance was found by exciting the dipole gap with a delta function of voltage and storing the current measured in the dipole gap (found from the discrete form of $I = \oint \underline{H}\, \underline{dL}$) for transformation to the frequency-domain. Fig. 7 shows the effect of the head on the dipole input impedance. The presence of the head lowers the resonant frequency from 977MHz to 900MHz and reduces the radiation resistance at resonance from 70.5Ω to 41.8Ω.

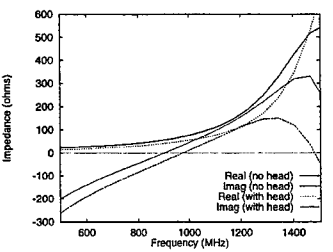

Figure 7: Input impedance of the antenna, with and without the head

The current flowing in the dipole for a Gaussian voltage excitation is shown in Fig. 8. The voltage excitation was e^{-k}, where $k = 8(N - N_{pk})^2/N_{pk}^2$, N is the time-step number and $N_{pk} = 100$ is the time-step corresponding to the function peak. The result is similar to the transient current found for the spherical head phantom in [9].

By exciting the antenna with a sinusoidal source of $V_b \sin \omega t$, where the dc source voltage of the mobile phone $V_b = 9$V and frequency $\omega = 2\pi \times 900 \times 10^6$, the specific absorption rate (SAR) at 900MHz can be calculated and is shown in Fig. 9. The SAR is calculated using the effective electrical conductivity at the source frequency ω, ie from equation (1) [7]

$$\sigma_e^{eff} = \sigma_e + \frac{\omega^2\, \varepsilon_0\, \chi_0\, \tau_0}{1 + \omega^2\, \tau_0^2} + \frac{\omega^2\, \varepsilon_0\, \chi_1\, \tau_1}{1 + \omega^2\, \tau_1^2} \tag{16}$$

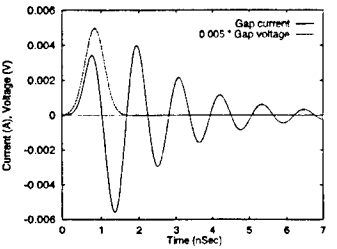

Figure 8: Antenna current for a transient voltage excitation

The SAR is found from

$$SAR = \frac{\sigma_e^{eff} E_{max}^2}{2\rho} \tag{17}$$

where E_{max} is the peak electric field at the sample point and the mass density of brain tissue $\rho = 1.05 \times 10^3 \text{kg m}^{-3}$. The SAR observed along the x axis of Fig. 6 shown in Fig. 9, the maximum power ($SAR_{max} \sim 12.1 \text{W kg}^{-1}$) is absorbed in the surface of the head closest to the antenna gap.

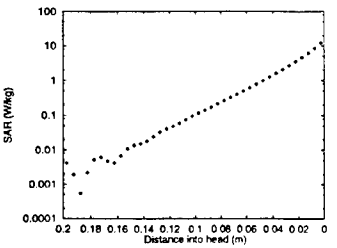

Figure 9: Specific absorption rate at 900MHz

The induced current in the cross-section of the head is calculated from the absolute electrical conductivity of the tissue at the source frequency [7], ie

$$\sigma_e^{abs} = abs\left(\sigma_e + j\omega\,\varepsilon_0\left(\varepsilon_\infty + \frac{\chi_0}{1 + j\omega\,\tau_0} + \frac{\chi_1}{1 + j\omega\,\tau_1}\right)\right) \tag{18}$$

The current I is obtained by summation of the currents in each cell over the cross section of the head,

$$I = \sum_{X-section} \frac{\sigma_e^{abs} E_{max}\,\Delta\ell^2}{\sqrt{2}} \tag{19}$$

The induced current in the plane $z = 0$ in the head was found to be 1.53A.

4 Conclusion

This paper has shown that the measured data of biological tissues can be approximated using a two relaxation Debye model with a static conductivity term. A phantom head close to a radiating antenna has been modelled in TLM and the results correlate with those presented by previous researchers. The model is currently being extended to other problems involving biological materials.

The authors acknowledge the support of the EPSRC, UK and the National Physical Laboratory, Teddington, UK.

References

[1] K. S. Cole and R. H. Cole. Dispersion and Absorption in Dielectrics—I.Alternating Current Characteristics. *Journal of Chemical Physics*, 9:341–351, April 1941.

[2] W. D. Hurt. Multiterm Debye Dispersion Relations for Permittivity of Muscle. *IEEE Transactions on Biomedical Engineering*, 32(1):60–64, January 1985.

[3] D. M. Sullivan, D. T. Borup and O. M. Gandhi. Use of Finite-Difference Time-Domain Method in Calculating EM Absorption in Human Tissues. *IEEE Transactions on Biomedical Engineering*, 32(2):148–157, February 1987.

[4] D. M. Sullivan. Frequency Dependant FDTD Methods using Z-transform. *IEEE Transactions on Antennas and Propagation*, 40(10):1223–1230, October 1992.

[5] O. P. Gandhi, B. Q. Gao and J. Y. Chen. A Frequency-Dependent Finite-Difference Time-Domain Formulation for General Dispersive Media. *IEEE Microwave and Guided Wave Letters*, 41(4):658–665, April 1993.

[6] J. Toftgard, S. N. Hornsleth and J. B. Andersen. Effect on Portable Antennas in the Presence of a Person. *IEEE Transactions on Antennas and Propagation*, 41(6):739–746, June 1993.

[7] H. Y. Chen and H. H. Wang. Current and SAR Induced in a Human Head Model by the Electromagnetic Fields Irradiated from a Cellular Phone. *IEEE Transactions on Microwave Theory and Techniques*, 42(12):2249–2254, December 1994.

[8] G. D'Inzeo. Proposal for Numerical Canonical Models in Mobile Communications. In *COST244: Biomedical Effects of Electromagnetic Fields: Roma-94: Reference Models in Mobile Communications*, pages 1–7, 1995.

[9] I. G. Marqvardsen. Numerical Solution to the COST244 Problems using FDTD. In *COST244: Biomedical Effects of Electromagnetic Fields: Roma-94: Reference Models in Mobile Communications*, pages 55–66, 1995.

[10] S. Gabriel, R. W. Lau and C Gabriel. The dielectric properties of biological materials: III. Parametric models for the dielectric spectrum of tissues. *Phys. Med. Biol.*, 41:2271–2293, 1996.

[11] R. Luebbers, F. Hunsberger, K. S. Kunz, R. B. Standler and M. Schneider. A Frequency-Dependent Finite-Difference Time-Domain Formulation for Dispersive Materials. *IEEE Transactions on Electromagnetic Compatibility*, 32(3):222–227, August 1990.

[12] L. de Menezes and W. J. R. Hoefer. Modelling Frequency Dependent Dielectrics in TLM. In *IEEE AP-S Symposium Digest*, pages 1140–1143, June 1994.

[13] L. de Menezes and W. J. R. Hoefer. Modeling of General Constitutive Relationships using SCN TLM. *IEEE Transactions on Microwave Theory and Techniques*, 44(6):854–861, June 1996.

[14] J. Paul, C. Christopoulos and D. W. P. Thomas. Modelling of RF Absorbing Materials for Anechoic Chambers. In *Second International Workshop on Transmission Line Matrix (TLM) Modeling Theory and Applications*, pages 165–176, October 1997.

[15] P. B. Johns. A Symmetrical Condensed Node for the TLM method. *IEEE Transactions on Microwave Theory and Techniques*, 35(4):370–377, April 1987.

[16] P. Naylor, and C. Christopoulos. A New Wire Node for Modelling Thin Wires in Electromagnetic Field Problems Solved by Transmission Line Modelling. *IEEE Transactions on Microwave Theory and Techniques*, 38(3):328–330, March 1990.

[17] J. A. Kong. *Electromagnetic Wave Theory*. Wiley, 1986.

[18] J. Paul, C. Christopoulos and D. W. P. Thomas. Perfectly Matched Layer for Transmission-Line Modelling (TLM) method. *Electronics Letters*, 33(9):729–730, April 1997.

SESSION 8:

ADVANCES IN PERFECTLY MATCHED LAYERS (PML)

Chairs: W.C. Chew and Q.H. Liu

Conformal Perfectly Matched Layer[†]

F. L. TEIXEIRA AND W. C. CHEW

CENTER FOR COMPUTATIONAL ELECTROMAGNETICS
ELECTROMAGNETICS LABORATORY
DEPARTMENT OF ELECTRICAL AND COMPUTER ENGINEERING
UNIVERSITY OF ILLINOIS
URBANA, IL 61801-2991 USA

1. Introduction

The simulation of open-region scattering problems using a partial differential equation (PDE) solver usually requires absorbing boundary conditions (ABC's) [1] to properly truncate the computational domain and to maintain the sparsity of the resultant matrices. In 1994, a new material ABC, the perfectly matched layer (PML), was introduced in the literature [2], [3] and since then, it has been extensively studied [4]-[14]. Being a material ABC, the PML leads naturally to sparse systems, is well-suited for parallel implementation, and, consequently, very attractive for computational purposes.

The original PML concept applied only to Cartesian coordinates (planar interfaces). To extend its range of applicability, the PML concept was later extended to non-orthogonal FDTD grids with good results [13], [14]. However, an approximate impedance matching condition was used, since the perfect matching condition was derived based on the assumption of the metric coefficients to be independent of the spatial coordinates

More recently, true PML's, in the sense of providing reflectionless absorption in the continuum limit) were derived for 2D cylindrical [15]-[19], 3D cylindrical [20], and 3D spherical interfaces [17], [18], [20].

As with any ABC, it is of interest to investigate the possibility to further extend the PML concept to a conformal PML. Along with its natural flexibility, a conformal ABC has the advantage of promoting, when used in combination with conformal computational grids, a further reduction on the amount of buffer space in the computational domain around the scatterer.

A previous attempt [21] to derive a conformal PML was only partially successful, in the sense that a *true* PML was not obtained, but only an approximate one. This quasi-PML gives a perfect matching condition only in the limit when the local radii of curvature go to infinity (then it recovers the Cartesian PML). However, even with this approximation, quite encouraging results were obtained in finite-element (FEM) simulations [21].

In this work, we present an analytic derivation of the true 3D conformal PML on a general orthogonal curvilinear coordinate system. It is demonstrated that the conformal PML can be expressed in terms of an anisotropic constitutive tensor depending on the local principal radii of curvatures of the termination surface. The derivation is based on the complex coordinate stretching approach [5], [6] through a complex stretching (analytic continuation to the upper half plane) of the *normal* coordinate along the PML (or termination surface). The previously derived PML in Cartesian, cylindrical and spherical coordinates are shown to be special cases of this conformal PML. The quasi-PML is shown to be the zeroth order approximation of the anisotropic conformal PML for large radii of curvature.

Throughout this work, the convention $e^{-i\omega t}$ is adopted.

[†]This work was supported by AFOSR under MURI grant F49620-96-1-0025, ONR under grant N00014-95-1-0872, and NSF under grant ECS93-02145, and a CAPES Fellowship.

2. Conformal Perfectly Matched Layer in Complex-Space

We start by introducing a *convex* (when viewed from the outside), closed surface S around the scatterer(s), representing the interface between free-space and the PML region, as illustrated in Fig. 1. For a concave scatterer or for a group of scatterers, such a surface can always be chosen given by considering its convex hull. Note that a convex surface S defines a *concave* surface PML as seen from inside the computational domain. The restriction to a concave PML is an important one, as will be discussed later on.

At any given point P on S, a *local*, right-handed reference frame can be defined through the orthonormal vectors $\mathbf{u}_1$, $\mathbf{u}_2$, $\mathbf{u}_3$, with $\mathbf{u}_1$ and $\mathbf{u}_2$ being tangent to S at P along the principal lines of curvature, and $\mathbf{u}_3 = \mathbf{u}_1 \times \mathbf{u}_2$ being outwardly normal to S at this point. In terms of local coordinates ξ_1, ξ_2, ξ_3, we write $\mathbf{u}_i = (\partial \mathbf{r}/\partial \xi_i) \,/\, \mid \partial \mathbf{r}/\partial \xi_i \mid$, $i = 1, 2, 3$, where $\mathbf{r}$ is the position vector. The first fundamental form induced by the coordinates ξ_1 and ξ_2 on the surface S is diagonal [22] and the curvilinear coordinate system ξ_1, ξ_2, ξ_3 is *orthogonal* (diagonal metric). Any point P' in this local reference frame is uniquely denoted by the local coordinates ξ_1, ξ_2, ξ_3. The equation $\xi_3 = 0$ represents the surface S. The points of constant ξ_3 corresponds to *parallel surfaces* in distance ξ_3 to S, and the unit vectors are functions of ξ_1 and ξ_2, only: $\mathbf{u}_1 = \mathbf{u}_1(\xi_1, \xi_2)$, $\mathbf{u}_2 = \mathbf{u}_2(\xi_1, \xi_2)$, $\mathbf{u}_3 = \mathbf{u}_3(\xi_1, \xi_2)$. If the principal radii of curvature at the point P in S are given by $r_{01}(\xi_1, \xi_2)$ and $r_{02}(\xi_1, \xi_2)$ (both positive for S convex), then at a point P', they will be given by $r_1(\xi_1, \xi_2, \xi_3) = r_{01}(\xi_1, \xi_2) + \xi_3$ and $r_2(\xi_1, \xi_2, \xi_3) = r_{02}(\xi_1, \xi_2) + \xi_3$.

In an orthogonal system of curvilinear coordinates ξ_1, ξ_2, ξ_3 defined by the diagonal metric $g_{ij} = g_{ii}\delta_{ij}$ with $g_{ii} = h_i^2$, $i = 1, 2, 3$, Faraday's equation for an isotropic medium is written as [23]:

$$\frac{1}{h_2 h_3}\left[\frac{\partial}{\partial \xi_2}(h_3 E_3) - \frac{\partial}{\partial \xi_3}(h_2 E_2)\right] - i\omega\mu H_1 = 0, \tag{1a}$$

$$\frac{1}{h_3 h_1}\left[\frac{\partial}{\partial \xi_3}(h_1 E_1) - \frac{\partial}{\partial \xi_1}(h_3 E_3)\right] - i\omega\mu H_2 = 0, \tag{1b}$$

$$\frac{1}{h_1 h_2}\left[\frac{\partial}{\partial \xi_1}(h_2 E_2) - \frac{\partial}{\partial \xi_2}(h_1 E_1)\right] - i\omega\mu H_3 = 0, \tag{1c}$$

The Ampere's equation follows by duality. Using the local coordinate system defined above, we have $h_1 = r_1/r_{01}$, $h_2 = r_2/r_{02}$, and $h_3 = 1$.

It has been previously observed [17]-[20], that the modified Maxwell's equations for PML media in Cartesian, cylindrical and spherical coordinates reduce to the ordinary Maxwell's equations on a complex space, where the x, y, z (Cartesian), ρ, z (cylindrical), and r (spherical) coordinates are analytically continued to a complex space.

In analogy to the Cartesian, cylindrical and spherical PML's, the conformal PML can be obtained through a complex stretching (analytic continuation to the upper-half complex plane) on the *normal* coordinate ξ_3:

$$\xi_3 \to \tilde{\xi}_3 = \int_0^{\xi_3} s(\zeta)d\zeta = \int_0^{\xi_3}\left(a(\zeta) + i\frac{\sigma(\zeta)}{\omega}\right)d\zeta = b(\xi_3) + i\frac{\Delta(\xi_3)}{\omega}, \tag{2}$$

where $a \geq 1$ and $\sigma \geq 0$

The effect of this stretching on a vector propagating wave can be seen, e. g., by locally expanding the wave in terms of a generalized Wilcox expansion [24], [25] in terms of the coordinates ξ_1, ξ_2, ξ_3:

$$\mathbf{E}(\xi_1, \xi_2, \xi_3) = \frac{e^{ik_0\xi_3}}{4\pi(r_1 r_2)^{1/2}} \sum_{n=0}^{+\infty} \frac{\mathbf{E}_n(\xi_1, \xi_2)}{(r_1 r_2)^{n/2}}, \tag{3}$$

where $k_0 = \omega/c$. Note that (as observed in [24]), the lowest order term in (6) corresponds to the geometrical optics spreading factor for a doubly curved wavefront. By applying the mapping (5) in (6), we arrive at:

$$\mathbf{E}(\xi_1, \xi_2, \tilde{\xi}_3) = \frac{e^{-c^{-1}\Delta(\xi_3)} e^{ik_0 b(\xi_3)}}{4\pi(\tilde{r}_1 \tilde{r}_2)^{1/2}} \sum_{n=0}^{+\infty} \frac{\mathbf{E}_n(\xi_1, \xi_2)}{(\tilde{r}_1 \tilde{r}_2)^{n/2}}, \tag{4}$$

where $\tilde{r}_1 = r_{01} + \tilde{\xi}_3$, $\tilde{r}_2 = r_{02} + \tilde{\xi}_3$, and the induced exponential decay along the normal coordinate for $\sigma \geq 0$ is evident. Also, if $a \geq 1$, additional attenuation can be achieved for evanescent waves, if they exist. This is in analogy to the Cartesian PML. Note also that the complex stretching on the normal coordinate preserves the transverse boundary conditions over the PML interface. However, the field in (7) does not obey Maxwell's equations: instead, the substitution of (5) in (1)-(4) lead to the following set of equations *inside* the conformal PML:

$$\frac{1}{\tilde{h}_2}\left[\frac{\partial}{\partial \xi_2}(E_3) - \frac{1}{s}\frac{\partial}{\partial \xi_3}\left(\tilde{h}_2 E_2\right)\right] - i\omega\mu H_1 = 0, \tag{5a}$$

$$\frac{1}{\tilde{h}_1}\left[\frac{1}{s}\frac{\partial}{\partial \xi_3}\left(\tilde{h}_1 E_1\right) - \frac{\partial}{\partial \xi_1}(E_3)\right] - i\omega\mu H_2 = 0, \tag{5b}$$

$$\frac{1}{\tilde{h}_1 \tilde{h}_2}\left[\frac{\partial}{\partial \xi_1}\left(\tilde{h}_2 E_2\right) - \frac{\partial}{\partial \xi_2}\left(\tilde{h}_1 E_1\right)\right] - i\omega\mu H_3 = 0, \tag{5c}$$

where we used $\tilde{h}_1 = \tilde{r}_1/r_{01}$, $\tilde{h}_2 = \tilde{r}_2/r_{02}$ (since these metric coefficients are functions of ξ_3 and must be changed accordingly), $h_3 = 1$, and $\partial/\partial\tilde{\xi}_3 = (1/s)(\partial/\partial\xi_3)$. No sources are assumed inside the PML.

A system of differential equations first order in time can be derived from (5) and their duals with the aid of auxiliary fields, in a manner very similar to [18]. A time-stepping scheme can then be easily implemented. The most salient feature of (5) (in addition to its complicated appearance!) is that the fields E_i, H_i inside the PML do not satisfy the original Maxwell's equations.

We can summarize some basic properties of this new system of partial differential equations, in the case of a concave PML, as follows:

(i) In the physical region (i.e., where $s = 1$), (5) and their duals reduce to the usual Maxwell's equations.

(ii) Any closed-form field solution of the Maxwell's equations in this general orthogonal curvilinear system can be mapped to solutions of this new system through a simple analytic continuation on the normal variable: $\xi_3 \to \tilde{\xi}_3$, as done in the passage from Eq. (3) to Eq. (4). No reflected field is induced due to this analytic continuation (in the continuum).

(iii) This analytic continuation preserves the analyticity of the solutions on the upper-half complex ω-plane, as long as we limit ourselves to positive radii of curvature ($r_{01} > 0$ and $r_{02} > 0$) (concave or planar PML). This means that, in this case, the resultant frequency-domain solutions are still causal in terms of a real-axis Fourier inversion contour, or, equivalently, that the solutions are dynamically stable. Otherwise (non-concave, non-planar PML), the solutions will contain singularities in the upper-half plane implying time-domain solutions that may grow unbounded. This will be discussed in more detail later on.

The fact that this system of equations is not the original Maxwell's equations is a drawback for some applications. In the next section, we show how to build a conformal PML formulation from (5) which satisfies Maxwell's equations with an anisotropic medium.

3. Anisotropic Conformal Perfectly Matched Layer

We start by introducing a new set of fields $\tilde{E}_i$, $\tilde{H}_i$ obtained by using the following transformations on the E_i, H_i fields of (5): $\tilde{E}_1 = (\tilde{h}_1/h_1)E_1$, $\tilde{E}_2 = (\tilde{h}_2/h_2)E_2$, $\tilde{E}_3 = sE_3$, $\tilde{H}_1 = (\tilde{h}_1/h_1)H_1$, $\tilde{H}_2 = (\tilde{h}_2/h_2)H_2$, $\tilde{H}_3 = sH_3$.

We note that, since the factors $(\tilde{h}_i/h_i)$ are continuous along the free-space- PML interface (both r_i and $\tilde{\xi}_3$ are continuous), the original tangential fields E_1, H_1, E_2, H_2, and the transformed tangential fields $\tilde{E}_1$, $\tilde{H}_1$, $\tilde{E}_2$, $\tilde{H}_2$ obey the same set of boundary conditions at the free-space-PML interface. Therefore, since E_1, H_1, E_2, H_2 are perfectly matched at this interface, $\tilde{E}_1$, $\tilde{H}_1$, $\tilde{E}_2$, $\tilde{H}_2$ are also perfectly matched.

Furthermore, by substituting the transformed fields into (5), we arrive at the equations:

$$\frac{1}{h_2}\left[\frac{\partial}{\partial\xi_2}\tilde{E}_3 - \frac{\partial}{\partial\xi_3}\left(h_2\tilde{E}_2\right)\right] - i\omega\mu\left(\frac{s\tilde{h}_1\tilde{h}_2}{h_1h_2}\right)\tilde{H}_1 = 0, \tag{6a}$$

$$\frac{1}{h_1}\left[\frac{\partial}{\partial\xi_3}\left(h_1\tilde{E}_1\right) - \frac{\partial}{\partial\xi_1}\tilde{E}_3\right] - i\omega\mu\left(\frac{s\tilde{h}_1h_2}{h_1\tilde{h}_2}\right)\tilde{H}_2 = 0, \tag{6b}$$

$$\frac{1}{h_1h_2}\left[\frac{\partial}{\partial\xi_1}\left(h_2\tilde{E}_2\right) - \frac{\partial}{\partial\xi_2}\left(h_1\tilde{E}_1\right)\right] - i\omega\mu\left(\frac{\tilde{h}_1\tilde{h}_2}{sh_1h_2}\right)\tilde{H}_3 = 0, \tag{6c}$$

Equations (6) are just the Faraday's equations on the original orthogonal curvilinear coordinates system of (1) characterized by the (real) metric $g_{ij} = g_{ii}\delta_{ij}$ with $g_{ii} = h_i^2$, $i = 1, 2, 3$, and $h_3 = 1$, but now for an *anisotropic* medium, whose constitutive parameters are given by $\bar{\bar{\mu}} = \mu\bar{\bar{\Lambda}}$ and $\bar{\bar{\epsilon}} = \epsilon\bar{\bar{\Lambda}}$, with

$$\bar{\bar{\Lambda}} = \mathbf{u}_1\mathbf{u}_1\left(\frac{sh_1\tilde{h}_2}{\tilde{h}_1h_2}\right) + \mathbf{u}_2\mathbf{u}_2\left(\frac{s\tilde{h}_1h_2}{h_1\tilde{h}_2}\right) + \mathbf{u}_3\mathbf{u}_3\left(\frac{\tilde{h}_1\tilde{h}_2}{sh_1h_2}\right). \tag{7}$$

The significance of this result is that it is possible to achieve reflectionless absorption of electromagnetic waves incident on a smooth, concave surface having anisotropic constitutive tensors given by (7), depending on the local principal radii of curvatures. Since (7) is a formula of a *constitutive* parameter, it is independent of any coordinate system. This means that, given a concave surface termination (as viewed from inside), we can apply this anisotropic conformal PML *in any coordinate system*, by expressing the local radii of curvature and the stretching as functions of the new coordinates, so that $\bar{\bar{\Lambda}} = \bar{\bar{\Lambda}}(\mathbf{r})$ is a function of $\mathbf{r}$ only.

An interesting point to observe is the local interplay between the physics of the medium and the geometry, as the (local) *constitutive* parameters depend on the (local) *geometry* of the termination.

4. Special Cases

The previously derived Cartesian [7], cylindrical [15], [20], and spherical [20] anisotropic PML are just special cases of (7). The Cartesian PML is obtained by setting $r_{01} = r_{02} = \infty$, so that $\tilde{h}_1 = \tilde{h}_2 = 1$. Furthermore, if $\mathbf{u}_1 = \mathbf{u}_x$, $\mathbf{u}_2 = \mathbf{u}_y$, $\mathbf{u}_3 = \mathbf{u}_z$, and $s = s_z(z)$ for attenuation in the z-direction, then (7) becomes

$$\bar{\bar{\Lambda}}_z(z) = \mathbf{u}_x\mathbf{u}_xs_z + \mathbf{u}_y\mathbf{u}_ys_z + \mathbf{u}_z\mathbf{u}_z\frac{1}{s_z}, \tag{8}$$

as first derived in [7]. Since $\bar{\bar{\Lambda}}_z(z)$ is a function of z only, we can combine it with simultaneous stretching in the x and y directions (orthogonal everywhere) also:

$$\bar{\bar{\Lambda}}_{x,y,z}(x,y,z) = \bar{\bar{\Lambda}}_x(x)\cdot\bar{\bar{\Lambda}}_y(y)\cdot\bar{\bar{\Lambda}}_z(z) = \mathbf{u}_x\mathbf{u}_x\frac{s_ys_z}{s_x} + \mathbf{u}_y\mathbf{u}_y\frac{s_zs_x}{s_y} + \mathbf{u}_z\mathbf{u}_z\frac{s_xs_y}{s_z}, \tag{9}$$

which is the most general expression for the Cartesian PML and corresponds to a corner region.

The cylindrical PML is obtained by setting $r_{01} = \infty$, $r_{02} = \rho$, so that $\tilde{h}_1/h_1 = 1$, and $\tilde{h}_2/h_2 = \tilde{\rho}/\rho$. Furthermore, $\mathbf{u}_1 = \mathbf{u}_\phi$, $\mathbf{u}_2 = \mathbf{u}_z$, $\mathbf{u}_3 = \mathbf{u}_\rho$, and $s = s_\rho(\rho)$ for attenuation in the ρ direction, so that (7) becomes

$$\bar{\bar{\Lambda}}_{\rho,\phi}(\rho) = \mathbf{u}_\phi \mathbf{u}_\phi \frac{\rho s_\rho}{\tilde{\rho}} + \mathbf{u}_z \mathbf{u}_z \frac{\tilde{\rho} s_\rho}{\rho} + \mathbf{u}_\rho \mathbf{u}_\rho \frac{\tilde{\rho}}{\rho s_\rho}, \tag{10}$$

as first derived using a graphical method in [15].

Since $\bar{\bar{\Lambda}}_\rho(\rho)$ is a function of ρ only, we can combine it with a simultaneous stretching (Cartesian) on the z direction (orthogonal to ρ everywhere) also:

$$\bar{\bar{\Lambda}}_{\rho,\phi,z}(\rho, z) = \bar{\bar{\Lambda}}_\rho(\rho) \cdot \bar{\bar{\Lambda}}_z(z) = \mathbf{u}_\phi \mathbf{u}_\phi \frac{\rho s_z s_\rho}{\tilde{\rho}} + \mathbf{u}_z \mathbf{u}_z \frac{\tilde{\rho} s_\rho}{\rho s_z} + \mathbf{u}_\rho \mathbf{u}_\rho \frac{\tilde{\rho} s_z}{\rho s_\rho}, \tag{11}$$

which is the most general expression for the 3D cylindrical PML, as derived in [20].

The spherical PML is obtained by setting $r_{01} = r_{02} = r$, so that $\tilde{h}_1/h_1 = \tilde{h}_2/h_2 = \tilde{r}/r$. Furthermore, $\mathbf{u}_1 = \mathbf{u}_\theta$, $\mathbf{u}_2 = \mathbf{u}_\phi$, $\mathbf{u}_3 = \mathbf{u}_r$, and $s = s_r(r)$ for attenuation in the r direction, so that (7) becomes

$$\bar{\bar{\Lambda}}_{r,\phi,\theta}(r) = \mathbf{u}_r \mathbf{u}_r \left(\frac{\tilde{r}}{r}\right)^2 \frac{1}{s_r} + \mathbf{u}_\phi \mathbf{u}_\phi s_r + \mathbf{u}_\theta \mathbf{u}_\theta s_r, \tag{12}$$

as derived in [20].

If $r_{01}, r_{02} >> \lambda$, then we have, as a zeroth-order approximation for (7)

$$\bar{\bar{\Lambda}} = \mathbf{u}_1 \mathbf{u}_1 s + \mathbf{u}_2 \mathbf{u}_2 s + \mathbf{u}_3 \mathbf{u}_3 \frac{1}{s}, \tag{13}$$

which is just the planar PML with stretching in the normal direction, as considered in [21]. This approximation should be more properly called 'quasi-PML', [26]. As demonstrated in [21], very good results can be obtained with this approximation, as long as large radius of curvature are considered, which is the case for large scatterers.

Care must be taken to derive higher-order approximations to (7). For instance, it is easy to show that the *first*-order approximation using a Taylor expansion in $\lambda/r_{01}, \lambda/r_{02}$ to (7) gives rise to constitutive tensors having poles on the upper-half ω plane for any $r_{01} \neq r_{02}$. This implies an active-medium behavior and the resultant time-domain equations may turn out to be dynamically unstable, as discussed in the next section.

5. Causality and Stability Issues for the Conformal PML

As discussed in more detail elsewhere [27], a condition that should be investigated for the frequency-dependent matrix $\bar{\bar{\Lambda}}$ (and also its inverse, $\bar{\bar{\Lambda}}^{-1}$) is that if it violates causality in the sense of the real axis Fourier inversion contour. This is equivalent to having the upper-half complex ω plane free of singularities (and zeros).

Using the stretching defined by (2), it can be easily shown that, for a concave or planar surface PML (more precisely, $r_{01} > 0$ and $r_{02} > 0$), all poles and zeros of $\bar{\bar{\Lambda}}$ are on the lower-half plane, so that causality is not violated. However, for a non-concave, non-planar surface PML (i. e., $r_{01} < 0$ or $r_{02} < 0$), there will be poles and zeros on the upper-half plane.

In the latter case, causality in the sense of real-axis integration is violated. In time-domain explicit methods, such as the FDTD, the causality will necessarily be enforced, which is equivalent to taking the Fourier inversion contour to be *above* all singularities [1]. In this case, the PML will behave as an active medium and the resultant time-domain equations

may turn out to be dynamically unstable, as, for instance, was found to be the case for simulations employing cylindrical and spherical convex PML's (inner boundary) [27]. An alternative to ensure a dynamically stable ABC when $r_{01} < 0$ or $r_{02} < 0$ (although not perfectly matched anymore), is to use the 'quasi-PML' described in the previous section.

This violation of causality can also be directly checked by an investigation of the singularities in the resultant analytic solutions, such as (4). For a concave PML, the denominator factors in (4) produce branch points and/or poles only in the *lower* half-plane (the singularities present on (3) are translated downwards in the complex ω plane). For a non-concave, non-planar PML however, these singularities are present on the *upper* half-plane (the singularities present on (3) are translated upwards in the ω complex-plane).

It is important to note that these conclusions are valid by considering the stretching defined by (2), which is the universally used in the literature. For other kinds of stretching (which would imply more involved time-domain equations), they are not necessarily valid.

6. Conclusions.

An analytic derivation of a conformal PML for concave grid-terminations is presented. The derivation is based on the complex stretching of the normal direction on a generalized orthogonal curvilinear coordinate system conformal to a termination surface.

It is shown that this conformal PML produces an exponential decay of the fields in the normal direction without any reflections in the continuum limit. In the complex-space formulation, the resultant fields do not obey Maxwell's equations. However, an alternative formulation is presented with anisotropic medium where the fields obey the Maxwell's equations everywhere. In analogy with the Cartesian, cylindrical and spherical PML's, in this Maxwellian formulation, the PML region is represented by an anisotropic artificial medium. For the conformal PML, the constitutive tensors depend on the local radii of curvature of the termination surface.

References

[1] W. C. Chew, *Waves and Fields in Inhomogeneous Media*, New York: Van Nostrand, 1990 (Reprinted by IEEE Press, 1995), ch. 4.

[2] J. Berenger, "A perfectly matched layer for the absorption of electromagnetic waves," *J. Comput. Phys.*, vol. 114, no. 2, pp. 185-200, 1994.

[3] J. Berenger, "Three-dimensional perfectly matched layer for the absorption of electromagnetic waves," *J. Comput. Phys.*, vol. 127, no. 2, pp. 363-379, 1996.

[4] D. S. Katz, E. T. Thiele, and A. Taflove, "Validation and extension to three dimensions of the Berenger PML absorbing boundary condition ," *IEEE Microwave Guided Wave Lett.*, vol. 4, no.8, pp. 268-270, 1994.

[5] W. C. Chew and W. Weedon, "A 3D perfectly matched medium from modified Maxwell's equations with stretched coordinates," *Microwave Opt. Tech. Lett.*, vol. 7, no. 13, pp. 599-604, 1994.

[6] C. M. Rappaport, "Interpreting and improving the PML absorbing boundary condition using anisotropic lossy mapping of space," *IEEE Trans. Magn.* , vol. 32, no. 3, pp. 968-974, 1996.

[7] Z. S. Sacks, D. M. Kingsland, R. Lee, and J.-F. Lee, "A perfectly matched anisotropic absorber for use as an absorbing boundary condition," *IEEE Trans. Antennas Propagat.*, vol. 43 , no. 12, pp. 1460-1463, 1995.

[8] S. D. Gedney, "An anisotropic PML absorbing media for the FDTD simulation of fields in lossy and dispersive media," *Electromagn.*, vol. 16, pp. 399-415, 1996.

[9] L. Zhao and A. C. Cangellaris, "GT-PML: generalized theory of perfectly matched layers and its application to the reflectionless trunction of finite-difference time-domain grids," *IEEE Trans. Microw. Theory and Tech.*, vol. 44, no. 12, pp. 2555-2563, 1996.

[10] W. C. Chew and J. M. Jin, "Perfectly matched layers in the discretized space: an analysis and optimization," *Electromagn.*, vol. 16, pp. 325-340, 1996.
[11] N. Kantartzis and T. Tsiboukis, "A comparative study of the Berenger perfectly matched layer, the superabsorption technique and several high-order ABC's for the FDTD algorithm in two and three dimensional problems," *IEEE Trans. Magn.* , vol. 33, no. 2, pp. 1460-1463, 1996.
[12] J. -Y. Wu, D. M. Kingsland, J. -F. Lee, and R. Lee, "A comparison of anisotropic PML to Berenger's PML and its application to the finite-element method for EM scattering," *IEEE Trans. Antennas Propagat.*, vol. 45, no. 1, pp. 40-50, 1997.
[13] E. A. Navarro, C. Wu, P. Y. Chung, and J. Litva, "Application of PML super-absorbing boundary condition to non-orthogonal FDTD method," *Electron. Lett.*, vol. 30, no. 20, pp. 1654-1655, 1994.
[14] J. A. Roden and S. D. Gedney, "Efficient implementation of the uniaxial-based PML media in three-dimensional nonorthogonal coordinates with the use of the FDTD technique," *Microwave Opt. Tech. Lett.* , vol. 14, no. 2, pp. 71-75, 1997.
[15] J. Maloney, M. Kesler, and G. Smith, "Generalization of PML to cylindrical geometries," in *Proc. of* 13^{th} *Annual Rev. of Prog. Appl. Comp. Electromag.* (Monterrey, CA), March 17-21, 1997, vol. 2, pp. 900-908.
[16] B. Yang, D. Gottlieb, and J. S. Hesthaven, "On the use of PML ABC's in spectral time-domain simulations of electromagnetic scattering," in *Proc. of* 13^{th} *Annual Rev. of Prog. Appl. Comp. Electromag.* (Monterrey, CA), March 17-21, 1997, vol. 2, pp. 926-933; see also B. Yang, D. Gottlieb, and J. S. Hesthaven, "Spectral simulations of electromagnetic wave scattering," *J. Comput. Phys.*, vol. 134, pp. 216-230, 1997.
[17] W. C. Chew, J. M. Jin, and E. Michielssen, "Complex coordinate system as a generalized absorbing boundary condition," in *Proc. of* 13^{th} *Annual Rev. of Prog. Appl. Comp. Electromag.* (Monterrey, CA), March 17-21, 1997, vol. 2, pp. 909-914; see also W. C. Chew, J. M. Jin, and E. Michielssen, "Complex coordinate stretching as a generalized absorbing boundary condition," *Microwave Opt. Tech. Lett.*, vol. 15, no. 6, pp. 363-369, 1997.
[18] F. L. Teixeira and W. C. Chew, "PML-FDTD in cylindrical and spherical grids," *IEEE Microw. Guided Wave Lett.*, vol. 7, no. 9, pp. 285-287, 1997.
[19] F. Collino and P. Monk, "The perfectly matched layer in curvilinear coordinates," private communication.
[20] F. L. Teixeira and W. C. Chew, "Systematic derivation of anisotropic PML absorbing media in cylindrical and spherical coordinates," *IEEE Microw. Guided Wave Lett.*, vol. 7, no. 11, pp. 371-373, 1997.
[21] M. Kuzuoglu and R. Mittra, "Investigation of nonplanar perfectly matched absorbers for finite-element mesh truncation," *IEEE Trans. Antennas Propagat.*, vol. 45, no. 3, pp. 474-486, 1997.
[22] H. W. Guggenheimer, *Differential Geometry*, New York: Dover, 1977, pp. 206-214.
[23] J. A. Stratton, *Electromagnetic Theory*, New York: McGraw-Hill, 1941, pp. 50-51.
[24] A. Chatterjee, J. L. Volakis, "Conformal absorbing boundary conditions for the vector wave equation," *Microwave Opt. Tech. Lett.* , vol. 6, no. 16, pp. 886-889, 1993; "Correction to conformal absorbing boundary conditions for the vector wave equation," *Microwave Opt. Tech. Lett.* , vol. 8, no. 6, pp. 323-324, 1995.
[25] C. H. Wilcox, "An expansion theorem for electromagnetic fields," *Comm. Pure Appl. Math.*, vol. 9, pp.115-1334, 1956.
[26] J. Q. He and Q. H. Liu, "A non-uniform cylindrical FDTD algorithm with Liao's and quasi-PML absorbing boundary conditions," private communication.
[27] F. L. Teixeira, W. C. Chew, "Causality and dynamical stability of perfectly matched layers for FDTD simulations," Research Report CCEM-27-97, Center for Computational Electromagnetics, University of Illinois at Urbana-Champaign, Sept. 1997.

Stability Analysis of Cartesian, Cylindrical and Spherical Perfectly Matched Layers[†]

F. L. Teixeira and W. C. Chew

Center for Computational Electromagnetics
Electromagnetics Laboratory
Department of Electrical and Computer Engineering
University of Illinois
Urbana, IL 61801-2991 USA

1. Introduction

The perfectly matched layer (PML) absorbing boundary condition (ABC) [1], [2] is a very efficient means to truncate the computational domain in the finite-difference time-domain (FDTD) simulations [1]-[10]. Being a material ABC, the PML retains the nearest-neighbor interaction characteristic of the FDTD method, making it particularly suitable for parallel simulations. It was also applied to finite-element (FEM) EM simulations [9], [11], [12], elastic-wave problems [13] and paraxial-wave problems [14] with similar success.

More recently, the recognition that the PML can be interpreted as an analytic continuation of Maxwell's equations (ME's) to complex-space [15] provided the basis for the extension of the PML to 2D cylindrical [18], [19], 3D cylindrical [20], and 3D spherical coordinates [18], [20] (extensions to 2D cylindrical coordinates are also considered in [16], [17]).

The artificial PML media in any of these coordinate systems should retain the causality conditions observed by the original ME's. This naturally leads to the study of the analytic properties on the complex ω plane of either the PML tensor constitutive parameters (in case of anisotropic formulations [6]-[8], [11], [12], [16], [20]) or the complex-space ME's closed-form solutions inside the PML (in case of complex-space formulation [3], [5], [9], [13]-[15], [18], [19]).

We study these analytic properties for the various coordinate systems PML's: Cartesian, cylindrical and spherical. We point out conditions under which causality is violated and the consequences of on the dynamical stability of the PML-FDTD simulations. Throughout this work, the $e^{-i\omega t}$ convention is used.

2. Causality and Dynamical Stability

The constitutive relation for the electric field is written as:

$$\mathbf{D}(t) = \int_{-\infty}^{\infty} \overline{\epsilon}(\tau) \cdot \mathbf{E}(t-\tau) d\tau. \tag{1}$$

Invoking causality, we have that $\overline{\epsilon}(t) = 0$ for $t < 0$, and it is possible to show [20] that this implies that $\overline{\epsilon}(\omega)$ must be analytic in the upper-half complex ω plane, whenever the Fourier inversion contour is carried out along the real ω axis.

However, when $\overline{\epsilon}(\omega)$ is not analytic in the upper-half plane, causality is preserved provided that the Fourier inversion contour is taken *above* any singularities [21]. In this case, the medium will behave as an *active* medium and its response will not be dynamically stable anymore. The definition of a dynamically stable system adopted here is such that all its

[†]This work was supported by AFOSR under MURI grant F49620-96-1-0025, ONR under grant N00014-95-1-0872, and NSF under grant ECS93-02145 and a CAPES Fellowship.

eigenmodes approach zero as $t \to \infty$ (asymptotically stable) or remain bounded as $t \to \infty$ (marginally stable). This stability criterion is distinct from the stability criterion that has to be satisfied by a particular numerical discretization scheme. It is also a distinct from the one incurred by a particular field-splitting of the modified PML equations, which may induce weakly well-posedness [22]. For a dynamically unstable system, no discretization schemes or field-splitting schemes prevent the solutions from growing unbounded. In FDTD simulations, causality is enforced, so that the inversion contour is always chosen to be above any singularities and violation of causality in the sense of real ω axis inversion contour implies a dynamically unstable FDTD method.

3. Dynamical Stability of the Cartesian PML

The PML was first proposed in Cartesian coordinates [1], [2], and since then, Cartesian FDTD codes have been implemented in several examples [1]-[10].

Since in the anisotropic formulation [6]-[8], [11], the fields inside the PML region obey the ME's, a useful test for violation of causality is to check if the resultant constitutive tensors (and their inverses), $\overline{\epsilon}(\mathbf{r},\omega) = \epsilon\overline{\Lambda}(\mathbf{r},\omega)$ and $\overline{\mu}(\mathbf{r},\omega) = \mu\overline{\Lambda}(\mathbf{r},\omega)$ satisfy, along with the crossing relation, the Kramers-Kronig relations [21], [23]-[25]. The $\overline{\Lambda}(\mathbf{r},\omega)$ tensor is given by:

$$\overline{\Lambda}(\mathbf{r},\omega) = \hat{x}\hat{x}\left(\frac{s_y s_z}{s_x}\right) + \hat{y}\hat{y}\left(\frac{s_z s_x}{s_y}\right) + \hat{z}\hat{z}\left(\frac{s_x s_y}{s_z}\right), \tag{2}$$

where the frequency-dependent complex stretching variables, s_ζ, $\zeta = x, y, z$, are given by

$$s_\zeta(\zeta,\omega) = a_\zeta(\zeta) + i\frac{\sigma_\zeta(\zeta)}{\omega}, \tag{3}$$

with $a_\zeta(\zeta) \geq 1$, and $\sigma_\zeta(\zeta) \geq 0$ in the practical cases. Note that this expression resembles the complex dielectric constant of a conductive media.

The expression (2) is the most general for a Cartesian PML media and corresponds to a 3-D PML at a corner interface. This tensor is the product of three simpler tensors [8], [11]:

$$\overline{\Lambda}(\mathbf{r},\omega) = \overline{\Lambda}_x(x,\omega)\cdot\overline{\Lambda}_y(y,\omega)\cdot\overline{\Lambda}_z(z,\omega), \tag{4}$$

with

$$\overline{\Lambda}_x = \hat{x}\hat{x}\left(\frac{1}{s_x}\right) + (\hat{y}\hat{y} + \hat{z}\hat{z})\, s_x, \tag{5}$$

and analogously for $\overline{\Lambda}_y(y,\omega)$ and $\overline{\Lambda}_z(z,\omega)$. In order for $\overline{\Lambda}(\mathbf{r},\omega)$ to satisfy causality each of the $\overline{\Lambda}_\zeta(\zeta,\omega)$, must satisfy it individually (there are no pole cancellations). Since the frequency dependence of $\overline{\Lambda}_\zeta(\zeta,\omega)$ and $\overline{\Lambda}_\zeta(\zeta,\omega)^{-1}$ is determined by $1/s_\zeta$ and s_ζ, the Kramers-Kronig relations must be satisfied by these functions individually. The Kramers-Kronig relations are a consequence of the application of the Cauchy's theorem to the function $\overline{\epsilon}(\omega) - \overline{\epsilon}(\infty)$ in the upper half-plane [21]. In their usual form [21], [23]-[25], it is implicitly assumed analyticity of $\overline{\epsilon}(\omega) - \overline{\epsilon}(\infty)$ over the real axis. However, this is *not* the case, for instance, of conductive media, in which the complex dielectric constant has a term $i\sigma/\omega\epsilon_0$, and therefore has a pole at $\omega = 0$. The Kramers-Kronig relations for conductive-like media must be modified to account for the deformation of the closed contour in the Cauchy's theorem to avoid the pole at the origin [23], [24]. This was overlooked in a previous study on this topic [25]. In this more general form, the Kramers-Kronig relations are [23], [24]:

$$\overline{\epsilon}_r(\omega) - \overline{\epsilon}(\infty) = \frac{1}{\pi} PV \int_{-\infty}^{+\infty} \frac{\overline{\epsilon}_i(\omega')}{\omega' - \omega} d\omega', \tag{6}$$

$$\overline{\epsilon}_i(\omega) = -\frac{1}{\pi} PV \int_{-\infty}^{+\infty} \frac{\overline{\epsilon}_r(\omega') - \overline{\epsilon}(\infty)}{\omega' - \omega} d\omega' + \frac{\overline{\sigma}}{\omega}, \tag{7}$$

where $\bar{\epsilon}_r(\omega)$ and $\bar{\epsilon}_i(\omega)$ are the real and imaginary parts of $\bar{\epsilon}(\omega)$, PV denotes the Cauchy principal value. The $\bar{\epsilon}_r(\omega)$ and $\bar{\epsilon}_i(\omega)$ are limiting values as ω approaches the real axis from above. To apply relations (7) and (8) to the expression (3), we identify: $\bar{\epsilon}_r(\omega) \to a_\zeta$, $\bar{\epsilon}(\infty) \to a_\zeta$, $\bar{\epsilon}_i(\omega) \to \sigma_\zeta/\omega_,$, so that (11) and (12) become (13) and (14) below:

$$0 = \frac{1}{\pi} PV \int_{-\infty}^{+\infty} \frac{\sigma_\zeta}{\omega'(\omega' - \omega)} d\omega', \tag{8}$$

$$\sigma_\zeta/\omega = 0 + \sigma_\zeta/\omega. \tag{9}$$

Eq. (9) verifies (7), and (8) verifies (6) since [30]:

$$\frac{1}{\pi} PV \int_{-\infty}^{+\infty} \frac{\sigma_\zeta}{\omega'(\omega' - \omega)} d\omega' = \pi \sigma_\zeta \delta(\omega), \tag{10}$$

so that (8) is true in the upper-half plane. As a result, expression (3) obeys the Kramers-Kronig relations and represents a causal function. The fact that in the real axis we get a Dirac delta function from (10) is related to the divergence of the integral in (1) for conductive media (real include the Dirac delta function since it should be treated as an analytic continuation from the upper-half plane, as a complex dielectric constant of conductive media.

It can also be shown that, if $a_\zeta \geq 1$ and $\sigma_\zeta \geq 0$, the function $1/s_\zeta$ satisfies the Kramers-Kronig relations.

In summary, the Cartesian anisotropic PML media with frequency-dependence given by (3) is causal in the sense of real axis inversion contour. No *dynamical* instability should be expected, consistent with the numerical results in the literature.

A second way to investigate the dynamical stability of the Cartesian PML is to write the closed-form field solutions for the modified ME's inside the PML and study its analytical behavior in the complex ω plane. This is done more expeditiously in the frequency domain since the solutions of the modified ME's inside the PML [3] are the analytic continuation of the closed-form solutions of the usual ME's [15], [18], [20]. It can be shown that the resultant PML Green's functions are analytic over the entire upper-half ω plane and causality in the sense of real-axis Fourier inversion contour is not violated [26], corroborating the previous analysis.

4. Dynamical Stability of the Cylindrical PML

The cylindrical PML is considered in [15]-[20]. The constitutive tensor, $\overline{\Lambda}(\rho, z; \omega)$, for the anisotropic 3D formulation is given by [20]:

$$\overline{\Lambda}(\rho, z; \omega) = \hat{\rho}\hat{\rho}\left(\frac{s_\phi s_z}{s_\rho}\right) + \hat{\phi}\hat{\phi}\left(\frac{s_z s_\rho}{s_\phi}\right) + \hat{z}\hat{z}\left(\frac{s_\rho s_\phi}{s_z}\right). \tag{11}$$

In the above, s_ρ and s_z are the stretching parameters in the ρ and z directions:

$$s_\rho(\rho, \omega) = a_\rho(\rho) + i\frac{\sigma_\rho(\rho)}{\omega}, \tag{12}$$

$$s_z(z, \omega) = a_z(z) + i\frac{\sigma_z(z)}{\omega}, \tag{13}$$

with $a_{\rho,z} \geq 1$ and $\sigma_{\rho,z} \geq 0$. The variable s_ϕ is a 'pseudo-stretching' parameter in the ϕ coordinate that accounts for the modification in the metric after the stretching:

$$s_\phi(\rho, \omega) = \frac{\tilde{\rho}}{\rho} = \frac{1}{\rho}\left(\rho_0 + \int_{\rho_0}^{\rho} s_\rho(\rho')d\rho'\right) = \frac{1}{\rho}\left(b_\rho(\rho) + i\frac{\Delta_\rho(\rho)}{\omega}\right), \tag{14}$$

where ρ_0 is on the physical (real) space and $a_\rho = 1$, $\sigma_\rho = 0$ in the physical space. The tensor in (22) can be written as the product of three simpler tensors:

$$\overline{\boldsymbol{\Lambda}}(\rho, z; \omega) = \overline{\boldsymbol{\Lambda}}_\rho(\rho, \omega) \cdot \overline{\boldsymbol{\Lambda}}_\phi(\rho, \omega) \cdot \overline{\boldsymbol{\Lambda}}_z(z, \omega) \tag{15}$$

with

$$\overline{\boldsymbol{\Lambda}}_\rho = \hat{\rho}\hat{\rho}\left(\frac{1}{s_\rho}\right) + \left(\hat{\phi}\hat{\phi} + \hat{z}\hat{z}\right) s_\rho, \tag{16}$$

and analogously for $\overline{\boldsymbol{\Lambda}}_\phi(\rho, \omega)$ and $\overline{\boldsymbol{\Lambda}}_z(z, \omega)$.

In order to $\overline{\boldsymbol{\Lambda}}(\rho, z; \omega)$ satisfy causality, each of the tensors in (15) must satisfy it individually (in general, there are no pole cancellations). $\overline{\boldsymbol{\Lambda}}_\rho$ and $\overline{\boldsymbol{\Lambda}}_z$ have the same analytical properties of the Cartesian PML tensors studied before. The frequency dependence of $\overline{\boldsymbol{\Lambda}}_\phi(\rho, \omega)$ (and $\overline{\boldsymbol{\Lambda}}_\phi(\rho, \omega)^{-1}$) is determined by s_ϕ and $1/s_\phi$, and therefore we must focus our attention on these factors. To ensure causality (in the sense of real-axis Fourier inversion contour) in $\overline{\boldsymbol{\Lambda}}_\phi(\rho, \omega)$, we must ensure that there are no poles due to s_ϕ or $1/s_\phi$ *above* the real-axis. For s_ϕ, this is evident, as the only pole is at $\omega = 0$ and it can be shown that this function satisfies the Kramers-Kronig relations of the form (6)-(7). However, a major difference arises in the angular factor $1/s_\phi$. It is due to the fact that the factor Δ_ρ in the imaginary part of s_ϕ can be, at certain instances, *negative*. This is in contrast to the correspondent σ factors in the imaginary part of s_x, s_y, s_z, or s_ρ which are also chosen to be positive to achieve absorption. Due to the fact that σ_ρ is positive, when used in (14) for a concave cylindrical PML (i.e., at an outer boundary), we will still have $\Delta_\rho > 0$. But for a *convex* cylindrical PML (inner boundary), we have $\Delta_\rho < 0$, as the integral in (14) is carried over decreasing values of ρ. The net effect of this is that the factor $1/s_\phi$ will then have poles at the upper half-plane, and the resultant $\overline{\boldsymbol{\Lambda}}(\rho, z; \omega)$ will be non-causal. As a consequence, dynamical instability on FDTD simulations employing a convex cylindrical PML is expected. This can also be concluded from an analysis of the properties of the field solutions on the cylindrical PML [26]. The solutions of the modified ME's in the cylindrical PML are just the analytic continuation of the solutions of the usual ME's in cylindrical coordinates.

For outer boundaries (concave PML), the analytic continuation preserves the analyticity on the upper-half ω plane of the resultant field. When $\rho \to \tilde{\rho}$ as in (14) with $\Delta_\rho > 0$, all singularities are translated *down* to the lower-half ω-plane, so that the upper half-plane is kept free of any singularity.

In contrast, for inner boundaries, the analytic continuation does not preserve analyticity in the upper-half plane as the variable $\tilde{\rho}$ now has $\Delta_\rho < 0$. Zeros of the denominator functions $H_n^{(1)}(\cdot)$ that appear on the Green's functions [26] and are located in the lower-half plane will eventually appear as poles on the upper-half ω-plane of the reflected field expressions under the complex stretching. Fig. 1(a) illustrates the location of the complex zeros of the function $H_n^{(1)}(\cdot), n = 7$. Branch points of the $H_n^{(1)}(\cdot)$ will similarly be translated to the upper-half ω-plane.

Fig. 1(b) shows the E_z field from a line source in the presence of a PEC cylinder computed using a cylindrical grid FDTD algorithm. The line source is located at $(r, \phi) = (4.25\lambda_c, 0^0)$ and the field is sampled at $(r, \phi) = (3.75\lambda_c, 0^0)$. The cylinder is centered at the origin and has a radius $a = \lambda_c$. The excitation pulse is the derivative of the Blackman-Harris pulse with $f_c = 300$ MHz. The grid is terminated at $r = 5\lambda_c$. An 8-layer concave cylindrical PML is used before the grid ends. The PML thickness is $0.5\lambda_c$. A quadratic taper on σ_ρ is used and $a_\rho = 1$ everywhere. The solid line in the Figure 2 shows the result when using only a concave cylindrical PML. The dotted line is the result of the simulation when a 8-layer convex cylindrical PML is placed around the inner PEC cylinder. The instability of the resultant FDTD algorithm in this case is dramatic, and an exponential growth appears soon after the wave reaches the convex PML.

An alternative to avoid instabilities in the convex case is to *impose* $\Delta_\rho \geq 0$ in for the inner boundary. In this manner, a dynamically stable scheme can be obtained. However, the

resultant cylindrical interface is not perfectly matched anymore. This useful approximation behaves as a true PML only in the limit $\rho \to \infty$, where the cylindrical PML reduces to the Cartesian PML. The two important features exhibited by this quasi-PML when compared to a true PML (when the latter is applicable) are (i) a non-zero reflection coefficient in the continuum limit and (ii) the need for a more finely tuned profile to achieve the best results.

Still, this quasi-PML may have important practical applications when $\rho \gg \lambda$, both for numerical simulations and as a physical basis for artificially engineered materials.

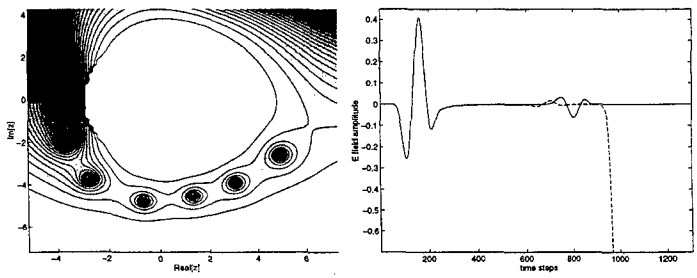

Fig. 1(a) *(left) - Contour map of the magnitude of the function $H_7^{(1)}(z)$. The darker regions represent smaller values. The zeros on the lower-half plane and the branch cut are clearly visible.* **Fig. 1(b)** *(right) - 2D FDTD solution with cylindrical PML. The solid line is the case with the concave PML only. Direct and the reflected pulse due to the inner cylinder are visible. No reflected fields due to the grid ends at the outer boundary are visible. The dashed line represents the FDTD simulation with the convex PML coating the inner cylinder. The dramatic instability incurred is evident.*

5. Dynamical Stability of the Spherical PML

The spherical PML is considered in [15], [18], [20]. The constitutive tensor $\overline{\boldsymbol{\Lambda}}(\rho, z; \omega)$ is given by [20]:

$$\overline{\boldsymbol{\Lambda}}(r;\omega) = \hat{r}\hat{r}\left(\frac{s_\theta s_\phi}{s_r}\right) + \hat{\theta}\hat{\theta}\left(\frac{s_\phi s_r}{s_\theta}\right) + \hat{\phi}\hat{\phi}\left(\frac{s_r s_\theta}{s_\phi}\right). \tag{17}$$

In the above, s_r is the stretching parameter in the r direction:

$$s_r(r,\omega) = a_r(r) + i\frac{\sigma_r(r)}{\omega}, \tag{18}$$

with $a_r \geq 1$ and $\sigma_r \geq 0$. The variables s_θ, s_ϕ are 'pseudo-stretching' parameters in the θ and ϕ angular coordinates that account for the modification in the metric after the stretching:

$$s_\theta(r,\omega) = s_\phi(r,\omega) = \frac{\tilde{r}}{r} = \frac{1}{r}\left(r_0 + \int_{r_0}^{r} s_r(r')dr'\right) = \frac{1}{r}\left(b_r(r) + i\frac{\Delta_r(r)}{\omega}\right), \tag{19}$$

where r_0 is on the physical (real) space and $a_r = 1$, $\sigma_r = 0$ in the physical space. Since $s_\theta = s_\phi$, the constitutive tensor in (32) can be simplified to

$$\overline{\boldsymbol{\Lambda}}(r;\omega) = \hat{r}\hat{r}\left(\frac{\tilde{r}}{r}\right)^2\left(\frac{1}{s_r}\right) + \left(\hat{\theta}\hat{\theta} + \hat{\phi}\hat{\phi}\right)s_r. \tag{20}$$

Following the same reasoning used in the cylindrical PML case, we conclude that $\overline{\boldsymbol{\Lambda}}(r;\omega)$ has no poles in the upper half plane for a concave spherical PML, and therefore the resultant

FDTD scheme will be dynamically stable. In the case of a convex spherical PML, we note that due to the pole cancellation in the angular terms $\hat{\theta}\hat{\theta}$ and $\hat{\phi}\hat{\phi}$ in (17) the tensor $\overline{\Lambda}(r;\omega)$ has no poles in the upper-half ω-plane. However, its inverse $\overline{\Lambda}(r;\omega)^{-1}$ has poles in the upper-half plane due to the factor $\hat{r}/r$ in the radial term $\hat{r}\hat{r}$ of (20). From this, we should also expect dynamical instability on FDTD simulation when employing a convex PML on spherical coordinates.

This is also predicted by a direct analysis of the field solutions in the frequency domain. The solutions of the modified ME's inside the spherical PML are the analytic continuation of the solutions of the usual ME's in spherical coordinates with the r coordinate mapped as in (19) [15], [18], [20]. When employing a convex spherical PML, the analyticity of the solutions in the upper-half plane is again not preserved. The only important distinction from the cylindrical case of the previous section is that the Hankel $H_n^{(1)}(\cdot)$ and Bessel $J_n(\cdot)$ functions are replaced by its spherical counterparts $h_n^{(1)}(\cdot)$, and $j_n(\cdot)$. Although not having branch points on the real axis as $H_n^{(1)}(\cdot)$, the *denominator* functions $h_n^{(1)}(\cdot)$ in the spherical case still have zeros on the lower-half plane, as illustrated in Fig. 2(a). These zeros will eventually appear as poles on the upper-half ω-plane of the field solutions under complex stretching.

Fig. 2(b) depicts the E_θ field from a θ-polarized Hertzian-dipole in the presence of a PEC sphere. The field is computed using a spherical-grid FDTD algorithm. The dipole is located at $(r,\theta,\phi) = (1.9\lambda_c, 90^0, 0^0)$ and the field is sampled at $(r,\theta,\phi) = (2.5\lambda_c, 90^0, 0^0)$. The PEC sphere is centered at the origin and has a radius $a = 0.5\lambda_c$. The grid is terminated at $r = 3.5\lambda_c$. The FDTD algorithm includes an 8-layer spherical PML before the grid ends. The PML thickness is $0.8\lambda_c$. The excitation is the same as before. The grid is terminated at $r = 3.5\lambda_c$. An 8-layer concave spherical PML is used before the grid ends. The PML thickness is $0.8\lambda_c$. A quadratic taper on σ_r is used, and $a_r = 1$ everywhere. The solid line in the Figure 5 shows the result when using only a concave spherical PML before the outward boundary. The dotted line is the result of the simulation when a 8-layer convex spherical PML is also placed around the inner PEC sphere. Again, a dramatic instability is present.

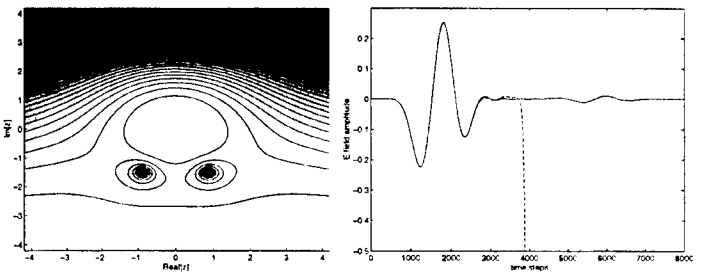

Fig. 2(a) *(left) - Contour map of the magnitude of the function $h_2^{(1)}(z)$ on the complex plane. The darker regions represent smaller values. The zeros on the lower-half plane are clearly visible.* **Fig.2(b)** *(right) - 3D FDTD solution with spherical PML. The solid line represents the case with the concave PML only. Direct and the reflected pulse due to the inner sphere are visible. No reflected fields due to the grid ends at the outer boundary are visible. The dashed line represents the FDTD simulation with the convex PML coating the inner sphere. The dramatic instability incurred is evident.*

6. Concluding Remarks

The analytic continuation of Maxwell's equations to complex space is a powerful tool to achieve the reflectionless absorption of electromagnetic waves in different coordinate systems. In this work we have pointed out some limitations of this approach. In particular, the analytic continuation should preserve analyticity on the upper-half of the complex ω plane. We have made the connection between the violation of causality and the dynamical instability of the resultant time domain scheme.

Contrary to previous claims, we have shown that the Cartesian PML with the frequency dependence as proposed by Berenger does not violate causality. The complex-space formulation of *concave* PML both in cylindrical and spherical coordinates preserves the analyticity of the solutions on the upper-half plane and therefore implies in a dynamically stable FDTD, but for the *convex* PML in cylindrical and spherical coordinates it violates causality (in the sense of real-axis inversion contour) and result on a dynamically unstable FDTD.

In principle, convex cylindrical and spherical surfaces PML are not ruled out by this analysis. It merely points out that the same method used to derive concave PML cannot be applied in a naive fashion to obtain a convex PML. The conclusions obtained here are based on the particular frequency dependence chosen for the stretching variables. Other choices are also possible but at the cost of increased complexity on the resultant time-domain equations.

References

[1] J. Berenger, "A perfectly matched layer for the absorption of electromagnetic waves," *J. Comput. Phys.*, vol. 114, pp. 185-200, 1994.

[2] J. Berenger, "Three-dimensional perfectly matched layer for the absorption of electromagnetic waves," *J. Comput. Phys.*, vol. 127, pp. 363-379, 1996.

[3] W. C. Chew and W. Weedon "A 3D perfectly matched medium from modified Maxwell's equations with stretched coordinates," *Microw. Opt. Tech. Lett.*, vol. 7, pp. 599-604, 1994.

[4] D. S. Katz, E. T. Thiele, and A. Taflove, "Validation and extension to three dimensions of the Berenger PML absorbing boundary condition ," *IEEE Microw. Guided Wave Lett.*, vol. 4, pp. 268-270, 1994.

[5] C. M. Rappaport,"Interpreting and improving the PML absorbing boundary condition using anisotropic lossy mapping of space," *IEEE Trans. Magn.* , vol. 32, pp. 968-974, 1996.

[6] Z. S. Sacks, D. M. Kingsland, R. Lee, and J.-F. Lee, "A perfectly matched anisotropic absorber for use as an absorbing boundary condition," *IEEE Trans. Antennas Propagat.*, vol. 43 , no. 12, pp. 1460-1463, 1995.

[7] S. D. Gedney, "An anisotropic PML absorbing media for the FDTD simulation of fields in lossy and dispersive media," *Electromagn.*, vol. 16, pp. 399-415, 1996.

[8] L. Zhao and A. C. Cangellaris, "GT-PML: generalized theory of perfectly matched layers and its application to the reflectionless trunction of finite-difference time-domain grids," *IEEE Trans. Microw. Theory and Tech.*, vol. 44, pp. 2555-2563, 1996.

[9] W. C. Chew and J. M. Jin, "Perfectly matched layers in the discretized space: an analysis and optimization," *Electromagn.*, vol. 16, pp. 325-340, 1996.

[10] N. Kantartzis and T. Tsiboukis, "Comparative study of the Berenger perfectly matched layer, the superabsorption technique and several high-order ABC's for the FDTD algorithm in two and three dimensional problems," *IEEE Trans. Magn.* , vol. 33, pp. 1460-1463, 1996.

[11] J. -Y. Wu, D. M. Kingsland, J. -F. Lee, and R. Lee, "A comparison of anisotropic PML to Berenger's PML and its application to the finite-element method for EM scattering," *IEEE Trans. Antennas Propagat.*, vol. 45, pp. 40-50, 1997.

[12] M. Kuzuoglu and R. Mittra, "Investigation of nonplanar perfectly matched absorbers for finite-element mesh truncation," *IEEE Trans. Antennas Propagat.*, vol. 45, pp.

474-486, 1997.
[13] W. C. Chew and Q. H. Liu, "Perfectly matched layers for elastodynamics: a new absorbing boundary condition," *J. Comp. Acoust.*, vol. 4, pp. 341-359, 1996.
[14] F. Collino, "Perfect matched absorbing layers for the paraxial equations," *J. Comput. Phys.*, vol. 131, pp. 164-180, 1997.
[15] W. C. Chew, J. M. Jin, and E. Michielssen, "Complex coordinate system as a generalized absorbing boundary condition," in *Proc. of* 13^{th} *Annual Rev. of Prog. Appl. Comp. Electromag.* (Monterrey, CA), March 17-21, 1997, pp. 909-914.
[16] J. Maloney, M. Kesler, and G. Smith, "Generalization of PML to cylindrical geometries," in *Proc. of* 13^{th} *Annual Rev. of Prog. Appl. Comp. Electromag.* (Monterrey, CA), March 17-21, 1997, pp. 900-908.
[17] B. Yang, D. Gottlieb, and J. S. Hesthaven, "On the use of PML ABC's in spectral time-domain simulations of electromagnetic scattering," in *Proc. of* 13^{th} *Annual Rev. of Prog. Appl. Comp. Electromag.* (Monterrey, CA), March 17-21, 1997, pp. 926-933.
[18] F. L. Teixeira and W. C. Chew, "PML-FDTD in cylindrical and spherical grids," *IEEE Microw. Guided Wave Lett.*, vol. 7, pp. 285-287, 1997.
[19] F. Collino and P. Monk, "The perfectly matched layer in curvilinear coordinates," private communication.
[20] F. L. Teixeira and W. C. Chew, "Systematic derivation of anisotropic PML absorbing media in cylindrical and spherical coordinates," *IEEE Microw. Guided Wave Lett.*, vol 7, pp. 371-373, 1997.
[21] W. C. Chew, *Waves and Fields in Inhomogeneous Media*, New York: Van Nostrand, 1990 (Reprinted by IEEE Press, 1995), pp. 211-215.
[22] S. Abarbanel, D. Gottlieb, "A mathematical analysis of the PML method," *J. Comput. Phys.*, vol. 134, pp. 357-363, 1997.
[23] E. M. Lifshitz and L. P. Pitaevskii, *Statistical Physics*, Part 1, Oxford: Pergamon, 1980, pp. 377-384.
[24] J. A. Kong, *Electromagnetic Wave Theory*, New York: Wiley, 1982, pp. 297-299
[25] M. Kuzuoglu and R. Mittra, "Frequency dependence of the consitutive parameters of causal perfectly matched anisotropic absorbers," *IEEE Microw. Guided Wave Lett.*, vol. 6, pp. 447-449, 1996.
[26] F. L. Teixeira, W. C. Chew, "Causality and dynamical stability of perfectly matched layers for FDTD simulations," Research Report CCEM-27-97, Center for Computational Electromagnetics, University of Illinois, Sept. 1997.

A UNIFIED APPROACH TO PML ABSORBING MEDIA

Douglas H. Werner and Raj Mittra
The Pennsylvania State University
Applied Research Laboratory
P.O. Box 30
State College, PA 16804-0030

Abstract: This paper offers an alternative interpretation of Berenger's Perfectly Matched Layer (PML) equations. This new formulation is based on a concept of field scaling rather than one that involves coordinate stretching. It is also demonstrated how the field scaling approach may be used to develop a methodology for unifying the Berenger and anisotropic PML formulations.

I. INTRODUCTION

The numerical solution of many electromagnetic radiation and scattering problems requires the imposition of Absorbing Boundary Conditions (ABCs) in order to truncate an otherwise infinite computational domain. An ABC which consists of a reflectionless lossy material, known as a Perfectly Matched Layer (PML), was recently introduced by Berenger [1]. The desired electromagnetic absorption characteristics of the PML medium are realized, in this case, by starting with a suitably modified form of Maxwell's equations. More recently, an alternative realization of a PML has been presented by Sacks et al. [2], which is based on an anisotropic layer whose complex permittivity and permeability tensors possess certain special properties.

The original form of the PML, first proposed by Berenger in [1], required the Cartesian field components to be split into two subcomponents, each of which is weighted by different constitutive parameters. A PML formulation based on complex coordinate stretching was later introduced by Chew and Weedon [3], which does not rely on field splitting. An unsplit form of Berenger's equations was derived by Mittra and Pekel [4] which only required 6 scalar equations instead of 12. It was also demonstrated in [4] that the unsplit form of Berenger's equations were identical to those obtained in [3] through the use of coordinate stretching. An alternative interpretation of Berenger's PML was recently proposed by Werner and Mittra [5] which is based on field scaling rather than coordinate stretching.

In this paper we present a review of the new field scaling formulation of Berenger's PML first introduced in [5]. We also demonstrate that one of the main advantages of this new field scaling approach is that it leads to a framework in which the Berenger and the anisotropic PML formulations may be easily unified.

II. THEORY

A. Coordinate Stretching Formulation of Berenger's PML

The coordinate stretching interpretation of Berenger's PML was first introduced by Chew and Weedon [3] and later refined by Wu et al. [6]. A Cartesian coordinate system was adopted in [3] such that the z-axis is normal to the interface between two homogenous half spaces. The first region is considered to be free space, whereas the second contains an anisotropic absorbing medium with material properties (ε_0, μ_0, σ, σ^*). If an $e^{j\omega t}$ time variation is assumed, then the modified Maxwell's equations for a source-free Berenger PML half-space may be expressed in the form [6]

$$\vec{\nabla}_e \times \vec{E} = -j\omega\mu_0\vec{H} \tag{1}$$

$$\vec{\nabla}_h \times \vec{H} = j\omega\varepsilon_0\vec{E} \tag{2}$$

$$\vec{\nabla}_h \cdot \varepsilon_0 \vec{E} = 0 \tag{3}$$

$$\vec{\nabla}_e \cdot \mu_0 \vec{H} = 0 \tag{4}$$

where $\vec{\nabla}_e$ *and* $\vec{\nabla}_h$ are complex coordinate stretching operators given by

$$\vec{\nabla}_e = \hat{x}\frac{1}{e_x}\frac{\partial}{\partial x} + \hat{y}\frac{1}{e_y}\frac{\partial}{\partial y} + \hat{z}\frac{1}{e_z}\frac{\partial}{\partial z} \tag{5}$$

$$\vec{\nabla}_h = \hat{x}\frac{1}{h_x}\frac{\partial}{\partial x} + \hat{y}\frac{1}{h_y}\frac{\partial}{\partial y} + \hat{z}\frac{1}{h_z}\frac{\partial}{\partial z} \tag{6}$$

The coordinate stretching variables e_x, e_y, e_z and h_x, h_y, h_z which appear in (5) and (6), respectively, are usually chosen to be

$$e_x = e_y = 1 \tag{7}$$

$$e_z = 1 - j\frac{\sigma^*}{\omega\mu_0} \tag{8}$$

$$h_x = h_y = 1 \tag{9}$$

$$h_z = 1 - j\frac{\sigma}{\omega\varepsilon_0} \tag{10}$$

The impedance of the PML medium is matched to that of the adjacent free space when [1]

$$\frac{\sigma}{\varepsilon_0} = \frac{\sigma^*}{\mu_0} \tag{11}$$

This matching condition is satisfied when $e_z = h_z$, which suggests that $\vec{\nabla}_e = \vec{\nabla}_h$. Hence, by incorporating this condition into (1)-(4), we arrive at the following set of modified Maxwell's equations:

$$\vec{\nabla}_e \times \vec{E} = -j\omega\mu_0\vec{H} \tag{12}$$

$$\vec{\nabla}_e \times \vec{H} = j\omega\varepsilon_0\vec{E} \tag{13}$$

$$\vec{\nabla}_e \cdot \varepsilon_0 \vec{E} = 0 \tag{14}$$

$$\vec{\nabla}_e \cdot \mu_0 \vec{H} = 0 \tag{15}$$

The corresponding set of modified vector Helmholtz equations for the electric and magnetic fields in Berenger's PML medium are then

$$\vec{\nabla}_e^2 \vec{E} + k_0^2 \vec{E} = 0 \tag{16}$$

$$\vec{\nabla}_e^2 \vec{H} + k_0^2 \vec{H} = 0 \tag{17}$$

where $k_0 = \omega\sqrt{\mu_0 \varepsilon_0} = \omega/c$ and

$$\vec{\nabla}_e^2 = \frac{\partial^2}{\partial x^2} + \frac{\partial^2}{\partial y^2} + \frac{1}{e_z^2}\frac{\partial^2}{\partial z^2} \tag{18}$$

Finally, we note that (18) may be used to express (16) and (17) in the explicit forms

$$\left(\frac{\partial^2}{\partial x^2} + \frac{\partial^2}{\partial y^2} + \frac{1}{e_z^2}\frac{\partial^2}{\partial z^2} + k_0^2\right)\vec{E} = 0 \tag{19}$$

$$\left(\frac{\partial^2}{\partial x^2} + \frac{\partial^2}{\partial y^2} + \frac{1}{e_z^2}\frac{\partial^2}{\partial z^2} + k_0^2\right)\vec{H} = 0 \tag{20}$$

B. Field Scaling Formulation of Berenger's PML

In this section, we introduce a new interpretation of Berenger's PML which is based on a field scaling approach rather than a coordinate stretching approach. The derivation begins by considering the unsplit form of Berenger's PML equations originally proposed by Mittra and Pekel [4]. The six unsplit scalar equations derived in [4] may be expressed in the following vector form [5]:

$$\vec{\nabla} \times ([\beta]\vec{E}) = -j\omega[\mu]\vec{H} \tag{21}$$

$$\vec{\nabla} \times ([\alpha]\vec{H}) = j\omega[\varepsilon]\vec{E} \tag{22}$$

where

$$[\varepsilon] = \varepsilon_0[\varepsilon_r] \quad \textit{and} \quad [\mu] = \mu_0[\mu_r] \tag{23}$$

$$[\varepsilon_r] = [\varepsilon_r'] - j[\varepsilon_r''] \quad \textit{and} \quad [\mu_r] = [\mu_r'] - j[\mu_r''] \tag{24}$$

$$[\varepsilon_r'] = [\mu_r'] = [I] = \begin{pmatrix} 1 & 0 & 0 \\ 0 & 1 & 0 \\ 0 & 0 & 1 \end{pmatrix} \tag{25}$$

$$[\varepsilon_r''] = \frac{1}{\omega \varepsilon_0}[\sigma] \quad \textit{and} \quad [\mu_r''] = \frac{1}{\omega \mu_0}[\sigma^*] \tag{26}$$

$$[\sigma] = \begin{pmatrix} \sigma & 0 & 0 \\ 0 & \sigma & 0 \\ 0 & 0 & 0 \end{pmatrix} \quad \textit{and} \quad [\sigma^*] = \begin{pmatrix} \sigma^* & 0 & 0 \\ 0 & \sigma^* & 0 \\ 0 & 0 & 0 \end{pmatrix} \tag{27}$$

$$[\alpha] = \begin{pmatrix} 1 & 0 & 0 \\ 0 & 1 & 0 \\ 0 & 0 & 1 - j\dfrac{\sigma}{\omega \varepsilon_0} \end{pmatrix} \quad \textit{and} \quad [\beta] = \begin{pmatrix} 1 & 0 & 0 \\ 0 & 1 & 0 \\ 0 & 0 & 1 - j\dfrac{\sigma^*}{\omega \mu_0} \end{pmatrix} \tag{28}$$

It is important to recognize here that the elements of the tensors $[\alpha]$ and $[\beta]$ are unitless. It is also of interest to point out that the elements of the electric and magnetic conductivity tensors which appear in (27) are all positive.

The impedance matching condition for the PML medium in this case is given by

$$\frac{[\varepsilon]}{\varepsilon_0} = \frac{[\mu]}{\mu_0} \tag{29}$$

which is satisfied provided $[\varepsilon_r'] = [\mu_r']$ and $[\varepsilon_r''] = [\mu_r'']$. The first of these conditions is automatically satisfied by (25), while the second is equivalent to (11), and suggests that $[\alpha] = [\beta]$. These facts may be used to show that the modified form of Maxwell's equations given in (21) and (22) for the Berenger PML may be written as

$$\vec{\nabla} \times \vec{E}' = -j\omega\mu_0 [\Lambda] \vec{H}' \tag{30}$$

$$\vec{\nabla} \times \vec{H}' = j\omega\varepsilon_0 [\Lambda] \vec{E}' \tag{31}$$

$$\vec{\nabla} \cdot \varepsilon_0 [\Lambda] \vec{E}' = 0 \tag{32}$$

$$\vec{\nabla} \cdot \mu_0 [\Lambda] \vec{H}' = 0 \tag{33}$$

where

$$\vec{E}' = [\alpha] \vec{E} \tag{34}$$

$$\vec{H}' = [\alpha] \vec{H} \tag{35}$$

$$[\alpha] = \begin{pmatrix} 1 & 0 & 0 \\ 0 & 1 & 0 \\ 0 & 0 & a \end{pmatrix} \tag{36}$$

$$a = 1 - j\frac{\sigma}{\omega\varepsilon_0} \tag{37}$$

and where $[\Lambda]$ has the property that

$$[\Lambda] = \frac{1}{\mu_0} [\mu] [\alpha]^{-1} = \frac{1}{\varepsilon_0} [\varepsilon] [\alpha]^{-1} = \begin{pmatrix} a & 0 & 0 \\ 0 & a & 0 \\ 0 & 0 & 1/a \end{pmatrix} \tag{38}$$

An inspection of (30)-(38) reveals that the curl and anisotropic tensor operations in the modified Maxwell's equations for the Berenger PML are carried out on the scaled version of the fields, i.e., $\vec{E}'$ and $\vec{H}'$, rather than directly on the actual fields $\vec{E}$ and $\vec{H}$. This field scaling approach offers an alternative to the coordinate stretching formulation of Berenger's PML discussed in the previous section. One of the main advantages is that the modified Maxwell's equations for the field scaling formulation of Berenger's PML have exactly the same form as those associated with the popular anisotropic PML formulation [2,5,6], the only difference being that

the former operates on a scaled version of the fields while the latter does not. In fact, if we define a generalized form of the tensor $[\alpha]$ according to

$$[\alpha] = \begin{pmatrix} 1 & 0 & 0 \\ 0 & 1 & 0 \\ 0 & 0 & d \end{pmatrix} \tag{39}$$

we obtain the anisotropic PML formulation when $d=1$, and the Berenger PML formulation when $d=a$.

It can be shown using (30)-(33) that the modified vector Helmholtz equations for the scaled field version of Berenger's PML are [5]

$$\frac{1}{a}\,\vec{\nabla}\cdot([\Lambda]\,\vec{\nabla})\,\vec{E}' + k_0^2\,\vec{E}' = 0 \tag{40}$$

$$\frac{1}{a}\,\vec{\nabla}\cdot([\Lambda]\,\vec{\nabla})\,\vec{H}' + k_0^2\,\vec{H}' = 0 \tag{41}$$

which may also be expressed in the form

$$\left(\frac{\partial^2}{\partial x^2} + \frac{\partial^2}{\partial y^2} + \frac{1}{a^2}\,\frac{\partial^2}{\partial z^2} + k_0^2\right)\vec{E}' = 0 \tag{42}$$

$$\left(\frac{\partial^2}{\partial x^2} + \frac{\partial^2}{\partial y^2} + \frac{1}{a^2}\,\frac{\partial^2}{\partial z^2} + k_0^2\right)\vec{H}' = 0 \tag{43}$$

Finally, by making use of (34) and (35), we recognize that if $\vec{E}'$ and $\vec{H}'$ represent solutions of (42) and (43), respectively, then so must $\vec{E}$ and $\vec{H}$.

III. CONCLUSION

A new unified approach to the treatment of PMLs has been introduced in this paper. This new approach allows both Berenger and anisotropic PMLs to be considered as special cases of a more general PML formulation.

REFERENCES

[1] J.-P. Bérenger, "A Perfectly Matched Layer for the Absorption of Electromagnetic Waves," *J. Comput. Phys.*, Vol. 114, No. 2, pp. 185-200, Oct. 1994.

[2] Z. S. Sacks, D. M. Kingsland, R. Lee and J. F. Lee, "A Perfectly Matched Anisotropic Absorber for Use as an Absorbing Boundary Condition," *IEEE Transactions on Antennas and Propagation*, Vol. 43, No. 12, pp. 1460-1463, Dec. 1995.

[3] W. C. Chew and W. H. Weedon, "A 3-D Perfectly Matched Medium From Modified Maxwell's Equations with Stretched Coordinates," *Microwave Opt. Tech. Lett.*, Vol. 7, No. 13, pp. 599-604, Sept. 1994.

[4] R. Mittra and Ü. Pekel, "A New Look at the Perfectly Matched Layer (PML) Concept for the Reflectionless Absorption of Electromagnetic Waves," *IEEE Microwave and Guided Wave Letters*, Vol. 5, No. 3, pp. 84-86, March 1995.

[5] D. H. Werner and R. Mittra, "A New Field Scaling Interpretation of Berenger's PML and its Comparison to Other PML Formulations," *Microwave Opt. Tech. Lett.*, Vol. 16, No. 2, pp. 103-106, Oct. 1997.

[6] J. Wu, D. Kingsland, J. Lee and R. Lee, "A Comparison of Anisotropic PML to Berenger's PML and its Application to the Finite-Element Method for EM Scattering," *IEEE Transactions on Antennas and Propagation,* Vol. 45, No. 1, pp. 40-50, Jan. 1997.

Comparison of the Performance of the PML and the Liao Absorbing Boundary Formulation

Merce Vall-llossera
Department of Signal Theory and Communications
Polytechnic University of Catalonia (UPC)
Barcelona
Merce@voltor.upc.es

Christopher W. Trueman
Electromagnetic Compatibility
Laboratory
Concordia University
Montreal
Trueman@ece.concordia.ca

Abstract-The cell space in the finite-difference time-domain method must be truncated with an absorbing boundary. The perfectly-matched layer (PML) formulation for the boundary offers much lower reflection than the Liao formula, but at the cost of much greater memory requirements and much longer execution time at each time step. But because the PML reflects much less and so interacts with the object being modelled much less, a much thinner layer of free space cells can be used to separate the object surfaces from the absorbing boundary. Thus a problem can be solved to a given accuracy with a much smaller cell space using the PML than using the Liao absorbing boundary. This paper examines the tradeoff in memory requirements and execution time of the PML compared to the Liao boundary, for computing the radar cross-section of a metallic rod target and of a dielectric cube.

Introduction

This paper compares radar cross-sections computed using FDTD with measured RCS data for a perfectly-conducting rod and for a high-permittivity, low-loss dielectric cube. The purpose is to compare the performance of the perfectly-matched layer (PML) absorbing boundary condition (ABC) [1,2] with the Liao second-order ABC [3]. The memory requirements for the FDTD cell space and for the absorbing boundary, and the CPU time requirements, are compared on the basis of equally good agreement with the measured RCS.

With the Liao ABC, a layer of free-space cells called the "whitespace" is used to separate the surfaces of the object from the outer boundary of the cell space layer. Using the PML, the whitespace separates the object from the inner surface of the PML, and PML itself has a thickness in cells. The cell space size is determined by the thickness of the whitespace plus the thickness of the PML, as shown in Fig. 1. To obtain good agreement with the measured data, how thick must the whitespace layer be using the Liao ABC? How thick must the PML be? How much whitespace must be used with the PML? The memory requirements to store the field components in Yee's FDTD [4,5] increase in proportion to the total number of cells, which in turn increases as the cube of the thickness of the whitespace plus the PML layers. The computation time thus increases as the cube of the whitespace thickness. The volume in cells of the PML layer increases in proportion to the area of the outer boundary in cells, which increases as the square of the whitespace size. The memory requirements of the PML thus increase as the square of the whitespace size. Since the PML ABC requires much more computation at each time step for the same space size than does the Liao ABC, it might be thought that a thicker whitespace used with the Liao absorbing boundary is more economical than a thin whitespace terminated with the PML. Indeed, it has been suggested that the Liao boundary be used for day-to-day investigations with FDTD, backed up by using the "expensive" PML to check the accuracy in individual

cases. This paper explores the trade-off between computer memory requirements and running time, comparing the Liao ABC with the PML for the same degree of agreement with measured RCS data.

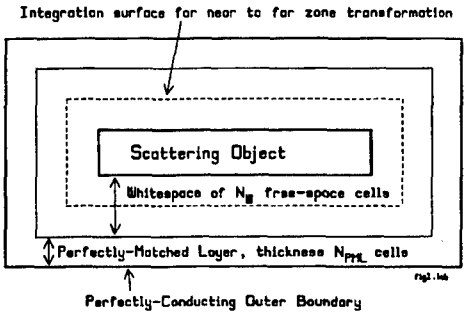

Figure 1 A cross-section of the FDTD cell space showing the scattering object in the center separated from the outer boundary by a layer of free-space cells and the PML absorbing boundary.

The Perfectly-Matched Layer

Fig. 1 shows the FDTD cell space terminated by a PML layer of thickness N_{PML} cells. The outside boundary of the cell-space is perfectly conducting, hence it has a reflection coefficient of unity. A layer of free-space cells separates the surface of the scattering object from the inside surface of the PML. To set up the problem, the user chooses the overall size of the cell space, N_x by N_y by N_z cells, which includes the PML layer, the whitespace, and the scattering object. The user defines the PML layer with the following parameters. The thickness of the PML, N_{PML} cells, is the most important choice. The variation of the conductivity with depth into the PML must be specified as either linear, or geometric, or parabolic. This paper uses parabolic evolution. The reflection coefficient for normal incidence on the surface of the PML must be specified. In this paper a reflection coefficient of 0.001 has been used.

The time of validity or "cutoff time" of the PML technique is governed [2] by the conductivity of the first layer of PML cells, which is determined by the thickness of the PML, whether geometric or parabolic evolution is chosen, and the reflection coefficient at the surface. Ref. [2] recommends cutoff times at least ten times the time interval over which FDTD is to be run to solve the problem.

The Perfectly-Conducting Rod

The rod target consists of an aluminum parallelepiped of square cross-section, whose length is ten times its cross-sectional size. The plane wave is incident end-on to the rod, with the electric field parallel to one edge of the cross-section. The rod scatters strongly from its front end and from its back end, and as the frequency changes the two scattered fields go in and out of phase, giving rise to the evenly-spaced set of maxima and minima shown in Fig. 2. The RCS was measured as described in reference [6]. The rod was modeled with 10 by 10 by 100 FDTD cells. The rod is excited by a Gaussian pulse plane wave, and the backscattered field as a function of time [7] is computed for 2048 time steps. The field is then Fourier-transformed and divided by the spectrum of the Gaussian pulse to determine the RCS as a function of frequency.

Using the Liao absorbing boundary with a whitespace eight cells thick, the agreement with the measured RCS is very poor. As the whitespace thickness is increased, the agreement gradually improves. With 16 cells of whitespace, the agreement with the measurement is good, as shown in Fig. 2. The maxima marked with the bracket are sensitive to the whitespace thickness and improve dramatically with increased whitespace. The minima also improve with whitespace thickness,

particularly the one marked with the arrow. The maximum at the low end of the frequency spectrum also improves. Increasing the whitespace to 20 cells leads to a small improvement in the agreement, and further increases to little improvement.

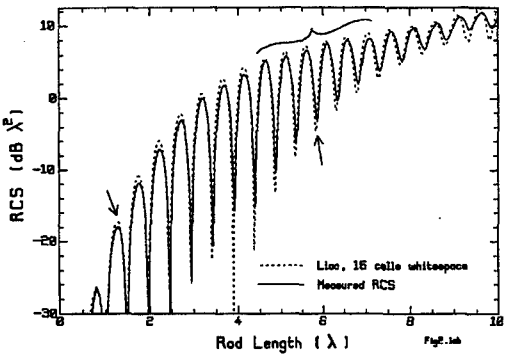

Figure 2 RCS of the rod target with the Liao ABC.

Table 1 summarizes the computer resources used for the rod problem when the Liao boundary is selected. The FDTD code was run on a 166 MHz Pentium with a 512 kb cache memory and 32 Mb of RAM. The code was compiled with the DEC Fortran-90 compiler [8] and run under Windows-95 to obtain the CPU times reported in this paper. FDTD was the only application running, and the machine had sufficient memory to run the code without paging to disk. Nevertheless, the CPU times from one run to another vary randomly by about 5%, for unknown reasons. For 16 cells of whitespace, the CPU time is 6,541 seconds. The code uses about 7.4 Mb for the FDTD cell space itself, and about 0.9 Mb for the storage associated with the Liao boundary. The agreement with the measurement is quite good. With 20 cells of whitespace, the storage rises to 11 Mb for the cell space and 1.7 Mb associated with the ABC, and the running time increases to 9,505 seconds. The agreement with the measurement is slightly improved over the 16 cell case.

Table 1
Computer Resources Needed to Solve the Rod Scatterer With the Liao Absorbing Boundary

Whitespace	Time	Cell Space Size	Cell Space Storage	Liao ABC Storage
12 cells	4,224 sec	125 x 35 x 35 cells	4,593,750 bytes	643,012 bytes
16	6,541	133 x 43 x 43	7,377,510	854,980
20	9,505	141 x 51 x 51	11,002,230	1,790,404

Using the PML for the PEC Rod

With an extremely thick perfectly-matched layer 10 cells deep, parabolic taper, a surface reflection of 0.001, and 10 cells of whitespace separating the surfaces of the rod from the surfaces of the PML, the agreement with the measured RCS is excellent. The cell space size corresponds to 20 cells of whitespace when the Liao boundary is used, and indeed the agreement with the measurement is about the same as found with Liao and 20 cells of whitespace. However, the PML algorithm is much slower than the Liao method, so the CPU time is much longer. Table 2 summarizes the computer resources needed with the PML. The cell space size is the same for Liao with a 20 cell whitespace and for a 10 cell PML and 10 cells of whitespace, hence the memory requirement for the cell space is the

same. But the storage associated with the PML at 6.1 Mb is much larger than that with Liao at 1.8 Mb. And the running time of 30,326 sec is much longer than Liao's 9505 sec. But a much thinner PML can be used with excellent agreement.

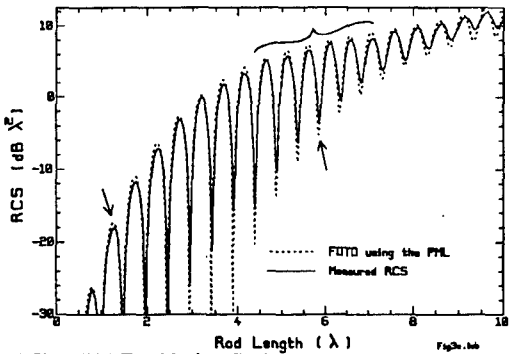

(a) Six cell PML with six cell whitespace.

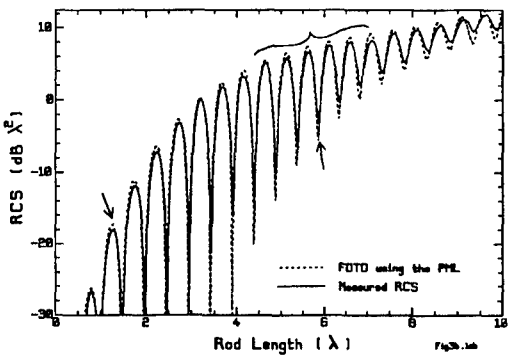

(b) Four cell PML with four cell whitespace.

Figure 3 RCS of the rod target using the PML.

Fig. 3(a) uses a PML 6 layers thick, and 6 cells of whitespace to separate the rod surfaces from the PML. With this formulation, the agreement with the measurement is good, but the storage requirement for the PML drops to 2.3 Mb, and the execution time to 11,842 seconds. Using a whitespace only 4 cells thick, the computed RCS is almost identical, and the storage drops to 1.9 Mb and the execution time to 9130 seconds. This execution time is comparable to the Liao case with 20 cells of whitespace, and the storage associated with PML is almost the same as that with the Liao ABC. But the memory required by the FDTD cell space is 11 Mb in the Liao case and only 3.5 Mb using the PML. This is a huge improvement. Even if we consider a 16 cell whitespace with the Liao boundary to be adequate, the total amount of storage at 8.2 Mb is still much larger than the total of 5.4 Mb for the PML, though the running time of 6541 sec is less than the PML's 9130 sec.

The FDTD program is time-stepped for a total of 3.9 microseconds to solve the rod problem for 2048 time steps. The cutoff time with 4 cells whitespace thickness and a 6 cell PML thickness is 15.6 microseconds, much longer than the FDTD time interval. Decreasing the PML thickness to four cell, Fig. 3(b), reduces the cutoff time to 4.6 microseconds, close to the FDTD time interval. But we find little difference between the computed RCS for a 6 cell PML and for a 4 cell PML. But reducing the PML thickness to 2 cells reduces the cutoff time to 0.6 microseconds, and the accuracy of the computed RCS is greatly reduced. With a 4 layer PML and 3 cells of whitespace the computed RCS is little different from Fig. 3(b). This PML formulation requires a total storage of 3.8 Mb and 5,845 seconds to run.

Table 2
Computer Resources for the Rod Scatterer
Using the PML Absorbing Boundary

PML Layers	Whitespace + PML Layers	Time	Cell Space Size	Cell Space Storage	PML ABC Storage
4	8	5,845 sec	117x27x27 cells	2,558,790 bytes	1,173,672 bytes
6	10	9,130	121x31x31	3,488,430	1,900,584
6	12	11,842	125x35x35	4,593,750	2,319,912
10	20	30,327	141x51x51	11,002,230	6,104,232

The Liao ABC with 16 cells of whitespace uses a total storage of 8.2 Mb and a CPU time of 6541 sec. With a 4 cell PML and 4 cells of whitespace, the total storage of 3.8 Mb is 46% less than that used by the Liao formulation, and the running time of 5,845 sec is 89% of that for Liao. Thus by selectively reducing the whitespace thickness and the thickness of the PML layer, we can reduce PML's CPU time and obtain the same degree of agreement with the measurement using much less storage. The PML has a clear advantage.

High-Permittivity, Low-Loss Dielectric Cube

This section compares the computer resources required to calculate the RCS of a dielectric cube resonator with ε_r=37.84, using both Liao and PML ABC. The results are compared with the measured RCS [9]. The side length of the cube is 8.99 mm and the cube was modeled using 15 by 15 by 15 cells to respect the restriction that the FDTD cell size must be smaller than $\lambda/10$. The RCS was measured and computed with a plane wave normally incident on a face of the cube, as a function of the frequency, spanning the cube's first four resonance peaks. The cube is excited with a Gaussian pulse plane wave. FDTD is used to compute the transient far field in the backscatterer direction for 8192 steps. A Prony's series [10] is generated from this FDTD data and is used to extend the time response until it subsides to zero, corresponding to about 131,000 FDTD time steps, with a great saving in computer time. Using the Liao absorbing boundary and an 8 cell whitespace, the agreement with the measured RCS is very, very poor. As the whitespace thickness is increased, the agreement gradually improves, and with 16 cells of whitespace the agreement is quite good, as shown in Fig. 4. As above, using 20 cells of whitespace gets a further small improvement, but more whitespace leads to little change in the RCS.

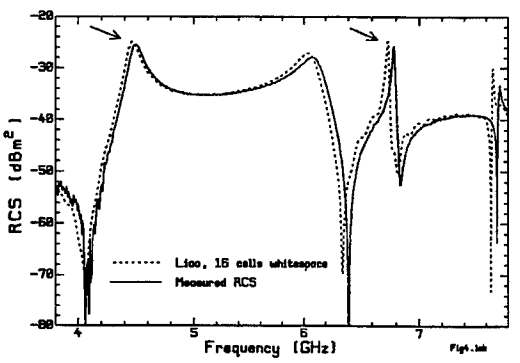

Figure 4 The RCS of the dielectric cube using the Liao ABC.

In Table 3, for 16 cells of whitespace, the FDTD space uses 3.3 Mb of storage, and the Liao boundary, 0.46 Mb, for a total of about 3.8 Mb. The running time is 12,134 sec. If the slightly improved agreement with 20 cells of whitespace is desired, the storage rises to 5.89 Mb and the running time to 18,408 sec.

Table 3
Computer Resources for the Dielectric Cube Scatterer
With the Liao ABC

Whitespace	Time	Cell Space Size	Cell Space Storage	Liao ABC Storage
16 cells	12,114 sec	48 x 48 x 48 cells	3,317,760 bytes	459,268 bytes
20	18,408	56 x 56 x 56	5,268,480	619,012
30	43,187	76 x 76 x 76	13,169,280	1,125,892

Cube Resonator using the PML

Using a 6 layer PML with 4 layers of whitespace, parabolic progression and a surface reflection of 0.001 obtains the RCS shown in Fig. 5(a). The agreement with the measurement is slightly better than in Fig. 4, especially near the first resonance peak. Thinning the PML to 4 layers still obtains excellent agreement with the measurement, as shown in Fig. 5(b). Note that the computed curve in part (b) is different from that in (a). The second resonance peak is taller than the measured peak in part (a), whereas it is shorter in (b).

The time interval corresponding to 8,192 steps is 9.43 nanoseconds. The cutoff time for the PML formulation with a six layer PML is 6 ns, suggesting that the PML is thin for the computation of Fig. 5(a). The cutoff time with four layers of PML is only 1 ns, suggesting that in part (b) the layer is very thin. If we increase the thickness of the PML to 8 layers, the cutoff time increases to 14 ns. But the computed RCS is almost identical to that in Fig. 5(a). Hence for this problem, a 6 layer PML is sufficient. The 6 cell PML with 4 cells whitespace uses 2.2 Mb, compared to Liao's 3.8 Mb, a 58% reduction. The running time of 15,366 sec is about 25% longer than Liao's 12,134 sec.

Table 4
Computer Resources for the Dielectric Cube Scatterer
With the PML ABC

PML Layers	Whitespace + PML Layers	Time	Cell Space Size	Cell Space Storage	PML ABC Storage
4	8	9852 sec	32x32x32 cells	983,040 bytes	477,072
6	10	15,366	36x36x36	1,399,680	800,784

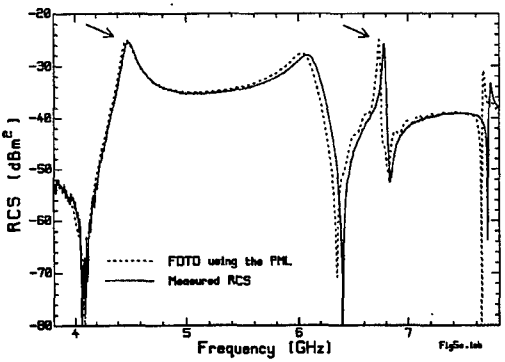

(a) Six cell PML with four cell whitespace.

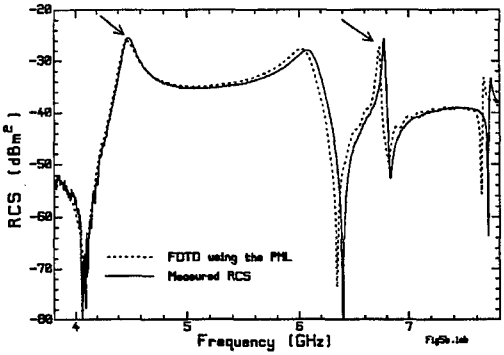

(b) Four cell PML with four cell whitespace.

Figure 5 The RCS of the cube target using the PML.

Conclusion

This paper has compared the memory requirements and CPU time for solving two scattering problems using the Liao second-order ABC and using the PML. The basis for comparison is equally-good agreement with the measured RCS. For the rod problem the PML used 46% less storage than the Liao formulation, and 89% less CPU time. For the dielectric cube problem, the PML used 58% less storage, but about 25% more CPU time. The PML has the clear advantage.

To use the PML effectively, the user must design an appropriate PML for the problem at hand. This paper has explored the parabolic progression of the PML's constitutive parameters. For very thin PML layers and thin whitespaces the geometric progression might offer better performance [2].

This paper shows good results with a 4 cell whitespace separating the scatterer surfaces from the PML surface. The cutoff time for the PML provides a good guide to the required thickness of the PML layer. Thus the user somewhat arbitrarily chooses a PML thickness and the FDTD code compares the cutoff time with the maximum time requested by the user, equal to the time step multiplied by the total number of steps. If the cutoff time is less than the total time, the code exits on an error, and the user must choose a thicker PML. The results of this paper suggest that a cutoff time 50% larger than the total running time is adequate for good agreement with the measurements.

The results reported in this paper fix the reflection coefficient at 0.001, corresponding to 60 dB. All cases were also solved with a reflection coefficient of 0.01 or 40 dB. The cutoff times are about 50% longer with the larger reflection coefficient. For the rod problem, the agreement of the maxima in the RCS in the bracketed region in Fig. 3 is poorer with the larger reflection coefficient. But for the cube problem, little difference in the results was seen.

The study of the computation of the RCS presented in this paper suggests that for the same degree of agreement with measured data, the perfectly-matched layer is comparable in CPU time and requires much less memory than the Liao absorbing boundary. Thus the PML has a clear advantage over the Liao formulation.

References

1. J.P. Bérenger, "A Perfectly Matched Layer for the Absorption of Electromagnetic Waves," *Journal of Computational Physics*, Vol. 114, No. 2, pp.185-200, Oct. 1994.
2. J. P. Bérenger, "Perfectly Matched Layer for the FDTD Solution of Wave-Structure Interaction Problems," *IEEE Trans. Antennas and Propagation*, Vol. 4, No. 1, pp. 110-117, January 1996.
3. Z. P. Liao, H.L. Wong, B.P. Yang and Y.F. Yuan "A Transmitting Boundary for Transient Wave Analysis," *Scientia Sinica*,Vol. XXVII, No. 10, p.1062-1076, October, 1984.
4. K.S. Yee, "Numerical Solution of Initial Value Problems Involving Maxwell's Equations in Isotropic Media," *IEEE Trans. On Antennas and Propagation*, Vol. AP-14, No. 3, pp. 302-307, May, 1966.
5. K.S. Kunz and R.J. Luebbers, "The Finite-Difference Time-Domain Method for Electromagnetics," CRC Press, 1993.
6. C.L Larose, S.R. Mishra, and C.W. Trueman, "Measured RCS Polar Contour Maps for Code Validation," *Applied Computational Electromagnetics Society Journal*, Vol. 11, No. 3, pp. 25-43, November, 1996.
7. R. J. Luebbers, K.S. Kunz, M. Schneider and F. Hunsberger, "A Finite-Difference Time-Domain Near-Zone to Far-Zone Transformation," *IEEE Trans. on Antennas and Propagation*, Vol. AP-39, No.4, pp. 429-433, April 1991.
8. DIGITAL Visual Fortran, Digital Equipment Corporation, Maynard, Mass., August 1997.
9. C.W. Trueman, S.J. Kubina, R. J. Luebbers, S.R. Mishra and C.L. Larose, "RCS of High Permittivity Cubes by FDTD and by Measurement," *9th Annual Review of Progress in Applied Computational Electromagnetics*, Naval Postgraduate School, Monterey, California, March 22-26, 1993.
10. M. L. Van Blaricum, R. Mittra, "A Technique for Extracting the Poles and Residues of a System Directly from its Transient Response," *IEEE Trans. on Antennas and Propagation*, Vol. AP-23, No. 6, pp.777-781, November 1975.

A Uniaxial PML Implementation for a Fourth Order Dispersion-Optimized FDTD Scheme

Gary Haussmann and Dr. Melinda Piket-May
Department of Electrical and Computer Engineering
Campus box 425, University of Colorado, Boulder CO 80309
phone 303-492-7891, fax 303-492-5323
haussman@ucsu.colorado.edu
mjp@boulder.colorado.edu

Abstract

This paper demonstrates the effectiveness of using a Uniaxial PML absorber to truncate the FDTD lattice for a dispersion-optimized fourth order scheme. The fourth order scheme is extended into the PML aborber, efficiently generating small truncation error. An attempt to reduce the computational work in the PML absorbing layer is also presented, and the results of this attempt are discussed.

1 Introduction

Recent developments in the Finite-Difference Time-Domain (FDTD) method have seen a surge of PML development, moving from the original split field absorber [1, 2] to unsplit or material based absorbers [3, 4, 5]. This paper examines the truncation of a fourth order dispersion-optimized FDTD grid (the "M24" scheme [6]) with a PML absorber. While the problem of terminating higher order methods has been examined [7, 8], previous examples implement the standard fourth order difference scheme throughout the FDTD grid, including the entire PML absorbers. Because computation of the curl using the dispersion-optimized fourth order method requires more computation than the traditional second order method, this paper also examines variations of the straightforward PML implementation, using second order difference approximations in an attempt to reduce amount of M24 updates in the PML aborber.

Although using a higher order method in the PML absorbers is required for maximum accuracy, a similar less accurate absorber can be modeled by partially implementing the PML absorber using the faster second order scheme [9]. The interface between space using a fourth order and a second order scheme produces a simulation discontinuity, causing a non-physical reflection. This reflection can be reduced somewhat by embedding the second/fourth order interface into the PML absorber, in which case the non-physical reflection is reduced by loss inherent to the PML absorber.

2 Initial Implementation

The test simulation consisted of a $20 \times 60 \times 20$ grid terminated in an 8 layer PML absorber. The PML boundary is implemented with a uniaxial absorbing material [10], using Maxwell's equations in the form

$$\begin{aligned} \nabla \times \vec{H} &= \frac{\partial}{\partial t}\overline{\varepsilon}\vec{E} \\ \nabla \times \vec{E} &= -\frac{\partial}{\partial t}\overline{\mu}\vec{H} \end{aligned} \tag{1}$$

where the anisotropic material parameters $\bar{\epsilon}$ and $\bar{\mu}$ are defined as

$$\bar{\epsilon} = \epsilon_0 \epsilon_r \begin{bmatrix} \frac{s_y s_z}{s_x} & 0 & 0 \\ 0 & \frac{s_x s_z}{s_y} & 0 \\ 0 & 0 & \frac{s_x s_y}{s_z} \end{bmatrix}$$

$$\bar{\mu} = \mu_0 \mu_r \begin{bmatrix} \frac{s_y s_z}{s_x} & 0 & 0 \\ 0 & \frac{s_x s_z}{s_y} & 0 \\ 0 & 0 & \frac{s_x s_y}{s_z} \end{bmatrix} \tag{2}$$

with values of $s_i = 1 + \frac{\sigma_i}{j\omega\epsilon_0}$. The value of $\sigma_{(x,y,z)}$ is chosen to be the traditional power curve, for example

$$\sigma_x(x) = \sigma \max \left(\frac{x}{d\Delta x} \right)^m \tag{3}$$

where d is the number of PML layers and m - the polynomial power - is set equal to 4, following [10].

The time derivative $\frac{\partial}{\partial t}$ is approximated with a standard second order difference approximation and the curl quantities $\nabla \times \vec{E}$ and $\nabla \times \vec{H}$ are approximated with either M24 style differences and second order differences. The whole interior space always uses the M24 update method; initially the PML layer is also implemented with M24 fourth order updates (figure 1).

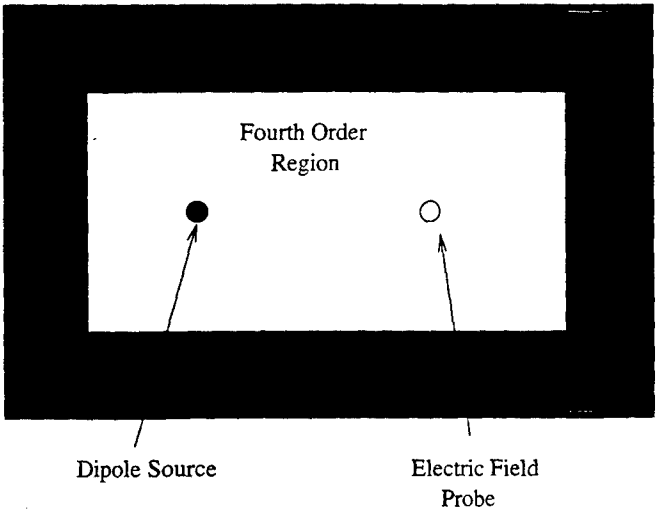

Figure 1: 2D cross section of the 3D test simulation. The PML layer is initially implemented with a standard second order FDTD scheme.

3 Varying the PML Configuration

The initial PML absorber is implemented using only fourth order accurate differences, the same as in the interior region. Then simulations are run which use the fourth order method in a limited region embedded in the PML absorber (figure 2). The remaining regions of the PML aborber are implemented using a faster second order accurate update. The embedding level determines how much of the PML absorber is implemented using fourth

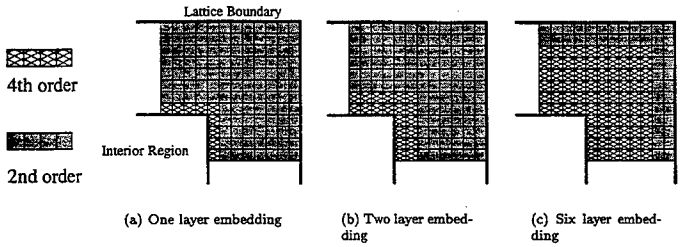

Figure 2: Varying the embedding depth of M24 fourth order updates into the PML absorber

order updates. This embedding can vary from 0 to d, where 0 indicates no fourth order updates in the PML, and d indicates only fourth order updates in the PML is the number of layers in the PML absorber. Since the PML factors in [4] are pre-calculated and stored in spatially-dependent arrays, switching from fourth to second order updates anywhere on the grid is simply a matter of redefining the curl operator. Various regions of the grid are blocked out with C++ template instantiations [11, p.306], using either second or fourth order differences as appropriate and accessing the PML coefficients from various spatial arrays.

4 Simulation Results

To examine the reflection from the absorber, an initial simulation is run with the FDTD grid large enough such that the grid boundaries are far enough to prevent any reflected waves from reaching the probe location during the simulation time. This "perfect" probe data is then compared with the probe data from simulation grids truncated with PML absorbers. The resulting ratio of output/transmitted signal to the error/reflected signal, as the frequency approaches DC [1] is tagged as the reflection amount, and plotted here as a function of the fourth order embedding depth (figure 3).

For the shallow configuration (only a few fourth order updates in the PML absorber), the mismatch between fourth and second order updates produces a large reflection error which propagates back out of the PML layer. As the embedding level is increased, the fourth order updates use more of the PML absorber; the reflection caused by the second/fourth order interface occurs deeper in the PML absorber, with higher loss coefficients. Therefore the second/fourth order discontinuity is increasingly damped by the higher PML aborber loss, resulting in a smaller overall reflection. Increasing the embedding level further eventually results in a full fourth order PML absorber, with only fourth order updates being used in the PML absorber.

A glance at the reflection values (figure 3) indicates that using a hybrid second/fourth order PML absorber does not provide efficient reflections compared to the full fourth order PML absorber; one possible problem is that the value of $\sigma_{\max}$ is optimized for a boundary reflection off the full 8 layer PML, when in fact the dominating reflection is from the second/fourth order interface. Re-optimizing the value of $\sigma_{\max}$ for the fourth order depth only improves the PML absorption by approximately 3dB – still not as effective as a pure fourth order PML absorber.

A plot of the total computation time versus fourth order embedding depth is shown in figure 4. For this graph, the CPU time for an FDTD simulation with pure fourth order PML is normalized to 1, and other times

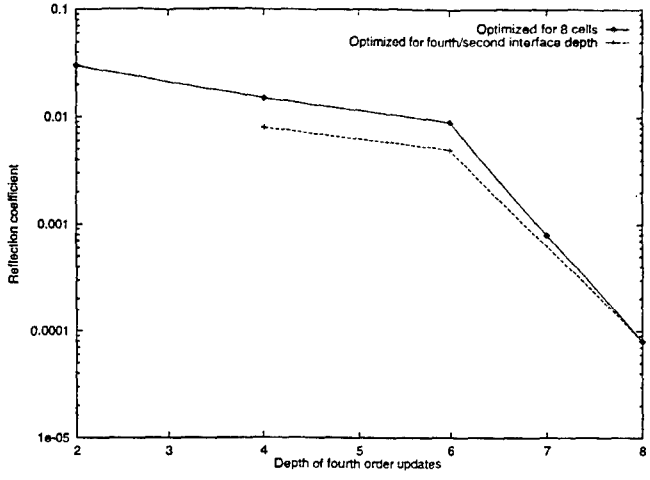

Figure 3: Reflection coefficient of an 8 layer PML absorber implemented with various fourth/second order updates. Embedding of 8 is fully fourth order PML, an embedding of 0 is fully second order PML

scaled accordingly. It is seen that when half of the PML is implemented with second order updates (embedding depth=4), the *overall* run time is approximately 80% that of an FDTD simulation using fourth order updates throughout all the PML. However, the reflection is also 18dB higher for the half/half hybrid PML absorber than for the pure fourth order absorber.

5 Summary

An implementation of a uniaxial PML absorber to truncate a fourth order dispersion-optimized FDTD scheme was discussed. Numerical results produce a reflection coefficient of 10^{-4} for 8 layer PML when the fourth order updates are used throughout the PML absorber.

We have examined the impact of replacing some or all of the higher order updates in a PML absorbing layer with simple second order updates, to examine the relative trade-offs between accuracy and speed. In general, it was seen that implementing all the PML with second order updates totally disrupts the absorbing characteristics, due to the non-physical reflection at the interface between fourth and second order updates. Re-optimizing the value of σ_{max} for the fourth order depth reduces this degradation by a small amount. However, the increase error that occurs due to using a hybrid absorber is too high of a price to pay for the given savings in CPU computation. In addition, the added complexity in programming both second and fourth order updates in the PML absorber further discourages use of a hybrid absorber in this case.

References

[1] J.P. Berenger. A perfectly matched layer for the absorption of electromagnetic waves. *Journal of Computational Physics*, 114:185–200, October 1994.

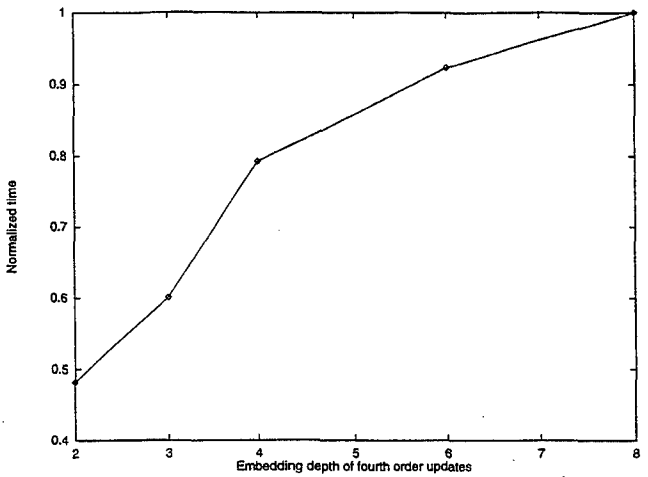

Figure 4: Relative computation time of various PML absorber configurations

[2] D. S. Katz, E. T. Thiele, and Allen Taflove. Validation and extension to three dimensions of the berenger PML absorbing boundary condition for FD-TD meshes. *Microwave and Guided Wave Letters*, 4(8):268–270, 1994.

[3] Richard W. Ziolkowski. The design of maxwellian absorbers for numerical boundary conditions and for practical applications using engineered artificial materials. *IEEE Trans. on Antennas and Propagat.*, 45(4):656–671, April 1997.

[4] Stephen D. Gedney. Efficient implementation of the uniaxial PML aborbing media for the finite-difference time-domain method. In *13th Annual Review of Progress in Apllied computation Electromagnetics* [12], pages 891–899.

[5] Yinchao Chen, Ming sze Tong, Mustafa Kuzuoglu, and Raj Mittra. A new artificial medium based on unsplit anisotropic PML for mesh truncation in FDTD analysis. In *13th Annual Review of Progress in Apllied computation Electromagnetics* [12], pages 920–925.

[6] Gary Haussmann and Melinda Piket-May. FDTD M24 dispersion and stability in three dimensions. In *13th Annual Review of Progress in Apllied computation Electromagnetics* [12], pages 82–89.

[7] Peter G. Petropoulos. The application of PML ABCs in high-order FD-TD schemes. In *13th Annual Review of Progress in Apllied computation Electromagnetics* [12], pages 884–890.

[8] A. R. Roberts and J. Joubert. PML absorbing boundary condition for higher-order FDTD schemes. *Electronics Letters*, 33(1):32–34, January 1997.

[9] K.S. Yee. Numerical solution of initial boundary value problems involving maxwell's equations in isotropic media. *IEEE Trans. on Antennas and Propagat.*, 14(4):302–307, 1966.

[10] Stephen D. Gedney. An anisotropic perfectly matched layer-absorbing medium for the truncation of FDTD lattices. *IEEE Trans. on Antennas and Propagat.*, 44(12):1630–1639, December 1996.

[11] John J. Barton and Lee R. Nackman. *Scientific and Engineering C++: an introduction with advanced techniques and examples.* Addison-Wesley Publishing Company, Inc., Reading, Massachusetts USA, 1994.

[12] *13th Annual Review of Progress in Applied computation Electromagnetics*, 1997.

SESSION 9:

VISUALIZATION IN CEM

Chairs:J. Karty and S.J. Kubina

Plate Scattering Visualization: Images, Near Fields, Currents, and Far Field Patterns

John Shaeffer
Marietta Scientific, Inc.
376 Powder Springs St. 240A
Marietta, Georgia 30064
(770) 425-9760

Kam Hom
NASA Langley Research Center
Hampton, Virginia 23665

ABSTRACT: This paper presents a case study of a simple yet robust target for demonstration of the EM visualization process. A five lambda square plate exhibits many scattering mechanisms depending on excitation angle and polarization: specular scattering, leading and trailing edge diffraction, traveling wave, and edge wave scattering. Bistatic k space radiation images, currents maps, and near scattered / total fields are examined for each of these scattering mechanisms.

Visualization in Computational Electromagnetics: The ultimate goal of computational modeling is to predict observed phenomena. Thus, for many years, computational scattering or antenna EM modeling output consisted of a backscatter or antenna radiation pattern that was compared to experimental results. In this mode, computational modeling did little to aid the identification and understanding of the physical mechanisms responsible for observed behavior. This limitation was unfortunate. Computational EM codes should in principle be able to provide a rich insight to the scattering or radiation process if we just ask the proper questions and use the rapidly developing graphical display capabilities to illustrate the basic phenomena. Our EM visualization inspiration is similar to efforts in computational fluid dynamics. We are attempting to better understand the interaction of an EM wave or local excitation with a structure, the nature of body-body interactions, and the nature of the resultant radiation.

Visualization diagnostics for electromagnetics involve the display of body currents, near fields and radiation images. Each display tells us something different about the radiation process. Taken together, these diagnostics produce a richer understanding of complex EM phenomena.

Currents (or effective tangential magnetic or electric fields) are the fundamental quantities which produce far field radiation patterns and are often the computational goal, e.g. MOM codes. Knowledge of the current amplitude and phase distribution on a geometric structure is sufficient to compute the radiation pattern. Although a graphical display of currents indicates the spatial amplitude distribution, it does not tell *how* the currents radiate in different directions in space.

Displays of near field E and H indicate how one part of a structure interacts with another part, how the surface currents and charges begin to form the eventual far-field radiation pattern and how various surface current modes are formed such as surface and edge traveling-wave mechanisms.

Bistatic k space imaging is yet another diagnostic tool for examining the scattering/radiation process. An image is not a picture of currents, but of the far field radiation produced by the currents. Images differ from a body current distribution in that an image shows *how* the currents radiate. An image from a given angle tells us which *parts* of the current distribution are producing radiation in that direction.

Far field radiation is the phasor sum of signals from *all* radiation centers on the body that radiate in the observed direction. An image identifies each center as a separate entity. The utility of images results from the ability to separate and identify the individual radiation centers that have collectively summed to produce the net result. This enables us to understand the nature of each radiation center and to modify it in ways that might be useful.

Visualization Parameters: Bistatic k-Space images [1-3] show the current distribution regions that radiate into the direction of the observer. These images do not require a frequency sweep, as do conventional experimental images. They are obtained by from the current distribution by evaluating the far field radiation integral over down and cross range directions in k-space and then performing a Fourier transform. One, two and three-dimensional images can be computed.

Surface currents, the computational goal of MOM codes, are the source of the observed visualization parameters: images, near fields, and far-scattered fields.

Currents and near fields are complex quantities. The real and imaginary parts represents the two independent time solution corresponding the phase of the incident excitation, time t = zero and –90 degrees of the excitation. Time harmonic animation is obtained by adding these two basis solutions. A time average root mean square (RMS) value is the value observed experimentally.

Near fields are computed from the current and charge distribution. Scattered fields are those produced directly by the currents. Total fields are the sum of the incident field with the scattered field.

Plate Geometry: The plate is square with side dimension of five wavelengths, Figure 1. The MOM code solution was obtained using MOM3D [4] and the visualization was obtained using EM ANIMATE [5]. Plane waves were used to excite the plate.

Far Field Backscatter Patterns: The traditional prediction code output for the backscatter patterns are shown in Figure 2. The elevation cut perpendicular to the plate edges, (a), show the backscatter magnitudes for specular, end region, traveling wave and edge diffraction. The elevation cut along the plate diagonal, (b), shows the backscatter due to specular, traveling wave and end region mechanisms. The azimuth cut in the plane of the plate for horizontal polarization, (c), has edge wave and edge specular scattering mechanisms.

Visualization: Current and field contour plots have a reverse gray scale. High value are black and low values are light.

Perpendicular Excitation: The induced plate currents, Figure 3, have the nominal physical optics value of twice the incident magnetic field along with a smaller component flashing back and forth between the edges forming a standing wave component. The scattered field produced by these currents radiates broadside to the plate on each side. Plate regions appear as line sources. The total field is perpendicular to the plate (as required by the PEC boundary conditions). The time average total field shows a shadow region behind the plate where the scattered and incident fields phase subtract. In front of the plate the total field shows a standing wave pattern resulting from the interference of the incident and scattered fields. The first peak occurs at $\lambda/4$ above the plate. The resultant backscatter from these currents is the broadside-specular value of $\sigma = 4\pi A^2 / \lambda^2 = 7854\, m^2 = 39\, dbsm$. The backscatter two-dimensional bistatic k space image shows a distributed source across the plate where each portion of the current distribution is contributing to the scattered field. The distributed image magnitude has a value that depends on the effective image resolution and coherent length [1].

45° Slant Angle Excitation: At 45° incidence with E parallel to the plate edge, Figure 4, the plate currents are still physical optics like with linear phase and a leading edge line source due to edge diffraction. The scattered field shows two major phenomena. The leading edge diffraction line currents are producing a cylindrical scattered wave while the physical optics currents are producing a forward and reflected scattered field symmetric about the plate. The total field shows the shadow formed on the plate backside and an interference pattern on the upper side. The backscatter bistatic k space image shows the leading and trailing edge of the plate as the major sources of radiation. The leading edge current line source is dominant.

0° Edge On Excitation: Edge illumination with E parallel to the edge, the major plate currents are the leading edge diffraction currents and two edge wave components which reflect from the rear plate vertices, Figure 5. The scattered field now is due mostly to leading edge diffraction line currents and is a cylindrical wave centered at the leading edge. The total field shows the shadow behind the plate and the interference pattern from the incident and scattered fields. The backscatter bistatic k space image shows the leading edge diffraction line source as the dominant scattering source. Secondary scattering sources are the two edge waves reflecting from the rear plate vertices. The line source backscatter magnitude is dependent on the plate edge length, $\sigma = L^2/\pi = 8\, m^2 = 9\, dbsm$.

Traveling Wave Excitation at 22.5°: For vertical polarization near grazing, backscatter is due to a traveling wave reflected by the rear edge, Figure 6. The angle up from grazing at which this mechanism peaks is given by $\theta = 49\sqrt{\lambda / L}$ = 22.5°. The traveling wave return is very similar to trailing edge diffraction for surface only a few wavelengths in size. The surface current display clearly shows the build up of the traveling wave as it builds in magnitude as it propagates aft on

the plate where it reflects. The scattered field shows: 1) the surface wave on the plate; 2) the specular forward and reflected wave; and 3) the field produced by the reflected traveling wave which appears to emanate from the trailing edge. The total field shows the shadow behind the plate as well as the interference pattern between the scattered and incident fields. The backscatter bistatic k space image clearly shows the entire plate contributing to the scattered field with the trailing edge being the peak. This is consistent with the notion that the surface current reflected wave loses energy via radiation after reflection from the back edge.

Edge Wave Excitation: When the plate is illuminated with horizontal polarization in plane the plane of the plate along the diagonal, backscatter is due to two edge waves reflected from the mid vertices, Figure 7. The current visualization clearly shows the edge currents flowing down the two illuminated edges. The scattered field in a plane along the plate diagonal shows the front tip diffraction. The total field shows the shadow and the interference pattern between scattering and incident fields. The backscatter bistatic k space image clearly shows the source as the two reflected edge waves. Note that the peak is at the mid vertices. The edge wave decays as it radiates away from the reflection point. A smaller amount of scattering is from the rear vertex due to edge waves that "turned" the first corner and are now being reflected from the back tip.

Traveling Wave Excitation Along Diagonal: For vertical polarization up 22.5° from grazing, a surface traveling wave is formed, Figure 8. Now, however, the rear reflection point is the rear vertex. The surface current visualization clearly shows the build up of the surface currents as the wave travels aft on the plate as it gains energy from the incident field. The scattered field in a plane along the plate diagonal shows the surface traveling wave on the plate. The scattered field from the rear vertex is apparently much smaller than the forward scattered energy and is not seen. The total field shows the interference pattern between the scattered and incident fields. The backscatter bistatic k space image shows the aft vertex region as the major source of backscatter. This is entirely consistent with the concept of the reflection of the surface traveling wave.

VFY218 Aircraft: A combined visualization for a non-simple scattering body is shown in Figure 9. The illumination is nose on, vertical polarization. Surface currents are displayed on the aircraft body. Scattered fields are shown in a vertical plane down the length of the vehicle. The backscatter bistatic k space image is shown in the horizontal plane.

Summary: Electromagnetic visualization shows many of the basic physical processes by which energy radiates, propagates, and reflects. Visualization aids in identifying scattering mechanisms. Once we are better able to understand how energy is scattered or how an antenna radiates, then we are better able to modify the scattering/radiating structure for more desirable results.

References

1. John Shaeffer, Kam Hom, Craig Baucke, Brett Cooper, and Noel Talcott, Jr., "Bistatic k-Space Imaging for Electromagnetic Prediction Codes for Scattering and Antennas", NASA Technical Paper 3569, July 1996.

2. John Shaeffer, Kam Hom, Craig Baucke, Brett Cooper, and Noel Talcott, Jr., "A Review of Bistatic k-Space Imaging for Electromagnetic Prediction Codes for Scattering and Antennas", IEEE Antennas and Propagation Magazine, Feature Article, vol. 39, no. 5, October, 1997.

3. Kam Hom, Noel Talcott, Jr., and John Shaeffer, "Computational Diagnostic Techniques for Electromagnetic Scattering: Analytical Imaging, Near Fields, and Surface Currents", ACES, March 17-21, 1997.

4. John Shaeffer, "MOM3D Method of Moments Code Theory Manual," NASA CR 189594, Contract NAS1-18603, March 1992.

5. Kam Hom, "EM Animate: A Computer Program for Displaying and Animating Electromagnetic Near Field and Surface-Current Solutions", NASA Technical Memorandum 4539, May 1994.

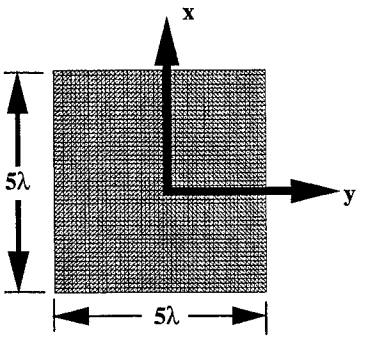

Figure 1. – Plate geometry and coordinate system.

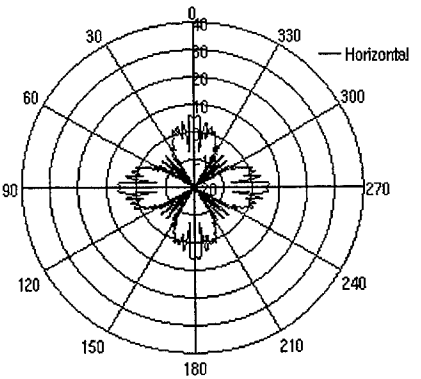

c) Azimuth cut, el = 0. deg.

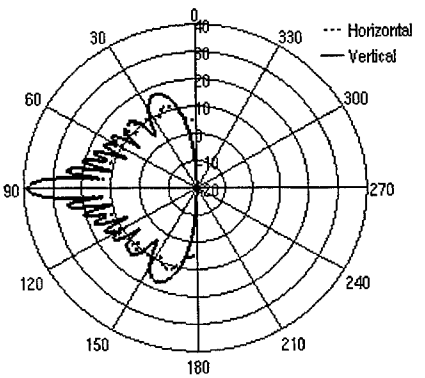

a) Elevation cut, az = 0. deg.

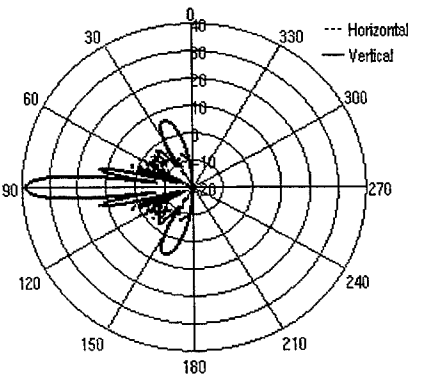

b) Elevation cut, az = 45. deg.

Figure 2. – Backscatter RCS patterns at different plane cuts.

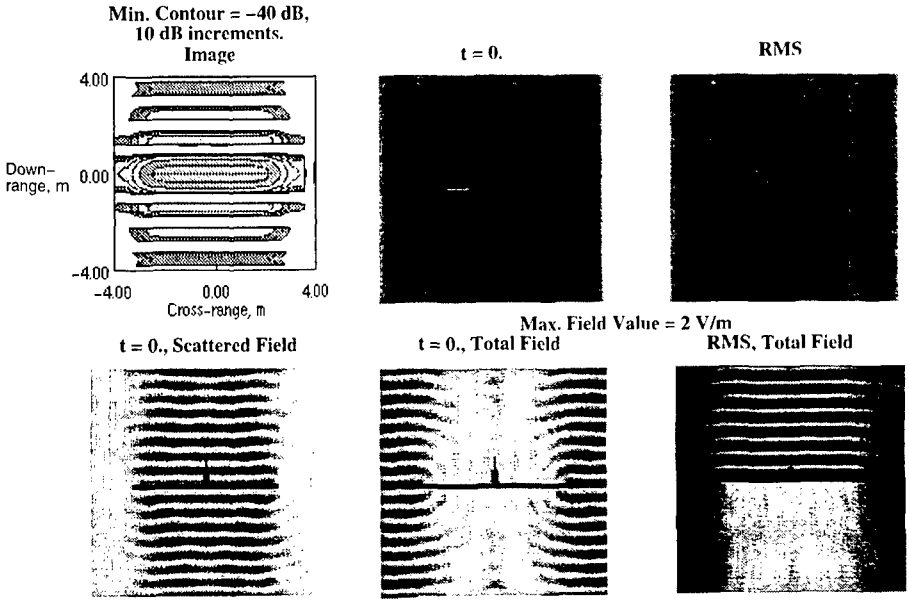

Figure 3. – Currents, radiation image, and fields: perpendicular to plate, E phi polariztion.

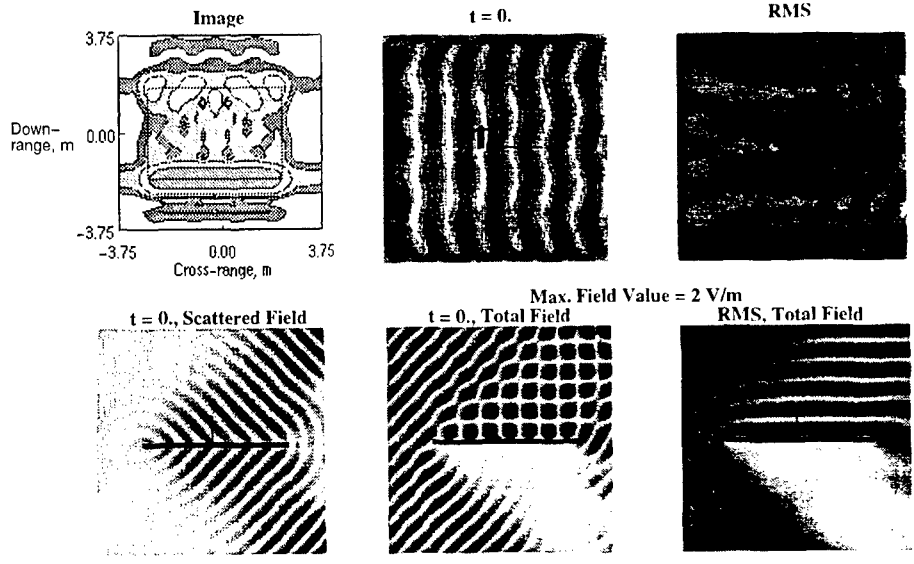

Figure 4. – Currents, radiation image, and fields: 45^{0} specular to plate, E phi polariztion.

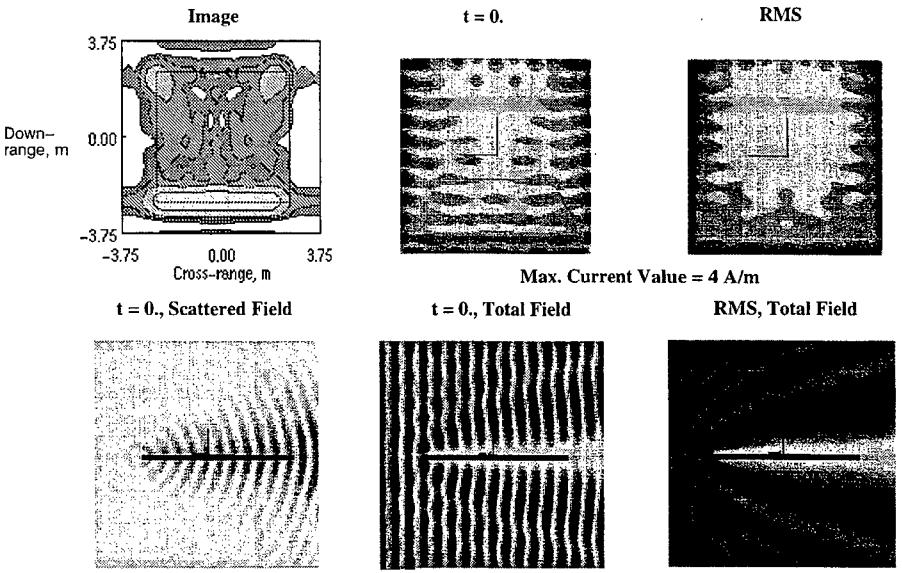

Figure 5. – Currents, radiation image, and fields: 0^{O} azimuth, 0^{O} elevation, E phi polariztion.

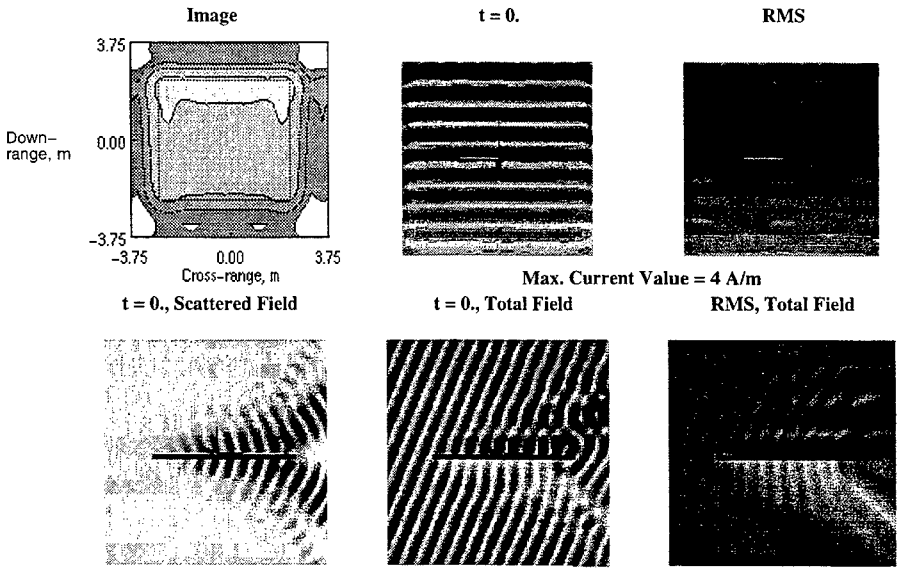

Figure 6. – Currents, radiation image, and fields: 0^{O} azimuth, 22.5^{O} elevation, E theta polariztion.

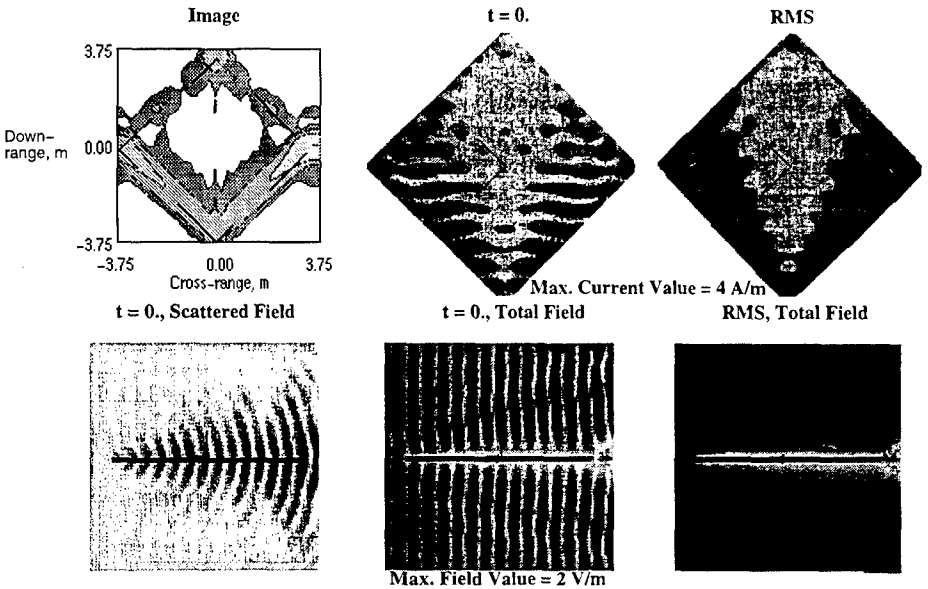

Figure 7. – Currents, radiation image, and fields: 45^{0} azimuth, 0^{0} elevation, E phi polariztion.

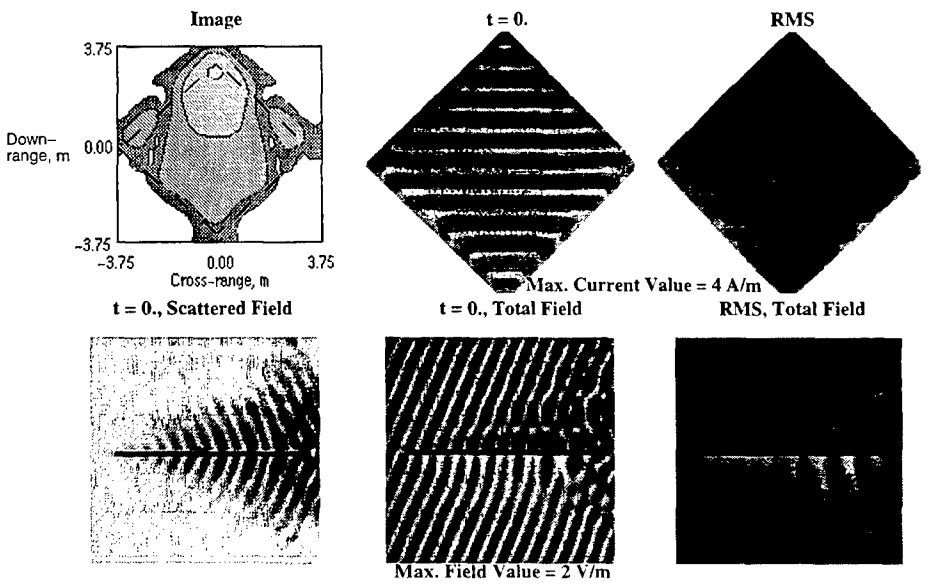

Figure 8. – Currents, radiation image, and fields: 45^{0} azimuth, 22.5^{0} elevation, E theta polariztion.

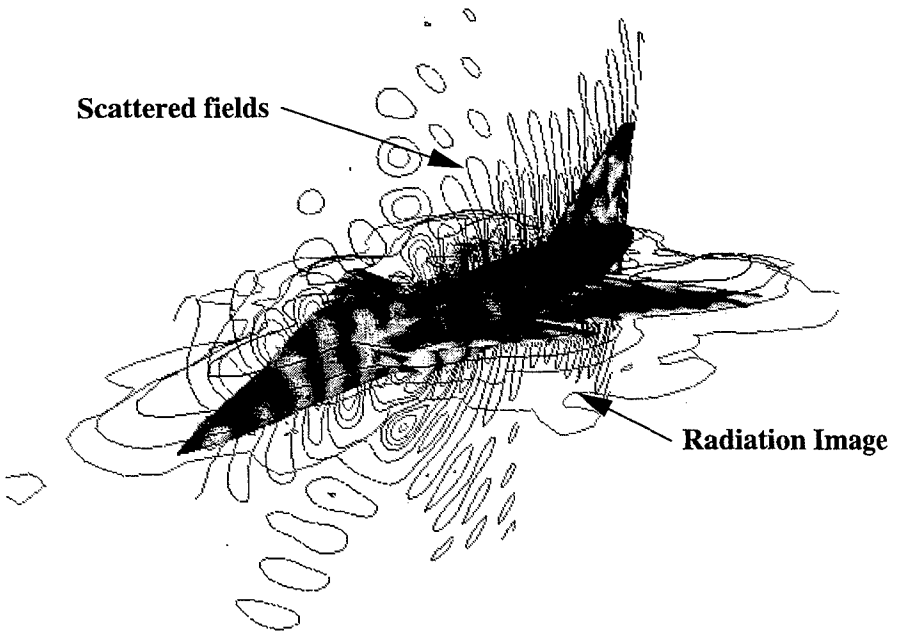

Figure 9. – Currents, radiation image, and scattered fields for VFY218, 0^{O} azimuth, 0^{O} elevation, E theta polariztion.

Visualization Aids for Effective Aircraft Antenna Simulations

Stanley J. Kubina, Christopher W. Trueman, Quan Luu and David Gaudine
EMC Laboratory, Concordia University
Montreal, Que. Canada

Abstract

Three-dimensional radiation patterns and associated current distributions, that are produced in a high resolution spectral analysis, can now be presented in a dynamic movie-like format, sequencing at 0.1MHz, through the entire 2-30 MHz HF frequency range. Such results are presented for an HF Notch antenna on the CL-600/CHALLENGER business jet built by Canadair. Impedance and performance vs. frequency data form the framework to which these displays apply. In addition, model development and model characteristics can be illustrated in a complete visualization process that produces an unusually integrated and complete grasp of the entire modeling process for aircraft antennas and of the rapid pattern changes when primary aircraft modes are excited.

Introduction

In the application of computational electromagnetics to complex structures, we have found it essential to develop a software system that keeps the creator in intimate contact with his EM simulation model. This applies particularly to the features which might govern its electromagnetic equivalence to the real structure. In addition, our system is intended to simplify the execution process and link a complete solution file to specific software display modules. These modules, while providing a self-validation component, are designed to be templates of the results as sets of operationally-relevant displays. In the earliest pre-ACES Progress Reviews [1] we coined our goal to create a **"thought amplifier"** for the difficult and error-prone task of electromagnetic analysis with complex models. The availability of meaningful and inter-related images is critical to this process.

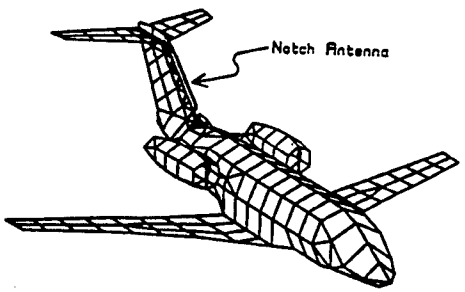

Fig.1 CL-600/CHALLENGER – 666 Segments

This paper is restricted to our experience with the Numerical Electromagnetics Code NEC [2] and its variants and other moment method codes. The basis of our model creation process has been the gathering of **GUIDELINES** [3] that should apply to a reliable simulation model. Our NEC modeling guidelines are summarized in Table 1. The implementation of these guidelines is tested in the model creation and checking segment of the **EMC Laboratory**

Integrated Software System [4], shown in the block diagram of Figure 2. It can be seen that displays of radiation patterns, maps of fields, currents and relevant parameters are the 'raison d'etre' of most of the software modules shown in the diagram.

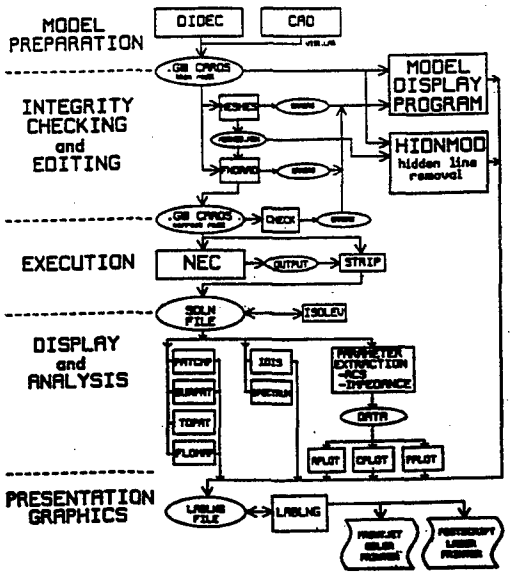

Fig. 2 EMC Lab Software System

The nature of the displays used to augment the visualization process can often produce unexpected results. The data integration, valuable in itself, can produce a perception of special features of the models that are being used and their response to specific excitations. An example of this phenomenon has been described in the rectangular and polar forms of the contour maps for both measured and computed Radar Cross Sections (RCS) of canonical shapes, presented as frequency sweeps for a range of orientations of the target by Trueman et al.[5]. In these results, the pattern features suggest the immediate association with important scattering centres of the targets.

In this paper, it is our intention to present the results of a high resolution spectral analysis [6] of an **HF "Notch"** antenna on the **CL-600/CHALLENGER** Canadair executive jet aircraft. The 666 segment model of this aircraft is shown in Figure 1. This extensive analysis lends itself to the exposition of the importance of visualization in the model creation process and in the several important phases of post-processing of the results. A similar result was presented for the BT-412 Utility helicopter at last year's ACES conference [7].

The Model and Its Essential Characteristics

The 666-segment model shown in Figure 1 was created by the systematic digitization of available aircraft drawings using the **DIDEC** [8] model creation software. DIDEC uses a multi-windowing system for the digitization of separate components, their attachment and reflection, etc. It can also import and export AUTOCAD files, and its output is compatible with other computer codes such as JUNCTION [9] and MBC[10].

Model verification and checking is performed by the FNDRAD/MESHES/CHECK combination [11,12] of software modules. Experienced modeling proponents might immediately identify key features of the final 'elegant' model shown in Figure 1. One summary of its features is the histogram of Figure 3, which shows the number of segments versus segment length. Although it is desirable to keep the segment lengths uniform, some variations are unavoidable. An example of the evolution of the vertical stabilizer is shown in Figure 4. It was found desirable to break up the small loops of the frontal edge and the number of small segments by using the design of Figure 4 b).

The various 'error' and 'warnings' that form the output from CHECK can be understood in the visualizations illustrated in Figure 5. Shown is the use of MODEL with the display of segment radii to illustrate segment-to-segment stepping and segment junction warnings. More extensive examples of model diagnosis for segments, junctions and meshes are presented in the referenced papers [11,12].

TABLE 1
SUMMARY OF THE MODELLING GUIDELINES
Δ = segment length
a = wire radius
λ = wavelength

INDIVIDUAL SEGMENTS	Warning	Error
segment length	$\lambda/10 < \Delta < \lambda/5$	$\Delta > \lambda/5$
radius	$30 < \lambda/a < 100$	$\lambda/a < 30$
segment to radius ratio	$0.5 < \Delta/a < 2$	$\Delta/a < 0.5$
JUNCTIONS		
segment length ratio		$\Delta_{big}/\Delta_{small} > 5$
radius ratio	$5 < a_{big}/a_{small} < 10$	$a_{big}/a_{small} > 10$
segment to radius ratio	$2 < \Delta/a < 6$	$\Delta/a < 2$

PC Workstations are now capable of 'windowing' all these aspects of the model in a comprehensive compendium of model characteristics. Note that all of these are directly linked to the implementation of the guidelines. Recall also that these have their roots in assuring the best possible electromagnetic equivalences of the wire grid model to the real aircraft. In some cases trial runs are undertaken, while in others, the model is considered good enough for a serious and complete analysis.

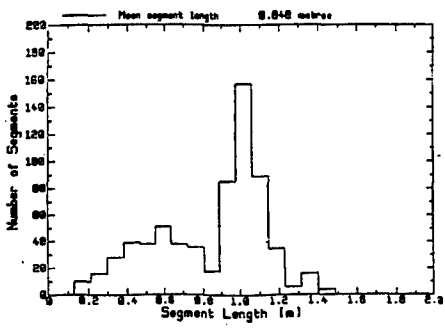

Fig. 3 Model Segment Profile

Indeed the model of Figure 1 was used to perform the high resolution spectral analysis [6] in the complete HF range 2-30 MHz at 0.1MHz frequency steps. Such a vast but complete data file now makes it possible to present the results in all its individual and composite aspects. Note from Figure 2 that impedance vs. frequency plots, current distributions at each frequency, radiation patterns in various formats and certain mission-related integrations of radiation patterns, such as plots of individual 'performance parameters' vs. frequency are available. The next section shows some typical examples. Some of them will be presented in a 'movie-like' format in the oral presentation.

Fig. 4 Evolution of the Tail Structure

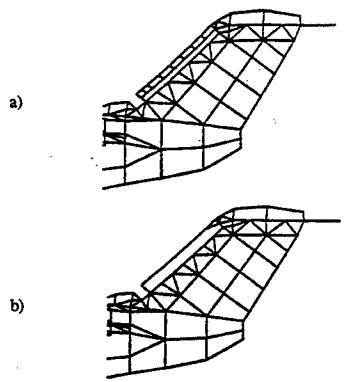

Fig. 5 Segment Radii Displays

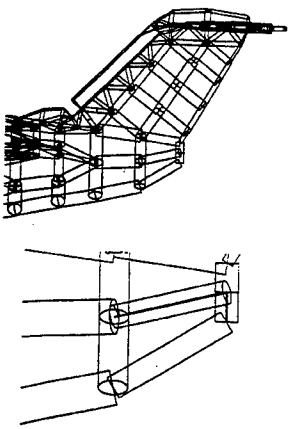

Simulation Results

Our practice is to archive NEC output files, 'stripped' to contain the essential geometry and solution data in the minimum disk space. The software module called **STRIPNEC** performs this function. In addition it is important for us to have radiation patterns calibrated to an isotropic reference level. This latter level is obtained by integrating the total radiated power in a standard conical data set [13] and then inserting the isotropic level into the output file. We also use this process for measured radiation patterns in order to obtain an exact amplitude equivalence for the two polarizations. This function is performed by the **ISOLEV** module (Fig.2). The 'performance parameters' [13]: radiation pattern efficiency, $\%E_\theta$, $\%E_\theta$* and HVIS, are also computed and inserted into the output file. All the modules listed under "Display and Analysis" in Fig.2, access this data base and provide the important visualization required by the analyst.

Validation will remain a critical component of computational electromagnetics [14]. When measurement results cannot obtained prior to an analysis, it is important to exploit any self-contained means to gain confidence in the computational analysis that is being done. Convergence tests are useful. However a productive approach is the close examination of current distributions that form the solution of a given code. These can produce the necessary insights into the characteristic response of a complex body, provided that the displays help in the diagnosis. In our software system the two modules **IDIS** and **SPECTRUM** produce colour-coded segments of the wire-grid corresponding to the amplitude and phase of the current. **IDIS** also enables selected rectangular plots of amplitude and phase and the display of current amplitude and phase as orthogonal lines to selected segments of the grid. Coupled with radiation patterns in any of the forms suggested by the software block diagram (Fig.2), one gains access to a visualization scheme that results in an understanding of model behaviour which is essential to the process.

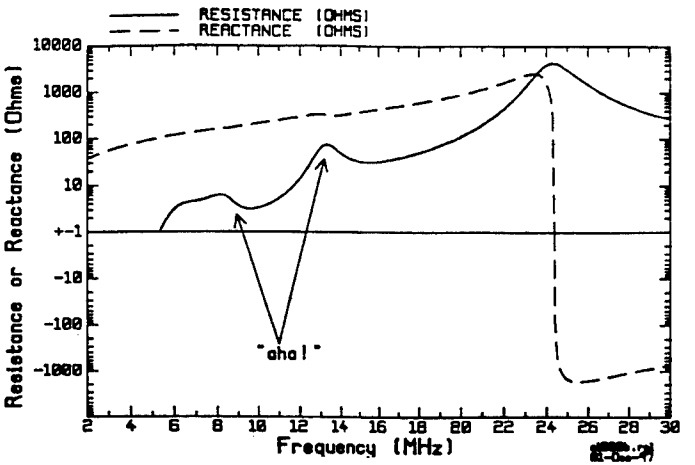

Fig. 6 a) Computed Impedance vs. Frequency – HF Notch Antenna

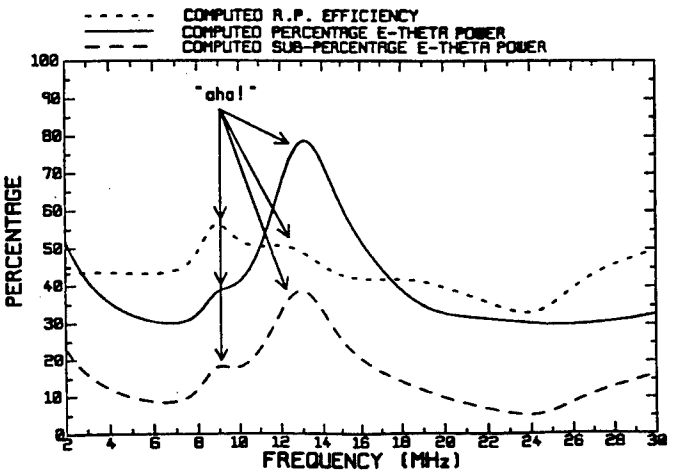

Fig. 6 b) Computed Performance Parameters vs. Frequency – HF Notch Antenna

Selections from a typical sequence are illustrated in Figures 6 and 7. Computed resistance and reactance of the antenna vs. frequency are plotted in Figure 6 a). The deviations from a monotonic increase in the resistance, noted by the 'aha!' label in the diagram are specially interesting. Figure 6 b) shows the plot of three of the performance parameters vs. frequency. The designated points in the impedance curve represent a coupling of the primary antenna element (loop) currents to primary modes of the aircraft structure [15]. These in turn result in rapid and radical changes in the radiation patterns as shown by the plots of the performance parameters. These characteristic shapes and rapid changes are illustrated for 9 MHz in Figure 7. It is impossible here to illustrate the meaningful colour-coded changes

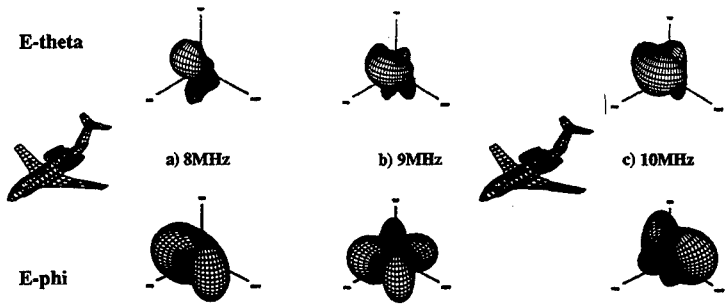

Fig. 7 – TDPAT Displays: 8, 9 & 10 MHz – HF Notch Antenna

in the current distributions that are actually shown alongside the 3-D radiation pattern displays on the computer screen for the **TDPAT** program.

An example of the diagnosis of a characteristic current path is illustrated in the referenced publication by Q. C. Luu [16]. He shows in rectangular plots of current amplitude and phase versus selected segments how constant phase of the current along this selected path is as an indication of a resonant condition. However, to see the sinusoidal amplitude distribution, corrections must be made for currents that are part of adjacent meshes.

Sequentially executed, this set of graphic images provides that valuable comprehension of what happens to the radiating structure and what the consequences are in the values of the operational parameters. Now however, a new powerful aspect can be introduced by the presentation of these complex data sets in a dynamic 'movie-like' format.

Dynamic Presentation of Frequency Sweep Results

What has been illustrated above in Figure 7 a) through c) is the composite visualization of the aircraft current distributions and the associated 3-D radiation patterns, for both polarizations. These are produced by the TDPAT module. Ed Miller introduced a dynamic movie presentation of currents some

time ago [17]. More recently Allan Nott [18] presented the movie-like display of radiation patterns in the 1996 ACES conference and we followed suit in 1997 [7] by a set similar to the present one, for the BT-412 Utility Helicopter.

This dynamic and complete sequence produces an integration of the results 'sans pareille'. It shortens the time of exposure of the mind to the entire data set while showing all its essential elements at each frequency. Multiple sweeps through the set quickly identify explicit regions for further detailed examination and analysis. Aircraft radio operators and mission analysts find the data easy to grasp and to translate into communications expectations.

The movie-like displays can be imagined as scanning along the impedance and parameter curves from left to right and seeing at once the consequences in aircraft current response and radiation pattern shape and intensity. With modern PC workstations, composite windowing can produce such complete exposition of the data. This had been the substance of our dreams in past decades. This present format has been so enthusiastically received that sponsors tend to forget about the necessity of the validation process and their commitment to corresponding scale-model measurements.

Summary

The visualization produced by specially designed graphics modules for model creation and analysis of NEC modeling results can now be incorporated into a coherent whole. Thus we can effectively create the simulation model and appreciate its characteristics. When the solution components are then displayed in relation to currents on the body and the operational parameters of the antenna, especially using the movie-medium, an integrated appreciation is obtained that had been out of reach for these complex simulations.

Acknowledgments

The wire-grid models used for our paper were generated for a Canadian Department of Defence study sponsored by Mr. Harvey Tremblay (DND/DTA3-5). This work formed part of the M. A.Sc. thesis of Q.C. Luu. Research assistance for the present set of high resolution spectral analysis sweeps was provided by Anne Luong.

References

[1] S. J. Kubina, " The E.M. Modeling Programs and Techniques at the EMC Laboratory", FUTURE-NEC, Naval Post Graduate School, Monterey, CA, 29-30 November 1983.

[2] G. J. Burke and A. J. Poggio, "Numerical Electromagnetics Code – Method of Moments, Part III: User's Guide", Technical Document 116, Naval Electronics Systems Command ELEX 3041), July, 1977.

[3] C. W. Trueman and S. J. Kubina, "Fields of Complex Surfaces Using Wire Grid Modeling", IEEE Transactions on Magnetics, Vol.27, No.5, September 1991.

[4] S.J. Kubina, C. W. Trueman, D. Gaudine and A. Ramos, "Creation, Visualization and Analysis – The Dynamics of Complex Models", Proceedings of the ACES 93 Conference, Monterey, CA.

[5] C. L. Larose, S. R. Mishra and C. W. Trueman, " Measured RCS Polar Contour Maps for Code Validation", ACES Journal Vol.11 No. 3, November 1996.

[6] Q.C. Luu, S. J. Kubina and C. W. Trueman, "Coupling Modes in Complex HF Aircraft Installations and Their Impact", 1993 East Coast Applied EM Symposium, Sydney, NS, Aug. 1993.

[7] S. J. Kubina, C. W. Trueman and David Gaudine, "Experiments with NEC3 and NEC4: Simulation of Helicopter HF Antennas", Proceedings of the 13th Annual Review of Progress in ACEM, Monterey CA, March 1997.

[8] S. J. Kubina, "An Interactive System of Model Creation for NEC: Helicopter Model Case Study", Proceedings of the Annual Review, Applications of Numerical Electromagnetics Code, LLNL, University of California, March 1985.

[9] S.U. Hwu and D. R. Wilton, "Electromagnetic Scattering and Radiation by Arbitrary Configurations of Conducting Bodies and Wires," AEL, Univ. of Houston, Tech Rept 87-17, May 1988.

[10] M. A. Tilston and K. G. Balmain, "A Multi-Radius Reciprocal Implementation of the Thin Wire Moment Method," AP-S Transactions, Oct. 1990.

[11] C. W. Trueman and S. J. Kubina, "Automated Radius Calculation for Wire-Grid Models", Proceedings of the 7th Annual Review in ACEM, Monterey, CA , March 1991.

[12] C. W. Trueman and S. J. Kubina, "Verifying Wire-Grid Model Integrity with Program CHECK", ACES Journal Vol. 5, No.2, Winter 1990.

[13] S. J. Kubina, "Measurement and Computer Simulation of Antennas on Ships and Aircraft for Results of Operational Reliability", Proceedings of AGARD Lecture Series 165, October 1989.

[14] S. J. Kubina and C. W. Trueman, "Some Practical Considerations in the Validation of EM Modelling Codes", IEEE 1988 AP-S Symposium, Syracuse, NY, 1989.

[15] J. V. Granger, "System Considerations in Aircraft Antenna Design", IRE Transactions on Airborne Electronics, Vol. AE-1, December 1951.

[16] Q.C. Luu, "Numerical Techniques for the Study of HF Coupling Modes on Large Aircraft", M. A.Sc. Thesis, ECE Dept. Concordia University, May 1994.

[17] E. K. Miller and J. A. Landt, "Time-Domain Computer Models for Wire Structures", 1974 URSI Symposium on Electromagnetic Wave Theory, Imperial College of Science and Technology, London, UK, July 1974. and pre-ACES presentations.

[18] H. A. Nott, "Electromagnetic Visualization Using Commercial Software", ACES 12th Annual Review of Progress in ACEM, Vol.1, Monterey CA, March 1996.

Visualization of Radiation from a Spiral Antenna Using EM-ANIMATE

R. A. Pearlman, M. R. Axe, J. M. Bornholdt, J. M. Roedder

The Boeing Company
Mail Code S0642263
P.O. Box 516
St. Louis, MO 63166

Abstract

A spiral antenna bent to conform with the leading edge of an aircraft wing was analyzed using a hybrid method of moments/high frequency technique. Analysis of such a large problem would not have been possible without using a hybrid technique. Free space near field radiation generated by the antenna was used to calculate impressed currents on the aircraft and resulting reradiation. The results show excellent agreement with measured data. Animation was used to investigate the differences between flat and bent spiral performance. Visualization was also used to locate which aircraft surface features perturb the antenna pattern. Such visualization allows a complex problem to be observed and provides clues for further study.

1. Introduction

A broadband spiral antenna mounted on an aircraft wing's leading edge was modeled with a hybrid method of moments/high frequency asymptotic technique using the preliminary HyPACED Code [1]. The code integrates elements of both CARLOS [2] and CADDSCAT [3,4] into an interactive hybrid with both low frequency and high frequency capability. The center feed and two spiral arms were modeled with approximately 3000 triangular facets as depicted in Figure 1. In the first step of this hybrid formulation the electric currents J flowing on the spiral arms were calculated exactly for a free space environment, i.e., in the absence of the aircraft. Rao-Wilton-Glisson rooftop basis functions were used in a standard Galerkin formulation resulting in a symmetric impedance matrix with 3324 unknowns.

The next step was to calculate the effect the presence of the aircraft has on the free space antenna pattern. It was assumed that the impressed currents on the surface of the aircraft could be closely approximated by assuming the surface to be locally flat with a total electric current equal to $2\mathbf{n} \times \mathbf{H}_p$, where $\mathbf{n}$ is the surface normal unit vector and $\mathbf{H}_p$ is the magnetic field at the surface due to radiation from the currents calculated in the first step. (This is the standard physical optics assumption.)

The aircraft on which the antenna was mounted was modeled as parametric bicubic surfaces, assumed to be perfectly conducting. Ray tracing was employed to determine which portions of the aircraft surface were directly illuminated by radiation from the antenna and which portions of the surface were shadowed using a CADDSCAT derived algorithm. Only portions with a direct line of sight to the antenna were assumed to reradiate energy into the far field. It was assumed that aircraft reradiation had negligible effect on antenna currents and the direct radiation it produces.

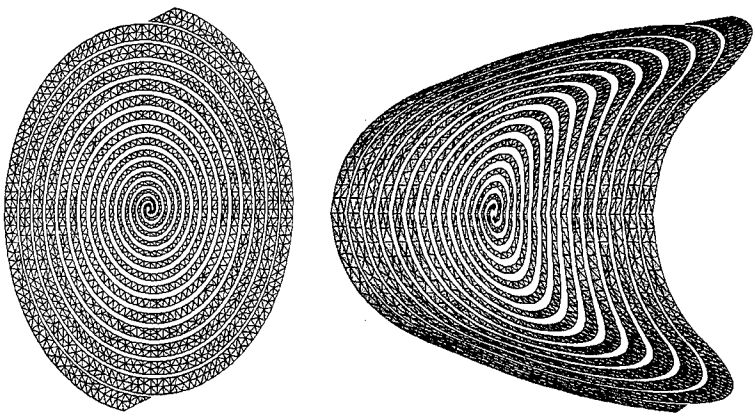

(a) Flat Spiral (b) Conformal Spiral

Figure 1- Spiral Antenna Faceted Model

The calculated currents on the spiral arms of the antenna were displayed using EM-ANIMATE [5], a computer code for displaying and animating electromagnetic near field and surface current solutions. This code takes the complex vector quantities representing sinusoidal steady state solutions for the currents and electromagnetic fields and translates them into time-dependent quantities as a linear combination of the real and imaginary terms with sine and cosine functions. The instantaneous value of the current or field is displayed in discrete time frames between the radian time period of 0 and 2π.

2. Formulation

An exact numerical solution for the entire system including the antenna and the aircraft on which it is mounted can be formulated as follows.

$[Z]\ [J] = [V]$

where $[J]$ = currents on antenna and aircraft

$[Z]$ = impedance matrix

$[V]$ = antenna voltage excitation

In this formulation the impedance matrix is full so that all portions of the system interact with all other portions. This exact formulation can be partitioned using domain decomposition into solutions for spiral currents and solutions for aircraft currents, resulting in the following two matrix equations:

$$[Z_{ss}]\ [J_s] + [Z_{sa}]\ [J_a] = [V]$$

$$[Z_{as}]\ [J_s] + [Z_{aa}]\ [J_a] = [0]$$

where $[Z_{ss}]$ = reaction of an element on the spiral with another element on the spiral

$[Z_{sa}]$ = reaction of an element on the aircraft with an element on the spiral

$[Z_{as}]$ = reaction of an element on the spiral with an element on the aircraft

$[Z_{aa}]$ = reaction of an element on the aircraft with another element on the aircraft

$[J_s]$ = currents on the spiral

$[J_a]$ = currents on the aircraft

The wavelength at 18 GHz, the highest frequency of interest, is about 2/3 of an inch. With a current discretization of 8 facets per wavelength, using a conventional method of moments, the required number of spiral current unknowns is 3324 and the required number of aircraft current unknowns is on the order of 50 million. Such size problems exceed available computer resources for an exact solution. Thus an alternative (hybrid) approach was used.

Assuming that the reaction of the aircraft current elements on the spiral elements is very small so that $[Z_{sa}]$ can be set to zero, the first equation decouples from the second equation and the spiral currents can be solved directly:

$$[J_s] = [Z_{ss}]^{-1}\ [V]$$

The electric and magnetic fields generated by these currents impinge on the aircraft. The magnetic field can be expressed as an integral operator K over the spiral currents as follows:

$$\mathbf{H} = \int - \mathbf{J}_s \times \nabla G \; dS = -K \mathbf{J}_s$$

where G is the free space Green's function. In matrix form the above equation becomes:

$$[H_p] = [K_{ps}] [J_s]$$

where $[H_p]$ is a column vector of the radiated magnetic field at points on the aircraft surfaceand $[K_{ps}]$ represents the magnetic field at point *p* due to current elements on the spiral.

The $[K_{ps}]$ terms are assumed to be non-zero only for direct line of sight between the current element and the aircraft surface point. Assuming a relatively smooth aircraft surface, locally flat with respect to a wavelength, the impressed current is assumed to be $2\mathbf{n} \times \mathbf{H}$ where **H** is the magnetic field due to the spiral currents and **n** is the surface normal vector on the aircraft.

$$[J_a] = 2\mathbf{n} \times [H_p]$$

The far field antenna pattern is the sum of contributions from the spiral currents and the aircraft surface currents. For a given polarization **P** the far field is:

$$\mathbf{E} = \mathbf{P} \bullet \{ \int_s G \; [\mathbf{J}_s] \; dS + \int_a G \; [\mathbf{J}_a] \; dS \; \}$$

3. Results

The calculated antenna patterns for vertical polarization at 10.4 GHz for 10 and 20 degrees elevation are shown in Figure 2a and 2b respectively. The patterns are calculated for both an antenna in free space (dotted line) and for an antenna installed on the aircraft (dashed line). The predictions show that the presence of the aircraft significantly alters the antenna pattern, especially in the right hand quadrant, where it introduces prominent peaks and nulls. These predictions closely match measured data (solid line). The predicted patterns are only shown for the angular sector -120 to 60 degrees corresponding to aspects radiating above the mounting surface for which the model is valid. Antenna boresight corresponds to -30 degrees azimuth. The results demonstrate that a complex problem whose exact solution is computationally intractable can be solved by a hybrid method with a great deal of fidelity.

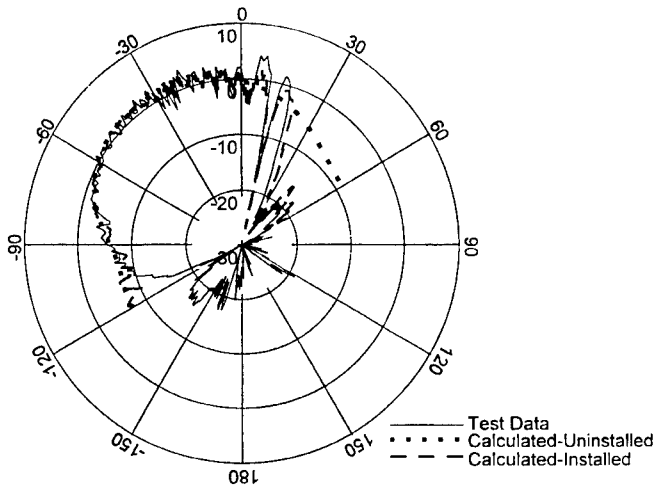

a) 10 degrees elevation

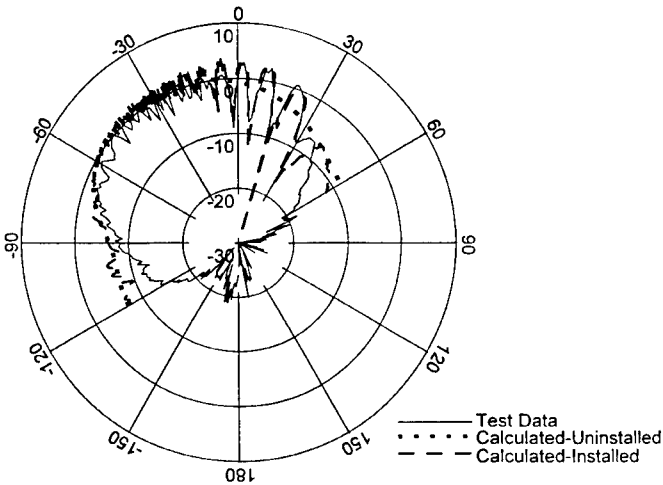

b) 20 degrees elevation

Figure 2-Spiral Antenna Mounted on Aircraft 10.4 GHz V-POL

The lobes that are significantly above the free space levels between 0 and 30 degrees were of particular interest. A color display was used to map portions of the aircraft generating the greatest contribution to the far field pattern at these aspects and viewed using MrPatches [6]. The color visualization enabled rapid identification of the major contributors.

A flat spiral antenna tends to have uniform broadband performance across its operating band with little difference between vertical and horizontal polarization. Its active radiating region is the spiral arm whose circumference is approximately a wavelength. Successive spiral arms moving radially outward tend to be like parasitic elements. The dynamics of radiation from a conformal spiral, on the other hand, is not well understood. It exhibits greater variations in gain with respect to polarization and frequency. Conventional outputs such as far field azimuthal patterns and spiral current magnitude plots for both flat and conformal antennas are similar and shed little light on the differences in performance.

When the spiral currents are displayed using EM-ANIMATE, a qualitative difference is seen. The flat spiral antenna exhibits tight coupling between successive spiral arms, giving rise to a pinwheel-like effect where a traveling wave spins around each arm at the same angular velocity. The currents appear to originate at the central feed point and propagate around the spiral toward the two outermost arms at this uniform angular rate until they reach the ends of the arms, at which point they reflect back in the opposite direction. This will be detailed in the video presentation accompanying this paper.

The conformal spiral antenna exhibits looser coupling between successive spiral arms. The currents are more disorganized and appear relatively random after a few spiral turns. The disorganized behavior of currents on the curved spiral is probably a causative factor in its relatively higher axial polarization ratio. In any event, this significant phenomenological difference in current propagation along the spiral arms could not have been discovered without the animation. Further study including animation of the near field radiation surrounding the antenna may shed more light on the physical mechanisms.

4. References

[1] "HyPACED Code, Hybrid Parallel Algorithms for Computational Electromagnetics Demonstrations", Technical Proposal, Volume 1, Submitted by the Boeing Company in response to Wright Laboratory PRDA 97-27-AAK, 23 July 1996.

[2] J. M. Putnam, M. B. Gedera, "CARLOS-3-D: A General Purpose Three Dimensional Method of Moments Scattering Code", IEEE A& P Magazine, Vol 35, No. 2, Apr 1993.

[3] D. M. Elking, J. M. Roedder, D. D. Car, S. Alspach, "A Review of High Frequency Radar Cross Section Analysis Capabilities at McDonnell Douglas Aerospace ", IEEE A & P Magazine, Vol 37, No. 5, Oct 1995.

[4] J. L. Karty, J. M. Putnam, J. M. Roedder, C. L. Yu, "Use of Near-Field Predictions In the Hybrid Approach ", presented at the 13th Annual Review of Progress in Applied Computational Electromagnetics, March 17-21, 1997.

[5] Kam W. Hom, "EM-ANIMATE, A Computer Program for Displaying and Animating Near-Field and Surface Current Solutions", NASA Technical Memorandum, May 31, 1996.

[6] D. D. Car, J. M. Roedder, "A Versatile Geometry Tool for Computational Electromagnetics: MrPatches", ACES Symposium Proceedings, Monterey, California, March 1997.

Evolution of an Antenna Training Aid using Electromagnetic Visualisation.

Alan Nott, BEE, CEng, MIEE
Senior Electromagnetics and Software Engineer
and
Deepak Singh BEng (Elec), Project Engineer
Army Technology and Engineering Agency (ATEA)
Department of Defence, Australia.
email:nott@atea.mat.army.defence.gov.au

Abstract:

This paper traces the evolution of a series of antenna training aids developed by the Australian Army's Army Technology and Engineering Agency (ATEA) for the Australian Army School of Signals. The training aids rely heavily on the ability to produce high-quality rendered images of antenna radiation patterns using electromagnetic visualisation techniques developed at ATEA. Adjustment of parameters such as frequency, antenna height, slope and sag, ground type and viewing angle controls the selection and display of the appropriate antenna pattern image. Interactive operation, coupled with the high quality images results in an aid that provides excellent insight into the intricacies of antenna radiation patterns.

Background:

Reliable communications depend on the best use of the available equipment, and effective exploitation of the communications medium. While this is true of any communications method, communications in the high frequency (HF) band, from 2 MHz to 30 MHz requires attention to matters considered by many to fall into the realm of 'the black arts'. Both the radio equipments and their antennas are generally required to operate over a wider range of frequencies (15:1) than equipment operating in other bands. Frequencies are often changed several times per day chasing that elusive optimum working frequency dictated by Mother Nature as she continues to massage the ionospheric conditions.

For some antennas, particularly wide band antennas, the radiation pattern shape can vary widely shape with frequency, and other parameters. And while the radio equipment - the transmitter and receiver - may function well over the required band, and even match the antenna system, unless due attention is paid to the choice of antenna, its configuration, siting and orientation, the shape of the radiation pattern at the chosen frequency may make communications difficult if not impossible. The use of low transmitter power to conserve battery life or for covert operation compounds the problem.

Proper antenna training will promote better understanding and exploitation of antenna radiation patterns, leading to improved communications availability and reliability. High performance personal computers, with high-capacity hard and compact disk drives are becoming more readily available and can provide a useful platform for which visual antenna training aids can be developed.

Earlier work at ATEA:

In 1991, ATEA began using NEC-2 for near field investigations. The code was obtained from the NEEDS 2.0 package, and although some graphical input and output routines were available, in general they required specialised hardware. Interfaces to AutoCAD Version 10 were quickly written (in AutoLISP). These allowed three dimensional graphical examination and creation of NEC input files (see figures 1 and 2). This work was reported in reference 1.

```
CM Frequency = 2.000 MHz
CM Excitation - 1000V on tag 1
CM NE 0 60 30 20 -3.0 -1.5 0.1 0.1 0.1 0.1
CM Finite ground, Sommerfeld/Norton method
CM Ground type = Average land, epr = 15.000, sigma = 0.028 mho/metre
CM No frequency adjustment applied to ground constants
CE
GW 0 1 -0.800 0.699 1.659 -0.800 -0.700 1.659 0.05000
GW 0 1 1.000 -0.750 1.110 0.750 -0.750 1.110 0.01000
GW 0 1 0.460 0.875 1.360 0.460 0.875 3.709 0.00600
.
.
.
GW 0 1 0.460 0.875 1.360 0.460 -0.875 3.709 0.00600
GW 0 1 0.460 0.875 1.360 0.460 0.875 3.709 0.00600
GW 0 1 0.460 0.875 1.209 0.460 0.850 1.110 0.00600
GW 0 1 0.460 0.875 1.209 0.460 0.875 1.360 0.00600
GE -1
GN 2 0 0 0 15.000 0.028
PT -1
FR 0 1 2.000 1.0
EX 0 1 1 0 1000.0 0.0
XQ
NE 0 60 30 20 -3.0 -1.5 0.1 0.1 0.1 0.1
EN
```

Fig 1: NEC input file for Land Rover (part)

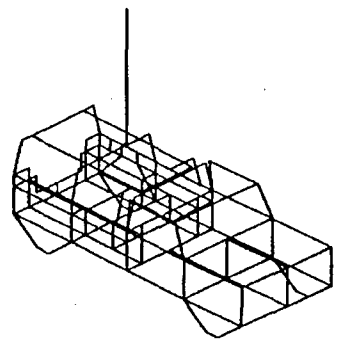

Fig 2: Wire model of Land Rover

The AutoCAD interfaces were extended to plot field contours and colour maps and to present far-field radiation pattern data as three dimensional meshes. Using the SlideShow capability of AutoCAD, screen-dumps were saved as .SLD files, and by stringing these files together with a script file, animations of field patterns were created. Although these ran fairly slowly, they showed considerable promise as a means of understanding pattern characteristics. An upgrade to AutoCAD Version 12 allowed rendered images to be created. These were used in a similar way to create radiation pattern images and animations. The images were more realistic, despite the minimal edge treatment of faces, and further demonstrated the potential of these techniques.

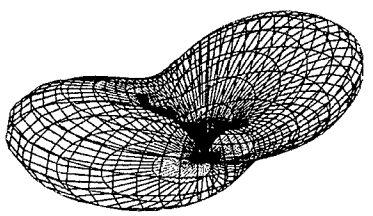

Fig 3: Mesh radiation pattern image (AutoCAD)

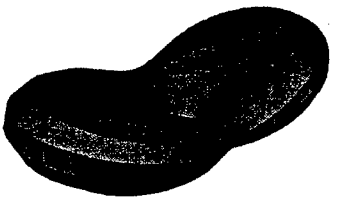

Fig 4: Rendered radiation pattern image (AutoCAD)

Encouraged by these successes, the rendering and animation package 3D Studio Version 2 was obtained. In addition to its stand-alone capabilities, it could create 'photographic quality' images from the 3D radiation pattern surfaces generated in AutoCAD.

Fig 5: Rendered radiation pattern image (3D Studio)

Fig 6: Rendered radiation pattern image in scene (3D Studio)

Suites of radiation pattern gain surfaces were created in AutoCAD from a series of NEC runs, using frequency, antenna height, or some other antenna variable as the independent parameter. These were output as .DXF files (Drawing eXchange Format), loaded into 3D Studio and saved as .3DS files, the native file format of 3D Studio. Morphing between radiation pattern surfaces provided a means to create pattern animations. As the independent parameter was changed, 3D Studio provided smooth interpolation between pattern shapes. (see reference 2)

Using the inherent capabilities of 3D Studio, animated frequency and other scales, backgrounds and other objects can be created to annotate the images. Careful attention to lighting, shadowing, camera positioning and control, the use of fog to suggest distance, choice of appropriate images, colour and textures for backgrounds, for the representation of the earth and of the antenna pattern itself, can all provide subtle clues which greatly enhance the perception and comprehension of the pattern (see figures 5 and 6). Creation of good images is not a process to be taken lightly, but requires considerable practice to develop and maintain the appropriate skills.

During the creation of an animation file, a series of keys (commands to move, rotate, morph etc) is assigned to each of the objects to be animated. In 3D Studio Version 2, these were created by hand. In one instance 11000 keys were created to produce an animation of a HF radiation pattern sweeping from 2 to 30 MHz, and viewed from 64 different viewpoints - a multi-dimensional set of radiation pattern images. Creation of the keys alone took almost three weeks but yielded an excellent result that could be saved as easily as an animation file, a videotape or a series of still images.

Neither the animation file or the videotape has a viable capability of interactively selecting the image of interest as a function of the parameters of interest (say) frequency and viewpoint. What was needed was an interactive viewer so that the user could select the parameters of interest and view the appropriate antenna pattern image. Because the computers of the Australian Army School of Signals at that time used a DOS 6.2 operating system, the target operating system for the viewer development was also DOS 6.2. This raised a number of interesting challenges during development including writing special colour palette handling and mouse driver procedures. (see reference 3)

A variety of still image formats is available in 3D Studio, including Tagged Image Format (.TIF), Windows BitMap (.BMP), Graphics Interchange Format (.GIF) and Joint Photographic Experts Group or JPEG (.JPG). To determine the best file format for the application, several runs were made using these formats and for a wide range of antenna images. With suitable compression selected, and providing there were no sharp edges in the image (text etc) the JPEG (Joint Photographic Experts Group) .JPG format easily gave the smallest file size for acceptable image quality. Using an image format of 640 X 480 pixels with 256 colours the average file size per image was about 13 kbyte, allowing some 50000 images to be stored on a single compact

disk (CD). The corresponding average file size for .GIF format was 120 kbyte, reducing the CD capacity to about 5500 images.

The choice of the JPEG format was not without its problems, as there was no readily available decompression code which could be embedded in the viewer. Thus to write the viewer it was necessary to become familiar with the .JPG processes. The Independent JPEG Group Internet site yielded source code for compression and decompression and this was adapted for the application. The involvement with JPEG processing yielded an unexpected benefit, leading to a process for the efficient compression and decompression of radiation pattern numerical data, as distinct from images (see reference 4) If disk space permits, it is planned to add a window to the training aid to display graphs of single cut radiation pattern data extracted from the compressed pattern data files.

A series of .JPG image sets was created for the Bidirectional Delta Antenna in service with the Australian Army. Each set comprised images for the patterns from 2 to 30 MHz in 0.25 MHz steps, viewed from 16 different azimuths (22.5° steps) and 4 different elevations (30° steps). Each set comprised 5537 images, only one viewing azimuth is necessary at 90° elevation (top view). Additional sets were created for three soil types, and three different antenna heights, giving 49833 images in all. These images, plus the viewer executive and other associated files occupied 643 Mbyte, essentially filling the CD.

A demonstrator disk was produced containing images for the Bidirectional Delta in two different configurations, and two different soil types. This was issued for client evaluation before embarking on further development. The viewer screen showed the pattern image, a wire drawing of the antenna seen from the same viewpoint, a text description of the antenna, and indicators showing frequency and viewing azimuth and elevation. A screen from this training aid is shown in figure 7.

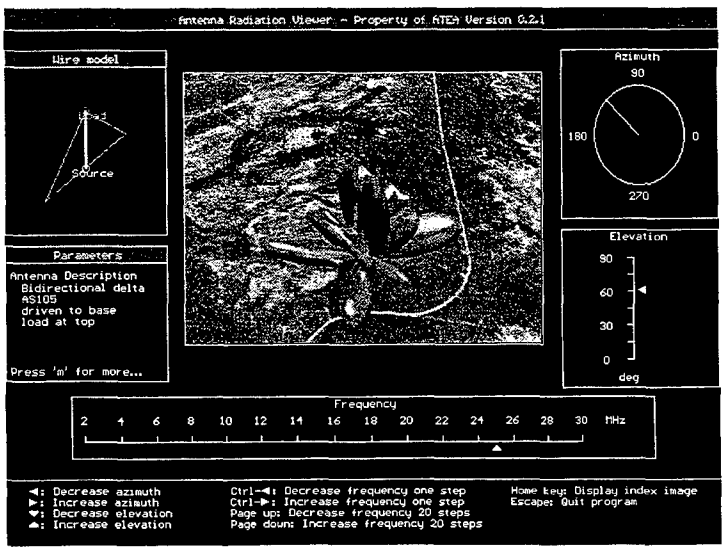

Fig 7: A screen from the DOS version of the Antenna Training Aid.

During the evaluation period a number of significant events took place.

- MIL-STD-498 documentation of the training aid software and associated processes was commenced
- The School of Signals changed operating systems from DOS to Windows 3.1 with UNIX servers.
- Discussions were held with the School to determine a prioritised list of antennas for which training aids were required.
- Geometric data for a range of antennas was obtained by field measurements, rather than using idealised data from the antenna handbooks.

Current work:

Work has now commenced on a Windows viewer, using a reduced number of frequency steps and viewing angles (figure 8). The number of images per set is currently 493, allowing the number of ground types, antenna heights and other parameters to be correspondingly increased. As each combination of antenna parameters other then frequency requires the creation of a separate 3D Studio file, the amount of manual file manipulation will increase. This effort, however, is offset by the greater versatility of the training aids.

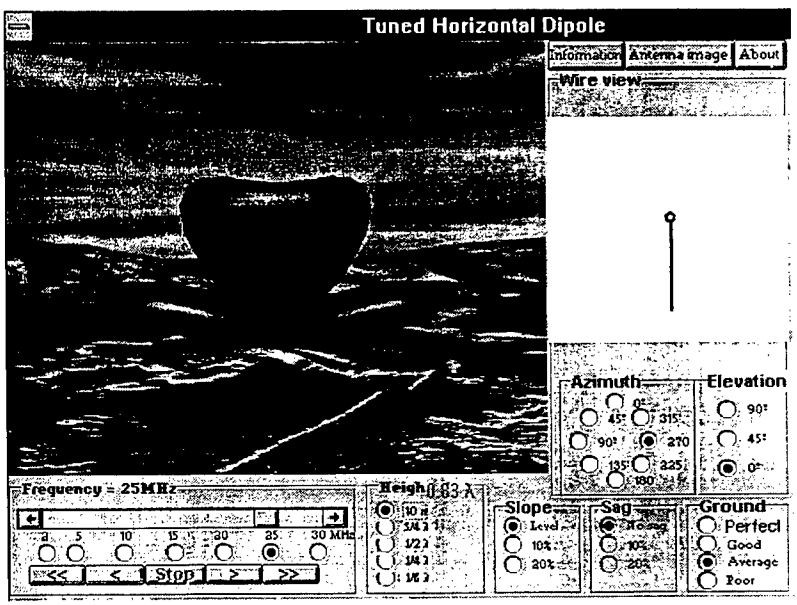

Fig 8: A proposed screen layout for the Windows-based training aid.

It became apparent that a single viewer could not easily cover the full range of antenna types because of the range of different variables associated with each antenna, and a series of purpose-written viewers is

envisaged. Each viewer will have the same generic layout incorporating the radiation pattern image and the antenna wire drawing, as well as frequency and ground selection controls, and an information window displaying textual information about the antenna type, configuration and other parameters. Controls specific to the particular antenna, such as height, slope, sag, included angle, load and source locations will also be required, giving rise to additional control functions on the viewer screen.

When 3D Studio creates a series of still image files from an animation file, the default file names are derived from the first four characters of the animation file name, plus a four character numeric field which is the frame number in the animation. With this arrangement, the DOS (and Windows 3.1n) limit of 8-character file names limits the maximum number of still images from a single run to 10000. To allow for a greater number of images, an hierarchical directory structure based on ground type, antenna height, slope and sag, and the other antenna parameters is used. In this way the default file names produced by 3D Studio can be reused in different directories, the frame number mapping into frequency, and viewpoint. This results in the 493 images per set, corresponding to 29 frequencies, 8 azimuths and 3 elevations.

The starting point in this process is a procedure written in TurboPascal which creates:

- The hierarchical directory structure,
- a series of NEC input files in each lowest level directory,
- a batch file in each lowest level directory to run the NEC jobs, collate the results, and create a .DXF file of radiation pattern data, and
- a 'master' batch file to call all the low-level batch files.

The master batch file initiates some 1800 NEC runs, and for the horizontal tuned dipole antenna this took just over three hours to complete. At the end of the run, sixty .DXF files, one in each lowest level directory, are ready for importing directly into 3D Studio. These are then imported (manually) into 3D Studio to create the corresponding .3DS files. Each .3DS file was then merged with a generic .3DS file containing all the objects necessary to complete the images. These objects include all lighting, cameras, pointers (for camera control), ground surfaces for the chosen ground types, and the sky. A process written in KeyScript (the key generation language embedded in 3D Studio) then creates all the keys necessary to produce the sequence of images in a single run. Once this is complete the renderer is invoked with the proper parameters, producing images at about two per minute. This process is performed once for each lowest level directory, creating the complete suite of images for the training aid. More detail of the preparation of the 3D Studio files and image creation is given in reference 3.

The radiation pattern images used in the DOS version were created with a 640 X 480 pixel format, and displayed at 320 X 200 screen resolution. This was found to give a better image quality than images created with 320 X 200 format and displayed at 320 X 200, but did not make best use of screen area. Scaling limitations prevented alternative (non-standard) sizes from being used. With the change to a Windows environment, this restriction was removed and images are now created to directly match the chosen radiation pattern image size of 350 X 280 pixels. As well as providing a larger image size with superior image quality, this arrangements result in significant reductions in image creation time, file storage requirements, and screen repaint time.

An antenna definition file (.ADX) is needed to provide additional information for the viewer. This includes the textual information about the antenna which is to be displayed in the information window, and geometric antenna data for creation of the antenna wire drawing. The file also contains data on the suite of images such as frequency range and steps, ground types, antenna geometries and configurations, and on the directory structure. This is used for viewer configuration and for navigation to the appropriate radiation pattern image in response to user input parameters

Future work:

The training aids described above use rendered images to display the characteristics of antenna radiation patterns, rather than the conventional method of graphs of pattern cuts. While these training aids have met with wide acclaim, there is still a place for the more conventional graphical display of single-cut pattern data. It is possible to provide this type of display as another window in the present training aid, the graphical data being calculated from pattern data stored in a compressed form (reference 4). Whether or not this is implemented will largely depend on the availability of additional space on the CD.

While meditating on the possibilities of simple graphical training aids, yet another variant was evolved. This 'simple' training aid has two screens - one for directly editing the geometry of the antenna using the 'click and drag' approach, while the other displays a selected cut of the antenna pattern. While this only currently exists as a two-dimensional demonstrator, it could be easily extended to three-dimensional adjustment of the antenna geometry, and selection of different antenna pattern cuts. Patterns are calculated in real time, and are based on techniques inspired by E.K. Miller's paper on Radiation Physics. (Reference 5). Because it is computationally intensive, it is best suited to simple antennas and requires a fast computer to provide sufficiently rapid response time. However its simple approach has considerable potential and should be the subject of further development.

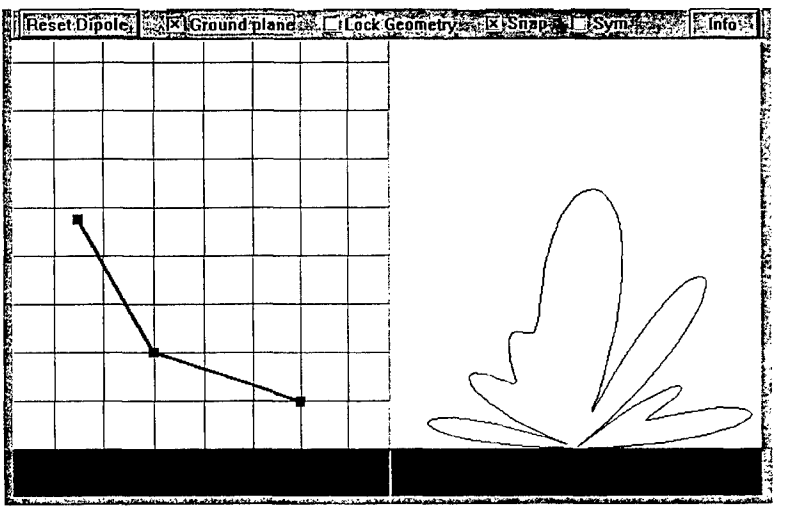

Fig 9: A screen from the 'simple' training aid.

Conclusions:

The evolution of a series of training aids developed by ATEA for the Australian Army's School of Signals has been presented. Strategies developed for the production of high-quality images of antenna radiation patterns derived from data generated from NEC output data has been discussed. The development of viewers for both DOS and Windows has also been covered. Using the processes described, training aids which provided excellent insight into the complexities of antenna radiation patterns can readily be developed. A new

type of training aid for simple antennas and based on a graphical rather than a rendered image displays of the radiation patterns has been briefly discussed, and further development of this approach is warranted.

References:

[1] Alan Nott. "AutoNEC - A marriage of convenience". Proceedings of the 10th ACES Review of Progress, March 21-26, 1994, Volume II, page 380.

[2] Alan Nott. "Electromagnetic Visualisation using Commercial Software". Proceedings of the 12th ACES Review of Progress, March 18-22, 1996, Volume II, page 326.

[3] Alan Nott. "An Antenna Training Aid using Electromagnetic Visualisation". Proceedings of the 13th ACES Review of Progress, March 17-21, 1997, Volume II, page 41.

[4] Alan Nott. "A Data Compression Technique for Antenna Pattern Storage and Retrieval". Proceedings of the 13th ACES Review of Progress, March 17-21, 1997, Volume II, page 56.

[5] E.K Miller. "An Exploration of Radiation Physics in Electromagnetics". Proceedings of the 13th ACES Review of Progress, March 17-21, 1997, Volume I, page 240.

The NEC-BSC Workbench: A Companion Graphical Interface Tool

G. F. Paynter and R. J. Marhefka
The Ohio State University
ElectroScience Laboratory
1320 Kinnear Road
Columbus, Ohio 43212-1191
paynter.5@osu.edu or marhefka.1@osu.edu

A companion graphical workbench has been developed for the NEC-BSC (Numerical Electromagnetic Code, Basic Scattering Code) [1]. The Workbench provides a rich set of tools for generating, validating, and visualizing model geometries prior to running the NEC-BSC, and for visualizing NEC-BSC results. The Workbench runs on Win95/NT platforms and uses the familiar windows 'look and feel'. Workbench features are described and some typical results of Workbench use are shown. Plans for future developments are discussed.

Background

The NEC-BSC is a computer code used to analyze large complex geometries at frequencies where the size of the object is large in terms of a wavelength. It will predict radiation patterns, scattering, and coupling. Two significant issues with the NEC-BSC are the difficulty of generating syntactically correct and meaningful input data sets, and the difficulty of interpreting the output data. The input format for the NEC-BSC is an ASCII file containing command digraphs and numerical data. The digraphs and data represent the 3D model geometry and ancillary data to be used in the NEC-BSC computation. This format, while human-readable, isn't very human-understandable. Generation of a complex problem geometry is tedious at best, and impossibly difficult at worst. Regarding interpretation of the NEC-BSC output, the ability to superimpose UTD ray results onto the model geometry allows the user to gain better insight than with pattern information alone. In recognition of the need for visualization support, the principal author of the NEC-BSC has collaborated with two other researchers at the Ohio State University's ElectroScience Laboratory to develop a tightly integrated, windows-based graphical workbench which acts as a pre- and post-processor for the NEC-BSC.

Lee Henderson, who worked at OSU-ESL until recently, defined and implemented the original architecture for the Workbench (released as NEC-BSC Workbench V2 [2]). The authors have extended and enhanced this user interface to be fully compatible with the commands and feature set of the currently available NEC-BSC V3, and the soon-to-be-released NEC-BSC V4.

Workbench Features

The Workbench Version 4 has been developed in parallel with NEC-BSC V4, and will be released as a companion product to it. The NEC-BSC input sets generated by the Workbench conform completely to the formats specified in the NEC-BSC V4 Users Manual. In general, a valid input data set produced

by any means can be read and manipulated using the Workbench. In addition to visualizing the geometry described by an input set, the Workbench facilitates the generation and manipulation of data sets. A geometry object can be interactively inserted, edited, removed, rotated, translated, and scaled. The effects of changes to the input set are immediately visible in a wireframe geometry model. Objects can be created in a convenient coordinate system, and then rotated/translated to another one for scattering analysis. Reference, local, and object coordinate origins are optionally viewable for any object. Sources and receivers can be single objects or arrays. Array elements can be generated with identical orientations, or oriented individually. Sources and receivers are displayed in distinctive colors. Output from the NEC-BSC is viewable as rectangular plots with a number of selectable parameters. Rays can be viewed superimposed on the model geometry.

One of the principle goals for the Workbench was to make it consistent with the widely used windows 'look and feel', so that users already familiar with other windows-based programs would not have to learn yet another interaction methodology. The current workbench uses standard windows graphical components and control features such as dialog boxes, document and view windows, and context-sensitive help.

Typical Operations

Some of the typical operations supported by the NEC-BSC Workbench are described below. These operations are the ones a user might employ to generate, edit, and validate an input set, submit the input set for NEC-BSC processing and then view the results.

Generate and visualize new objects

The first step in preparing a problem for electromagnetic analysis is to generate a valid input set that is representative of the problem geometry and the frequency or frequencies of interest. A new input document is created by launching the Workbench and selecting 'FILE|NEW|BSC Input'. This creates a blank input document. New NEC-BSC commands can be entered manually, or can be automatically formatted and entered into the input data set. In Figure 1, a new blank document has been created, and the 'New Command' dialog box showing all available NEC-BSC commands has been launched by pressing the 'New Command Wizard' toolbar button ( ).

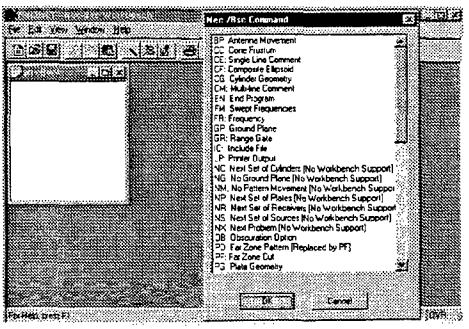

Figure 1. Creating a new input data set

When a new command is selected, a dialog box appropriate for the command is displayed for user parameter entry, as shown in Figure 2.

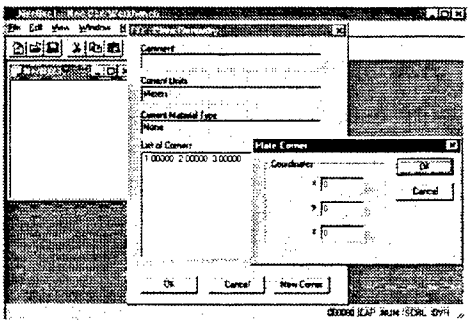

Figure 2: Adding a PG (plate) object

Note that the dialog boxes use the familiar windows interface elements. After (or as) a geometry model is constructed, the user can view the object as the NEC-BSC code would see it. Figure 3 shows the input data set and wireframe view of a simple truck model

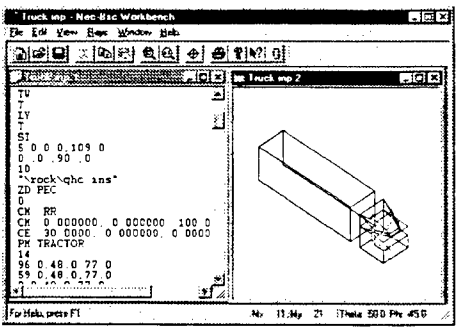

Figure 3: Simple truck geometry model

NEC-BSC provides a number of geometric primitives, and the Workbench supports them all In addition to the basic plate (PG), there are multiple-plate (PM), cone frustum (CF), Cylinder (CE), and test cylinder (TC) primitives. The Workbench supports each primitive with its own customized dialog box

Rotate/Translate objects from the reference coordinate origin

The Workbench supports the NEC-BSC RR & RT commands These two commands allow the user to rotate and/or translate a geometry object. The RT command rotates/translates from the original or

'reference' origin, and the RR command (new to V4) rotates/translates relative to the current or 'local' origin (the local origin is the reference coordinate system transformed by any preceding RR or RT commands). In addition, some objects incorporate a separate 'object' coordinate system. To assist a user in determining an object's 'reference', 'local', and 'object' (if any) coordinate system origin and orientation, display of the local and object coordinate axes can be turned on or off for each individual object contained in the input data set. Figure 4 is the same truck model shown in Figure 3, except now a RT command was used to rotate/translate the model from the reference origin. As can be seen by the local coordinate system axis (the 'primed' axis), the truck geometry was originally created at the origin for convenience, with the front of the truck oriented along the X-axis. Then the entire object was rotated and translated using the RT command.

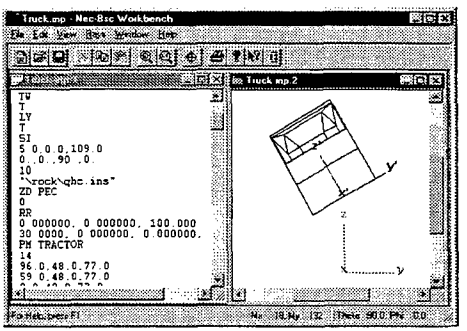

Figure 4: Truck model rotated and translated from reference origin

Generate and visualize pattern cuts

Generation and visualization of both 'Far Zone' (PF/VF) and 'Near Zone' (PN/VN) pattern cuts are supported by the Workbench. Generation of both types is accomplished via fill-in fields in customized dialog boxes. Once either of these commands are in the input data set, they are represented in the wireframe view by a pattern of dots. The pattern traces are oriented in the same way as the actual pattern cut is oriented.

Generate and visualize sources and source arrays

Generation and visualization of sources, receivers, source arrays, and receiver arrays are supported by the Workbench. Generation of these objects is done in the same manner as for any other object, with the addition that source. and/or receiver objects can be set up to 'move' through the model geometry space. Moving receiver or source objects are displayed with the receiver/source geometry shown on the pattern trace. Figure 5 shows an array of sources on a flat plate, modeling a phased array geometry. Note that in this figure, the source array and backing plate were created at the origin and then translated/rotated away. This can be seen from the blue 'primed' coordinate axes.

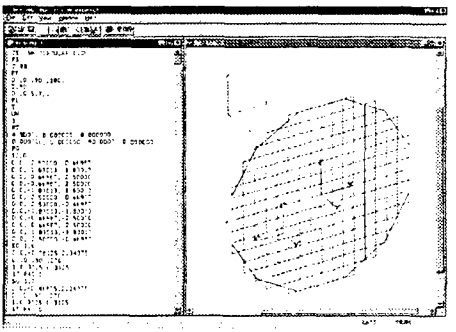

Figure 5: Phased array source model

Source/Receiver Movement

The NEC-BSC and the Workbench supports antenna (source and/or receiver) movement along near-zone pattern paths. Both single cut (PN) and multiple cut (VN) features are supported To help the user achieve the desired antenna orientation, the Workbench allows the user to step the antenna through all defined pattern points. At any point, the antenna is depicted with the orientation specified by the user. This allows the user to immediately see if the actual orientation is what was intended Keyboard accelerator keys are provided to 'fly' the antenna through its entire range of motion

Edit and manipulate input data

Input data sets can be easily edited and manipulated The effect of any manipulations becomes visible as soon as the user refreshes the wireframe view by clicking in the wireframe view window or by selecting the refresh function. This allows a user to quickly adapt a model to a new situation, or troubleshoot problems. Selected input lines may be commented out or in by simply selecting the lines. right-clicking on the selection, and selecting the desired operation from a pop-up context menu In Figure 5 above, the source array and backing plate were isolated from a larger model by commenting out all the other lines. If the user double-clicks on a line containing the start of a command block, then the edit dialog box for that object is displayed for user edit. User changes (if any) to dialog box data are validity checked and then written back to the input data set The user is notified of any problems with the data (a warped plate, for instance). User edits of a model geometry object can also be accomplished by double clicking on an object in the wireframe view. This brings up the same dialog box as if the user had double-clicked on the first line of that command block in the input set. This means that the user doesn't have to know where an object's command block is located in a long input set; the block can be accessed naturally via its representation in the model geometry window

As with most windows applications, the user can freely zoom and scroll within the geometry model In addition, the user can adjust the angle from which the model is viewed either with a graphical 'drag ring' or via the arrow keys

Include 'canned' model geometry

Version 4 of the NEC-BSC supports the use of an 'include' file (IC command). This allows the user to incorporate relatively static aspects of a model with a two-line command. For instance, if an antenna which takes five lines to describe in an input set is added to a complex 1000 line aircraft model, the entire input set can be 7 lines instead of 1005. All coordinate transformations, material changes and object scaling commands in the included file are properly incorporated into the model geometry. The Workbench fully supports insert, delete, and edit operations on included files. The user can insert an IC file into an input data set via the command wizard or manually in the same manner as for other objects. Changes to an included file are accomplished by opening and editing the file in a second window (display and edit for the second window are supported in the same manner as for the 'parent' input set). The parent model geometry wireframe view will be updated when the user saves any changes back to the included disk file and selects the 'refresh' function in the parent wireframe view. Included files are 'read-only in the parent input set, and included file objects cannot be selected in the parent wireframe view. If an IC command block is commented out, the entire IC file's model geometry contributions disappear from the wireframe view. If it is commented back in, then it all reappears. To avoid slowdowns due to repetitive disk accesses to large IC files, included file objects are cached in RAM. The disk file is re-read only if it has been modified.

Run NEC-BSC and view output

Once the user has verified that the input data set is in fact the geometry that the user wishes to address, the file is saved and NEC-BSC is run. NEC-BSC can be run independently from the Workbench, or the Workbench can be used to launch NEC-BSC with the currently active file as the input set. In either case, the output from NEC-BSC is the form of an *.OAA (plot description) file, and possibly a *.ORY (ray description) file. The *.OAA file can be viewed in the Workbench by simply opening the file. Figure 6 shows a typical output plot. The NEC-BSC also outputs a *.OUT file containing 'raw' numerical results, but this file is not used by the Workbench.

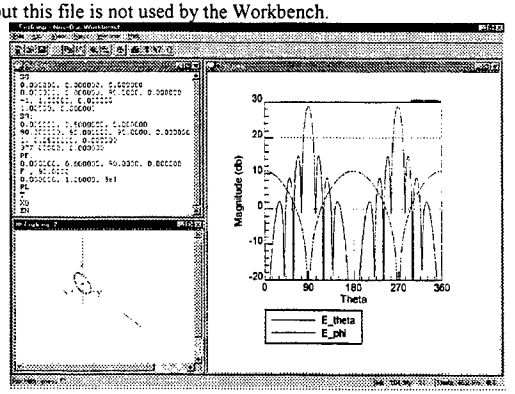

Figure 6: Typical output plot

Viewing NEC-BSC output in terms of ray paths and interactions is accomplished by opening a *.INP file in a wireframe view window, and then opening the corresponding *.ORY file. The ray paths are

shown in blue by default. Additional information about each ray is available by double clicking on a particular ray. This action brings up a dialog box that shows the field strength, the normalized field strength, and the number of interactions. Figure 7 shows a simple input set and a filtered subset of the ray interactions resulting from the selected test conditions

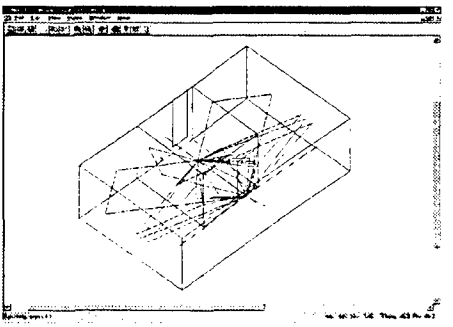

Figure 7: Typical ray trace output

Access help files

Consistent with the windows application model, NEC-BSC Workbench V4 incorporates fairly extensive on-line help features. Help topics include text from the NEC-BSC command reference (Chapter 4 in the user's guide), along with individual help sections for each (non-trivial) command dialog box. Dialog box help is also accessible via F1 when the dialog box is displayed

Other features

- Advanced users can directly edit the 'terms' (*.INT) file associated with the 'Execute Terms' (XT) command. This allows fine control over what terms are retained or neglected in the NEC-BSC computations.
- Plots and other outputs can be printed on any of the huge variety of printers and other output devices supported by Windows 95.
- Input data sets, wireframe models and plots can be easily captured and included in reports and/or presentations.
- Because the Workbench is a standard windows application, it can even be run across the internet using any of the available 'whiteboard' products. In one instance, this capability was even used to graphically demonstrate the presence of a bug in the Workbench code.

Conclusion

The NEC-BSC Workbench is a useful companion tool for use with the NEC-BSC. Use of the familiar windows 'look and feel' allows users to use it without having to learn yet another interaction

methodology. Because it was developed in collaboration with the principal author and developer of NEC-BSC V4, the Workbench incorporates and supports all V4 features and capabilities.

Future plans for the NEC-BSC Workbench include the following

- Incorporate 3D solid modeling.
- Apply pseudo-color amplitude coding to ray plots.
- Extend the help files to include the entire reference manual.
- Port the Workbench 'look and feel' to other ESL codes, such as the reflector, aircraft, and ESP5 codes.

References

[1] "Implementation of the NEC-BSC on a PC," 7th Annual Review, Applied Computational Electromagnetic Society, Naval Postgraduate School, Monterey, California, March 18-22, 1991

[2] "A Graphical User Interface for the NEC-BSC," L. W. Henderson and R. J. Marhefka, 11th Annual Review, Applied Computational Electromagnetic Society, Naval Postgraduate School, Monterey, California, March 20-24, 1995.

A New Tool to Assist Use of Legacy Programs

Bob Joseph
Armand Paboojian
Stan Woolf
Edward Cohen
ARCON Corporation
260 Bear Hill Rd.
Waltham, MA 02154

ABSTRACT

We introduce a new software product called *ArconViz*©, which facilitates the use of older established codes such as GEMACS[1] or NEC[2]. Since these legacy codes were developed before the availability of graphical workstations, they lack the ease of use extended to the user by a 'Windows' type user interface. *ArconViz* provides an envelope around these codes providing them the look and feel that modern computer users expect.

INTRODUCTION

We have developed a software package which will provide for legacy codes, such as GEMACS or NEC, some of the facilities typical of modern windows based applications. In addition to GEMACS and NEC, other codes accommodated include the Radar Cross Section code GRECO[3], particle transport code ITS[4] and the heat transfer code SINDA/G[5].

Formerly, these codes required a fully text-based input format reminiscent of the punch card. *ArconViz* provides to the user a Graphical User Interface (GUI) typical of Windows or X-Windows applications.

In addition, all of these codes require specification of a geometric situation. With the exception of GRECO, which has its own geometry translation facility, *ArconViz* provides a facility which will allow the user to specify the problem using a Computer Aided Design (CAD) program, import the output from the CAD into *ArconViz* which will then translate the data into a format recognized by the particular scientific modeling program.

In this paper we will show some of the steps taken in the specification of a simple GEMACS problem.

DEVELOPMENT

We have developed two versions of *ArconViz*, one for the UNIX workstation and one for 32-bit Windows PC. The UNIX version was developed using C++, with Motif for the User Interface and OpenGL[6] for the various graphics screens. The PC version was developed using Microsoft Visual C/C++ and again OpenGL for visualization.

PROGRAM FUNCTION

In this paper we will demonstrate some of the capabilities of *ArconViz* by examining the analysis of a communications hut with a radiating T antenna on top using GEMACS modeling code.

1. Geometry Design.

The user would first design the geometric situation using a standard CAD program, then output the geometric data in the IGES[7] format. The user is then able to import the geometry into *ArconViz*, which will allow the user to visualize the input situation (Figure 1).

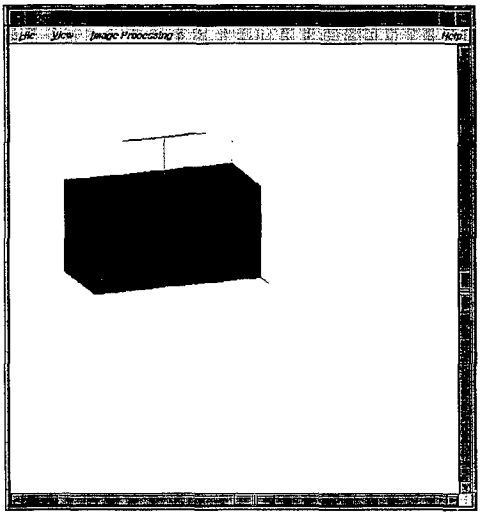

Figure 1. Input geometry visualization.

2. Setting Physical Properties

After importing the geometry into *ArconViz*, the user is able to set physical properties. For instance, the user may 'click' one of the sides of the block house which would bring up a dialog box as shown in Figure 2.

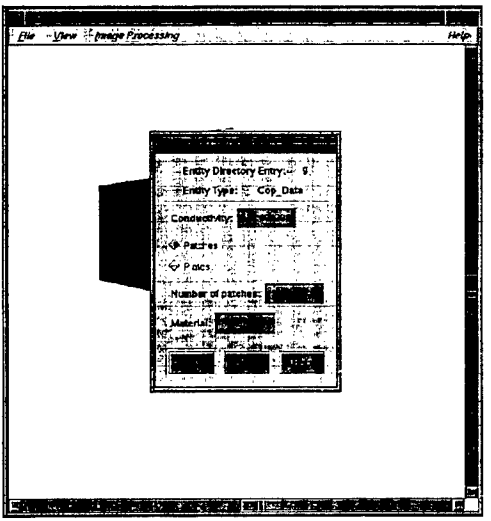

Figure 2. Setting physical properties of a panel.

With the aid of the dialog box (Figure 2), the user may specify the conductivity of the panel (-1 indicates perfect conductivity), whether the panel will be analyzed as patches or plates, and the number of patches or plates the panel will be divided into. The specification of material enters into the analysis of the geometry as required by other modeling packages such as ITS or SINDA/G.

In addition to being able to set the panel properties as in Figure 2, the user may also set the properties of a wire, as in Figure 3. In this case the program will provide the locations of the end points of the wire, allow the user to specify properties such as conductivity, request that the wire be segmented, and specify a voltage excitation source on one or more of the segments.

Complex Shapes

In addition to the analysis of simple shapes such as panels and wires, *ArconViz* provides the user other capabilities. For instance, for GEMACS, *ArconViz* is able to examine the geometric data and recognize entities such as cylinders and end caps. For other codes, *ArconViz* is able to recognize shapes such as cone, sphere, ellipsoid, wedge, and others. Also *ArconViz* is able to analyze complex shapes encoded using NURBSs and recast them in a format which GEMACS understands.

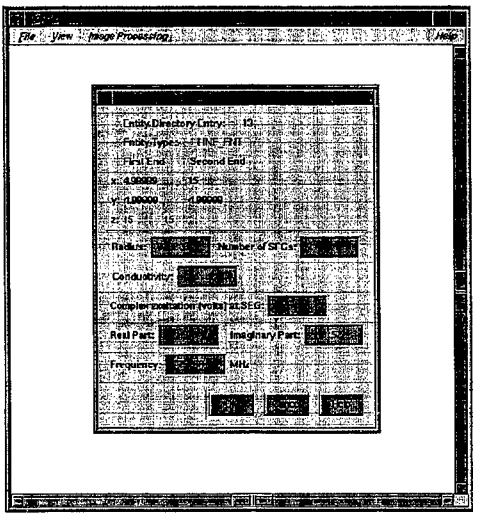

Figure 3. Setting wire properties.

CONCLUSION

ArconViz will facilitate the use of a number of classic scientific modeling codes such as GEMACS and NEC. It will provide a modeling environment where the user may choose the type of analysis to be done on a particular situation. In addition to providing input into these modeling codes, *ArconViz* will also provide the user immediate output visualization.

ACKNOWLEDGMENT

The work described here was supported by the Air Force Material Command under contract F30602-95-C-0226.

REFERENCES

[1] D. L. Kadlec and E. L. Coffey, "General Electromagneti Model for the Analysis of Complex Systems (GEMACS) User Manual (Version 3)", Final Technical Report RADC-TR-83-217, Rome Air Development Center, AFSC, Griffiss AFB, NY, 13441. Sept. 1983.

[2] G. J. Burke and A. J. Poggio, "Numerical Electromagnetics Code (NEC)", Lawrence Livermore Laboritory, Livermore, CA, Jan. 1981.

[3] J. M. Rius, M. Ferrando, and L. Jofre, "GRECO: Graphical Electromagnetic Computing for RCS Prediction in Real Time", *IEEE Antennas and Propagation Magazine*, Vol. 35, No. 2, April 1993..

[4] J. A. Halbleib et al, "ITS Version 3.0, The Integrated TIGER Series of Coupled Electron/Photon Monte Carlo Transport Codes", ORNL RSIC Computer Code Collection, CCC-467, 1993.

[5] R. Behee, "Introduction to Thermal Modeling Using SINDA/G", Network Analysis Associates, Inc., Fountain Valley, CA.

[6] J. Neider, T. Davis, and M. Woo, OpenGL Programming Guide, Addison-Wesley Publishing Co., Reading, MA, June, 1993.

[7] IGES - Initial Graphics Exchange Specification (Ver. 5.2), US PRO/IPO-100, U.S. Product Data Association, Fairfax, VA, January 1993.

Visual EMag: A 2-D Electromagnetic Simulator for Undergraduates

by
Dion Garner
Electronics Engineer
NSWC Crane
Crane, IN 47522
diong@smtp803.nwscc.sea06.navy.mil

Jovan Lebaric
Associate Professor of Electrical and Computer Engineering
Naval Postgraduate School
Monterey, CA 93943
lebaric@ece.nps.navy.mil

David Voltmer
Professor of Electrical and Computer Engineering
Rose-Hulman Institute of Technology
Terre Haute, IN 47803
voltmer@rose-hulman.edu

Abstract - Visual EMag (VEM) is a 2-D static electromagnetic simulator intended as a visualization aid for students in undergraduate electromagnetic courses. VEM utilizes finite difference techniques in electrostatic and magnetostatic environments. TGT techniques are incorporated for compact simulation of open boundaries. The VEM code, written in Matlab 5 for Windows 95, provides a user friendly graphical interface which is inexpensive and platform independent. The presentation includes a demonstration of the simulator.

> *"Teaching and learning 0's and 1's is easier than teaching and learning electromagnetics."*
> Robert MacIntosh

Introduction - Students in undergraduate electromagnetics courses are faced with challenging learning tasks. Firstly, they must master the basic principles—Gauss's law, Ampere's law, Faraday's law. Secondly, they must learn the to "speak" the underlying mathematical language used to describe the phenomena. Thirdly, they must learn to visualize abstract potentials and vectors as representations of fields in space. Fourthly, they must be able to "connect" the mathematical and the physical world. The symbols and equations must impart the meaning of the physical phenomena and vice-versa. These learning tasks are all focused upon students gaining an intuitive sense of the behavior of electromagnetic fields.

To this end, EMAG, Manke[1], was developed as a menu-driven, networked computational tool. But with revolutionary increases in computational power and rapidly developing numeric techniques for electromagnetic problems, EMAG has been redesigned recently to include the highly-interactive, rich graphical environment of modern computers. VEM provides a powerful, yet inexpensive, tool for the visualization of electromagnetic potentials and fields commonly encountered in undergraduate courses.

Features - The salient features of VEM are summarized below:

- *Geometry*: 2-dimensional geometries in rectangular coordinates and rotationally symmetric cylindrical coordinates.
- *Domain*: Electrostatic and magnetostatic.
- *Stimuli*: Voltages and charges in electrostatic mode; currents in magnetostatic mode.
- *Material*: PECs, PMCs, conductors, dielectrics, and magnetics.
- *Grid Size*: User selected.
- *Boundary conditions*: Standard Dirichlet and Neumann boundary conditions and Open boundaries via pre-calculated or user-calculated Transparent Grid Termination (TGT) Lebaric [2].
- *Structure-Layout window*: Objects and materials can be added, positioned, modified, and deleted by standard windows drawing tools.
- *Solution Method*: Finite Differences.
- *Solution Window*: Equipotential surfaces or contours, modified quiver plots of vector fields, adjustable visualization viewing angle.
- *GUI*: Standard windows assortment of sliders, buttons, and menus for user interaction while providing input in structure layout and observing results in solution windows.

Results - This work is in progress up to the date of the conference. Demonstration of the software will be included in the presentation.

References

1. Manke, Roger P., Jr., "EMAG: a 2-D Electrostatic and Magnetostatic Solver in Matlab," MS Thesis, Rose-Hulman Institute of Technology, October, 1992.

2. Lebaric, Jovan, "Transparent Grid Termination: A Boundary Simulation Technique for Solving Problems Involving Poisson's Equation," unpublished notes.

EXPLORING ELECTROMAGNETIC PHYSICS USING THIN-WIRE TIME-DOMAIN (TWTD) MODELING

E. K. Miller
3225 Calle Celestial, Santa Fe, NM 87501-9613
505-820-7371, emiller@esa.lanl.gov

0. ABSTRACT

Among the various applications for which numerical electromagnetics models can be productively employed is that of conducting computer experiments for the purpose of exploring fundamental physics phenomenology such as radiation. A time-domain model is especially well-suited for this purpose since it provides a convenient way of isolating local effects in a manner not as readily achieved using its frequency-domain counterpart. This paper reports on some computer experiments using TWTD (Thin-Wire Time-Domain), an integral-equation, time-domain model based on the electric-field integral equation.

The main question investigated here using TWTD is to examine where and how much energy is lost as a function of time when a wire object is impulsively excited as either and antenna or scatterer. It will be demonstrated that a space integral over an object of $I(s,t)^2$ and $[Q(s,t)c]^2$, where c is the speed of light in the medium in which the object is located, provides a measure of the energy stored on it and whose time variation can thus exhibit its rate of radiation. Furthermore, when related to the time-dependent spatial source distribution, this measure indicates from where radiation occurs, thus shedding some light on the question "Why and from where does an object radiate?"

1. BACKGROUND

Maxwell's equations are now routinely solved using first-principles models (FPMs) developed in either the time domain (TD) or frequency domain (FD) and based on either integral-equation or differential-equation formulations, or their equivalents. The predominant application of these numerical models seems to be for analysis and design of specific objects of interest, demonstrating the degree of maturity of computational modeling. A no-less valuable role for FPMs is their use for exploring more fundamental aspects of electromagnetic physics, one of which is that of the radiation process. While it can be established analytically that accelerated charge is the cause of radiation, quantitatively identifying where charge acceleration occurs on an object and how much radiation is produced on an incremental basis from over its surface, has so far not proven to be straightforward.

As is demonstrated here, a TD model can evidently provide a measure of the energy represented by the source distribution on an object, i.e. its electric current and charge, that appears that offers some insight into where and how much radiation the object generates as a function of time. This measure, as discussed earlier by Miller and Landt (1980), is given by the energy quantities $W_I(t) = \int I(s,t)^2 ds$ and $W_Q(t) = \int [Q(s,t)c]^2 ds$[1], where c is the speed of light in the medium in which the object is located and the integrals are over the object's surface. Miller and Landt's earlier results did not examine the behavior

[1]Miller and Landt computed W_I and $W_Q' = W_Q/c^2$, which results in the average value of $W_Q' \approx W_I/c^2$. The c^2 proportionality factor not only puts Qc and I in the same units but then yields $W_I \approx W_Q$ which seems reasonable if the energy is approximately shared between the electric field of moving charge and the magnetic field due to the charge motion. Bevensee (1997) derives a result containing I^2 and $(Qc)^2$ as an energy measure, but using their difference rather than their sum. Consideration of E and H energy integrals also suggests this result.

of $W_T(t) = W_Q(t) + W_Q(t)$, however, but displayed their time variations separately. While W_I and W_Q individually can be useful, it is their sum that is needed if the rate of energy loss, and therefore, of radiation, is to be determined.

We begin by hypothesizing that the total energy stored in the near fields of an object is proportional to W_T, with W_I representing the magnetic-field energy and W_Q the electric-field energy. While there may be some uncertainty about whether the energy in the near fields can be determined from the source distribution itself, rather than from a volumetric integral of E^2 and H^2, it's obvious that were there no boundary-source distribution, there would be no near field. Thus it appears reasonable, since the sources terminate the fields through the appropriate boundary conditions, to assume that the stored energy is proportional to the source distribution, which is the approach explored here, but there is one important caveat to this assumption that is discussed below.

3. THE RADIATION PROBLEM

We first examine the case of a wire driven at its center by a Gaussian voltage pulse $V = \exp(-a^2t^2)$. The modeling parameters employed, using the Lawrence Livermore National Laboratory TWTD code (thanks to Jerry Burke for providing a Macintosh version), are:

TABLE I

Time step = 1.515e-10 s: Nominal number of time steps = 500: Pulse parameter a = 3.25e9/s
Wire length = 4 m: Wire diameter = 0.001 m: Number of space segments = 199

It should be noted that some initial calculations were done using a single-precision version of TWTD (32 bits) that sometimes produced divergent results but which were eliminated when a double-precision version was used.

A plot of the broadside radiated field for this problem is shown in Fig. 1. Note that the first pulse is produced due to the initial charge acceleration caused by the driving voltage. The next pulse is caused by the first end reflection of the outward-propagating current/charge (I/Q) pulse, and is of opposite sign because the charge acceleration is reversed relative to that initially caused. The lower-amplitude radiation field between these two pulses is caused by a partial, continuing reflection of the I/Q pulse as it propagates away from the feed region. As might be expected, the subsequent radiation field consists of a series of oppositely signed pulses as the current and charge change direction upon each end reflection. Also, the radiation field continues to diminish in amplitude due to the energy loss associated with these reflections.

Results for W_T, W_I and W_Q are shown in Fig. 2. However, contrary to what should be expected on physical grounds, the result for W_T does not monotonically decrease after the driving voltage goes to zero; instead it exhibits slight increases upon each end reflection. This is of course where a near zero occurs in W_I and where W_T is dominated by W_Q. Recall that W_Q involves a proportionality constant, c^2, which as shown below in Fig. 3 results in essential equality between the current and charge terms away from the wire ends and away from the wire center where the pulses meet, i.e., $I \approx Qc$. It's not clear that this equality should hold in the vicinity of the wire ends, though, and were a smaller value to be used, possibly as a function of distance from the ends, then W_T could be apparently made to have a monotonic-decreasing behavior. The maximum decrease in W_T occurs at each end reflection, while a smaller decrease is associated with the pulse propagation away from the ends.

The snapshots of I and Qc presented in Fig. 3 demonstrate these effects in a different way. As the I/Q pulses leave the source region, it can be seen that I and Qc are graphically indistinguishable, where they have the same signs. This equality is disrupted during end reflection as well as when they meet at the

wire's center where the charge pulses cancel, being of opposite sign. The pulse amplitudes decrease more slowly in the propagation phase than during end reflection, although their collective effects, as far as the amount of radiation that results is concerned, may not be too dissimilar. It would be necessary to examine the radiation field more completely over the far-field sphere to more fully separate these contributions.

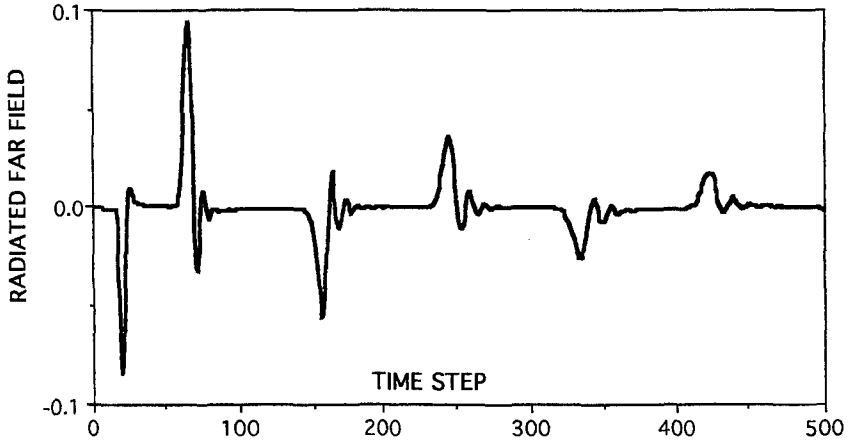

Figure 1. The broadside-radiated field for the antenna problem over the entire 500 time steps of the computation. The various field components are connected with various changes in the acceleration of the charge flowing on the wire.

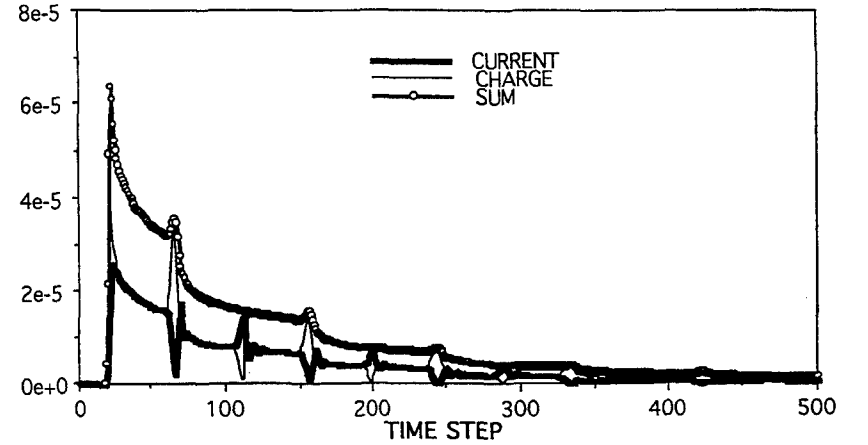

Figure 2. The energy for the radiation problem. While their sum is approximately monotonic decreasing, W_I and W_Q widely oscillate in value, with the latter a maximum as the I/Q pulses meet at the wire's center and the latter on each end reflection.

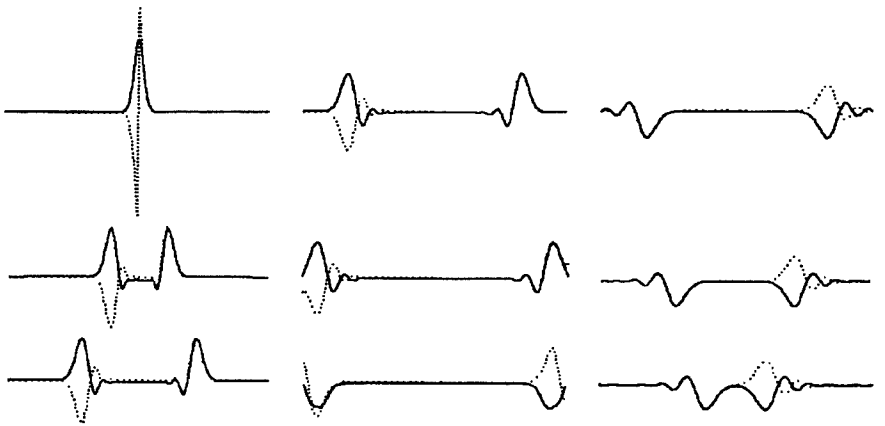

Figure 3. Snapshots of the current (solid line) and charge times c (dashed line) on a wire excited at its center by a Gaussian voltage pulse. Time steps progress in units of 10 from 21 (upper left) to 101 (lower right). A slight decrease in the pulse amplitudes is seen as they propagate down the wire with a more pronounced amplitude decrease upon end reflection.

3. THE SCATTERING PROBLEM

Not surprisingly, a quite different picture is seen when the wire is instead excited by a broadside-incident, Gaussian-pulse plane wave, although qualitatively the associated phenomena are quite similar to the antenna case just considered. As before, we present first the broadside scattered field for the first in Fig. 4. Aside from the absence of a second pulse in this interval as caused by end reflection for the antenna problem, the radiated field is otherwise quite similar. An initial "specular flash" occurs due to the incident field setting charge on the wire into motion, which is then followed by a lower-amplitude field of opposite sign which is evidently also due to slowing of the I/Q waves, as exhibited more clearly in Fig. 6. A continuing decrease in the scattered field with time is seen in Fig. 4 due to the shedding of energy, a result more clearly demonstrated in the energy plots of Fig. 5.

The W_T, W_I and W_Q results shown in Fig. 5 for the scattering problem, where it may be see in contrast to the antenna problem, that W_T appears to decline monotonically in time. The maximum change in W_T occurs approximately at maxima in W_I and the minimum occurs approximately at maxima in W_Q. This implies that radiation is predominantly controlled in this case by a small amount of of charge reflection along the wire's length rather than by end reflection as occurs for the antenna case.

Snapshots of I and Qc are presented in Fig. 6 for the scattering problem. The spatially uniform current initially produced decays in time after the incident field is no longer present, consistent with the previous observation that a partial reflection of the I/Q wave takes place along the wire. The ends of the current, on the other hand, collapse inward due to end reflection, a more abrupt phenomenon.

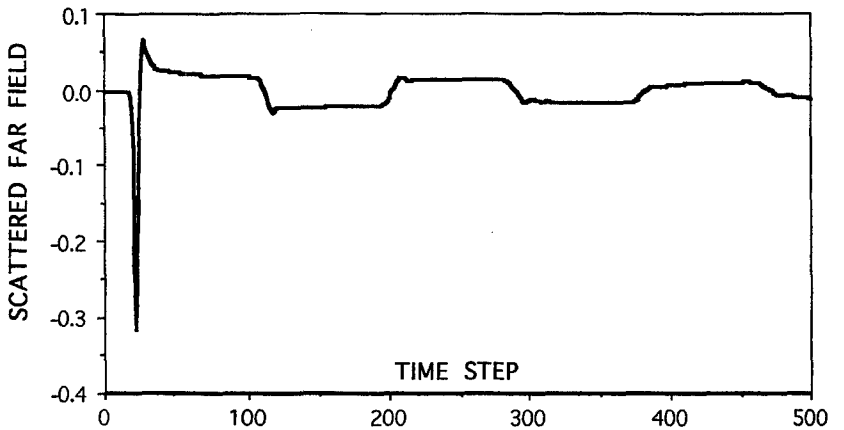

Figure 4. Broadside scattered field from a wire illuminated by a broadside-incident, Gaussian-pulse pulse plane wave. After an initial specular flash caused by charge acceleration due to the incident field, the field reverses sense as the I/Q waves undergo a partial reflection as they propagate along the wire.

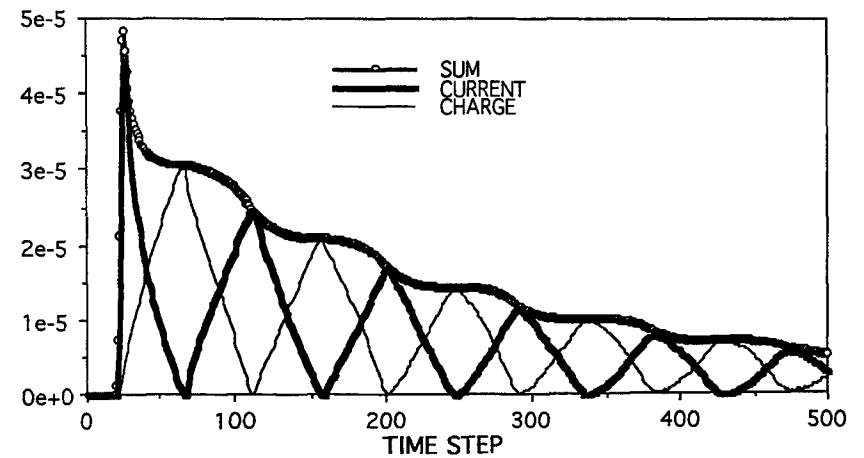

Figure 5. The energy quantities for the scattering problem. In contrast with the radiation problem, W_T here is essentially a monotonic decreasing function, evidently because end reflection is not as important as for the radiation case.

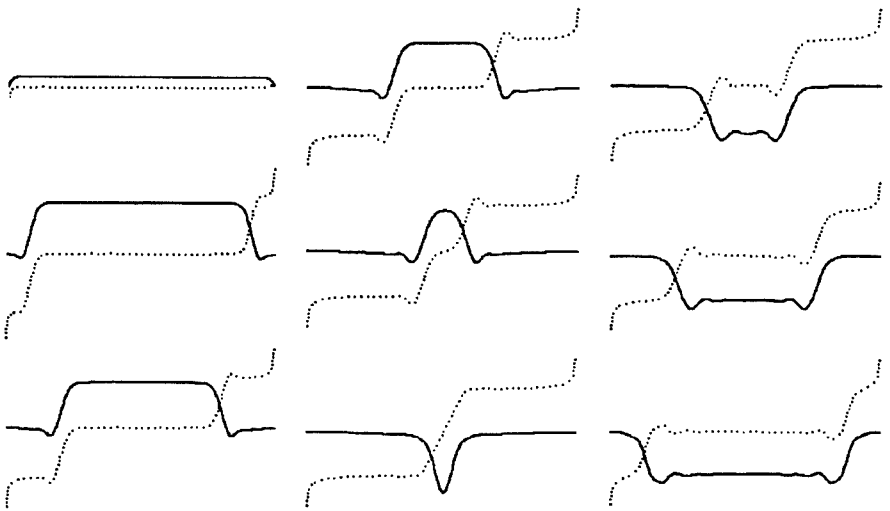

Figure 6. Current (solid line) and charge times c (dashed line) on a long wire illuminated from broadside by a Gaussian-pulse plane wave. Time advances in units of 10 from 21 (upper left) to 101 (lower right). After a uniform current flow is established by the incident pulse, it decreases in amplitude due to a partial reflection of the I/Q waves propagating along the wire and collapses inwards due to end reflection.

4. CONCLUDING REMARKS

Results for a long wire center-excited by a Gaussian voltage pulse or excited from broadside by a Gaussian-pulse plane wave have been presented. In particular, two energy measures are used as indicators of when and, by inference, from where the wire radiates as a function of time. These measures are given by $W_I(t) = \int I(s,t)^2 ds$ and $W_Q(t) = \int [Q(s,t)c]^2 ds$ for the current and charge, respectively, whose total is $W_T = W_I + W_Q$. The change with time of W_T appears to provide a way to estimate the rate at which the energy stored by a pulse-excited object is lost due to radiation.

5. REFERENCES

Bevensee, R. M. (1997), "Formulae for Total Energy and Time-Average Power Radiated from Charge-Current Distributions," in 13th ACES Review, pp. 248-255.

Miller, E. K. and J. A. Landt (1980), "Direct Time-Domain Techniques for Transient Radiation and Scattering from Wires", Invited Paper in *Proceedings of the IEEE*, **68**, pp. 1396-1423.

AUTHORS INDEX

Abrams, R. I-20
Aidam, M. II-983
Alexopoulos, N.G. I-151, 179
Allard, R.J. II-964
Allen. J.M. I-36
Alperl, B.K. II-600
Archambeault, B. II-880, 888
Ares, F. II-1100
Arkko, A. I-121
Axe, M.R. I-554
Aygun, K. II-838, 866, 873
Azar, T. I-216
Baghal-Wadji, A.R. I-297, 305
Beng, B. II-1087
Bernstein, D. II-750
Beyer, A. I-344
Bindiganavale, S. I-405
Biswas, R. I-144
Blake , D.C. II-808
Bleszynski, E. I-441
Bleszynski, M. I-441
Blocher, T.W. I-36
Bogolyubov, A.N.
Bomholdt, J.M. I-554
Boots, B. II-687
Botros, Y.Y. II-639
Brauer, J.R. II-763
Brennan, C. I-390
Bridges, G. I-326
Burkholder, R. I-243
Bush, G.G. I-167
Byers, A. II-687
Cangellaris , A.C. II-721
Cai, M. I-73
Canino, L.S. I-413
Canning, F.X. I-449
Carroll, Jr., C.E. I-36
Caputa, K. I-476
Cascio, L I-367
Castro, F. I-173
Chamberlin, K. II-880
Chang, Y. I-20
Cherkashin, Y.N. I-278
Chew, W.C. I-397, 420, 434,
Chew, W.C. I-500, 507, II-712
Christopoulos, C. I-490
Chung, Y-C. II-795
Cohen, E. I-576
Cohen, N. II-1047, 1051
Coren, R. I-216
Cown, B.J. I-270
Crosta, G.F. I-210
Crouch, D.D. I-144
Cuhaci, M. I-326
Cown, B.J. I-270
Crosta, G.F. I-210
Crouch, D.D. I-144
Cuhaci, M. I-326
Cummins, W.F. II-1043
Davey, K. I-188, 1106
Dawson, T.W. I-258, 476
De Cogan, D. I-331
DeLyser, R.R. I-105 359, 374
Demkowicz, L. II-799
Diaz, R.E. I-159, 179
Dinesen, P.G. II-858
Dionigi, M. II-952
Dombowsky, P. II-1006
Donepudi, , K. II-712
Drewniak, J.L. II-672, 905
Drozd, A.L.S. I-36
DuBroff, R. II-905
Dunn, J.M. II-1120
Ehmann, R. II-825
El Hachemi, M. II-1066
Elsherbeni, A.Z. I-99
Eriksson, G. I-87, II-1134
Eremenko, V.A. I-278
Ergin, A.A. II-838, 866, 873
Estrada, J.P. I-270
Evans, J. I-9, 15
Fan , G-X. II-655
Felsen, L.B. II-952
Feng, M. I-204
Filipovic, D.S I-405
Fisher, S.E. II-838
Fujiwara, K. II-779
Furse, C.M. I-482
Fuzi , J. I-283, 291
Gallivan, K. II-732
Garner, D. I-581
Gaudine, D. I-546
Gisin, F. I-313
Gong, J. II-750
Gottlieb, D. II-607
Goverdhanam, K. I-127
Gravrok, R. II-687
Greengard, L.F. II-600
Greenwood , A.D. II-756
Grimes, C.A. I-194
Grimes, D.M. I-194
Gutschling, S. II-832
Hagstrom, T. II-600
Hallatt, D.M. I-15
Hantman, B. I-20
Hariharan, S.I. II-600
Haupt, R. II-1095
Haussmann, G. I-113, 531
He , J-Q. II-631, 845
Hecht, R.W. II-1058
Hesthaven, J.S. II-858
Hill, K.C. I-50
Ho, K.M. I-144
Hoefer, W.J.R. I-367
Hom, K. I-538
Hori, T. I-66
Hubing, T. II-905, 928
Ingersoll, G. I-28
Ivanyi, A. I-283
Jakobus, U. II-920, 936
Jandhyala, V. I-204, 434
Jaroszewicz, T. I-441
Jensen, M.A. I-428, 470
Ji, Y. II-928
Jin, J-M. I-250, 397, II-712, 756
Joseph, B. I-576
Kagoshima, K I-66
Kang, T-W. II-795
Kantartzis, N.V. II-623
Kashyap, N. II-905
Katehi, L.P.B. I-127, II-647
Kettunen, L I-121
Kim, B-W. II-795
Kim, K.W. I-462
Kopylov, Y.V. I-381
Kyriazidou, S.A. I-151, 179
Kruger, H. II-832
Kubina, S.J. I-93, 546
Kuester, E.F II-1112
Kun, C. I-331
Kurokhtin, A.N. I-381
LaBelle, J. I-20
Landstorfer, F.M. II-936
Lauber, W.R. I-93
Lebaric, J. I-581
Lee, J-F. II-787
Lee , Y.H. II-991, 999
Leskiw, D.M. I-28
Levy, M.F. I-455
Ljepojevic, N. I-73
Lindenmeier, S. I-320
Ling, F. I-250
Liu , C. II-787
Liu , F. II-695
Liu, G. I-194
Liu, Q-H. II-631, 655, 845, 852, 972
LoVetri, J. I-326
Lu, C.C. I-397
Lu, Y. II-991, 999, 1087
Luu, Q. I-546
Lynov, J.P II-858

Lysiak. K. II-1006, 1012
MacMillan, H. II-1120
Mangold, T. I-351
Mannikko, P.D. II-1074
Marhefka, R.J. I-568
Martin, T. I-79
Maruyama, T. I-66
McFarlane, R. I-367
Merrill, M. I-151
Michielssen, E. I-204, 434, II-732, 838
Michielssen, E. II-866, 873
Miller, E.K. I-583, II-958
Minaev, D.V.
Mittra, R. I-515
Miyazaki, Y. II-911
Monglardo, M. II-952
Muller, U. I-344
Nabet, B. I-173
Nguyen, N. II-972
Nott , A. 560
O'Brien, P.J. II-1074
Ommodt, K.W. II-1074
Ong, K.G. I-194
Ottusch, J.J. I-413
Paboojian, A. I-576
Packer, M.J. II-1028
Pantic-Tanner, F. I-313
Paul, J. I-490
Paynter, G.F. I-568
Pearlman, R.A. I-554
Perez, R. II-895
Pertz, O, I-344
Peterson, A.F. II-771
Petropoulos, P.G. II-615, 623
Pflug, D.R. I-42
Pierantoni, L. I-320
Piket-May, M. I-113, 531, II-687
Poltz, J. II-680
Popov, A.V. I-381
Rachowicz, W. II-799
Rahmat-Samii, Y. I-462
Rahola, J. II-1126
Ramahi, O.M. II-592, 880
Rebel, J. I-336
Redmond, R. I-28
Regarajan, S. I-264
Remis , R.F. II-704
Righi, M. I-367
Riley , D.J. II-816
Robertson, R. II-647
Rodriguez, J.A. II-1100
Rodriguez-Pereyra, V. I-99
Roedder, J.M. 554
Rogovin, K. I-449
Routier, R. I-243, 270
Roy, J.E. I-93
Ruoss, H-O. II-936
Russer, P. I-320, 336, 351, II-952, 983
Sandlin , B.S. II-1080
Savage, J.S. II-742
Schutt-Aine, J.E. II-695
Schwengler, T. II-1112
Selormey, P. II-911
Sengupta, D. I-204
Sertel, K. I-405
Severns, R. II-1036
Shaeffer, J. I-538
Shang, J.S. II-808
Shanker, B. I-204, 434, II-838, 866,873
Shen, C.Y. I-57
Sheng, X.Q. I-397
Shi, H. II-672
Shlepnev, Y.O. II-664
Siarkiewicz, K.R. I-2
Sigalas, M. I-144
Simons, N. I-326
Singh, D. I-560
Siushansian, R. I-326
Skochinski, E. I-264
Smith, C.E. I-99
Song, J.M. I-397, 420
Soukoulis, C.M. I-144
Speciale, R.A. I-224
Stach,J. II-979
Stalzer, M.A. I-413
Stillman, G. I-204
Stuchly, M.A. I-476
Sugiyama, K. II-779
Suzuki, T. I-136
Takahashi, N. II-779
Takehara, K. II-779
Tardioli, G. I-367
Tarhasaari, T. I-121
Teixeira, F.L. I-500, 507
Tentzeris, E. I-127, II-647
Terzuoli, A.J. II-1080
Thibblin, U. I-87, II-1134
Thomas, D.W.P. I-490
Thomas, K. I-113
Tosser-Roosey, A. II-1066
Tosser-Roussey, C. II-1066
Trueman, C.W. I-93, 523, 546
Tsiboukis, T.D. II-623
Turner, C.D. II-816
Uehara, K. I-66
Ulander, L. I-79
Vall-llossera, M. I-93, 523
van den Berg, P.M. II-704
Vardapetyan, L. II-799
Van Doren, T. II-905
Vidoni. T. I-28
Vinogradov, A.V. I-381
Visher, J.L. I-413
Volakis, J.L. I-405, II-639
Voltmer, D. I-581
Walker, M.J. II-944
Wandzura, S.M. I-413
Wang, C-F. I-250
Wassef, K.N. II-771
Wedge, S. II-750
Weiland, T. II-825, 832
Weile, D.S. II-732
Werner, D.H. I-515, II-964
Werner, P.L II-964
Wharton, T. I-9
Wheless, Jr. W.P. II-1019
Wood, Jr., W.D. I-50
Woolf, S. I-576
Wright, H. I-20
Wurtz, L.T. II-1019
Yang, B. II-607
Yeo, K. II-1087
Yu, P.K.L I-136
Zaporozhets, A.A. I-455
Zhao, L. II-721
Zheng, D. II-1106
Zmyslo, J.S. II-964
Zunoubi, M. II-712